



UNIVERSITY OF LEEDS

Ionised Jets Associated With Massive Young Stellar Objects

Simon John Derek Purser
School of Physics and Astronomy
University of Leeds

Submitted in accordance with
the requirements for the degree of

Doctor of Philosophy

September 2017

The candidate confirms that the work submitted is his own, except where work which has formed part of jointly authored publications has been included. The contribution of the candidate and the other authors of this work has been explicitly indicated. The candidate confirms that appropriate credit has been given within this thesis where reference has been made to the work of others.

This copy has been supplied on the understanding that it is copyright material and that no quotation from the thesis may be published without proper acknowledgement.

© 2017 The University of Leeds and Simon John Derek Purser.

Dedicated to the men of the Parachute Regiment

who gave their tomorrow for our today.

They are in fact, men apart.

Every man an emperor.

Preface

This thesis contains work presented in the following jointly authored publication:

- I. “A search for ionized jets towards massive young stellar objects”
– **S. J. D. Purser**, S. L. Lumsden, M. G. Hoare, J. S. Urquhart,
N. Cunningham, C. R. Purcell, K. J. Brooks, G. Garay, A. E. Gúzman,
M. A. Voronkov, 2016, MNRAS, 460, 1039-1053. 26, 27.

Paper I forms the basis of chapter 2. The paper involves the analysis of general ionised jet properties, using radio data, towards an RMS survey derived sample of MYSOs. Sample selection was performed by the first 3 co-authors, while observations were conducted by the fourth co-author. All data reduction, analysis and writing was carried out by the primary author, S. J. D. Purser. All co-authors provided comments on various drafts which proved invaluable to the final version.

Acknowledgements

For their advice, guidance and support over the last four years, I would like to thank both of my supervisors, Stuart Lumsden and Melvin Hoare. Their open door policy has certainly been beneficial to the progress of my PhD, but maybe not to their sanity at times. That latter point also applies to Luke Maud, who was my unofficial third supervisor during my first year and his last. My gratitude also extends to the astrophysics group as a whole for making Leeds an enjoyable, fantastic place to study.

Of course, no university experience, at any level, would be complete without a good(ish) set of blokes lurking in the background. So without further ado, I'd like to say cheers to Fernando, Marc, Rob and the other astrophysics PhD students for all the Fenton Fridays, Otley runs and making the office such a crackin' place to work.

To my mum and late dad, from the bottom of my heart, thank you for all the opportunities you have given me in my life. I know without your support (in every sense of the word), I wouldn't have been able to get this far and I'm eternally grateful to you both. In the future I can only hope to do for my children what you have done for me, you're both an inspiration.

Abstract

This thesis focuses on the phenomena of ionised jets associated with massive young stellar objects. Firstly a study was conducted with the aim to establish a statistical sample of such objects. Radio observations towards a sample of 49 MYSOs resulted in the detection of 28 objects classified as ionised jets. The jets' radio luminosities scaled with their MYSOs' bolometric luminosities in the same way as for low-mass examples. This infers that the jet launching and collimation mechanisms of high-mass jets are very similar to that in their low-mass counterparts and they are ejected for the last ≤ 65000 yr of the MYSO phase. Interestingly non-thermal emission was regularly detected towards spatially distinct radio lobes (associated with $\sim 50\%$ of the jets), suggesting the presence of synchrotron emission and therefore, magnetic fields. With an average spectral index of $\bar{\alpha} = -0.55$ (indicative of the 1st order Fermi acceleration mechanism) it is concluded these lobes are the result of shocks in the jets' stream.

My second science chapter is a study of radio variability, precession and proper motions towards a subset of objects from the first chapter. Over a two year time period, no significant variability and only one example of proper motion ($1800 \pm 600 \text{ km s}^{-1}$) was detected. Precession was found to be commonplace however and if it arises as the

result of binary interactions, we infer orbital radii between 30 and 1800 au for the binary companions.

Lastly, high-resolution, VLA observations at C and Q-bands were analysed to extend the known sample of MYSOs harbouring ionised jets into the northern hemisphere. Only 3 radio sources were detected possessing jet-like characteristics towards the work's sub-sample of 8 IRDCs containing 44 mm-cores (in our field of view), highlighting the radio-quiet ($\gtrsim 30 \mu\text{Jy}$) nature of this early phase in massive star formation. Towards the RMS survey derived sample of 48 MYSOs, a total of 38 radio sources with jet-like characteristics were detected, of which 14 were bona-fide jets (10 of which were associated with shock-ionised lobes). Comparing the analysis of the MYSO sample to statistical surveys of molecular outflows, it was inferred from their total momenta that the jets alone are mechanically capable of entraining the outflows. Measurement of the physical extent of the radio emission showed no evolution of the opening angle with bolometric luminosity, and that a trapped HII region alone was not enough to explain the radio emission. Most interestingly, jets associated with shock ionised lobes were found to occupy later evolutionary IR colours than those without, suggesting them to be an evolutionary stage in ionised jet, and MYSO, evolution.

Abbreviations

ALMA	Atacama Large Millimeter Array
APEX	Atacama Pathfinder EXperiment
ATCA	Australian Telescope Compact Array
ATLASGAL	APEX Telescope Large Area Survey of the Galaxy
BeSSeL	Bar and Spiral Structure Legacy survey
CHII	Compact HII region
CMC	Cold Molecular Core
CMF	Core Mass Function
CTTs	Classical T Tauri stars
FIR	Far-Infrared
FWHM	Full Width Half Maximum
GLIMPSE	Galactic Legacy Infrared Mid-Plane Survey Extraordinaire
GMC	Giant Molecular Cloud
HCHII	Hyper-Compact HII region
HMC	Hot Molecular Core
HMPO	High Mass Protostellar Object
HR	Hertzsprung-Russell
IMF	Initial Mass Function
IR	Infrared
IRAC	InfraRed Array Camera
IRAS	InfraRed Array Satellite
ISM	Interstellar Medium
KH	Kelvin-Helmholtz
MIR	Mid-Infrared
MSF	Massive Star Formation

MSX	Midcourse Space eXperiment
MYSO	Massive Young Stellar Object
NIR	Near-Infrared
NOEMA	NOrthern Extended Millimeter Array
PAH	Polycyclic Aromatic Hydrocarbon
PdBI	Plateau de Bure Interferometer
PMS	Pre-Main Sequence
RMS	Red MSX Source (survey)
SED	Spectral Energy Distribution
SMA	Sub-Millimeter Array
SNR	Singal-to-Noise Ratio
TTs	T Tauri stars
UCHII	Ultra-Compact HII region
UV	Ultra-Violet
VLA	Karl G. Jansky Very Large Array
YSO	Young Stellar Object
ZAMS	Zero Age Main Sequence
2MASS	2 Micron All Sky Survey

Contents

1	Introduction	1
1.1	Environments of MSF	3
1.2	Paradigms of star formation	6
1.2.1	Low mass star formation	6
1.2.2	Massive star formation	7
1.2.3	Turbulent core model	8
1.2.4	Competitive Accretion	9
1.2.5	Stellar Mergers	10
1.3	Massive Molecular Outflows	10
1.4	Ionised jets	12
1.4.1	How are they launched?	12
1.4.2	How are they ionised?	17
1.4.3	What do they look like?	20
1.4.4	Previous Observations	27
1.5	The RMS Survey	32
1.6	Thesis outline	34
2	An RMS Survey for Ionised Jets Around MYSOs	37

CONTENTS

2.1	Sample Selection	38
2.2	Observations	39
2.2.1	Radio observations with the ATCA	39
2.2.2	Data reduction	41
2.2.3	Flux recovery with the 6km configuration	44
2.2.4	Extragalactic radio sources	47
2.3	Results	48
2.3.1	A word on calculating fluxes and their errors	49
2.3.2	Classification of the radio emission	51
2.3.3	Object results	55
2.4	Analysis and Discussion	57
2.4.1	Radio luminosity vs. bolometric luminosity	58
2.4.2	Radio luminosity vs. Clump Mass	62
2.4.3	Radio luminosity vs. IR colours	64
2.4.4	Coincidence with maser and line emission	66
2.4.5	Ionised jets and their general properties	66
2.4.6	HII regions and their general properties	75
2.5	Summary and Conclusions	77
3	Deep Radio Continuum Observations of Ionised Jets Around Four MYSOs	81
3.1	Observations	84
3.2	Multi-epoch Synthetic Observations	87
3.3	Results	96
3.3.1	Image alignment	96

3.3.2	New radio flux clean maps	102
3.4	Discussion	112
3.4.1	Natures of newly detected emission	112
3.4.2	Variability and proper motions	116
3.4.3	Precession	120
3.5	Summary and Conclusions	132
4	A statistical JVLA C and Q-band survey of ionised jets on the 100 au scale	135
4.1	The Sample	137
4.1.1	The IRDC sample	138
4.1.2	The MYSO sample	146
4.2	Observations	146
4.3	Results	149
4.4	Analysis	160
4.4.1	IRDCs and their radio evolution	160
4.4.2	Radio luminosity against bolometric luminosity	162
4.4.3	Spectral Indices and dust contribution	166
4.4.4	Jet opening angle and its evolution	172
4.4.5	Mechanical jet properties	178
4.4.6	Ionised jets or gravitationally trapped HII regions?	184
4.5	Summary and Conclusions	187
5	Conclusions	191
5.1	Summary and synthesis	192
5.2	Future Work	195

CONTENTS

5.2.1	Updating radio jet models	195
5.2.2	Further temporal studies	197
5.2.3	Sub-mm/mm follow-up campaigns	197
5.2.4	Jet studies in the SKA era	199
A	Supporting figures	201
B	Supporting tables	279
C	Object Notes	367
C.1	Southern MYSO sample	367
C.1.1	Jets, candidates and a disc wind	367
C.1.2	‘Embedded’ HCHII regions	396
C.1.3	A curious case - G301.1364-00.2249	401
C.2	Northern IRDC/MYSO sample	405
C.2.1	IRDC Sample	405
C.2.2	MYSO Sample	414
	References	479

List of Figures

1.1	Mid-infrared image of the HII region RCW 79	2
1.2	Observations of Cygnus X and its hierarchical substructure	5
1.3	Physics of the disc-wind model	14
1.4	Physics of the X-wind model	15
1.5	Calculated ionisation fractions within an MYSO's accretion disc using the α -disc model	19
1.6	Optical and near-infrared images of HH111	26
1.7	Radio luminosity against bolometric luminosity for RMS sources	33
2.1	Flux and structure recovery of ATCA over the observed frequencies	45
2.2	Comparison of flux measurement accuracy using either IMFIT or 3σ contours	49
2.3	Flowchart of the source classification algorithm	53
2.4	Radio luminosity against bolometric luminosity for all detected MYSOs/HII regions	60
2.5	Radio luminosity against ATLASGAL-derived clump mass	64
2.6	Radio luminosity against MSX $21\mu\text{m}/8\mu\text{m}$ flux ratio	65
2.7	Jet mass loss rate against ATLASGAL-derived clump mass	70

LIST OF FIGURES

2.8	Momentum rate against bolometric luminosity for jet-like sources	72
2.9	Radio spectral index histogram for jet-like sources and their associated lobes	74
2.10	Histogram of lobe spatial separations	76
2.11	Emission measure against radius for detected HII regions	77
3.1	Comparison of $S(u, v)$ for 2013 and 2014 observations	88
3.2	Temporal profile of T_{sys} employed for the synthetic observations .	89
3.3	Synthetic clean maps at 9 GHz	90
3.4	Flux differences between the two epochs' synthetic clean maps . .	91
3.5	Deviations of the derived properties of each lobe from the model .	95
3.6	Radio flux contour plots of G263.7434+00.1161	97
3.7	Radio flux contour plots of G310.0135+00.3892	98
3.8	Radio Herbig-Haro objects near G310.0135+00.3892 at 6 GHz . .	99
3.9	Radio flux contour plots of G310.1420+00.7583A	100
3.10	Radio flux contour plots of G313.7654−00.8620	101
3.11	Radio flux contour plot of the variable source S2 located south of G263.7434+00.1161	104
3.12	Radio flux contour plot of component F located in the field of G313.7654−00.8620	108
3.13	Radio SED for the SE component of G263.7434+00.1161	113
3.14	Radio contour map of G313.7654−00.8620 and its environment at 2 and 6 GHz	114
3.15	Pixel-to-pixel flux differences towards G310.1420+00.7583A be- tween 2013 and 2014	119

3.16	Illustration of the precession model	123
3.17	χ^2 parameter space for precession modelling of G310.1420+00.7583A	124
3.18	Position angle against separation for shock-ionised lobes relative to the powering jet of G310.1420+00.7583A	127
3.19	Radio and MIR image of G310.1420+00.7583A overlaid with the best-fitting precessing jet model	128
3.20	Position angle against separation for shock-ionised lobes relative to the powering jet of G313.7654–00.8620	130
3.21	Radio and MIR image of G313.7654–00.8620 overlaid with the best-fitting precessing jet model	131
3.22	Precession angle against inferred orbital radii	132
4.1	Mid-infrared flux ratios against bolometric luminosity for the IRDC cores/MYSOs of the sample	147
4.2	Radio luminosity against parental core luminosity-to-mass ratio for the IRDC sample	161
4.3	Radio luminosity against bolometric luminosity for detected sources	163
4.4	Subplots of bolometric and radio luminosity against MIR 70 μm to 24 μm flux ratio	164
4.5	Cumulative distribution functions of the FIR ratios, radio lumi- nosities and bolometric luminosities of northern hemisphere MYSOs with jets	165
4.6	Spectral index histograms for jet-like sources	168
4.7	Jet opening angle against MYSO mass	178
4.8	Jet mass loss rate against bolometric luminosity for jet-like sources	179

LIST OF FIGURES

4.9	Jet momentum rate against bolometric luminosity	182
4.10	Total jet momentum against bolometric luminosity	183
4.11	Jet power against bolometric luminosity	185
4.12	Subplots of IMFIT-derived major and minor axes against bolometric luminosity	186
5.1	Initial RADIORT results for a standard jet model	196
A.1	ATCA radio images of G010.8411−02.5919	202
A.2	ATCA radio images of G012.9090−00.2607	202
A.3	ATCA radio images of G014.9958−00.6732	203
A.4	ATCA radio images of G251.2337−01.9535	203
A.5	ATCA radio images of G254.0491−00.5615	204
A.6	ATCA radio images of G254.0548−00.0961	205
A.7	ATCA radio images of G263.2283−01.5712	206
A.8	ATCA radio images of G263.7434+00.1161	207
A.9	ATCA radio images of G263.7759−00.4281	207
A.10	ATCA radio images of G265.1438+01.4548	208
A.11	ATCA radio images of G274.0649−01.1460	208
A.12	ATCA radio images of G284.2438−01.1302	209
A.13	ATCA radio images of G286.2086+00.1694	209
A.14	ATCA radio images of G287.3716+00.6444	210
A.15	ATCA radio images of G298.2620+00.7394	211
A.16	ATCA radio images of G300.9674+01.1499	211
A.17	ATCA radio images of G301.1364−00.2249	212
A.18	ATCA radio images of G305.2017+00.2072A	212

A.19 ATCA radio images of G305.5610+00.0124	213
A.20 ATCA radio images of G308.9176+00.1231A	213
A.21 ATCA radio images of G310.0135+00.3892	214
A.22 ATCA radio images of G310.1420+00.7583A	215
A.23 ATCA radio images of G313.7654−00.8620	215
A.24 ATCA radio images of G317.4298−00.5612	216
A.25 ATCA radio images of G317.8908−00.0578	216
A.26 ATCA radio images of G318.9480−00.1969A	217
A.27 ATCA radio images of G326.6618+00.5207	218
A.28 ATCA radio images of G327.1192+00.5103	219
A.29 ATCA radio images of G331.3576+01.0626	220
A.30 ATCA radio images of G331.5414−00.0675	220
A.31 ATCA radio images of G332.0939−00.4206	221
A.32 ATCA radio images of G332.8256−00.5498A	222
A.33 ATCA radio images of G332.9868−00.4871	223
A.34 ATCA radio images of G337.8442−00.3748	223
A.35 ATCA radio images of G338.9196+00.5495	224
A.36 ATCA radio images of G339.6221−00.1209	224
A.37 ATCA radio images of G339.8838−01.2588	225
A.38 ATCA radio images of G340.0543−00.2437D	225
A.39 ATCA radio images of G340.2480−00.3725	226
A.40 ATCA radio images of G343.1261−00.0623	226
A.41 ATCA radio images of G343.5213−00.5171	227
A.42 ATCA radio images of G345.4938+01.4677	227
A.43 ATCA radio images of G345.5043+00.3480	228

LIST OF FIGURES

A.44 ATCA radio images of G345.9561+00.6123	229
A.45 ATCA radio images of G348.6972−01.0263	229
A.46 Mid-infrared, ATLASGAL and VLA radio images of the IRDC G018.82−00.28	230
A.47 Mid-infrared, ATLASGAL and VLA radio images of the IRDC G024.08+00.04	231
A.48 Mid-infrared, ATLASGAL and VLA radio images of the IRDC G024.33+00.11	232
A.49 Mid-infrared, ATLASGAL and VLA radio images of the IRDC G024.60+00.08	233
A.50 Mid-infrared, ATLASGAL and VLA radio images of the IRDC G028.28−00.34	234
A.51 Mid-infrared, ATLASGAL and VLA radio images of the IRDC G028.37+00.07	235
A.52 Mid-infrared, ATLASGAL and VLA radio images of the IRDC G028.67+00.13	236
A.53 Mid-infrared, ATLASGAL and VLA radio images of the IRDC G33.69−00.01	237
A.54 Near-infrared and VLA radio images of the MYSO IRAS 18517+ 0437	238
A.55 Mid-infrared and VLA radio images of the MYSO IRAS 18556+ 0136	239
A.56 Mid-infrared and VLA radio images of the MYSO G033.6437− 00.2277	240

A.57 Near-infrared and VLA radio images of the MYSO G056.3694– 00.6333	241
A.58 Near-infrared and VLA radio images of the MYSO G077.5671– 00.6333	241
A.59 Near-infrared and VLA radio images of the MYSO G078.8699+ 02.7602	242
A.60 Near-infrared and VLA radio images of the MYSO G079.8855+ 02.5517	243
A.61 Near-infrared, mid-infrared and VLA radio images of the MYSO G081.8652+00.7800	244
A.62 Near-infrared and VLA radio images of the MYSO G083.7071+ 03.2817	245
A.63 Near-infrared and VLA radio images of the MYSO G084.9505– 00.6910	245
A.64 Near-infrared and VLA radio images of the MYSO G094.2615– 00.4116	246
A.65 Near-infrared and VLA radio images of the MYSO G094.3228– 00.1671	246
A.66 Near-infrared and VLA radio images of the MYSO G094.4637– 00.8043	247
A.67 Near-infrared and VLA radio images of the MYSO G094.6028– 01.7966	247
A.68 Near-infrared and VLA radio images of the MYSO G100.3779– 03.5784	248

LIST OF FIGURES

A.69 Near-infrared, mid-infrared and VLA radio images of the MYSO G102.8051–00.7184	248
A.70 Near-infrared, mid-infrared and VLA radio images of the MYSO G103.8744+01.8558	249
A.71 Near-infrared and VLA radio images of the MYSO G105.5072+ 00.2294	250
A.72 Near-infrared and VLA radio images of the MYSO G107.6823– 02.2423A	250
A.73 Near-infrared, mid-infrared and VLA radio images of the MYSO G108.18+5.51	251
A.74 Near-infrared and VLA radio images of the MYSO G108.4714– 02.8176	251
A.75 Mid-infrared and VLA radio images of the MYSO G108.5955+ 00.4935C	252
A.76 Mid-infrared and VLA radio images of the MYSO G108.7575– 00.9863	253
A.77 Near-infrared and VLA radio images of the MYSO G110.0931– 00.0641	254
A.78 Near-infrared and VLA radio images of the MYSO G111.2348– 01.2385	255
A.79 Near-infrared and VLA radio images of the MYSO G111.2552– 00.7702	256
A.80 Near-infrared and VLA radio images of the MYSO G111.5671+ 00.7517	257

A.81 Near-infrared and VLA radio images of the MYSO G114.0835+ 02.8568	258
A.82 Near-infrared and VLA radio images of the MYSO G118.6172– 01.3312	258
A.83 Near-infrared and VLA radio images of the MYSO G126.7144– 00.8220	259
A.84 Near-infrared and VLA radio images of the MYSO G133.7150+ 01.2155	260
A.85 Near-infrared and VLA radio images of the MYSO G133.7150+ 01.2155	261
A.86 Near-infrared and VLA radio images of the MYSO G134.2792+ 00.8561	262
A.87 Near-infrared and VLA radio images of the MYSO G136.3833+ 02.2666	263
A.88 Near-infrared and VLA radio images of the MYSO G138.2957+ 01.5552	264
A.89 Near-infrared and VLA radio images of the MYSO G139.9091+ 00.1969A	265
A.90 Near-infrared and VLA radio images of the MYSO G141.9996+ 01.8202	266
A.91 Near-infrared and VLA radio images of the MYSO G143.8118– 01.5699	267
A.92 Near-infrared and VLA radio images of the MYSO G148.1201+ 00.2928	268

LIST OF FIGURES

A.93 Near-infrared and VLA radio images of the MYSO G160.1452+ 03.1559	269
A.94 Near-infrared, mid-infrared and VLA radio images of the MYSO G173.4839+02.4317	270
A.95 Near-infrared and VLA radio images of the MYSO G174.1974– 00.0763	271
A.96 Near-infrared and VLA radio images of the MYSO G177.7291– 00.3358	272
A.97 Near-infrared and VLA radio images of the MYSO G183.3485– 00.5751	273
A.98 Near-infrared and VLA radio images of the MYSO G188.9479+ 00.8871	274
A.99 Near-infrared and VLA radio images of the MYSO G189.0307+ 00.7821	275
A.100 Near-infrared and VLA radio images of the MYSO G192.6005– 00.0479	276
A.101 Near-infrared and VLA radio images of the MYSO G196.4542– 01.6777	277
A.102 Near-infrared and VLA radio images of the MYSO/HII region W48, or G035.1992–01.7424	278
C.1 Spectral index map for G263.7434+00.1161 between 5 and 9 GHz	372
C.2 Spectral index map of G310.0135+00.3892 between 5 and 9 GHz .	376
C.3 Mid-infrared image of G310.1420+00.7583A overlaid with 9 GHz radio flux contours	378

C.4 Spectral index map of G310.1420+00.7583A between 5 and 9 GHz	379
C.5 Mid-infrared image of G313.7654–00.8620 overlaid with 9 GHz radio flux contours	380
C.6 Spectral index map of G313.7654–00.8620 between 5 and 9 GHz .	381
C.7 Spectral index map of G339.8838–01.2588 between 5 and 9 GHz .	388
C.8 Mid-infrared image of G343.1261–00.0623 overlaid with 17 GHz radio flux contours	390
C.9 Spectral index map of G343.1261–00.0623 between 17 and 22 GHz	392
C.10 Flux against channel velocity for hydrogen recombination lines detected towards G301.1364–00.2249 and G301.1364–00.2235 . . .	403
C.11 Fitted precessing jet model of G35.20–0.74N overlaid on radio flux contour map	417
C.12 Relative separations of shock-ionised lobes from the central thermal jet of G133.7150+01.2155	448
C.13 Radio image of G138.2957+01.5552 employing a fully natural robustness	453
C.14 Radio SED for source A of G160.1452+03.1559	460
C.15 Radio image of G173.4815+02.4459 overlaid on top of 1.2 mm PdBI observations	462
C.16 Uniform ($R = -1$) radio image of source B (AFGL 5172) from the G174.1974–00.0763 field	466
C.17 Near-infrared and VLA radio images of G189.0323+00.8092 . . .	472

LIST OF FIGURES

List of Tables

1.1	Properties of GMCs and their substructures	4
1.2	Properties of different outflow phenomena towards MSF regions .	11
2.1	Observable RRLs within the bandwidth of the ATCA observations	40
2.2	Target sources for the southern survey	42
2.3	Predicted radio galaxy populations	47
2.4	Number of detected objects by type	57
2.5	Calculated Kendall-Tau coefficients	58
3.1	Flux, bandpass and phase calibrator properties	86
3.2	Target sources for the 2014 ATCA observations	86
3.3	Deconvolved component properties of the model and images produced from the synthetic datasets	92
3.4	IMFIT-derived radio properties of objects from the 2014 data . . .	110
3.5	Proper-motion derived velocities and fluxes	116
3.6	Derived properties of the best fitting precession models for each jet	128
4.1	Target IRDC cores and their properties	139
4.2	Target MYSOs and their properties	142

LIST OF TABLES

4.3	Detected source counts within $1'$ of the pointing centres	150
4.4	Number of detected objects by type	150
4.5	Bolometric luminosities and classifications of all radio sources . . .	151
4.6	Detection statistics towards target IRDC cores	160
4.7	Classifications, opening angles and mass loss rates for all jet-like radio sources detected.	174
5.1	Telescope specifications for the SKA and its precursors	199
B.1	Deconvolved positions of jet-like sources and their associated lobes at 5.5 and 9 GHz from the ATCA survey	280
B.2	Deconvolved positions of jet-like sources and their associated lobes at 17 and 22.8 GHz from the ATCA survey	283
B.3	Fluxes and calculated values for α of jet-like sources and their associated lobes from the ATCA survey	286
B.4	Deconvolved major axes for all jet-like sources and their associated lobes from the ATCA survey	291
B.5	Deconvolved minor axes for all jet-like sources and their associated lobes from the ATCA survey	293
B.6	Deconvolved major axis position angles and calculated values for γ for all jet-like sources and their associated lobes from the ATCA survey	297
B.7	Deconvolved positions for sources of unknown classification from the ATCA survey	301
B.8	Fluxes and calculated values for α for sources of unknown classifi- cations from the ATCA survey	301

B.9	Deconvolved major axis position angles and calculated values for γ for sources of unknown classification from the ATCA survey . . .	302
B.10	Positions, fluxes and deconvolved sizes of the HII regions from the ATCA survey	302
B.11	Derived properties of jet-like sources from the ATCA survey . . .	305
B.12	Derived properties of HII regions from the ATCA survey	307
B.13	Positions, fluxes and calculated values for α of field sources from the ATCA survey	309
B.14	Positions, fluxes and deconvolved dimensions of sources from the 6 GHz ATCA observations from 2014	313
B.15	Positions, fluxes and deconvolved dimensions of sources from the 9 GHz ATCA observations from 2014	315
B.16	Flux/bandpass calibrators and observing dates for the VLA survey	317
B.17	Phase calibrators used in the VLA survey	318
B.18	C-band positions and fluxes for all objects detected in the VLA survey	322
B.19	Q-band positions and fluxes for all objects detected in the VLA survey	335
B.20	C-band deconvolved sizes and position angles for all sources from the VLA survey	342
B.21	Q-band deconvolved sizes and position angles for all sources from the VLA survey	351
B.22	Calculated values for α , γ and major axis position angle differences for sources detected in the VLA survey	355

LIST OF TABLES

Chapter 1

Introduction

Massive stars are defined as those stars with masses exceeding 8 times that of our sun (spectral types of B3 or earlier). This definition has been accepted throughout the literature as it is the mass at which a star can fuse carbon within its core (see section 6.3.1 of Ryan & Norton 2010), ultimately leading to a Type II supernova (i.e. core-collapse at the red supergiant stage). During earlier stages in their evolution we can define massive stars as those that can produce a sizeable HII (ionised hydrogen) region as a result of significant, ionising far-UV output ($E_\gamma \geq 13.6$ eV or $\lambda_\gamma \leq 912$ Å). Either way, the lower mass limit for this classification remains the same and forms the definition for the stellar mass regime which this work investigates. A common theme for both characterizations is the idea that the massive star is a source of feedback and influences the environment around it, whether at the beginning of its relatively short ($\sim 10^{6.5} - 10^{7.5}$ yr) life or, more spectacularly, at the end as a supernova, the sole mechanism responsible for seeding the universe with heavy elements (Hoyle 1954). It is this intrinsic nature of massive stars to disrupt their surroundings that makes them so important on

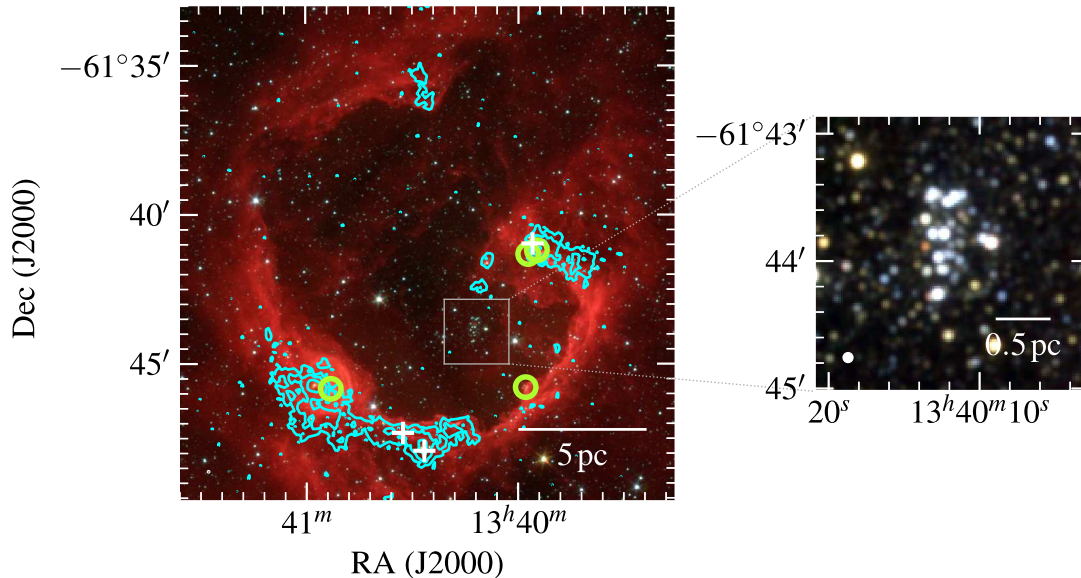


Figure 1.1: A GLIMPSE RGB image of the HII region RCW 79 (large-scale, diffuse, reddened emission). A close up of the powering cluster is shown as a 2MASS RGB image (right). Cyan contours ($-3, 3, 6, 13$ and $27 \times 83 \text{ mJy beam}^{-1}$) represent $870 \mu\text{m}$ emission (from the ATLASGAL survey, Urquhart *et al.* 2014b), while HII regions (green circles) and MYSO positions (white crosses) from the RMS survey (Lumsden *et al.* 2013) are shown.

local, galactic and even extra-galactic scales and this effect is termed as ‘feedback’.

Feedback occurs through many mechanisms including bipolar, molecular outflows, large radiative outputs and other types of mass loss in a variety of forms. It has the ability to stifle, or trigger, star formation across a significant range of scales through disruption of local gas and dust. In Figure 1.1, an example of how previous, massive star formation has triggered more star formation further afield is shown. In this case it is the classical HII region RCW 79 (powered by a cluster of a dozen O-type stars, Martins *et al.* 2010), which is responsible for the disruption of its environmental material. Physically, the expansion of the ionisation front (i.e. Strömgren sphere) into the surrounding, molecular cloud pushes

material outwards, increasing the density, and therefore decreasing the Jean’s mass (Equation 1.1), leading to further star formation at the Strömngren radius. This is known as the ‘collect-and-collapse’ mechanism (Elmegreen & Lada 1977). Various stages of a massive star’s pre-main sequence life are shown, including a second generation of HII regions, massive young stellar objects (MYSOs) and their collapsing, natal clumps of material. It is obvious therefore that massive star formation (MSF) plays a crucial role in galactic evolution.

$$M_J = \left(\frac{5kT}{G\mu} \right)^{\frac{3}{2}} \left(\frac{3}{4\pi\rho} \right)^{\frac{1}{2}} \quad (1.1)$$

Where M_J is the Jean’s mass (minimum mass for collapse to occur), ρ is the density, T is temperature and μ is the mean particle mass.

1.1 Environments of MSF

Massive stars form exclusively within giant molecular clouds (GMCs) with only 25% of O-stars and 2% of B-stars being found in isolation and classed as ‘runaway OB-stars’ (on account of their high velocities of $> 40 \text{ km s}^{-1}$). Originally these runaways belonged to massive star forming complexes within GMCs, but were ejected either as the result of asymmetrical supernovae or binary interactions (see §2.3.3 of Zinnecker & Yorke 2007).

Giant molecular clouds are positioned at the top of a hierarchy of substructure and are intrinsically inhomogeneous (i.e. ‘clumpy’) in nature. Below GMCs, hierarchically speaking, are ‘clumps’ which are agglomerations of material which will eventually collapse to form clusters or OB associations, and are coherent regions in $l-b-v$ (galactic longitude – galactic latitude – velocity) space (Blitz &

Table 1.1: The typical properties of the substructures commonly found within GMCs, the GMCs themselves and InfraRed Dark Clouds (taken from: Beuther *et al.* 2007a; Garay *et al.* 2004; Stahler & Palla 2008; Tan *et al.* 2014; Zinnecker & Yorke 2007).

Structure	n_H (cm^{-3})	T (K)	M (M_\odot)	R (pc)	σ (km s^{-1})
IRDC	$10^5 - 10^6$	< 20	$10^3 - 10^4$	$1 - 10$	$0.5 - 4.0$
GMC	$10^2 - 10^3$	$10 - 20$	$10^4 - 10^{6.5}$	$10 - 100$	$1 - 8$
Clump	$\sim 10^5$	$10 - 30$	$10^2 - 10^3$	$1 - 1.5$	$0.5 - 3$
CMC	$> 10^5$	< 20	$100 - 1000$	$0.2 - 0.3$	–
HMC	$\sim 10^7$	≥ 100	< 100	~ 0.1	$0.2 - 0.5$

Williams 1999). Again, the clumps are inhomogeneous and their subsequent substructures are termed ‘cores’, defined as those substructures which will eventually go on to form single stellar systems (which may or may not display multiplicity). Depending on the exact stage of evolution of the cores, they are either classed as cold molecular cores (CMCs) or hot molecular cores (HMCs), due to the degree of internal heating by forming stars (some may be externally heated by nearby HII regions). Observationally HMCs are typically rich in sub-mm molecular line transitions (e.g. Orion KL, see Figure 3a–5d of Beuther *et al.* 2005), whereas CMCs tend to possess featureless spectra. In Table 1.1 each step of this hierarchy is defined in terms of its average, physical parameters while in Figure 1.2, different images sensitive to each scale are compared with each other. Also included are the properties for infrared dark clouds (IRDCs) which were initially identified as patches of extinction against the background, thermal, IR emission from MSX observations (Egan *et al.* 1998). They appear to be contained within the GMCs (Hernandez & Tan 2015, who defined GMC boundaries by $^{13}\text{CO}(1 - 0)$ observations), and contain quiescent cores or active star formation, though generally at a much earlier stage than those ongoing in the surrounding molecular cloud. As a note, these terminologies shall be adhered to throughout the rest of this thesis.

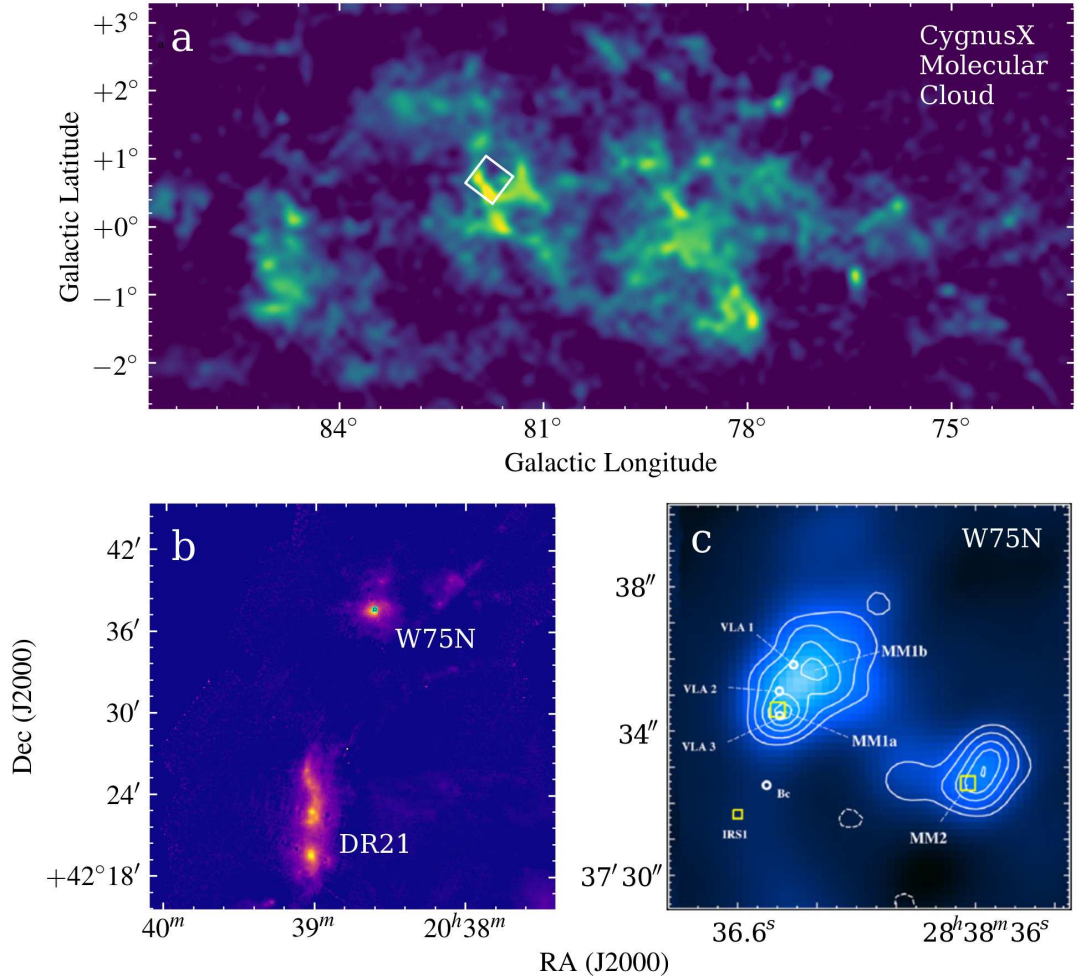


Figure 1.2: A plot showing the hierarchical substructure of a giant molecular cloud. Sub-plots are: a.) Colour-scale plot of the Cygnus X molecular cloud in CO (utilising multiple transitions) whereby the white box represents the field of view of panel b. Data is taken from Dame *et al.* (2001); b.) Both the DR21 and W75N clump at 1.2 mm whereby the light blue square centred on W75N represents the field of view of panel c. Data is taken from Motte *et al.* (2007) ; c.) Continuum emission at 217 GHz (contour) and 347 GHz (colour image), adapted from Figure 1 of Minh *et al.* (2010).

The ATLASGAL sub-mm survey (Urquhart *et al.* 2014b), investigated the 870 μm fluxes and sizes of a sample of clumps harbouring forming massive stars in stages of evolution from the MYSO to HII region phase. Importantly, they identified that clump mass is strongly correlated with the bolometric luminosity of the MYSO contained within, and concluded that the most massive stars form in the most massive clumps.

1.2 Paradigms of star formation

1.2.1 Low mass star formation

Although it is not within the remit of this thesis, it is helpful to give a brief overview of the generally accepted formation mechanism for low-mass stars, especially since some theories paint massive star formation as a scaled-up version of this mechanism (see subsection 1.2.3).

A seminal review by Shu *et al.* (1987) tied together and summarised previous works on low-mass star formation, and concluded that this process starts with slowly rotating density enhancements (‘cores’) within molecular clouds. These cores are either sub-critical, whereby the internal pressure support the cores against collapse, or super-critical, whereby the cores cannot support themselves and collapse due to self-gravity. In the sub-critical case, turbulent and magnetic (through ambipolar diffusion) support slowly leak out of the core until it turns super-critical. It is important to note that either way, collapse proceeds from the inside-out. Due to the overall angular momentum vector of the initial rotating core, the collapse forms an accretion disc through which accretion proceeds upon

a central protostar. Stellar winds/jets drive molecular outflows out of cavities formed along the poles of the rotation axis, which eventually dissipate the surrounding circumstellar envelope as they widen, leaving a remnant disc from which planets may eventually form.

Due to the relative flux contributions at various wavelengths from separate components of different temperatures, the spectral energy distribution can be used to establish an evolutionary classification system. Measurement of the spectral index between $1\ \mu\text{m}$ and $20\ \mu\text{m}$ allows low-mass protostars to be categorised as class 0 (undetectable at $\lambda > 10\ \mu\text{m}$; Andre *et al.* 1993), class I, class II or class III ($0 < \alpha < 3$, $-2 < \alpha < 0$ or $-3 < \alpha < -2$ respectively; Lada 1987). The reader is directed to Figure 1 of Feigelson & Montmerle (1999) and Figure 1.1 of Isella (2006) for a complete description and illustration of each evolutionary class.

1.2.2 Massive star formation

The astrophysical community remains divided between the prominent paradigms of massive star formation. On one hand we have the idea that it is the core that collapses to form a massive star of a defined fraction ('star formation efficiency') of its mass, and on the other is the idea that the massive star's mass can exceed that of its core by sourcing material from the surrounding clump. More extreme processes involving the collision of two forming stars to form a protostar of higher mass have also been considered.

1.2.3 Turbulent core model

Essentially the turbulent core model (McKee & Tan 2002, 2003) is similar to the accepted mechanism for low-mass star formation (see subsection 1.2.1), whereby the material a massive star accretes during its formation comes directly from the initial prestellar core it evolves from. Observationally-speaking this translates into a similarity of the core mass function, or CMF, (distribution of prestellar core masses as a function of a mass) with the IMF (as well as a stellar mass to core mass ratio of ~ 0.5 , Tan *et al.* 2014). This approach conserves angular momentum in the form of a rotating, flattened, accretion disc and associated bi-polar jets. Direct observations of ‘massive rotating structures’ (i.e. potential accretion discs) of comparable mass to the accreting star (upto $\sim 20 M_{\odot}$) are commonplace (see Cesaroni *et al.* 2007, for a review) supporting this view. Disc-jet systems have been observed in a handful of examples in the mm/cm regime, (see subsection 1.4.4) however when it comes to the most massive stars (O4–O8 type), only toroids of material around the central star have been observed (e.g. NIR observations of W33a by Davies *et al.* 2010). This may be due to the small sample size of O4–O8 type stars, their distance, the relative luminosity of the tori to discs, or other effects. Criticisms on the basis of the increased radiative forces on the disc of gas and dust from the high radiative output of an MYSO do produce a problem of accretion being counteracted by radiation pressure (Zinnecker & Yorke 2007). It is thought this issue can be alleviated as the disc forms only a small cross-sectional area (i.e. non-spherical accretion/non-Bondi Hoyle), to the radiation’s direction (Krumholz *et al.* 2009). This means only exposing a small fraction of the disc to its full force, and thus avoiding dispersion.

1.2.4 Competitive Accretion

Simulations by Bonnell *et al.* (1997), who considered a strongly gravitationally-bound clump, showed that the protostars in the central regions had much higher accretion rates than average, spawning the idea of competitive accretion. This process operates on two main principles, the first being that protostars at the centre of clumps will become the largest, as there is simply more matter (denser environments) within their accretion domains. The second principle is that those protostars that have formed first, have more time to accrete and hence are gravitationally more attractive (i.e. larger accretion radius) compared to their neighbourhood siblings.

In comparison to core accretion, the material that forms the protostar is siphoned from all parts of its natal clump ('clump-fed') as the accreting MYSO moves internally through the clump. The knock-on effect is that the core mass function should no longer mirror the initial mass function (Tan *et al.* 2014). Other predictions include changing accretion disc rotation axes (due to chaotic mass flows to the forming star and dynamical interactions in crowded environments), which observationally should present itself in the precession of outflow directions. Massive stars should also be seen to always form at the centre of clumps and with relatively small accretion disks.

However, due to the Bondi-Hoyle process which this model employs, radiative forces impeding accretion become a problem at $M_{\star} > 10 M_{\odot}$ (Tan *et al.* 2014). Outflows, regularly observed towards sites of massive star formation (see section 1.3), further exacerbate this issue by halting accretion along their axis of motion. Indeed, simulations of this mechanism have yielded poor accretion

rates of $4.6 \times 10^{-5} M_{\odot} \text{yr}^{-1}$ for even the most massive ($46 M_{\odot}$) star formed in the simulated clump (Wang *et al.* 2010), which are an order of magnitude too small. Possible solutions include a higher accretion efficiency, in order to reduce the time for massive stars to form, or time-variable accretion rates (such as the accretion-driven bursts seen in the simulations of Meyer *et al.* 2017) since those shown in Wang *et al.* (2010) were relatively constant. This last possibility has intriguing implications on the mass loss of collimated jets, since accretion and mass loss mechanisms are generally linked (see subsection 1.4.1).

1.2.5 Stellar Mergers

Also referred to as coalescence in the literature, this process essentially forms massive stars by the physical merging of multiple, lower-mass precursors (Bonnell *et al.* 1998). Originally it was a concept designed to overcome the radiation pressure problem, however it was found to be an unlikely candidate for the dominant process of MSF due to the high stellar densities required for significant merger rates ($\sim 10^8 \text{pc}^{-3}$). As such it shall not be discussed in any more detail, however it has been included here for completeness and may still contribute to the formation of the highest mass stars.

1.3 Massive Molecular Outflows

Towards sites of massive star formation, molecular outflows with typical velocities, momenta and mass loss rates of $10 - 50 \text{km s}^{-1}$, $\lesssim 10^2 M_{\odot} \text{km s}^{-1}$ and $\lesssim 10^{-3} M_{\odot} \text{yr}^{-1}$ respectively are almost always observed (Beuther *et al.* 2002b). Despite their common nature however, we do not definitively understand how

Table 1.2: A table of the typical values of various, physical parameters for different types of outflow phenomena arising from forming, massive stars. Parameters for ionised jets are taken from a plethora of observational examples (see subsection 1.4.4) while disc wind, molecular outflow and stellar wind parameters are taken from Hoare (2006), Beuther *et al.* (2002b)/Hatchell *et al.* (1999) and Dyson & Williams (1980) respectively.

Type	v (km s^{-1})	ρ (cm^{-3})	T (K)	\dot{M} ($M_{\odot} \text{ yr}^{-1}$)
Ionised jet	500 – 1000	10^{8*}	10^4	10^{-5}
Disc wind	$> 10^2$	10^3	10^4	$10^{-8} - 10^{-7\dagger}$
Molecular outflow	20 – 100	$10^4 - 10^6$	> 50	$10^{-5} - 10^{-3}$
Stellar wind	2000	$\sim 10^{3\dagger}$	10^5	10^{-6}

they are driven. Prevailing view points (see the review by Arce *et al.* 2007) are that they could be driven by a wind from the central source, result from non-accreted inflow streams, are ionisation-driven (e.g. Klaassen *et al.* 2013) or driven by a highly collimated, high-velocity, ionised jet that sweeps up and entrains the surrounding molecular material (e.g. G023.01–00.41, whereby jet and outflow momenta are of order unity, Sanna *et al.* 2016).

Properties of these outflows, such as mass flow rate, momentum and force, have been shown to correlate well with the bolometric luminosities of their parental MYSOs, as well as natal clump mass (Maud *et al.* 2015). Other studies in the literature (e.g. Cabrit & Bertout 1992) derive similar relationships, which in turn bear resemblances to equivalent relationships for ionised jets (see section 1.4). This final point is intriguing and begs the question of whether the outflows truly are entrained by ionised jets, a query of direct relevance to this work.

1.4 Ionised jets

In this work, the specific phenomenon of ionised jets resultant from the mechanisms of massive star formation is studied. However, within the literature there is much ambiguity with regard to terms employed to describe any of the outflows associated with regions of massive star formation. Therefore I choose to define the main outflow phenomena as ionised jets, photo-evaporative disc winds, molecular outflows and stellar winds, whose typical physical parameters are outlined in Table 1.2. Qualitatively ionised jets are defined as collimated, high-velocity ejections of ionised material driven by one of the possible mechanisms of subsection 1.4.1, disc winds are the high-velocity outflows comprised of the radiatively ablated surface of the accretion disc and moving perpendicular to the disc’s rotation axis, molecular outflows are defined in section 1.3 and stellar winds are isotropically driven by the radiation pressure in a young star’s photosphere.

1.4.1 How are they launched?

A pure ‘disc-wind’ (not to be confused with the photo-evaporative disc winds mentioned above) model was developed by Blandford & Payne (1982), for application to extragalactic phenomena, who suggested that a poloidal magnetic field, originating from an accretion disc, acts as a launching mechanism for ionised material travelling near the surface of the disc (see Figure 1.3 for a diagrammatic representation). This material is accelerated centrifugally along the field lines and away from the disc, accurately adhering to the analogy of ‘beads on a wire’. As the accretion disc rotates, these field lines become more twisted (due to magnetic coupling) further from the disc and eventually jet collimation is in-

duced by ‘hoop stresses’ from the field’s increasing toroidal component. A later paper by Pudritz & Norman (1983) further developed this work in to the field of star formation providing an efficient way to remove angular momentum from accreting material and a general model accommodating for ranges in magnetic field geometry was presented by Pelletier & Pudritz (1992). Crucially that last work also predicted an accretion to jet mass loss ratio of 10 : 1. Simulations by Seifried *et al.* (2012) showed that massive protostellar jets were likely driven by this mechanism, with varying hoop stresses (enhanced by weaker magnetic fields, and suppressed by sub-Keplerian disc motions in the presence of strong fields) affecting the degree of collimation. This result predicted that collimation should relate to the evolutionary stage of the MYSO, with lower degrees of collimation for younger MYSOs. An observational result in support of this picture is the jet in W75N VLA 2 whereby collimation has been shown to increase over subsequent observations spread over 18 years (Carrasco-González *et al.* 2015), although the inferred velocity of the driven outflow was an order of magnitude higher than that predicted by the theoretical work.

On the other hand, Shu *et al.* (1994) proposed a model with a magnetic field originating from the central protostar, referred to as the ‘X-wind model’. This is so named because the launching radius for the jet in the disc is located at the X-shaped lines of equipotential (balancing points of gravitational and centrifugal forces) located near the truncated (by strong stellar magnetic fields), inner surface of the disc itself. With the inward flow of material in the accretion disc, magnetic coupling bows the field lines inwards. Consequently, magneto-centrifugal processes accelerate the inflowing gas supersonically in a direction parallel to the poloidal field lines, resulting in an outflowing wind (see Figure 1.4). Twisted

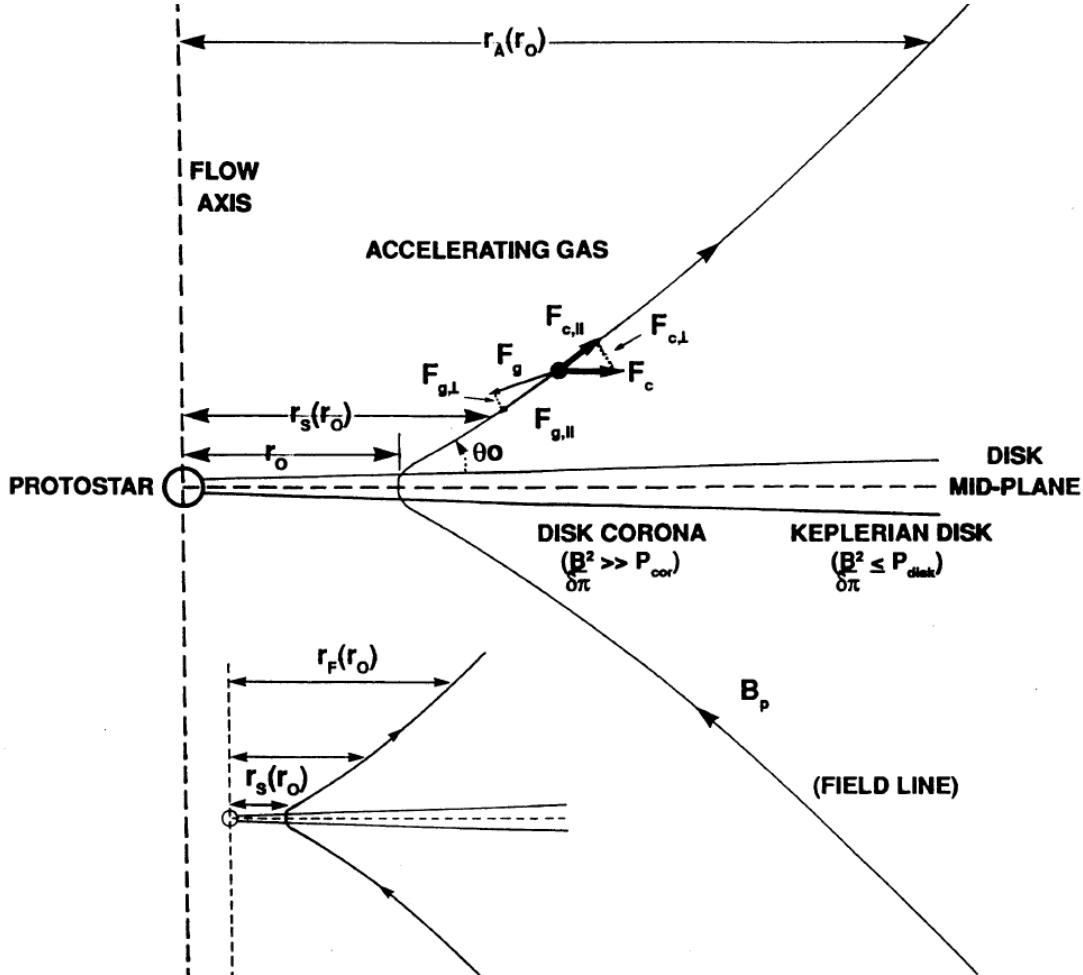


Figure 1.3: Representation of the pure disc-wind model (reproduced from Pelletier & Pudritz 1992) showing forces acting on a particle coupled to the disc's magnetic field lines (i.e. 'bead on a wire'). F_g and F_c are the gravitational and centrifugal forces respectively, with the perpendicular and parallel components of each force to the poloidal magnetic field's direction shown with an extra \perp or \parallel subscript. Important radii are r_0 , the radius in the disc at which the line is embedded, r_s , the slow magnetosonic radius (the point at which centrifugal force dominates gravity and the particle accelerates away from the disc), r_F , the fast magnetosonic radius (the point at which centrifugal acceleration ceases and an increasing toroidal magnetic field collimates the flow) and r_A , the Alfvén radius.

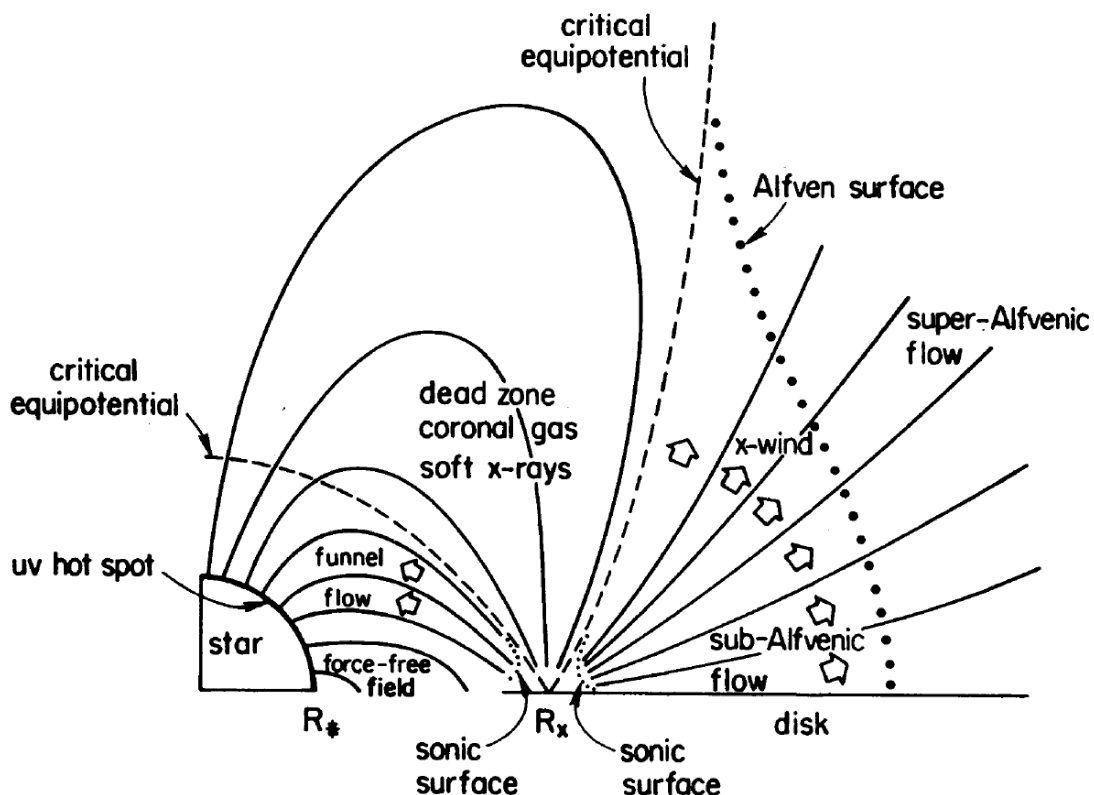


Figure 1.4: Representation of the X-wind model (reproduced from Shu *et al.* 1994) showing jet streamlines and the X-point (R_x) where the material is launched from.

magnetic fields further away from the disc’s mid-plane focus the ionised material, resulting in a collimated, ionised jet. When applied to massive star formation, the X-wind model presents a problem since stellar magnetic fields are intrinsically related to the convective nature of their protostars. For low-mass protostars, these convective models adhere well to reality with the onset of deuterium burning (Stahler 1988). Simulations of the protostellar evolution of MYSOs, (e.g. Hosokawa & Omukai 2009) show them to evolve through radiative as well as convective stages, meaning the window for stellar magnetic fields is limited in time.

Differentiating between these two models presents an observational challenge

due to the small spatial scales on which differences are apparent. In terms of the launching radius from the disc itself, the pure disc-wind model suggests material launches from a range of radii from the disc (< 100 au), almost asymptotically from the disc's surface to its rotation axis (see figures within Zanni *et al.* 2007, for MHD simulations showing such). A X-wind model suggests that the launching radius is well defined, limited in range and not far from the inner truncation radius of the disc itself (≤ 10 au) where the X-shaped lines of centrifugal/gravitational equipotential are located. Morphologically the degree of collimation for the launched jet with disc-winds will be greater, while X-winds have a lower collimation (Pudritz *et al.* 2007) and wider opening angle. Observations of collimated, parsec-scale jets (e.g. HH 80-81, IRAS 17527-2439, IRAS 13481-6124 from Marti *et al.* 1993; Varricatt 2011; Kraus *et al.* 2010, respectively) may therefore show that the X-wind model does not apply, however Shu *et al.* (2000) suggest that the highest density material at the centre of the jet encounters the lowest density material in the surrounding envelope at the poles of the evacuated cavities, thus offering a mechanical form of collimation. Magnetically, disc-winds only require a magnetic field originating in the disc whose field lines are $\leq 60^\circ$ from the disc's surface (Blandford & Payne 1982), whereas X-winds require protostellar magnetic fields, however polarimetric observations close to the forming massive star/disc are difficult. Primarily therefore, differentiating between the two models could be achieved by measurements of the launching radius whereby large radii would signify the dominance of the disc-wind model.

Due to current resolution limitations however, differentiating between these mechanisms on the scale of the launching radii (i.e. ≤ 10 au) is impossible for even the nearest massive star forming regions. Other differentiating characteristics

would be investigating ejection/accretion ratios, investigating the cross-sectional profile of the jets (which should be layered for disc winds) or (perhaps solely for the low mass case where there is a defined disc truncation radius) looking for the presence of dust in the flow. For studies at current resolutions, the former method is likely the most promising. However, it suffers from poor determination of both accretion (using NIR line proxies for accretion rates e.g. Cooper *et al.* 2013) and ejection mass loss rates, which can be overcome by large scale statistical surveys.

1.4.2 How are they ionised?

From the discussions of subsection 1.4.1, a common prerequisite for the launching of collimated jets is the coupling of jet material to magnetic fields achieved through the ionised state of the material itself. However the exact method by which the inflowing gas is ionised *prior* to launch is uncertain. Therefore this poses the question, if we were to track material as it flows from clump to core to disc to MYSO, at what point do the constituent atoms become ionised and how? Available mechanisms for the ionisation of a gas are those of thermal ionisation at high temperatures, photoionisation ($E_\gamma > 13.6$ eV in the case of hydrogen) or collisional (shock) ionisation.

Considering the case of thermal ionisation first, the structure of an accretion disc can be approximated using the α -disc model of Shakura & Sunyaev (1973) and consequently, using typical MYSO disc parameters (Ilee *et al.* 2013), the mid-plane temperatures, densities and, with the use of the Saha equation (Equation 1.2), ionisation fractions in the disc can be calculated. Results are shown in Figure 1.5 and show that the number density of electrons in the mid-plane (i.e.

at its highest) is only of the order 10^6 cm^{-3} . Considering that observationally established jet number densities *away* from the launching site are $\geq 10^5 \text{ cm}^{-3}$ (Caratti o Garatti *et al.* 2015), this would appear too low as a source of ionisation. Alternatively, collimation at significant heights above the disc may increase the density to observed values, if sourced from a range of radii.

$$\begin{aligned} \frac{\chi_i^2}{1 - \chi_i} &= \frac{1}{n} \frac{(2\pi m_e kT)^{\frac{3}{2}}}{h^3} e^{-\frac{13.54 \text{ eV}}{kT}} \equiv \alpha \\ \Rightarrow \chi_i &= \frac{-\alpha + \sqrt{\alpha^2 + 4\alpha}}{2} \end{aligned} \quad (1.2)$$

Where χ_i is ionisation fraction, n is gas number density and T is gas temperature.

Photoionisation is considered next, whereby the photons are emitted as the result of high stellar photospheric temperatures. On average MYSOs in the mass range $8 M_\odot < M_\star < 25 M_\odot$ have jet mass loss rates of $\sim 10^{-5} M_\odot \text{ yr}^{-1}$ (Purser *et al.* 2016) requiring a minimum UV photon flux of $N_{Ly} > 4 \times 10^{44} \text{ sec}^{-1}$ to ionise their flow, an estimate which does not take into account geometrical (i.e. disc exposure), dust shielding or optical depth effects thereby assuming every photon is absorbed exclusively by jet material. This flux corresponds to an $8 - 9 M_\odot$, B2 ZAMS-type (zero age main sequence) star (Davies *et al.* 2011), however how this relates to an MYSO which has not yet settled into its ZAMS configuration is unclear. Models incorporating high accretion rates of $10^{-3} M_\odot \text{ yr}^{-1}$ (Hosokawa & Omukai 2009) predict that a forming massive star remains in a bloated state with low surface temperature ($< 7000 \text{ K}$), and therefore low UV-flux production, for its entire evolution on to the main sequence. The same work also showed that low accretion rates of $10^{-5} M_\odot \text{ yr}^{-1}$ led to much higher photospheric temperatures

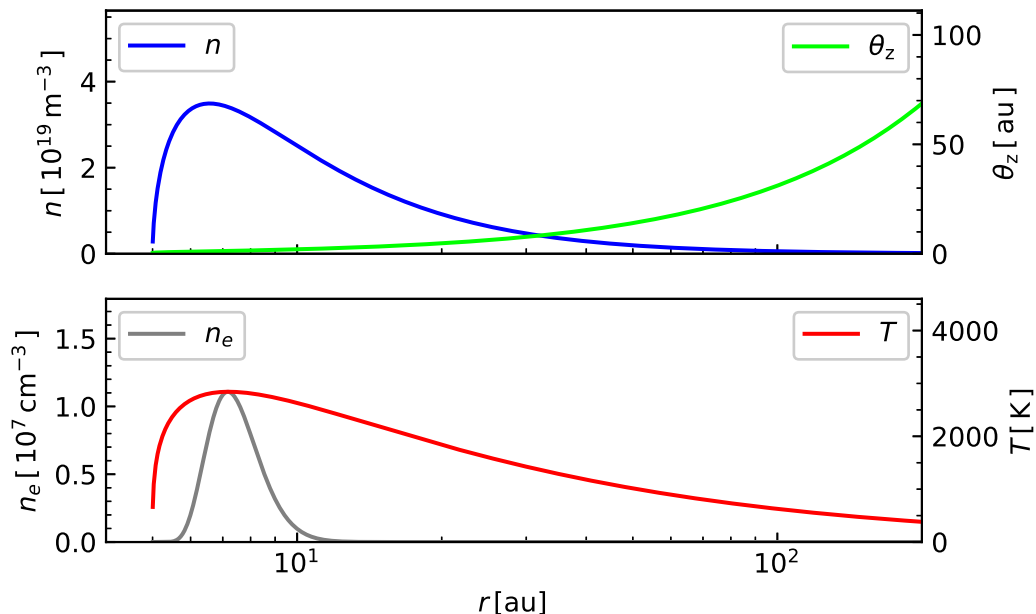


Figure 1.5: Calculated values of number density, disc FWHM (θ_z), temperature and ionisation fraction (χ_i) using the α -disc model of Shakura & Sunyaev (1973). Values used in the model were $\alpha = 1$ (i.e. a fully viscous disc), $R_i = 5$ au (inner disc radius), $\dot{M} = 10^{-3} M_{\odot} \text{yr}^{-1}$ (mass accretion rate) and $M_{\text{MYSO}} = 20 M_{\odot}$ (mass of the central object).

capable of producing significant Lyman fluxes from a mass of $4 M_{\odot}$ and greater, but considering the high mass loss rates observed, constant low accretion rates are unlikely.

Collisional ionisation presents itself through a range of potential scenarios. Parkin *et al.* (2009) modelled the interaction between radiatively driven stellar and disc winds with material in the cavity walls (and disc surface) for a $30 M_{\odot}$ MYSO. Not only did this reproduce the X-ray emission seen towards some MYSOs (Broos *et al.* 2007), but in doing so shock-ionised material to temperatures of up to $\sim 10^8$ K. However their simulations were initiated with cavities already pre-evacuated via jet activity and therefore did not attempt to ascertain how jets'

material ionises prior to launch. An attractive consequence of the X-wind model (described in subsection 1.4.1) is the production of accretion ‘hotspots’ on the protostellar surface (a result of protostellar magnetic fields) which would become significant sources of UV radiation, in turn photoionising disc material in the inner disc and outer disc surface. In the low-mass regime, a mechanism of shock-ionisation from a stellar wind on ambient material is favoured (Curiel *et al.* 1987), though this mechanism also applies for accretion shocks in the disc.

Generally the assumption in the literature is that either a high-velocity protostellar wind provides a source of collisional ionisation (as with low mass cases where photoionisation is insufficient, Anglada 1995), or that ionised material is already present in the disc itself. However, from the range of possible solutions to this problem, no conclusive supporting evidence establishing the dominance of a particular ionisation mechanism has been found for the massive case.

1.4.3 What do they look like?

1.4.3.1 Radio

Continuum radio emission from ionised jets is dominated by two processes, thermal free-free and non-thermal free-free (synchrotron) emission. Thermal emission processes take place throughout the ionised gas component of the jet while the latter traces magnetically-accelerated, relativistic, unbound electrons within the jet’s stream. Since average velocities of the ionised jet are of the order $\sim 500 - 1000 \text{ km s}^{-1}$ (for MYSOs, see subsection 1.4.4) and using the Maxwell-Boltzmann distribution for electron velocities, only $\sim 1\%$ of electrons ($v_{\text{jet}} = 1000 \text{ km s}^{-1}$ and $T_e = 10000 \text{ K}$) possess speeds whereby $\frac{v}{c} > 0.001$ with a vanish-

ingly small number with $\frac{v}{c} > 0.1$. Therefore to attain relativistic velocities, other mechanisms must be found to accelerate the radiating particles to a significant fraction of c . Realistically this can only be accomplished within shocks via the first order Fermi acceleration mechanism, whereby energy is imparted to electrons each time they cross a shock's boundary from 'upstream' to 'downstream' or vice versa.

From these considerations, we expect to see emission at radio wavelengths from:

1. Direct emission from the jet's ionised gas (free-free)
2. Indirect emission from shock-ionised gas (synchrotron and free-free):
 - (a) Internal shocks within the jet possibly resulting from time-variable ejection velocities.
 - (b) External shocks by the jet impinging upon surrounding material (e.g. cavity walls).

$$t_{rec} = \frac{1}{n_e \alpha(H, 10^4 \text{ K})} \quad (1.3)$$

Where t_{rec} is the recombination time (s), n_e is the electron density (cm^{-3}) and $\alpha(H, T)$ is the recombination coefficient for hydrogen at temperature, T ($= 2.3 \times 10^{-13} \text{ cm}^3 \text{ s}^{-1}$ where $T = 10^4 \text{ K}$ Stahler & Palla 2008). It is important to note this recombination coefficient only takes into account recombinations to energy levels with $n \geq 2$ since the ground state recombination results in the emission of an ionising photon which re-ionises a nearby HI atom.

When it comes to the direct emission from the jet’s ionised gas, one may expect recombination rates to play an important role in the physical extent of the emission (in the absence of further ionisation mechanisms). The recombination timescale for ionised hydrogen (with $T = 10^4$ K) is shown in Equation 1.3 and for typical ionised jet number densities at shock sites ($\sim 10^4 \text{ cm}^{-3}$, e.g. Curiel *et al.* 2006) is of the order ~ 7 yr. At the base of the jet, much higher densities ($\sim 10^9 \text{ cm}^{-3}$) should make the recombination timescale much shorter (< 1 day). However, because the jet’s cross-section increases along its propagation axis (i.e. $n_e(r) \propto r^{-2}$) and the process of recombination itself subsequently emits an ionising photon, which re-ionises a nearby atom, this scale will be much greater.

An analytic work by Reynolds (1986) properly quantified the behaviour of an ionised jet’s properties with frequency. As well as assuming no (overall) recombination in the flow in the majority of models, power-law behaviour was expected for a number of observable quantities based upon the ratio of optically thick to thin emission along the length of the jet’s beam. Consequently a jet’s major-axis extent (from launch to its $\tau = 1$ surface) is expected to be $\sim 200 - 3000$ au ($0.07'' - 1''$ for $D = 3$ kpc), over the frequency range 1 GHz – 50 GHz, for the ‘standard’ spherical case (using $n_0 = 10^9 \text{ cm}^{-3}$, launch radius of 10 au and initial jet half-width of 5 au). This reduction in the jet’s length with frequency is a power law (Equation 1.4) with spectral index γ defined in Equation 1.5, where β is the power-law index for the electron number density with radius (Equation 1.6). Radio flux from the jet’s stream also obeys a power-law with frequency (Equation 1.7) with a spectral index α (Equation 1.8). A typical value of $\gamma = -0.7$ and $\alpha = 0.6$ is derived for a conical, non-collimated, non-recombining jet (i.e. the ‘standard case’), a value which is commonly observed towards real examples (e.g.

Cepheus A HW2; W75N(B)-VLA 2; S140-IRS1 from Curiel *et al.* 2006; Carrasco-González *et al.* 2015; Maud *et al.* 2013, respectively) and also mimics that of a spherical (i.e. $n_e \propto r^{-2}$) wind (Panagia & Felli 1975).

$$\theta_\nu = \theta_{\nu_0} \left(\frac{\nu}{\nu_0} \right)^\gamma \quad (1.4)$$

$$\gamma = -\frac{2.1}{2\beta - 1} \quad (1.5)$$

$$n_e(r) = n_e(r_0) \left(\frac{r}{r_0} \right)^\beta \quad (1.6)$$

$$S_\nu = S_{\nu_0} \left(\frac{\nu}{\nu_0} \right)^\alpha \quad (1.7)$$

$$\alpha = -\frac{4\beta - 6.2}{2\beta - 1} \quad (1.8)$$

Synchrotron emission on the other hand possesses typical negative spectral indices (in its optically thin regime) of $\alpha = -0.5$ since $S_\nu \propto \nu^{\frac{(1+p)}{2}}$ where p is the electron energy distribution index (Rybicki & Lightman 1979) with a typical value of -2 . In the optically thick case synchrotron emission produces a spectral index of $+2.5$. With regard to jets, for synchrotron emission, the physical mechanism of ionisation confines the extent of the flux to the vicinity of the shocked surface. Should this shocked surface move (e.g. as a result of jet precession), the position of the radio flux would move with it.

Aside from continuum emission, there are several important masing lines commonly seen towards thermal jets in massive star forming regions. The CH_3OH $5_1 - 6_0$ 6.67 GHz line is radiatively pumped by infrared photons and is exclusively seen towards sites of massive star formation (Minier *et al.* 2003) naturally lending itself to studies of MYSOs. Both the disc surface and cavity walls of

an MYSO would be likely emission sites due to exposure to pumping radiation, high methanol column densities ($> 2 \times 10^{15} \text{ cm}^{-3}$ required) and limiting hydrogen number densities (must be $< 10^8 \text{ cm}^{-3}$). Other common maser lines seen are the collisionally/radiatively pumped $\text{H}_2\text{O } 6_{16} - 5_{23}$ 22.24 GHz line and both the main (1665 MHz/1667 MHz) and satellite (1612 MHz/1720 MHz) lines of the radiatively pumped hydroxyl molecule. Although these emission lines do not trace jet material, they can be used to measure magnetic fields through Zeeman splitting at high resolution with VLBI (e.g. Sanna *et al.* 2015; Surcis *et al.* 2015) and, of direct relevance to this work, pinpoint the location of accretion discs (for CH_3OH masers) and therefore constrain exact positions of MYSOs.

1.4.3.2 mm/Sub-mm

In the sub-mm regime, continuum emission is dominated by cold ($T < 50 \text{ K}$) dust heated by local star formation activity. Massive star forming clumps are particularly well revealed at these wavelengths (e.g. Urquhart *et al.* 2014b) but the most relevant observations come from line emission by molecules entrained in molecular outflows (see section 1.3). Depending on the exact species and transition, these outflows can trace further away from, or closer to, the (presumably) driving ionised jet. SiO is particularly useful since it only emits in its gas phase into which it is liberated by the action of shocks upon dust grains from collimated jets. A particularly good low mass example can be found towards HH212 (Codella *et al.* 2007) whereby the SiO emission is confined to $< 4^\circ$ from the jet axis. High mass examples are also present in the literature (e.g. the collimated SiO outflow towards the MYSO G24.78+0.08, Codella *et al.* 2013), though at much lower effective resolution and in lower numbers. Other commonly used molecules are CO

and its isotopes, HCO^+ or CH_3OH , with transitions at higher excitation temperatures generally tracing regions nearer to the powering jet. Many active, massive star-forming regions are particularly complex, powering multiple outflows leading to source confusion.

At mm wavelengths, continuum emission from both the accretion disc and envelope is seen, however depending on the exact spectral indices of both the dust and jet, the exact contribution from both warm and ionised materials varies from case to case. In comparison with observations at cm-wavelengths, the structures observed tend to be perpendicular in major axis orientation from the jet's outflow axis (e.g. Cepheus A HW2, Patel *et al.* 2005), or can have quadrupolar morphology if contributions from both jet and disc are present (e.g. HH80/81, Carrasco-González *et al.* 2012).

1.4.3.3 Infrared

Observational technology in the far-infrared precludes the scales required to image direct and indirect emission from a jet upon the surrounding material (e.g. resolution of Herschel at $200\ \mu\text{m}$ is $\sim 17''$).

In the near-infrared, several relevant atomic and molecular line transitions are found. The most important are the $1.644\ \mu\text{m}$ [FeII] and $2.122\ \mu\text{m}$ $\text{H}_2(v = 1 - 0)$, S(1) shock-excited lines. Since a jet interacts with ambient material at high velocities, these shocks are common along the jets' paths (e.g. left panel of Figure 1.6) and several studies have made use of this to study collimated outflows from all mass regimes of star formation (e.g. Caratti o Garatti *et al.* 2015; Navarete *et al.* 2015, who found the shock features to align well with overall molecular outflow directions). Near-infrared continuum emission towards embedded MYSOs is typ-

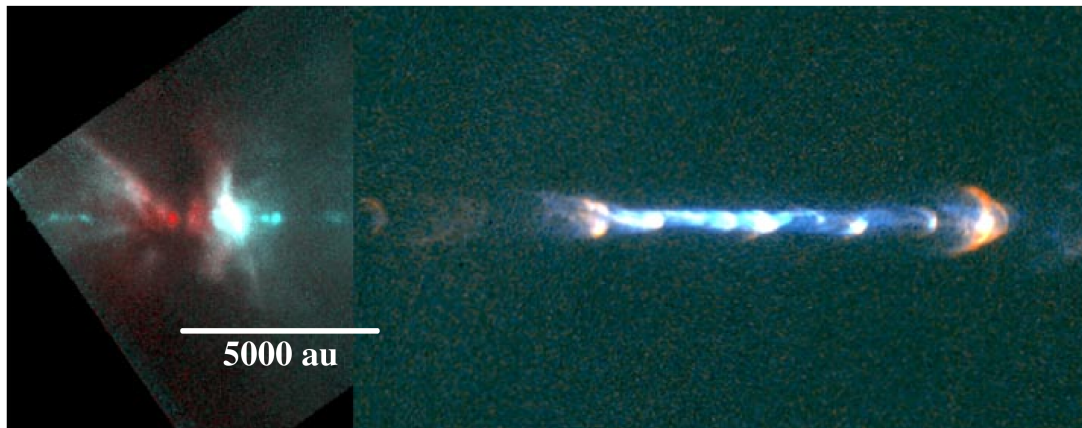


Figure 1.6: Hubble space telescope image of HH111 at optical (right) and near-infrared (left) wavelengths taken from Reipurth *et al.* (1999). In the optical image, [SII] is coloured blue and H α as orange, while in the near-infrared image, blue represents $1.4 - 1.7 \mu\text{m}$ (which includes the $1.64 \mu\text{m}$ [FeII] line) and red represents $1.7 - 2.3 \mu\text{m}$ (which includes the $2.12 \mu\text{m}$ H $_2$ line).

ically dominated by scattered light from the outflow cavities surrounding the jet propagation axis.

At mid-infrared wavelengths, $8.0 \mu\text{m}/4.5 \mu\text{m}/3.6 \mu\text{m}$ RGB imagery (i.e. GLIMPSE wavebands) is a useful tool for observing indirect emission from a jet due to the presence of extended green objects (EGOs). These $4.5 \mu\text{m}$ excesses are the result of shock-excited line emission increasing the flux for the overall $4.5 \mu\text{m}$ continuum band. Lines included in the $4.5 \mu\text{m}$ IRAC band, which is sensitive to wavelengths in the range $4 \mu\text{m} - 5 \mu\text{m}$, are the fundamental CO ($1 - 0$) ro-vibrational (centred on $4.5 \mu\text{m}$ but extending over the whole bandpass) and H $_2(v = 1 - 0)$, S(9, 10, 11) ($4.18 \mu\text{m}$, $4.41 \mu\text{m}$ and $4.69 \mu\text{m}$ respectively) transitions. An unbiased survey using GLIMPSE data which looked for EGOs showed strong correlations between 6.7 GHz CH $_3\text{OH}$ maser activity (see subsection 1.4.3.1) and the green excesses suggesting them to track protostellar outflows from MYSOs specifically (Cyganowski *et al.* 2008).

1.4.3.4 Optical

Optical jets towards low-mass YSOs are commonly seen and a plethora of HST observations towards such objects exist (e.g. HH1/2, HH30, HH47 and HH111; Hester *et al.* 1998; Burrows *et al.* 1996; Heathcote *et al.* 1996; Reipurth *et al.* 1997, respectively). Typically continuum observations in V and R bands (551 nm and 658 nm) show the jet's emission due to the presence of shock-excited, bright lines in such bands (most notably $[\text{S II}]_{\lambda 6717}$, $[\text{S II}]_{\lambda 6731}$, $[\text{H}\alpha]_{\lambda 6300}$ and $[\text{O I}]_{\lambda 6300}$). However in the high-mass case, because throughout their entire evolution MYSOs are obscured by optically thick material, no optical observations are possible and this wavelength regime remains unstudied.

1.4.4 Previous Observations

The HH80–81 jet

At a distance of 1.7kpc (Rodriguez *et al.* 1980) the infrared source IRAS 18162–2048 (G010.8411–02.5919 in this work) is the powering object of the Herbig-Haro objects HH80 and HH81. A study by Marti *et al.* (1993) using VLA observations at 1.5, 5, 8 and 15 GHz revealed a multitude of radio knots separated by an average of ~ 1400 au, with IRAS 18162–2048 ($L_{\text{bol}} \sim 2 \times 10^4 L_{\odot}$) at their geometric centre. A central, elongated source with a derived spectral index of $\alpha = 0.2 \pm 0.1$ and centred on the infrared source, was suggested to represent a biconical, ionised jet in keeping with the models of Reynolds (1986). The radio lobes were interpreted to represent working surfaces upon which the neutral jet acted upon, with spectral indices of $\alpha = -0.3 \pm 0.1$ for the lobes HH80, HH81 and HH80 North. Furthermore, the jet was shown to be highly collimated, with

an opening angle of $\sim 1^\circ$. Careful analysis of the radio lobe positions along the jet's axis, showed a sinusoidal path indicating a precession in the outflow axis with a period of 5500 years. Proper motions in the lobes ranging from 600 to 1400 kms^{-1} were found in a later work combining observations over a time period of 4 years (Marti *et al.* 1995). Compared to other ionised jets in the literature, this example is one of the most extended, with a distance between the terminal shocks of HH80 North and HH80 of 5.1pc.

A later study by Carrasco-González *et al.* (2010a) observed polarised, synchrotron emission in the radio lobes close ($\sim 0.5 \text{ pc}$) to the jet's launching point. Inferred magnetic field lines ran parallel to the jet's outflow axis, a configuration expected of a helical, magnetic field confining the flow of the ionised material at its centre. This represents the only occurrence of this type of observation for ionised jets around MYSOs.

Cepheus A HW2

Located in the cloud complex, Cepheus OB3, Cepheus A hosts a great deal of star formation activity (see Rodriguez *et al.* 1994, and references therein). Observations between 1.5 and 43 GHz with the VLA (Rodriguez *et al.* 1994) towards Cepheus A HW2, showed an elongated ($\theta_{P.A.} \sim 40^\circ$) structure in the maps of radio flux, with an asymmetric tail to the south west (interpreted to be shock ionisation as a result of the jet's interaction with surrounding material). A spectral index of $\alpha = 0.69 \pm 0.06$ and power-law constant for the variation of major axis length with frequency of $\gamma = -0.57 \pm 0.02$ were inferred. These values are close to the typical values expected of a non-confined, biconical jet ($\alpha \sim 0.6, \gamma \sim -0.7$; Reynolds 1986). The jet's elongation axis corresponded well to a HCO^+ molecular outflow's

red/blue (south west/north east respectively) axis (Gómez *et al.* 1999), while barely resolved SiO emission tentatively showed elongation perpendicular to the outflow direction. More up to date observations with the Sub-Millimeter Array (SMA) (Patel *et al.* 2005) conclusively identified a dusty disc with an inclination angle of $62 \pm 10^\circ$, radius of 330AU and mass between 1 and 8 M_\odot (protostellar mass was inferred to be $15 M_\odot$) whose major axis lay perpendicular to the jet. This represented the first bona fide example of a jet-disc system in a high-mass protostellar case. Multi-epoch observations constrained the proper motions of the outer radio lobes to $\sim 480 \text{ km s}^{-1}$ and inferred an asymmetric, episodic style of ejection in the jet (Curiel *et al.* 2006).

IRAS 16547–4247

Using ATCA radio observations (Garay *et al.* 2003) an ionised jet system was identified with a familiar central component/outer lobe structure in association with the infrared source IRAS 16547–4247 ($L_{\text{bol}} = 1.9 \times 10^4 L_\odot$). Spectral indices were found to be 0.49 ± 0.12 , -0.33 ± 0.04 and -0.61 ± 0.26 for the central component, southern lobe and northern lobe respectively. The position angle of the outflow axis was deduced to be 161° , with a scale between outer lobes of 0.28 pc (for a distance of 2.7 kpc). Mass loss rates in the jet of $\dot{M} \sim 8 \times 10^{-6} M_\odot \text{ yr}^{-1}$ were derived, significantly exceeding the low mass case of $10^{-7} - 10^{-9} M_\odot \text{ yr}^{-1}$. A set of observations with a noise ~ 2.5 times lower than the first set (Rodríguez *et al.* 2005), detected many more radio lobes associated to the jet. These two complementary datasets show how deep radio observations should be used to reveal the full extent of ionised material emanating from the phenomena forming the subject of this thesis.

Further observations performed at different epochs over 2.68 years showed no ($> 4\sigma$) proper motions in the outer lobes of the jet, which also displayed a large precession in its outflow axis of $0.08^\circ \text{ yr}^{-1}$ (Rodríguez *et al.* 2008). The lack of any motions indicated that the outer radio lobes were the result of shock-ionisation along working surfaces where jet material collided with ambient material.

Most recently, ALMA 0.85mm observations detected a dusty, compact ($1620 \text{ au} \times 1450 \text{ au}$) component coincident with IRAS 16547 – 4247, oriented at a position angle of $115 \pm 5^\circ$. Concurrent line observations of high-excitation temperature transitions of both CH_3OH and CH_3SH , showed that at smaller scales ($< 1000 \text{ au}$), a compact, rotating structure whose major axis was perpendicular to that of the ionised jet was present, and from Keplerian arguments was inferred to be in rotation around a central mass of $20 M_\odot$ (Zapata *et al.* 2015).

IRAS 16562–3959

Although not as extensively studied as the other examples of ionised jets reviewed here, the radio free-free emission associated to this target proves morphologically interesting. Radio observations are comprised of a thermal ($\alpha = 0.85 \pm 0.15$) central component centred on the infrared source ($L_{\text{bol}} = 7 \times 10^4 L_\odot$) and 4 aligned radio lobes with flat spectral indices ($\alpha \sim -0.1$) symmetrically arranged either side (Guzmán *et al.* 2010), similar to other examples. The inferred mass loss rate was $\dot{M} \sim 2 \times 10^{-6} M_\odot \text{ yr}^{-1}$, and proper motions in the inner/outer radio lobes were extrapolated to determine terminal velocities in the jet of ~ 360 and $\sim 280 \text{ km s}^{-1}$, for eastern and western components respectively. A quadrupolar morphology of $\text{CO}(6 \rightarrow 5)$ and $\text{CO}(7 \rightarrow 6)$ was observed by Guzmán *et al.* (2011), suggesting the presence of two molecular outflows, one aligned with the radio jet

($\dot{P} = 3.0 \times 10^{-2} M_{\odot} \text{ km s}^{-1} \text{ yr}^{-1}$) and another oriented in the N-S direction. In this thesis the designation, G345.4938+01.4677, is adopted for this object.

Two previous radio surveys

Guzmán *et al.* (2012) surveyed 7 out of 33 potential high mass young stellar object (HMYSO) candidates for ionised jets, in the southern hemisphere. Criteria used to select the sample were a positive radio spectral index, large bolometric luminosity ($L_{\text{bol}} > 2 \times 10^4 L_{\odot}$) of which most lies in the infrared (due to dust extinction), an association with a luminous IRAS source and an under-luminosity in the radio compared to that expected from an optically-thin HII region. These potential jet-harboring YSOs were consequently followed up by ATCA radio observations at 1.4, 2.4, 4.8, and 8.6 GHz whose respective resolutions were 7'', 4'', 2'', and 1''.

Following radio observations, spectral index calculations and consideration of other wavelength observations, 2 out of the 33 candidates were definitively identified as MYSOs with ionised jets; G337.4032–00.4037 and G345.4938+01.4677. Another five of the sample were categorised as either HCHII or UCHII regions based on their physical sizes and emission measures (size $< 0.03 \text{ pc}$, $\text{EM} > 10^8 \text{ pc cm}^{-6}$ for HCHII; size $< 0.1 \text{ pc}$, $\text{EM} > 10^6 \text{ pc cm}^{-6}$ for UCHII). On the basis that 37.5 %, 37.5 % and 25 % of the observed objects were categorised as jets (including G343.1261–00.0623), HCHII regions and UCHII regions respectively, it was inferred that the ‘jet-stage’ of a forming massive star lasts $\sim 4 \times 10^4 \text{ yr}$.

Another survey by Moscadelli *et al.* (2016) aimed to detect collimated outflow activity using a combination of multi-epoch, VLBI observations of water/methanol masers and high-sensitivity ($\sigma \sim 10 \mu\text{Jy}$) JVLA continuum observations (C, Ku

and K bands). A distance-limited ($D < 9$ kpc) sample of 40 high-mass star forming regions were selected from the BeSSeL maser survey under the criteria that they were radio weak (< 50 mJy), compact ($\theta_{maj} < 1''$), possessed a bolometric luminosity corresponding to ZAMS types B3 - O7 and possessed 10, or more, bright (> 1 Jy) maser spots (to map the outflow kinematics effectively). Of these 40 regions a sub-sample of 11 were reported upon. Five of the objects were categorised as collimated, ionised jets on the basis of radio continuum morphology, spectral index and maser spatial and 3D velocity distribution. The other six were complex in the relationship of these two aspects and no definitive conclusions were drawn about them. Two of the five jets showed associated non-thermal emission in lobes spatially distinct from, but definitely associated to, the central, thermal jet.

1.5 The RMS Survey

In order to guide future surveys of ionised jets towards MYSOs, reliable samples of radio weak MYSOs are required as a sample base. The RMS survey (Lumsden *et al.* 2013) is a systematic search for MYSOs using previous surveys as well as mm, radio and infrared follow-up observations to aid in the classification of objects catalogued by the Midcourse Space eXperiment (MSX).

In order to extract genuine MYSO candidates from the MSX database, contaminant objects such as planetary nebulae, old dusty stars and resolved ultra-compact HII regions had to be removed. Since most of the bolometric luminosity of a MYSO lies at infrared wavelengths (due to dust reprocessing), a comparison of fluxes at a variety of IR-wavelengths (based on known MYSOs) was employed.

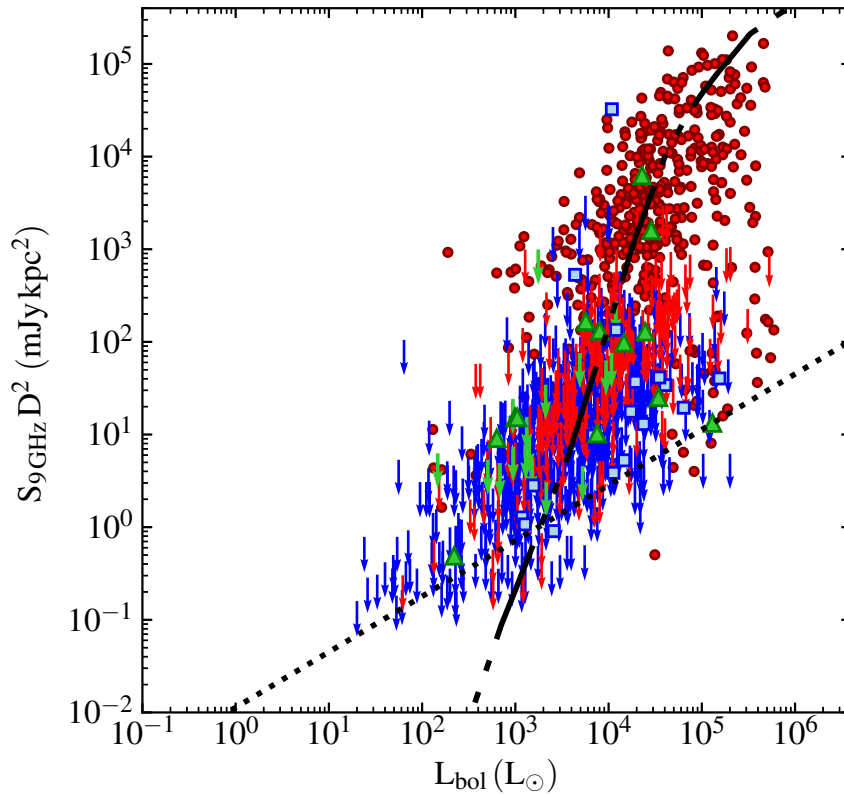


Figure 1.7: A plot of all HII regions and YSOs catalogued by the RMS survey. All data points are contained in the full catalogue (Lumsden *et al.* 2013). Circles (red) represent HII regions, squares (blue) are YSOs and green triangles are ambiguous classifications as HII regions or YSOs. Lower limits for those HII regions (red), YSOs (blue) and HII/YSOs (green) not detected are also shown. The dot-dashed line represents the ionised flux expected from the Lyman continuum, taken from stellar models by Davies *et al.* (2011) for $L_{\text{bol}} > 10^3 L_{\odot}$, and Thompson (1984) for $L_{\text{bol}} \leq 10^3 L_{\odot}$. The dotted line represents the empirical relation derived for the low-mass regime (Anglada 1995; Shirley *et al.* 2007; AMI Consortium *et al.* 2011), normalized to 9 GHz (assuming $\alpha = 0.6$).

The exact colour-cuts used in the sample selection were, $2.5 \text{ Jy} > F_{21 \mu\text{m}} > F_{14 \mu\text{m}} > F_{8 \mu\text{m}} > 5F_{\text{K}} > 10F_{\text{J}}^*$ where $F_{21 \mu\text{m}} > 2F_{8 \mu\text{m}}$ (Lumsden *et al.* 2013).

VLA and ATCA observations at 5 GHz ($\theta_{\text{res}} \sim 1''$) helped to remove resolved UCHIIIs (Urquhart *et al.* 2007a, 2009b), while CO observations by MOPRA

*Where J and K-band data were taken from the 2-micron all sky survey (2MASS).

($^{13}\text{CO}(1-0)$) and JCMT ($^{13}\text{CO}(3-2)$) allowed the removal of close, low-mass YSOs by the determination of kinematic distances and therefore absolute luminosities (Urquhart *et al.* 2007b). The relative strength of the CO lines helped eliminate dusty, evolved stars (stronger in young stars) while those evolved stars lying along the line of sight to molecular clouds were picked out on the basis of their distinct near-IR spectra.

After this selection process, the resulting RMS database catalogues ~ 1600 embedded, young massive stars (Urquhart *et al.* 2014a) of which both HII regions and MYSOs are included. In Figure 1.7, the radio fluxes recorded for these objects are plotted against their infrared-derived bolometric luminosities.

1.6 Thesis outline

As shown throughout this chapter, the study of forming massive stars and their associated ionised jet phenomena, is an observationally demanding discipline. Not only do high confusion rates, which arise from their naturally clustered environments, play a role in this difficulty, but so also do their distances, embedded natures and rarity. To further progress our knowledge of massive star formation and ionised jet launching/collimation mechanisms, large, statistical samples are required, exacerbating our problems further.

Therefore, in light of the absence of large-scale statistical surveys (see subsection 1.4.4) of MYSO jets, this work makes use of the RMS survey to provide a statistically-sized sample of MYSOs, with which to progress our understanding of their associated ionised jets. Radio interferometry is used to negate the effects of their dense environments, in fine enough detail and resolution, to glean the

properties of the sample's objects. It is this sample, towards which radio interferometric observations have been conducted using the ATCA, whose analysis forms the basis of chapter 2, which aims to identify how common ionised jets are towards massive forming stars, and establish their general properties. After that, a smaller, more sensitive set of observations were conducted towards a small subset (4 objects) of the sample from chapter 2, in chapter 3. Purposes of this investigation were to look for faint radio emission, variability and proper motions of the ionised jets, in an effort to constrain jet-formation models. The last major work is presented in chapter 4, which turned its attention to ionised jets associated with MYSOs located in the northern sky. Using the superior resolution and sensitivity of the VLA, at both C (6 cm) and Q (7 mm) bands, the general properties of the ionised jets are investigated, as well as the scales whereby collimation may take place. Although this line of inquiry mirrors that of chapter 2, it differs from that work, not only in the spatial scales probed, but also by the inclusion of a sample of IRDC cores with which the earliest phases of massive star formation, and therefore of jet production, are investigated. These 3 major works, and the conclusions stemming from them, are tied together and summarised in chapter 5 to conclude this thesis.

Chapter 2

An RMS Survey for Ionised Jets Around MYSOs

An in depth review of possible mechanisms for massive star formation has already been discussed (subsection 1.2.2), with the main similarity between the two competing concepts of core accretion McKee & Tan (2003) and competitive accretion (Bonnell *et al.* 2001) being the presence of a flattened disc. Because outflows are likely powered by accretion processes, the disc and jet can be thought of as being intrinsically linked. However observations of discs or ionised jets towards MYSOs are rare in comparison to low-mass studies (e.g. Anglada 1996; Furuya *et al.* 2003; Scaife *et al.* 2011; AMI Consortium *et al.* 2011; Ainsworth *et al.* 2012), as shown in subsection 1.4.4. In response to this lack of bonafide examples of collimated jets from MYSOs, two previous surveys (Guzmán *et al.* 2012; Moscadelli *et al.* 2016) have been conducted which identified 7 jets associated to MYSOs between them. In order to increase knowledge of both the driving mechanisms and properties of ionised jets towards MYSOs, a statistically sized sample is required. Therefore

it is the purpose of this chapter to provide the first large sample of such objects, by making use of the RMS survey from which to draw a distance-limited sample of MYSOs. Radio observations are used due to the unimpeded view of a jet's ionised gas that can be attained in this wavelength regime and I report on jets discovered, their properties and relationship to their parental clumps.

2.1 Sample Selection

In total the sample consists of 49 individual objects which are listed in Table 2.2. Of these, 34 were selected to form a distance-limited ($D < 7 \text{ kpc}$) sample of MYSOs due to the completeness limit of the RMS survey ($> 10^4 L_{\odot}$ for $D < 15 \text{ kpc}$, or $> 2 \times 10^3 L_{\odot}$ for $D < 7 \text{ kpc}$; Urquhart *et al.* 2011a). An even spread in the luminosities of the objects was required for unbiased sampling in terms of bolometric luminosity and consequently 6 of these objects fall in the range $700 L_{\odot} \leq L_{\text{bol}} < 3000 L_{\odot}$, 11 in the range $3000 L_{\odot} \leq L_{\text{bol}} \leq 10000 L_{\odot}$, 9 in the range $10000 L_{\odot} \leq L_{\text{bol}} \leq 30000 L_{\odot}$ and 8 with $L_{\text{bol}} > 30000 L_{\odot}$. It is worth noting that derived bolometric luminosities have changed for some of the sample since the observations. The previous observations of Urquhart *et al.* (2007a) have demonstrated them all to be radio weak at 8 GHz with $S_{\nu} < 2 \text{ mJy}$ and therefore not powering compact, optically-thin HII regions (for those with $L_{\text{bol}} > 10^4 L_{\odot}$ Davies *et al.* 2011). These sources are at elevations conducive to more circular synthetic apertures with the ATCA, whereby $\delta < -34^{\circ}$. Targets with declinations greater than the quoted cut-off have been included due to their scientific value, as well as filler objects for allocated times when the other sources were not fully risen above the horizon (i.e. elevation $< 20^{\circ}$). A further 8 sources were added

to complete the observations (at 17 and 22.8 GHz) which Guzmán *et al.* (2012) performed from 1.4 to 8.6 GHz with the ATCA. One of the Guzmán sample (G317.4298-00.5612) was observed at 5 and 9 GHz to check for variability. Four of the objects were added on the basis of being associated to $4.5 \mu\text{m}$ excesses, or extended green objects (EGOs Cyganowski *et al.* 2008), a signature of shocks possibly caused by jet activity (Smith & Rosen 2005). The latter two samples were not distance-limited and also were used to fill in coverage in right ascension.

2.2 Observations

2.2.1 Radio observations with the ATCA

All radio observations were made using the Australia Telescope Compact Array (ATCA; See chapter 1, §1 of Frater *et al.* 1992, for an overview) in the 6A and 6B configurations, over a period of 12 days, spread over 4 years. A total of 49 individual, compact objects were observed at 4 different frequency bands (centred on 5.5, 9.0, 17.0 and 22.8 GHz). These frequencies were observed using a bandwidth of 2048 MHz (XX, YY, XY, and YX polarizations) split evenly either side of the central frequencies (an overview of the CABB correlator’s capabilities can be found in Wilson *et al.* 2011). This bandwidth was split into channels of width 1 MHz (minimising the averaging out effect of RFI over broad channels and giving the ability to easily recognise and flag it). From this point on the frequency bands observed shall be referred to as the 5.5, 9, 17 and 22.8 GHz bands.

The highest frequency band has been also chosen to incorporate the $\text{H}_2\text{O}(6 \rightarrow 5)$ transition at 22.235 GHz, in order to observe masing activity and allow more

Band (GHz)	ν_{RRL} (GHz)	RRL	Δv (km s ⁻¹)
5.5	4.61879	H112 α	64.9
	4.74418	H111 α	63.2
	4.87416	H110 α	61.5
	5.00892	H109 α	59.9
	5.14870	H108 α	58.2
	5.29373	H107 α	56.6
	5.44426	H106 α	55.1
	5.60055	H105 α	53.5
	5.76288	H104 α	52.0
	5.93154	H103 α	50.5
	6.10686	H102 α	49.1
	6.28914	H101 α	47.7
	6.47876	H100 α	46.3
9	8.04560	H93 α	37.3
	8.30938	H92 α	36.1
	8.58482	H91 α	34.9
	8.87257	H90 α	33.8
	9.17332	H89 α	32.7
	9.48782	H88 α	31.6
	9.81686	H87 α	30.5
17	16.56329	H73 α	18.1
	17.25821	H72 α	17.4
	17.99256	H71 α	16.7
22.8	22.36417	H66 α	13.4
	23.40428	H65 α	12.8

Table 2.1: A table of the observable radio recombination lines for each observed band, and the associated velocity resolution per 1 MHz channel.

accurate, phase-only self-calibration from the relevant channels.

Due to the broad radio recombination lines (half-widths at zero intensities of $> 400 \text{ km s}^{-1}$) observed in pre-HCHII regions (Figure 5 of Hoare & Franco 2007), RRLs may be observable in the strongest sources of the sample, giving some degree of kinematic information for the ionised gas. Table 2.1 shows the radio recombination lines falling within the observed bands and their effective, velocity resolutions for a channel width of 1 MHz.

The range of scales the instrument was sensitive to were $2.0\text{--}16.5''$, $1.2\text{--}10.1''$,

0.6 – 5.4'' and 0.5 – 4.0'' over the 5.5, 9, 17 and 22.8 GHz frequency bands respectively. These correspond to a maximum baseline length of 6 km and a minimum of ~ 300 m.

Individual scan times on flux and phase calibrators were typically 5 minutes and 90 seconds respectively and on target sources were between 5 and 20 minutes dependent on observing frequencies. The average total integration time on each science target, τ_{int} , was ~ 75 minutes. Observations at 5.5 and 9 GHz were all conducted during February 2013, with a typical RMS noise level calculated to be 17 and 20 $\mu\text{Jy beam}^{-1}$ respectively. The upper two frequency bands were observed during the months of February 2010, April 2011, September 2011 and January 2012, giving a range of conditions particularly affecting the 22.8 GHz band which is more sensitive to atmospheric water vapour content (greater during the southern hemisphere's summer months). Theoretical RMS noise levels therefore range between 40 – 41 and 73 – 106 $\mu\text{Jy beam}^{-1}$ for the 17 and 22.8 GHz bands respectively, during the months of September (lower noise) and January. As a note, the typical values for the RMS noise were calculated assuming the removal of 200 channels (100 at each edge of the bandwidth), RFI interference, typical weather during the relevant months, $\delta \sim -50^\circ$ and a robustness of 0.

2.2.2 Data reduction

For calibrating and cleaning the data, the Multichannel Image Reconstruction Image Analysis and Display (MIRIAD) software package (Sault *et al.* 1995) was used. For the measurement of various parameters, the Common Astronomy Software Applications (CASA) was implemented (McMullin *et al.* 2007).

Table 2.2: Target sources observed by ATCA between 12/02/2010 and 28/02/2013, their RMS survey names, positions, bolometric luminosities, distances (Lumsden *et al.* 2013), which epoch they were observed in and their final classification.

RMS Name	α (J2000)	δ (J2000)	D (kpc)	L_{bol} (L_{\odot})	5.5/9 (GHz)	17/22.8 (GHz)	Class.
G010.8411–02.5919*	18 ^h 19 ^m 12.09 ^s	–20°47′30.90″	1.9 ^a	2.40×10^{4b}	–	E2	Jet
G012.9090–00.2607*	18 ^h 14 ^m 39.56 ^s	–17°52′02.30″	2.4 ^c	3.20×10^{4a}	–	E3	Jet (C)
G014.9958–00.6732*	18 ^h 20 ^m 19.47 ^s	–16°13′29.80″	2.0 ^c	1.30×10^{4c}	–	E3	Jet (C)
G251.2337–01.9535	08 ^h 02 ^m 42.97 ^s	–34°31′48.70″	4.6 ^a	8.20×10^{3a}	E5	E4	Jet (C)
G254.0491–00.5615	08 ^h 15 ^m 57.12 ^s	–36°08′06.80″	3.0 ^a	1.70×10^{3a}	E5	E1	Jet
G254.0548–00.0961	08 ^h 17 ^m 52.62 ^s	–35°52′47.60″	2.8 ^a	1.90×10^{3a}	E5	E1	Jet (L)
G263.2283+01.5712	08 ^h 53 ^m 09.46 ^s	–42°13′07.60″	0.7 ^d	1.20×10^{3b}	E5	E1	Jet
G263.7434+00.1161	08 ^h 48 ^m 48.64 ^s	–43°32′29.00″	0.7 ^d	1.20×10^{3a}	E5	E1	Jet (L)
G263.7759–00.4281	08 ^h 46 ^m 34.84 ^s	–43°54′29.80″	0.7 ^d	1.30×10^{3a}	E5	E1	Jet (L)
G265.1438+01.4548	08 ^h 59 ^m 27.40 ^s	–43°45′03.70″	0.7 ^d	7.19×10^{2c}	–	E1,E4	Jet/DW
G268.3957–00.4842	09 ^h 03 ^m 25.08 ^s	–47°28′27.50″	0.7 ^d	3.00×10^{3a}	–	E1	N/D
G274.0649–01.1460A	09 ^h 24 ^m 42.54 ^s	–52°01′50.60″	5.7 ^a	6.00×10^{3a}	E5	E4	HCHII
G282.2988–00.7769	10 ^h 10 ^m 00.32 ^s	–57°02′07.30″	3.7 ^a	4.00×10^{3b}	–	E1	N/D
G283.9146–01.0485	10 ^h 18 ^m 49.96 ^s	–58°10′11.30″	4.9 ^a	6.00×10^{3a}	–	E1	N/D
G284.2438–01.1302	10 ^h 20 ^m 35.17 ^s	–58°25′07.10″	4.2 ^a	4.40×10^{3a}	E5	E1	CHII
G286.2086+00.1694	10 ^h 38 ^m 32.70 ^s	–58°19′14.30″	2.3 ^a	8.00×10^{3a}	–	E1	Jet (L,C)
G287.3716+00.6444	10 ^h 48 ^m 04.55 ^s	–58°27′01.50″	4.5 ^a	1.80×10^{4b}	E5	E1	CHII
G298.2620+00.7394	12 ^h 11 ^m 47.68 ^s	–61°46′18.80″	4.0 ^a	1.50×10^{4a}	E5	E3	DW
G300.9674+01.1499†	12 ^h 34 ^m 53.22 ^s	–61°39′40.00″	4.3 ^a	4.50×10^{4c}	–	E4	UCHII
G301.1364–00.2249†	12 ^h 35 ^m 35.13 ^s	–63°02′31.60″	4.3 ^a	3.80×10^{5a}	–	E3	HCHII
G305.1940–00.0051‡	13 ^h 11 ^m 14.44 ^s	–62°47′25.50″	4.0 ^b	7.00×10^{3a}	E5	–	N/D

Notes: Sample selection is indicated by the superscripted symbol on each source’s name, whereby \star indicates a filler object of scientific value, \dagger indicates an object which is part of the Guzmán *et al.* (2012) sample and \ddagger indicates an MYSO associated to an EGO (Cyganowski *et al.* 2008). Any source without a symbol is part of the distance limited sample. The footnote marks for the distances indicate how they were calculated: a) kinematic distance determined using the source velocity; b) spectrophotometric distance; c) maser parallax distance; d) distances taken from the literature. The footnote marking for the bolometric luminosities show the relevant calculation methods which were: a) spectral energy distribution (SED) fit to the available infrared fluxes (e.g., 2MASS, MSX) including HiGAL (Mottram *et al.*, in prep.); b) SED fit to infrared and either MIPS GAL 70 μm or IRAS Galaxy ATLAS 60 μm fluxes (Mottram *et al.* (2010), Mottram *et al.* (2011b)); c) MSX 21 μm band flux using a scaling relationship determined from a comparison with sources where SED fits have been possible (Mottram *et al.* 2011b). Also included are the epochs during which their data was recorded by the ATCA for the 5.5/9 GHz setup and 17/22.8 GHz setup. The epoch notation corresponds to the following dates: E1, 12/02/2010–13/02/2010; E2, 16/04/2011; E3, 10/09/2011–11/09/2011; E4, 05/01/2012–07/01/2012; E5, 25/02/2013–28/02/2013. Date ranges include all dates in between those provided. Hyphenated table cells denote the source not being observed at the relevant frequencies. The final column denotes each object’s final classification, whereby HII regions follow the accepted acronyms, N/D indicates a non-detection, U/K indicates where no robust classification could be made, DW indicates a disc-wind, while Jet/DW indicates an ambiguous classification and the presence of an (L) and/or (C) after ‘jet’ indicates whether lobes were present and/or the object was only classified as a jet candidate, respectively.

Table 2.2: Continued

RMS Name	α (J2000)	δ (J2000)	D (kpc)	L_{bol} (L_{\odot})	5.5/9 (GHz)	17/22.8 (GHz)	Class.
G305.2017+00.2072A	13 ^h 11 ^m 10.45 ^s	−62°34′38.60″	4.0 [†]	$3.00 \times 10^{4\dagger}$	–	E4	U/K
G305.5610+00.0124	13 ^h 14 ^m 26.36 ^s	−62°44′30.40″	4.0 [†]	$1.20 \times 10^{4*}$	E5	E4	HCHII
G308.9176+00.1231A	13 ^h 43 ^m 01.70 ^s	−62°08′51.20″	5.3 [*]	$9.00 \times 10^{4*}$	–	E4	UCHII
G310.0135+00.3892	13 ^h 51 ^m 37.85 ^s	−61°39′07.50″	3.2 [*]	$6.70 \times 10^{4*}$	E5	E3	Jet (L)
G310.1420+00.7583A	13 ^h 51 ^m 58.27 ^s	−61°15′41.70″	5.4 [*]	$8.00 \times 10^{3*}$	E5	E4	Jet (L)
G313.7654−00.8620 [‡]	14 ^h 25 ^m 01.53 ^s	−61°44′57.60″	7.8 [*]	$6.10 \times 10^{4*}$	E5	–	Jet (L)
G317.4298−00.5612 [†]	14 ^h 51 ^m 37.59 ^s	−60°00′19.40″	14.2 [*]	$3.50 \times 10^{5*}$	E5	–	HCHII
G317.8908−00.0578 [†]	14 ^h 53 ^m 06.16 ^s	−59°20′59.40″	13.6 [*]	$6.30 \times 10^{4*}$	–	E2	UCHII
G318.9480−00.1969A	15 ^h 00 ^m 55.31 ^s	−58°58′52.60″	2.4 [*]	$1.00 \times 10^{4*}$	E5	E3	Jet/DW
G326.6618+00.5207	15 ^h 45 ^m 02.84 ^s	−54°09′03.00″	1.8 [†]	$1.40 \times 10^{4*}$	E5	E2	Jet (C)
G327.1192+00.5103	15 ^h 47 ^m 32.80 ^s	−53°52′39.30″	4.9 [*]	$3.70 \times 10^{4*}$	E5	E2	Jet
G331.3576+01.0626	16 ^h 06 ^m 25.78 ^s	−50°43′22.00″	4.5 [*]	$1.80 \times 10^{4*}$	E5	E3	Jet (C)
G331.5414−00.0675 [‡]	16 ^h 12 ^m 09.00 ^s	−51°25′47.00″	5.0 [*]	$6.00 \times 10^{4*}$	E5	–	UCHII
G332.0939−00.4206	16 ^h 16 ^m 16.46 ^s	−51°18′25.20″	3.6 [†]	$9.30 \times 10^{4*}$	E5	E2	Jet (L)
G332.8256−00.5498A	16 ^h 20 ^m 11.06 ^s	−50°53′16.20″	3.6 [†]	$1.30 \times 10^{5*}$	E5	E2	UCHII
G332.9868−00.4871	16 ^h 20 ^m 37.81 ^s	−50°43′49.60″	3.6 [†]	$1.80 \times 10^{4*}$	E5	E4	Jet (C)
G337.8442−00.3748 [†]	16 ^h 40 ^m 26.68 ^s	−47°07′13.10″	3.0 [*]	$3.70 \times 10^{4*}$	–	E2	HCHII
G338.9196+00.5495	16 ^h 40 ^m 34.04 ^s	−45°42′07.90″	4.2 [*]	$3.20 \times 10^{4\dagger}$	E5	E3	Jet (C)
G339.6221−00.1209	16 ^h 46 ^m 05.99 ^s	−45°36′43.90″	2.8 [*]	$1.90 \times 10^{4*}$	E5	–	Jet (L,C)
G339.8838−01.2588	16 ^h 52 ^m 04.66 ^s	−46°08′33.60″	2.7 [*]	$6.40 \times 10^{4\dagger}$	E5	E2	Jet (L)
G340.0543−00.2437A	16 ^h 48 ^m 13.69 ^s	−45°21′42.50″	3.8 [*]	$2.90 \times 10^{4*}$	E5	–	Jet (C)
G340.2480−00.3725 [†]	16 ^h 49 ^m 29.97 ^s	−45°17′44.40″	3.7 [*]	$3.40 \times 10^{4*}$	–	E2	UCHII
G343.1261−00.0623 [†]	16 ^h 58 ^m 17.20 ^s	−42°52′07.10″	2.8 [*]	$1.90 \times 10^{4*}$	–	E2, E4	Jet (L)
G343.5213−00.5171	17 ^h 01 ^m 34.04 ^s	−42°50′19.70″	3.2 [*]	$6.70 \times 10^{3*}$	E5	E4	Jet (L,C)
G345.4938+01.4677 [†]	16 ^h 59 ^m 41.61 ^s	−40°03′43.30″	2.4 [†]	$1.50 \times 10^{5\dagger}$	–	E2	Jet (L)
G345.5043+00.3480	17 ^h 04 ^m 22.87 ^s	−40°44′23.50″	2.0 [*]	$1.00 \times 10^{5*}$	E5	E4	Jet (C)
G345.9561+00.6123	17 ^h 04 ^m 43.00 ^s	−40°13′13.40″	2.5 [*]	$2.40 \times 10^{3*}$	E5	E3	U/K
G348.6972−01.0263 [‡]	17 ^h 19 ^m 58.91 ^s	−38°58′14.80″	2.8 [†]	$1.30 \times 10^{5*}$	E5	–	UCHII

Multi frequency synthesis was used to image the visibility datasets, and at 5.5, 9 and 17 GHz, the multi-frequency CLEAN algorithm (MFCLEAN in miriad) was used to account for the variation in intensity distribution with frequency, since the fractional bandwidth is $> 12.5\%$ (Sault & Wieringa 1994). In Fourier transforming the data, the visibilities were weighted according to T_{sys} in order to down-weight data taken at times of increased atmospheric instability and thus improve the signal-to-noise ratio of the resultant images. This acted to improve the accuracy of recorded fluxes, at the cost of more elongated restoring beams.

Phase only self-calibration was performed on any strong point source (extended sources give erroneous solutions for the limited baseline numbers of the ATCA) in the field of view, and solutions were applied only if they converged over the course of multiple iterations (in terms of the rms deviations on the gain phases). Time intervals over which to produce calibration solutions took account of the calibrating source's flux and the frequency of the observations (since the atmosphere is more stable at lower frequencies). At 22.8 GHz, if masing activity was present for the 22.23508 GHz water line, the strongest channel was imaged and used as a model for phase-only self-calibration. Simultaneous amplitude and phase self calibration was not performed on any of the datasets since there are not enough constraints with 15 baselines to solve for both the real and imaginary parts of the gains.

2.2.3 Flux recovery with the 6km configuration

As a check, modelling was performed on a synthetic dataset in order to calculate how much flux is resolved out at each observing frequency. This is an expected ef-

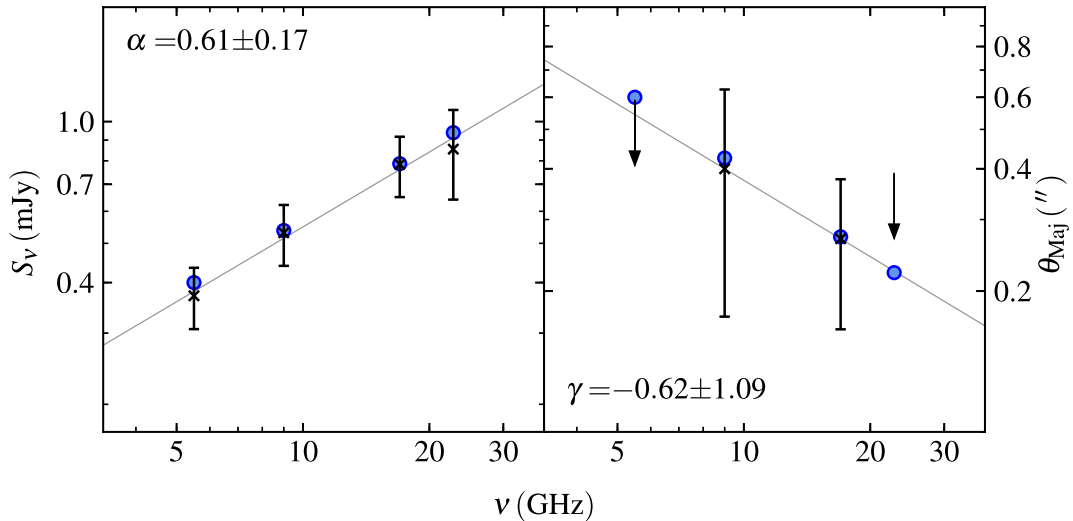


Figure 2.1: The plotted fluxes (left) and deconvolved major axes (right) for both the model (blue circles) and those recovered through deconvolution with a Gaussian (crosses), for a synthetic dataset. The best fits to the measured fluxes and major axes are shown as grey lines. Error bars on the recovered fluxes include the adopted absolute flux-scale uncertainties expected from observations using the ATCA (see subsection 2.3.1). Upper limits on the recovered major axes are also shown. Model parameters used were, $\alpha = 0.6$, $\gamma = -0.7$, $\theta_{\text{maj}} = 0.6''$ (major axis at 5.5 GHz) and $\theta_{\text{min}} = 0.21''$ (minor axis at 5.5 GHz).

fect of interferometry, since the shortest baseline (in units of wavelength) increases in size with increasing frequency and consequentially, the array’s scale-sensitivity drops for larger spatial scales.

The synthetic dataset was created with the use of the miriad task, UVGEN, and mirrors the real observations. Total time on target (positioned at the pointing/phase centres) for the fake observations was 90 minutes, split into five separate 18 minute scans with visibility integration times of 5 seconds. An elevation limit of 30° was imposed (equivalent to a range in hour angle of $-5^{\text{h}} \leq \tau \leq 4^{\text{h}}$), and the source declination used (-60°) is conservative (for the sample) in terms of the maximum elevations for scans ($< 60^\circ$). Typical values of the system temperature

of 30K, 35K, 45K and 100K were used for the 5.5, 9, 17 and 22.8 GHz bands respectively. For the model a source with a spectral index $\alpha = 0.6$, a major axis index $\gamma = -0.7$, and a total flux (at 5.5 GHz) of 0.4 mJy was used. Both spectral indices, α and γ were defined in Equations 1.7/1.8 and 1.4/1.5 respectively and the values employed here are representative of a typical ionised wind or jet (see subsection 1.4.4). The major and minor axes at 5.5 GHz were defined as $0.60''$ (position angle of 0°) and $0.21''$ respectively, corresponding to an opening angle in the jet of 20° . Restoring beams were oriented at a position angle of 175° , with major axes approximately 30% larger than minor axes.

In Figure 2.1, the model fluxes, the recovered fluxes (using the IMFIT task) and the derived spectral index/fit are shown. Flux recovered varied between 91% (at 22.8 GHz) and $> 99\%$ (at 17 GHz). A spectral index of 0.61 ± 0.17 was derived, with a derived value for γ of ~ -0.6 (physical sizes could not be deconvolved at 5.5 and 22.8 GHz). This test of the array's performance towards the types of object this paper focusses on, shows that the ATCA effectively recovers the flux and spectral index of a typical ionised jet/wind. The deconvolved sizes were not recovered at both the lower (due to SNR) and upper (due to SNR and the small spatial scales involved) frequencies, while errors were approaching 100% of the deconvolved size at 9 GHz. This shows that even for moderate SNR objects ($\sim 20\sigma$), the deconvolved dimensions may be unreliable, even though the recovered value for γ in this case is reasonably close to the model's value. Further to this point, the position angles recovered at 9 and 17 GHz ($145^\circ \pm 46^\circ$ and $126^\circ \pm 10^\circ$ respectively), were not in agreement with the model. The major implication of this result for analysis of low radio SNR sources would be upon the credibility of deconvolved position angles, which should not be taken as absolute.

Type	ν (GHz)	Field of View		
		$1^\circ \times 1^\circ$	$10' \times 10'$	$6'' \times 6''$
FRI	5.5	222	2.2	0.002
	9.0	161	1.6	0.001
	17.0	88	0.881	0.001
	22.8	41	0.414	< 0.001
FRII	5.5	22	0.225	< 0.001
	9.0	16	0.163	< 0.001
	17.0	9	0.108	< 0.001
	22.8	9	0.089	< 0.001
Star-forming	5.5	1061	11	0.008
	9.0	770	7.7	0.006
	17.0	391	3.9	0.003
	22.8	147	1.5	0.001
Total	5.5	1305	13	0.010
	9.0	947	9.5	0.007
	17.0	488	4.9	0.004
	22.8	197	2.0	0.001

Table 2.3: Predicted radio galaxy populations, interpolated from the study by Jackson (2004) using simple power laws for each population. For each frequency, different flux density limits are used (60 μJy at 5.5/9 GHz, 90 μJy at 17 GHz and 300 μJy at 22.8 GHz) typical of the observations.

Extended sources, such as UCHII regions, will likely not mirror these results.

2.2.4 Extragalactic radio sources

A study by Jackson (2004) examined the theoretical, radio, AGN population as a function of flux density and angular density. It considered and predicted FRI, FRII and star-forming galaxy populations on the celestial sphere for three flux-density limits (10 μJy being the highest) at a frequency of 1.4 GHz. From this work, the predicted populations are extrapolated to a conservative 3σ limit (60 μJy at 5.5/9 GHz, 90 μJy at 17 GHz and 300 μJy at 22.8 GHz) of this study, and further reduce the populations at each frequency in accordance with the observed average spectral index of radio galaxies ($\bar{\alpha} = -0.65$ Bornancini *et al.* 2010). In Table 2.3, the number of expected radio galaxies within 3 fields of view are listed.

This estimate shows that even at 5.5 GHz only one radio galaxy is expected, within 5'' of the pointing centre, for every 50 fields of view. Moreover the star-forming galaxy population has been overestimated, since a power-law is a rough approximation which overestimates the counts. Point-like profiles were also assumed, however this is not valid for all and it is likely that the observations will resolve many of the closer radio galaxies out, especially at the higher frequencies.

Another study by Anglada *et al.* (1998) provides extragalactic source number density estimates (their equation A2), which can be extrapolated to other frequencies (using the average spectral index value quoted above). This alternate approach produces number densities ~ 5 times lower than those calculated above across all 4 frequencies. On this basis, it is not expected that this type of object will be a concern of this chapter's analysis.

2.3 Results

Emission in 45 of the 49 fields observed is detected. All maps of radio flux are shown in Appendix A (Figures A.1–A.45) at each observed frequency. For the ionised jets identified (and other associated emission), deconvolved positions, fluxes/spectral indices and sizes/derived values for γ are again contained in Appendix B (Tables B.1–B.6). Fluxes, sizes and other derived properties of radio sources identified as HII regions are given in Table B.10. Any sources that were not part of the sample, but identified within the primary beam of the observations at 5.5 and 9 GHz, have both their fluxes (primary-beam corrected) and positions listed in Table B.13. For the measurement of all of these properties, the CASA task, IMFIT is used in the case of a compact, Gaussian-like flux distribution

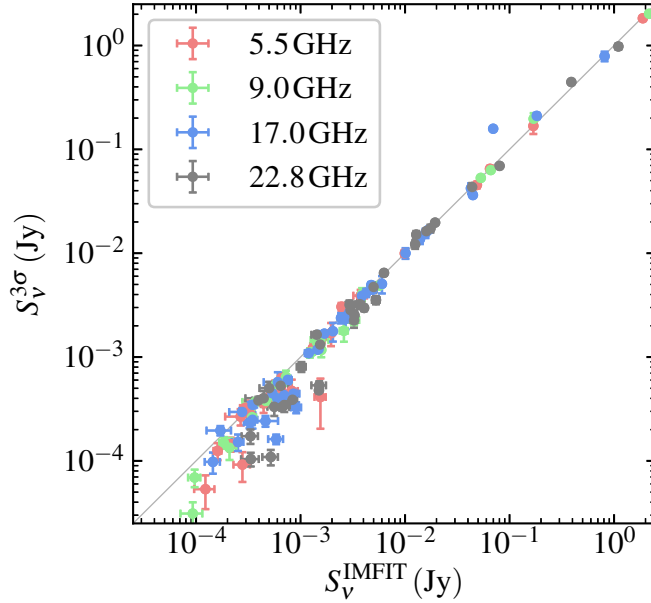


Figure 2.2: A plot of fluxes towards all object in the sample calculated via integrating pixel values contained within a 3σ aperture against those calculated by fitting a two-dimensional Gaussian to flux distribution in the image plane (CASA’s IMFIT).

whereas for extended sources (i.e. UCHII regions) flux measurement is detailed in subsection 2.3.1, while source size is deduced using Equation 2.1.

$$\theta_G = \sqrt{\theta_{\text{FWHM}}^2 - \theta_{\text{beam}}^2} \quad (2.1)$$

where θ_G , θ_{FWHM} and θ_{beam} are the deconvolved size, measured full width half maximum of the convolved flux distribution and beam full width half maximum respectively.

2.3.1 A word on calculating fluxes and their errors

Derivation of the fluxes, and their errors, calculated over finite regions in images of flux are rarely stated explicitly. This section therefore intends to clearly define the

process for the calculation of both flux and its associated error for astronomical (especially extended) objects. As a note, it must be said that calculation of flux and its errors via the fitting of a 2-dimensional Gaussian (i.e. using the IMFIT task) in the image plane, is *always* preferred for sources which are obviously of compact/Gaussian morphology. This is justified in Figure 2.2, whereby the fluxes included in the fit with a Gaussian and those in a 3σ region are indicated, showing that the summing of pixels' fluxes within the 3σ regions misses flux outside this area that the Gaussian fitting does not. This effect becomes significant for low dynamic range images and/or low signal-to-noise sources whereby the missing flux is a sizeable proportion of the source's flux. As a word of caution however, should the source be of low signal-to-noise and non-Gaussian, both methods are only an approximation of the object's true flux.

In Equation 2.2, the sum flux, ΣS_ν , is defined as the sum of all the pixels' fluxes within a defined region of an image. The sum flux is in turn equal to the product of the number of pixels, N , within the region and \bar{S}_ν , the average flux for each pixel. The flux of an object is consequently related to this image-derived sum flux by Equation 2.3, whereby θ_{maj} and θ_{min} are the major and minor axes of the clean beam and Δx is the pixel size.

$$\Sigma S_\nu = \sum_{n=1}^N S_n = S_0 + S_1 + S_2 + \dots + S_N = N\bar{S}_\nu \quad (2.2)$$

$$S_\nu = \frac{\Sigma S_\nu}{\theta_{maj}\theta_{min}} \frac{4 \ln 2 \Delta x^2}{\pi} \quad (2.3)$$

Consequently, there are two sources of error in the calculation of the flux, which are the number of pixels in the defined region and the average flux of those

pixels. From Poisson statistics, the error in the number (count) of pixels is defined to be $\sigma_N = \sqrt{N}$ and the error in the average flux is $\sigma_{\bar{S}_\nu} = \sigma_{rms} N^{-\frac{1}{2}}$. For both the error in the sum flux and error in the flux, the equations are presented in Equations 2.5 and 2.6 respectively.

$$\sigma_{\Sigma S_\nu} = \sqrt{\left(\sqrt{N}\bar{S}_\nu\right)^2 + \left(\sqrt{N}\sigma_{rms}\right)^2} \quad (2.4)$$

$$= \sqrt{\frac{\Sigma S_\nu^2}{N} + \left(\sqrt{N}\sigma_{rms}\right)^2} \quad (2.5)$$

$$\sigma_{S_\nu} = \frac{\sqrt{\frac{\Sigma S_\nu^2}{N} + \left(\sqrt{N}\sigma_{rms}\right)^2}}{\theta_{maj}\theta_{min}} \frac{4 \ln 2 \Delta x^2}{\pi} + \epsilon S_\nu \quad (2.6)$$

In Equation 2.6, the final term (ϵS_ν) is a consequence of the systematic, absolute flux-scale uncertainty. This error comes about as a result of both the intrinsic errors in the models used during flux calibration, which are a consequence of variability in the flux calibrator models since they were last updated, and atmospheric/phase stability over the course of the observations. Usually values of $0.05 \leq \epsilon \leq 0.10$ are common in the cm-radio domain and are a function of frequency, with higher frequencies prone to larger values of ϵ due to increased atmospheric instabilities. For the observations of this chapter, values of 0.05 for the 5.5, 9 and 17 GHz bands and 0.1 for the 22 GHz observations are adopted.

2.3.2 Classification of the radio emission

At the observational resolutions of this work, HCHII regions, ablated disc winds, thermal radio jets, extragalactic radio sources and Herbig-Haro objects all share

similar morphology and flux densities. This high degree of similarity between these different types of object is, by and large, the main problem in classifying compact radio sources. Determination of a radio source's exact nature is therefore an issue for which a multi-wavelength approach is adopted here. In summary, morphology, radio/bolometric flux comparison, radio-spectral features and correlation with previous observations of shock tracing lines, molecular outflows and infrared continuum form the bulk of this process. Figure 2.3 shows a more comprehensive view of the classification algorithm developed and employed here.

An initial inspection of the radio emission's morphology is usually enough to remove extended HII regions from the sample. For the more compact radio sources (some of which may be embedded in extended emission), a comparison of the measured radio fluxes with those expected from the bolometric luminosities (inferred from the models of Davies *et al.* 2011) aids in the separation of HCHIIIs and other types of objects. For this study, a cut-off of 20% of the expected radio flux (at the highest observed frequency, thus limiting optical depth effects) was used for identification. A potential pitfall at this point originates from the optical depths towards the prospective HII regions. If still in the optically thick regime (typical for HCHIIIs at the frequencies in this work), the radio flux may be underestimated leading to a false classification as a jet candidate further down the line. Therefore, to avoid an ambiguous classification as a jet/HII region, if strong, narrow Br γ emission is seen (from NIR spectra of Lumsden *et al.*, in prep.), an automatic classification as an HII region is enacted. The 1.644 μm [FeII] transition is also of interest as it is indicative of J-type shocks with shock velocities $> 50 \text{ km s}^{-1}$ (Hollenbach & McKee 1989). These shocks arise from the

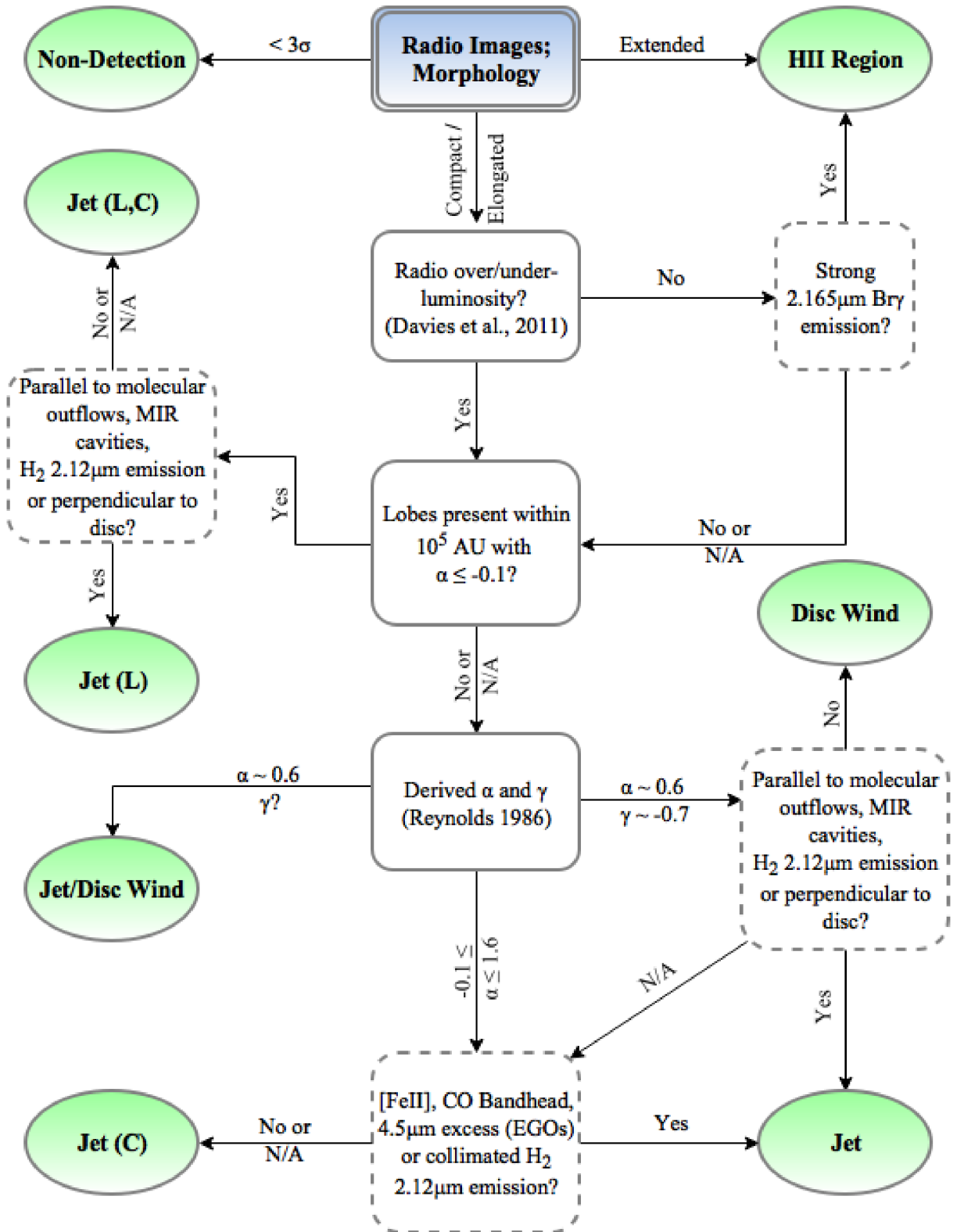


Figure 2.3: A flowchart illustrating the classification algorithm employed upon the sample of MYSOs. ‘N/A’ signifies if data is not available.

interaction of the jets with ambient material and therefore the presence of this line within the spectra is taken as evidence of ionised jets or winds. Further to this, detection of RRLs (see subsection 2.2.1) would be another method for separating jets and HII regions since jets should have much broader linewidths than HII regions (see Figure 5 of Hoare & Franco 2007).

From the radio flux maps, measurement of both α and γ enables the differentiation between various jet scenarios in accordance with the models of Reynolds (1986). The deconvolved position angle for the major axis of the jet's emission is taken to be the jet's propagation axis, which can then be compared to position angles for molecular outflows present in the literature. In cases whereby the difference between these two position angles is $< 45^\circ$ (i.e. parallel), this is taken as enough evidence to warrant classification as a jet. Should this alignment be perpendicular whilst $\alpha \sim 0.6$ and $\gamma \sim -0.7$, a disc wind scenario is deduced. Molecular outflows can be significantly decollimated however, with major to minor axis ratios of $\bar{f}_c \sim 2.1$ (Beuther *et al.* 2002b), corresponding to large opening angles of $\bar{\theta}_{\text{OA}} \sim 60^\circ$, sometimes making this comparison difficult. Another indicator in the literature for the outflow axis (to which position angles can be compared) is $2.122 \mu\text{m}$ H_2 emission (such as in G310.0135+00.3892, Caratti o Garatti *et al.* 2015) which is indicative of collisional excitation of molecular hydrogen through shocks attributable to protostellar outflows and/or large Lyman continuum fluxes (Wolfire & Konigl 1991). This emission can arise in both C and J-type shocks, unlike the [FeII] line.

Optically-thin ($\alpha \sim -0.1$, e.g. G345.4938+01.4677, Guzmán *et al.* 2010) and/or non-thermal lobes of emission ($\alpha < -0.1$, e.g. G343.1261-00.0623, Garay *et al.* 2003), may be present where the jet shock-ionises its environment through

collisional interaction at working surfaces. The alignment angle of these lobes with the central, thermal jet defines the jet's axis for which comparison with observations in the literature can be conducted. As with the deconvolved position angles of the thermal jet component, should the derived outflow axis be parallel to molecular outflows and/or $2.12\ \mu\text{m}$ H_2 emission, this is taken as evidence of a jet and classification as a jet with lobes is made. If perpendicular, classification as a candidate jet with lobes is instead decided on account of the disparity between outflow axes inferred in the literature and in this work.

It is important to emphasize at this point that classification is not an absolute procedure and each case is assessed individually. Although the process presented above provides a robust algorithm in the majority of cases, proper consideration is still required especially in low signal to noise examples where full information cannot be recovered.

2.3.3 Object results

From the sample I report the identification of 28 sources with the characteristics expected of ionised jets, two of which can be identified as either disc-winds or ionised jets (G265.1438+01.4548 and G318.9480-00.1969A) and twelve of which are given the classification of jet candidate. One source (G298.2620+00.7394) is identified as a disc wind. Of the original sample, 14 HII regions (5 HCHII, 7 UCHII and two compact HII regions) have been identified, with 6 other UCHII regions identified in the fields of view for the images. The conditions for classification of the UCHII regions are based on those of Wood & Churchwell (1989). It is also important to note that in cases where there is no clear cut distinction, based

upon radius and emission measure, the measured, physical radius of the HII region takes precedence in the classification process.

Four of the sources were not detected at any observing frequency (G268.3957–00.4842, G282.2988–00.7769, G283.9146–01.0485, and G305.1940–00.0051). Figure 2.4 shows these non-detections as upper-limits, assuming spectral indices of $\alpha = 0.6$ in cases where no 9 GHz data was available.

Two objects evaded classification, G305.2017+00.2072A and G345.9561+00.6123. G305.2017+00.2072A imaging displayed extended, partially resolved-out emission $\sim 10''$ to the SSW of the pointing centre complicating its deconvolution through dynamic range limitations. Removing shorter baselines did not help to improve the images significantly. Although a faint, compact component was present at 17 and 22.8 GHz coincident with both the MSX point source position and a 6.7 GHz methanol maser, a spectral index of -1.1 ± 1.5 was calculated. With a bolometric luminosity of $2.4 \times 10^3 L_{\odot}$, G345.9561+00.6123 is one of the less luminous MYSOs in the sample. For the radio emission from an optically thin HII region, a value for $S_{9\text{GHz}} D^2$ (see subsection 2.4.1) of 1.6 mJy kpc^2 is expected for $L_{\text{bol}} = 2400 L_{\odot}$, the measured value being $(0.56 \pm 0.13) \text{ mJy kpc}^2$ at 9 GHz and $(1.75 \pm 0.44) \text{ mJy kpc}^2$ at 17 GHz. Either this may represent an optically thin (at 17 GHz or above), small, emergent HII region or an ionised jet with a large range of possible spectral indices, hence why it remains unclassified.

In summary, the objects reported here have had their classifications tabulated in Table 2.4.

Table 2.4: A summary of the numbers and types of objects within the sample, as well as their incidence rate with water masers in the 22.8 GHz band (which takes account of which sources were observed at 22.8 GHz and which were not).

Type	Sub-type	Count	Masers?	(%)
Ionised Jet	with lobes	10	7	78
	w/o lobes	4	2	50
Ionised Jet (C)	with lobes	3	1	50
	w/o lobes	9	4	50
Jet/Disc Wind	-	2	1	50
Disc wind	-	1	0	0
HII region	HCHII	3	1	50
	(embedded)			
	HCHII	2	1	50
	(isolated)			
	UCHII	7	5	100
	Compact HII	2	1	50
Unknown	-	2	0	0
Non-detection	-	4	-	-

2.4 Analysis and Discussion

The analyses presented in this section make use of the Kendall-tau rank correlation test (Kendall 1938) in order to examine the degree of correlation between various observables. It is used on the basis that it is a non-parametric test, making no assumptions of underlying distributions. Results for each of the correlations presented throughout this section are summarised in Table 2.5. For consistency, the Kendall-tau correlation coefficient for measured flux (not distance flux, $S_\nu D^2$) with distance is calculated to be $\tau = 0.18$ with a p-value of 0.38, showing an absence of a Malmquist bias (i.e. brighter objects are preferentially detected at larger distances) in the distance-limited sample. For fitting the data, a simple power-law is assumed and the method of least squares employed.

Table 2.5: A summary values for the Kendall-Tau coefficient of correlation, the associated p-value, for both the distance-limited (D/L) sample of detected jets and all jets detected (the second column). Presence of (J) next to the sample type denotes jet classifications only, while the absence denotes jets and candidate jets. The size of each sample is tabulated in the third column. τ_p represents the partial Kendall-Tau correlation coefficient and the associated p-value (p_p), whilst controlling for distance.

(x, y)	S	n	τ	p	τ_p	p_p
(L _{bol}	D/L (J)	10	0.674	0.007	0.479	0.023
vs.	D/L	22	0.418	0.006	0.294	0.062
S _{νD²})	All (J)	14	0.552	0.006	0.479	0.023
	All	28	0.423	0.002	0.351	0.010
(M _{clump}	D/L (J)	05	0.800	0.050	0.802	0.102
vs.	D/L	14	0.626	0.002	0.548	0.009
S _{νD²})	All (J)	08	0.643	0.026	0.645	0.042
	All	17	0.603	< 0.001	0.551	0.039
(M _{clump}	D/L (J)	05	0.400	0.327	0.535	0.276
vs.	D/L	14	0.473	0.019	0.476	0.023
M _{Jet})	All (J)	08	0.357	0.216	0.382	0.228
	All	17	0.485	0.007	0.486	0.009
(L _{bol}	D/L (J)	10	0.809	0.001	0.742	0.005
vs.	D/L	21	0.600	< 0.001	0.550	< 0.001
F _{Jet})	All (J)	14	0.818	< 0.001	0.796	< 0.001
	All	25	0.617	< 0.001	0.586	< 0.001

2.4.1 Radio luminosity vs. bolometric luminosity

Using the parameters of stellar atmospheres reported in Davies *et al.* (2011) (for $L_{\text{bol}} > 10^3 L_{\odot}$), it is possible to infer both the spectral type, and UV photon flux, of a ZAMS star with a specific bolometric luminosity. Since the Lyman flux is intrinsically associated with the amount of material which a young protostar can ionise, the radio continuum flux expected from an optically thin HII region produced by such a UV flux can be inferred. Therefore, using this expected radio flux from the bolometric luminosities of the objects, can help to distinguish between HII regions and less evolved phases of massive star formation (see subsection 2.3.2). The specific radio luminosity expected for ionised jets and winds

is not as easy to constrain, due to a lack of theoretical models which incorporate all the variables likely influencing the radio luminosity of jets. Therefore, in order to establish an idea of the fluxes expected of these objects, the empirical relations of radio luminosity with bolometric luminosity derived by Anglada (1995), Shirley *et al.* (2007) and AMI Consortium *et al.* (2011) of $S_\nu D^2 \propto L_{\text{bol}}^{0.6}$, $S_\nu D^2 \propto L_{\text{bol}}^{0.51 \pm 0.26}$ and $S_\nu D^2 \propto L_{\text{bol}}^{0.71 \pm 0.01}$ respectively, are utilised. As these relations are derived from low-mass samples with maximum bolometric luminosities $< 10^3 L_\odot$, they serve as a comparison for the fluxes expected for thermal jets from MYSOs. Should the mechanism for ionisation/jet production be different to the, assumed in the low-mass case, models of shock-ionisation (Curiel *et al.* 1987), a deviation towards the higher masses of the MYSOs should be seen.

Figure 2.4 shows structure attributable to the clear divide between the bright, HII regions near the expected Lyman-continuum line and the jet-like objects which are not as bright as expected from their bolometric luminosities. The HII regions which occupy radio luminosities similar to those of the jets are either resolved out extended regions (higher bolometric luminosities), or are small HCHII regions around lower bolometric luminosity objects. Those HII regions which have lower than expected radio fluxes are usually still in the optically thick regime. It is worth noting that lower radio luminosities for the HII regions may be seen in comparison to those expected from the models of Davies *et al.* (2011), due to significant dust absorption of Lyman continuum photons (Wood *et al.* 1988).

For 9 GHz radio luminosity against bolometric luminosity, the jets themselves can be fitted (distance-limited sample) with a power-law with an index of 0.63 ± 0.21 ($\tau = 0.67$, p-value= 0.007). Fitting all jets/candidate (28 sources) yields an index value of 0.75 ± 0.17 . It must be added that fitting the low-mass jet

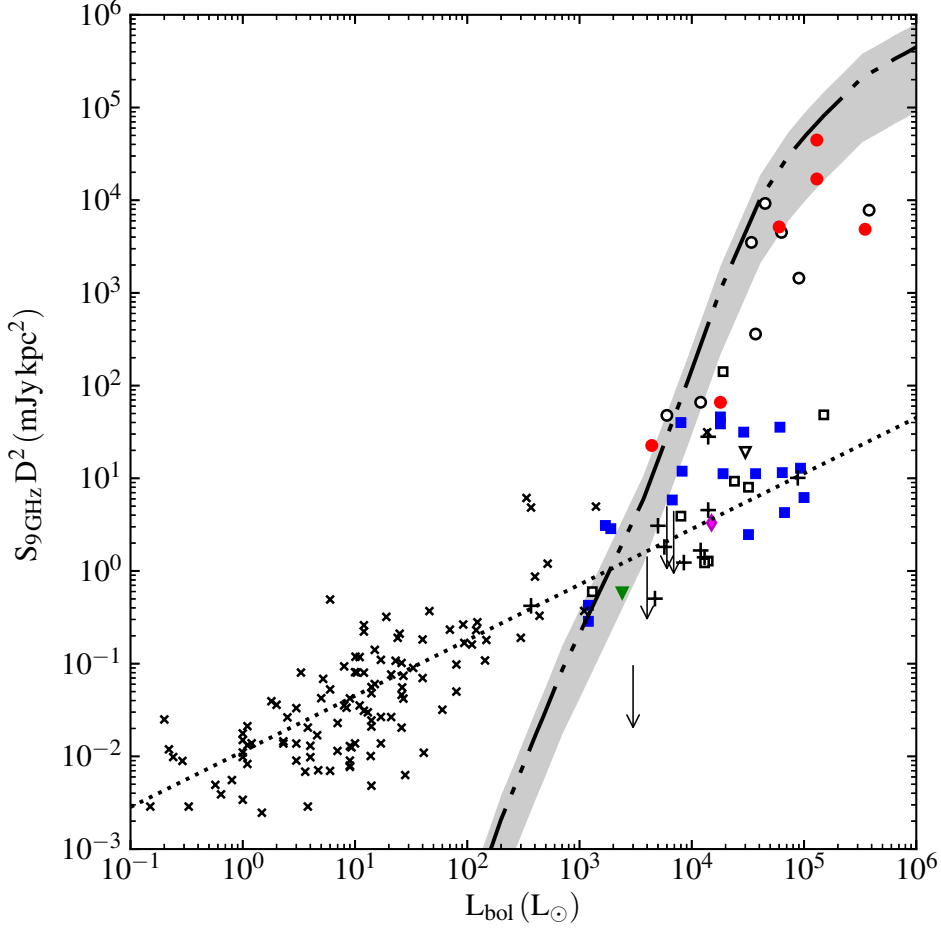


Figure 2.4: A plot of the 9 GHz distance-luminosities against bolometric luminosity for all detected objects (apart from non-thermal lobes) in the sample. Circles represent HII regions, squares represent ionised jets, diamonds represent disc-winds, triangles represent unknown sources and ‘ \times ’ markers mark low-mass cases normalized to 9 GHz (assuming $\alpha = 0.6$ in the case of flux at only one frequency, Anglada 1995; Furuya *et al.* 2003; AMI Consortium *et al.* 2011). Coloured (red for HII regions, blue for jets, magenta for disc-winds and green for unknown) symbols show cases where the flux has been directly measured at 9 GHz, while hollow symbols show cases where the flux has been interpolated from measured spectral indices and higher frequency observations. The ‘+’ symbols represent the sample of high-mass jets from Moscadelli *et al.* (2016). Lower limits ($< 3\sigma$) of non-detections are shown. The dot-dashed line represents the ionised flux expected from the Lyman continuum, taken from stellar models by Davies *et al.* (2011) for $L_{\text{bol}} > 10^3 L_{\odot}$, and Thompson (1984) for $L_{\text{bol}} \leq 10^3 L_{\odot}$. Grey shading represents the area where the radio-luminosity is between 20 – 180% of that expected from the bolometric luminosity (for a HII region). The dotted line represents the empirical relation derived for the low-mass case (Anglada 1995; Shirley *et al.* 2007; AMI Consortium *et al.* 2011), normalized to 9 GHz (assuming $\alpha = 0.6$).

sample of Anglada (1995) with the same algorithms as employed upon the high-mass sample yields a higher coefficient of 0.67 ± 0.10 ($\tau = 0.55$, p-value < 0.001) than that recorded by Anglada (1995). When fitting both the high-mass and low-mass sample of jets together, a coefficient value of 0.64 ± 0.04 ($\tau = 0.73$, p-value $\simeq 0$) is calculated. These results imply that similar processes explain the ionisation within the high-mass jets, as with their lower mass counterparts (i.e. the shock-ionisation models of Curiel *et al.* 1987). Some jets however have higher fluxes similar to that expected from HII regions (such as G310.1420+00.7583A). This may be explained by a developing HCHII at small radii around the MYSO, existing with the collimated jet contemporaneously, although higher resolution observations would be required to determine this (sub-milliarcsecond for 15 au at a distance of 3 kpc). In such cases, these objects perhaps may represent transition objects between jet and HII phases (e.g. the case of G345.4948+01.4677 in the work by Guzmán *et al.* 2016).

Of the 34 MYSOs from which the distance-limited sample is comprised, a total of 22 objects displaying the characteristics of ionised jets are detected. Of these, 10 (3 of which are candidates) are associated with radio lobes, 10 without (7 of which are candidates) and 2 are ambiguously categorized as jets or disc winds. The mean (and its standard error) bolometric luminosities of isolated jets and jets with lobes are $(2.6 \pm 0.9) \times 10^4 L_{\odot}$ and $(2.7 \pm 1.0) \times 10^4 L_{\odot}$ with medians of $1.8 \times 10^4 L_{\odot}$ and $8.0 \times 10^3 L_{\odot}$ respectively, showing only small differences between the two populations in this respect.

2.4.2 Radio luminosity vs. Clump Mass

An ATLASGAL survey by Urquhart *et al.* (2014b), recorded the 870 μm fluxes and sizes of a sample of clumps, 35 of which coincide with sources in this survey. Of those 35 sources, 21 have been classified as exhibiting jet-like characteristics. The clump mass was calculated using the referenced dataset in conjunction with Equation 2.7 (Hildebrand 1983), where M_{clump} is the calculated clump mass, D is distance (m), S_ν is the flux at 870 μm ($\text{W m}^{-2} \text{Hz}^{-1} \text{sr}^{-1}$), T_{dust} is the dust temperature (assumed to be 20 K), R is the gas to dust mass ratio (assumed to be 100), $B_\nu(T_{\text{dust}})$ is the Planck function (shown explicitly in Equation 2.8 with units of $\text{W m}^{-2} \text{Hz}^{-1} \text{sr}^{-1}$) and κ_ν is the dust absorption coefficient (assumed to be $0.185 \text{ m}^2 \text{ kg}^{-1}$). Values used for T_{dust} , R and κ_ν are the same as those assumed by Urquhart *et al.* (2014b).

$$M_{\text{clump}} = \frac{S_\nu D^2 R}{B_\nu(T_{\text{dust}}) \kappa_\nu} \quad (2.7)$$

$$B_\nu(T_{\text{dust}}) = \frac{2h\nu^3}{c^2} \frac{1}{e^{\frac{h\nu}{k_B T_{\text{dust}}}} - 1} \quad (2.8)$$

In Figure 2.5 the radio luminosities at 9 GHz have been plotted against the calculated clump masses and a relation of $S_\nu D^2 \propto M_{\text{clump}}^{1.38 \pm 0.27}$ is derived for all jets and candidates (1.33 ± 0.29 for the jets and candidates from the distance-limited sample). There appears to be two outliers toward the heavier end of the clump masses. G014.9958–00.6732 suffered from elongated beams and noisier data as a result of its observed times and environment. G338.9196+00.5495 is known to be in an extremely active star formation region in general, as well as being located at

the edge of its natal clump, which is unusual for the sample (see subsection 2.4.5).

Neglecting the two outliers, as well as G012.9090–00.2607 (for the same justification as for G014.9958–00.6732), a correlation coefficient between the clump masses and distance fluxes at 9 GHz (for the distance-limited sample of jets and candidates, neglecting G012.9090–00.2607, G014.9958–00.6732 and G338.9196+00.5495) of $\tau = 0.63$ with a p-value of 0.002 is calculated. This indicates a high likelihood of a positive correlation between the two quantities and justifies the empirical power-law, fitted in Figure 2.5. For the partial Kendall correlation coefficient for distance-flux with clump mass (controlling for distance) a value of $\tau = 0.55$ with a p-value of 0.009 is found. This statistical result again supports the correlation between jet luminosity and clump mass, as well as the fact that the most massive stars form in the most massive clumps.

As a further note, the two objects classified as unknown are consistent with the fitted power-law for the jets and candidates. This provides evidence that these objects may be ionised jets, a classification which higher signal-to-noise observations will help to definitively clarify.

It is intriguing that the derived relationship between radio luminosity and clump mass is very similar to the prediction that $L_{\text{rad}} \propto M_{\text{clump}}^{\frac{4}{3}}$ (Equation 6 of Scaife 2012, and references therein) for the low-mass, Class 0 case. Furthermore, lower power exponents for this relation are expected for more evolved Class 1 objects (Bontemps *et al.* 1996; Scaife *et al.* 2011). This latter point provides an alternate explanation for the presence of outliers if these objects represent more evolved stages of high mass star formation. Most importantly, these points suggest a similarity between the high-mass and low-mass evolutionary case outlined by Bontemps *et al.* (1996), whereby \dot{M}_{acc} decreases with age.

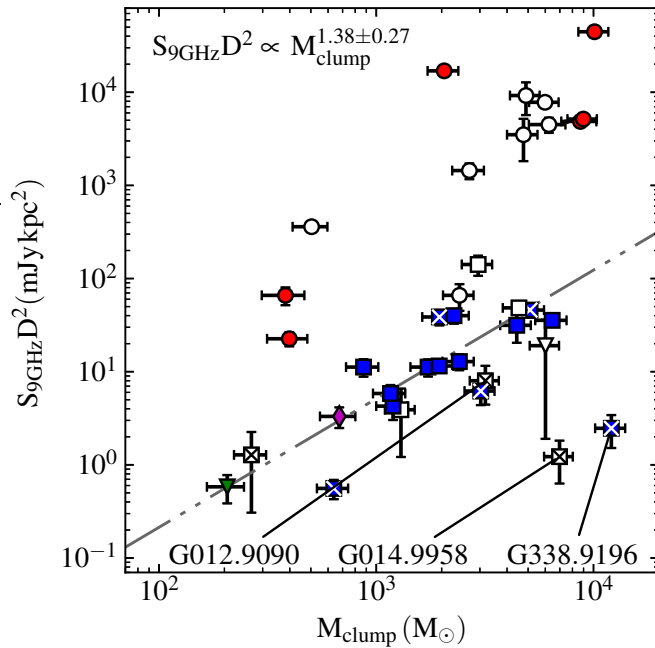


Figure 2.5: A plot of the 9 GHz distance fluxes against associated clump masses for HII regions and objects displaying properties associated with either ionised jets or disc winds. The coefficient to the fitted power-law fit is displayed in the top left corner and is represented as the dot-dashed line. Symbols have the same meanings as in Figure 2.4.

2.4.3 Radio luminosity vs. IR colours

As discussed in section 1.5, the reddening of sources in infrared surveys can be an accurate indicator of youth since the greater the degree of reddening, the more embedded a source will be in its environment. Extrapolating this reasoning to the MYSO phase, the radio luminosity at 9 GHz has been plotted against the MSX ($21\ \mu\text{m}$ - $8\ \mu\text{m}$) colour in Figure 2.6.

While the HII regions appear to show higher radio luminosities with the more reddened mid-infrared colours, the jets show no correlation, holding similar fluxes over the sampled colour-space. This may indicate that the jet phase occupies a relatively large portion of an MYSO's lifetime and therefore it stands to rea-

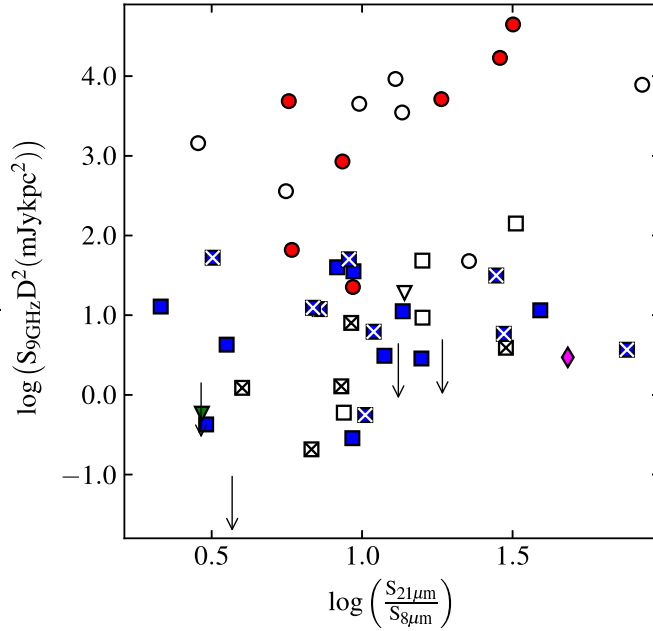


Figure 2.6: A logarithmic plot of the 9 GHz distance luminosities against the MSX 21 $\mu\text{m}/8 \mu\text{m}$ colour for the nearest associated MSX point source. Symbols follow the conventions of Figure 2.4, apart from for jets with a ‘ \times ’ marker in them signifying them to be jet candidates.

son that the X-wind model may not apply in many cases, due to the lack of a stellar magnetic field for the majority of an MYSO’s lifetime. Non-detections occupy the same range of colours as the detected jets themselves. Considering the average bolometric luminosities for the detections and non-detections of the sample are $3.7 \times 10^4 L_{\odot}$ and $3.7 \times 10^3 L_{\odot}$ respectively, the signal to noise ratio may be insufficient to detect any free-free emission, should it exist coincident with the MSX sources with no detected radio flux. It is also interesting to note that the sources exhibiting disc-wind properties occupy a wide range of colours. However, of these, the unambiguous disc wind (G298.2620+00.7394) holds one of the reddest colours of the jets/disc-winds in the sample. Definite conclusions about whether disc winds represent separate evolutionary stages in MYSO evolution

would require a larger sample of such objects than that presented in this work.

2.4.4 Coincidence with maser and line emission

With regard to the water line at 22.23508 GHz, within $10''$ of 22 of the 42 sources, maser emission is observed. Two more of the 42 sources have a detection of water maser activity in previous studies (Forster & Caswell 1999), making a total of 24 of 42 sources. The exact breakdown in terms of object type is summarised in Table 2.4.

In comparison with the survey by Urquhart *et al.* (2009a), a detection rate of 52% is found compared to their rate of 27%. This is likely due to the SNR (~ 50 times lower) of this survey since it is continuum oriented (i.e. 1 MHz channels), compared to the previous line oriented study ($4\sigma \sim 1$ Jy). Given the (spectrally) low-resolution nature of continuum observations, no kinematic information could be derived.

2.4.5 Ionised jets and their general properties

Using Equation 2.9 (Reynolds 1986), it is possible to infer a mass loss rate in the jet:

$$\dot{M}_{\text{Jet}} = \frac{9.38 \times 10^{-6} v_8 \mu S_{\text{mJy}}^{3/4} d_{\text{kpc}}^{3/2} \theta_{\text{OA}}^{3/4}}{x_0 \nu_{10}^\alpha \nu_{m10}^{0.45 - \frac{3\alpha}{4}} T_4^{0.075} (\sin i)^{1/4} F^{3/4}} \quad (2.9)$$

where α is the derived spectral index, μ is the average particle mass (as a fraction of the proton mass), x_0 is the ionisation fraction, v_8 is the terminal velocity of the jet (assumed to be 500 km s^{-1} from proper motion studies in the literature e.g. subsection 1.4.4), S_ν is the integrated flux density, D is the distance to the

source, ν_{m10} is the turnover frequency, i is the inclination angle (assumed to be $\sim 39^\circ$), T is the electron temperature, θ_0 is the opening angle at the base of the jet (Equation 2.10 from Eisloffel *et al.* 2000) and F is defined in Equation 2.11:

$$\theta_{\text{OA}} = 2 \tan^{-1} \left(\frac{\theta_{\text{min}}}{\theta_{\text{maj}}} \right) \quad (2.10)$$

$$F \equiv F(q_\tau, \alpha) \equiv \frac{4.41}{q_\tau(\alpha - 2)(\alpha + 0.1)} \quad (2.11)$$

$$q_\tau = \frac{2.1(1 + \epsilon + q_T)}{\alpha - 2} \quad (2.12)$$

where q_τ is the power-law coefficient with which the opacity falls with distance along the jet propagation axis (i.e. $\tau(r) = \tau_0(r/r_0)^{q_\tau}$ where r_0 is the launching radius), q_T is the equivalent of q_τ for temperature, ϵ is the equivalent of q_τ for jet width and α is the spectral index.

Equations 2.9 and 2.11 necessitate assumptions to be made for the non-observable parameters contained within them. A higher ionisation fraction than in the low-mass case (~ 0.1 , Hartigan *et al.* 1994) of 0.2 is assumed, a typical jet velocity of 500 km s^{-1} , (as seen in subsection 1.4.4 for other examples of ionised jets around MYSOs) and an electron temperature of 10^4 K in line with optical/near-IR line estimates from low-mass jets (see §3.1 of Frank *et al.* 2014). For the inclination angle, a value of 39.54° is adopted since the average value for $\sin(i)$ (for uniformly distributed, random inclinations) is found to be ~ 0.64 . These values are used for all of the jets in the sample. The turnover frequency is assumed to be 50 GHz , apart from for the jets whereby $\alpha < 0$, in which case they are already in the optically thin regime and the lowest observed frequency is used.

The highest (i.e most resolving) frequency measurements of the minor/major axes are used in the calculation of the opening angle, for which I find a range between $16 - 80^\circ$ and a median value of 41° , higher than the range of opening angles found by Moscadelli *et al.* (2016) towards their sample of MYSOs ($10 - 30^\circ$), and much greater than typical low-mass cases ($5 - 10^\circ$ Tsinganos *et al.* 2009). The widest opening angle was found towards G313.7654–00.8620, which represents a morphologically complex MYSO in the radio, which may have affected the deconvolution (reflected in opening angle errors of 42°). It is important to note at this point that in cases where the opening angle could not be directly measured, a value of $(20 \pm 15)^\circ$ was adopted in line with typical values within the literature.

A more complex approach is used when assuming values for q_r . Since (from Equation 2.12) it is dependent on values for ϵ and q_T , one of three models is assumed. In the case of $0.4 \leq \alpha < 0.8$, I assume $\epsilon = 1$ and $q_T = 0$, the “standard” spherical model. Where α is measured to be less than 0.4, I assume $\epsilon = 2/3$ and $q_T = 0$, the “standard” collimated model. Finally, in the instances where $\alpha \geq 0.8$, values of $\epsilon = 1$ and $q_T = -0.5$ are assigned, a conical, recombining jet model.

Derived mass loss rates range between $(0.3 - 64) \times 10^{-6} M_\odot \text{ yr}^{-1}$ for all jets and jet candidates. A corresponding average mass loss rate of $(1.5 \pm 0.3) \times 10^{-5} M_\odot \text{ yr}^{-1}$ is calculated, with a median value of $8 \times 10^{-6} M_\odot \text{ yr}^{-1}$. Plotting the derived mass loss rates against the clump masses (Figure 2.7) shows a power law with an index of 1.05 ± 0.24 . For this correlation $\tau = 0.485$ with an associated p-value of ~ 0.007 is calculated. For those objects comprising the distance limited sample, $\tau = 0.473$ and a p-value of 0.019 is derived. As shown in Table 2.5, these values do not appreciably change for the partial correlation coefficients, whilst

controlling for distance. This confirms that the mass loss rates in the jets are related to the clump masses, without a distance related bias.

The same three sources were neglected from the correlation tests (G012.9090–00.2607, G014.9958–00.6732 and G338.9196+00.5495) as in subsection 2.4.2. W33A (G012.9090–00.2067) and the Kleinmann-Wright (Kleinmann & Wright 1973) object (G014.9958–00.6732) both lie at declinations conducive to elongated beam shapes, thus adversely affecting their deconvolved sizes. Indeed, W33A was found to have a deconvolved size of $(0.53'' \pm 0.14) \times (0.27'' \pm 0.11)$ at 43 GHz by van der Tak & Menten (2005), giving an opening angle at the base of the jet of 0.94 rads, in contrast to the derived value in this work of 0.18 rads. This would in turn derive $\dot{M}_{\text{jet}} = (1.7 \pm 1.0) \times 10^{-5} M_{\odot} \text{ yr}^{-1}$ (I calculate a value is $\sim 1 \times 10^{-6} M_{\odot} \text{ yr}^{-1}$ for this work). W33A is also known to be composed of at least 3 separate sources at very high resolutions, Q1, Q2 and Q3 (Q1 represents the main jet). This complicates the analysis, requiring higher resolutions observations (at all frequencies) in order to separate and determine the natures of each source.

The KW object is positioned at the edges of two ATLASGAL ($R_{\text{eff}} \sim 60''$ and $R_{\text{eff}} \sim 90''$) clumps, the membership to which is uncertain. If the accretion, and hence jet mass loss rates, are intrinsically tied to the reservoir of material from the clump, this may explain (in combination with the elongated beam) its current (relatively low) mass loss rate of $\sim 4 \times 10^{-6} M_{\odot} \text{ yr}^{-1}$.

G338.9196+00.5495 images had low signal to noise ratios, showed the presence of 5 HCHII/UCHIIs within $1'$ of the source, and displayed partially resolved out extended emission at the lowest frequencies. In a competitive accretion scenario, the busy nature of the environment could affect the reservoir of available material to the MYSO and hence affect jet outflow rates, as well as the quality of the images

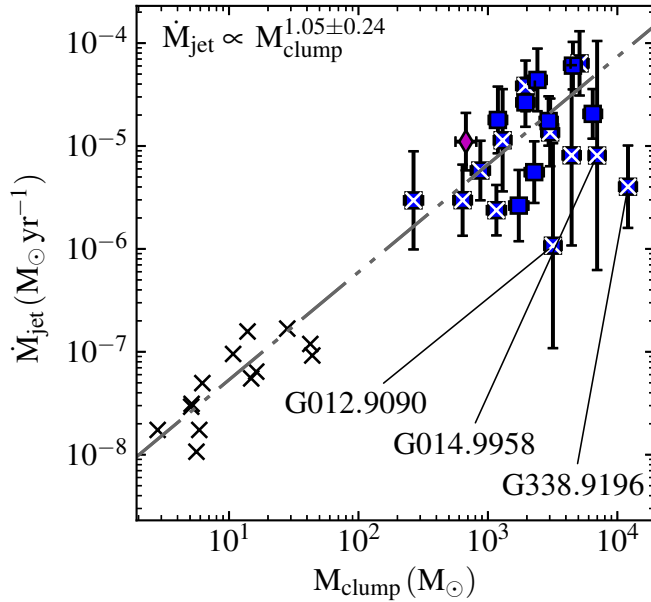


Figure 2.7: A plot of the inferred mass loss rates against ATLASGAL derived clump masses (Urquhart *et al.* 2014b) in the jet for all the sources in the sample displaying jet-like characteristics. The dot-dashed line represents the power-law fit to the data, with the power-law index indicated in the top left of the plot. Data for low-mass jets from Ainsworth *et al.* (2012) is represented by ‘×’ symbols.

and deconvolved dimensions of the object itself (which is unresolved at 17 and 22.8 GHz). ATLASGAL images of G338.9196+00.5495 also show its parental clump to be comprised of two, non-resolved clumps, with the source offset on the southern edge of the smaller, thus the clump’s mass may be overestimated. Considering that G338.9196+00.5495 is also an outlier in Figure 2.5, it is likely that the clump mass is poorly constrained as discussed above.

As a check with the rest of the data, all sources apart from the KW object, G338.9196+00.5495 and G345.9561+00.6123 (which is still of uncertain classification) are positioned within the inner 25% of their parental clumps (c.f. Urquhart *et al.* 2014b, who found 90% of embedded objects were separated by less than 0.5pc from their associated clump’s peak flux position).

Inferred momentum rates (assuming a terminal velocity for the jet of 500 km s^{-1}) against the bolometric luminosities of the powering sources, are plotted in Figure 2.8. For those MYSOs comprising the distance limited sample (derived values change little between jet and jet/candidate sub-samples) the relation represented in Equation 2.13 is found. Comparing this to the CO outflow momentum rate/bolometric luminosity relations found by Cabrit & Bertout (1992) (Equation 2.14) and Maud *et al.* (2015) (Equation 2.15):

$$\log_{10} F_{\text{jet}} = (-6.11 \pm 0.49) + (0.87 \pm 0.12) \log_{10} L_{\text{bol}} \quad (2.13)$$

$$\log_{10} F_{\text{CO}} = (-4.36 \pm 0.12) + (0.69 \pm 0.05) \log_{10} L_{\text{bol}} \quad (2.14)$$

$$\log_{10} F_{\text{CO}} = (-4.60 \pm 0.46) + (0.61 \pm 0.11) \log_{10} L_{\text{bol}} \quad (2.15)$$

From these relations, the momentum rate of ionised jets appears to depend more heavily on the bolometric luminosities than the molecular outflows. However the incidence rate of massive molecular outflows in the (6 kpc distance-limited) MYSO sample of Maud *et al.* (2015) was found to be 66%, similar to the incidence rate of jets and candidates for the distance-limited sample of 65%. The power-law coefficient for the relation between the molecular mass outflow rate and clump mass was found to be 0.55 ± 0.10 . In comparison with the fitted value of 1.05 ± 0.24 for the jet outflow rate, this indicates a heavier dependence of the outflow rates on the clump mass for ionised jets, than for the molecular outflows.

In Figure 2.9, the histogram of the spectral indices derived for all jets in the sample is presented. This shows a peak in the jet's spectral indices of ~ 0.6 as per the standard, conical jet model. All detected jets exhibit spectral indices

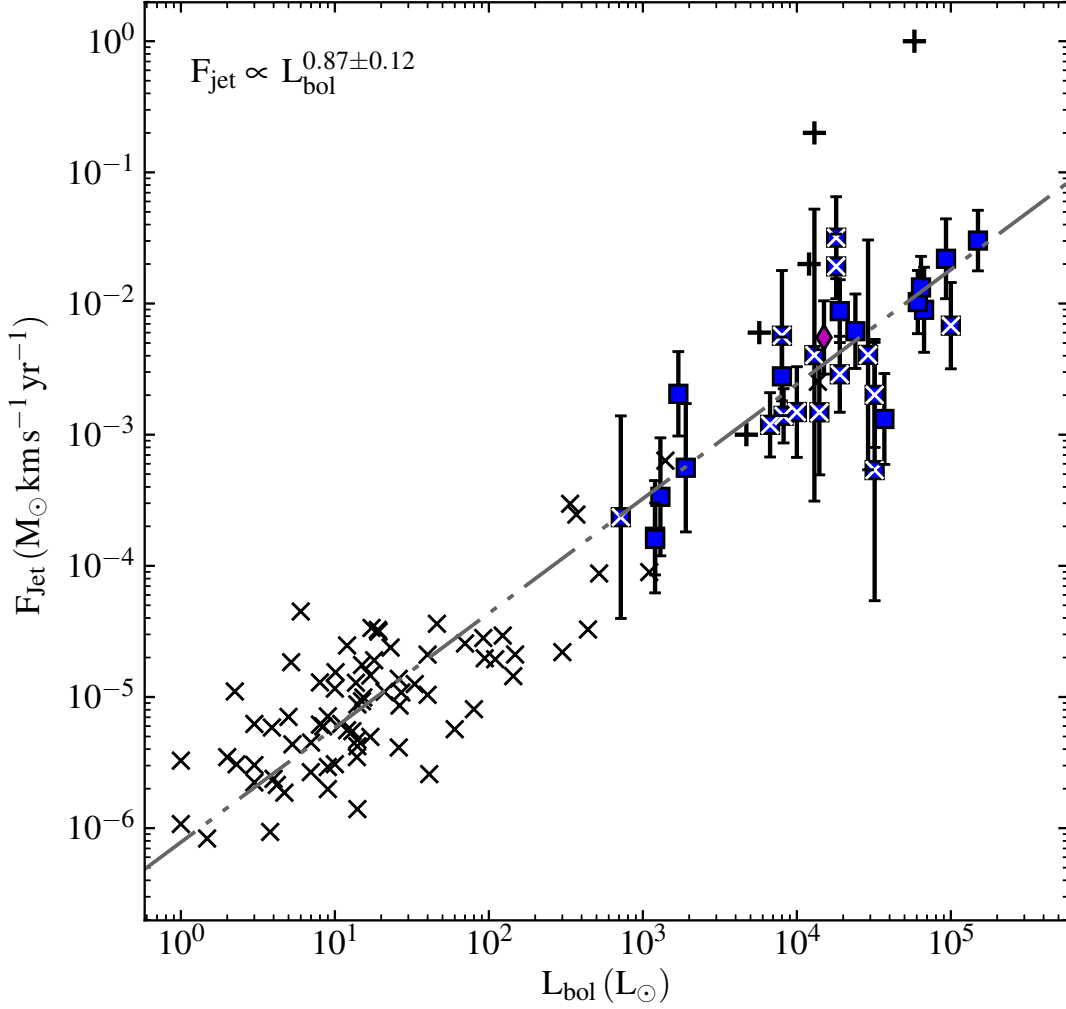


Figure 2.8: A plot of the inferred momentum rate against bolometric luminosity for the sources in the sample displaying jet-like characteristics. The dot-dashed line represents the power-law fit to the data, with the power-law index indicated in the top left of the plot. Data for low-mass jets from Ainsworth *et al.* (2012) is represented by ‘ \times ’ symbols, assuming a velocity of 200 km s^{-1} unless otherwise indicated in the literature. The ‘+’ symbol indicates data for the high mass sample from Moscadelli *et al.* (2016).

expected from the models of Reynolds (1986) between -0.1 and 1.6 within errors.

As for the lobes of emission associated to the thermal jets, non-thermal spectral indices for lobes associated to 10 of the 13 jets are found (blue bars in Figure 2.9). An average spectral index in the non-thermal lobes of -0.55 is also calculated showing that synchrotron emission is the dominant emission mechanism in these cases and therefore magnetic fields are present in the environments of ionised jets from MYSOs. This result also agrees with radio lobes being produced via Fermi acceleration at shocks (see subsection 1.4.3.1), whereby $\alpha = -\frac{(1-p)}{2}$ is expected, where p is the power-law coefficient for the electron energy distribution ($p = 2$ in head-on shocks). It can also be said that, due to the lack of spectral steepening due to spectral aging (i.e. depletion of the highest energy electrons), these electron populations are relatively young and therefore produced at the shock sites, as expected. Four of the jets show associated lobes with thermal spectral indices, G310.0135+00.3892 (SW), G310.1420+00.7583A (B), G313.7654-00.8620 (B2) and G332.0939-00.4206 (E). For all four cases, apart from G313.7654-00.8620, the spectra of the components are not well fitted by simple power-laws suggesting these components may represent extended emission (i.e. resolved out at higher frequencies), the natures of which are indeterminate. G313.7654-00.8620 was observed at the lower two frequencies only, and so the presence of this effect is unknown, raising another possibility of multiplicity. For the SW component of G310.0135+00.3892, the alignment between the central radio source and this component is parallel to derived outflow directions in the literature. Therefore, it is likely this represents thermal emission from the jet material however more sensitive observations with higher signal-to-noise are required to conclude this definitively (part of the motivation for chapter 3).

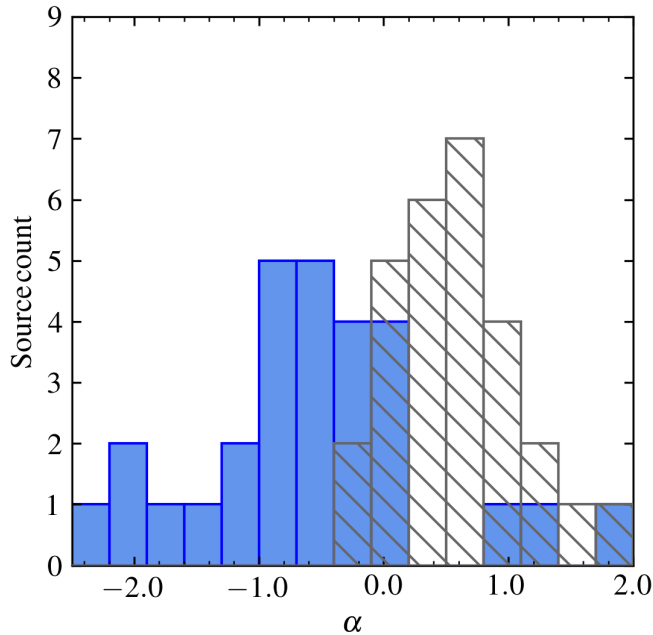


Figure 2.9: A histogram of all the spectral indices derived for those sources determined to exhibit jet-like characteristics (hatched). The solid blue bars are for the associated lobes. Binning starts at $\alpha = -2.5$ and bin widths are set at 0.3 due to the sample size.

For those jets identified which had associated lobes of emission, the separation of these lobes from the central jet was calculated (assuming an inclination of 90°) and in Figure 2.10, the histogram of logarithmic lobe separations is plotted. A peak at $\sim 10^4$ au from the central object is evident, with a mean value of 2.0×10^4 au (and a median value of 1.3×10^4 au). The minimum separation calculated (~ 600 au) was for the NW component of G263.7759–00.4281, while the maximum (~ 90000 au) was for component D of G313.7654–00.8620. If these lobes represent internal shocks within the jet as a result of periodic ejection, coupled with non-constant ejection velocities, the typical time between these ejections can be calculated. Assuming an ejection velocity of 500 km s^{-1} for the first ejection, which increases by 10% for the second, and using the typical value

for lobe separations of 1.3×10^4 au, it can be inferred that the time between these ejections is typically ~ 10 yr.

It is important to note that the population of small separation lobes is under-sampled and I cannot reliably comment on lobe separations for distances < 4000 au, due to the minimum resolvable scales of the observations. In order to investigate the spectral consequences of this resolution limit, the spectral indices for the combined fluxes of north and south lobes, for both G263.7434+00.1161 and G310.0135+00.3892 (due to their relative morphological simplicities) were analysed. Derived values for the spectral index of the combined emission were found to be $\alpha = 0.09 \pm 0.13$ and $\alpha = 0.42 \pm 0.17$ for G263.7434+00.1161 and G310.0135+00.3892 (for the thermal jets alone, $\alpha = 0.39 \pm 0.18$ and $\alpha = 1.27 \pm 0.18$) respectively, with the combined fluxes being fitted well with a simple power law. This indicates that any unresolved, optically thin lobes which are inseparable from their powering, thermal jets, would flatten the jet's spectrum without strongly distorting its power law profile. This effect could act to decrease the measured spectral index for jets, whose flux incorporates those of optically thin or non-thermal lobes, offering another explanation for a slightly larger proportion of jets with spectral indices < 0.6 (see Figure 2.9).

2.4.6 HII regions and their general properties

From the HII regions that were included in the overall sample, I have calculated both the emission measures and physical radii (deconvolved). The three HCHII regions displaying a compact core have been separated from their extended background emission, with both components analysed separately. Both

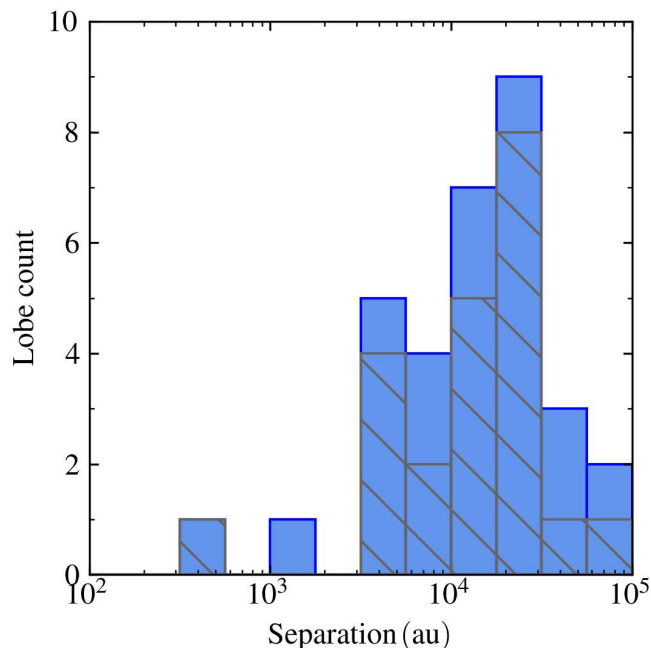


Figure 2.10: A logarithmic histogram of the spatial separations between all lobes (solid bars), and lobes where $\alpha < 0$ (hatched bars), and their powering central jets.

emission measures and radii are plotted in Figure 2.11.

For the HCHII regions of the sample an average emission measure of $6.51 \times 10^8 \text{ pc cm}^{-6}$, and corresponding electron density of $2.28 \times 10^5 \text{ cm}^{-3}$, is found. For the ultra-compact HII regions detected, values of $1.09 \times 10^8 \text{ pc cm}^{-6}$ and $5.13 \times 10^4 \text{ cm}^{-3}$ for the average emission measure and electron density respectively are calculated. Average radii were calculated to be 0.013 pc and 0.041 pc, while average bolometric luminosities were calculated to be $(1.6 \pm 0.4) \times 10^5 L_{\odot}$ and $(7.9 \pm 1.1) \times 10^4 L_{\odot}$, for HCHII and UCHII respectively (assuming a 34% error in the bolometric luminosities, as in Mottram *et al.* 2011b). Although HII regions are not the focus of this work, the derived properties provide a consistency check in conjunction with typical values reported in the literature (Mezger *et al.* 1967; Wood & Churchwell 1989; Hoare *et al.* 2007).

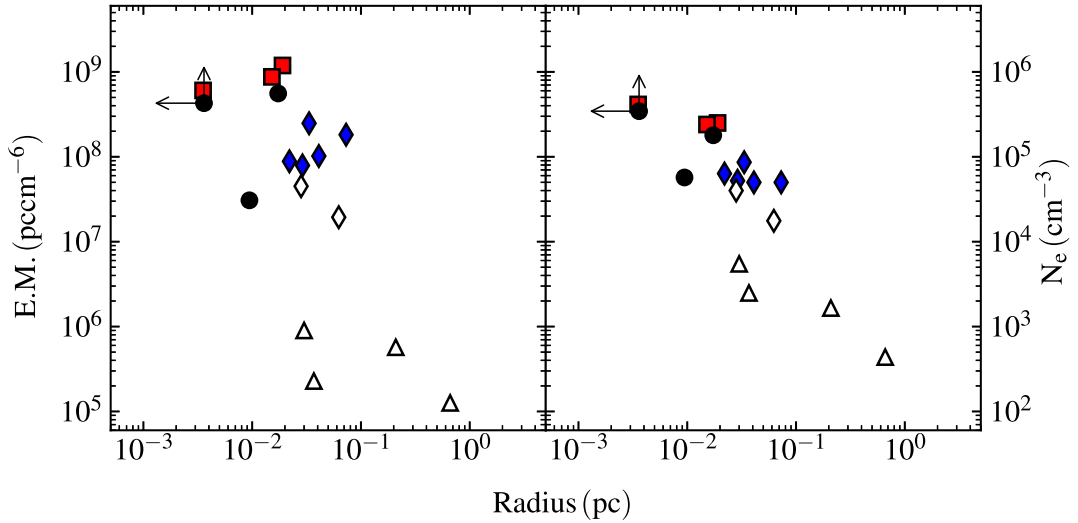


Figure 2.11: A plot of the calculated emission measures against radius for the HII regions detected (top) and the corresponding electron densities inferred against radius (bottom). Circles (black) represent the compact HCHII ‘core’ seen in 3 HII regions, squares (red) represent other HCHII regions, diamonds (blue) represent UCHII regions, and triangles represent compact and classical HII regions. Any symbols in white suffer from resolving out effects due to their scale.

2.5 Summary and Conclusions

In this chapter, the results of radio observations made towards 49 massive young stellar objects potentially harbouring ionised jets have been presented, 34 of which form a distance-limited sample. Establishing a statistically-sized sample of ionised jets and, by extension, how common this phenomenon is during the formation process of massive stars was the main objective. Relations to possible accretion processes and/or jet models and the physical parameters typical of the jets themselves were also investigated. In summary, the main results and conclusions of this chapter are:

1. From the distance-limited sample of 34 MYSOs, 22 ionised jets and jet candidates are detected showing this to be a common phenomenon in forming

massive stars. Disc based accretion processes are therefore the dominant mechanism of accretion (up to masses of at least $25 M_{\odot}$).

2. Ionised jets are more common than photo-evaporative disc winds, by at least an order of magnitude, suggesting that either ionised jets are generally brighter than disc winds (if they are concurrent), or that a distinct disc-wind phase exists and is relatively short in comparison.
3. From the jet fraction observed, and assuming a MYSO phase lifetime of $\sim 10^5$ yr (McKee & Tan 2002), a jet-phase lasting $(2.9 - 6.5) \times 10^4$ yr is implied from the incidence rate of jets and jet candidates. Since some objects potentially represent a transition phase between ionised jet and HII region, this time range is placed at the later end of an MYSO's lifetime, implying accretion doesn't completely halt after the initial production of an HII region.
4. The luminosity and momenta of massive, ionised jets scale with bolometric luminosity in the same way as low-mass jets, supporting the idea that these jets are produced in the same way over YSO mass ranges upto at least $25 M_{\odot}$.
5. For the mass range, $8 M_{\odot} \leq M_{\star} \leq 25 M_{\odot}$, typical jet mass-loss rates and momenta rates are $1.4 \times 10^{-5} M_{\odot} \text{ yr}^{-1}$ and $0.7 \times 10^{-2} M_{\odot} \text{ km s}^{-1} \text{ yr}^{-1}$ respectively, assuming an average ionisation fraction of 20% and jet velocity of 500 km s^{-1} . This suggests an average mass of $\sim 1 - 2 M_{\odot}$ (corresponding to $\sim 10^{48}$ ergs) is lost through the ionised jet mechanism, to the ISM, over the course of an MYSO's jet-phase.

6. Jet outflow rates (and hence accretion rates) are closely related to the mass of the molecular clump from which they form, which agrees with the idea that the most massive stars form in the most massive clumps. This is also supported by the fact that 88% of the jets are found in the inner 25% of their associated clump. Furthermore, the relation found between jet radio luminosity and clump mass supports an evolutionary model similar to the low-mass case.

7. Synchrotron emission is commonplace (present in $\sim \frac{1}{2}$ of the jets) in the form of spatially distinct, associated lobes of emission. Since magnetic fields are required for this type of non-thermal emission, this lends support to the idea of magnetic collimation in ionised jets around MYSOs, as in the low mass case. It is established, that with an average spectral index of $\bar{\alpha}_{\text{lobe}} \sim -0.5$, the emission arises as the results of the 1st order Fermi mechanism at shock sites.

Chapter 3

Deep Radio Continuum

Observations of Ionised Jets

Around Four MYSOs

From previous observations of ionised jets (see subsection 1.4.4 and chapter 2), their general, radio morphology seems takes the form of an elongated component with a thermal, spectral index centred on the MYSO. Theoretical studies indicate that the value for the spectral index can range from -0.1 to 1.4 (see subsection 1.4.3.1, Reynolds 1986), with observational studies seemingly averaging a spectral index of ~ 0.6 (Figure 2.9). In $\leq 50\%$ of cases this is associated with separate lobes of emission (incidence rates of $\sim 65\%$, see chapter 2), which are the result either external shocks as the result of collision with ambient material, or internal shocks within the jet as a result of variability in ejection velocity (such as in the low mass case of HH 211, Moraghan *et al.* 2016). These lobes tend to be spatially distinct and separate in the majority of cases (average separations

of $\sim 10^4$ au, see Figure 2.10), with little radio emission seen in between thermal and non-thermal components (e.g. IRAS 16547–4247 and IRAS 16562–3959 of Rodríguez *et al.* 2005; Guzmán *et al.* 2010, respectively). This suggests one of two possibilities, that the ejection of material is highly variable/episodic (possibly a result of fragmentation in the accretion disc, Meyer *et al.* 2017), or that a constant, collimated outflow of material only sporadically impinges upon the surrounding matter to form shocks.

In cases where multiple lobes are seen, a positional offset for of lobe from the overall position angle of the jet (e.g. IRAS 16547–4247; see subsection 1.4.4) would suggest the outflow axis changes over time. Precession of collimated outflows are predicted in the simulations of Sheikhnezami & Fendt (2015) who performed 3D MHD simulations of a disc-jet system influenced by the gravitational potential of a binary companion. They find that the tidal interactions for separations of ~ 200 inner disc radii (~ 2000 au in reality) warp the accretion disc of the YSO, resulting in disc, and therefore jet, precession. Considering the high companion fraction observed towards massive stars (see §3.5 of Duchêne & Kraus 2013, and references therein) it might be expected that jet precession is a relatively common phenomenon. Interestingly their simulations also predict variable accretion and outflow rates which would be seen in observations as flux variability (AMI Consortium *et al.* 2011).

Radio observations of both variability and precession of massive jets are present in the literature, but are few and far between. For example, Rodríguez *et al.* (2008) observed the MYSO IRAS 16547–4247 at two epochs separated by ~ 1000 days. From comparison of the flux maps in both epochs, no proper motions along the outflow axis were seen, however precession was apparent in the

non-thermal lobes with a rate of $0.08^\circ \text{ yr}^{-1}$ and therefore derived period of 4500 yr. Both the central jet and a non-thermal lobe (component S-1) increased in flux over time by 9% and 36% respectively. As far as proper motion observations, several works have reported radio-lobe velocities ranging from $300 - 1000 \text{ km s}^{-1}$ in massive cases (such as HH80-81 and Cep A HW2 from Martí *et al.* 1998; Curiel *et al.* 2006, respectively) or $\lesssim 200 \text{ km s}^{-1}$ in low mass cases (e.g. knot A of DG Tau, which also showed morphological evolution and variability over time, Lynch *et al.* 2013).

Considering the discussion above, this chapter aims to investigate how ionised jets, and their lobes, change over time (specifically their flux variability, precession and proper motions) and uses the results of the previous survey of ionised jets (that discussed in chapter 2), which employed a well-selected sample of MYSOs from the RMS (Red MSX Source) survey (Lumsden *et al.* 2013), as its foundation. In that work a total of 28 jet-like radio sources were detected from a sample of 49 objects, of which 11 of the 28 were associated with non-thermal emission. Using a new set of radio observations towards 4 of these 11 sources, this work increases the sensitivity by a factor of $2 - 3$ ($\sim 10 \mu\text{Jy beam}^{-1}$) in comparison to chapter 2. Specific questions this chapter aims to answer are, do the radio jets, or shock-ionised lobes, exhibit variability over the period of time between observations ($\sim 2 \text{ yr}$)? Despite these short time-baselines, can large proper motions towards the lobes still be detected? Do they show precession in their propagation axes? Is there any fainter emission previously undetected and therefore is mass loss a continuous, yet variable, process? In light of answers to the previous questions, can models of massive star/jet formation be constrained any further?

3.1 Observations

All radio observations were made using the Australian Telescope Compact Array (ATCA) in the 6A configuration, on the 19th, 20th and 21st December 2014. For reference, the previous observations (subsection 2.2.1) were conducted from the 25th to 28th of February 2013. A total of 4 individual objects were observed at 2 different frequency bands (centred on 6.0 and 9.0 GHz). These frequencies were observed using a bandwidth of 2048 MHz (XX, YY, XY, and YX polarizations) split evenly either side of the central frequencies, which was subsequently divided into 1 MHz channels. From this point on the observed frequencies are referred to as the 6 and 9 GHz bands.

The range of scales the instrument was sensitive to were $1.8 - 18.5''$ and $1.2 - 12.3''$ for the 6, and 9 GHz frequency bands respectively, corresponding to a minimum baseline length of 337 m and a maximum of 5939 m. Differing scale sensitivities can manifest in the results by a decrease in the amount of flux recovered at higher frequencies (i.e. on larger spatial scales). In subsection 2.2.3 I conducted synthetic observations towards an idealised jet model, representative of the sample in both spatial scale, and spectral index. This investigation showed that for the ATCA in the 6A configuration, $> 92\%$ of the flux was recovered at 5.5 and 9.0 GHz, and the recovered spectral index did not vary from the idealised model. Thus, these effects can be neglected in the further analysis of this paper. Furthermore, the synthetic observations showed that the signal to noise ratio was insufficient to accurately recover the physical dimensions of the object. However, with the deeper integration times (and therefore better signal-to-noise ratio) of this dataset, more accurate dimensions should be deconvolved from the data.

Scan times on the flux calibrator, phase calibrators and science targets were approximately 8, 2 and 15 minutes respectively. In order to provide more coherent phase solutions between the two epochs, therefore increasing the reliability of image comparison and analysis, the phase calibrators were the same quasars as those used in chapter 2. For the flux calibrator, an absolute flux scale uncertainty of 5% is adopted for both frequencies. Listed in Tables 3.1 and 3.2 are the observed calibrators and science targets.

Table 3.1: A table of the positions, calibration types and fluxes for the calibrators used in the reduction of the data. The science target which the phase calibrators are used to transfer complex gain solutions to are also listed (in an abbreviated form).

Calibrator	R.A. (J2000)	Dec. (J2000)	Type	Freq. (GHz)	S_ν (Jy)	Science Target(s)
0826–373	08 ^h 28 ^m 04.78 ^s	−37°31′06.3″	Phase	6	1.55 ± 0.09	G263.7434
				9	1.30 ± 0.10	
1352–63	13 ^h 55 ^m 46.63 ^s	−63°26′42.6″	Phase	6	1.22 ± 0.14	G310.0135, G310.1420, G313.7654
				9	1.08 ± 0.29	
1934–638	19 ^h 39 ^m 25.03 ^s	−63°42′45.6″	Bandpass, Flux	6	4.51 ± 0.35	
				9	2.72 ± 0.16	

8

Table 3.2: A table of the target sources, their positions, associated IRAS sources, distances, bolometric luminosities, ZAMS stellar masses (from the models of Davies *et al.* 2011, assuming a 30% error in L_{bol}), total integration times and theoretical image noise levels per beam (utilising a robustness of 0) at 6 and 9 GHz.

Object	R.A. (J2000)	Dec. (J2000)	IRAS	D (kpc)	L_{bol} (L_\odot)	M_\star (M_\odot)	$\tau_{\text{int.}}$ (hrs)	σ_6 (μJy)	σ_9 (μJy)
G263.7434+00.1161	08 ^h 48 ^m 48.64 ^s	−43°32′29.0″	08470–4321	0.7	1.2×10^3	$6.3_{-0.2}^{+0.6}$	7.33	7.3	8.4
G310.0135+00.3892	13 ^h 51 ^m 37.85 ^s	−61°39′07.5″	13481–6124	3.2	6.7×10^4	$24.3_{-3.2}^{+3.1}$	6.19	7.9	9.1
G310.1420+00.7583A	13 ^h 51 ^m 58.27 ^s	−61°15′41.7″	13484–6100	5.4	8.0×10^3	$11.2_{-1.2}^{+1.0}$	2.99	11.4	13.1
G313.7654–00.8620	14 ^h 25 ^m 01.53 ^s	−61°44′57.6″	14212–6131	7.8	6.1×10^4	$23.4_{-3.0}^{+2.7}$	5.29	8.6	9.9

For reducing the data, the Multichannel Image Reconstruction Image Analysis and Display (MIRIAD) software package (Sault *et al.* 1995) was used.

In the event that methanol masers or bright (> 10 mJy) continuum sources were present in the field of view, phase-only (due to ATCA's limited number of baselines) self-calibration was iteratively performed until no further improvement in the RMS scatter of the phase solutions was achieved.

3.2 Multi-epoch Synthetic Observations

A problem with comparing multi-epoch observations taken by a radio interferometer is the difference in the uv sampling function (or synthetic aperture), $S(u, v)$, between each observation. Since an interferometer is essentially a limited Fourier filter whereby each orientation of each baseline samples a separate Fourier component, if one set of observations is not a perfect copy of another (i.e. same times of year, hour angles etc.), different Fourier sampling is performed and subsequent deconvolved flux distributions may not match, even for a non-changing object. Generally for arrays with excellent uv -coverage, such as the VLA or ALMA, this effect is likely to be negligible regardless of the exact temporal format of the observations. However for the sparse uv -sampling of east-west arrays such as ATCA, whereby gaps in hour angle coverage mean position angle gaps in uv -coverage, this effect becomes significant. In Figure 3.1, the difference between 2013 and 2014 observations outlined in section 3.1 is illustrated by plotting each epoch's uv -coverage. Compounding this problem are imperfections in complex gain calibrations which, when it comes to imaging, leave artefacts in the clean maps of flux which are essentially residual parts of the dirty beam. The morphology of

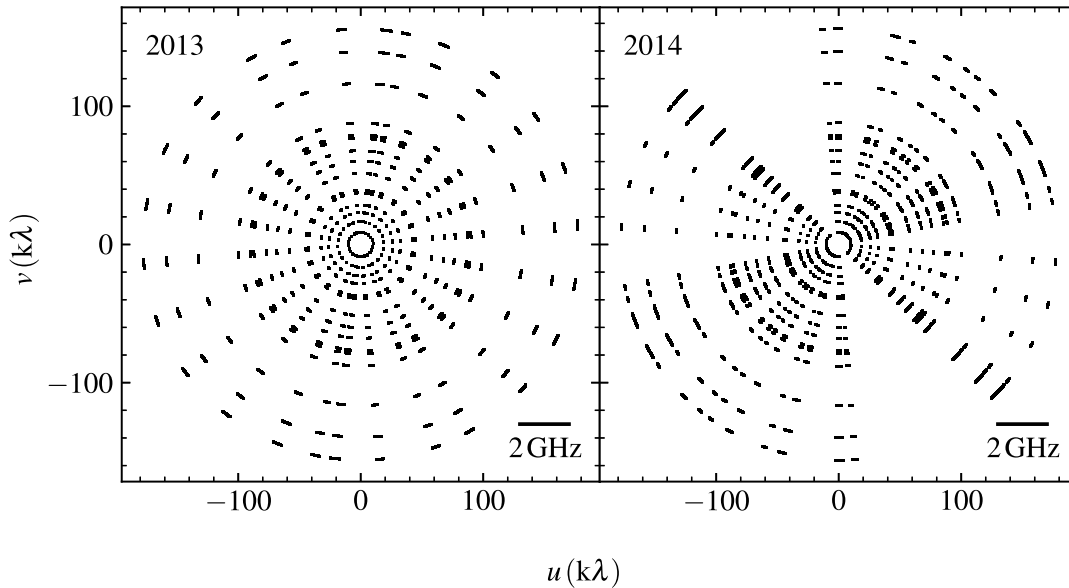


Figure 3.1: Plots of the sampling functions (single channels at 9 GHz) for the 2013 and 2014 datasets towards G310.1420+00.7583A. Illustrated in the bottom right of each plot is a scale bar showing the radial uv coverage over the 2 GHz bandwidth (for the longest (6 km) baseline), highlighting the increased sampling of the uv-plane for multi-frequency synthesis.

these imperfections is therefore directly related to the format of the observations since the dirty beam is the inverse Fourier transform of the sampling function.

In light of this discussion, it had to be determined if pixel-to-pixel changes in flux distribution between 2013 and 2014 were reliable. This involved creating two sets of synthetic observations designed to mirror the actual data using MIRIAD’s task UVGEN. The flux model employed was an approximation of the known flux distribution towards G310.1420+00.7583A, based upon the deconvolved positions, fluxes and dimensions of the 6 prominent lobes of emission (A1, A2, A3, A4, C and D) from the 2013 dataset (see Table 3.3 for exact values). Due to the irregular nature of the scans during the real observational cycles, each mimic, synthetic scan was generated separately and then all were concatenated

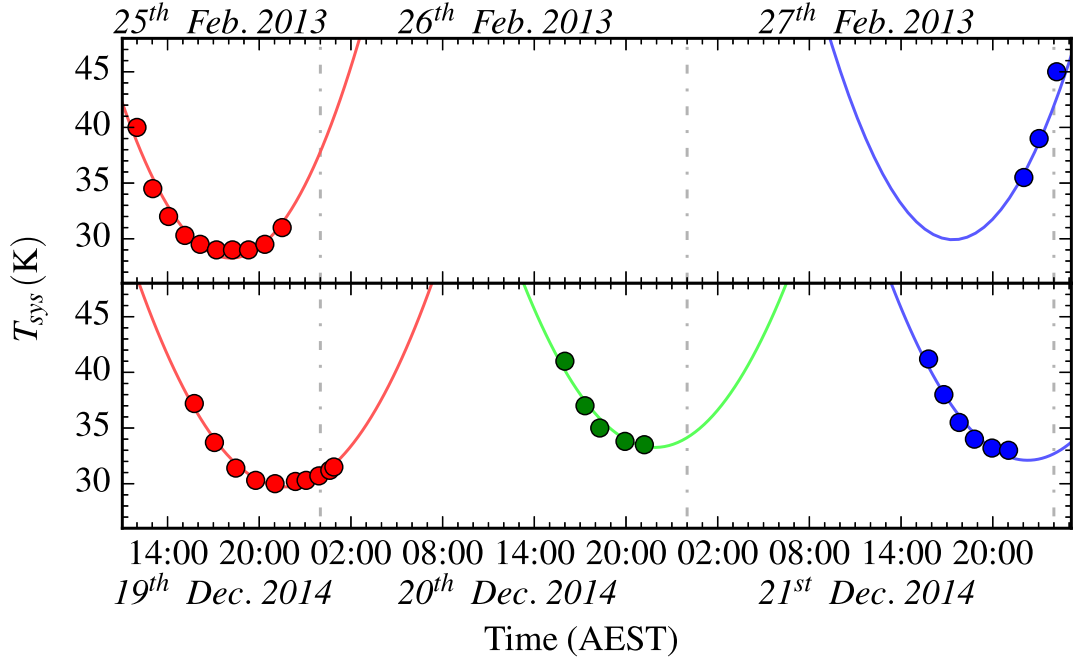


Figure 3.2: A plot of the T_{sys} profiles used for the synthetic observations during both epochs. Different colour points/lines represent the separate observational days, where the lines are the quadratic fit to T_{sys} on that day.

into single visibility files, one for each observational epoch. Integration times were set to 10 seconds, all linear polarizations were sampled, leakage between feeds was set to 2% and the antenna positions mirrored the ATCA’s 6A-configuration. In general, during radio observations the system temperature, T_{sys} , varies with time with a quadratic profile due to day to night atmospheric temperature variations (whereby the ‘minima’ occur during the night). Since the real, dirty maps of flux were produced using the `systemp` option, whereby the visibilities are weighted to the inverse of the noise variance, the system temperature for each synthetic scan was set to the average value for T_{sys} during the real scan. This variability in system temperature is plotted in Figure 3.2 for clarity.

After the datasets were created the usual imaging process was performed for

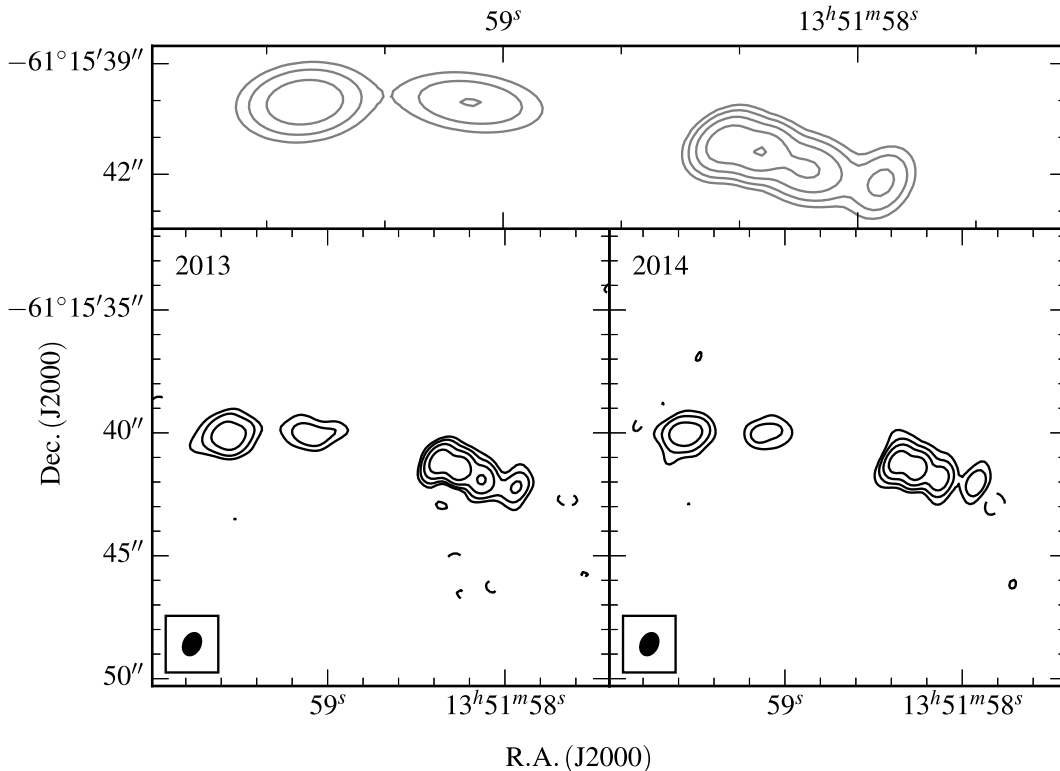


Figure 3.3: Clean maps of the synthetic data at 9 GHz (bottom left and right plots). The top plot represents the model used to generate the synthetic visibilities convolved with the common beam used in both synthetic clean maps ($0.94'' \times 0.68''$, $\theta_{PA} = -26.3^\circ$, shown bottom left of each clean map). All contours are logarithmically spaced from 3σ (where $\sigma = 23.0 \mu\text{Jy}/\text{beam}$, the noise in the 2013 synthetic clean map) to 95% the maximum flux in the model’s image, specifically $-3, 3, 6, 14, 29$ and 63σ .

each synthetic epoch with the resulting clean maps shown in Figure 3.3. Comparison of those clean maps shows that not all of the model’s flux is recovered (as is usual with radio interferometric observations) and that there are subtle changes in the low-level flux morphology, particularly towards the two eastern, extended lobes. Pixel-to-pixel subtraction of both synthetic maps results in the flux changes shown in Figure 3.4. From this map it is clear that flux differences between two epochs can result from differing uv-coverage for each set of observations. In light of this, any pixel-to-pixel changes in flux should be cautiously

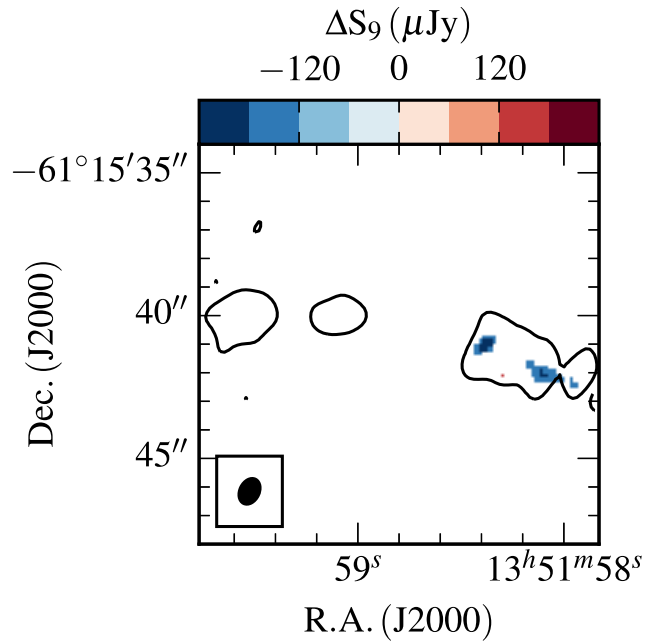


Figure 3.4: A map of pixel-to-pixel flux differences between 2013 and 2014 synthetic clean maps (colour-scale). The contour shows the 3σ flux as per Figure 3.3.

regarded as showing real variability, when this kind of analysis is performed towards ATCA data.

With regard to deconvolved properties of the emission the positions, fluxes and dimensions of each lobe, for each synthetic dataset as well as the model, have been recorded in Table 3.3. Consequently, lobe-to-lobe deviations of these parameters from the model's values for both epochs are plotted in Figure 3.5.

Table 3.3: A table of the deconvolved properties for the emission from each synthetic dataset, as well as the model. From left to right, the columns represent lobe/component name, the dataset used to make the synthetic image, offsets in right ascension and declination (taken from the pointing centre at α (J2000) = $13^{\text{h}}51^{\text{m}}58.27^{\text{s}}$ and δ (J2000) = $-61^{\circ}15'41.7''$), deconvolved major axis, deconvolved minor axis, deconvolved position angle, proper-motion derived velocity (calculated by comparing 2014 and 2013 offsets, using a distance of 5.4 kpc) and position angle of the proper motion. The abbreviation ‘P/S’ stands for point source i.e. convolved dimensions were beam sized and therefore the deconvolution failed to resolve finite dimensions for the lobe.

Lobe	Dataset	Flux (mJy)	R.A. offset ($''$)	Dec. offset ($''$)	θ_{maj} ($''$)	θ_{min} ($''$)	θ_{PA} ($^{\circ}$)	Δv (km s^{-1})	$\theta_{\Delta v}$ ($^{\circ}$)
A1	Model	1.73	+0.70	+0.53	0.56	0.37	133		
	2013	1.59 ± 0.04	$+0.72 \pm 0.01$	$+0.54 \pm 0.01$	0.55 ± 0.03	0.17 ± 0.06	132 ± 3	762 ± 200	-158 ± 15
	2014	1.50 ± 0.04	$+0.67 \pm 0.01$	$+0.52 \pm 0.01$	-0.64 ± 0.05	-0.27 ± 0.03	141 ± 4		
A2	Model	1.27	-0.03	+0.26	P/S	P/S	P/S		
	2013	1.50 ± 0.04	-0.08 ± 0.01	$+0.25 \pm 0.01$	P/S	P/S	P/S	447 ± 200	-162 ± 26
	2014	1.43 ± 0.04	-0.11 ± 0.01	$+0.24 \pm 0.01$	-0.33 ± 0.06	-0.25 ± 0.04	161 ± 42		
A3	Model	1.62	-0.90	-0.16	1.09	-0.41	61		
	2013	1.07 ± 0.05	-1.01 ± 0.01	-0.22 ± 0.01	-0.64 ± 0.05	-0.25 ± 0.07	49 ± 5	860 ± 314	$+99 \pm 14$
	2014	-0.80 ± 0.04	-1.02 ± 0.01	-0.16 ± 0.02	-0.63 ± 0.10	-0.36 ± 0.09	176 ± 16		
A4	Model	-0.61	-2.44	-0.52	-0.86	-0.35	167		
	2013	-0.58 ± 0.05	-2.38 ± 0.02	-0.51 ± 0.03	-0.71 ± 0.10	-0.44 ± 0.10	146 ± 15	2864 ± 746	$+123 \pm 12$
	2014	-0.44 ± 0.05	-2.49 ± 0.03	-0.34 ± 0.05	-0.99 ± 0.18	-0.28 ± 0.09	156 ± 5		

Table 3.3: Continued

Lobe	Dataset	Flux (mJy)	R.A. offset ($''$)	Dec. offset ($''$)	θ_{maj} ($''$)	θ_{min} ($''$)	θ_{PA} ($^\circ$)	Δv (km s^{-1})	$\theta_{\Delta v}$ ($^\circ$)
C	Model	1.05	+5.91	+1.64	1.84	-0.47	78	583 ± 1274	+14 ± 68
	2013	-0.77 ± 0.08	+5.93 ± 0.07	+1.67 ± 0.02	1.68 ± 0.19	-0.41 ± 0.12	86 ± 3		
	2014	-0.55 ± 0.07	+5.97 ± 0.06	+1.68 ± 0.04	1.27 ± 0.20	-0.40 ± 0.23	87 ± 11		
D	Model	1.85	+9.27	+1.65	1.38	-0.82	93	860 ± 323	+81 ± 34
	2013	1.66 ± 0.08	+9.27 ± 0.03	+1.58 ± 0.01	1.32 ± 0.07	-0.74 ± 0.05	92 ± 4		
	2014	1.39 ± 0.07	+9.28 ± 0.02	+1.64 ± 0.02	1.19 ± 0.08	-0.59 ± 0.11	93 ± 7		

As expected for any radio interferometric observation, gaps in uv-coverage have acted to decrease the amount of recovered flux for each of the lobes with mean flux differences (between model and data) of -11% and -25% for the 2013 and 2014 fake observations respectively. Predictably this effect is amplified for the more extended components such as C and D but the percentage change is apparently greater for A3 (a relatively compact lobe). Further to this, the deconvolved flux actually increases for A2 in both epochs. Both of these effects however are not due to the resolving out of flux, but more to do with the inaccuracy of deconvolution for multiple, closely-spaced, Gaussian distributions of flux. This is reflected again in the inability of the 2014 synthetic observations to deconvolve A2 as a point source, and subsequently it was measured to have finite angular size and position angle. Component A4 also appears to significantly relocate by $\sim 0.19''$, at a position angle of -16° , for the 2014 dataset compared to the model. This is equivalent to a proper motion derived velocity of $\sim 2900 \text{ km s}^{-1}$ for G310.1420+00.7583A's distance of 5.4 kpc.

From the results presented above, the following can be concluded:

- Fluxes recovered by the synthetic observations are on average -11% and -25% lower than actual values supplied by the model, with extended sources C and D worst affected.
- Percentage of flux recovered for the 2014 observations is lower than for the 2013 observations, whereby, on average, 14% less flux is recovered.
- Source confusion leads to the wrong distribution of flux being deconvolved for lobes A2 and A3, with the compact source A2 'leeching' flux from A3.

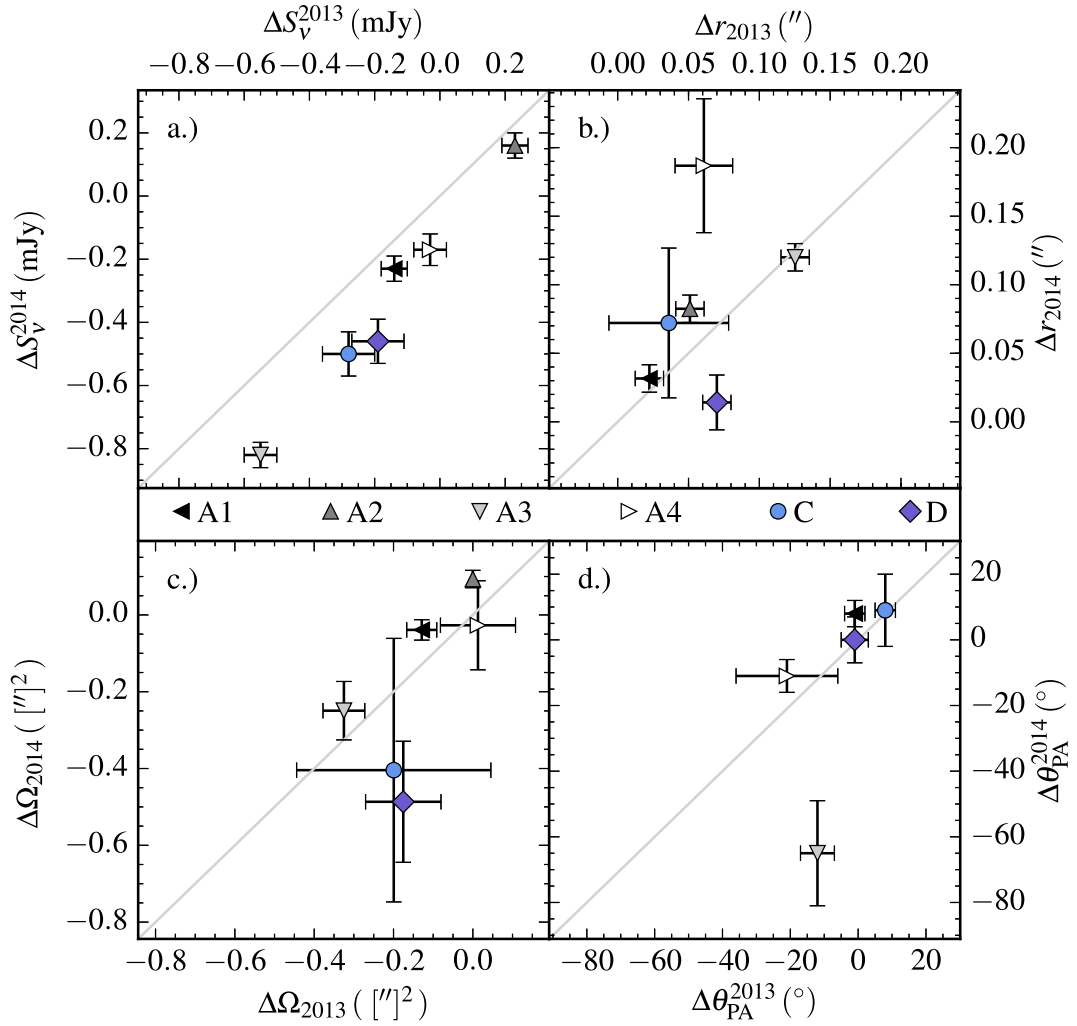


Figure 3.5: Deviations for the deconvolved properties of each lobe from the model, for the 2013 synthetic data (x-axis) and 2014 synthetic data (y-axis). Plots represent: a.) difference between deconvolved, synthetic and model fluxes; b.) angular offset between synthetic and model positions; c.) difference between deconvolved, synthetic and model angular sizes; d.) difference between deconvolved, synthetic and model position angles.

- Lobe positions are deduced with $> 0.1''$ accuracy in non-source confused components.
- Deconvolved position angles are relatively well recovered by deconvolution with average deviations of just -2° and 6° (ignoring source confused lobes, A2 and A3) for the former and latter epochs respectively.

This analysis implies that for the real-world ATCA images presented in the rest of this chapter, any proper motions $\lesssim 3000 \text{ km s}^{-1}$ are likely too affected by poor uv-coverage and source confusion to draw any conclusions from. Negative variations over time in lobe fluxes between 2013 and 2014 should be considered suspect. Pixel to pixel comparisons of the maps of flux also show non-real negative flux variations centred on components A1, A2, A3 and A4. These considerations will be taken into account during the rest of this chapter.

3.3 Results

3.3.1 Image alignment

Measurement of the positional changes of radio lobes allows a direct measurement of the ionised gas' velocity. In order to do this, accurate positional measurements are required due to the great distances involved. For example with two measurements separated by a period of 2 yr and assuming a jet velocity of 500 km s^{-1} , at a distance of 3 kpc, an angular shift (assuming the jet's path lies in the plane of the sky) of $0.07''$ is calculated. However due to imperfections in calibration, as well as astrometric inaccuracy, coordinates have an absolute positional uncertainty. In an effort to negate this effect, the same phase calibrators were used for the new

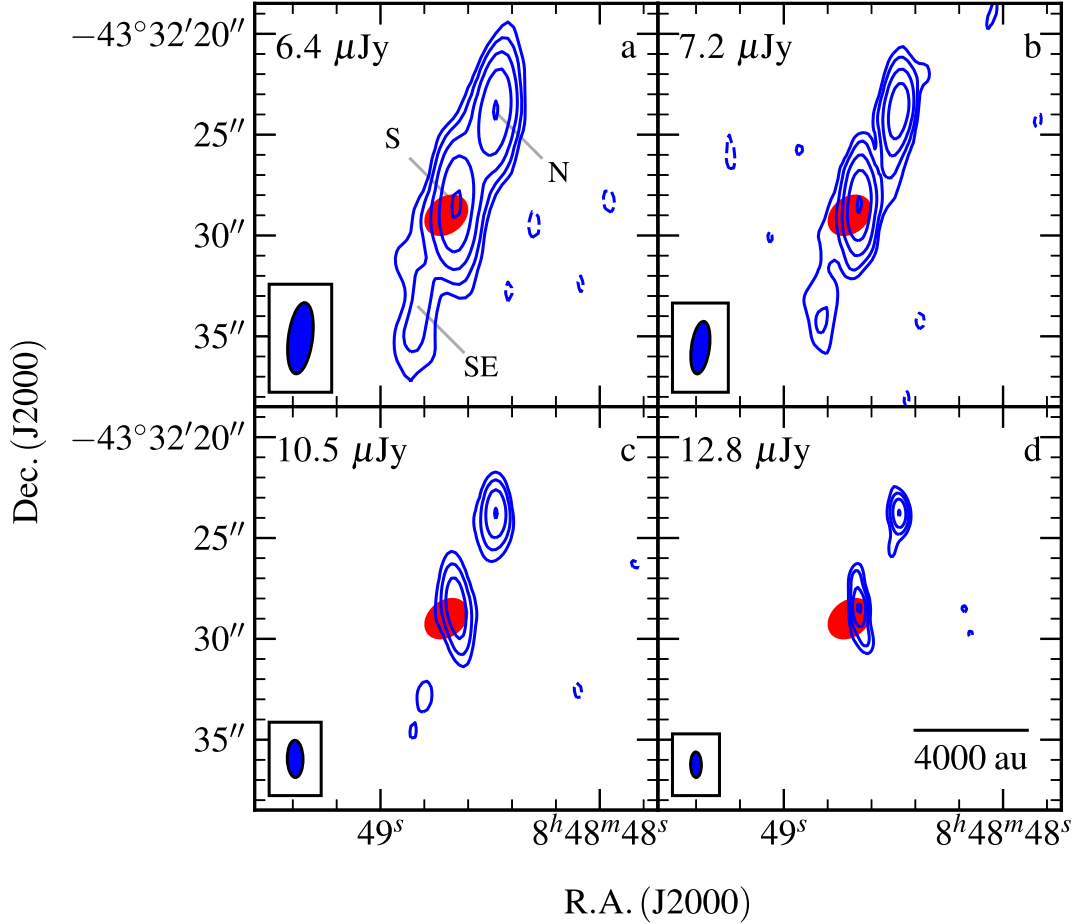


Figure 3.6: Contour plots of radio flux density for observations made towards G263.7434+00.1161. RMS noise is marked in the top-left of each of the sub-plots which are: a.) Image of 6 GHz data using a robustness of 0.5 where contours are $(-3, 3, 7, 15, 35, 79) \times \sigma$; b.) Image of 9 GHz data using a robustness of 0.5 where contours are $(-3, 3, 7, 15, 35, 78) \times \sigma$; c.) Image of 6 GHz data using a robustness of -1 with contours located at $(-3, 3, 7, 18, 42) \times \sigma$; d.) Image of 9 GHz data using a robustness of -1 with contours located at $(-3, 3, 7, 15, 33) \times \sigma$. Restoring beams are indicated in the bottom left corner of each plot and are $3.55'' \times 1.20''$ at $\theta_{PA} = -7.48^\circ$, $2.62'' \times 0.89''$ at $\theta_{PA} = -7.76^\circ$, $1.84'' \times 0.78''$ at $\theta_{PA} = 1.07^\circ$ and $1.27'' \times 0.53''$ at $\theta_{PA} = 0.98^\circ$ for sub-plots a, b, c and d respectively. The 3σ positional error ellipse for the MSX point source associated with the MYSO is plotted in red.

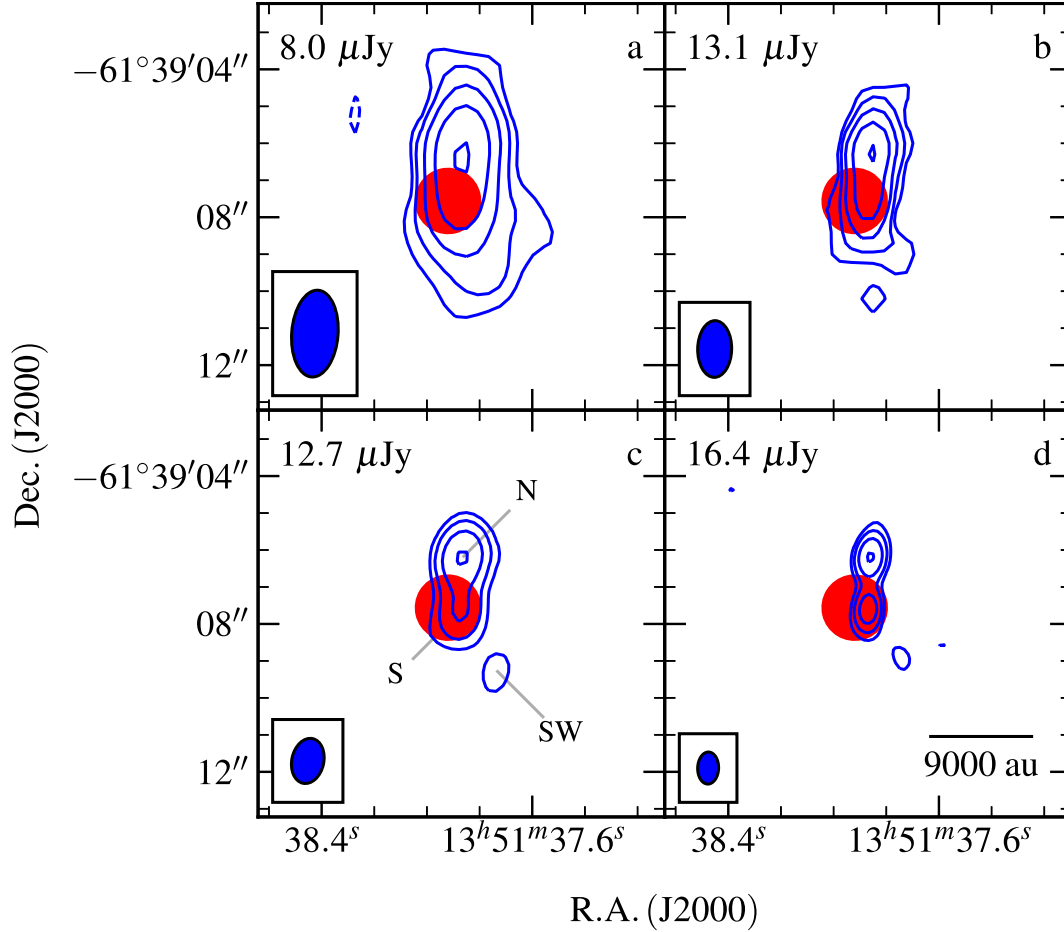


Figure 3.7: Contour plots of radio flux density for observations made towards G310.0135+00.3892. RMS noise is marked in the top-left of each of the sub-plots which are: a.) Image of 6 GHz data using a robustness of 0.5 where contours are $(-4, 4, 9, 20, 44, 97) \times \sigma$; b.) Image of 9 GHz data using a robustness of 0.5 where contours are $(-4, 4, 8, 14, 27, 52) \times \sigma$; c.) Image of 6 GHz data using a robustness of -1 with contours located at $(-4, 4, 9, 21, 49) \times \sigma$; d.) Image of 9 GHz data using a robustness of -1 with contours located at $(-4, 4, 8, 17, 36) \times \sigma$. Restoring beams are indicated in the bottom left corner of each plot and are $2.35'' \times 1.25''$ at $\theta_{PA} = -4.43^\circ$, $1.53'' \times 0.92''$ at $\theta_{PA} = -1.13^\circ$, $1.23'' \times 0.87''$ at $\theta_{PA} = -12.29^\circ$ and $0.87'' \times 0.57''$ at $\theta_{PA} = -1.84^\circ$ for a.), b.), c.) and d.) respectively. The 3σ positional error ellipse for the MSX point source associated with the MYSO is plotted in red.

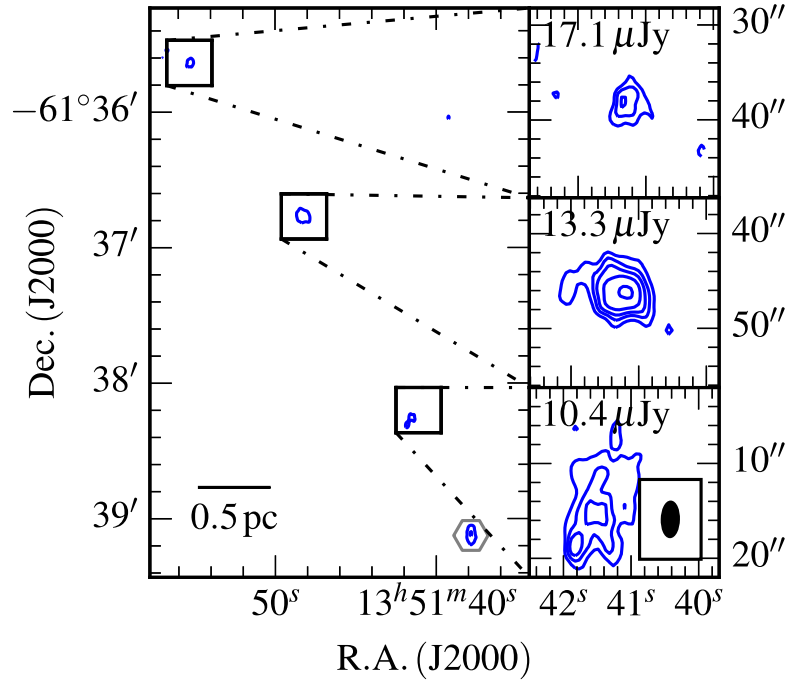


Figure 3.8: Primary beam corrected 6 GHz image (robustness of 2) of G310.0135+00.3892 and its associated radio Herbig-Haro objects. Each plot is: a.) the overall area presented with 4 and 50 σ contours where $\sigma = 17.1 \mu\text{Jy beam}^{-1}$ with G310.0135+00.3892 is located in the bottom right (hexagonal marker); b.) Sub-plot of HH3 ($\sigma = 17.1 \mu\text{Jy}$); c.) Sub-plot of HH2 ($\sigma = 13.3 \mu\text{Jy}$); d.) Sub-plot of HH1 ($\sigma = 10.4 \mu\text{Jy}$). Contours are set at $(-3, 3, 5, 7, 10, 15) \times \sigma$ and the field of view is $22''$, for b, c and d.

observations as for those of 2013. Extragalactic background sources were subsequently identified from the clean maps of radio flux (on the basis of spectral index and lack of IR counterparts) and any positional shift of these objects between the two images was assumed to be due to positional errors. This provided corrections which were applied to the 2014 images using spline interpolation, therefore aligning the two images.

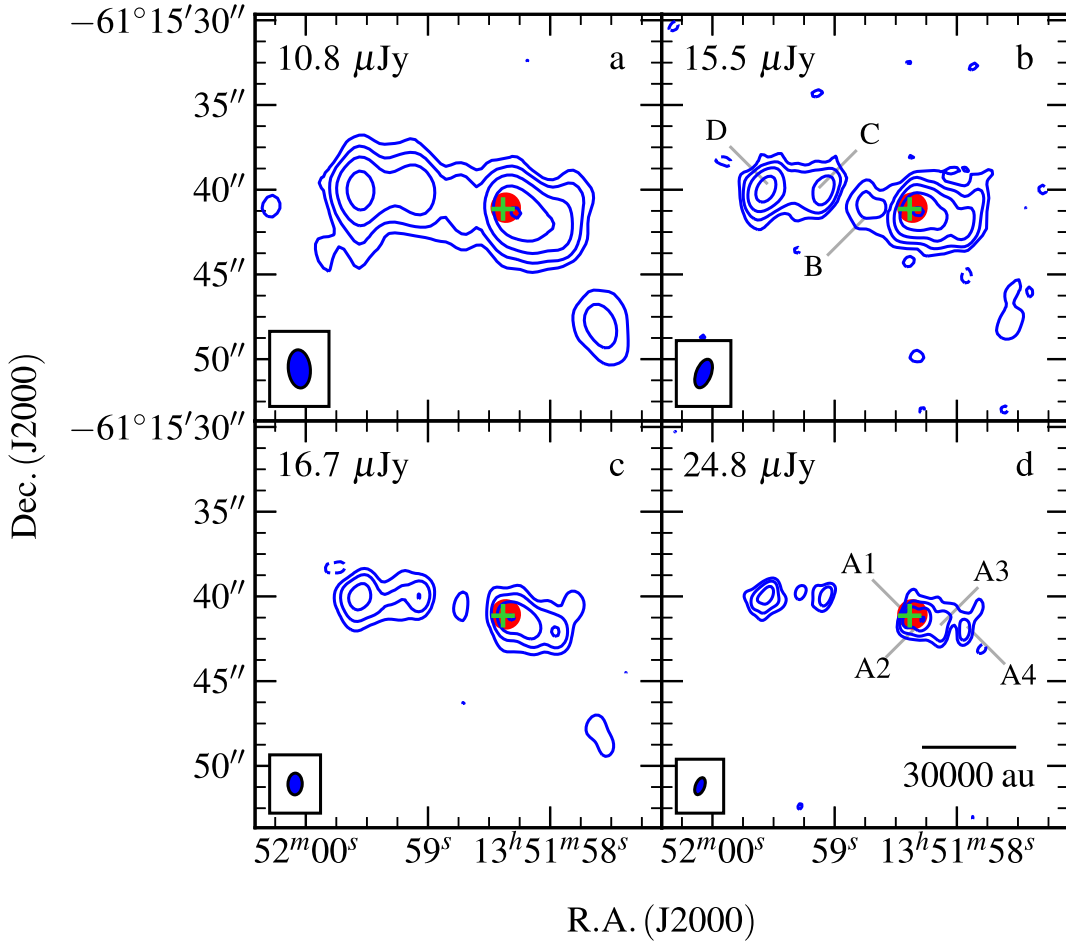


Figure 3.9: Contour plots of radio flux density for observations made towards G310.1420+00.7583A. RMS noise is marked in the top-left of each of the sub-plots which are: a.) Image of 6 GHz data using a robustness of 0.5 where contours are $(-3, 3, 6, 13, 27, 58) \times \sigma$. The restoring beam was $2.26'' \times 1.30''$ at $\theta_{PA} = 5.73^\circ$; b.) Image of 9 GHz data using a robustness of 0.5 where contours are $(-3, 3, 6, 13, 26, 54) \times \sigma$. The restoring beam was $1.77'' \times 0.89''$ at $\theta_{PA} = -21.04^\circ$; c.) Zoomed in image of 6 GHz data using a robustness of -1 with contours located at $(-3, 3, 7, 15, 32) \times \sigma$. The restoring beam was $1.28'' \times 0.84''$ at $\theta_{PA} = -1.86^\circ$; d.) Zoomed in image of 9 GHz data using a robustness of -1 with contours located at $(-3, 3, 6, 13, 27) \times \sigma$. The restoring beam was $1.05'' \times 0.54''$ at $\theta_{PA} = -20.89^\circ$. The 3σ error ellipse in the position of the MSX point source is shown in red, while the detected methanol maser is shown as a green cross.

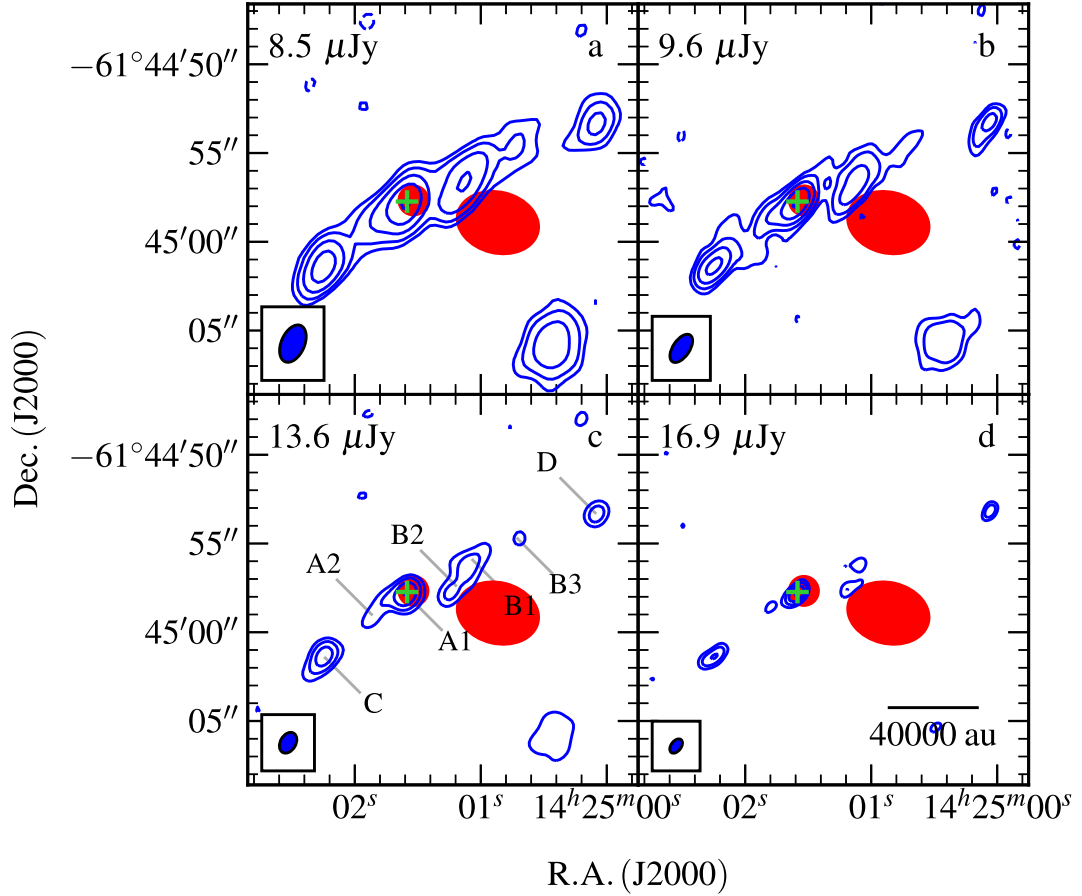


Figure 3.10: Contour plots of radio flux density for observations made towards G313.7654–00.8620. RMS noise is marked in the top-left of each of the sub-plots which are: a.) Image of 6 GHz data using a robustness of 0.5 where contours are $(-3, 3, 6, 13, 27, 58) \times \sigma$. A restoring beam of $2.22'' \times 1.31''$ at $\theta_{PA} = -23.69^\circ$ was used; b.) Image of 9 GHz data using a robustness of 0.5 where contours are $(-3, 3, 6, 13, 26, 54) \times \sigma$. A restoring beam of $1.80'' \times 0.95''$ at $\theta_{PA} = -33.80^\circ$ was used; c.) Zoomed in image of 6 GHz data using a robustness of -1 with contours located at $(-3, 3, 7, 15, 32) \times \sigma$. A restoring beam of $1.25'' \times 0.87''$ at $\theta_{PA} = -29.68^\circ$ was used; d.) Zoomed in image of 9 GHz data using a robustness of -1 with contours located at $(-3, 3, 6, 13, 27) \times \sigma$. A restoring beam of $0.91'' \times 0.57''$ at $\theta_{PA} = -37.09^\circ$ was used. Both MSX (larger) and GLIMPSE error ellipses (smaller) are shown in red. A green cross marks the position of a detected methanol maser.

3.3.2 New radio flux clean maps

Maps of radio flux towards each MYSO are shown in Figures 3.6–3.10 with separate clean maps produced at each frequency and each utilised robustness of -1 and 0.5 . Robustness (Briggs 1995) is a parameter which gives a continuous visibility weighting scheme between natural and uniform weighting. While the former gives constant weight to all visibilities, the latter gives each visibility a weight which is inversely proportional to the density of the sampling function, $S(u, v)$. Having a continuous weighting scheme between these two extremes allows for compromises between resolution, sidelobe prominence and noise levels. While a more negative robustness gives improved resolution and reduced effects from residual side-lobes, more positive values lead to lower noise levels and better flux recovery from large-scale emission. Any channels displaying strong maser emission in the 6 GHz band were imaged and the positions of the brightest maser spot plotted as a green cross in the relevant contour plots. Values for the integrated fluxes (derived using the CASA task IMFIT), spectral indices (α) and power-law coefficient for the variation of the deconvolved major-axis length with frequency (γ) are presented in Table 3.4 for each identified radio lobe. In each case, the robustness of the clean maps used to derive these quantities is listed, with spatially-distinct lobes generally utilising a natural robustness and more confused sources making use of the enhanced resolution of the more uniformly weighted clean map (at the cost of increased noise).

I now move on to give brief reviews of previous observations and discuss the results of the 2014 images, on a per object basis.

3.3.2.1 G263.7434+00.1161

G263.7434+00.1161 is the nearest and lowest-luminosity object of the sample, located in the Vela molecular ridge cloud D at a distance of 0.7 pc. Observations at 1.2mm by *Massi et al.* (2007) revealed an $18 M_{\odot}$ compact core (MMS12, 0.13pc in size) peaking $\sim 5''$ to the east of this work's pointing centre. This mm-core is coincident with 'complex and intense' H₂ emission at $2.12 \mu\text{m}$ (*de Luca et al.* 2007), indicative of collisional excitation of molecular hydrogen through shocks attributable to protostellar outflows (*Wolfire & Konigl* 1991). In chapter 2 two radio sources were identified (see Figure A.8), one centred on the MYSO's position (S) and the other offset $\sim 4''$ to the NW. Derived spectral indices were thermal ($\alpha = 0.4 \pm 0.2$) and non-thermal ($\alpha = -0.5 \pm 0.3$) for S and N respectively.

Figure 3.6 shows this work's maps of radio flux towards G263.7434+00.1161. Three lobes of emission, N, S and SE, are detected at both frequencies and aligned along a position angle of $\sim 158^{\circ}$. Most obviously in the more uniformly-weighted images (panels c and d of Figure 3.6), the thermal jet (S) is in fact elongated along a different axis to that running through all three components (see subsection 3.4.3 for further discussion of this). Component SE, whose peak is located $\sim 4''$ from S at a position angle of $\sim 160^{\circ}$, is clearly elongated along a position angle of 178° with a length of $\sim 5''$ (3500 au at a distance of 0.7 pc) and is calculated to possess a spectral index of 0.17 ± 0.68 . Approximately $29''$ to the south ($\alpha_{\text{J2000}} = 08^{\text{h}}48^{\text{m}}48.63^{\text{s}}$, $\delta_{\text{J2000}} = -43^{\circ}32'57.8''$) a new source is detected (shown in Figure 3.11) in both the 6 and 9 GHz clean maps which does not appear in the 2013 epoch's images, which is designated S2. With integrated fluxes of 319 ± 28 and $363 \pm 31 \mu\text{Jy}$ at 6 and 9 GHz, it possesses a thermal spectral

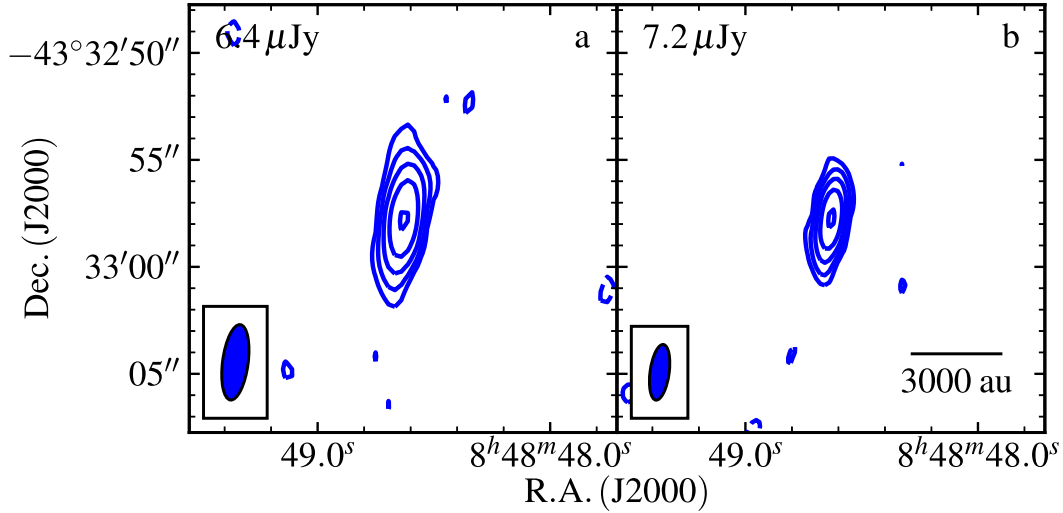


Figure 3.11: Primary beam corrected, radio contour maps of lobe S2 detected in the primary beam of our observation of G263.7434+00.1161 utilising a robustness of 0.5 at: a.) 6 GHz; b.) 9 GHz. Restoring beams used are illustrated in the bottom left corners (same dimensions as in Figure 3.6) and contours are $(-3, 3, 6, 11, 22, 44) \times \sigma$ and $(-3, 3, 6, 11, 22, 42) \times \sigma$ for the 6 and 9 GHz data respectively, where σ is the noise in the image indicated in the top-left corner of each sub-plot.

index of $\alpha = 0.32 \pm 0.30$ and has a GLIMPSE, mid-IR counterpart.

3.3.2.2 G310.0135+00.3892

G310.0135+00.3892 (or IRAS 13481–6124) is well-studied across a broad range of wavelengths. Kraus *et al.* (2010) used NIR interferometric observations ($\theta_{\text{res}} = 2.4\text{mas}$ or 8.4 au at $\theta_{\text{PA}} = 114^\circ$) to directly observe a hot, dusty, compact (13 au \times 19 au) disc. The disc’s orientation was found to be perpendicular to a collimated, (opening angle $\sim 6^\circ$) CO, bipolar outflow. Furthermore, inspection of IRAC images showed two lobes of excess emission at $4.5\mu\text{m}$ separated by $7'$ (indicative of shocked molecular hydrogen) and aligned with the outflow axis. Corroborating these findings, diffraction limited MIR imaging at $20\mu\text{m}$ by Wheelwright *et al.*

(2012) suggested that the dominant emission at $20\ \mu\text{m}$ was from the walls of cavities evacuated by outflows (along a NE-SW axis). Ilee *et al.* (2013) detected CO bandhead emission and subsequent modelling found temperature gradients consistent with Kraus *et al.* (2010) and with a flared, irradiated disc around a MYSO with $M_\star = 21.8 M_\odot$. Broad linewidths ($25.5\ \text{km s}^{-1}$) in the CO are also present, as well as high-velocity wings attached to the P-cygni profile of the Br γ line (Stecklum *et al.* 2012), suggestive of an ionised wind. Caratti o Garatti *et al.* (2015) observed the H₂ 2.122 μm transition, detecting lobes of emission spread over 6.9 pc at a position angle of -154° , coincident with the NW-SE outflow centred on IRAS 13481-6124. These lobes appeared to be more spread out to the NE (red lobe) showing that a density gradient exists in this direction. In chapter 2 I found 3 radio lobes associated with the MYSO designated N, S and SW (see Figure A.21) with spectral indices of -0.2 ± 0.1 , 1.3 ± 0.2 and 0.7 ± 1.7 respectively. While the S and SW lobes are aligned to the general outflow direction, N is offset by $\sim 30^\circ$ to the west. It was deduced that while S represents the MYSO and base of the jet, the SW component is the faint thermal emission from the jet itself while N is likely optically thin and/or non-thermal emission as the result of wide-angle shocks from the jet on the surrounding material. The reason for the offset was unclear, however Caratti o Garatti *et al.* (2016) observed spatially, and spectrally, resolved Br γ emission whose spatial velocity profile (their Figure 2) seemed to show a wide range in outflow angle. This could possibly account for shock sites significantly deviating from the jet's outflow angle (26° according to Caratti o Garatti *et al.* 2015).

In the clean maps presented in Figure 3.7, the previously established N, S and SW components are detected at both frequencies. The SW lobe appears to ‘break

up' into two separate components from 6 to 9 GHz (comparing panels a and b of Figure 3.7), separated by $1.4''$. However this may be due to image defects caused by strong, residual, sidelobes from a ~ 27 mJy source $\sim 470''$ to the NW of the pointing centre. Imaging the whole of the primary beam at 6 GHz also shows three extended lobes of emission, designated as HH1, HH2 and HH3 (shown in Figure 3.8, with positions recorded in Table B.14 of the Appendix). These sources lie at separations of 0.88, 2.47 and 3.78 pc with position angles of 30° , 27° and 31° from the MYSO respectively. No spectral indices could be computed since 9 GHz clean maps resolved out much of the extended emission of these lobes.

3.3.2.3 G310.1420+00.7583A

G310.1420+00.7583A is associated with IRAS 13484–6100 and is offset by $\sim 8''$ from a cometary UCHII (G310.1420+00.7583B). The radio observations of chapter 2 detected 7 separate components (Figure A.22), named A1 (MYSO), A2, A3, A4, B, C and D, roughly aligned east to west with a total, integrated flux of ~ 10 mJy. Previous to that Urquhart *et al.* (2007a) detected radio emission (observations conducted in November 2004) at 4.8 GHz coincident with components A1 and A2, with an integrated flux of 2.92 ± 0.75 mJy (fitted from the archived image using IMFIT). Different masing species have been detected towards this source (OH, H₂O and CH₃OH: Walsh *et al.* 1998; Urquhart *et al.* 2009a; Green *et al.* 2012, respectively), with the methanol maser coincident (multibeam survey positional accuracy is $< 0.1''$) with A1. Caratti o Garatti *et al.* (2015) observed two knots of H₂ emission, one of which also displayed Br γ emission indicative of strong dissociative shocks ('knot 1' or D as in Figure A.22) with shock velocities > 90 km s⁻¹ within a medium of density $\sim 10^5$ cm⁻³. Jet properties

inferred from the H₂ observations included a length of 0.4 pc, precession of 17° and electron density, n_e , of $(4 \pm 1) \times 10^4 \text{ cm}^{-3}$. An extended green object was also detected offset from knot 1 by $\sim 16''$ at a PA of 57° (Cyganowski *et al.* 2008).

The clean maps shown in Figure 3.9 show all components detected (see Figure) aligned in a jet-like morphology along a position angle of $\sim 78^\circ$. One previously-undetected component is seen at the 6σ level (panel a), located $\sim 5.5''$ to the east of component D. At 9 GHz it is not detected and an upper limit to the spectral index of $\alpha < 0$ is derived from the peak flux at 6 GHz. Radio emission roughly connecting lobe C to D is also detected, which is especially well shown in panels b and c of Figure 3.9, and methanol maser emission coincident with A1. Fluxes and positions for A1, A2, A3 and A4 proved difficult to measure via IMFIT due to source confusion. Using clean maps with a robustness of 0.5, the emission from A1 and A2 could not be separated and only at 9 GHz, using a robustness of -1 , could each be deconvolved individually. For components B, C and D this was not the case and consequently sizes and integrated fluxes are derived from the clean map with a robustness of 0.5 to maximise the signal to noise ratio. A resolved out HII region is also seen to the south west of A1 (RMS survey alias G310.1420+00.7583B or component E of Figure A.22) which is not discussed further.

3.3.2.4 G313.7654–00.8620

Associated to IRAS 14212–6131, 6 associated lobes were previously detected in chapter 2 named A1 (MYSO), A2, B1, B2, C and D (Figure A.23). Both hydroxyl (Caswell 1998) and methanol (Green *et al.* 2012) masers have been previously observed, the latter of which was separated from A1 by $\sim 1''$ at a

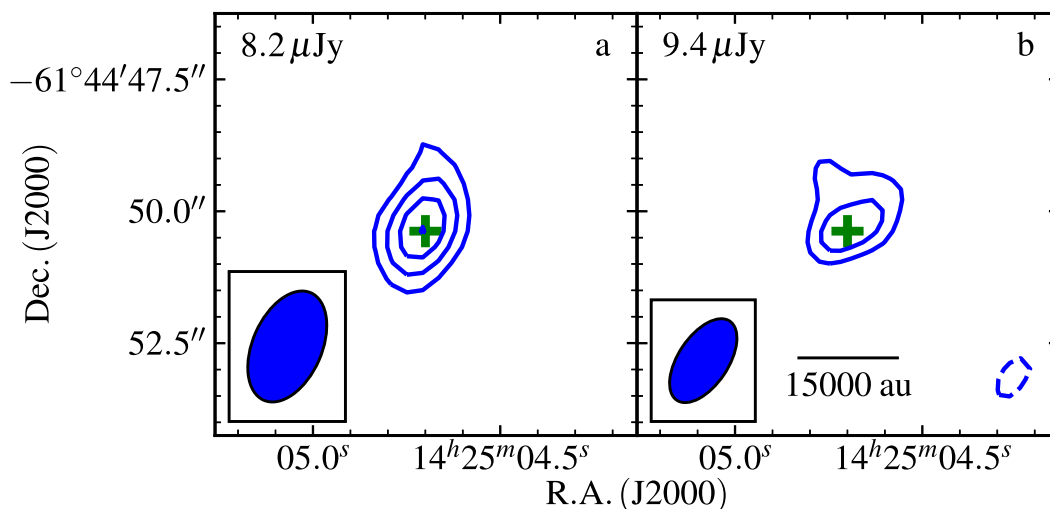


Figure 3.12: Primary beam corrected, radio contour maps of ‘F’ towards G313.7654-00.8620 utilising a robustness of 0.5 at: a.) 6 GHz; b.) 9 GHz. Restoring beams used are illustrated in the bottom left corners (same dimensions as in Figure 3.10) and contours are $(-3, 3, 5, 7) \times \sigma$ where σ is the noise in the image indicated in the top-left corner of each sub-plot. The green cross indicates a CH_3OH maser detected in the 6 GHz band whose positional uncertainties are $< 0.1''$.

position angle of 108° . Caratti o Garatti *et al.* (2015) detected 4 knots of H_2 emission which, if tracing a jet, show evidence of a precession in the jet’s axis of 32° . Knot 1 (coincident with B1 of Figure A.23) has an inferred electron density of $(1 \pm 0.5) \times 10^4 \text{ cm}^3$, while knot 4 (most distant) displays $\text{Br}\gamma$ emission indicative of strong J-type shocks with a shock speed of $\sim 60 \text{ km s}^{-1}$. Currently the jet axis is defined at a position angle of 125° , with a length (on one side) of 1.4 pc. GLIMPSE images show diffuse $4.5 \mu\text{m}$ excesses in the general area of previously established radio emission, an extended HII region $\sim 30''$ to the west and a compact HII region $\sim 10''$ to the south west (E of Figure A.23).

Two new components are seen in the clean maps of Figure 3.10 compared to Figure A.23. One is situated $\sim 2''$ to the NW of B1 which is designated

B3, and the other approximately halfway between A2 and C, which is relatively diffuse and is therefore unnamed. For B3 a spectral index of $\alpha = -0.9 \pm 1.0$ is derived. Outside the field of view for Figure 3.10, a radio source (shown in Figure 3.12) is detected $\sim 24''$ to the NE of A1, named F, for which integrated fluxes of $85 \pm 18 \mu\text{Jy}$ and $85 \pm 21 \mu\text{Jy}$ are measured at 6 and 9 GHz respectively, and therefore $\alpha = 0.0 \pm 1.0$ is calculated. It is also interesting to note that there is an extended radio lobe with spectral index $\alpha = -3 \pm 1$ (suffering from resolving-out effects at 9 GHz) detected $\sim 33''$ from A1 at $\theta_{\text{PA}} \sim -81^\circ$, named G. Two 6.7 GHz methanol maser spots are also detected, one coincident with A1 (see Figure 3.10) and the other coincident with F. For the calculation of spectral indices, a robustness of -1 was employed at all frequencies to allow for the effective deconvolution and subsequent measurement of all component's (apart from B3) integrated fluxes. Component B3 was only detected in the clean maps with a robustness of 0.5 but was sufficiently separated from B1/B2 to allow the accurate deconvolution and measurement of its flux. For all lobes, calculated spectral indices agree with the values obtained in chapter 2 (see Table B.3).

Table 3.4: A table of the integrated fluxes (whose errors take into account a 5% absolute flux error at 6 and 9 GHz), derived spectral indices for flux (α) and major axis length (γ), for all objects in the 2014 epoch observations.

Name	Comp.	S_6 (μJy)	S_9 (μJy)	α	θ_{maj}^6 ($''$)	θ_{maj}^9 ($''$)	γ	R
G263.7434+00.0161	N	626 ± 43	594 ± 44	-0.13 ± 0.25	1.40 ± 0.19	1.40 ± 0.14	-0.01 ± 0.41	0.5
	S2	319 ± 28	363 ± 31	0.32 ± 0.30	1.13 ± 0.49	1.04 ± 0.27	-0.20 ± 1.25	0.5
	S	767 ± 52	837 ± 58	0.22 ± 0.24	2.24 ± 0.13	1.85 ± 0.10	-0.47 ± 0.19	0.5
	SE	126 ± 22	135 ± 29	0.17 ± 0.68	5.18 ± 1.09	5.29 ± 1.27	0.05 ± 0.79	0.5
G310.0135+00.3892	N	707 ± 53	695 ± 66	-0.04 ± 0.30	0.28 ± 0.07	—	—	-1
	S	347 ± 37	481 ± 53	0.81 ± 0.38	0.50 ± 0.16	—	—	-1
	SW	126 ± 35	93 ± 32	-0.75 ± 1.09	< 2.60	—	—	-1
G310.1420+00.7583A	A1	$\left. \begin{array}{l} \\ \end{array} \right\} 2744 \pm 177$	1459 ± 122	—	$\left. \begin{array}{l} \\ \end{array} \right\} 0.84 \pm 0.03$	0.66 ± 0.28	—	-1
	A2		1852 ± 147	—		0.62 ± 0.06	—	-1
	A3	2053 ± 144	1295 ± 160	-1.14 ± 0.35	1.09 ± 0.04	1.36 ± 0.14	0.53 ± 0.28	-1
	A4	888 ± 83	570 ± 94	-1.09 ± 0.47	0.93 ± 0.10	1.00 ± 0.22	0.18 ± 0.60	-1
	B	205 ± 65	117 ± 61	-1.38 ± 1.50	2.78 ± 0.94	—	—	-1
	C	568 ± 56	511 ± 74	-0.26 ± 0.43	< 0.51	0.50 ± 0.17	$> -0.03 \pm 0.82$	-1
	D	1896 ± 137	1684 ± 157	-0.29 ± 0.29	1.09 ± 0.05	0.98 ± 0.08	-0.25 ± 0.22	-1
	G313.7654-00.8620	A1	506 ± 46	537 ± 55	0.15 ± 0.34	< 0.57	0.43 ± 0.10	$> -0.67 \pm 0.60$
A2		183 ± 39	170 ± 60	-0.18 ± 1.02	< 3.00	1.92 ± 0.76	$> -1.10 \pm 0.98$	-1

Table 3.4: Continued

Name	Comp.	S₆ (μJy)	S₉ (μJy)	α	θ_{maj}^6 ($''$)	θ_{maj}^9 ($''$)	γ	R
	B1	350 ± 54	240 ± 76	-0.93 ± 0.87	1.74 ± 0.25	1.92 ± 0.62	0.24 ± 0.87	-1
	B2	116 ± 27	167 ± 46	0.90 ± 0.89	–	1.20 ± 0.41	–	-1
	B3	118 ± 30	81 ± 27	-0.93 ± 1.03	2.15 ± 0.90	1.97 ± 1.11	-0.22 ± 1.73	0.5
	C	420 ± 44	399 ± 57	-0.13 ± 0.44	0.85 ± 0.12	1.06 ± 0.15	0.53 ± 0.50	-1
	D	138 ± 25	157 ± 28	0.32 ± 0.62	–	–	–	-1
	F	85 ± 22	85 ± 25	0.00 ± 0.97	< 2.2	–	–	0.5
	G	171 ± 59	51 ± 18	-2.98 ± 1.02	4.75 ± 1.56	–	–	0.5

3.4 Discussion

Observations presented in section 3.3 have detected new radio emission towards a small sample of young stellar objects across a range in bolometric luminosity. Now I move on to discuss these results and their implications upon the natures of newly detected faint emission, the variability/proper motions of the jets and their lobes and precession in the jets' outflow axes.

3.4.1 Natures of newly detected emission

Towards all of the objects in the sample, apart from G310.1420+00.7583A, sources of radio emission below the detection threshold of previous observations are detected, resulting from many different processes.

In the case of G263.7434+00.1161's SE component, morphology of the emission at 6 GHz shows it to be extended in a jet-like, elongated structure ($5.2 \times 0.6''$) at a position angle of 179° . However the spectral index derived from 6 to 9 GHz ($\alpha = 0.17 \pm 0.68$) was unable to establish whether it was thermal or non-thermal in nature. In an attempt to constrain the emission processes at work, the data shown in Figure A.8 were re-imaged with a robustness of 2 (in order to maximise sensitivity) and a 3σ component was detected, coincident with the new SE lobe, at 5.5, 9 and 17 GHz. Least squares fitting to the first epoch's data alone yields a spectral index of 1.06 ± 0.61 , while for the combined fluxes of data from all epochs a spectral index of $\alpha = 0.51 \pm 0.41$ is calculated (see Figure 3.13). This value for the spectral index (0.51 ± 0.41) determines it to be the partially thermal emission, likely from the jet's stream, and is compatible with a wide variety of scenarios from the models of Reynolds (1986), including the 'standard' spheri-

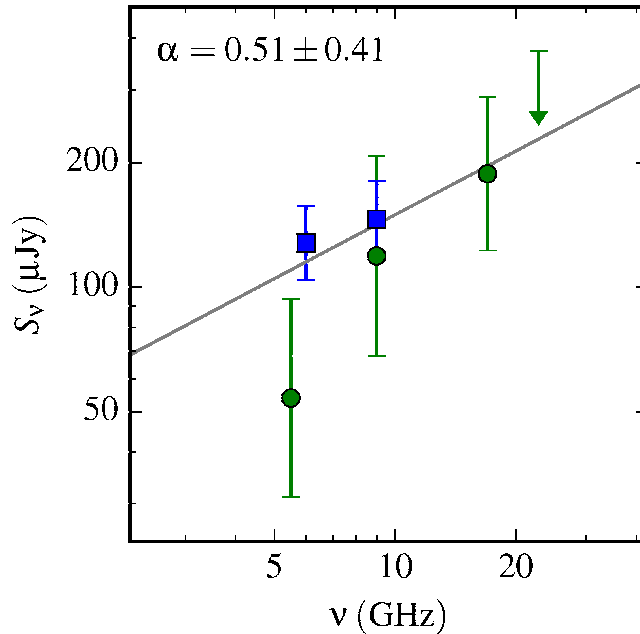


Figure 3.13: A plot of integrated flux against frequency for the SE component of G263.7434+00.1161. Green circles and blue squares represent data from chapter 2 and this work respectively, with the upper limit being that of the 22.8 GHz data from chapter 2. All error bars shown include a 5% uncertainty in the absolute flux calibration. The grey line shows the (log-space) weighted, least-squares fit of the combined data from both epochs, with the derived spectral index shown in the top-left corner.

cal case of a freely flowing ionised jet. Considering its properties and alignment with the North-South component axis, this likely represents the fainter, direct, thermal emission from the jet’s stream. A discussion of the new radio object, S2, detected 29'' to the south of G263.7434+00.1161 is reserved for subsection 3.4.2.

With G310.0135+00.3892, in comparison to other objects in this sample, the previously undetected emission (HH1, HH2 and HH3) is found to be greatly separated from the MYSO itself (up to 3.78 pc) but still roughly aligned along the same axis of $\sim 30^\circ$ with respect to S, much like the HH80-81 system (which has Herbig-Haro objects spread over 5.3 pc, Marti *et al.* 1993). In comparison with a previous near-infrared study (Caratti o Garatti *et al.* 2015), HH1, HH2

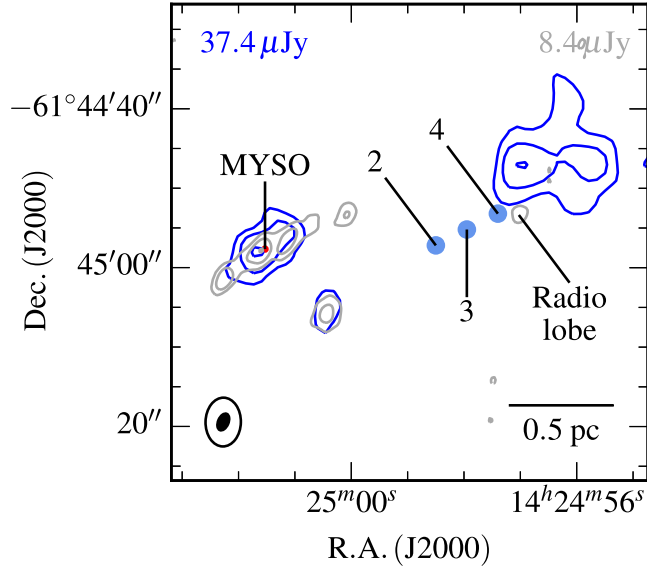


Figure 3.14: Radio contour map of the general area towards G313.7654–00.8620 utilising a robustness of 0.5, at 2 GHz (blue contours) and 6 GHz (grey contours). Restoring beams are illustrated in the bottom left corner and the 2 GHz beam has dimensions of $6.14'' \times 4.45''$ at $\theta_{PA} = -1.24^\circ$. Contours are set at $(-4, 4, 6, 10) \times \sigma$ and $(-4, 4, 15, 58) \times \sigma$ for the 2 and 6 GHz data respectively. The value employed for σ is indicated in the top-left corner (for 2 GHz) and top-right (for 6 GHz). Filled, blue circles indicate the $2.12 \mu\text{m}$ knots, ‘knot 2’, ‘knot 3’ and ‘knot 4’ from Caratti o Garatti *et al.* (2015). The radio lobe detected at 6 GHz, which suggests an overall precession, in the outflow axis is annotated.

and HH3 are spatially coincident with their $2.122 \mu\text{m}$, H_2 lobes ‘E red’, ‘D red’ and ‘bow-shock A Red’. Considering that this type of emission is the result of shocks with velocities $> 15 \text{ km s}^{-1}$ (Elias 1980), this confirms HH1, HH2 and HH3’s status as radio Herbig-Haro lobes. From their integrated fluxes and size, average emission measures of 5350 ± 825 , 9590 ± 1250 and $9990 \pm 2110 \text{ pc cm}^{-6}$ are calculated, while average electron densities are found to be 303 ± 55 , 351 ± 61 and $549 \pm 116 \text{ cm}^{-3}$ for HH1, HH2 and HH3 respectively.

Diffuse faint emission between the previously established lobes, A2 and C of G313.7654–00.8620 was detected, which is likely ‘filling in’ the jet’s emission as

a result of the increased sensitivity of this set of observations. Component F on the other hand is distinctly separated from the main radio emission, compact and has a methanol maser detected towards it meaning it is likely another MYSO in the vicinity. However it has no clear near or mid-IR counterpart and therefore must be deeply embedded within the clump and/or relatively unevolved. Maps of $2.122 \mu\text{m}$ H_2 emission from Caratti o Garatti *et al.* (2015) shows the other new radio component B3 to be coincident with their ‘knot 1’, a fact which, in conjunction with B3’s alignment to the presumed jet outflow axis, classifies it as a likely jet-shocked surface. Unfortunately B3’s spectral index was calculated to be -0.9 ± 1.0 meaning the exact emission processes at work could not be constrained. Further from the obvious string of jet-lobes is radio lobe G detected $33''$ to the west. Considering the relative position angle of the emission from the thermal jet (A1) and coincidence with a NIR H_2 , $2.122 \mu\text{m}$ lobe (knot 4 of Caratti o Garatti *et al.* 2015), I propose this to be another surface upon which the jet of outflowing material is impinging. This position also sits at the head of a cometary HII region’s bow-shock, from which extended, partially resolved out emission is detected at 6 GHz . It is therefore possible that this new radio emission is attributable to the HII region and not with a shocked surface along the jet’s axis. However archival observations, taken on 09/12/2011 at 2 GHz , show the HII region’s emission to be offset to the detected radio lobe (Figure 3.14), and extended along a position angle of $\sim 95^\circ$ across an extent of $\sim 10''$ (perpendicular to the MIR HII region’s ‘front’). Since the HII region at 2 GHz is not co-located with the radio lobe at 6 GHz , which itself is coincident with NIR shock emission, this lobe may still be attributable to jet activity.

3.4.2 Variability and proper motions

To examine both the flux variability and motion of radio sources, a comparison of both the IMFIT-derived lobe positions and integrated 9 GHz fluxes from chapter 2 (Tables B.1 and B.3 respectively) with those recorded here was performed (tabulated in Table 3.5). Considering the short time-baseline between the two datasets, the 3σ lower-limits (assuming $\sim 0.1''$ positional uncertainty) on the proper motions are relatively high, ranging from $600 - 6000 \text{ km s}^{-1}$ and therefore realistically their detection was not expected.

Table 3.5: A table of the proper motion-derived velocities/position angles and integrated flux changes from the first to second epochs. These quantities are calculated from the IMFIT-derived positions/fluxes at 9 GHz. Upper limits given are the 3σ upper limits. Velocities incorporate errors on distances of 1 kpc (i.e. spiral arm width) apart from for G263.7434+00.1161 whose distance error is 0.2 kpc (Liseau *et al.* 1992).

Source	Lobe	r ($''$)	v_{PM} (km s^{-1})	θ ($^\circ$)	ΔS_9 (μJy)	R
G263.7434+00.1161	N	0.032 ± 0.062	< 339	29 ± 66	< 270	0.5
	S	0.060 ± 0.032	< 183	245 ± 63	< 375	0.5
	SE	0.716 ± 0.388	< 2208	241 ± 54	< 276	0.5
	S2	—	—	—	$> 283 \pm 41$	0.5
G310.0135+00.3892	N	0.101 ± 0.035	< 1188	307 ± 24	< 324	−1
	S	0.071 ± 0.052	< 1431	346 ± 24	< 276	−1
	SW	0.092 ± 0.140	< 3582	338 ± 42	< 219	−1
G310.1420+00.7583A	A1	0.097 ± 0.012	1376 ± 308	97 ± 26	< 591	−1
	A2	0.115 ± 0.036	< 1791	35 ± 13	933 ± 171	−1
	A3	0.238 ± 0.043	3371 ± 867	309 ± 12	< 726	−1
	A4	0.453 ± 0.079	6409 ± 1627	351 ± 3	< 505	−1
	B	0.318 ± 0.121	< 5718	186 ± 8	< 285	0.5
	C	0.128 ± 0.035	1806 ± 596	70 ± 26	< 552	0.5

Table 3.5: Continued

Source	Lobe	r ($''$)	v_{PM} (km s^{-1})	θ ($^\circ$)	ΔS_9 (μJy)	R
G313.7654–00.8620	D	0.068 ± 0.049	> 2145	344 ± 16	< 699	0.5
	A1	0.063 ± 0.020	< 1320	244 ± 27	< 321	–1
	A2	0.754 ± 0.149	15404 ± 3631	309 ± 13	304 ± 82	0.5
	B1	0.196 ± 0.109	< 6825	195 ± 17	< 225	0.5
	B2	0.511 ± 0.100	10444 ± 2449	327 ± 8	< 135	0.5
	C	0.043 ± 0.104	< 6363	161 ± 68	< 372	–1
	D	0.110 ± 0.052	< 3279	326 ± 24	< 258	–1

From the IMFIT-measured 2013 and 2014 9 GHz fluxes, only two components directly attributable to the jets show significant ($> 3\sigma$) variability, being component A2 of G310.1420+00.7583A and A2 of G313.7654–00.8620. However, since many of the sources' flux distributions (especially these two) are not simple it is unclear whether this change is due to inaccuracies in either deconvolution, measurement of the emission using IMFIT, or both. A pixel-to-pixel comparison and analysis helped to reveal that variability is likely present towards G310.1420+00.7583A, without relying on accurate deconvolution by a multiple set of gaussians in the image plane. In Figure 3.15, the absolute change in the flux for each pixel is plotted for G310.1420+00.7583A (Figure 3.15) showing well-ordered variability towards the western side of the jet (i.e. A2, A3 and A4). However, as discussed in section 3.2, this was an expected effect of differing sampling functions for the two sets of observations (comparing Figure 3.15 to its synthetic equivalent in Figure 3.4). Unexpectedly from considerations of uv -coverages, component D shows an increase in the pixel fluxes towards its peak flux position,

not reflected in its integrated flux (via measurement with IMFIT or integrating flux within the 3σ contours). Therefore I suggest that D is a spatially-resolved shock-site which is evolving over time.

Away from the obvious emission along the ionised jets' axes, a highly variable radio source (S2) was detected $29''$ to the south of G263.7434+00.1161 which should have been seen at the $\sim 12\sigma$ level in the 2013 data and as such possesses a lower-limit on its 9 GHz flux change of $> 283 \pm 41 \mu\text{Jy}$. The thermal nature of the radio emission precludes extragalactic origins since only starburst galaxies rich in HII regions should display thermal spectral indices, but their fluxes should not be variable on the time-scale of ~ 2 yr. At a position angle of 181° from S, which is roughly aligned with the deconvolved position angle of S's major axis, it is possible that this source may be a highly variable radio Herbig-Haro object. On the other hand, it is separated by $0.17''$ (which is likely coincident within astrometric errors) from a 2MASS source (J08484864 – 4332578) which is likely to be a reddened main sequence star and therefore may alternatively be a highly-variable radio star. On the basis of these results however, no definitive classification could be made.

With regard to lobe proper motions, only the morphologically complex sources (i.e. A1, A2, A3 and A4 of G310.1420+00.7583A and A2, B1 and B2 of G313.7654–00.8620) showed significant proper motions in the fitted positions for the lobes. Derived velocities for some of the lobes (i.e. $\sim 10^4 \text{ km s}^{-1}$ for B2 and A2 of G313.7654–00.8620) are extremely high and, considering typical, proper-motion values in the literature ($300 - 1000 \text{ km s}^{-1}$, Marti *et al.* 1995; Rodríguez *et al.* 2008; Guzmán *et al.* 2010), likely due to errors during deconvolution and/or using the IMFIT task (as with flux variability). Towards G310.1420+00.7583A's

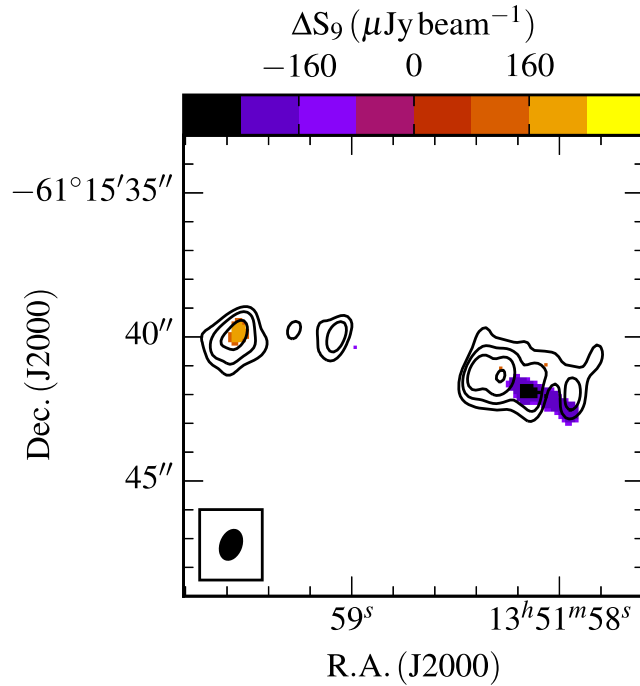


Figure 3.15: A plot of the absolute flux difference between the 2014 and 2013 9 GHz clean maps (robustness = -1) of radio flux for G310.1420+00.7583A (colourscale). Only the pixels whose flux difference was $\Delta S_\nu \leq -4\sigma$ | $\Delta S_\nu \geq 4\sigma$ were included (where $\sigma = 34.5 \mu\text{Jy beam}^{-1}$, the rms noise in the map of absolute flux difference). The common restoring beam's dimensions were $1.05'' \times 0.69''$ at $\theta_{\text{PA}} = -20.9^\circ$. Contours represent the 9 GHz data taken in 2014 with $-4, 4, 9, 21$ and 47σ shown ($\sigma = 22.4 \mu\text{Jy beam}^{-1}$).

lobe C however a more reasonable, and statistically-significant, proper motion of $1806 \pm 596 \text{ km s}^{-1}$ is calculated. A derived position angle of $70 \pm 26^\circ$ places the proper motion along the jet's propagation axis supporting the case that the observed motion is real.

3.4.3 Precession

3.4.3.1 Precession Model

A basic illustration of the model used for a precessing jet is presented in Figure 3.16, which uses the following assumptions:

- Ballistic trajectories are adhered to.
- Bi-axial symmetry of the jet at the point of collimation and ejection (i.e. identical, but opposite, jet and counter-jet).
- Velocity assumed to be constant along the length of the jet.
- Precession occurs at a constant angle and period.

Consequently, for a jet of position angle, inclination and phase of 0° , the x , y and z coordinates of any point along the jet as a function of time are defined by Equations 3.1 to 3.3, where t is time, $\theta_{Pr.}$ is the jet's precession angle and $P_{Pr.}$ is the precession period.

$$r(t) = vt \sin\left(\frac{\theta_{Pr.}}{2}\right)$$

$$x(t) = r \cos\left(\frac{2\pi t}{P_{Pr.}}\right) \quad (3.1)$$

$$y(t) = r \sin\left(\frac{2\pi t}{P_{Pr.}}\right) \quad (3.2)$$

$$z(t) = vt \cos\left(\frac{\theta_{Pr.}}{2}\right) \quad (3.3)$$

Once the (x, y, z) coordinates of this initial jet model are established, a rotation is then applied around the x , y and z -axes for position angle, inclination and

phase (θ_{PA} , i and ϕ) respectively. For any point on the jet, $p(x, y, z)$, the final rotated coordinate, p_{rot} , is calculated according to Equation 3.7:

$$R_x(\theta_{PA}) = \begin{bmatrix} 1 & 0 & 0 \\ 0 & \cos(\theta_{PA}) & -\sin(\theta_{PA}) \\ 0 & \sin(\theta_{PA}) & \cos(\theta_{PA}) \end{bmatrix} \quad (3.4)$$

$$R_y(i) = \begin{bmatrix} \cos(i) & 0 & \sin(i) \\ 0 & 1 & 0 \\ -\sin(i) & 0 & \cos(i) \end{bmatrix} \quad (3.5)$$

$$R_z(\phi) = \begin{bmatrix} \cos(\phi) & -\sin(\phi) & 0 \\ \sin(\phi) & \cos(\phi) & 0 \\ 0 & 0 & 1 \end{bmatrix} \quad (3.6)$$

$$p_{rot} = R_y(i) \cdot (R_x(\theta_{PA}) \cdot (R_z(\phi) \cdot p(x, y, z))) \quad (3.7)$$

Axes are defined so that the x axis points towards the observer and, therefore, y and z axes represent right ascension and declination respectively. This allows us to compare the observables r and θ (radial distance and position angle from the jet origin, respectively) with the model, since the (y, z) coordinate of any point in the rotated model is equivalent to (α, δ) offsets from the jet's origin. Due to the assumption of bi-axial symmetry, it is possible to rotate any lobe coordinate through π radians in position angle.

For fitting observational data, a number of models are produced using a range of values for i , $\theta_{Pr.}$, ϕ , $P_{Pr.}$ and θ_{PA} . For each model the reduced χ_ν^2 value is calculated (Equation 3.8) and the model which minimizes χ_ν^2 is chosen. From jets with multiple lobes, it is possible to place an initial, lower limit on $\theta_{Pr.}$,

approximate θ_{PA} and in some circumstances place an upper limit on P_{Pr} . (should the lobes appear to move through $> \frac{3\pi}{2}$ rads) from inspection of the (r, θ) lobe coordinates. This allows the constraint of the extent of parameter space covered during the fitting process.

$$\chi_{\nu}^2 = \frac{1}{\nu} \sum_{i=1}^k \frac{(|O_i - E_i| - Y)^2}{\sigma_i^2} \quad (3.8)$$

where χ_{ν}^2 is the reduced χ^2 statistic, k is the number of data-points, ν is the degrees of freedom (k - number of open parameters), O_i is the observed value, E_i is the expected value from the model, σ_i is the measurement error and Y is Yates' correction factor ($Y = 0.5$ if $\nu = 1$, otherwise $Y = 0$).

A shortcoming of this approach is that any number of models can be fitted through any number of points by reducing P_{Pr} to shorter times. Therefore the simplest model with the longest precession period is chosen as the 'correct' one.

3.4.3.2 Estimating model errors

Because the precession model was not fitted analytically in the standard way (i.e. fitting an equation to the data) but involved the minimization of χ_{ν}^2 over a finite range of models (much like fitting data to radiative-transfer derived SEDs by Robitaille *et al.* 2007), error-estimation on the derived parameters (such as period or inclination) is a non-trivial problem.

In order to try to overcome this problem, the value for χ_{ν}^2 was plotted in parameter space (fixing the position angle at 77° for G310.1420+00.7583A), between every pair of non-constrained parameters, the results for which are shown in Figure 3.17. From these plots, it is evident that all parameters are relatively well

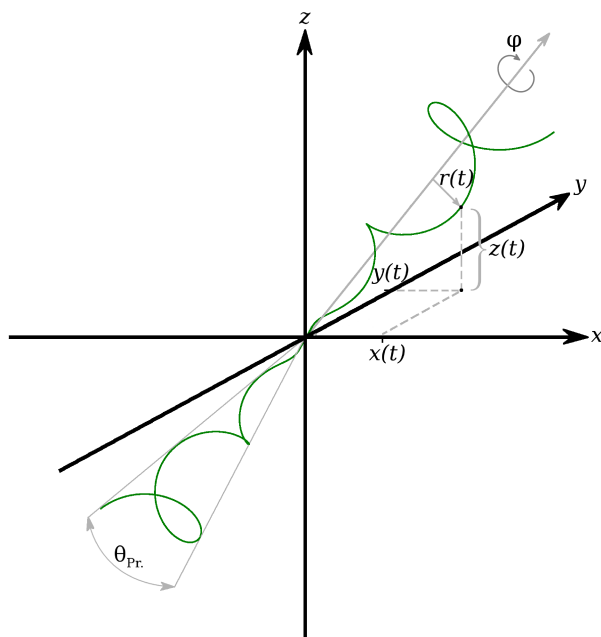


Figure 3.16: An illustration showing the basic setup of the jet model used to fit radio lobe positional data in the main text. Symbols in the diagram are as follows, i is inclination angle, θ_{PA} is position angle in the sky, θ_{Pr} is the precession angle and $x(t)$, $y(t)$ and $z(t)$ are the (x, y, z) coordinates of a point in the jet's stream (green line) at a time, t .

constrained, with precession angle being the most, and inclination angle being the least, constrained of all free parameters.

From these values of χ_ν^2 across parameter space it is possible to infer the standard error on each parameter since the value for χ_ν^2 at a set confidence interval (68.27% or 1σ for Gaussian errors) is defined by Equation 3.9 (Wall & Jenkins 2012). Conservatively, the largest confidence interval for each parameter (since the parameter-space of each is explored three times) is taken as the error.

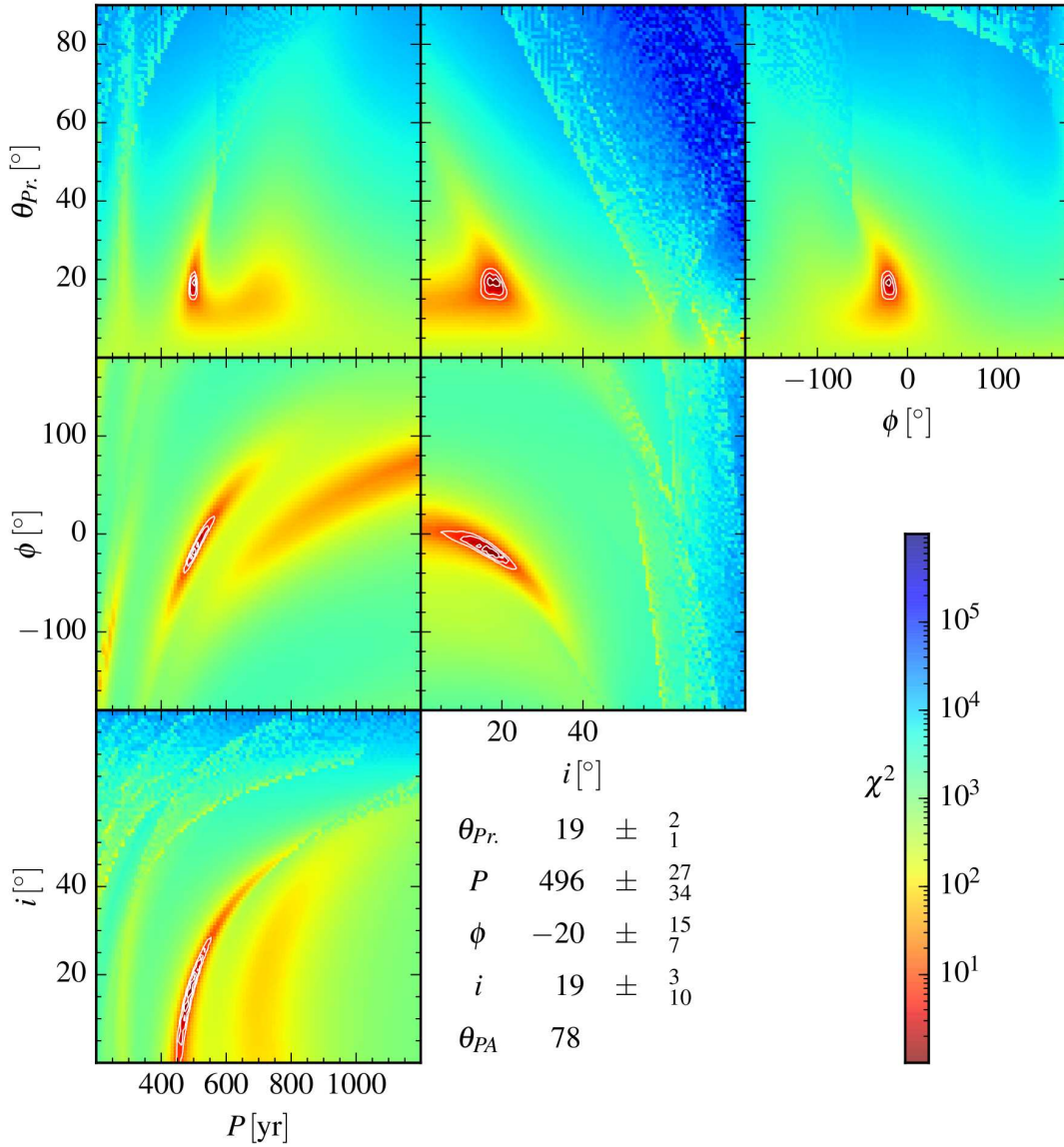


Figure 3.17: Values for χ_ν^2 in parameter space (logarithmic colourscale) for each combination of free parameters in the jet-model fitting to 2013, 9 GHz lobe radii/positions for G310.1420+00.7583A. The black contours represent the 3σ uncertainties.

$$\chi_{\nu,\alpha}^2 = \chi_{\nu,min}^2 + \Delta(\nu, \alpha) \quad (3.9)$$

$$f(\chi_\nu^2) = \frac{(\chi^2)^{\frac{\nu}{2}-1} e^{-\frac{\chi^2}{2}}}{2^{\frac{\nu}{2}} \Gamma(\nu/2)} \quad (3.10)$$

$$\Delta_{\chi_\nu^2}(\chi_\nu^2) = \int_0^\alpha f(\chi_\nu^2) d\chi^2 \quad (3.11)$$

3.4.3.3 Observed precession properties

Various forms of evidence for precession are found towards all 4 objects of the sample with a large range in both derived precession periods and angles.

In the case of G263.7434+00.1161 the deconvolved position angles for the thermal jet at S of $6 \pm 2^\circ$, at both 6 and 9 GHz, suggest that the jet's current axis is offset by $35.7 \pm 1.6^\circ$ w.r.t. the axis running through N, S and SE ($\theta_{PA} = -29.9 \pm 0.24^\circ$). Assuming a jet velocity of 500 km s^{-1} , $i = 90^\circ$ and N to be optically thin emission from jet material (or a shock) which was therefore ejected on a ballistic trajectory from S 33 ± 10 yr ago (assuming a distance error of 200 pc), a precession rate of $1.1^\circ \text{ yr}^{-1}$ is estimated, much higher than precession rates for other ionised jets found in the literature. Assuming the precession over a period of 33 yr is a result of a binary interaction and half the total period, a separation of 30 ± 6 au is inferred (using Equation 3.12, where P is period, M is

the total mass of the binary system and r is the orbital semi-major axis). The complex, $2.122\ \mu\text{m}$, H_2 emission previously observed (Figure A9 of de Luca *et al.* 2007) could be the result of a jet with a high precession rate creating shock sites over a wide range in angles, over a relatively short period, or multiple sources. It must be conceded that YSO/outflow multiplicity is an alternative explanation for these results.

$$r = \left(\frac{P^2 GM}{4\pi^2} \right)^{\frac{1}{3}} \quad (3.12)$$

For G310.0135+00.3892, variations in the position angles of the Herbig-Haro radio lobes are seen, HH1, HH2 and HH3, with respect to S. Fitting the 6 GHz peak positions of these HH objects, and the SW component with a jet model, via minimization of χ^2 as described in subsection 3.4.3.1 (with fixed values of $i = 42^\circ$ and $\theta_{PA} = 31^\circ$, Boley *et al.* 2016), yields a precession angle and period of $6_{-2}^{+1^\circ}$ and 15480_{-2248}^{+3409} yr respectively. Should this precession be due to a regular orbiting body, it should be separated by 1797_{-191}^{+275} au from the MYSO. It must be noted that a precession angle and period of 8° and 8300 yr (inferring an orbital radius of 1200 au) fit the (limited) data equally as well, but a period of 15480 yr represents the simplest model. Since the position angle for the established HH jet lies at an angle of 29° , as discussed previously, the exact nature of the lobe N is an open question since it lies at a position angle of -3° from the MYSO/thermal jet at S. If N is an optically thin HII region, on the basis of its radio flux (and assuming a distance of 3.2 kpc), a bolometric luminosity of $\sim 4000 L_\odot$ (ZAMS type B2, Davies *et al.* 2011) is implied, with a calculated average emission measure of $\sim 7 \times 10^6 \text{ pc cm}^{-6}$ and electron density of $\sim 5000 \text{ cm}^{-3}$, both of which are

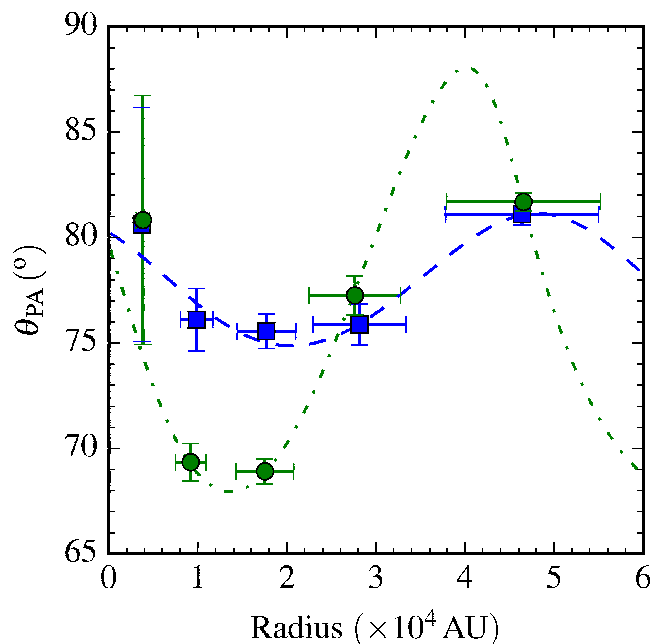


Figure 3.18: A plot of the radii and position angle of components A2, A3, A4, C and D of G310.1420+00.7583A, relative to A1, during both the 2013 (green circles) and 2014 (blue squares) epochs with their fitted curves (green dot-dashed line and blue dashed line respectively). Parameters derived for each curve are listed in Table 3.6.

possibly too low for such a highly-compact (~ 650 au) HII region. On the other hand, if a more rapid and wider angle precession is present compared to that found by analysis of the radio HH lobes, then this may support N as being the site of shock emission from the jet. However, SE lies along the accepted jet outflow axis and is roughly the same separation from S as N is. This suggests that if a wider angle precession is present, it is only affecting the northern jet. It is interesting to note that Wheelwright *et al.* (2012) see this lobe asymmetry in their mid-IR observations too. Unfortunately 2MASS and GLIMPSE imagery is saturated, with image defects at N's position prohibiting its nature from being established any further.

In Figure 3.18 the position angle of the peak emission for each of G310.1420+00.7583A's

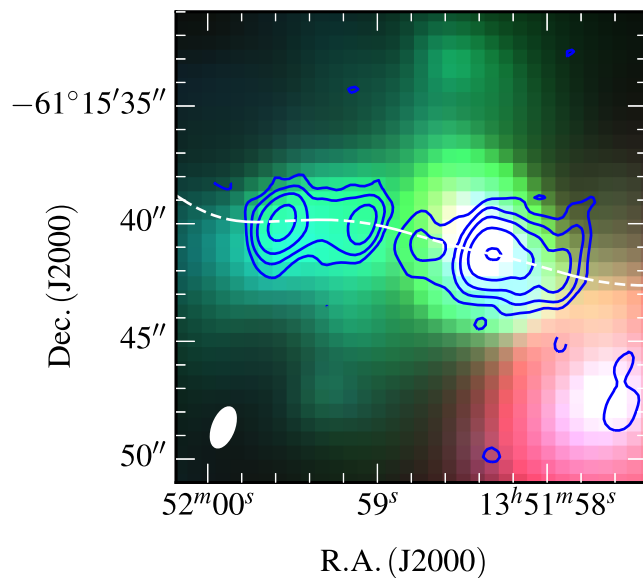


Figure 3.19: A GLIMPSE RGB image of G310.1420+00.7583A overlaid with contours of the 9 GHz radio flux (contour levels are the same as in panel b.) of Figure 3.9). The jet model uses the fitted values for the 2014 data (see Figure 3.18).

Table 3.6: A table of the derived parameters from χ^2 fitting of model in parameter space. Errors are calculated by consideration of the distribution of χ^2 in parameter space. Any value with a * next to it was held as a fixed parameter, so that the number of degrees of freedom, $\nu = N_{\text{points}} - N_{\text{op}}$ (N_{op} is the number of open parameters in the fit) is always 1.

Source	Year	$\theta_{Pr.}$ ($^{\circ}$)	$P_{Pr.}$ (yr)	ϕ ($^{\circ}$)	i ($^{\circ}$)	θ_{PA} ($^{\circ}$)
G310.0135	2014	6_{-2}^{+1}	15480_{-2248}^{+3409}	308_{-26}^{+43}	42*	31*
G310.1420	2013	19_{-1}^{+2}	496_{-34}^{+27}	340_{-7}^{+15}	19_{-10}^{+3}	78*
	2014	6_{-3}^{+3}	568_{-126}^{+318}	313_{-57}^{+88}	16_{-16}^{+26}	78*
G313.7654	2014	12_{-1}^{+2}	920_{-32}^{+82}	338_{-26}^{+11}	51_{-2}^{+3}	121*

lobes is plotted as a function of radius and position angle from A1 (i.e. the MYSO), which shows evidence for precession in the jet’s axis. These positions were fitted with a precessing jet model with inclination left as a free parameter. For both the 2013 and 2014 data, the best fitting model’s parameters are tabulated in Table 3.6. In Figure 3.19 this model derived for the 2014 data is plotted over GLIMPSE, MIR images. It can be seen that the jet model’s path traces both the east, MIR 4.5 μm excess (EGO) and general, extended, radio morphology well. Comparison of the 2013 and 2014 best fit models shows the derived quantities largely agree, apart from the precession angles (19° and 6° for the 2013/2014 data respectively). This discrepancy between the two models is likely due to deconvolution/imaging errors discussed in section 3.2 and subsection 3.4.1. As with G310.0135+00.3892, assuming that the jet precession is due to a binary whose orbital period is the same as the precession period, an orbital radius of 141_{-8}^{+7} au or 155_{-24}^{+58} au is inferred, depending on whether the fit parameters for the 2013 or 2014 data are used respectively.

In the case of G313.7654–00.8620, the radii and position angles of A2, B1, B3, C and D were calculated with respect to the MYSO, A1 (plotted in Figure 3.20). Because only the 2014 images detected B3, fitting with inclination as a free parameter was only attempted towards the 2014 lobe positions (in order to have at least one degree of freedom). Component B2 is neglected from this analysis due to its unknown nature and its deviation from the position angles of the other lobes. Fitting yields a precessing jet model with a precession angle of $12_{-1}^{+2^\circ}$, period of 920_{-32}^{+82} yr and inclination of $51_{-2}^{+3^\circ}$ which is shown overlayed upon a GLIMPSE RGB image in Figure 3.21. As with the other objects, if a binary companion has induced this precession, a separation for the binary companion

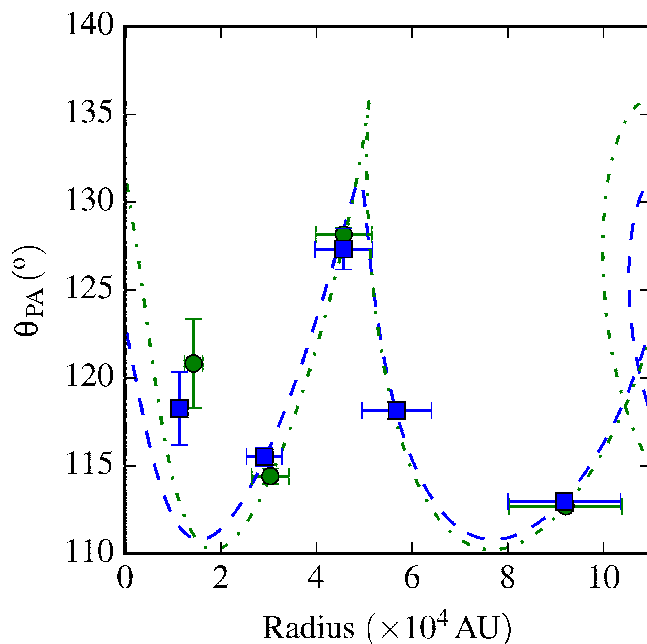


Figure 3.20: A plot of the radii and position angles for components A2, B1, B3, C and D of G313.7654–00.8620 (relative to A1) where symbols and fitted lines have the same meaning as in Figure 3.19. For 2013 and 2014 data, values for θ_{PA} of 123° and 121° , P_{pr} of 950 and 920 yr, i of 54° and 51° , θ_{pr} of 15° and 12° and ϕ of 35° and 338° were used for the 2013 and 2014 models respectively.

of 270_{13}^{+19} au is inferred. The fitted model does not accurately trace the MIR $4.5 \mu\text{m}$ excess, in comparison with G310.1420+00.7583A, the diffuse radio emission detected between A2 and C, or the radio lobe, G (which is coincident with the H_2 $2.122 \mu\text{m}$ emission lobe, ‘knot 4’ from Caratti o Garatti *et al.* 2015). It is possible that G313.7654–00.8620 is a more complex system, and (in addition to periodic precession) a large overall shift in the precession axis may have occurred, on account of G’s position and the results of Caratti o Garatti *et al.* (2015), from $\sim 98^\circ$ to 121° over a period of approximately 4100 yr, or $5.6 \times 10^{-3} \text{ }^\circ \text{ yr}^{-1}$.

In Figure 3.22 the four, inferred precession angles for the sample, and the relevant orbital radii, are plotted. Fitted power laws for precession angle against

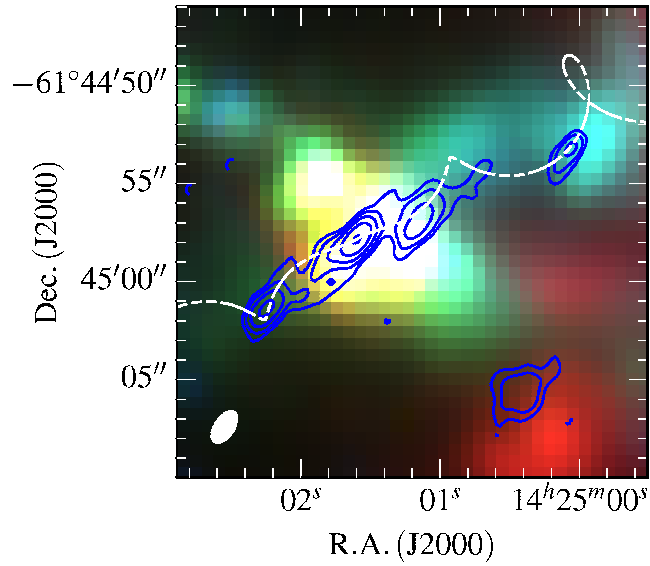


Figure 3.21: A GLIMPSE RGB image of G313.7654–00.8620 overlaid with contours of the 9 GHz radio flux (contour levels of $-4, 4, 8, 15, 28$ and 54σ where $\sigma = 9.0 \mu\text{Jy beam}^{-1}$). The jet model uses the fitted values for the 2014 data (see Figure 3.20).

both period and inferred orbital radius are explicitly stated in Equation 3.13 and Equation 3.14 respectively. These relations show that for shorter precession periods/smaller orbital radii for the hypothesised binary companions, a larger precession angle is observed. This agrees with the idea that a closer companion would deflect a jet’s stream to a greater degree through gravitational influence on the ballistic trajectory of jet material. However to establish this explanation would require both a larger sample than that presented here and direct confirmation of the existence of binary companions.

$$\log_{10}(\theta_{\text{Pr}}) = (2.20 \pm 0.13) - (0.36 \pm 0.05) \log_{10}(P_{\text{Pr}}) \quad (3.13)$$

$$\log_{10}(\theta_{\text{Pr}}) = (2.23 \pm 0.08) - (0.45 \pm 0.04) \log_{10}(r) \quad (3.14)$$

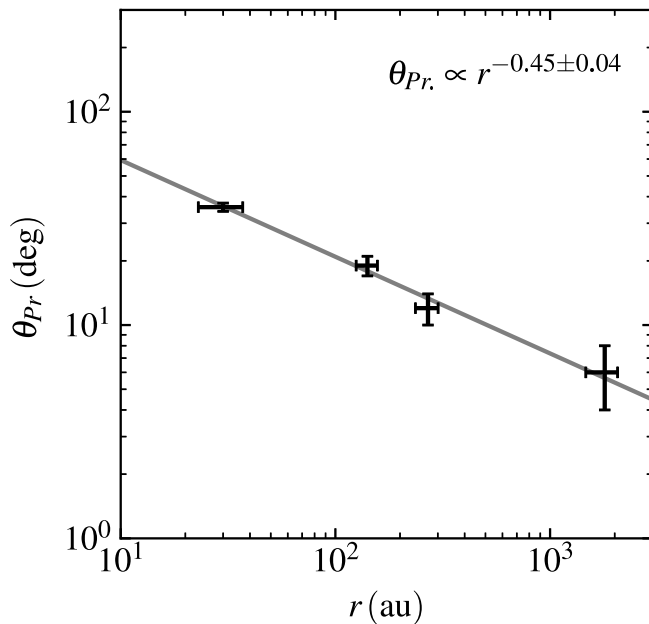


Figure 3.22: A plot of the precession angle against inferred orbital radii. Orthogonal distance regression (taking into account errors in both variables) was used to fit the power law which is plotted in grey and explicitly stated in Equation 3.14.

3.5 Summary and Conclusions

Sensitive radio observations at 6 and 9 GHz were conducted towards a sample of 4 MYSOs known to harbour ionised jets associated with shock-ionised lobes. This sample was selected from the previous work of chapter 2 in order to investigate their temporal evolution, faint emission and precession of their outflow axes. From careful consideration of the observational differences between each epoch’s dataset, their subsequent comparison and modelling of the relative lobe positions from their sourcing jets, the following can be concluded:

- Fainter emission is detected towards 3 of 4 jets, which is sources directly from the thermal jet itself in one object (G263.7434+00.1161), radio Herbig-Haro objects in G310.0135+00.3892 and extra non-thermal emission in

G313.7654–00.8620. This suggests that mass loss in MYSOs is a variable, yet continuous, process.

- Proper motions are detected at the $> 3\sigma$ level towards one lobe (C) of G310.1420+00.7583A, with a derived velocity of $1806 \pm 596 \text{ km s}^{-1}$, in agreement with other examples of proper motions in the literature, parallel with the jet's propagation axis.
- Change in the flux morphology is seen towards a non-thermal lobe (D) of G310.1420+00.7583A, supporting the hypothesis the emission is the result of shocked material, rather than direct emission from the jet's stream.
- Evidence for precession is found in all objects within the sample, with inferred precession angles ranging from $6 \pm 3^\circ$ to $36 \pm 2^\circ$ and periods from 66 ± 20 to 15480^{+3409}_{-2248} yr. If the assumed precession of jet outflow axes is caused by the bound orbits of binary companions, estimated orbital radii of 30 ± 6 au, 1797^{+275}_{-191} au, 141^{+7}_{-8} au and 270^{+19}_{-13} au are found for G263.7434+00.1161, G310.0135+00.3892, G310.1420+00.7583A and G313.7654–00.8620 respectively.

Considering the apparent precessions of the MYSOs observed, it is clear that these 4 ionised jets are not restricted to a single outflow angle over time. Compared to precession seen towards low-mass examples, it is both more extreme and also more rapid. Definitive variability or proper motions were not observed over a 2 year period towards the shock ionised lobes or thermal jets, however future studies, with longer time baselines, towards a larger sample of objects from chapter 2 will inform more reliably on these matters. The results presented

here therefore form the foundation for such studies and hint that it will produce interesting results in the future.

Chapter 4

A statistical JVLA C and Q-band survey of ionised jets on the 100 au scale

Source confusion and large distances are the main observational constraints in studying MYSOs and their collimated outflow phenomena at radio wavelengths. As already discussed, these factors are responsible for the small number of large scale surveys for jets conducted up to this point (see subsection 1.4.4). From the work of chapter 2, this was somewhat alleviated by utilising radio observations at 4 frequencies from 5 to 22 GHz to detect 28 radio sources exhibiting the characteristics of ionised jets, from a southern sample of 49 objects. That sample drew its targetted MYSO fields directly from the Red MSX Source (RMS) multi-wavelength survey (Lumsden *et al.* 2013) and was comprised of a smaller, distance-limited (< 7 kpc) sub-sample (34 objects) spaced evenly over a wide range of bolometric luminosities. In order to advance knowledge of this field fur-

ther, expanding that work into the northern hemisphere and, by extension, the number of known ionised jets associated with MYSOs, is paramount.

Extending the sample into the northern sky allows for the use of the VLA up to frequencies of ~ 50 GHz. In its most extended (A) configuration, the VLA possesses synthesised beam widths of $\gtrsim 0.05''$, which is equivalent to ~ 40 au at the distance of the closest MYSOs (in the Vela molecular cloud at a distance of 700 pc) from the sample of chapter 2. As discussed in subsection 1.4.1, probing scales < 100 au is required in order to spatially resolve the collimation radius of the jets, however the launching radius is likely too small to be detected without even larger (i.e. SKA era) baselines. Recently the VLA also underwent a major upgrade to its correlator, which effectively increased its sensitivity by an order of magnitude. With this increase in sensitivity, surveys of radio-faint phenomena can be efficiently performed and, more specifically, the extremely weak ($\ll 1$ mJy) radio emission from MYSOs, or even earlier phases of massive star formation. A relatively poorly investigated question in this field is when exactly the weak radio emission from an MYSO ‘switches on’ (i.e. the jet phase, *not* the HII phase). In order to establish this, surveys of IRDCs (the earliest phase in MSF) with extremely high radio sensitivities are required.

Considering those points discussed above, this work attempts to perform a similar, RMS-derived, survey towards a northern sample of 45 MYSOs, as in chapter 2, utilising the VLA at its highest possible resolution. The main goal is to establish a statistical sample of identified, northern, ionised jets to augment the southern sample, and study them on scales previously unstudied in order to possibly examine their collimation radii. Further to this, this chapter intends to investigate the emergence of ionised outflow phenomena towards even earlier

stages of massive star formation within IRDCs, for which 12 fields from a previous millimetre survey (Rathborne *et al.* 2010) have been chosen. Full details of the sample, its constituting two sub-samples and their selection procedure are discussed in section 4.1. In section 4.2 we subsequently describe the VLA observations conducted towards our sample the results of which are further discussed in section 4.3. During the analysis of these results, the jets' derived physical properties are compared to their associated molecular outflows, models of gravitationally trapped HII regions and their evolution with the MYSOs' luminosities is further examined. Based upon these analyses, the conclusions stemming from this work are then discussed in section 4.5 to conclude this chapter.

4.1 The Sample

Membership criteria for the observational sample of this work has been tailored to represent a wide range of evolutionary statuses, from the earliest phase of massive star formation represented by the IRDC stage, to the mid-infrared bright, pre-UCHII phase just as a massive star starts its journey along its Hayashi track (evolutionary path in the stellar luminosity-temperature plane) to join the main sequence. Increasing mid-infrared luminosities are brought about by the dispersion of the extinguishing circumstellar material by radiative and mechanical means, as an MYSO increases both its luminosity and mass. Selection criteria for the sample are therefore formed upon the basis of bolometric luminosity and infrared colour, assumed to be indicators of mass and evolutionary status respectively.

4.1.1 The IRDC sample

Evolutionarily-speaking, the first sub-sample is based upon the work by Rathborne *et al.* (2010), who surveyed a number of IRDCs at mm wavelengths, and subsequently derived many of their filial cores' physical properties. They employed the same classification system as Chambers *et al.* (2009), whereby each core was categorised based upon IR evolutionary indicators, specifically the presence of $4.5\ \mu\text{m}$ excesses ('green fuzzies' or EGOs), bright $8\ \mu\text{m}$ and/or $24\ \mu\text{m}$ emission. Core classifications include (in order of evolution) quiescent (Q), intermediate (I), active (A) or red (R). Details for each can be found in Table 4 of Chambers *et al.* (2009).

A requirement of the IRDCs selected for observation were that they contained cores of either a 'red' or 'active' classification, though numerous stages can be seen in cores encompassed by the primary beam of the lowest frequency observations. Quantitatively, the selection criteria included IRDC cores with luminosities $> 10^3 L_{\odot}$, distances $< 7\ \text{kpc}$ and infrared flux ratios, $S_{70\mu\text{m}}/S_{24\mu\text{m}} \gtrsim 50$. This led to a sample size of 8 IRDCs, incorporating 44 cores in total, of which 14 possessed bolometric luminosities greater than the cut-off (see Table 4.1 for a full list). All luminous cores of the sample which have MIPS GAL data are shown as green markers in Figure 4.1.

Table 4.1: Target IRDC cores and their properties (taken from Rathborne *et al.* 2010). Columns, from left to right, are IRDC name, core designation, right ascension (J2000), declination (J2000), distance (with a quoted 15% error in the kinematic distances from Simon *et al.* 2006), bolometric luminosity, core mass, IR classification, C-band and, finally, Q-band observation dates (see Table B.16 of Appendix B for details). Any core name superscripted with a ‘*’ denotes the C-band/Q-band pointing centre, with the exception of G033.69–00.01, whose pointing centre at C-band was $18^{\text{h}}52^{\text{m}}54^{\text{s}}$, $+00^{\circ}39'39''$. At Q-band, it was imaged as a 3-piece mosaic comprised of a pointing towards the C-band pointing centre, one towards $18^{\text{h}}52^{\text{m}}49.9^{\text{s}}$, $+00^{\circ}37'57''$ and the other towards $18^{\text{h}}52^{\text{m}}58.1^{\text{s}}$, $+00^{\circ}41'20''$. For core luminosity/mass, a superscript † symbol denotes that the number is the midpoint in the lower/upper limit range given by Rathborne *et al.* (2010).

IRDC	Core	α (J2000)	δ (J2000)	Distance	L_{bol}	M_{C}	Class.	Date of Observation(s)	
		(hh:mm:ss)	(dd:mm:ss)					(kpc)	(L_{\odot})
G018.82–00.28	MM2*	18:26:23.4	–12:39:37	4.6 ± 0.7	8990	87	R	C3	Q2, Q3
G018.82–00.28	MM4	18:26:15.5	–12:41:32	4.6 ± 0.7	198	228	I	C3	Q2, Q3
G018.82–00.28	MM5	18:26:21.0	–12:41:11	4.6 ± 0.7	237 [†]	118 [†]	Q	C3	Q2, Q3
G024.08+00.04	MM1*	18:34:57.0	–07:43:26	3.8 ± 0.6	14847	71	R	C4, C5	Q2, Q3
G024.08+00.04	MM2	18:34:51.1	–07:45:32	3.8 ± 0.6	321	115	Q	C4, C5	Q2, Q3
G024.08+00.04	MM3	18:35:02.2	–07:45:25	3.8 ± 0.6	245 [†]	77 [†]	Q	C4, C5	Q2, Q3
G024.08+00.04	MM4	18:35:02.6	–07:45:56	3.8 ± 0.6	60	55	Q	C4, C5	Q2, Q3
G024.08+00.04	MM5	18:35:07.4	–07:45:46	3.8 ± 0.6	171 [†]	63 [†]	Q	C4, C5	Q2, Q3
G024.33+00.11	MM1*	18:35:07.9	–07:35:04	6.3 ± 0.9	47387	472	R	C4, C5	Q2, Q3
G024.33+00.11	MM4	18:35:19.4	–07:37:17	3.7 ± 0.6	161 [†]	301 [†]	Q	C4, C5	Q2, Q3
G024.33+00.11	MM6	18:35:07.7	–07:34:33	3.7 ± 0.6	239 [†]	175 [†]	Q	C4, C5	Q2, Q3

Table 4.1: Continued

IRDC	Core	α (J2000)	δ (J2000)	Distance (kpc)	L_{bol} (L_{\odot})	M_C (M_{\odot})	Class.	Date of Observation(s)	
		(hh:mm:ss)	(dd:mm:ss)					C-band	Q-band
G024.33+00.11	MM8	18:35:23.4	-07:37:21	3.7 ± 0.6	66 [†]	239 [†]	Q	C4, C5	Q2, Q3
G024.33+00.11	MM9	18:35:26.5	-07:36:56	3.7 ± 0.6	697	81	R	C4, C5	Q2, Q3
G024.33+00.11	MM10	18:35:27.9	-07:35:32	3.7 ± 0.6	187	36	I	C4, C5	Q2, Q3
G024.33+00.11	MM11	18:35:05.1	-07:35:58	3.7 ± 0.6	110 [†]	552 [†]	Q	C4, C5	Q2, Q3
G024.60+00.08	MM1*	18:35:41.1	-07:18:30	3.6 ± 0.5	964	163	A	C4, C5	Q2, Q3
G024.60+00.08	MM2	18:35:39.3	-07:18:51	6.5 ± 1.0	3544	249	I	C4, C5	Q2, Q3
G024.60+00.08	MM3	18:35:40.2	-07:18:37	3.6 ± 0.5	338 [†]	108 [†]	I	C4, C5	Q2, Q3
G028.28-00.34	MM1*	18:44:15.0	-04:17:54	3.2 ± 0.5	4768	150	R	C4, C5	Q2, Q3
G028.28-00.34	MM2	18:44:21.3	-04:17:37	3.2 ± 0.5	4565	132	R	C4, C5	Q2, Q3
G028.28-00.34	MM3	18:44:13.4	-04:18:05	3.2 ± 0.5	2951	23	R	C4, C5	Q2, Q3
G028.37+00.07	MM1*	18:42:52.1	-03:59:45	4.8 ± 0.7	26062	507	A	C4, C5	Q2, Q3
G028.37+00.07	MM2	18:42:37.6	-04:02:05	4.8 ± 0.7	23329	184	I	C4, C5	Q2, Q3
G028.37+00.07	MM4	18:42:50.7	-04:03:15	4.8 ± 0.7	2113	140	A	C4, C5	Q2, Q3
G028.37+00.07	MM6	18:42:49.0	-04:02:23	4.8 ± 0.7	727 [†]	277 [†]	I	C4, C5	Q2, Q3
G028.37+00.07	MM9	18:42:46.7	-04:04:08	4.8 ± 0.7	283 [†]	675 [†]	Q	C4, C5	Q2, Q3
G028.37+00.07	MM10	18:42:54.0	-04:02:30	4.8 ± 0.7	1200	172	A	C4, C5	Q2, Q3

Table 4.1: Continued

IRDC	Core	α (J2000)	δ (J2000)	Distance (kpc)	L_{bol} (L_{\odot})	M_C (M_{\odot})	Class.	Date of Observation(s)	
		(hh:mm:ss)	(dd:mm:ss)					C-band	Q-band
G028.37+00.07	MM11	18:42:42.7	-04:01:44	4.8 ± 0.7	353	173	A	C4, C5	Q2, Q3
G028.37+00.07	MM14	18:42:52.6	-04:02:44	4.8 ± 0.7	99 [†]	68 [†]	Q	C4, C5	Q2, Q3
G028.37+00.07	MM16	18:42:40.2	-04:00:23	4.8 ± 0.7	288 [†]	599 [†]	Q	C4, C5	Q2, Q3
G028.37+00.07	MM17	18:43:00.0	-04:01:34	4.8 ± 0.7	82 [†]	190 [†]	Q	C4, C5	Q2, Q3
G028.67+00.13	MM1*	18:43:03.1	-03:41:41	4.8 ± 0.7	11997	46	R	C4, C5	Q2, Q3
G028.67+00.13	MM2	18:43:07.1	-03:44:01	4.8 ± 0.7	145	245	I	C4, C5	Q2, Q3
G028.67+00.13	MM5	18:43:10.1	-03:45:08	4.8 ± 0.7	132 [†]	151 [†]	Q	C4, C5	Q2, Q3
G028.67+00.13	MM6	18:43:12.2	-03:45:39	4.8 ± 0.7	103 [†]	106 [†]	Q	C4, C5	Q2, Q3
G033.69-00.01	MM1	18:52:58.8	+00:42:37	7.1 ± 1.1	2003	751	R	C4, C5	Q6, Q7
G033.69-00.01	MM2	18:52:49.9	+00:37:57	7.1 ± 1.1	22373	563	R	C4, C5	Q6, Q7
G033.69-00.01	MM3	18:52:50.8	+00:36:43	7.1 ± 1.1	5108	98	R	C4, C5	Q6, Q7
G033.69-00.01	MM4	18:52:56.4	+00:43:08	7.1 ± 1.1	246	485	A	C4, C5	Q6, Q7
G033.69-00.01	MM5	18:52:47.8	+00:36:47	7.1 ± 1.1	18213	99	A	C4, C5	Q6, Q7
G033.69-00.01	MM6	18:52:48.7	+00:35:58	7.1 ± 1.1	374 [†]	310 [†]	Q	C4, C5	Q6, Q7
G033.69-00.01	MM8	18:52:53.9	+00:41:16	7.1 ± 1.1	534 [†]	908 [†]	Q	C4, C5	Q6, Q7
G033.69-00.01	MM9	18:52:58.1	+00:41:20	7.1 ± 1.1	5621	43	I	C4, C5	Q6, Q7

Table 4.1: Continued

IRDC	Core	α (J2000)	δ (J2000)	Distance	L_{bol}	M_C	Class.	Date of Observation(s)	
		(hh:mm:ss)	(dd:mm:ss)					(kpc)	(L_{\odot})
G033.69–00.01	MM10	18:52:52.7	+00:38:35	7.1 ± 1.1	427 [†]	174 [†]	Q	C4, C5	Q6, Q7
G033.69–00.01	MM11	18:52:56.2	+00:41:48	7.1 ± 1.1	510 [†]	142 [†]	Q	C4, C5	Q6, Q7

Table 4.2: All targets within our MYSO sample observed during the 7 years of observations. Superscript numbers depict the reference from which that distance or bolometric luminosity is adopted, otherwise they are taken from the RMS survey (Lumsden *et al.* 2013). These are ¹: Zhang *et al.* (2009), ²: Lu *et al.* (2014), ³: Zhang *et al.* (2013), ⁴: Fujisawa *et al.* (2012), ⁵: Rygl *et al.* (2012), ⁶: Rygl *et al.* (2010), ⁷: Sugitani *et al.* (1989), ⁸: Moscadelli *et al.* (2009), ⁹: Imai *et al.* (2000), ¹⁰: Hachisuka *et al.* (2006), ¹¹: Kawamura *et al.* (1998), ¹²: Burns *et al.* (2017), ¹³: Oh *et al.* (2010), ¹⁴: Minier *et al.* (2005), ¹⁵: Burns *et al.* (2016), ¹⁶: Honma *et al.* (2007). *: Indicates that the luminosity from the reference has been adapted to take account of more recent, more accurate distance estimates.

MYSO	α (J2000)	δ (J2000)	Distance	L_{bol}	Date of Observation(s)	
	(hh:mm:ss)	(dd:mm:ss)			(kpc)	(L_{\odot})
18517+0437	18:54:13.8	+04:41:32	1.88 ± 0.08^1	7100 ^{2*}	C7	Q2, Q4
18556+0136	18:58:13.0	+01:40:38	2.19 ± 0.24^1	150000 ³	C7	Q2, Q4
G033.6437–00.2277	18:53:32.6	+00:31:39	4.0 ± 1.0^4	14000 ⁴	C4, C5	Q6, Q7
G056.3694–00.6333	19:38:31.6	+20:25:19	5.9 ± 1.0	8700	C3	Q2, Q4
G077.5671+03.6911	20:12:33.7	+40:47:41	5.7 ± 1.0	4500	C3	Q5

Table 4.2: Continued

MYSO	α (J2000)	δ (J2000)	Distance (kpc)	L_{bol} (L_{\odot})	Date of Observation(s)	
	(hh:mm:ss)	(dd:mm:ss)			C-band	Q-band
G078.8699+02.7602	20:20:30.6	+41:21:27	1.40 ± 0.08^5	6500	C3	Q5
G079.8855+02.5517	20:24:31.5	+42:04:18	1.40 ± 0.08^5	2200	C3	Q5
G081.8652+00.7800	20:38:36.4	+42:37:35	1.30 ± 0.07^5	3600	C3	Q5
G083.7071+03.2817	20:33:36.5	+45:35:44	1.40 ± 0.08^5	3900	C3	Q5
G084.9505−00.6910	20:55:32.5	+44:06:10	5.5 ± 1.0	13000	C3	Q5
G094.2615−00.4116	21:32:31.6	+51:02:20	5.2 ± 1.0	9000	C1, C6	Q11, Q12
G094.3228−00.1671	21:31:45.1	+51:15:35	4.4 ± 1.0	5700	C1, C6	Q11, Q12
G094.4637−00.8043	21:35:09.1	+50:53:10	5.0 ± 1.0	21000	C1, C6	Q11, Q12
G094.6028−01.7966	21:39:58.3	+50:14:21	4.9 ± 1.0	43000	C1, C6	Q11, Q12
G100.3779−03.5784	22:16:10.4	+52:21:35	3.7 ± 1.0	17000	C1, C6	Q11, Q12
G102.8051−00.7184	22:19:09.2	+56:05:02	4.0 ± 1.0	2300	C1, C6	Q11, Q12
G103.8744+01.8558	22:15:09.1	+58:49:08	1.6 ± 0.5	6800	C1, C6	Q11, Q12
G105.5072+00.2294	22:32:24.0	+58:18:58	4.6 ± 1.0	7000	C1, C6	Q1, Q10
G107.6823−02.2423A	22:55:29.8	+57:09:25	4.7 ± 1.0	4100	C1, C6	Q1, Q10
G108.1844+05.5187	22:28:51.4	+64:13:41	0.78 ± 0.10^6	*873 ^{7*}	C1, C6	Q1, Q10
G108.4714−02.8176	23:02:32.0	+56:57:53	4.5 ± 1.0	5100	C1, C6	Q1, Q10

Table 4.2: Continued

MYSO	α (J2000)	δ (J2000)	Distance	L_{bol}	Date of Observation(s)	
	(hh:mm:ss)	(dd:mm:ss)	(kpc)	(L_{\odot})	C-band	Q-band
G108.5955+00.4935A	22:52:38.1	+60:01:01	4.3 ± 1.0	3000	C1, C6	Q1, Q10
G108.7575−00.9863	22:58:47.3	+58:45:02	4.3 ± 1.0	14000	C1, C6	Q1, Q10
G110.0931−00.0641	23:05:25.2	+60:08:15	4.3 ± 1.0	17000	C1, C6	Q1, Q10
G111.2348−01.2385	23:17:21.0	+59:28:48	4.4 ± 1.0	42000	C1, C6	Q8, Q9
G111.2552−00.7702	23:16:10.4	+59:55:28	3.5 ± 1.0	11000	C1, C6	Q8, Q9
G111.5671+00.7517	23:14:01.8	+61:27:20	2.65 ± 0.12^8	23000	C1, C6	Q8, Q9
G114.0835+02.8568	23:28:27.8	+64:17:38	4.2 ± 1.0	7100	C1, C6	-
G118.6172−01.3312	00:15:27.8	+61:14:19	2.8 ± 1.0	4900	C1, C6	Q13
G126.7144−00.8220	01:23:33.2	+61:48:48	0.7 ± 0.22	2600	C2	Q13
G133.7150+01.2155	02:25:40.8	+62:05:52	1.83 ± 0.14^9	123300*	C2	Q13
G134.2792+00.8561	02:29:02.0	+61:33:32	2.04 ± 0.07^{10}	5691*	C2	Q13
G136.3833+02.2666	02:50:08.1	+61:59:52	3.2 ± 1.0	7800	C2	Q13
G138.2957+01.5552	03:01:31.3	+60:29:13	2.9 ± 1.0	17000	C2	Q13
G139.9091+00.1969A	03:07:24.5	+58:30:43	3.2 ± 1.0	11000	C2	Q13
G141.9996+01.8202	03:27:38.8	+58:47:00	0.8 ± 0.2	5500	C2	Q13
G143.8118−01.5699	03:24:51.0	+54:57:31	2.4 ± 1.0	9200	C2	Q13

Table 4.2: Continued

MYSO	α (J2000)	δ (J2000)	Distance	L_{bol}	Date of Observation(s)	
	(hh:mm:ss)	(dd:mm:ss)	(kpc)	(L_{\odot})	C-band	Q-band
G148.1201+00.2928	03:56:15.4	+53:52:13	3.2 ± 1.0	3400	C2	Q13
G160.1452+03.1559	05:01:39.9	+47:07:20	1.9 ± 1.0	2100	C2	-
G173.4839+02.4317	05:39:09.9	+35:45:17	2.0 ± 0.6^{11}	2900	C2	-
G174.1974-00.0763	05:30:46.1	+33:47:53	2.14 ± 0.05^{12}	5900	C2	-
G177.7291-00.3358	05:38:47.2	+30:41:18	2.0 ± 0.6^{11}	2300	C2	-
G183.3485-00.5751	05:51:11.1	+25:46:16	2.0 ± 0.6^{11}	3800	C2	-
G188.9479+00.8871	06:08:53.3	+21:38:29	1.76 ± 0.11^{13}	7000^{14*}	C2	-
G189.0307+00.7821	06:08:40.5	+21:31:00	2.0 ± 0.6^{11}	24000	C2	-
G192.6005-00.0479	06:12:54.0	+17:59:23	1.78 ± 0.12^{15}	36000^*	C2	-
G196.4542-01.6777	06:14:37.1	+13:49:37	5.28 ± 0.24^{16}	94000	C2	-
W48	19:01:46.7	+01:13:24	3.27 ± 0.49^1	170000	C7	Q2, Q4

4.1.2 The MYSO sample

For the second sub-sample, the RMS survey database* was used from which to draw mid-IR bright targets of interest, representing a more evolved phase of massive star formation than the IRDCs of subsection 4.1.1. For both their luminosities and distances, the same criteria as for the IRDCs ($> 10^3 L_{\odot}$ and $< 7 \text{ kpc}$) are imposed. Other requirements include a MSX $21 \mu\text{m}$ to $8 \mu\text{m}$ flux ratio of > 2 and previous radio non-detection, or flux of $< 1 \text{ mJy}$ (Urquhart *et al.* 2009b), in order to ensure the sources are not in the UCHII phase. These extra criteria ensure selection of different evolutionary stages compared to those comprising the sample of subsection 4.1.1 and resulted in a sample size of 48 MYSOs. Comparing their MIPS GAL $S_{70\mu\text{m}}/S_{24\mu\text{m}}$ ratios to the IRDCs, the mid-IR bright MYSOs have values of $\lesssim 100$ (red circles in Figure 4.1) meaning that between the MYSO and IRDC samples, a continuous range in evolutionary stages is represented (highlighting the previous point). Near-infrared ancillary data (Cooper *et al.* 2013) has also shown that they are still accreting (due to the presence of CO bandhead emission, e.g. Ilee *et al.* 2013) and likely driving ionised winds (weak Br γ emission relative to that expected from HII regions). In total this provides a sample size of 48 MYSOs which are listed, along with their basic properties, in Table 4.2.

4.2 Observations

All observations were taken with the Very Large Array (VLA) in its A-configuration, between 13th October 2012 and 27th December 2012 for 5.8 GHz observations

*http://rms.leeds.ac.uk/cgi-bin/public/RMS_DATABASE.cgi

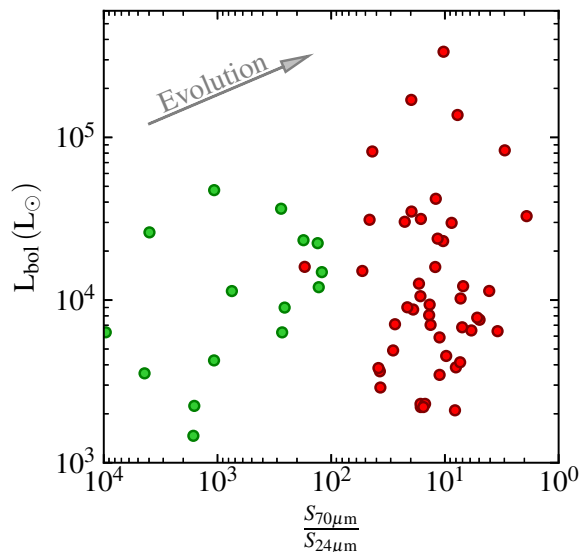


Figure 4.1: A plot of the ratio between the IRAS/MIPSGAL $S_{70\mu\text{m}}$ fluxes and MSX $S_{24\mu\text{m}}$ fluxes versus bolometric luminosity for the luminous ($L_{\text{bol}} > 10^3 L_{\odot}$) IRDC cores (green circles) and MYSOs (red circles) of the sample. The arrow represents the general evolutionary trend for an IRDC to MYSO.

and between 16th March 2014 and 27th July 2015 for 44 GHz observations. The WIDAR correlator was set up in full continuum mode, with bandwidths of 2 GHz (16 spectral windows of 64×2 MHz channels with 8-bit samplers) and 8 GHz (64 spectral windows of 64×2 MHz channels with 3-bit samplers) centred on frequencies of 5.8 and 44 GHz respectively. These shall be referred to as C and Q-bands from this point on. In the A-configuration, the VLA has a minimum and maximum baseline length of 680 m and 36400 m, corresponding to C and Q-band largest, recoverable, angular scales of $8.9''$ and $1.2''$ respectively. Synthesised beam widths, with uniform weighting, of $0.33''$ and $0.04''$ are typically representative.

In total, 56 target fields were observed at C-band and 49 at Q-band (3 of which comprise a mosaic of the C-band field of view towards G033.69–00.01). General

and observational properties of the sample are summarised in Tables 4.1 and 4.2, including basic target properties, coordinates and the dates of their observation.

Depending on elevation curves and the LST of the observation, different flux and bandpass calibrators were used to bootstrap the flux density scale and calibrate the frequency dependent gains. For calibration of the time-varying gains, a phase calibrator was observed every 12 minutes at C-band, for between 30 – 60 s dependent on calibrator flux. Full flux/bandpass and phase calibrator details can be found in Tables B.16 and B.17 of Appendix B, respectively. At Q-band, due to increased atmospheric instability, a calibrator cycle time of 2 minutes, including slew times and phase-calibrator scan lengths of between 30 – 40 s, was adopted. On source times for the science targets were 24 – 26 and 15 – 17 minutes, achieving a theoretical RMS noise of $6 \mu\text{Jy}$ and $27 \mu\text{Jy}$ at C and Q-bands respectively. Target fields in the MYSO sample labelled between G118 and G148 only received half of the Q-band observing time required to achieve this sensitivity, resulting in a theoretical RMS noise of $38 \mu\text{Jy}$. Convolved beam sizes and RMS noise levels achieved in the final images are shown in each plot (and caption) in Figures A.46–A.102 of Appendix A.

For the flagging, editing, calibration and subsequent deconvolution/imaging, the CASA software package (McMullin *et al.* 2007) was used in conjunction with the CASA pipeline (version 4.7.2). Manual flagging was performed first before running the pipeline, after which output calibration tables were manually inspected. In cases where erroneous calibration solutions were found, flagging was repeated and the pipeline was rerun until the time-varying gains, bandpass solutions and bootstrapped flux densities were of a high quality comparable to standard, non-automated results.

4.3 Results

Every field was imaged out to 25% of the primary beam’s peak response at each observed frequency ($\sim 5'$ and $\sim 40''$ from the pointing centre at C and Q-bands respectively) using a typical robustness of 0.5 and cell sizes of $0.07''$ and $0.01''$ respectively. Appendix A contains the resulting clean maps of radio flux in Figures A.46–A.53 for the IRDC sample and Figures A.54–A.102 for the MYSO sample. At C-band, spectral cube imaging of the 6.7 GHz CH_3OH maser line was conducted with maser positions recorded (green ‘ \times ’ in any contour plots) and the relevant channels subsequently flagged prior to continuum imaging. Hanning smoothing was employed in the reduction process, and therefore maser fluxes are not recorded as they are physically meaningless, however their positions remain unaffected by this process.

For the measurement of fluxes, and physical sizes, the same methods discussed in section 2.3 of chapter 2 were adopted. A full list of sources detected (i.e. $> 5\sigma$ where σ is the RMS noise in each image) in the field are recorded, along with their derived fluxes and physical sizes, in Tables B.18–B.21. Calculated spectral indices (α and γ) between 5.8 GHz and 44 GHz are recorded in Table B.22. At C-band, for the MYSO sample, only sources within $60''$ from the pointing centre are recorded (i.e. within the field imaged at Q-band for spectral comparison), with the total number of detections summarised in Table 4.3.

Classification of the compact radio sources follows the algorithm presented in Figure 2.3 of subsection 2.3.2 and resulting classifications are summarised in Table 4.4 with a detailed breakdown in Table 4.5, along with adopted bolometric luminosities. These new luminosities were calculated to compensate for either

Table 4.3: A table of the total number of radio sources detected within $60''$ of the pointing centres, for all fields.

Type	C and Q	C Only	Q Only	Total
IRDCs	5	11	3	19
MYSOs	48	144	17	209
All	53	155	20	228

Table 4.4: A table of the number of sources of each classification detected towards the IRDC samples' cores (2nd column), the MYSO samples' targets (3rd column) and within $1'$ of the target cores/MYSOs (4th column).

Classification	IRDC cores	MYSO targets	Within $60''$
Disc Wind	0	1	1
Extragalactic	0	0	11
Evolved	0	0	16
HII Region	6	3	25
Ionised Jet	1	4	7
Ionised Jet (C)	2	21	38
Ionised Jet (L)	0	10	11
Ionised Jet (L,C)	0	3	7
Lobe	0	0	54
Unknown	1	2	58
Not detected	37	4	0

source confusion at mid-IR wavelengths, or for updated distances since the registered luminosities were calculated (scaled by a factor of $\frac{D_{\text{new}}^2}{D_{\text{old}}^2}$). In case of source confusion, the overall luminosity is either divided equally between all thermal radio components within the resolution element of the IR surveys responsible for the original value of L_{bol} , or are apportioned based on high-resolution sub-mm fluxes from the literature. It must be conceded that this is only an approximation, especially since the SEDs of each component may be at various stages in evolution, however it provides values for L_{bol} closer to the true luminosities. Detailed discussion of the classifications and results for each member of the sample are contained in section C.2 of Appendix C for the interested reader.

Table 4.5: A table of the classifications for all radio sources of the sample and adopted values for L_{bol} . Superscript text next to the component names shows that that component is associated with the target IRDC core (if an ‘MMXX’ superscript), or target MYSO (an asterisk superscript), from the original sample.

Source	Component	Class.	L_{bol} (L_{\odot})	L_{bol} Ref.
IRDCs				
G018.82–00.28	Core ^{MM2}	HII	9000	Rathborne <i>et al.</i> (2010)
G024.08+00.04	A ^{MM1}	HII	15000	Rathborne <i>et al.</i> (2010)
G024.08+00.04	B	EG		
G024.33+00.11	A ^{MM1}	Jet	47837	Rathborne <i>et al.</i> (2010)
G024.33+00.11	B	UK		
G024.33+00.11	C	UK		
G024.60+00.08	A	EG		
G024.60+00.08	B	Evolved		
G028.28–00.34	A	EG		
G028.28–00.34	HII ^{MM1}	HII	4768	Rathborne <i>et al.</i> (2010)
G028.37+00.07	A ^{MM1}	Jet(C)	13031	Rathborne <i>et al.</i> (2010)
G028.37+00.07	A2 ^{MM1}	UK		
G028.37+00.07	A3 ^{MM1}	Jet(C)	13031	Rathborne <i>et al.</i> (2010)
G028.37+00.07	B	EG		
G028.37+00.07	C	UK		
G028.37+00.07	D ^{MM2}	HII	23329	Rathborne <i>et al.</i> (2010)
G028.67+00.13	HII ^{MM1}	HII	11997	Rathborne <i>et al.</i> (2010)
G033.69–00.01	A ^{MM2}	HII	22373	Rathborne <i>et al.</i> (2010)
G033.69–00.01	E	UK		
MYSOs				
18517+0437	A	Jet(C)		

Table 4.5: Continued

Source	Component	Class.	L_{bol} (L_{\odot})	L_{bol} Ref.
18517+0437	B*	Jet(C)	7100	Lu <i>et al.</i> (2014)
18517+0437	C	Jet(C)		
18556+0136	13	UK		
18556+0136	14	Lobe		
18556+0136	15	Lobe		
18556+0136	4	Lobe		
18556+0136	5	HII		
18556+0136	6	HII		
18556+0136	7*	Jet(L)	75000	Zhang <i>et al.</i> (2013)
18556+0136	7b	Lobe		
18556+0136	8	Lobe		
18556+0136	8b	Lobe		
18556+0136	Core A	UK	75000	Zhang <i>et al.</i> (2013)
18556+0136	EX-N	Lobe		
18556+0136	EX-S	Lobe		
G033.6437−00.2297	A*	Jet(C)	14000	Fujisawa <i>et al.</i> (2012)
G033.6437−00.2297	B	Evolved		
G033.6437−00.2297	C	EG		
G033.6437−00.2297	D	UK	14000	Fujisawa <i>et al.</i> (2012)
G056.3694−00.6333	A	Lobe		
G056.3694−00.6333	B	Lobe		
G056.3694−00.6333	C*	Jet(L,C)	8700	RMS
G056.3694−00.6333	D	Lobe		
G077.5671+03.6911	A	EG	4500	RMS
G078.8699+02.7602	A*	Jet	5972	Aspin <i>et al.</i> (1994)
G078.8699+02.7602	B	Jet(C)	528	Aspin <i>et al.</i> (1994)

Table 4.5: Continued

Source	Component	Class.	L_{bol} (L_{\odot})	L_{bol} Ref.
G078.8699+02.7602	C	Evolved	1080	Lumsden <i>et al.</i> (2012)
G078.8699+02.7602	D	EG		
G078.8699+02.7602	E	UK		
G079.8855+02.5517	A	Jet(C)	120	RMS
G079.8855+02.5517	B	EG		RMS
G079.8855+02.5517	C1*	UK	1100	RMS
G079.8855+02.5517	C2	UK	1100	RMS
G079.8855+02.5517	D	UK		RMS
G081.8652+00.7800	A*	Jet(C)	3600	RMS
G081.8652+00.7800	HII	HII	11000	RMS
G081.8652+00.7800	VLA1	Jet(C)		
G081.8652+00.7800	VLA2	Jet(C)		
G081.8652+00.7800	VLA3	Jet	3600	RMS
G081.8652+00.7800	VLA4	Lobe		
G081.8652+00.7800	VLA5	Lobe		
G081.8652+00.7800	VLA6	Lobe		
G081.8652+00.7800	VLA7	Lobe		
G081.8652+00.7800	W75NBc	Lobe		
G081.8652+00.7800	W75NBc2	Lobe		
G083.7071+03.2817	A*	Jet	3900	
G083.7071+03.2817	B	UK		
G084.9505−00.6910	A	Jet(C)	13000	RMS
G084.9505−00.6910	B*	Jet(C)	13000	RMS
G094.2615−00.4116	A1*	Jet(L)	9000	RMS
G094.2615−00.4116	A2	Lobe		
G094.2615−00.4116	B	EG		

Table 4.5: Continued

Source	Component	Class.	L_{bol} (L_{\odot})	L_{bol} Ref.
G094.3228−00.1671	A*	Jet(C)	5700	RMS
G094.4637−00.8043	A*	Jet(C)	10500	RMS
G094.4637−00.8043	A2	Jet(C)	10500	RMS
G094.4637−00.8043	B	Lobe		
G094.4637−00.8043	C	Jet(C)		
G094.4637−00.8043	D	Lobe		
G094.4637−00.8043	E	Lobe		
G094.6028−01.7966	A*	Jet(C)	43000	RMS
G100.3779−03.5784	A*	Jet	17000	RMS
G100.3779−03.5784	B	HII		
G102.8051−00.7184	A	Evolved	2300	RMS
G103.8744+01.8558	A	HII	3400	RMS
G103.8744+01.8558	B*	Jet(L)	3400	RMS
G103.8744+01.8558	C	Jet(C)		
G103.8744+01.8558	D	Lobe		
G103.8744+01.8558	E	Lobe		
G103.8744+01.8558	F	Lobe		
G105.5072+00.2294	A*	Jet(C)	7000	RMS
G107.6823−02.2423A	A*	Jet(C)	4100	RMS
G107.6823−02.2423A	HII	HII		
G108.1844+05.5187	A*	Jet(C)	870	Sugitani <i>et al.</i> (1989)
G108.1844+05.5187	B	EG		
G108.4714−02.8176	A*	DW	5100	RMS
G108.5955+00.4935A	B	Jet(C)	3200	RMS
G108.5955+00.4935A	C	HII	3000	RMS
G108.5955+00.4935A	D	Evolved		

Table 4.5: Continued

Source	Component	Class.	L_{bol} (L_{\odot})	L_{bol} Ref.
G108.7575−00.9863	A*	Jet(C)	14000	RMS
G108.7575−00.9863	B	UK		
G108.7575−00.9863	C	UK		
G108.7575−00.9863	D	UK		
G108.7575−00.9863	E	UK		
G110.0931−00.0641	A1	Lobe		
G110.0931−00.0641	A2	Lobe		
G110.0931−00.0641	B*	Jet(L)	17000	RMS
G110.0931−00.0641	C	Lobe		
G110.0931−00.0641	D	HII	17000	RMS
G110.0931−00.0641	E	UK		
G110.0931−00.0641	F	UK		
G111.2348−01.2385	A*	Jet(C)	42000	RMS
G111.2552−00.7702	A1*	Jet(L)	11000	RMS
G111.2552−00.7702	A2	Lobe		
G111.2552−00.7702	B	UK		
G111.2552−00.7702	C	UK		
G111.2552−00.7702	D	UK		
G111.5671+00.7517	A*	Jet(L)	23000	RMS
G111.5671+00.7517	B1	Lobe		
G111.5671+00.7517	B2	Lobe		
G111.5671+00.7517	C	Lobe		
G111.5671+00.7517	D	UK		
G114.0835+02.8568	A1*	UK	7100	RMS
G114.0835+02.8568	A2	UK	7100	RMS
G114.0835+02.8568	B	UK	7100	RMS

Table 4.5: Continued

Source	Component	Class.	L_{bol} (L_{\odot})	L_{bol} Ref.
G114.0835+02.8568	C	UK		
G114.0835+02.8568	D	UK		
G118.6172−01.3312	A	Jet(C)	4900	RMS
G118.6172−01.3312	B	UK		
G126.7144−00.8220	A*	Jet(C)	1300	RMS
G126.7144−00.8220	A2	Jet(C)	1300	RMS
G133.7150+01.2155	A	HII		
G133.7150+01.2155	B	HII		
G133.7150+01.2155	C1	Lobe		
G133.7150+01.2155	K8	Lobe		
G133.7150+01.2155	Q1/K2	Lobe		
G133.7150+01.2155	Q10	Lobe		
G133.7150+01.2155	Q2/K3	Jet(L,C)	14000	Rodón <i>et al.</i> (2008)
G133.7150+01.2155	Q3/K4	Jet(L)	25000	Rodón <i>et al.</i> (2008)
G133.7150+01.2155	Q4/K6	Jet(C)	15000	Rodón <i>et al.</i> (2008)
G133.7150+01.2155	Q4b	Lobe		
G133.7150+01.2155	Q5/K7*	Jet(L)	73000	Rodón <i>et al.</i> (2008)
G133.7150+01.2155	Q6/K5	Jet(C)		
G133.7150+01.2155	Q7	Lobe		
G133.7150+01.2155	Q8	Lobe		
G133.7150+01.2155	Q9	Lobe		
G133.7150+01.2155	QE1	UK		
G133.7150+01.2155	QE2	UK		
G134.2792+00.8561	A*	Jet(C)	5700	RMS
G134.2792+00.8561	B	UK		
G134.2792+00.8561	C	EG		

Table 4.5: Continued

Source	Component	Class.	L_{bol} (L_{\odot})	L_{bol} Ref.
G136.3833+02.2666	A*	Jet(C)	7800	RMS
G136.3833+02.2666	B	HII		
G136.3833+02.2666	C	UK		
G136.3833+02.2666	D	UK		
G136.3833+02.2666	E	UK		
G138.2957+01.5552	A*	Jet(L)	17000	RMS
G138.2957+01.5552	B	Lobe		
G138.2957+01.5552	C	Evolved		
G138.2957+01.5552	D	Evolved		
G138.2957+01.5552	E	Evolved		
G138.2957+01.5552	HII	HII		
G139.9091+00.1969A	A*	Jet(L)	11000	RMS
G139.9091+00.1969A	Ab	Lobe		
G139.9091+00.1969A	Ac	Lobe		
G139.9091+00.1969A	B	UK		RMS
G139.9091+00.1969A	HII	HII	10000	RMS
G141.9996+01.8202	A*	Jet(C)	5500	RMS
G141.9996+01.8202	B	UK		
G141.9996+01.8202	C	UK		
G143.8118-01.5699	A*	Jet(C)	9200	RMS
G143.8118-01.5699	B	UK		
G143.8118-01.5699	C	UK		
G148.1201+00.2928	A*	Jet(C)	3400	RMS
G148.1201+00.2928	A2	UK	3400	RMS
G148.1201+00.2928	B	UK		
G148.1201+00.2928	C	UK		

Table 4.5: Continued

Source	Component	Class.	L_{bol} (L_{\odot})	L_{bol} Ref.
G148.1201+00.2928	D	UK		
G160.1452+03.1559	A*	Jet	2100	RMS
G160.1452+03.1559	B	UK		
G173.4839+02.4317	A1*	HII	2900	RMS
G173.4839+02.4317	A2	UK	2900	RMS
G173.4839+02.4317	B	UK		
G173.4839+02.4317	C	UK		
G173.4839+02.4317	D	UK		
G173.4839+02.4317	E1	Jet(L,C)	7600	RMS
G173.4839+02.4317	E2	Lobe		
G173.4839+02.4317	E3	Lobe		
G173.4839+02.4317	E4	Lobe		
G173.4839+02.4317	E5	Lobe		
G173.4839+02.4317	E6	Lobe		
G173.4839+02.4317	F	UK		
G173.4839+02.4317	G	Evolved		
G174.1974−00.0763	A*	HII	6800	RMS
G174.1974−00.0763	B	Jet	3300	Palau <i>et al.</i> (2011)
G174.1974−00.0763	C	Evolved		
G177.7291−00.3358	A*	Jet(C)	2300	RMS
G177.7291−00.3358	B	UK		
G183.3485−00.5751	A*	Jet(C)	3800	RMS
G183.3485−00.5751	B	Evolved		
G188.9479+00.8871	A*	Jet(C)	7000	Minier <i>et al.</i> (2005)
G188.9479+00.8871	B1	Jet(L,C)	37000	Minier <i>et al.</i> (2005)
G188.9479+00.8871	B2	Lobe		

Table 4.5: Continued

Source	Component	Class.	L_{bol} (L_{\odot})	L_{bol} Ref.
G188.9479+00.8871	C	Evolved		
G188.9479+00.8871	D	HII		
G189.0307+00.7821	A1*	Jet(L,C)	24000	RMS
G189.0307+00.7821	A2	Lobe		
G189.0307+00.7821	B	Lobe		
G189.0307+00.7821	C	Jet(L,C)	24000	RMS
G189.0307+00.7821	D	UK		
G189.0307+00.7821	E	UK		
G189.0307+00.7821	F	Evolved		
G192.6005−00.0479	A*	Jet(L)	36000	RMS
G192.6005−00.0479	B	UK		
G192.6005−00.0479	C	Lobe		
G192.6005−00.0479	D	Lobe		
G192.6005−00.0479	E	UK		
G192.6005−00.0479	F	Lobe		
G192.6005−00.0479	G	Lobe		
G192.6005−00.0479	H	Evolved		
G192.6005−00.0479	I	HII		
G196.4542−01.6777	A1*	Jet(L,C)	94000	RMS
G196.4542−01.6777	A2	Lobe		
G196.4542−01.6777	B	HII		
G196.4542−01.6777	C	Evolved		
G196.4542−01.6777	D	Evolved		
W48	A	UK	170000	RMS
W48	B	UK		
W48	HII*	HII	170000	RMS

Table 4.6: A table of the radio detection rates towards the cores of our sample. The type column denotes the core classification system of Chambers *et al.* (2009).

Core class.	Count	Radio?	Radio (%)	Maser?	Maser (%)
Q	19	0	0.0	0	0.0
I	8	1	12.5	2	25.0
A	7	1	14.3	0	0.0
R	11	6	54.5	2	18.2

4.4 Analysis

4.4.1 IRDCs and their radio evolution

Rathborne *et al.* (2010) employed a classification scheme (Chambers *et al.* 2009) for their 1.2 mm detected cores, which is summarised in subsection 4.1.1. The purpose of this scheme was to establish a qualitative, evolutionary measure for the cores from completely inactive (‘quiescent’) to harbouring active sites of star formation (‘red’). With the radio observations towards these IRDCs presented here, it is found that the only radio detections are overwhelmingly found towards the ‘red’ cores (Table 4.6) and that no weak ($\gtrsim 30 \mu\text{Jy}$) radio emission at all was detected towards the quiescent cores.

To try and establish when the radio emission from a YSO ‘switches on’, both the core luminosity to mass ratios, (determined from the results of Rathborne *et al.* 2010) a proxy for the transition from ‘cold’ (or quiescent) to ‘hot’ (intermediate/active/red) molecular cores, and IR ratios are used as evolutionary indicators. The resulting plot is shown in Figure 4.2, where the only radio detections are found towards cores whose luminosity to mass ratios are $\gtrsim 40$. We also find

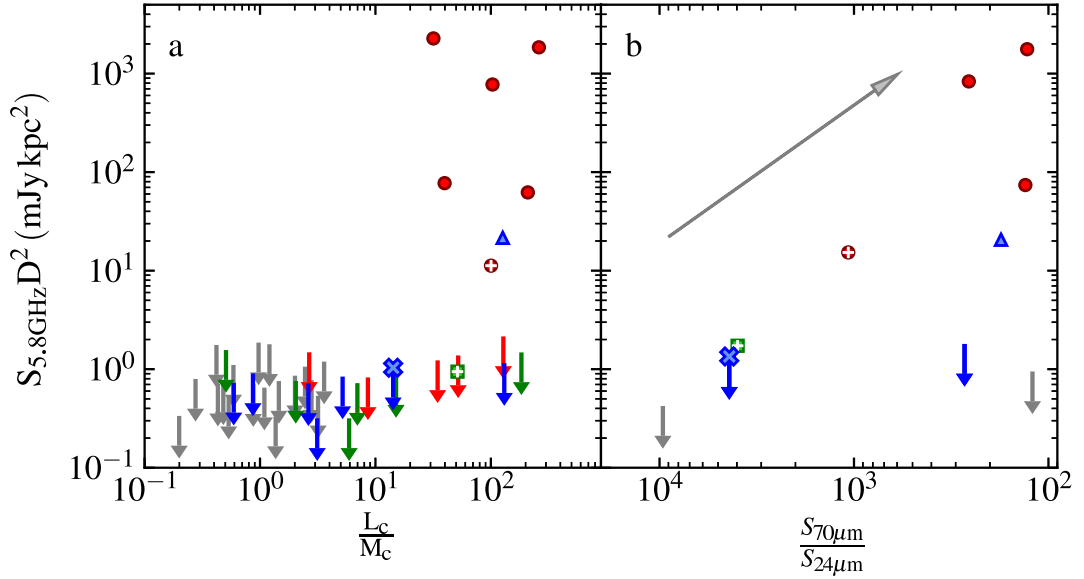


Figure 4.2: Plots of the 5.8 GHz distance luminosities against (a) parental core luminosity to mass ratios (from Rathborne *et al.* 2010) (b) 70 μm to 24 μm flux ratios, for detected radio objects towards the IRDC sample. Red circles, green squares and blue triangles mark radio detections towards cores with ‘R’, ‘A’ and ‘I’ classifications respectively. Red, green, blue and grey upper distance luminosity limits are also plotted for cores with ‘R’, ‘A’, ‘I’ and ‘Q’ classifications respectively. The blue ‘x’ marker denotes the IRDC core for which a maser was detected, but not continuum emission, markers with a white ‘+’ within them denote the sources classified as jets or jet candidates and the grey arrow highlights the general evolutionary trend.

an intermediate-class (‘I’) core for which maser emission is present with no corresponding radio continuum source (MM2 of G024.60+00.08). Weak radio emission typical of ionised jets is seen towards the ‘R’ and ‘A’ cores, G024.33+00.11 MM1 (the most massive of the sample) and G028.37+00.07 MM1 (which harbours two jet candidates), with higher luminosity to mass ratios than the maser-only source. Strong radio emission from HII regions is observed towards six (five ‘R’ class and one ‘I’ class) cores possessing high L/M ratios. Evolutionarily, these observations make sequential sense. First, collapse-induced heating consequently liberates volatile species into the gas phase via desorption from icy mantles (Viti *et al.*

2004), providing the conditions for maser emission from the desorbed CH_3OH . As the core collapses further, accretion and ejection phenomena in the form of discs and jets (the ‘Class 1’ phase of low-mass star formation) produce weak radio emission, after which the newly formed massive protostar’s UV flux increases to the point whereby an HII region is formed. Although the radio detected sample of IRDC cores are not statistical in size, this result may guide future surveys in terms of sensitivity requirements, especially in the SKA era (see discussion in subsection 5.2.4).

4.4.2 Radio luminosity against bolometric luminosity

One of the key results of chapter 2 was the segregation of MYSOs determined to harbour ionised jets in radio/bolometric luminosity parameter space. While the jets were found to occupy a region which adhered to the low-mass power-law for jets found by Anglada (1995), HII regions were roughly as radio luminous as their inferred Lyman fluxes would predict (Davies *et al.* 2011). In line with, and to compare to, that analysis, the inferred distance luminosities at 9 GHz ($S_{9\text{GHz}} D^2$) were calculated by using the derived values for the spectral index between 5.8 and 44 GHz. In cases identified as HII regions where the loss of flux with increasing resolution becomes an issue (i.e. $\alpha_{\text{measured}} < -0.1$), an optically thin spectral index is assumed and the flux at 9 GHz is extrapolated from that at 5.8 GHz. For the cases of jets and jet candidates where detection was only made at one of the two frequency bands, a similar process is adopted, this time assuming a spectral index of 0.6 to extrapolate the flux to 9 GHz, as per the mean value for α derived in subsection 2.4.5 (see Figure 2.9).

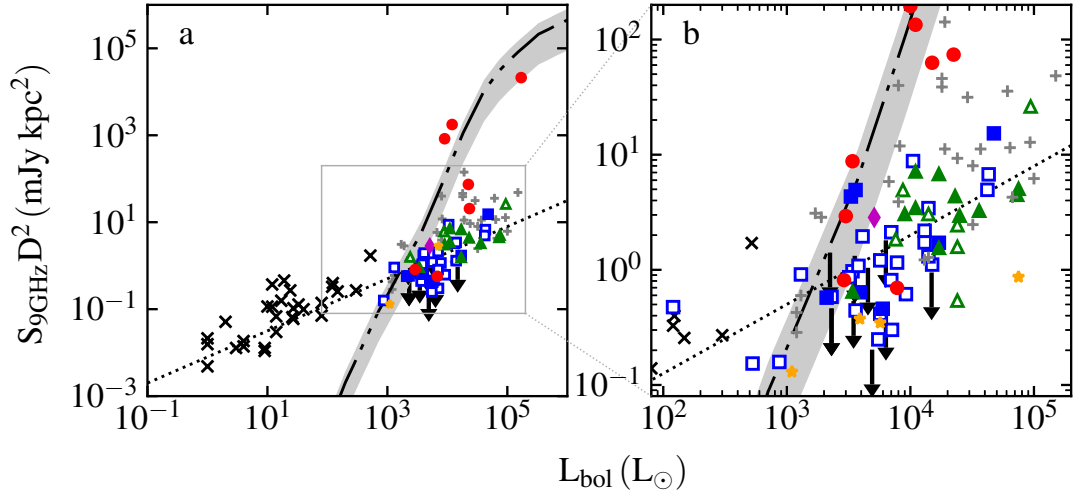


Figure 4.3: A plot of the distance luminosities (interpolated to 9 GHz) against bolometric luminosity for detected sources. The dot-dashed line represents the ionised flux expected from the Lyman continuum, calculated using the stellar models by Davies *et al.* (2011) for $L_{\text{bol}} > 10^3 L_{\odot}$, and Thompson (1984) otherwise. Grey shading represents the area where the radio-luminosity is between 20 – 180% of that expected from the bolometric luminosity for an optically thin HII region. The dotted line represents the empirical relation derived for the low-mass case (Anglada 1995; Shirley *et al.* 2007; AMI Consortium *et al.* 2011), normalized to 9 GHz (assuming $\alpha = 0.6$). Different sub-classifications are marked as blue squares for jets, hollow squares for jet candidates, green triangles for jets with lobes, hollow triangles for candidate jets with lobes, red circles for HII regions, magenta diamonds for disc winds, orange stars for sources of an unknown classification and grey ‘+’ markers for the detected jets from chapter 2. Black ‘x’ markers are the low-mass cases normalized to 9 GHz (assuming $\alpha = 0.6$ in the case of flux at only one frequency, Anglada 1995; Furuya *et al.* 2003; AMI Consortium *et al.* 2011). Panel (a) only includes detected sources directly associated to the target core or MYSO. Panel (b) includes all sources within the 60'' field of view.

In Figure 4.3, the calculated distance luminosities are plotted against bolometric luminosity for only radio detections associated to the sample targets (panel a) and also for all radio detections within an arcminute of the pointing centres (panel b). Those sources classified as ionised jets occupy the same part of parameter space as the jets from chapter 2 and also that predicted by the low-mass jet relations (dotted line). Fitting the sample of jets with a power law yields the

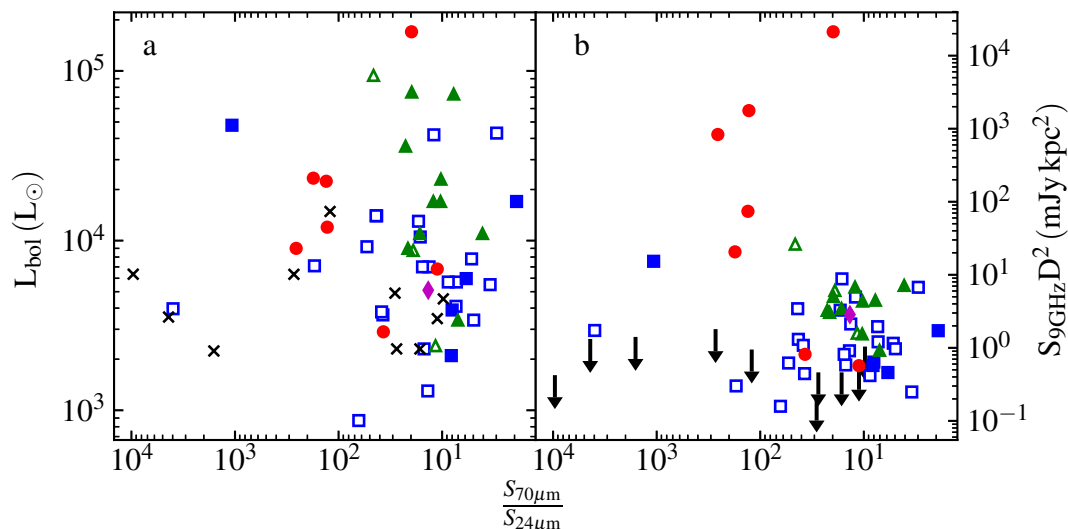


Figure 4.4: A plot of a.) bolometric luminosity and b.) distance luminosity at 9 GHz, against the $70\ \mu\text{m}$ to $24\ \mu\text{m}$ flux ratios. All symbols have the same meaning as in Figure 4.3.

relations found in Equation 4.1 for the jets/jet candidates from this chapter’s work, and Equation 4.2 if those from chapter 2 are also incorporated. From those relations, the power law is very similar to the low mass jet power law (Anglada 1995), as in chapter 2, and therefore the conclusions about the relation of jet luminosity with bolometric luminosity remain unchanged.

$$\log_{10}(S_{9\text{GHz}}D^2) = (-2.40 \pm 0.35) + (0.69 \pm 0.09) \log_{10}(L_{\text{bol}}) \quad (4.1)$$

$$\log_{10}(S_{9\text{GHz}}D^2) = (-2.29 \pm 0.38) + (0.71 \pm 0.09) \log_{10}(L_{\text{bol}}) \quad (4.2)$$

Since the sample was initially selected using the $70\ \mu\text{m}$ to $24\ \mu\text{m}$ flux ratios, in Figure 4.4 the bolometric luminosities (panel a) and 9 GHz distance luminosities (panel b) are plotted against these ratios. Superficially, the sources classified

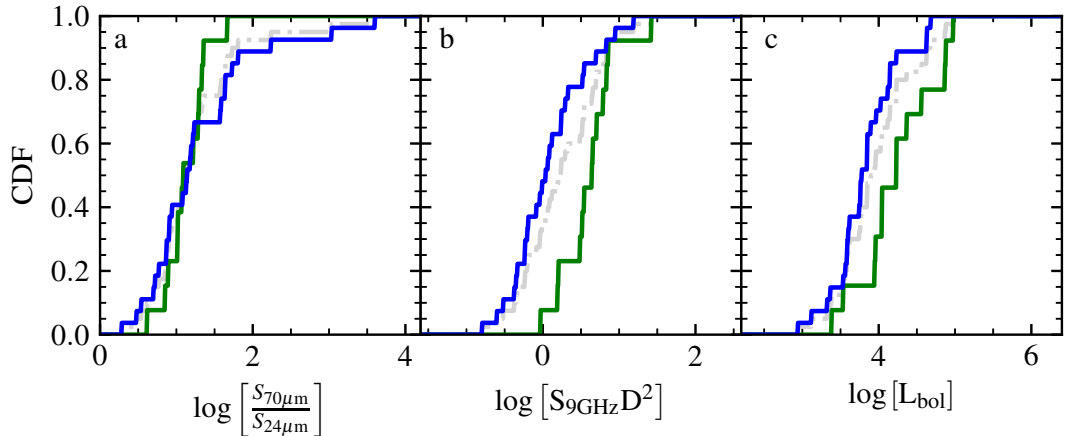


Figure 4.5: Calculated cumulative distribution functions for the $70\ \mu\text{m}$ to $24\ \mu\text{m}$ flux ratios (panel a), 9 GHz radio luminosities (panel b) and bolometric luminosities of MYSOs harbouring ionised jets. CDFs for jets with lobes including candidate jets with lobes (green line), jets without lobes including candidates (blue line) and all jets and candidates (dashed grey line) are plotted.

as jets with associated lobes of shock emission seem to occupy a select part of parameter space with regard to their radio luminosities and FIR ratios (higher than average jet radio luminosity coupled with relatively small IR ratios of $\lesssim 30$). From this observation, it could be that the ‘jets with lobes’ phase is an evolutionary step towards the end of the MYSO phase. In order to examine this conclusion more thoroughly, the Kolmogorov-Smirnov test was performed to see if the jets with, and those without, lobes were drawn from the same distribution in FIR luminosity ratios, 9 GHz radio luminosities and bolometric luminosities. For the FIR ratios a K-S test statistic of 0.256 and p-value of 0.544 were calculated, for the radio luminosities these were calculated to be 0.553 and 0.005 respectively and for bolometric luminosity values of 0.513 and 0.012 were calculated respectively. Although this shows that the two samples could be drawn from the same FIR ratio distribution, the opposite is true for the radio luminosities and bolometric

luminosity. This result is reflected in the cumulative distribution functions shown in Figure 4.5. Should the lobes come about as the result of induced precession in outflow axes (see chapter 3), this may be a piece of supporting evidence for competitive accretion as being a more important process towards the heavier end of massive star formation (see subsection 1.2.2). Other explanations include episodic accretion leading to ejection bursts or increasing variability in jet launching velocities consequently leading to the prevalence of internal shocks within a jet's stream.

4.4.3 Spectral Indices and dust contribution

At cm-wavelengths, emission from an MYSO is generally dominated by free-free emission from the ionised gas. However at shorter cm-wavelengths, and certainly in the mm-regime, thermal emission from dust grains significantly contributes to the spectral energy distribution. At the frequencies probed in this chapter, especially at Q-band, thermal dust emission is likely to contribute a significant amount to the total flux. Fortunately power-law contributions can be validly assumed for both the ionised and dust components, since turnover frequencies of ionised jets are generally higher than 44 GHz and mm-wavelengths fall under the Rayleigh-Jeans approximation ($h\nu \ll kT_{\text{Dust}}$). While the ionised jet's flux is given by Equation 1.7 of chapter 1, the dust's flux is related to frequency by Equation 4.3 (where β is the dust opacity index) with the total flux given in Equation 4.4. In the ISM, the dust opacity index, β , possesses an average value of $\beta = 1.8 \pm 0.2$, while in protoplanetary discs, where grain agglomeration leads to increased dust grain sizes, this value can fall to $\beta \approx 1$ (Draine 2006), or even

less if observing an optically-thick, hot, accretion disc. Typically, for MYSOs the value for the dust opacity index falls in the range $1 \leq \beta \leq 2$ (e.g. $\beta = 1$, $\beta = 1.3$ and $\beta = 1.5$ for Zhang *et al.* 2007; Galván-Madrid *et al.* 2010; Chen *et al.* 2016, respectively). In order to accurately attribute the correct flux and spectral index to each ionised jet, the thermal dust contributions must be subtracted.

$$S_{\nu}^{\text{Dust}} \propto \nu^{\beta+2} \quad (4.3)$$

$$S_{\nu} = c_1 \nu^{\alpha} + c_2 \nu^{\beta+2} \quad (4.4)$$

where $c_1 = S_0^{\text{Ion}} \nu_0^{-\alpha}$, $c_2 = S_0^{\text{Dust}} \nu_0^{-\beta+2}$ and S_0^{Ion} and S_0^{Dust} are the flux contributions at some reference frequency, ν_0 , from the ionised and dust components respectively.

For the majority of sources, fluxes are only available at the two frequencies presented here. For individual objects, discerning how much contribution comes from thermal dust emission, and how much from the ionised gas, is not possible with the radio data alone. In cases where a single (sub-)millimetric flux can be found it is possible, using an assumed value for β , to approximate the dust contribution. With an increasing number of millimetric observations, β can be left as a free parameter whilst fitting a double power law model (Equation 4.4) and therefore provide a higher reliability measurement of the dust's flux. A caveat of this approach is that the mm or sub-mm observations need to be of roughly the same resolution as the data provided here so that the emission from the envelope and clump (which may also have differing dust properties to further complicate the matter) does not contribute to that measured towards the core. An example

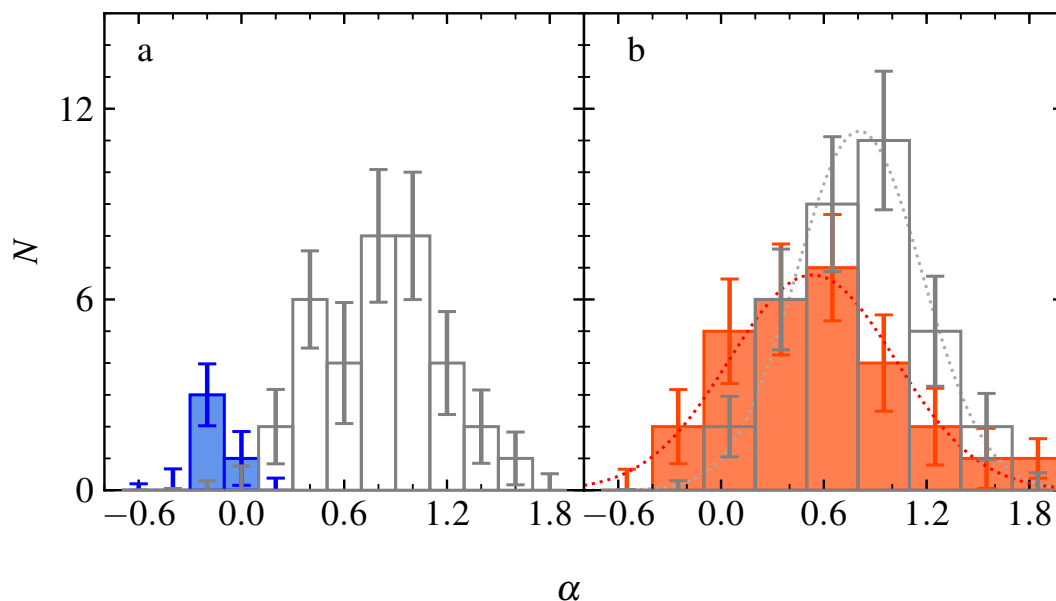


Figure 4.6: Histograms of spectral indices for: a.) All lobes (blue) and jet-like sources (grey) for whom a spectral index between C and Q-bands was derived. b.) All jet-like sources with a derived spectral index from this chapter (grey) and those from chapter 2 (orange). Normal distributions have been fitted to the VLA jets (grey dotted line) and ATCA jets (red dotted line). Binning is defined as $s + w(n - 1) \leq \alpha < s + wn$, where s is the left edge value for the left-most bin ($\alpha = -0.7$), n is the bin number (starting at 1 with the left-hand bin) and w is the bin width (0.2 for panel a and 0.3 for panel b). All bin errors are calculated using the method described in subsection 4.4.3.1.

of this analysis was performed towards G160.1452+03.1559 (see Figure C.14 in section C.2 of Appendix C) whereby values of $\alpha_{\text{jet}} = 0.74 \pm 0.48$ and $\beta = 1.41 \pm 0.36$ were deduced. Unfortunately, the only large-scale, sub-mm/mm, statistical surveys that have so far been conducted used single-dish observations (e.g. a mm IRDC survey, BGPS and ATLASGAL, Rathborne *et al.* 2006; Rosolowsky *et al.* 2010; Urquhart *et al.* 2014b, respectively) and therefore only serendipitous small-scale surveys, or single-object studies, can provide the necessary information for the purposes of this investigation, limiting this analysis to a handful of objects.

An alternative approach in determining dust contribution is to construct his-

tograms (errors of which are discussed in subsection 4.4.3.1) of the spectral indices found towards the ionised jets (Figure 4.6), and compare this to the lower frequency survey (i.e. minimised dust contribution) of chapter 2 (Figure 2.9). The resulting histograms are plotted in Figure 4.6 which seems to follow a (possibly negatively skewed) normal distribution, with a median spectral index of $\alpha = 0.85$ and mean of $\alpha = 0.81$ for all jet-like radio sources in the sample. There is an indication of two spectral index populations, of which there are hints of in panel a of Figure 4.6, which admittedly uses a smaller, and therefore less reliable, bin size than that of panel b. Each of the possible, two populations appear to be centred on spectral index bins of $0.3 < \alpha < 0.5$ and $0.7 < \alpha < 0.9$, which according to the models of Reynolds (1986) would indicate a ‘collimated’ and ‘spherical’ (i.e. non-collimated) population of jets. However, considering the statistical non-significance of this result, an even larger sample size is required to draw any firm conclusions.

As for the comparison between those spectral indices recorded in chapter 2 and those here, it is clear that those jets observed with the VLA have a higher mean spectral index, than those observed with the ATCA. This can not be an instrumental effect since the VLA’s changing scale sensitivity from C to Q-band could only lower recovered spectral indices (Q-band resolves out more extended flux). Fitting a normal distribution to each sample yields a mean spectral index of $\bar{\alpha}_{\text{ATCA}} = 0.53$ and $\bar{\alpha}_{\text{VLA}} = 0.81$ for the jets from the ATCA and VLA samples respectively. Since there should be no intrinsic differences between southern and northern hemisphere jets this difference is therefore attributable to dust contributions at Q-band which increase the derived values for $\bar{\alpha}$. Consequently this corresponds to an average dust contribution, at 44 GHz, of $43 \pm 11\%$ that of

the total flux, showing it to be a significant effect for the VLA data. Without a full description of both the cm, and mm, portions of the SED however, exact case-by-case contributions are impossible to discern.

As for the shock-ionised lobes and their spectral index distribution, unfortunately the population with calculated spectral indices is too small (four lobes), as a result of the negative spectral indices lowering the flux densities of these objects below the detection threshold at Q-band. Resolving out effects also can not be ruled out, and as the result of the small sample size with calculated values for α , no further analysis could be performed.

4.4.3.1 A word on histogram errors

In the literature, typically the approximation is made that the standard error on the count for each of a histogram's bins follows Poisson statistics (i.e. $\sigma_N = \sqrt{N}$ where N is the bin count and σ_N is its associated error). However when errors are present on measured data values, this is inadequate (as highlighted by errors of 0 on 'empty' bins) and addressing this problem requires moving away from Poisson statistics. Instead a more thorough consideration of the probability distribution of each result in the dataset is performed, since if the error of a particular result increases, so too does the probability that its true value lies in the surrounding bins of that in which it was counted.

For the rest of this discussion the example of radio spectral index, α , is used which plays an important part in the classification of sources throughout this thesis (a typical error for which is ± 0.2). The probability that the true value for α lies in the j^{th} histogram bin (whose edges are defined by the range $a \leq \alpha \leq b$)

given its observed value, $\alpha_{obs} \pm \sigma_\alpha$, is given by Equation 4.5.

$$p(j) = \int_a^b \frac{1}{\sqrt{2\pi}\sigma_\alpha} e^{-\frac{\alpha - \alpha_{obs}}{2\sigma_\alpha^2}} d\alpha \quad (4.5)$$

This probability can also be written as the difference between the values for the cumulative distribution function (Equation 4.6) at b and a .

$$F(\alpha) = \frac{1}{2} \left[1 + \operatorname{erf} \left(\frac{\alpha - \alpha_{obs}}{\sqrt{2}\sigma_\alpha} \right) \right] \quad (4.6)$$

$$\operatorname{erf} \left(\frac{\alpha - \alpha_{obs}}{\sqrt{2}\sigma_\alpha} \right) = \frac{2}{\sqrt{\pi}} \int_0^{\frac{\alpha - \alpha_{obs}}{\sqrt{2}\sigma_\alpha}} e^{-\frac{t^2}{2}} dt \quad (4.7)$$

Where erf is the error function (Equation 4.7) which defines the probability of a randomly sampled point from a Gaussian distribution being in the range $[\alpha_{obs} - \alpha : \alpha_{obs} + \alpha]$.

A histogram is essentially the sum of a collection of Bernoulli random variables, whereby a Bernoulli distribution has two, discrete states whose probabilities are p (i.e. ‘in’ a bin) and $(1 - p)$ (i.e. ‘out’ of a bin). The variance of a Bernoulli distribution is $p(1 - p)$ and therefore the standard error on the total count in bin j , σ_j , is defined in Equation 4.8.

$$\sigma_j = \sqrt{\sum_{i=1}^N p_i(j) (1 - p_i(j))} \quad (4.8)$$

In light of this discussion, the method detailed in this section is that which is used to determine histogram errors in subsection 4.4.3.

4.4.4 Jet opening angle and its evolution

A theoretical work by Vaidya *et al.* (2011) investigated the effects of radiative forces (from the central MYSO and/or hot inner disc) on the launch and collimation of ionised jets. After switching on the radiation after an initial, pure MHD-phase, it was observed that the radiative forces acted to specifically decollimate the ionised jet which, from an observational standpoint, would result in wider opening angles. Since higher luminosities and stellar masses are directly related, they re-ran their simulations for stellar masses ranging from $20 - 60 M_{\odot}$, over which opening angles in the jet were found to change from 20° to 32° .

With the high-resolution observations of this chapter, potentially the point of collimation and/or launch of the jet itself can be probed (scales of $10 - 100$ au). An estimate of the opening angle (using Equation 2.10) at this scale consequently tests the theoretical predictions of Vaidya *et al.* (2011). In Figure 4.7, the opening angles deduced from the observations are plotted against MYSO mass (columns 4 and 5 of Table 4.7) for all sources displaying jet-like characteristics, apart from the C-band component A of the MYSO, G126.7144-00.8220. This particular source was neglected since at Q-band, the source was resolved into two (unresolved) components, which were spatially confused at 5.8 GHz. Over the entire sample, average opening angles of 47° at C-band and 48° at Q-band are found, with ranges of $20 \pm 16^{\circ}$ to $86 \pm 36^{\circ}$ and $23 \pm 14^{\circ}$ to $83 \pm 61^{\circ}$ respectively. Large errors are calculated for the opening angles whereby the median/mean errors of $27^{\circ}/31^{\circ}$ and $20^{\circ}/27^{\circ}$ were found for C and Q-bands respectively. A sliding window average was calculated across MYSO mass (inferred from L_{bol} using the models of Davies *et al.* 2011) for the derived opening angles using a window width of $8 M_{\odot}$. It is

worth noting that C and Q-band measurements of the same source were taken as two independent measurements of the opening angle and subsequently averaged. As shown in Figure 4.7, within errors, there is no definitive increase of opening angle with MYSO mass. There is tentative evidence that the opening angle does increase from the low/intermediate mass end up to $\sim 20 M_{\odot}$, however this apparent increase ($\sim 10^{\circ}$) is within the average's standard deviation throughout the mass range. The apparent decrease at masses $> 20 M_{\odot}$ is likely due to small sample sizes for the sliding window average. Unfortunately, the well sampled range of MYSO mass for this study only extends from $8 M_{\odot}$ to $20 M_{\odot}$, lower than the mass ranges studied by Vaidya *et al.* (2011), and thus no comment can be made on their predictions. As a note, a similar, sliding-average analysis was performed using the evolutionary indicator of $\frac{S_{70\mu\text{m}}}{S_{24\mu\text{m}}}$, rather than MYSO mass, and no correlation (or tentative suggestion of such) was found for opening angle with FIR ratio either.

A Kendall-tau rank correlation test for opening angle with M_{\star} was also performed, resulting in a correlation coefficient of $\tau = 0.10$ and corresponding p -value of 0.33. A similar calculation for opening angle and the FIR ratio results in $\tau = -0.11$ and a p -value of 0.35. These values indicate the absence of a correlation for MYSO mass (or FIR ratio) and opening angle in the jet for this study. For consistency, the correlation coefficient for opening angle with distance was calculated to be $\tau = 0.09$ with an associated p -value of 0.38, showing that resolution effects upon opening angle with distance are not an issue. As a final note to this section, it must be conceded that spatially unresolved multiplicity may play a factor in derived opening angles, whose significance would require higher resolution observations, exceeding the capabilities of the VLA, to fully establish.

Table 4.7: Classifications, opening angles and mass loss rates for all jet-like radio sources detected.

MYSO	Lobe	Class	$\theta_{\text{OA}}^{\text{C}}$ ($^{\circ}$)	$\theta_{\text{OA}}^{\text{Q}}$ ($^{\circ}$)	$\dot{M}_{\text{jet}}^{\text{C}}$ ($\times 10^{-6} M_{\odot} \text{ yr}^{-1}$)	$\dot{M}_{\text{jet}}^{\text{Q}}$ ($\times 10^{-6} M_{\odot} \text{ yr}^{-1}$)
18517+0437	A	Jet(C)	-	-	0.30 ± 0.25	-
18517+0437	B	Jet(C)	-	-	1.26 ± 0.78	1.26 ± 0.78
18517+0437	C	Jet(C)	-	-	0.58 ± 0.46	-
18556+0136	7	Jet(L)	52.3 ± 4.4	31.0 ± 14.5	9.18 ± 2.07	6.20 ± 2.55
G024.33+00.11	A	Jet	63.6 ± 43.8	26.4 ± 13.1	28.07 ± 17.38	14.50 ± 7.34
G028.37+00.07	A	Jet(C)	-	32.0 ± 16.6	6.91 ± 5.05	9.83 ± 5.97
G028.37+00.07	A3	Jet(C)	-	44.5 ± 10.3	12.21 ± 8.03	22.24 ± 8.50
G033.64-00.21	A	Jet(C)	67.8 ± 33.8	42.9 ± 42.4	5.71 ± 4.14	4.05 ± 3.92
G056.3694-00.6333	C	Jet(L,C)	72.1 ± 26.6	-	3.58 ± 3.16	-
G078.8699+02.7602	A	Jet	-	53.5 ± 6.9	2.73 ± 1.61	5.72 ± 1.15
G078.8699+02.7602	B	Jet(C)	34.5 ± 34.7	60.1 ± 55.5	0.49 ± 0.48	0.75 ± 0.69
G079.8855+02.5517	A	Jet(C)	-	64.4 ± 49.2	1.05 ± 0.64	2.51 ± 1.56
G081.8652+00.7800	A	Jet(C)	-	-	1.24 ± 0.75	1.24 ± 0.75
G081.8652+00.7800	VLA1	Jet(C)	82.8 ± 6.9	52.6 ± 5.5	3.08 ± 1.04	2.19 ± 0.75
G081.8652+00.7800	VLA2	Jet(C)	41.4 ± 3.6	44.0 ± 43.7	0.72 ± 0.33	0.75 ± 0.66
G081.8652+00.7800	VLA3	Jet	27.9 ± 16.2	52.4 ± 2.1	10.00 ± 4.61	16.01 ± 2.46

Table 4.7: Continued

MYSO	Lobe	Class	$\theta_{\text{OA}}^{\text{C}}$ ($^{\circ}$)	$\theta_{\text{OA}}^{\text{Q}}$ ($^{\circ}$)	$\dot{M}_{\text{jet}}^{\text{C}}$ ($\times 10^{-6} M_{\odot} \text{ yr}^{-1}$)	$\dot{M}_{\text{jet}}^{\text{Q}}$ ($\times 10^{-6} M_{\odot} \text{ yr}^{-1}$)
G083.7071+03.2817	A	Jet	21.5 ± 28.6	30.5 ± 24.2	0.65 ± 0.68	0.85 ± 0.57
G084.9505-00.6910	B	Jet(C)	-	-	-	2.92 ± 2.05
G094.2615-00.4116	A1	Jet(L)	20.1 ± 15.5	-	2.04 ± 1.87	2.03 ± 1.84
G094.3228-00.1671	A	Jet(C)	-	-	3.76 ± 2.67	3.76 ± 2.67
G094.4637-00.8043	A	Jet(C)	38.4 ± 13.2	56.4 ± 54.2	5.04 ± 2.69	6.72 ± 5.78
G094.4637-00.8043	A2	Jet(C)	-	-	-	3.69 ± 2.60
G094.4637-00.8043	C	Jet(C)	-	-	5.50 ± 3.78	5.50 ± 3.78
G094.6028-01.7966	A	Jet(C)	63.4 ± 33.2	-	9.18 ± 5.35	3.86 ± 2.74
G100.3779-03.5784	A	Jet	-	-	2.77 ± 2.13	2.77 ± 2.13
G103.8744+01.8558	B	Jet(L)	51.4 ± 20.5	-	0.68 ± 0.63	-
G103.8744+01.8558	C	Jet(C)	56.8 ± 22.3	-	0.38 ± 0.36	-
G105.5072+00.2294	A	Jet(C)	27.6 ± 67.3	82.7 ± 61.4	5.23 ± 9.84	11.92 ± 8.41
G107.6823-02.2423A	A	Jet(C)	-	-	4.97 ± 4.04	4.97 ± 4.04
G108.1844+05.5187	A	Jet(C)	61.0 ± 16.8	22.7 ± 13.5	1.45 ± 0.56	0.69 ± 0.38
G108.5955+00.4935A	B	Jet(C)	-	-	0.93 ± 0.83	-
G108.7575-00.9863	A	Jet(C)	-	-	5.09 ± 3.60	5.09 ± 3.60
G110.0931-00.0641	B	Jet(L)	48.1 ± 7.4	57.9 ± 41.2	4.25 ± 2.98	4.88 ± 4.27

Table 4.7: Continued

MYSO	Lobe	Class	$\theta_{\text{OA}}^{\text{C}}$ ($^{\circ}$)	$\theta_{\text{OA}}^{\text{Q}}$ ($^{\circ}$)	$\dot{M}_{\text{jet}}^{\text{C}}$ ($\times 10^{-6} M_{\odot} \text{ yr}^{-1}$)	$\dot{M}_{\text{jet}}^{\text{Q}}$ ($\times 10^{-6} M_{\odot} \text{ yr}^{-1}$)
G111.2348–01.2385	A	Jet(C)	-	50.3 ± 13.5	9.14 ± 6.24	18.27 ± 7.97
G111.2552–00.7702	A1	Jet(L)	44.9 ± 18.9	-	1.30 ± 1.12	0.71 ± 0.69
G111.5671+00.7517	A	Jet(L)	49.6 ± 25.8	61.7 ± 14.5	10.36 ± 4.46	12.21 ± 3.11
G118.6172–01.3312		Jet(C)	-	-	-	-
G118.6172–01.3312	A	Jet(C)	-	47.3 ± 47.0	-	2.58 ± 2.54
G126.7144–00.8220	A	Jet(C)	6.4 ± 19.5	-	0.62 ± 1.46	1.47 ± 1.08
G126.7144–00.8220	A2	Jet(C)	-	-	-	0.45 ± 0.35
G133.7150+01.2155	Q2/K3	Jet(L,C)	-	-	0.66 ± 0.51	0.66 ± 0.51
G133.7150+01.2155	Q3/K4	Jet(L)	-	37.0 ± 27.4	3.90 ± 2.38	6.19 ± 3.72
G133.7150+01.2155	Q4/K6	Jet(C)	-	-	2.15 ± 1.33	2.15 ± 1.33
G133.7150+01.2155	Q5/K7	Jet(L)	-	53.4 ± 14.0	5.17 ± 3.09	10.79 ± 3.05
G133.7150+01.2155	Q6/K5	Jet(C)	-	14.0 ± 20.5	1.57 ± 1.15	1.20 ± 1.44
G134.2792+00.8561	A	Jet(C)	70.9 ± 61.1	-	1.61 ± 1.38	-
G136.3833+02.2666	A	Jet(C)	-	-	2.16 ± 1.74	2.16 ± 1.74
G138.2957+01.5552	A	Jet(L)	-	-	2.04 ± 1.72	2.04 ± 1.72
G139.9091+00.1969A	A	Jet(L)	22.6 ± 41.9	76.3 ± 49.7	3.63 ± 5.46	9.05 ± 6.77
G141.9996+01.8202	A	Jet(C)	25.2 ± 36.5	-	0.43 ± 0.53	0.36 ± 0.29

Table 4.7: Continued

MYSO	Lobe	Class	$\theta_{\text{OA}}^{\text{C}}$ ($^{\circ}$)	$\theta_{\text{OA}}^{\text{Q}}$ ($^{\circ}$)	$\dot{M}_{\text{jet}}^{\text{C}}$ ($\times 10^{-6} M_{\odot} \text{ yr}^{-1}$)	$\dot{M}_{\text{jet}}^{\text{Q}}$ ($\times 10^{-6} M_{\odot} \text{ yr}^{-1}$)
G143.8118−01.5699	A	Jet(C)	21.2 ± 116.9	-	0.88 ± 3.69	-
G148.1201+00.2928	A	Jet(C)	-	-	1.77 ± 1.52	1.77 ± 1.52
G160.1452+03.1559	A	Jet	36.2 ± 46.1	-	1.23 ± 1.66	-
G173.4839+02.4317	E1	Jet(L,C)	-	-	1.89 ± 1.71	-
G174.1974−00.0763	B	Jet	28.6 ± 6.7	-	4.70 ± 2.68	-
G177.7291−00.3358	A	Jet(C)	-	-	0.80 ± 0.73	-
G183.3485−00.5751	A	Jet(C)	-	-	1.27 ± 1.15	-
G188.9479+00.8871	A	Jet(C)	-	-	1.03 ± 0.81	-
G188.9479+00.8871	B1	Jet(L,C)	-	-	0.76 ± 0.60	-
G189.0307+00.7821	A1	Jet(L,C)	86.1 ± 35.5	-	5.05 ± 3.89	-
G189.0307+00.7821	C	Jet(L,C)	78.3 ± 16.9	-	6.51 ± 4.70	-
G192.6005−00.0479	A	Jet(L)	-	-	2.91 ± 2.29	-
G196.4542−01.6777	A1	Jet(L,C)	34.2 ± 4.0	-	20.78 ± 11.47	-

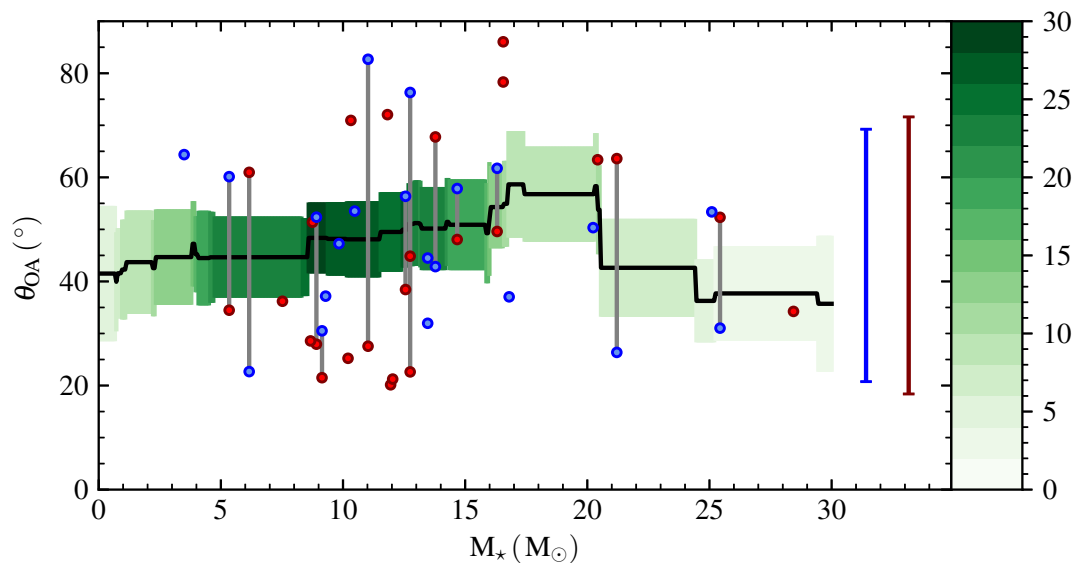


Figure 4.7: A plot of the opening angle for all jet-like sources against the MYSO mass inferred from the bolometric luminosity. Red circles represent the C-band derived properties, while blue circles represent the Q-band derived properties. A grey line connecting two data points signifies that the C and Q-band data are for the same object. The black line represents a sliding window average (using a window width of $8 M_{\odot}$), with the standard error on the mean represented by the coloured area's height. The colour-scale represents the number of samples for each window sampling. Representative errorbars for θ_{OA} are shown towards the right edge of the plot.

4.4.5 Mechanical jet properties

4.4.5.1 Jet mass loss rates and accretion rates

Using Equation 2.9 of chapter 2, it is possible to infer the jet mass loss rates from the observables of α , S_{ν} , distance and θ_{OA} . Values for jet mass loss rate are therefore calculated and tabulated in Table 4.7, with average/median values of $5 \times 10^{-6}/3 \times 10^{-6} M_{\odot} \text{ yr}^{-1}$ across the entire sample. From these rates, it is possible to infer other valuable quantities, such as jet force, power, or momentum, all of which can be important in establishing the relationships between jets and accretion, or molecular outflow phenomena. In this section, these quantities are calculated and

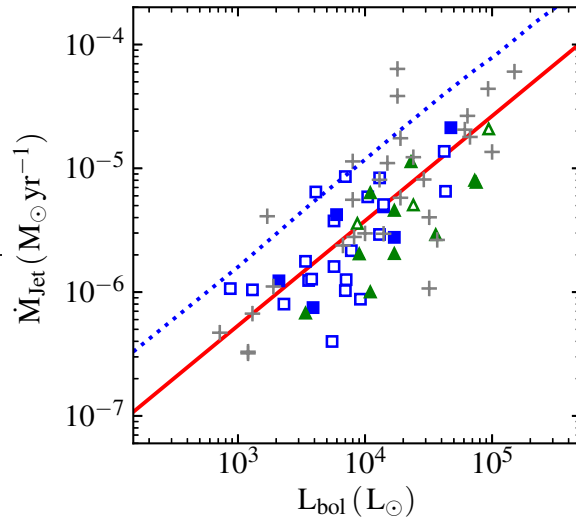


Figure 4.8: A plot of the jet mass loss rate against bolometric luminosity for jet-like sources detected towards the targets only. Symbols have the same meaning as in Figure 4.3, while the red line is the fit to both the data presented here and that of chapter 2. The dotted line represents the accretion rate (assuming $L_{\text{acc}} = 0.1L_{\text{bol}}$).

subsequently fitted with simple power laws, using orthogonal distance regression. For this, an error of 30% for all MYSO bolometric luminosities is assumed (as detailed in Mottram *et al.* 2011b).

In Figure 4.8, the jet mass loss rates for all radio sources exhibiting characteristics of ionised jets are plotted (only for those coincident with the target sources from the sample). Mass loss rates calculated in subsection 2.4.5 are also over-plotted and consequently two power laws are derived for the relation of mass loss rate with bolometric luminosity. Equations 4.10 and 4.11 show the two relations derived for the VLA only, and combined VLA/ATCA, sources respectively which agree within errors. Comparing these to the accretion rates, which are inferred from the accretion luminosities (assuming $\frac{L_{\text{acc}}}{L_{\text{bol}}} = 0.1$ as per Figure 8 of Cooper *et al.* 2013) using Equation 4.9 (whereby the results of Davies *et al.* 2011, are used to compute R_{\star} and M_{\star}) shows that $\frac{\dot{M}_{\text{jet}}}{\dot{M}_{\text{acc}}} \sim 0.3$ across the high-mass regime, which

is significantly higher than those found towards low mass cases ($\sim 0.01 - 0.1$; Hartigan *et al.* 1994). Though seemingly higher than the ratio predicted for a disk wind model of 0.1 (see subsection 1.4.1), the large approximations involved in this calculation require a more accurate follow-up survey to constrain the accretion rates of each object and hence ratio of jet mass loss to accretion rates.

$$\dot{M}_{\text{acc}} = \frac{R_{\star} L_{\text{acc}}}{GM_{\star}} \quad (4.9)$$

$$\log_{10}(\dot{M}_{\text{jet}}) = (-8.28 \pm 0.36) + (0.70 \pm 0.09) \log_{10}(L_{\text{bol}}) \quad (4.10)$$

$$\log_{10}(\dot{M}_{\text{jet}}) = (-8.83 \pm 0.33) + (0.85 \pm 0.08) \log_{10}(L_{\text{bol}}) \quad (4.11)$$

4.4.5.2 Jet momentum and molecular outflows

As discussed in section 1.3, how molecular outflows are driven is as yet unknown, with a possibility being entrainment by ionised jets. The work by Sanna *et al.* (2016) showed that the ratio between the momentum of a $40000 L_{\odot}$ MYSO's jet and that of its associated molecular outflow, over the dynamical timescale of the outflow, was of order unity. This in turn indicated that it was possible (from a mechanical point of view) to drive the outflow with the ionised jet. However, since this was a single object study, its application to MYSOs and their molecular outflows in general necessitated a larger sample. Therefore, combining the work presented in this chapter and that of chapter 2, an opportunity to compare the momenta of outflows and jets, on a *statistical* scale, is available.

$$\log_{10}(F_{\text{CO}}) = (-4.60 \pm 0.46) + (0.61 \pm 0.11) \log_{10}(L_{\text{bol}}) \quad (4.12)$$

$$\log_{10}(p_{\text{CO}}) = (-0.59 \pm 0.42) + (0.67 \pm 0.10) \log_{10}(L_{\text{bol}}) \quad (4.13)$$

A large, distance-limited sample of massive, molecular outflows by Maud *et al.* (2015), derived the relationships presented in Equation 4.12 and 4.13 for outflow force and momentum, with bolometric luminosity, respectively. Consequently they also established an average dynamical timescale for the molecular outflows, which was constant across the luminosity range, of 8.4×10^4 yr, roughly the same as known timescales for massive star formation ($\sim 10^5$ yr, McKee & Tan 2003; Mottram *et al.* 2011a). In order to calculate the total momentum of an ionised jet, the jet's outflow force (i.e. momentum rate) is integrated over these timescales, which itself is the product of mass loss rate and the jet's velocity. In Figure 4.9, the momentum rate of the jet (assuming $v_{\text{jet}} = 500 \text{ km s}^{-1}$) is plotted against bolometric luminosity with the power laws for this chapter's sample only and then also including jets from chapter 2, stated in Equations 4.14 and 4.15 respectively. From this plot, within errors, the jets' momentum force and the outflows' momentum force seem to scale in the same way as each other, however the outflows have a higher momentum rate. As a consistency check, a partial correlation test was performed, whilst controlling for distance, with a Kendall-tau correlation coefficient value of $\tau = 0.38$ and corresponding p -value $\ll 0.001$. Therefore, although distance factors heavily in the overall values for jet momentum (i.e. from Equation 2.9), the correlation between a jet's momentum and its parental MYSO's bolometric luminosity is statistically significant regardless, as

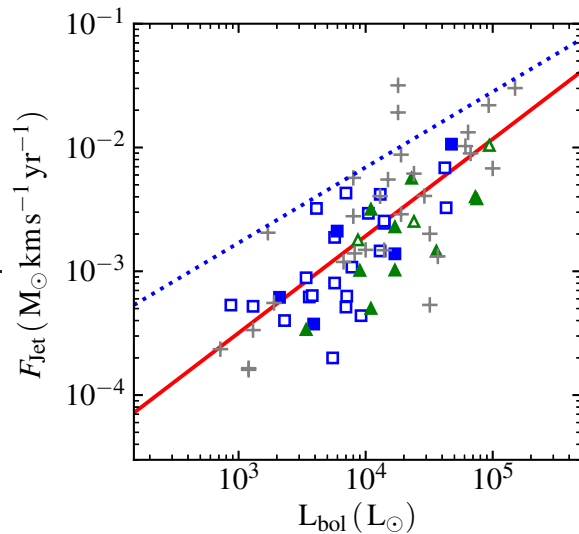


Figure 4.9: A plot of the jet momentum rates (i.e. $\dot{M}_{\text{jet}} v_{\text{jet}}$, where v_{jet} is assumed to be 500 km s^{-1}) against bolometric luminosity. Symbols have the same meaning as in Figure 4.3, while the red line is the fit to both the data presented here and that of chapter 2. The dotted line is the relationship between F_{CO} and L_{bol} presented in Equation 4.12 (Maud *et al.* 2015).

per the conclusions of chapter 2.

$$\log_{10}(F_{\text{Jet}}) = (-5.36 \pm 0.34) + (0.65 \pm 0.08) \log_{10}(L_{\text{bol}}) \quad (4.14)$$

$$\log_{10}(F_{\text{Jet}}) = (-5.87 \pm 0.31) + (0.79 \pm 0.07) \log_{10}(L_{\text{bol}}) \quad (4.15)$$

In Figure 4.10, the total jet momentum (i.e. F_{jet} integrated over the dynamical scale of the outflows of $1 \times 10^5 \text{ yr}$) is plotted with the relationship for the molecular outflows from Equation 4.13 overplotted also. As with the single object study of Sanna *et al.* (2016), the ratio of the jet and outflow momenta are of order unity as shown by comparison of the outflow momentum, with jet momentum, relations shown in Equations 4.13 and 4.17 respectively. In turn this goes to show that

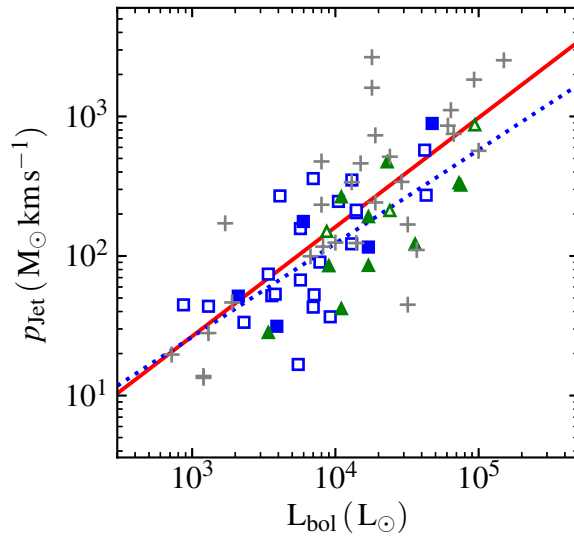


Figure 4.10: A plot of the total jet momentum against bolometric luminosity. Symbols have the same meaning as in Figure 4.3, while the red line is the fit to both the data presented here and that of chapter 2. The dotted line is the relationship between p_{CO} and L_{bol} presented in Equation 4.13 (Maud *et al.* 2015).

ionised jets are quite possibly the driving forces behind the molecular outflows.

$$\log_{10}(p_{\text{Jet}}) = (-0.44 \pm 0.34) + (0.65 \pm 0.08) \log_{10}(L_{\text{bol}}) \quad (4.16)$$

$$\log_{10}(p_{\text{Jet}}) = (-0.95 \pm 0.31) + (0.79 \pm 0.07) \log_{10}(L_{\text{bol}}) \quad (4.17)$$

4.4.5.3 Jet power and accretion

An important question to address is how much energy is contained in the jet's themselves. Establishing this in turn helps to determine their input to the ISM (and role pertaining to turbulence in molecular clouds), contribution to the overall energy budget of an MYSO and to examine the ratio of jet to accretion power which, assuming a scaling relation between accretion luminosity and rate, is a key

diagnostic tool in constraining jet launching mechanisms (see subsection 1.4.1). The work by Cooper *et al.* (2013) used the luminosity of the NIR Br γ line to infer the accretion luminosities for a sample of MYSOs using empirical relationships of $L_{\text{Br}\gamma}$ and L_{acc} in the literature. In conjunction with low mass accretion studies they found that, across all mass regimes, accretion luminosity is $\sim 10\%$ that of the bolometric luminosity. As with the jet mass loss and accretion rates in subsection 4.4.5.1, this allows for the comparison of accretion power with jet power. In order to convert the mass loss rate to power Equation 4.18 was employed, where v_{jet} was, again, assumed to be 500 km s^{-1} across the sample. Consequently, the results are plotted in Figure 4.11.

$$\begin{aligned}
 P_{\text{jet}} &= \frac{\dot{M}_{\text{jet}} v_{\text{jet}}^2}{2} + \frac{3k_B T \dot{M}_{\text{jet}}}{2m_{\text{H}}} \approx \frac{1}{2} \dot{M}_{\text{jet}} v_{\text{jet}}^2 \\
 \Rightarrow \left[\frac{P_{\text{jet}}}{L_{\odot}} \right] &= 82.4 \left[\frac{\dot{M}_{\text{jet}}}{M_{\odot} \text{ yr}^{-1}} \right] \left[\frac{v_{\text{jet}}}{\text{km s}^{-1}} \right]^2
 \end{aligned} \tag{4.18}$$

By comparison of accretion power to that of the jet, it appears that the jet power is approximately an order of magnitude less than the accretion power and consequently around two orders of magnitude smaller than the total MYSO luminosity.

4.4.6 Ionised jets or gravitationally trapped HII regions?

Early expansion of HII regions is governed by the interplay between pressure outwards (due to the contrasting temperature between ionised and ambient gas) and gravitational forces inwards (Keto 2002). Towards more evolved HII regions,

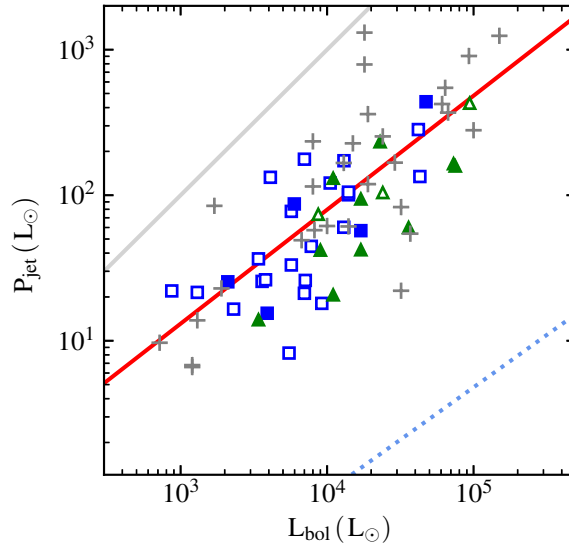


Figure 4.11: A plot of the jet power against bolometric luminosity. Symbols have the same meaning as in Figure 4.3, while the red line is the fit to both the data presented here and that of chapter 2. The dotted, blue line is the relationship for CO molecular outflow power with bolometric luminosity (from Maud *et al.* 2015, whereby $\log_{10}(P_{\text{CO}}) = (-2.92 \pm 0.62) + (0.72 \pm 0.15) \log_{10}(L_{\text{bol}})$) while the grey line represents 10% of the bolometric luminosity (i.e. the accretion luminosity from Cooper *et al.* 2013).

the gas pressure far exceeds the gravitational forces (i.e. $\frac{GM^2}{rnkT} \ll 1$) at their Strömgen radii where expansion is halted due to equality of Lyman fluxes and recombination rates. However, an MYSO with limited UV photon flux has a much smaller Strömgen radius whereby $\frac{GM^2}{rnkT} \gg 1$, and therefore the HII region can become trapped only to expand when its radius exceeds that of the ‘gravitational radius’, r_g (Equation 4.19). Pertinent to this work, these lines of thought lead to the question of whether observed thermal, free-free, radio emission originates in a trapped HII region, or an ionised jet.

$$r_g = \frac{GM_\star}{2v_s^2} \quad (4.19)$$

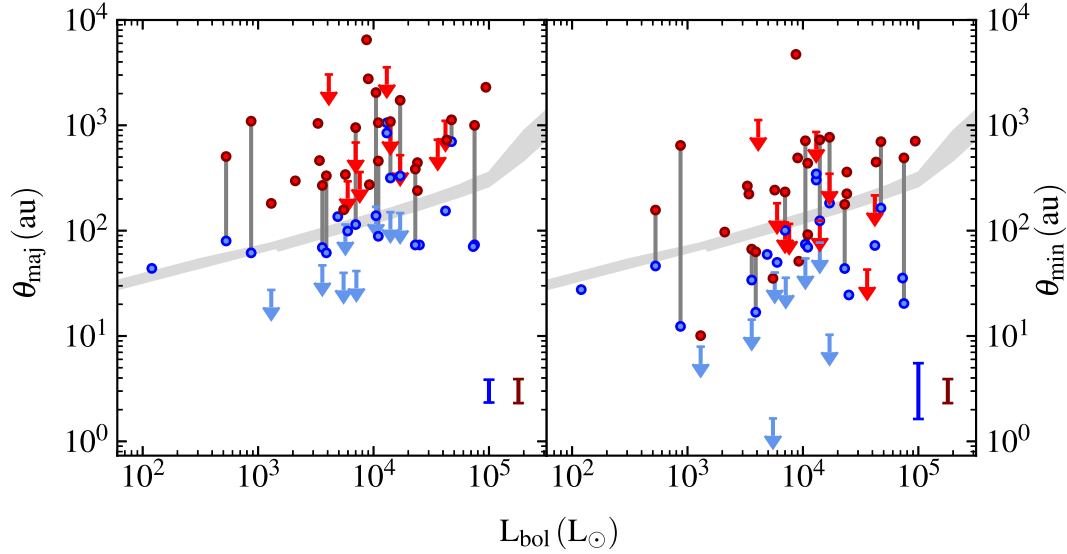


Figure 4.12: Plots of both θ_{maj} (left) and θ_{min} (right), as derived using IMFIT, against bolometric luminosity for all sources displaying jet-like characteristics. Red circles represent the C-band derived properties, while blue circles represent the Q-band derived properties. A grey line connecting two data points signifies that the C and Q-band data are for the same object. The grey areas represents twice the gravitational radius (Equation 4.19) for the relevant bolometric luminosity, with a 30% error, (Davies *et al.* 2011). Representative errorbars are shown in the bottom right of each subplot.

Where M_* is the MYSO mass and v_s is the sound speed ($v_s = \sqrt{\frac{kT}{m_H}}$ where $T \sim 10^4$ K and m_H is the mass of hydrogen).

In order to differentiate between the two possibilities, the gravitational radius of the MYSO and physical extent of the ionised gas must be compared, with similarity between the two quantities favouring a trapped HII region. It is possible to infer MYSO mass from bolometric luminosity using the models of Davies *et al.* (2011), and therefore calculate gravitational radius using Equation 4.19. A measure of the plasma's physical extent can be deduced from the radio clean maps using IMFIT which returns the FWHM along both major and minor axes, assuming the radio component adheres to Gaussian morphology.

In Figure 4.12, the deduced major and minor axes are separately plotted against bolometric luminosity for all sources with jet-like characteristics. On each plot the gravitational radii, calculated over the entire range in bolometric luminosity, are over-plotted. It is apparent that the major and minor axes at C-band generally exceed the gravitational radii (in all cases for the major axes), while at Q-band, around half of the major axes (and all of the minor axes) are smaller than the corresponding gravitational radius. As a note, this difference between C and Q-band sizes is due to the changing location of the optical depth ~ 1 surface, with frequency. Median and mean differences between C-band major axes lengths and corresponding values for r_g are 670 au and 1050 au respectively over a range of differences between 170 au – 6490 au. From Keto (2002), the ionisation front of an expanding HII region moves with an approximate velocity of $\sim 5 \text{ km s}^{-1}$, corresponding to mean and median dynamical times for the ionisation front of $\sim 640 \text{ yr}$ and 1000 yr respectively. Considering the whole process of massive star formation is thought to last $\sim 10^5 \text{ yr}$ (Davies *et al.* 2011), only a small percentage of the jet-candidates observed could potentially be recently untrapped HII regions, while the vast majority must have an elongated, ionised jet component to explain the large extent over which ionised material is found.

4.5 Summary and Conclusions

Radio observations towards forming massive stars at a variety of evolutionary stages has resulted in the detection of a total of 15 (non-candidate) ionised jets, of which 10 are determined to be associated to shock-ionised lobes. Including those radio sources detected towards the targets which also hold candidacy status

as ionised jets, this increases to a total of 41, of which there are 13 associated to shock-ionised lobes. Within $60''$ of the pointing centres, a further 22 ionised jets (5 of which are associated to lobes) are found. Using this new, northern-hemisphere sample of ionised jets, as well as those from chapter 2, analyses to determine ionised jets' role in massive star formation, as well as their properties have resulted in the following conclusions:

- Radio emission ($\gtrsim 30 \mu\text{Jy}$) towards IRDCs is not present in cores with a luminosity to mass ratio of < 40 .
- In agreement with the previous statistical study of chapter 2, jet radio luminosities are found to scale with MYSO bolometric luminosity in the same way as for low mass jets. This indicates a common mechanism for the launch of ionised jets across the mass regime.
- Dust emission accounts for an average of $43 \pm 11\%$ of an ionised jet's observed, Q-band flux, from comparison of the 'dust-free' studies of chapter 2, to those of this work, highlighting the importance of well sampled cm/mm/sub-mm SEDs in the deduction of ionised jet properties.
- No evidence is found for the evolution of jet opening angle with bolometric luminosity, with an average opening angle of 48° representative of ionised jets across the entire high-mass regime.
- Jets associated to shock-ionised lobes have larger radio luminosities which, inconjunction with the relationship between radio luminosity and bolometric luminosity, indicates them to be more common towards more massive MYSOs.

- Using previous, statistically sized studies of massive, molecular outflows, it has been shown that ionised jets and massive molecular outflows have momenta ratios of ~ 1 . This indicates that the outflows can indeed, and are therefore likely, powered by the ionised jets through mechanical entrainment.
- From the maximum physical sizes of the radio emission from ‘jet-like’ sources, an ionised jet is required to explain the presence of ionised gas past the gravitational radius for each MYSO, but does not preclude the existence of contemporaneous, gravitationally-trapped HII regions.

For future works, it has been shown that constraining the spectral properties of the jets themselves, at sub-mm, mm and cm wavelengths, is crucial in accurately determining the jets properties. With these future works, the relationships between the jets and various parameters and properties of the MYSOs themselves would be constrained further and ultimately the mechanisms for launch, collimation and relationship with their environment elucidated.

Chapter 5

Conclusions

Despite the observationally challenging nature of studying forming, massive stars, the original purpose of this thesis was to further our understanding of the MSF process and examine both the physics and prevalence of its associated ionised jets. For the first time, a statistical sample of MYSOs harbouring ionised jets was established to accomplish this, using both northern and southern hemisphere radio interferometers towards MYSO samples derived from the RMS survey. In this chapter, each work's main findings and conclusions are briefly summarised and concurrently tied together into a synthesis containing a discussion of how these overall findings further our understanding and knowledge. Unresolved and new questions raised throughout these works are subsequently examined, with a deliberation of the future lines of scientific inquiry aimed at answering them included.

5.1 Summary and synthesis

Ionised jets are intimately linked to the formation process of massive stars through accretion discs, an integral component of MSF mechanisms. Establishing a statistical sample of such objects potentially allows for the general inference of accretion processes as well as elucidation of the physics behind their launch and collimation.

In this thesis, chapter 2 analysed the results of multi-frequency, radio observations using the ATCA, towards a sample of 49 MYSOs drawn from the RMS survey (Lumsden *et al.* 2013). From the detection of 28, compact, radio sources which exhibited the characteristics of ionised jets, it was inferred that collimated ejection phenomena are common in massive star formation and their phase lasts for the $\lesssim 65000$ yr leading up to (and likely beyond, e.g. G345.4938+01.4677 Guzmán *et al.* 2016) the production of a non-gravitationally trapped HII region. Calculations of their radio luminosities and mass loss rates showed that these properties were ‘scaled up’ from low-mass examples, showing that jet formation/collimation processes were much the same across all mass ranges. Most interestingly however was the frequent, and relatively unexpected, detection of spatially distinct radio lobes, exhibiting non-thermal spectra with an average spectral index ($\bar{\alpha} = -0.55$) typical of the 1st order Fermi acceleration mechanism within shocks.

Given the uncertain origin of those shocked lobes, the question as to how they are produced naturally arose. In light of the recent confirmation of variable accretion/ejection towards an MYSO (Caratti O Garatti *et al.* 2017), it is possible the radio knots are a result of that process in combination with the collision with

either ambient material (e.g. the case of HH80/81, Masqué *et al.* 2015) or internal shocks in the jet’s stream. What’s more, previous works in the literature show that precession of these lobes is seen in some cases, however the origin of this precession is not fully understood. Chapter 3 therefore set about to study the ionised jets, and the shock-ionised lobes, in the temporal domain. Towards a sub-sample of 4 objects classified as ‘jets with lobes’ from chapter 2, similar radio observations to those described in subsection 2.2.1 were conducted ~ 2 yr later. Although significant flux variability and proper motions were not reliably detected (aside from in one shocked lobe with inferred velocities of $\sim 1800 \pm 600 \text{ km s}^{-1}$), faint radio emission between lobes and evidence for precession in the jet axes were observed (the latter towards all 4 objects). Detection of the faint radio emission between the, presumably, episodic accretion/ejection of the non-thermal lobes suggests that low, constant accretion rates can still be found in between these episodes (as per the findings of Meyer *et al.* 2017, their Figure 2). Primarily however, these results pave the way as a pilot study for a future, more extensive study (see subsection 5.2.2) aiming to explore these properties towards a more statistically-sized sample. Tentative (due to small sample size) evidence for a relation between precession angle and period was also found, hinting that multiplicity (or disc fragmentation) may be an underlying cause.

Given the relatively coarse, effective resolutions of the above studies, the collimation and launching mechanisms involved in ionised jet production could not be constrained. Therefore, not only did chapter 4 set out to extend the sample of known massive, ionised jets into the northern hemisphere but also aimed to examine, with the use of high-resolution, VLA observations, previously inaccessible scales. In addition to this, the questions of when jet activity ‘switches on’

in massive star formation, if ionised jets were mechanically able to entrain the massive molecular outflows and if the compact radio sources could be alternatively explained purely by the presence of gravitationally trapped HII regions, were addressed. An IRDC sample of mm-cores (from Rathborne *et al.* 2010) was exploited to examine the former question and it was found that (non-HII region) radio emission $\gtrsim 30 \mu\text{Jy}$ was not detected towards the vast majority of the cores. As for the chapter’s mid-IR bright MYSO sample, the properties of its 14 detected jets (with a further 24 candidates) were deduced in order to answer both the second and latter questions posed above. Importantly it was found that, as with chapter 2, radio luminosities scaled in the same way with bolometric luminosity as for low-mass examples. Deduction of the ionised jets’ physical properties showed that their momenta are of the same magnitude found for molecular outflows and therefore it was physically possible for them to be driven by jet-entrainment alone. Most intriguing, though somewhat more speculative than those findings already discussed, was the location of the jet sources associated to lobes of shocked emission within IR-colour (i.e. evolutionary) parameter space. This jet sub-class was seen to have lower $\frac{S_{70\mu\text{m}}}{S_{24\mu\text{m}}}$ ratios, corresponding to later evolutionary stages, than those jets without associated lobes. In turn this suggests that if lobes are the result of time-variable accretion/ejection bursts, or a direct consequence of precession, then these phenomena are more common towards the end of an MYSO’s evolution. If, as chapter 3 suggests, precession is a consequence of binarity or disc fragmentation, this would support the findings of previous theoretical works showing heavier, later-stage MYSOs are subject to an increasing likelihood of disc fragmentation (Kratte & Matzner 2006; Klassen *et al.* 2016) and, by extension, episodic accretion. Unfortunately observations were inadequate to resolve the

collimation radii necessary to establish the dominant method of jet production. A statistical approach comparing mass loss rates in the jet to accretion rates was used, however given the highly assumptive determination of accretion rates, again the physics behind jets could not be elucidated. This work's successes and shortcomings naturally now lead to a discussion of the future lines of research which may progress the answer to the posed question ever further.

5.2 Future Work

5.2.1 Updating radio jet models

Studies of radio jets over all mass regimes have solely relied on the seminal work by Reynolds (1986) to infer the jets' physical conditions, based upon spectral indices of both flux and major axis length. For that work many assumptions were made about the supply and ejection of material in the jet, including the steady state mass flux in the jet stream and constant ejection velocity. However recent works have shown that accretion and, by extension, mass loss do not occur at a constant rate (Caratti O Garatti *et al.* 2017) in MYSOs. Variable ejection velocities, leading to internal shocks within a jet shown via the presence of shocked 'knots' in the jet stream, are also observed (most readily seen in the low-mass case of HH111, Reipurth *et al.* 1999). At radio wavelengths, these knots are consistently seen towards MYSO jets (see Chapters 2–4), however their origin in either internal or external (i.e. jet impinging on material outside its stream) shocks is not certain. Considering these findings since the work of Reynolds (1986), I believe it is time to update our radio models for ionised jets

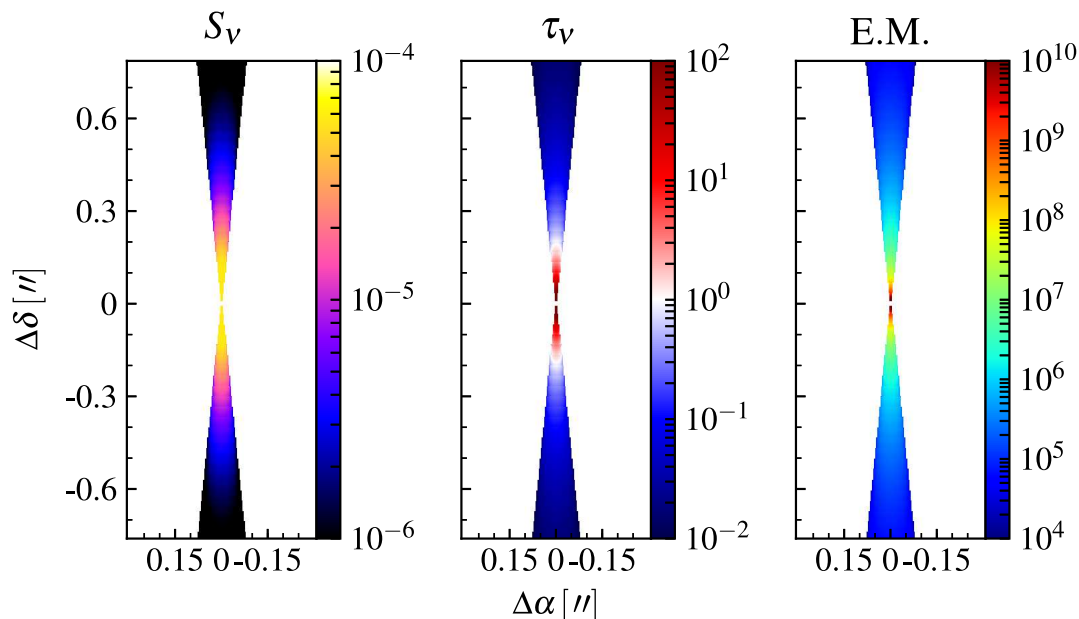


Figure 5.1: Output from the RADIORT code for a standard jet model. From left to right are plots of flux (in mJy pixel^{-1}), optical depth (where white shows the transition from optically thick to thin regimes) and emission measure (units of pc cm^{-6}). Pixel size is 1.7mas , observed frequency is 5.5GHz and $1''$ is the equivalent of 1500au .

to incorporate these effects.

In order to improve our understanding, a new set of jet models (temperature, density and pressure) would constitute the input to the RADIORT (radio continuum and recombination line radiative transfer code, H.G. Steggle and J.M. Pittard) code developed at the University of Leeds. Subsequently the output from RADIORT could be fed in to CASA to perform synthetic observations which could then be quantitatively compared to real radio images allowing the inference of jet properties. Figure 5.1 shows an example of the output of this code, for which I used the steady-state, ‘standard, spherical’ jet model ($\alpha = 0.6$, $\epsilon = 1$, $q_n = -2$, Reynolds 1986) as a proof of concept. This line of inquiry would ultimately incorporate variabilities in ejection velocity and mass flux in order to bring these

models up to date with the most recent observational results.

5.2.2 Further temporal studies

Given the temporal nature of the study presented in chapter 3, a natural extension to that work would be to expand both its sample size and time baselines. Therefore a new set of ATCA observations was approved and consequently conducted in February 2017, towards the whole southern sample of ionised jets from chapter 2. This new data permits a statistical, more sensitive study of both precession and variability, tripling the size of the sample from chapter 3 and extending the time baseline from 2 to 7 years. This latter improvement lowers the detection threshold for proper motions (across the range in distances of 2.0 – 7.8 kpc) from 470 – 1850 down to 140 – 530 km s⁻¹. Considering typical values in the literature, proper motions should therefore be seen in the majority of cases.

Not only will this help to constrain both the jet velocities and therefore mass loss rates, but will also establish the prevalence of the radio variability in MYSOs associated with episodic accretion events.

5.2.3 Sub-mm/mm follow-up campaigns

In order to properly constrain the contribution from dust to the recorded fluxes at cm-wavelengths, high-resolution, sub-mm/mm observations are required to accurately measure the core properties. As discussed in subsection 4.4.3, only small, serendipitous studies of the same objects that were studied in chapter 4 were present in the literature, for only a handful of sources, with the bulk of previous work being devoted to large-scale, statistical, single-dish surveys. In order to

accurately constrain the spectral properties of the cores/jets from cm to sub-mm regimes, a large-scale, high-resolution study is necessary. The required sensitivity and resolution could be attained by NOEMA and ALMA in the northern and southern hemispheres respectively.

Concurrent to these continuum observations, line studies would help to image the molecular outflows towards each of the objects, and disentangle their multiplicitous nature towards each of the MYSOs. In turn this would aid in attributing each outflow to an individual core, and therefore ionised jet, allowing an accurate study of the relationship between jet and outflow (i.e. refining the results of subsection 4.4.5.2). Using high-density tracers, such as HCN, would also constrain accretion disc properties, which would allow, for the first time, a statistical study of the relationship between an ionised jet's physical properties and those of its launching accretion disc. With current sub-mm interferometers and their small synthesised beam widths/high sensitivities, line tracers could also be used to calculate accretion rates. A good example of this type of study was performed towards NGC7538 IRS 1 by Sandell *et al.* (2009). Using CARMA observations of the $\text{HCO}^+ J = 1 \rightarrow 0$ transition, they inferred an accretion rate of $2 \times 10^{-4} M_{\odot} \text{yr}^{-1}$ from the line's inverse P Cygni profile. It is unknown how much the larger scale material of the envelope potentially pollutes such a profile, however using ALMA/NOEMA at their highest possible resolutions would resolve out much from the large scale providing more reliable estimates of the accretion rates. In turn, comparison of the ionised jet mass loss rate to the derived accretion rates would lead to accurate determination of mass loss to accretion ratios, a constraining parameter of jet launching and collimation mechanisms.

Table 5.1: Relevant telescope specifications for future observations using the SKA and its precursors, with the ATCA and EVLA shown for comparison. Columns 3, 4, 5, 6 and 7 are for maximum baseline length, maximum bandwidth, frequency ranges, noise level for a 1 hr integration and finest resolution attainable, respectively. System temperatures have been conservatively assumed as 40 K for calculations of sensitivity, however this will increase for K or Q-band observations. For the SKA2-MID, a final array size of 2000 antennae was used. An asterisk denotes a possible upgrade to the relevant specification of the instrument.

Telescope	Operational (Year)	B_{\max} (km)	$\Delta\nu_{\max}$ (GHz)	$[\nu_{\min}, \nu_{\max}]$ ([GHz, GHz])	$\sigma_{\text{RMS}}^{\text{1hr}}$ ($\mu\text{Jy}/\text{beam}^{-1}$)	θ_{\max} (mas)
ATCA	1989	6	2	[1.00, 50.0]	26.28	234
EVLA	2011	26	4	[0.06, 50.0]	2.97	48
MeerKAT	2018	20	2 (4*)	[0.58, 14.5]	4.56	213
SKA1-MID	2022	100	2.5	[0.35, 13.8]	0.87	45
SKA2-MID	2028	180	2.5	[0.05, 24.0]	0.11	14

5.2.4 Jet studies in the SKA era

From this work, it is apparent that much higher resolutions and sensitivities are required than those available with current technology to further our knowledge of ionised jets and massive star formation in general. Future radio astronomical instrumentation will be dominated by the Square Kilometer Array (SKA) and its precursors until final light on the finished array. To understand the science that will, and will not, be accessible, we must first consider the specifications for each stage of the SKA project. In Table 5.1, the specifications relevant to observers are shown.

Looking at the short term prospects for science, using MeerKAT would allow for the southern hemisphere survey presented in chapter 2, to be enhanced to the sensitivity of the northern hemisphere survey of chapter 4. Just as importantly, the fuller *uv*-coverage of MeerKAT compared to ATCA would drastically increase the images' dynamic range, which was low and therefore heavily affected the

quality of some ATCA images. Considering the resolution of MeerKAT however, only the phase-1 SKA could subsequently allow for high resolution studies. With an effective resolution at 1 kpc of 45 au at 13.8 GHz, this may help to resolve the collimation radii of ionised jets due to the relatively dust-free emission at these frequencies. However, only the final SKA could truly resolve this scale with prospects of probing the launching radii predicted by the disc wind model.

Certainly the most promising study to be completed with the SKA in phase 1 and 2 would be an extremely sensitive survey of IRDCs in the southern hemisphere. This would, once and for all, allow us to detect the extremely faint radio emission expected (using the results of subsection 4.4.1) from the first production of ionised emission towards the earliest stages of massive star formation. To emphasize this point, a full 12 hour integration with the phase 1 or phase 2 SKA would provide an image noise level of ~ 250 nJy or ~ 30 nJy respectively.

Appendix A

Supporting figures

In this Appendix, Figures A.1–A.45 are included in support of Chapter 2, while Figures A.46–A.102 support Chapter 4.

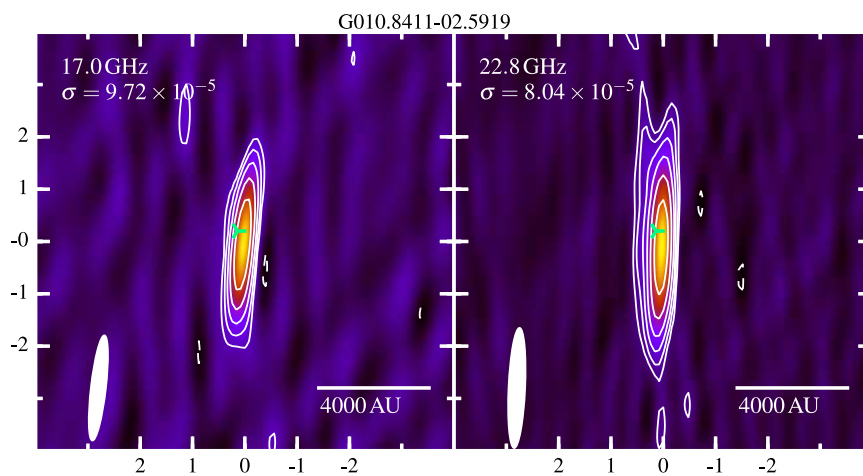


Figure A.1: Radio flux density contour plots of G010.8411–02.5919. Each panel has the observed frequency and noise level indicated in the top left corner of each sub-plot. Convolving beam sizes are represented by the white ellipse in the bottom left corner, whilst in the bottom right, a scalebar assuming the distance of Table 2.2 is plotted. Green markers with 3 vertices, blue ‘×’ markers and pink ‘+’ markers represent CH₃OH (Walsh *et al.* 1998), H₂O (Caratti o Garatti *et al.* 2015) and OH (Caswell 1998) masers from the literature, respectively.

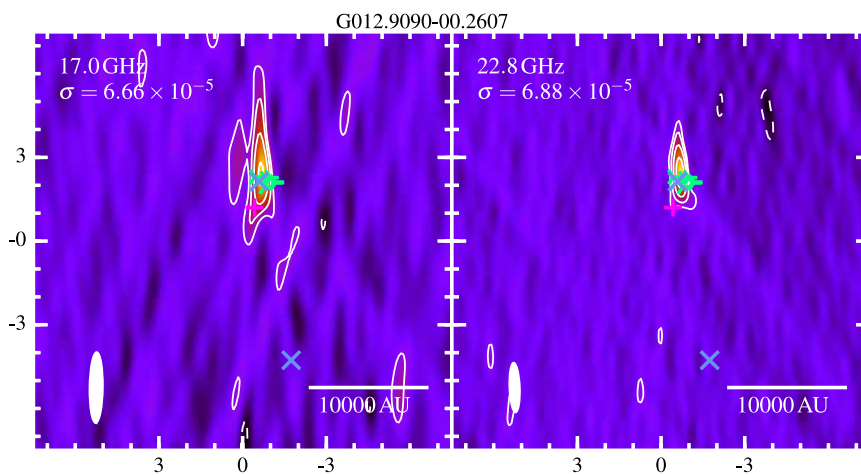


Figure A.2: As in Figure A.1, but towards G012.9090–00.2607.

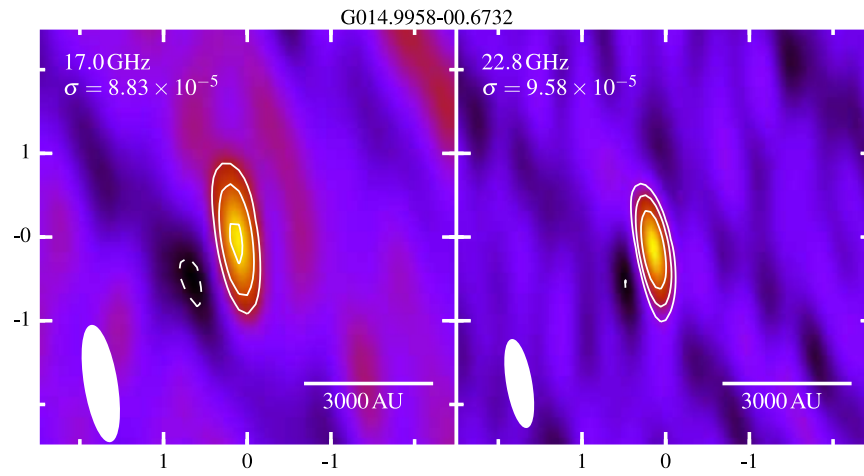


Figure A.3: As in Figure A.1, but towards G014.9958–00.6732.

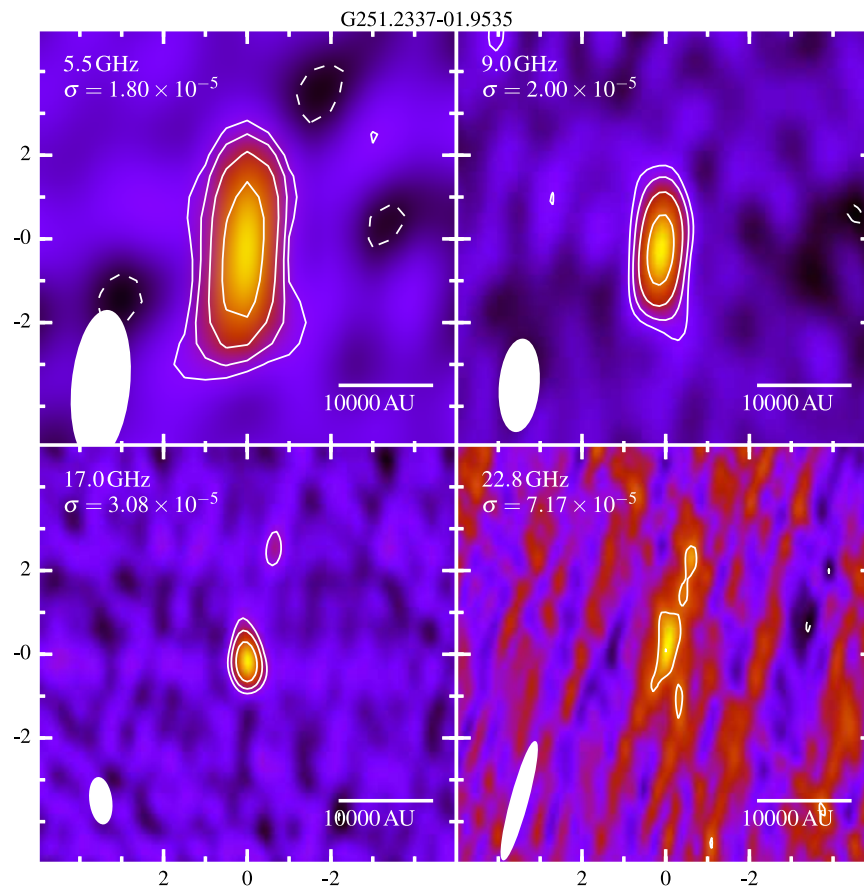


Figure A.4: As in Figure A.1, but towards G251.2337–01.9535.

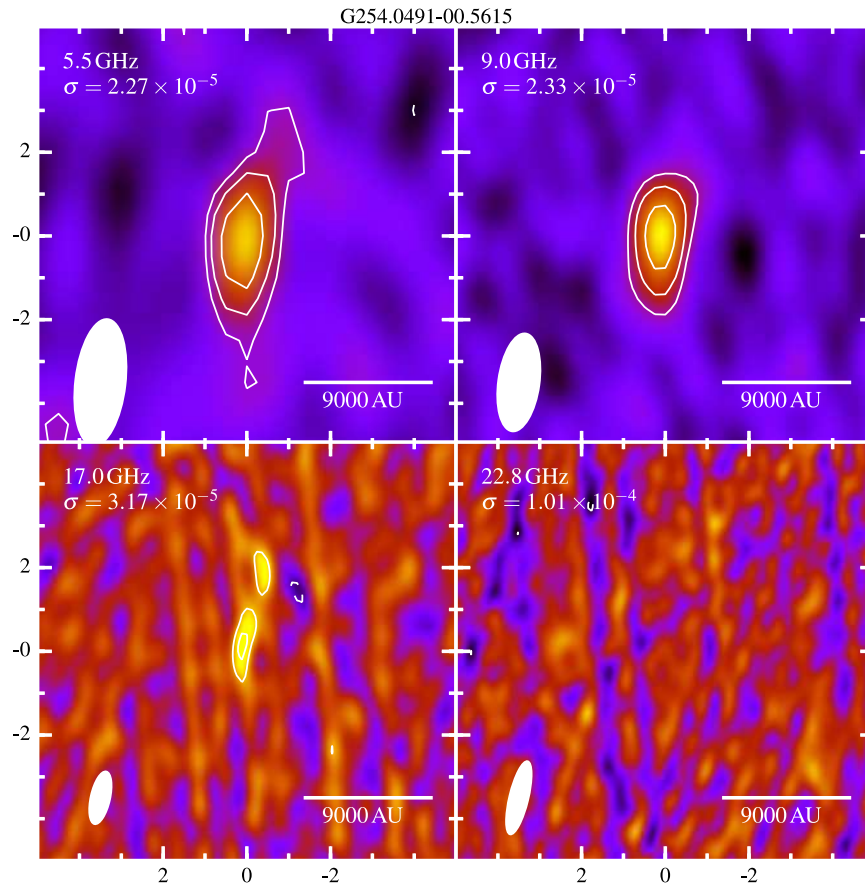


Figure A.5: As in Figure A.1, but towards G254.0491–00.5615.

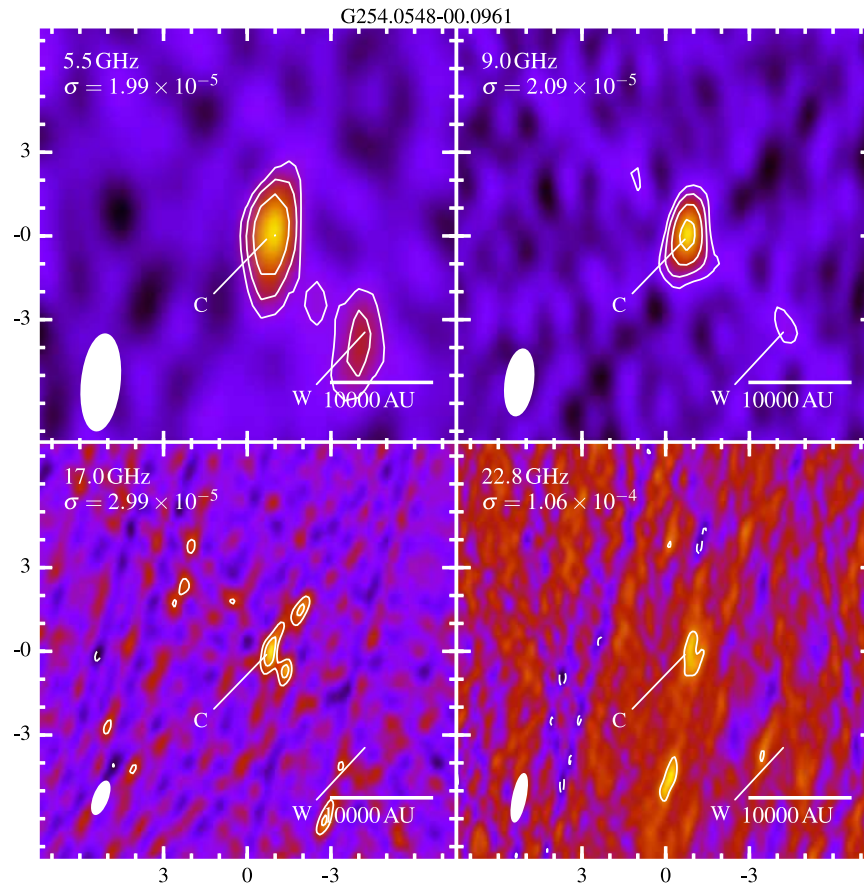


Figure A.6: As in Figure A.1, but towards G254.0548–00.0961.

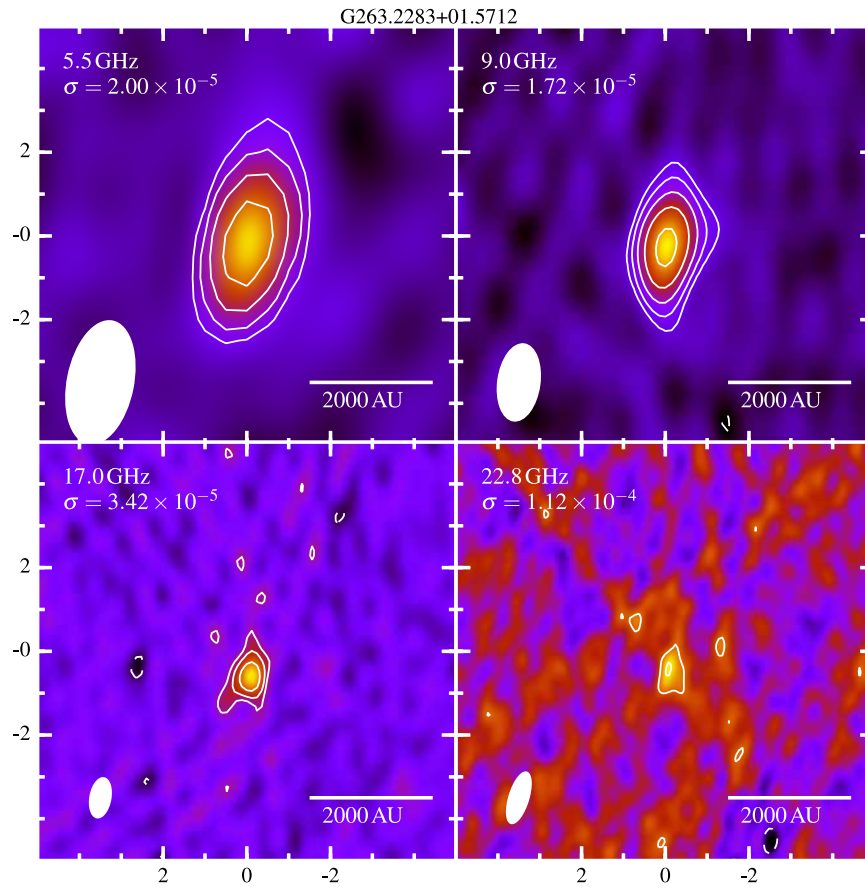


Figure A.7: As in Figure A.1, but towards G263.2283–01.5712.

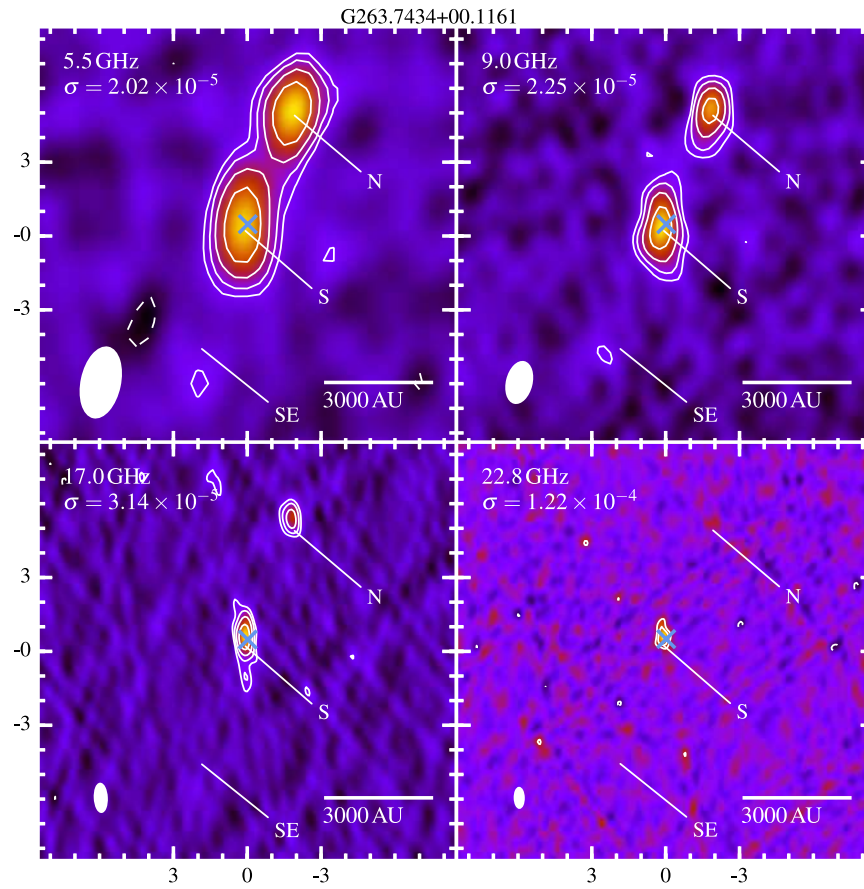


Figure A.8: As in Figure A.1, but towards G263.7434+00.1161.

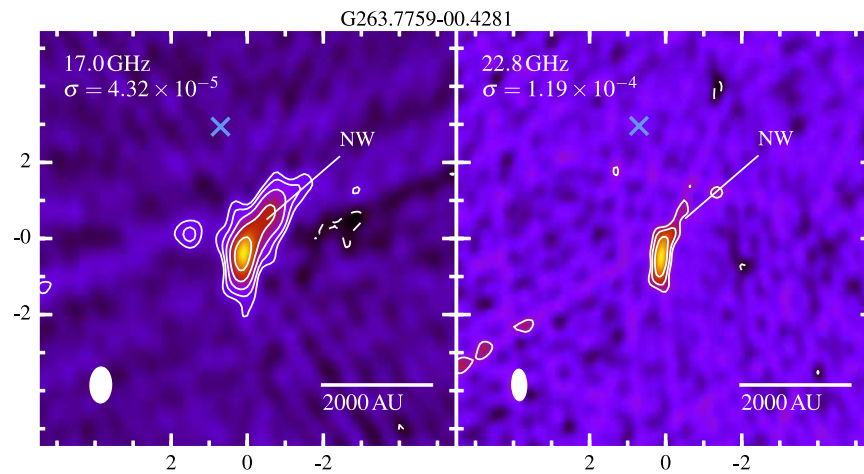


Figure A.9: As in Figure A.1, but towards G263.7759-00.4281.

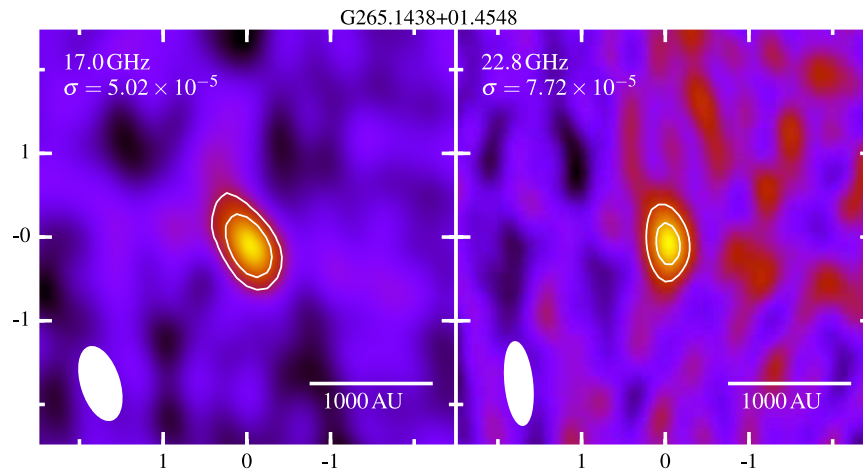


Figure A.10: As in Figure A.1, but towards G265.1438+01.4548.

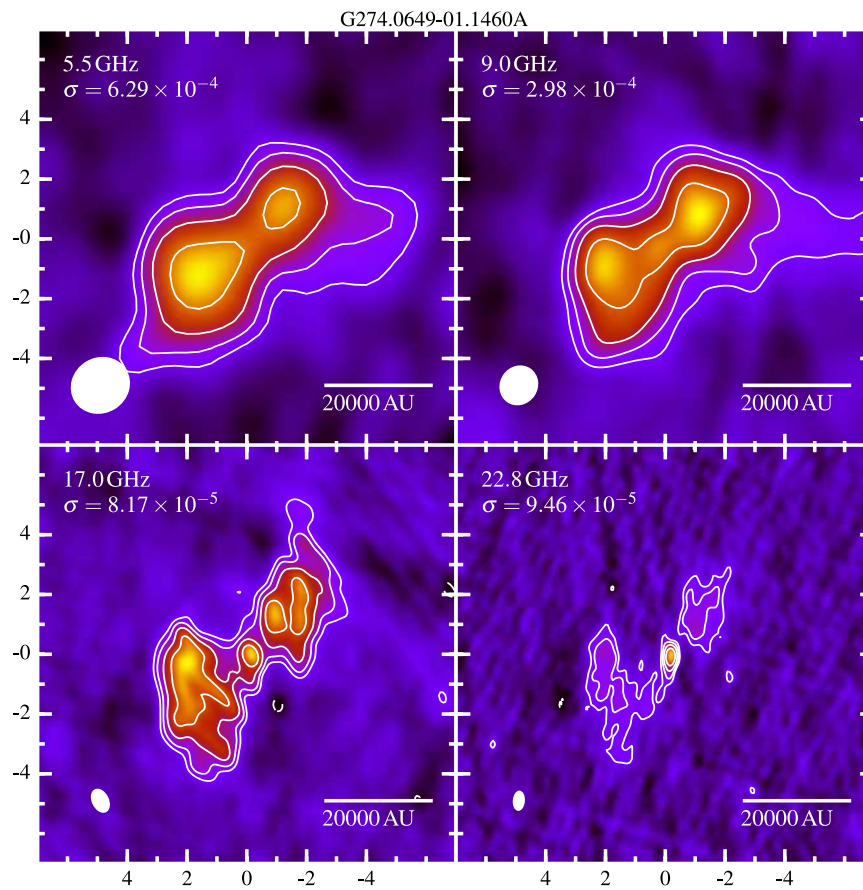


Figure A.11: As in Figure A.1, but towards G274.0649-01.1460.

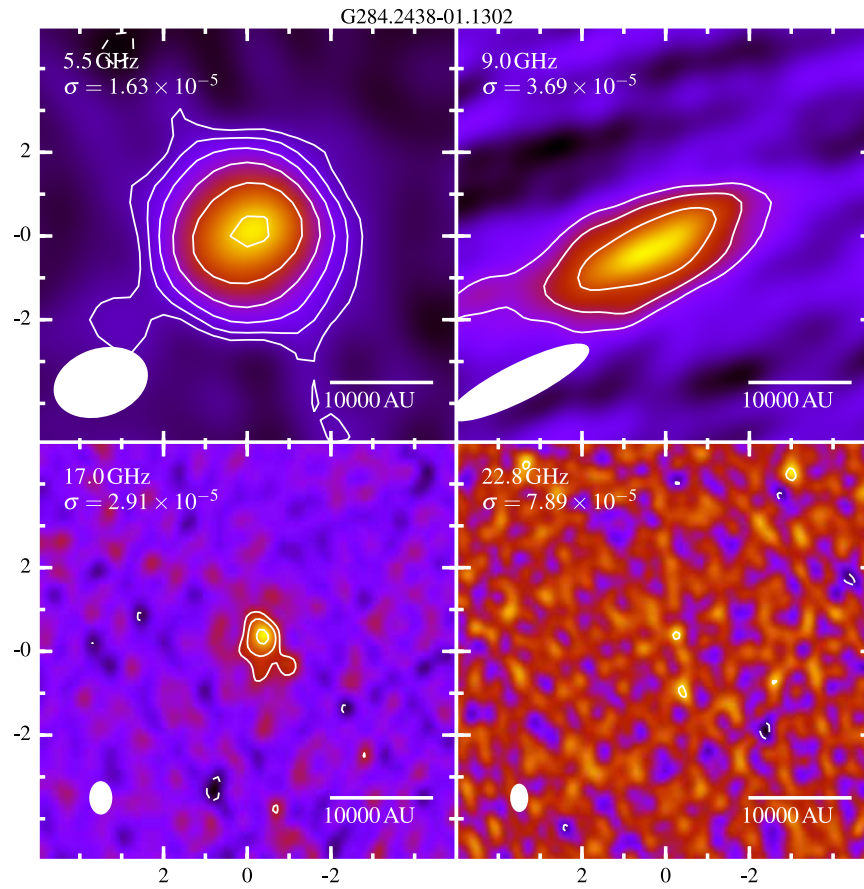


Figure A.12: As in Figure A.1, but towards G284.2438–01.1302.

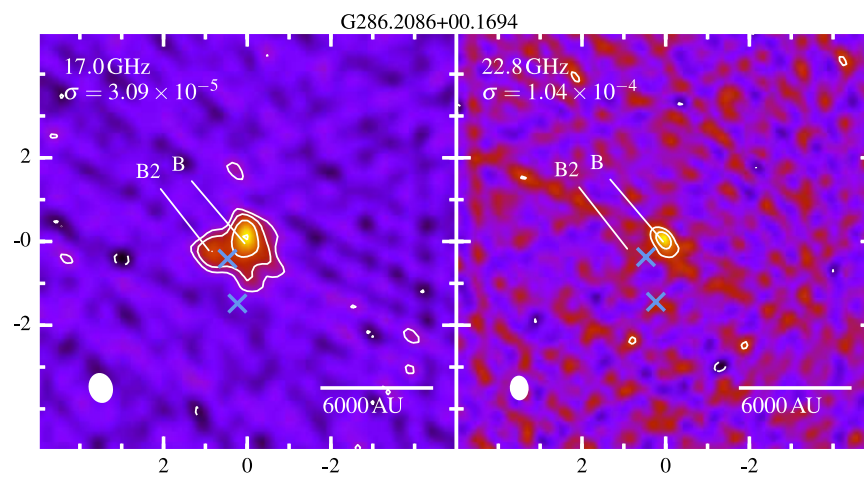


Figure A.13: As in Figure A.1, but towards G286.2086+00.1694.

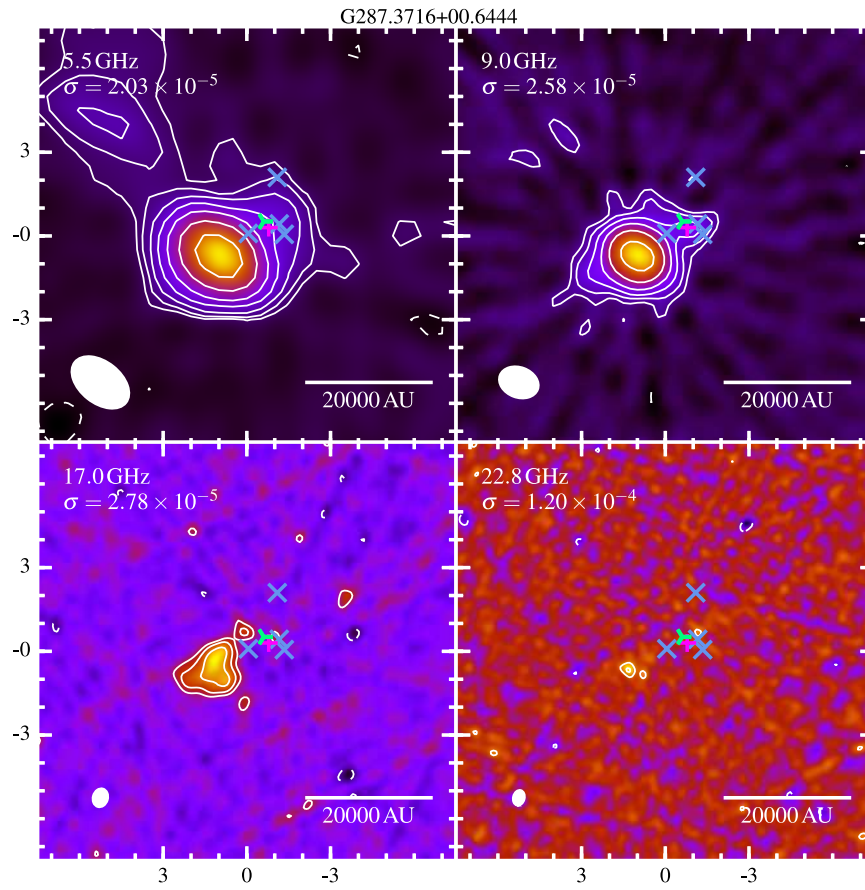


Figure A.14: As in Figure A.1, but towards G287.3716+00.6444.

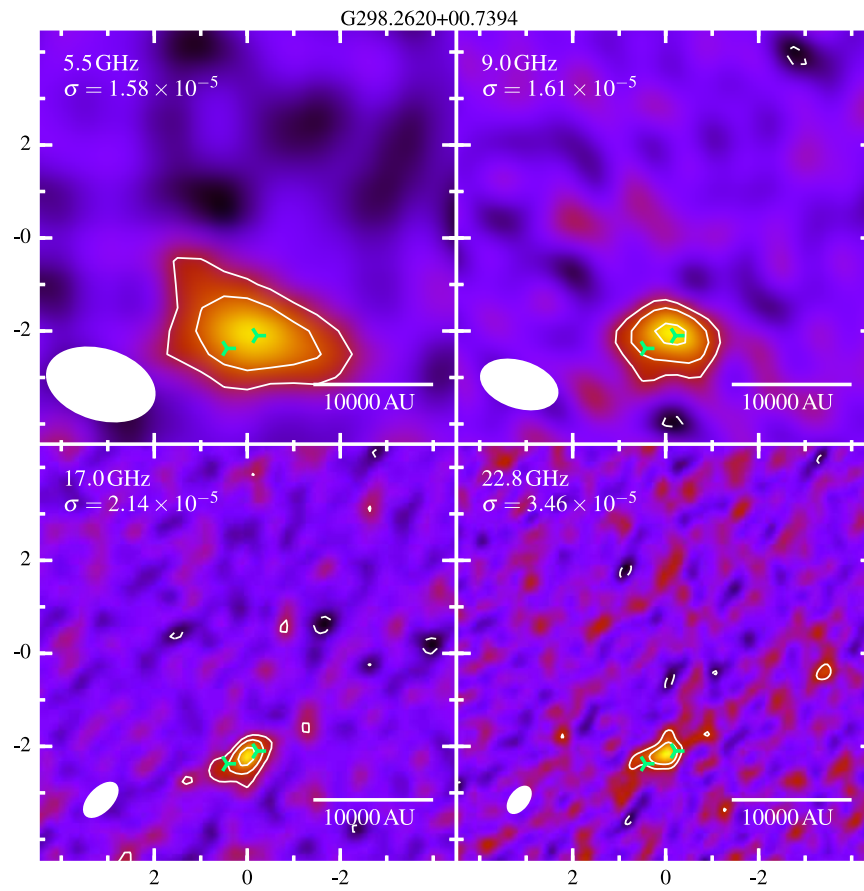


Figure A.15: As in Figure A.1, but towards G298.2620+00.7394.

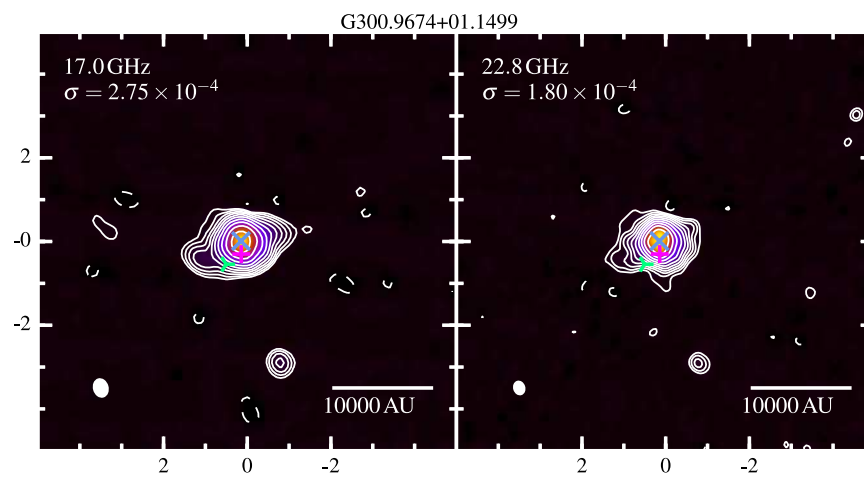


Figure A.16: As in Figure A.1, but towards G300.9674+01.1499.

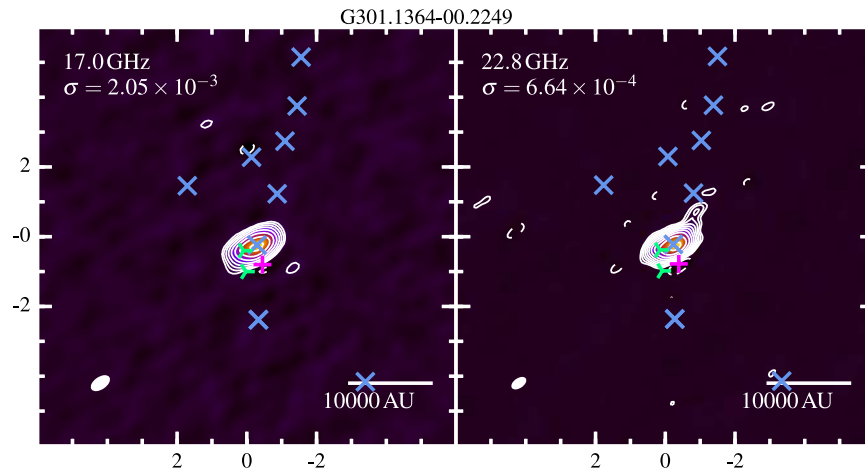


Figure A.17: As in Figure A.1, but towards G301.1364–00.2249.

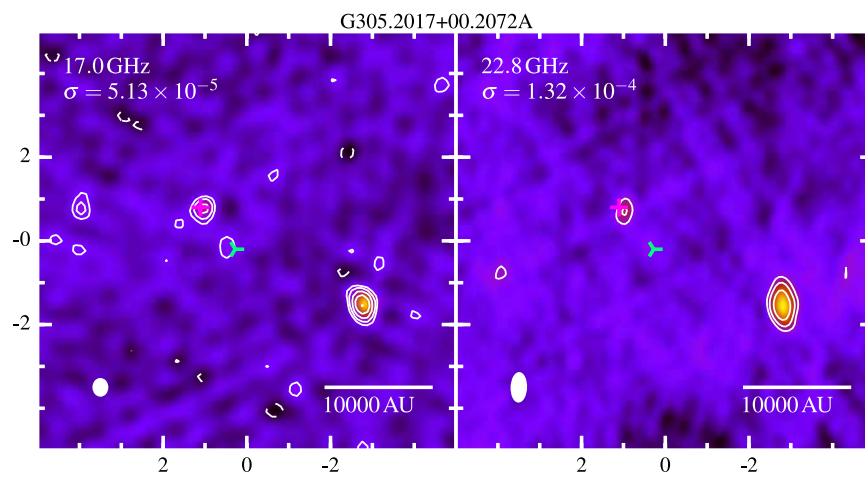


Figure A.18: As in Figure A.1, but towards G305.2017+00.2072A.

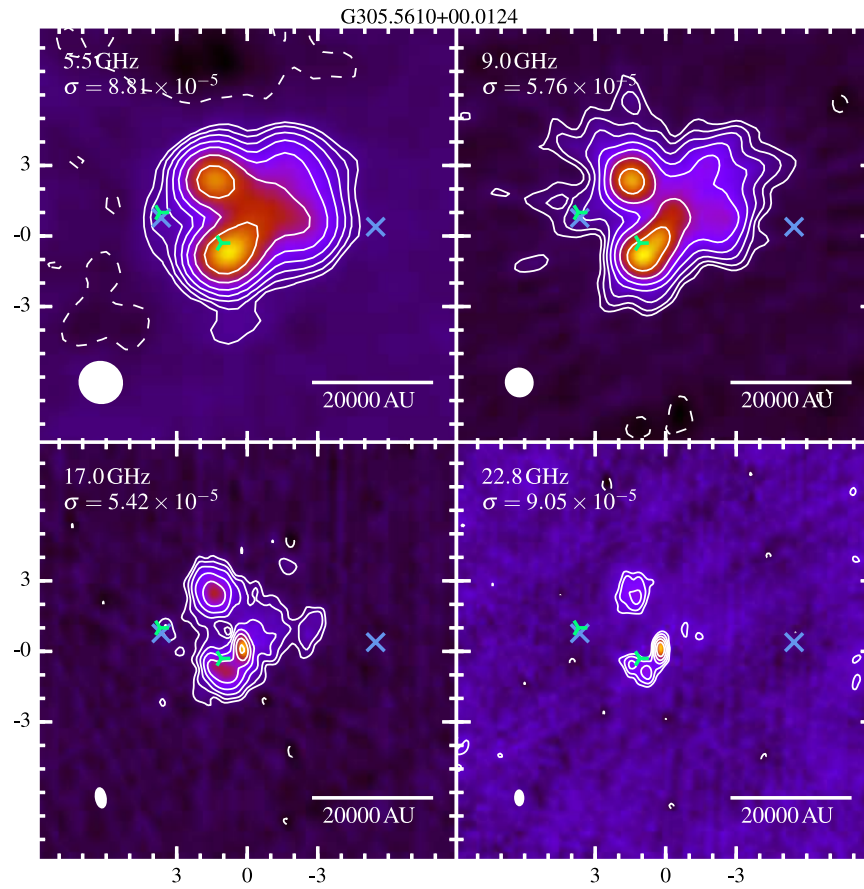


Figure A.19: As in Figure A.1, but towards G305.5610+00.0124.

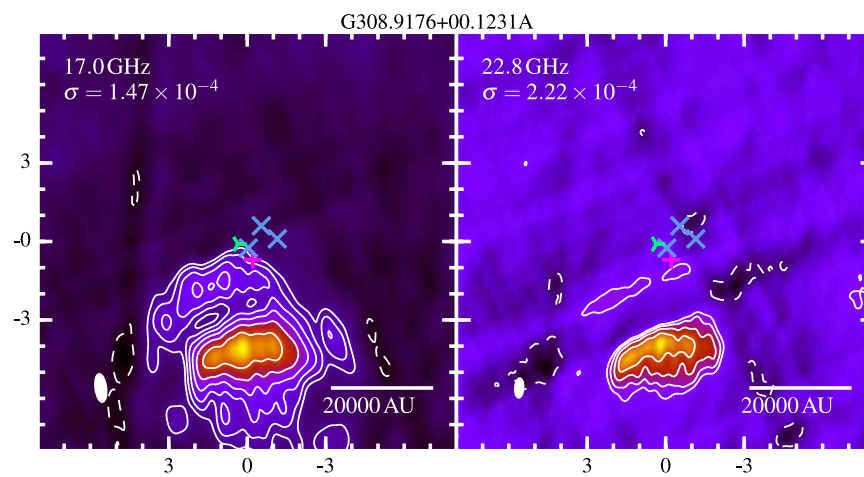


Figure A.20: As in Figure A.1, but towards G308.9176+00.1231A.

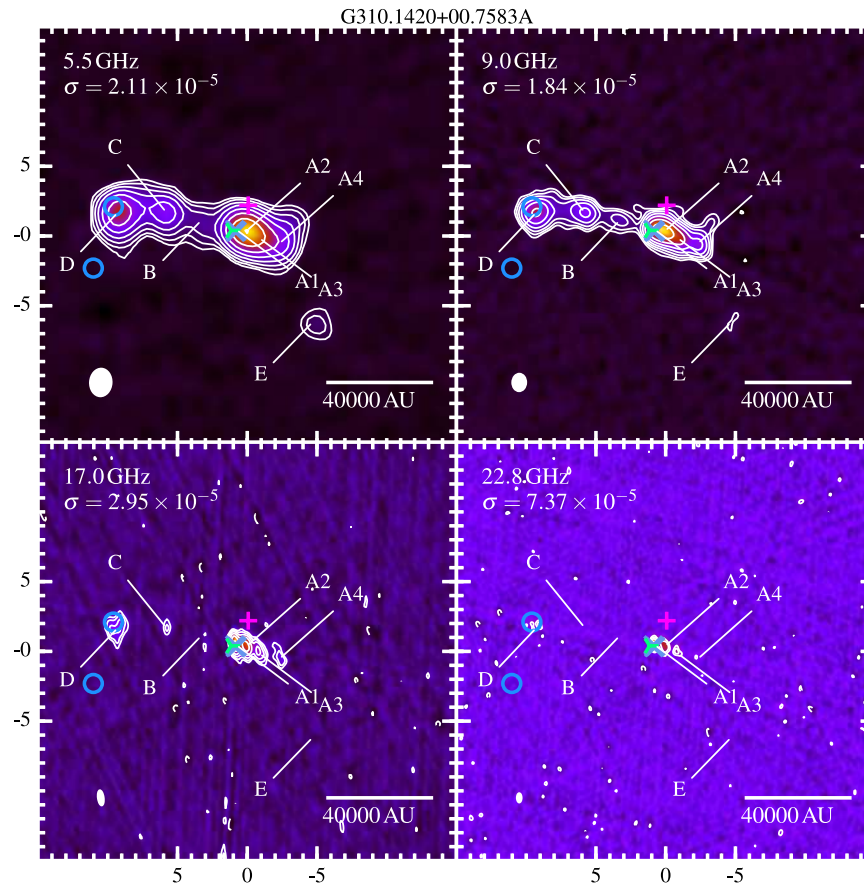


Figure A.22: As in Figure A.1, but towards G310.1420+00.7583A.

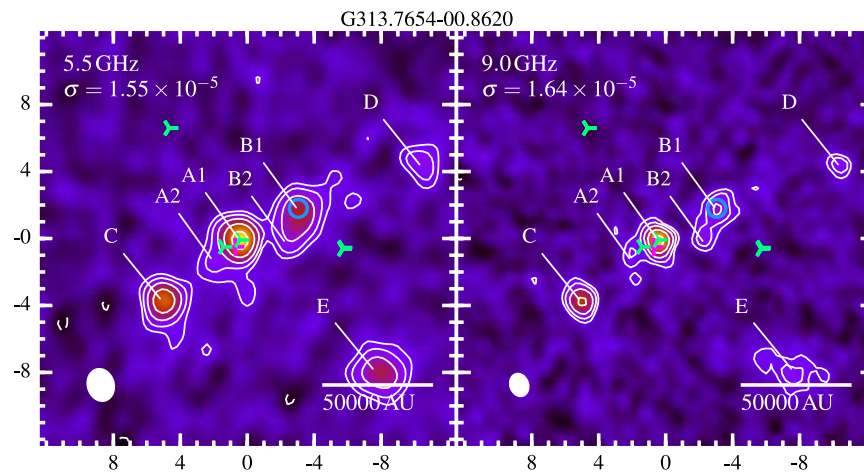


Figure A.23: As in Figure A.1, but towards G313.7654-00.8620.

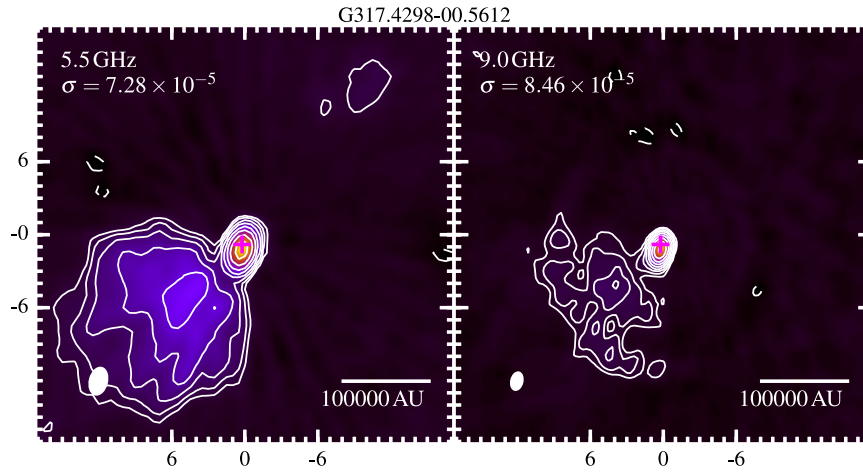


Figure A.24: As in Figure A.1, but towards G317.4298–00.5612.

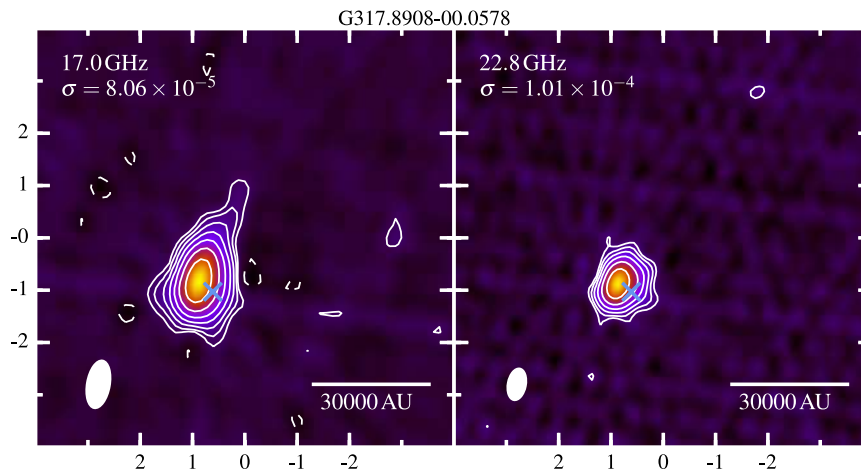


Figure A.25: As in Figure A.1, but towards G317.8908–00.0578.

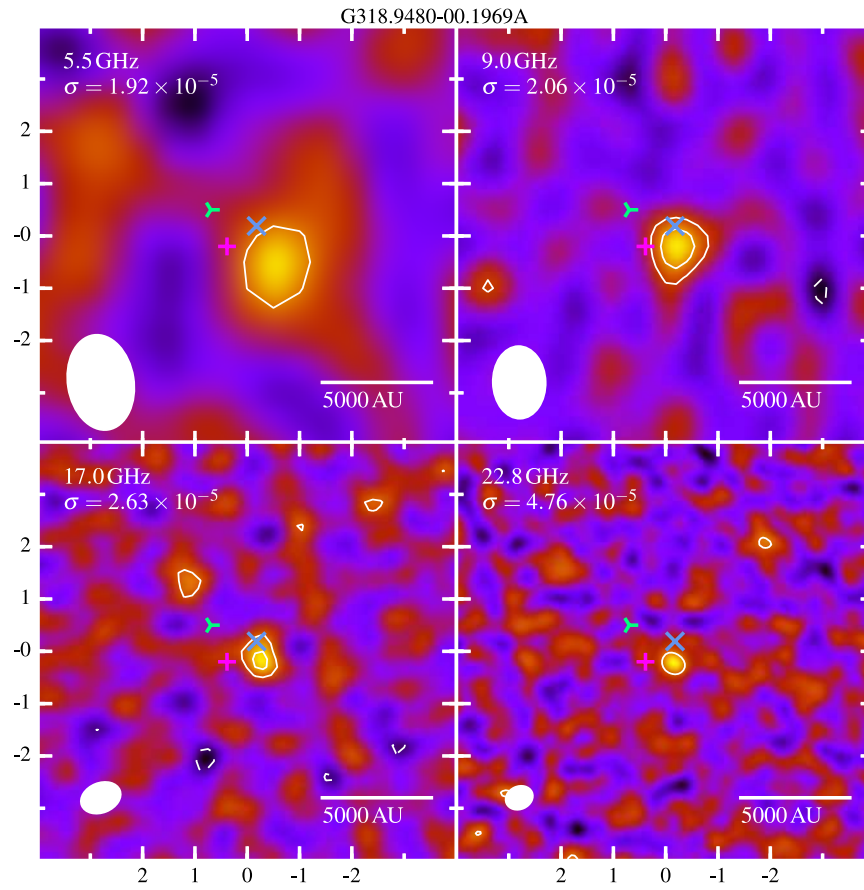


Figure A.26: As in Figure A.1, but towards G318.9480–00.1969A.

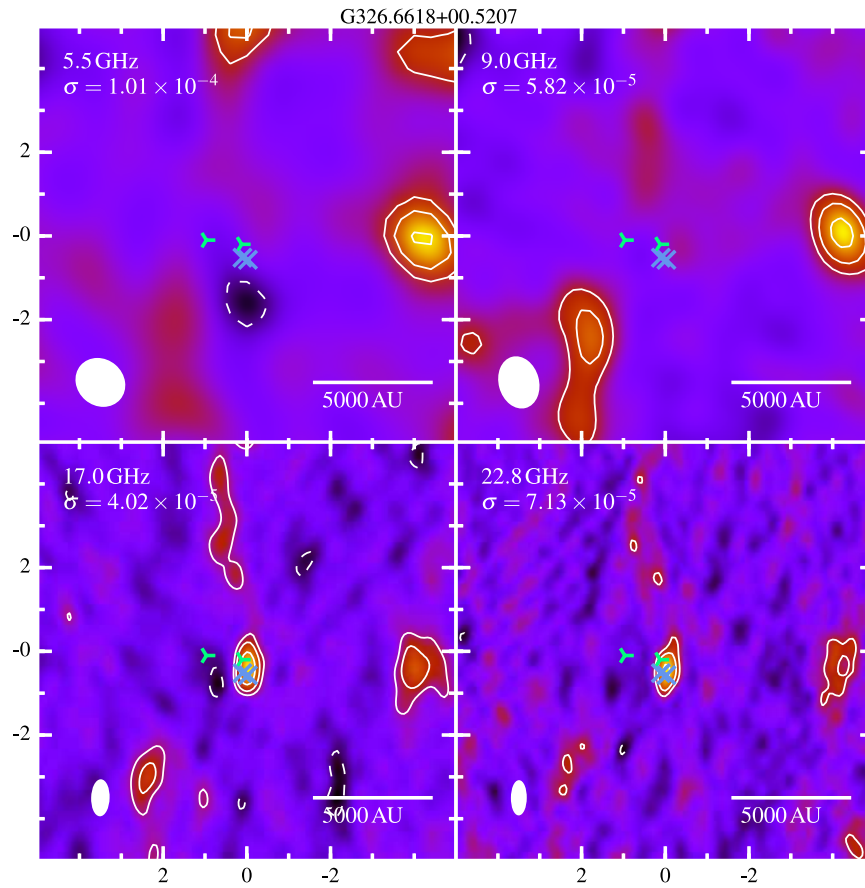


Figure A.27: As in Figure A.1, but towards G326.6618+00.5207.

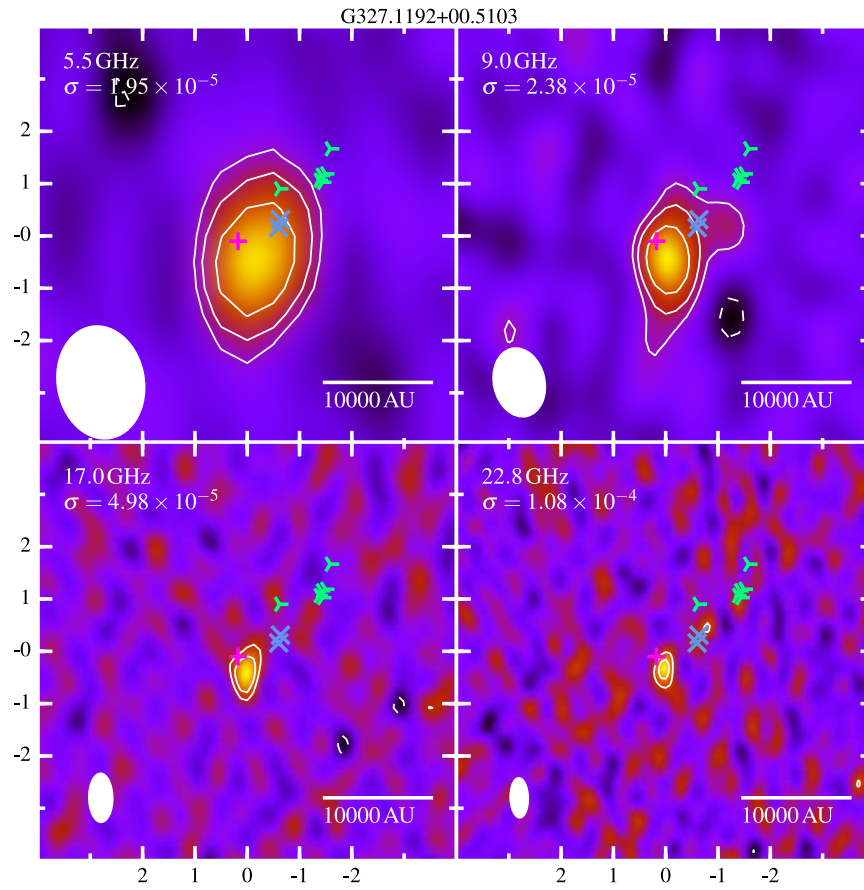


Figure A.28: As in Figure A.1, but towards G327.1192+00.5103.

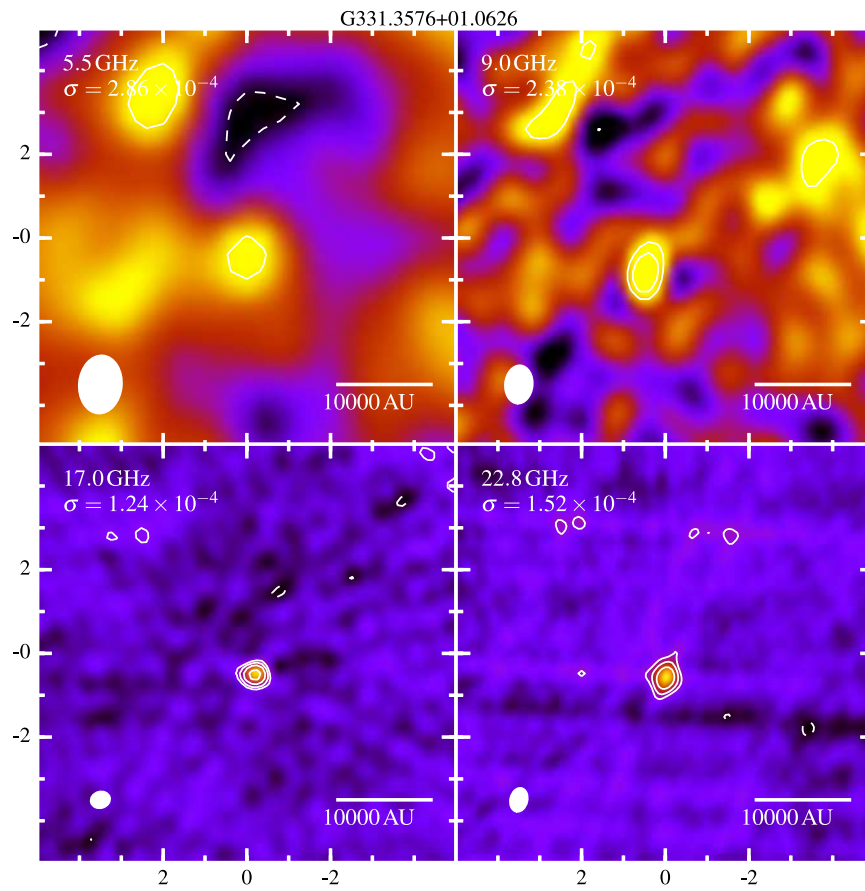


Figure A.29: As in Figure A.1, but towards G331.3576+01.0626.

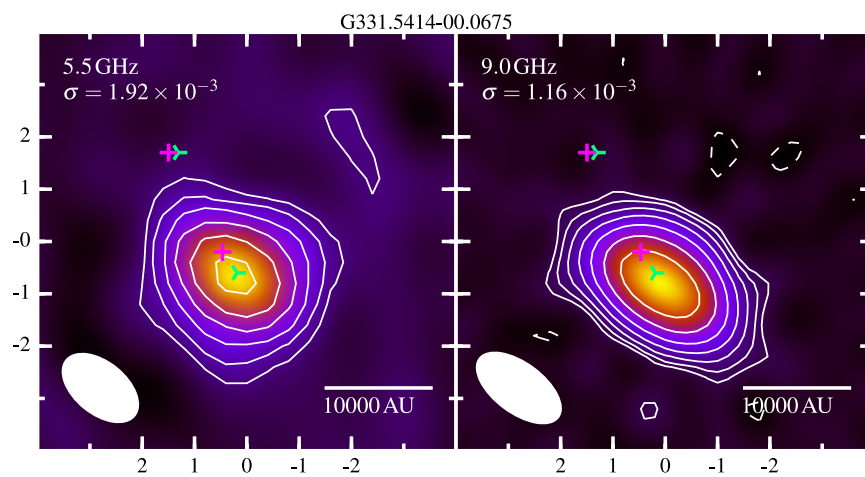


Figure A.30: As in Figure A.1, but towards G331.5414-00.0675.

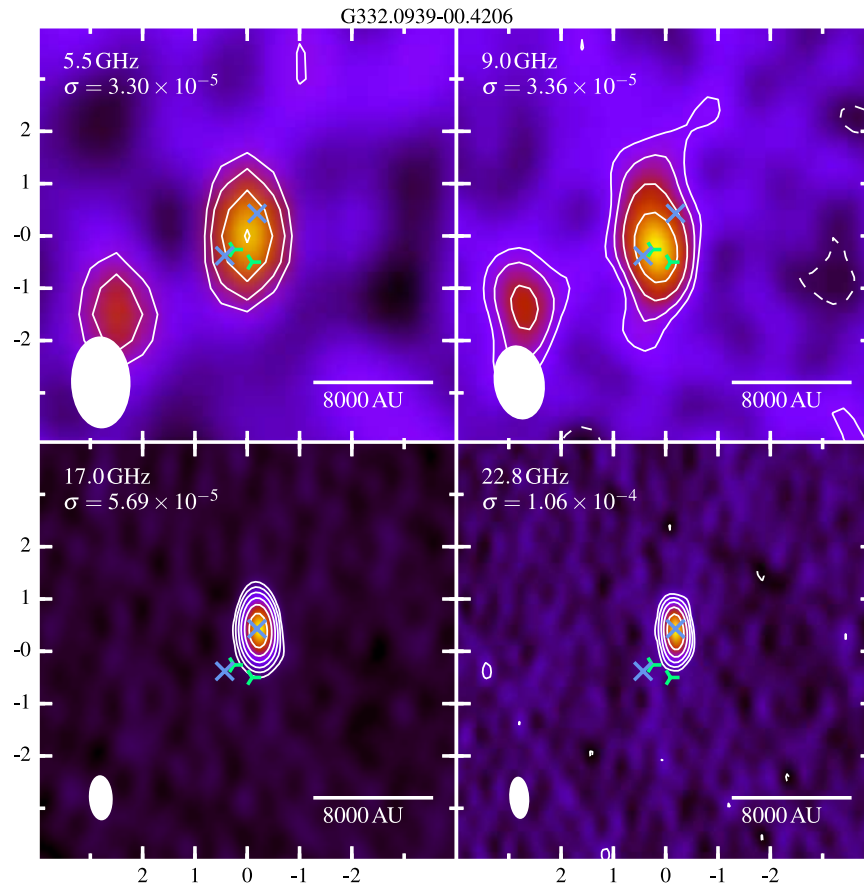


Figure A.31: As in Figure A.1, but towards G332.0939–00.4206.

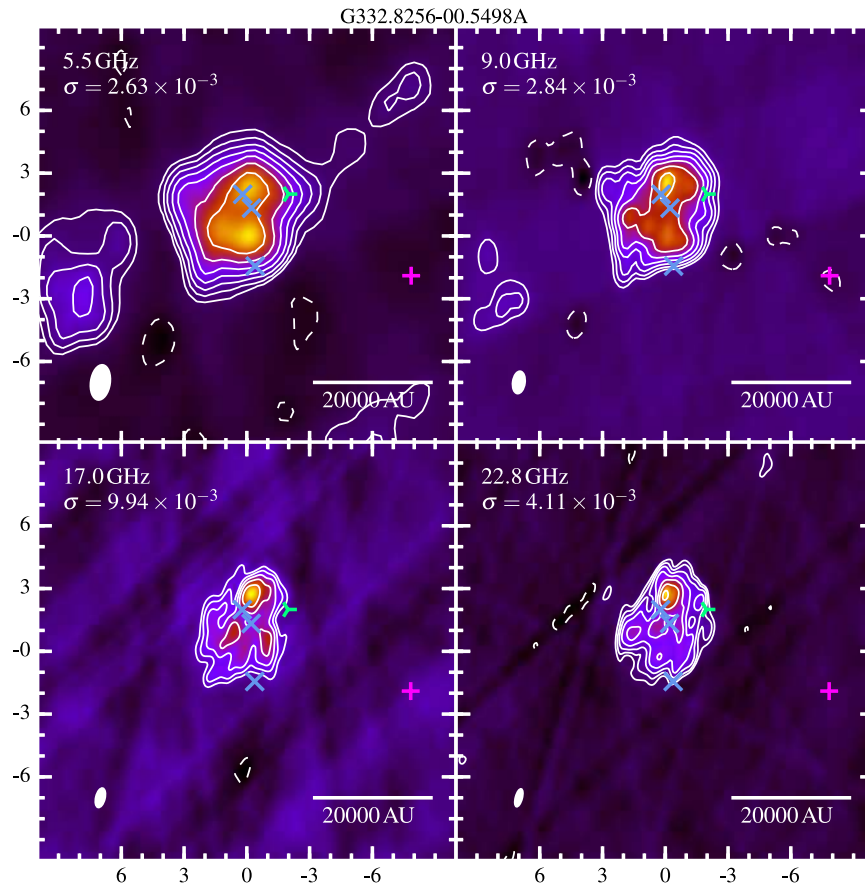


Figure A.32: As in Figure A.1, but towards G332.8256–00.5498A.

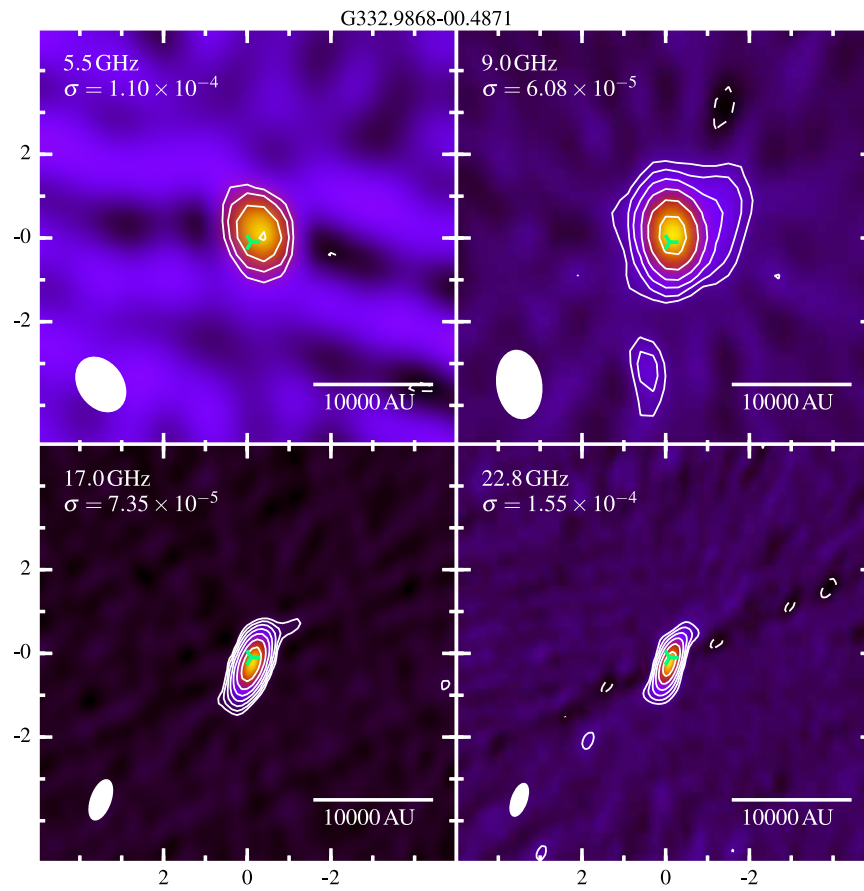


Figure A.33: As in Figure A.1, but towards G332.9868–00.4871.

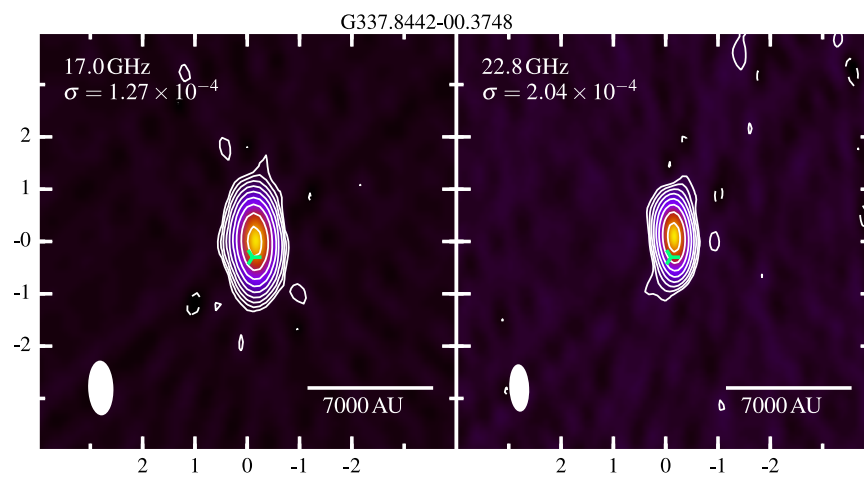


Figure A.34: As in Figure A.1, but towards G337.8442–00.3748.

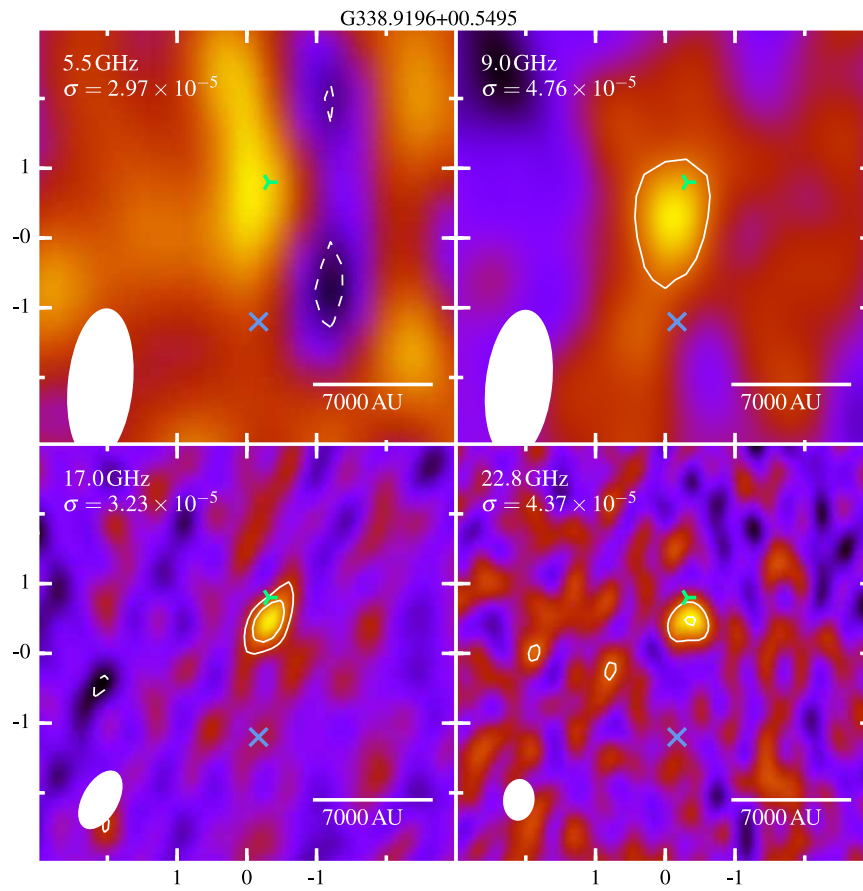


Figure A.35: As in Figure A.1, but towards G338.9196+00.5495.

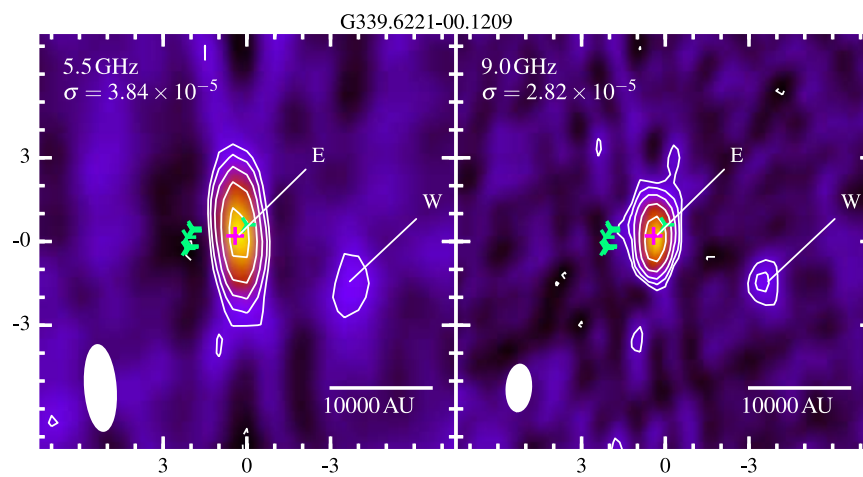


Figure A.36: As in Figure A.1, but towards G339.6221-00.1209.

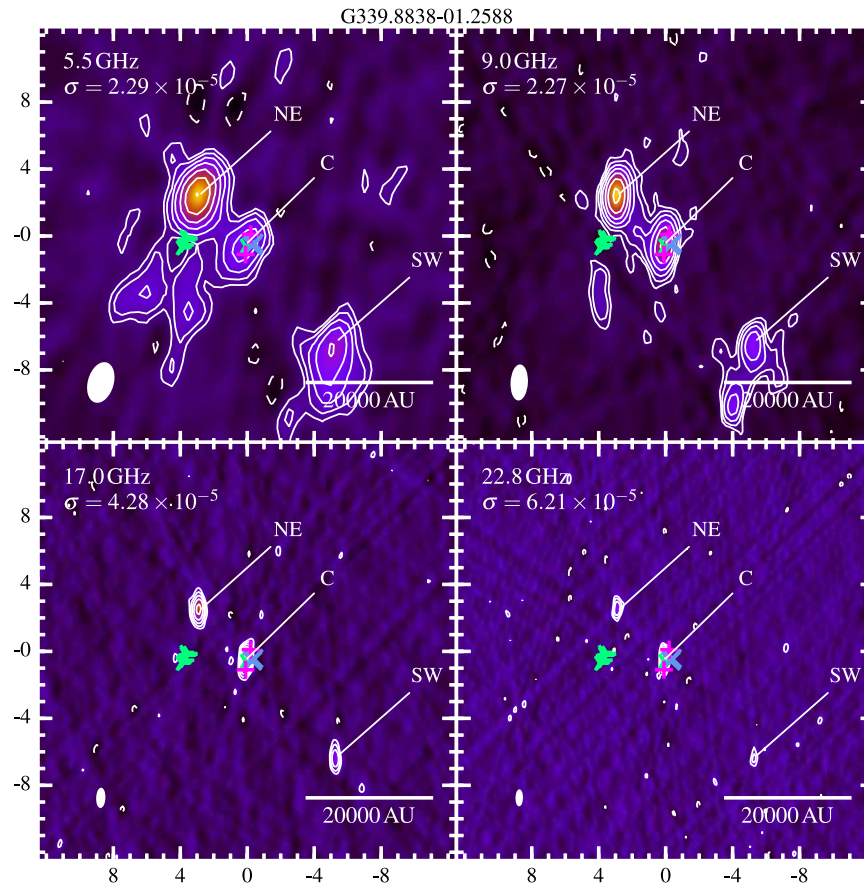


Figure A.37: As in Figure A.1, but towards G339.8838–01.2588.

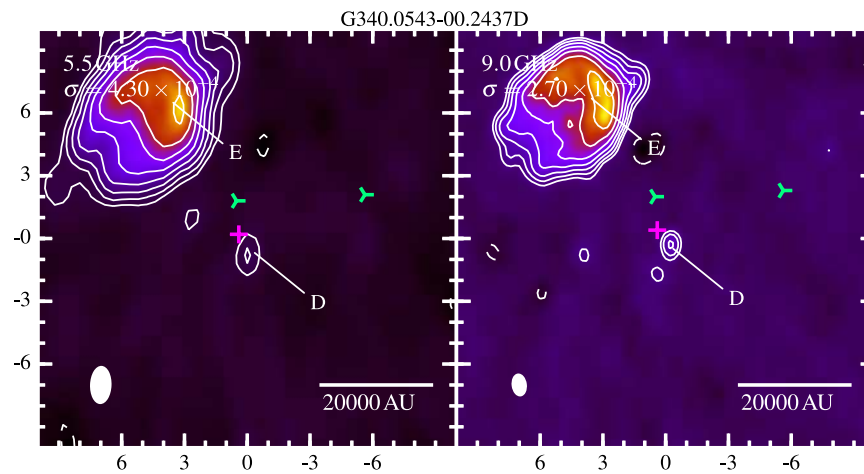


Figure A.38: As in Figure A.1, but towards G340.0543–00.2437D.

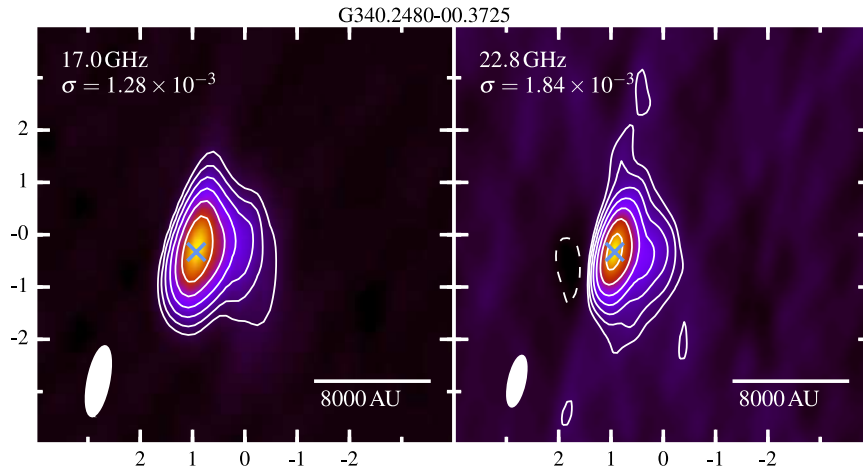


Figure A.39: As in Figure A.1, but towards G340.2480–00.3725.

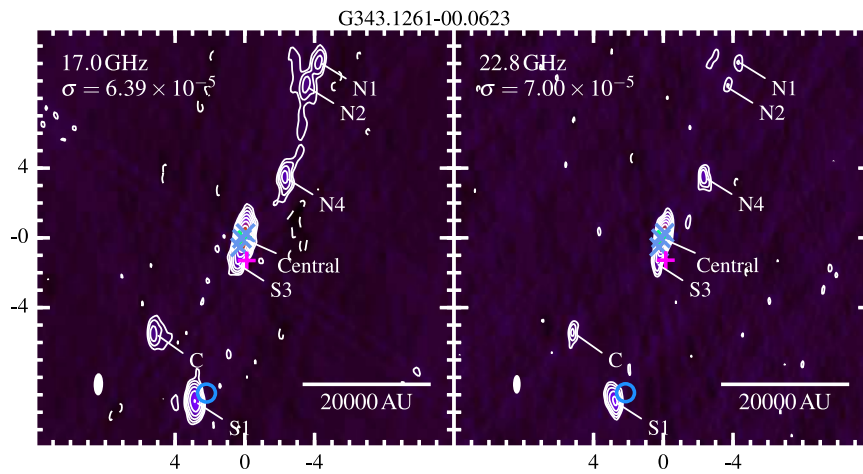


Figure A.40: As in Figure A.1, but towards G343.1261–00.0623.

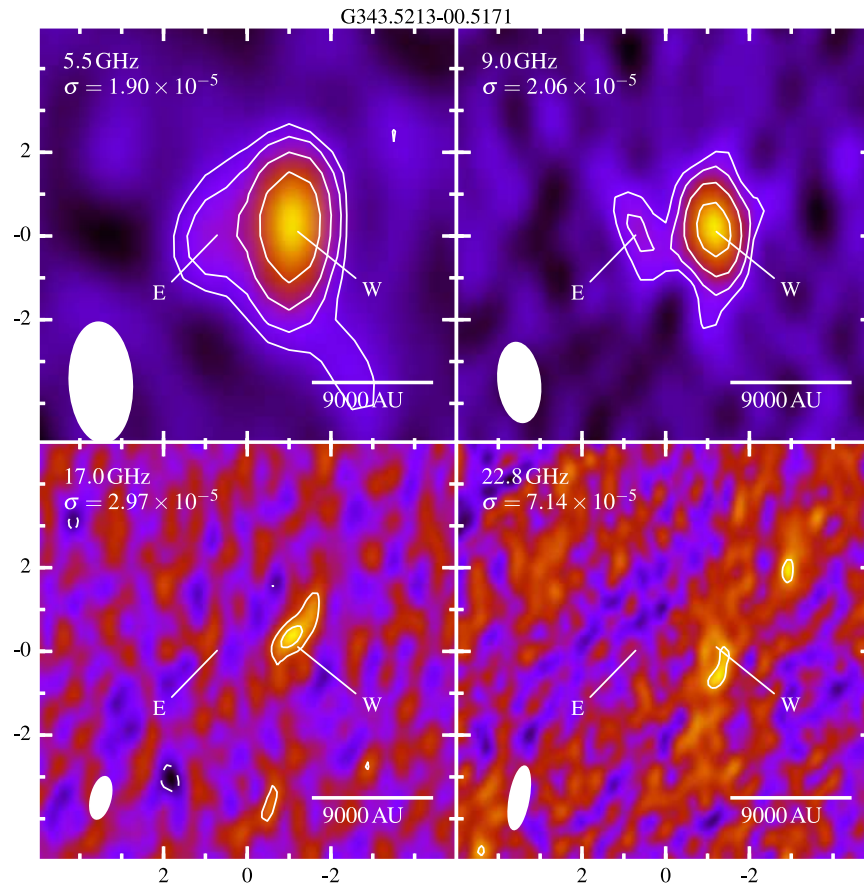


Figure A.41: As in Figure A.1, but towards G343.5213–00.5171.

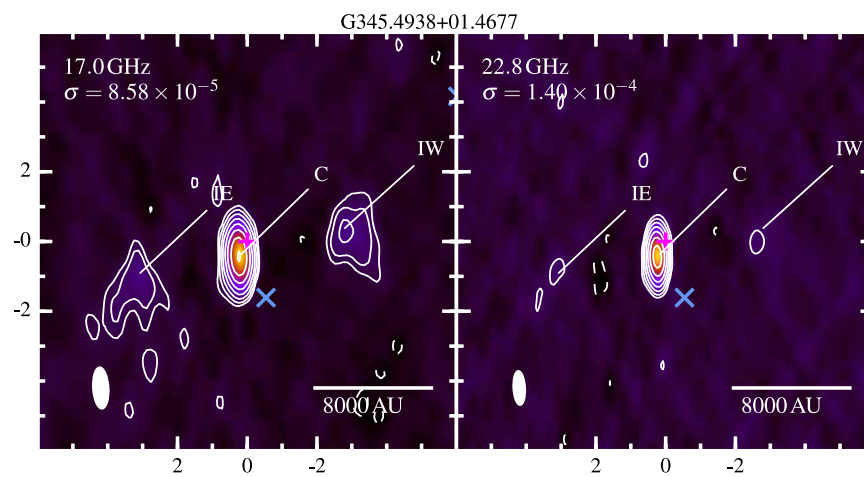


Figure A.42: As in Figure A.1, but towards G345.4938+01.4677.

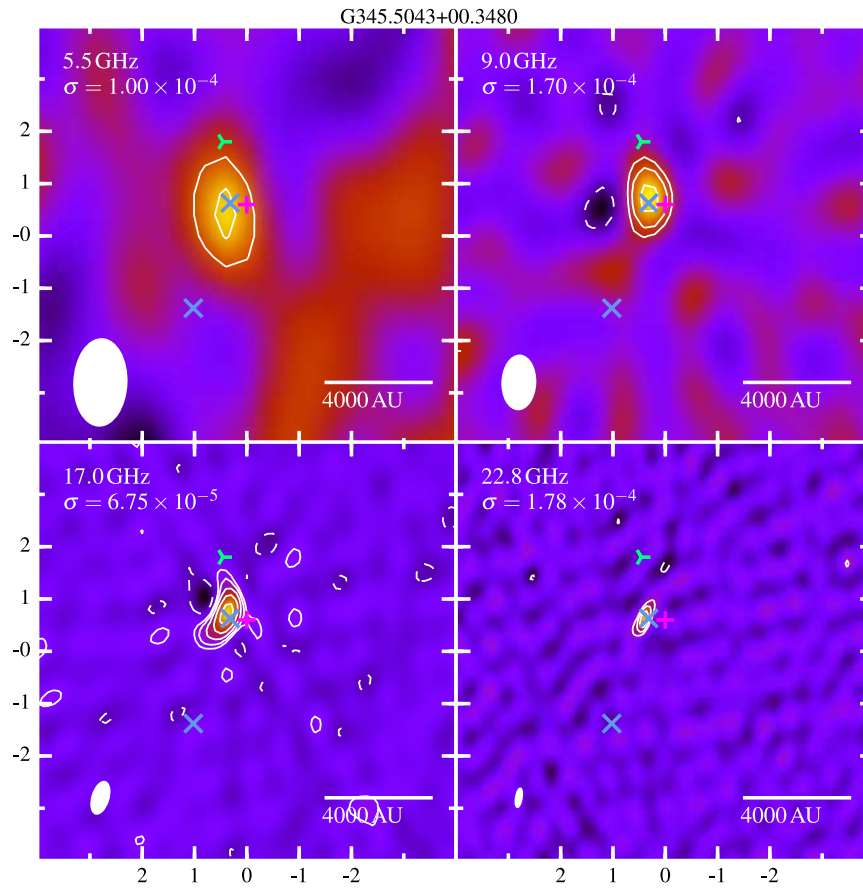


Figure A.43: As in Figure A.1, but towards G345.5043+00.3480.

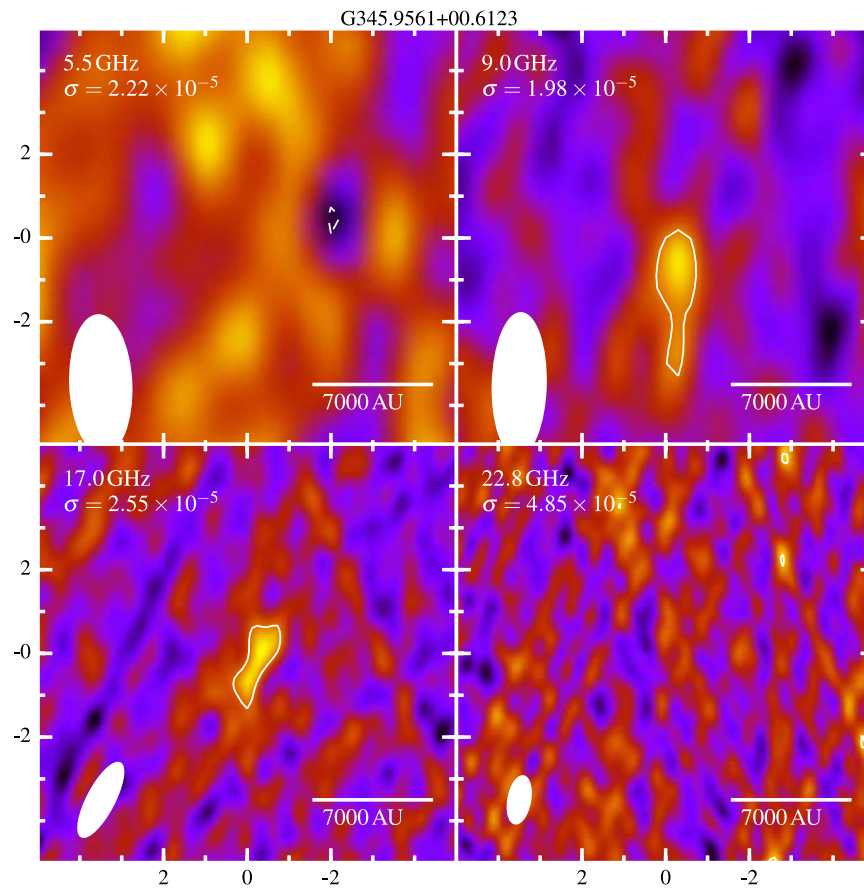


Figure A.44: As in Figure A.1, but towards G345.9561+00.6123.

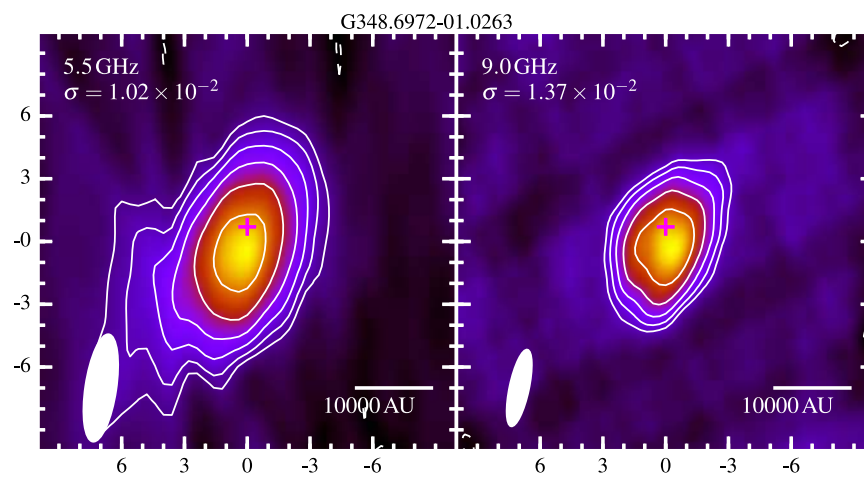


Figure A.45: As in Figure A.1, but towards G348.6972-01.0263.

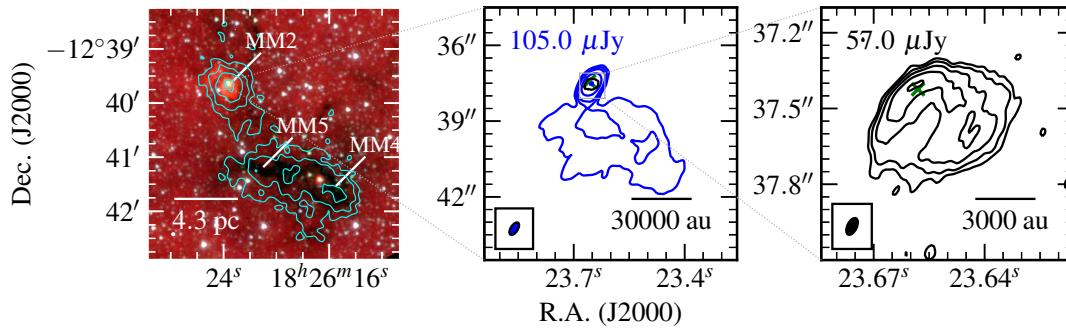


Figure A.46: Mid-infrared (GLIMPSE 8.0, 4.5, 3.6 μm R, G, B image; left panel), sub-mm (ATLASGAL 870 μm cyan contours; left panel) and radio maps of G018.82–00.28 at C-band (blue contours; middle) and Q-band (black contours; right). Restoring beams were $0.558'' \times 0.283''$ at -33° and $0.072'' \times 0.038''$ at -26° , while contour levels are $(-3, 3, 6, 12, 44, 171) \times \sigma$ and $(-3, 3, 6, 11, 21, 40) \times \sigma$ for C and Q-band respectively and ATLASGAL contours are set at $(-3, 3, 5, 9, 15) \times \sigma$ where $\sigma = 82 \text{ mJy/beam}$. All other symbols/values have the usual meaning.

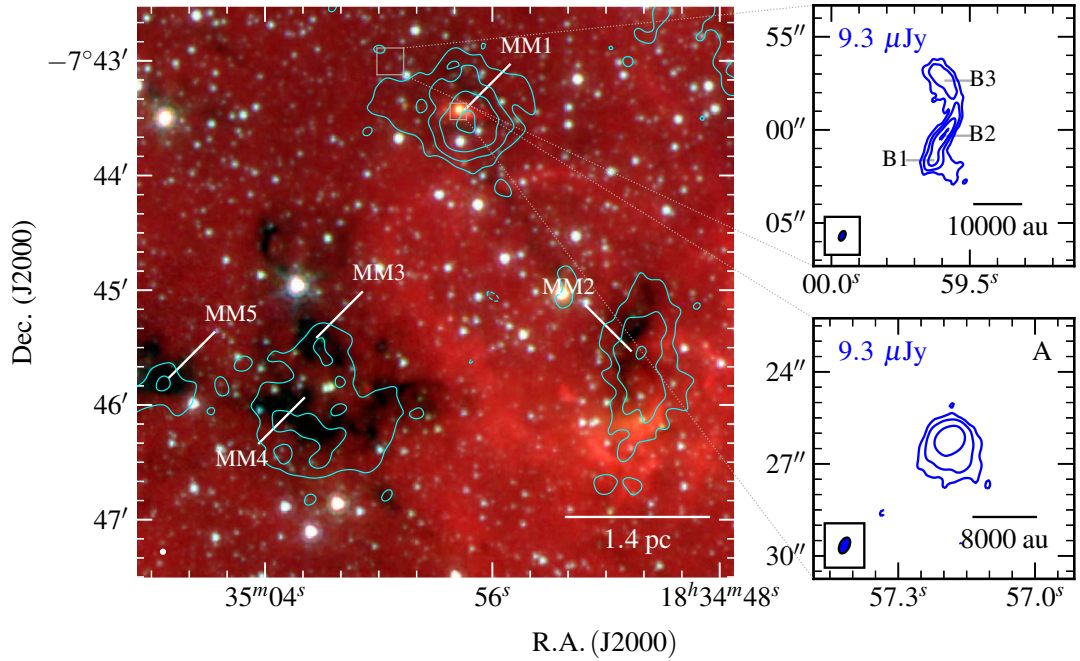


Figure A.47: Mid-infrared (GLIMPSE 8.0, 4.5, 3.6 μm R, G, B image; left panel), sub-mm (ATLASGAL 870 μm cyan contours; left panel) and C-band (blue contours; right panels) images of G024.08+00.04. The C-band restoring beam was $0.551'' \times 0.313''$ at -25° . The right panels show enlarged C-band maps of components A, B1, B2 and B3. Contour levels are $(-3, 3, 6, 10, 19) \times \sigma$ and ATLASGAL contours are set at $(-3, 3, 5, 9, 15) \times \sigma$ where $\sigma = 75 \text{ mJy/beam}$. All other symbols have their usual meaning.

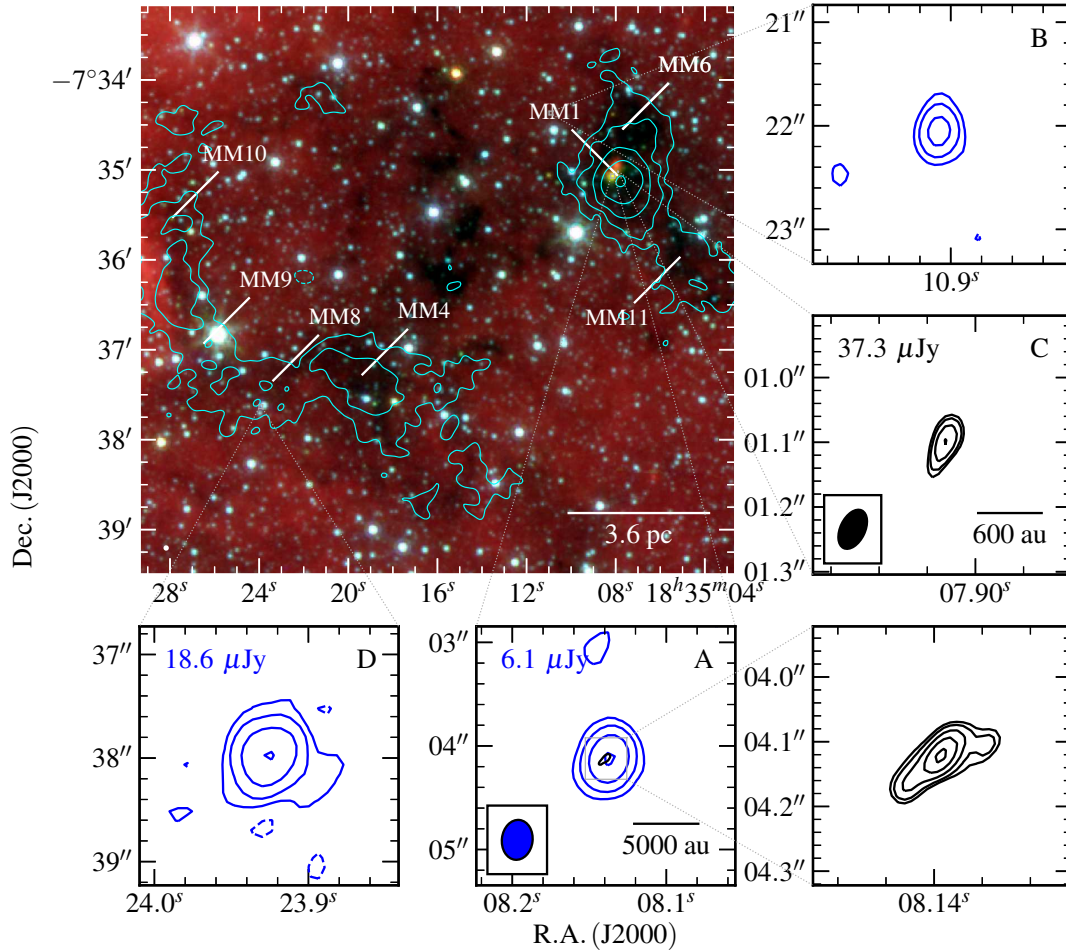


Figure A.48: Mid-infrared (GLIMPSE 8.0, 4.5, 3.6 μm R, G, B image; top left panel), sub-mm (ATLASGAL 870 μm cyan contours; left panel) and radio contour maps of the IRDC, G024.33+00.11, at C-band (top and right panels; blue contours) and Q-band (middle and right panels; black contours). Restoring beams were $0.386'' \times 0.297''$ at -7° and $0.064'' \times 0.038''$ at -26° while contour levels are $(-3, 3, 7, 16, 36) \times \sigma$ and $(-3, 3, 4, 6, 9, 13) \times \sigma$ for C and Q-band respectively and ATLASGAL contours are set at $(-3, 3, 7, 15, 32, 70) \times \sigma$ where $\sigma = 80 \text{ mJy/beam}$. An exception to the contour levels is for component D which was much brighter than the other C-band sources and so we set its contour levels to $(-4, 4, 12, 37, 111) \times \sigma$. All other values have the usual meaning.

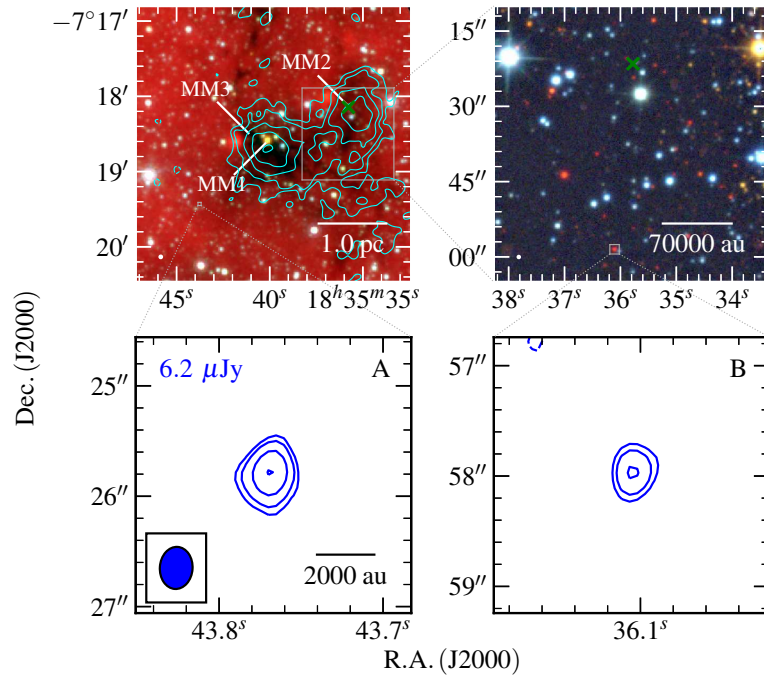


Figure A.49: Mid-infrared (GLIMPSE 8.0, 4.5, 3.6 μm R, G, B image; top left panel), near-infrared (top right panel; UKIDSS, K, H, J bands in R, G, B colour-scale), sub-mm (ATLASGAL 870 μm cyan contours; top left panel) and C-band (blue contours; bottom panels) images of the IRDC, G024.60+00.08. The C-band restoring beam was $0.382'' \times 0.297''$ at -4° . C-band contour levels are $(-3, 3, 5, 10, 18) \times \sigma$ and ATLASGAL contours are set at $(-3, 3, 5, 8, 14, 24) \times \sigma$ where $\sigma = 69 \text{ mJy/beam}$. All other values have their usual meaning.

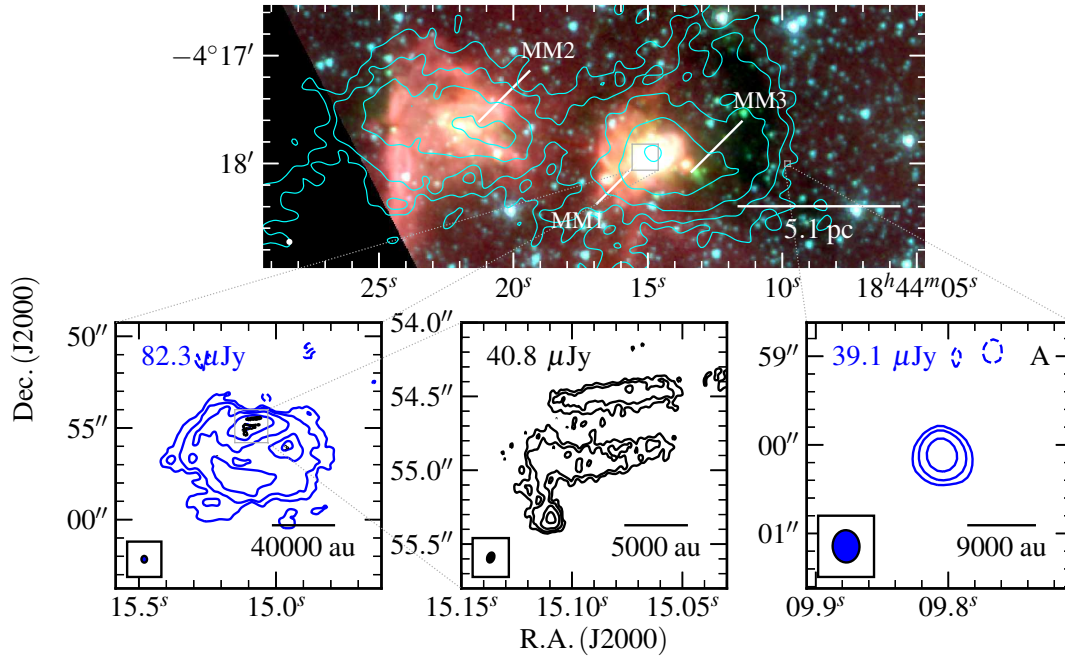


Figure A.50: Mid-infrared (GLIMPSE 8.0, 4.5, 3.6 μm R, G, B image; top panel), sub-mm (ATLASGAL 870 μm cyan contours; top panel) and radio maps of G028.28–00.34 at C-band (blue contours; middle) and Q-band (black contours; bottom). Restoring beams were $0.364'' \times 0.303''$ at 3° and $0.069'' \times 0.047''$ at -20° , while contour levels are $(-3, 3, 10, 33, 108) \times \sigma$ and $(-3, 3, 5, 9, 17) \times \sigma$ for C and Q-band respectively. ATLASGAL contours are set at $(-3, 3, 6, 11, 20, 39) \times \sigma$ where $\sigma = 68 \text{ mJy/beam}$. All other symbols/values have the usual meaning.

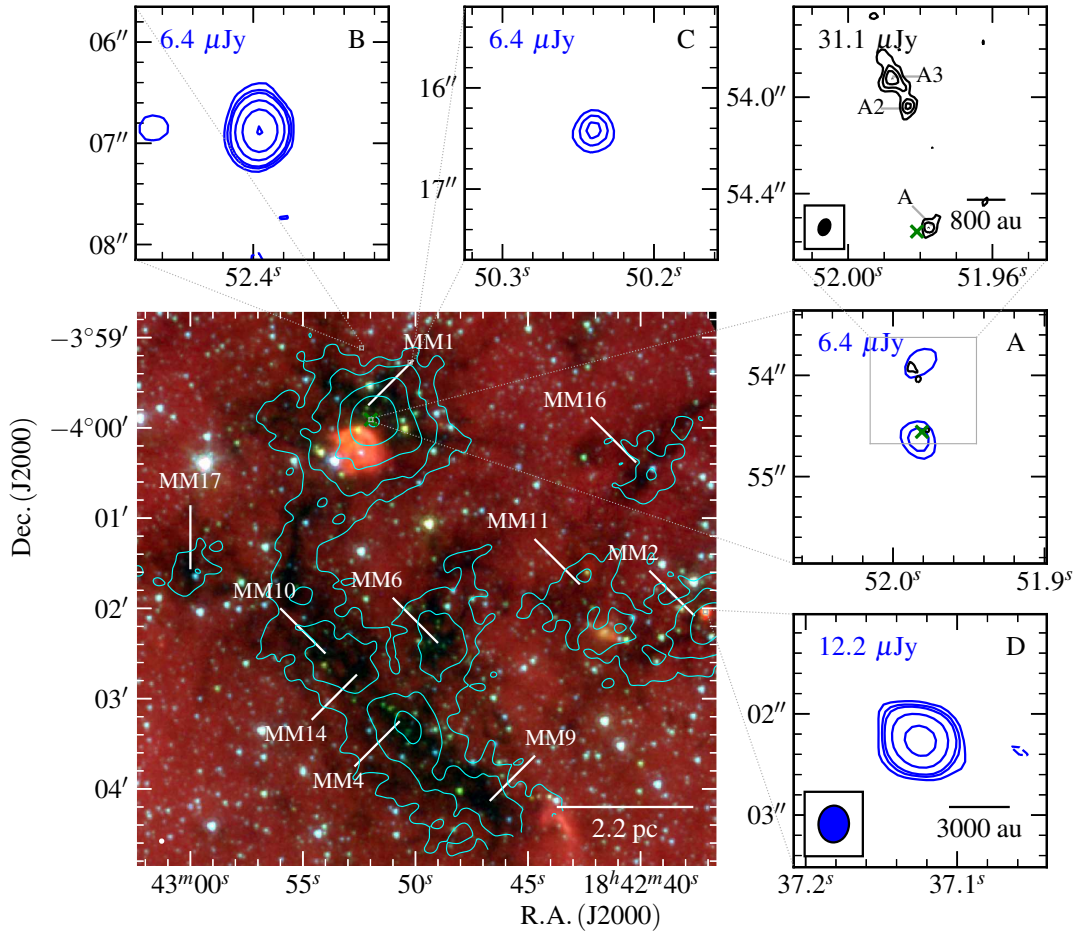


Figure A.51: Mid-infrared (GLIMPSE 8.0, 4.5, 3.6 μm R, G, B image; left panel), sub-mm (ATLASGAL 870 μm cyan contours; left panel) and radio maps of G028.37+00.07 at C-band (blue contours; middle panels) and Q-band (black contours; right panel). Restoring beams were $0.364'' \times 0.301''$ at -3° and $0.068'' \times 0.046''$ at -21° , while contour levels are $(-3, 3, 5, 7, 15, 34, 77) \times \sigma$ and $(-3, 3, 5, 7, 9) \times \sigma$ for C and Q-band respectively, while ATLASGAL contours are set at $(-3, 3, 6, 13, 28, 59) \times \sigma$ where $\sigma = 87 \text{ mJy/beam}$. All other symbols/values have the usual meaning.

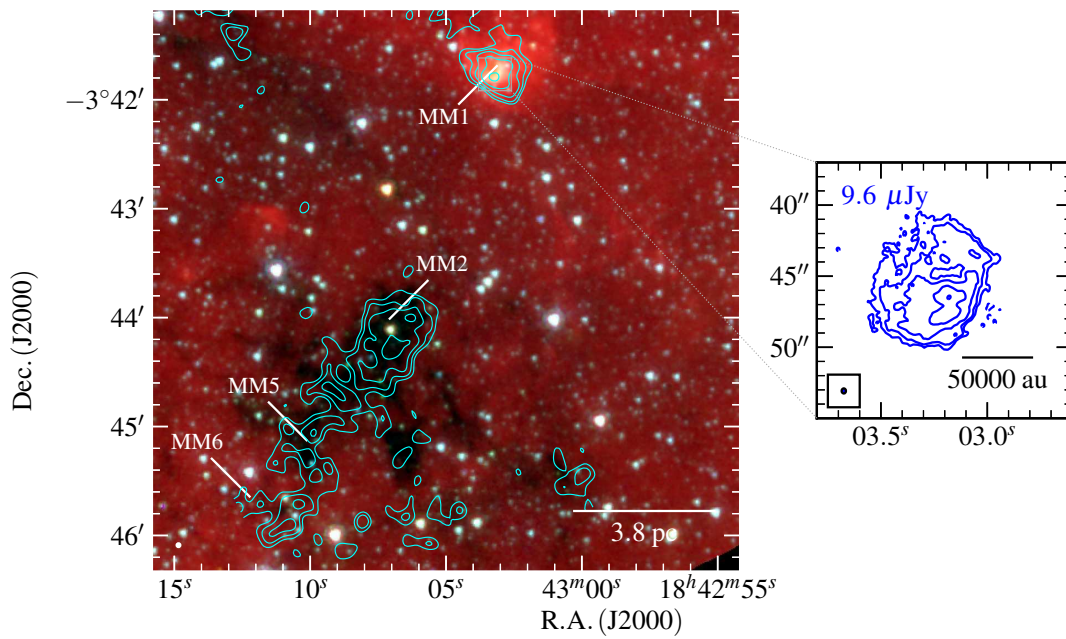


Figure A.52: Mid-infrared (GLIMPSE 8.0, 4.5, 3.6 μm R, G, B image; left panel), sub-mm (ATLASGAL 870 μm cyan contours; left panel) and C-band radio map of G028.67+00.13 (right panel). The restoring beams used was $0.358'' \times 0.303''$ at 1° , while contour levels are set to $(-4, 4, 9, 20, 43, 96) \times \sigma$. All other symbols/values have the usual meaning.

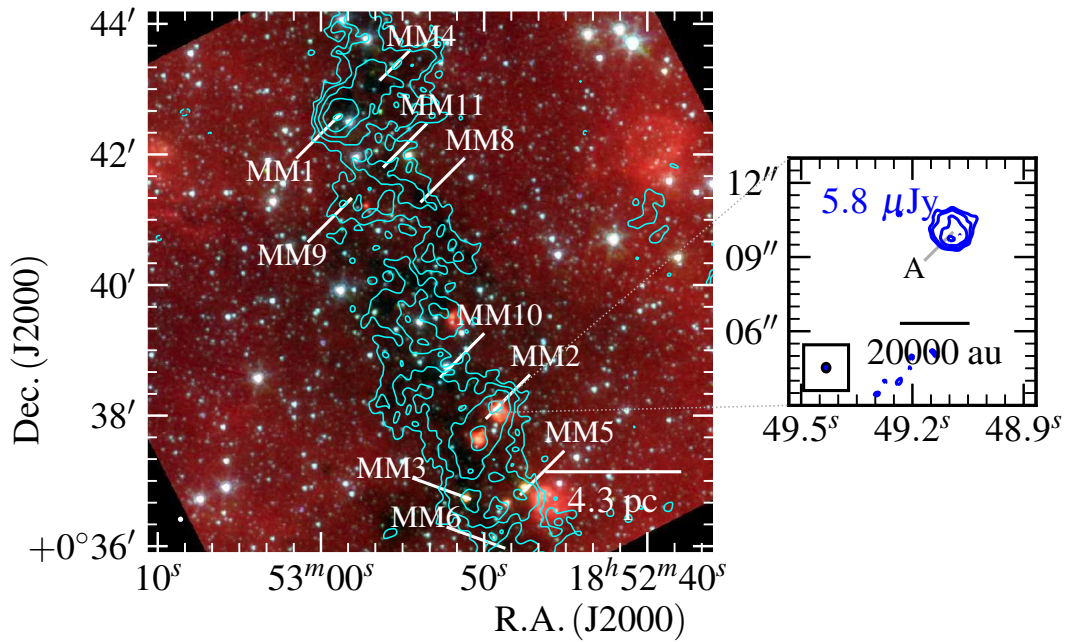


Figure A.53: Mid-infrared (GLIMPSE 8.0, 4.5, 3.6 μm R, G, B image; left panel), sub-mm (ATLASGAL 870 μm cyan contours; left panel) and C-band radio map of G33.69–00.01 MM2 (right panel). The restoring beams used was $0.445'' \times 0.364''$ at -53° , while contour levels are set to $(-4, 4, 7, 13, 22) \times \sigma$, while ATLASGAL contours are set at $(-3, 3, 5, 9, 15, 25) \times \sigma$ where $\sigma = 85 \text{ mJy/beam}$. All other symbols/values have the usual meaning.

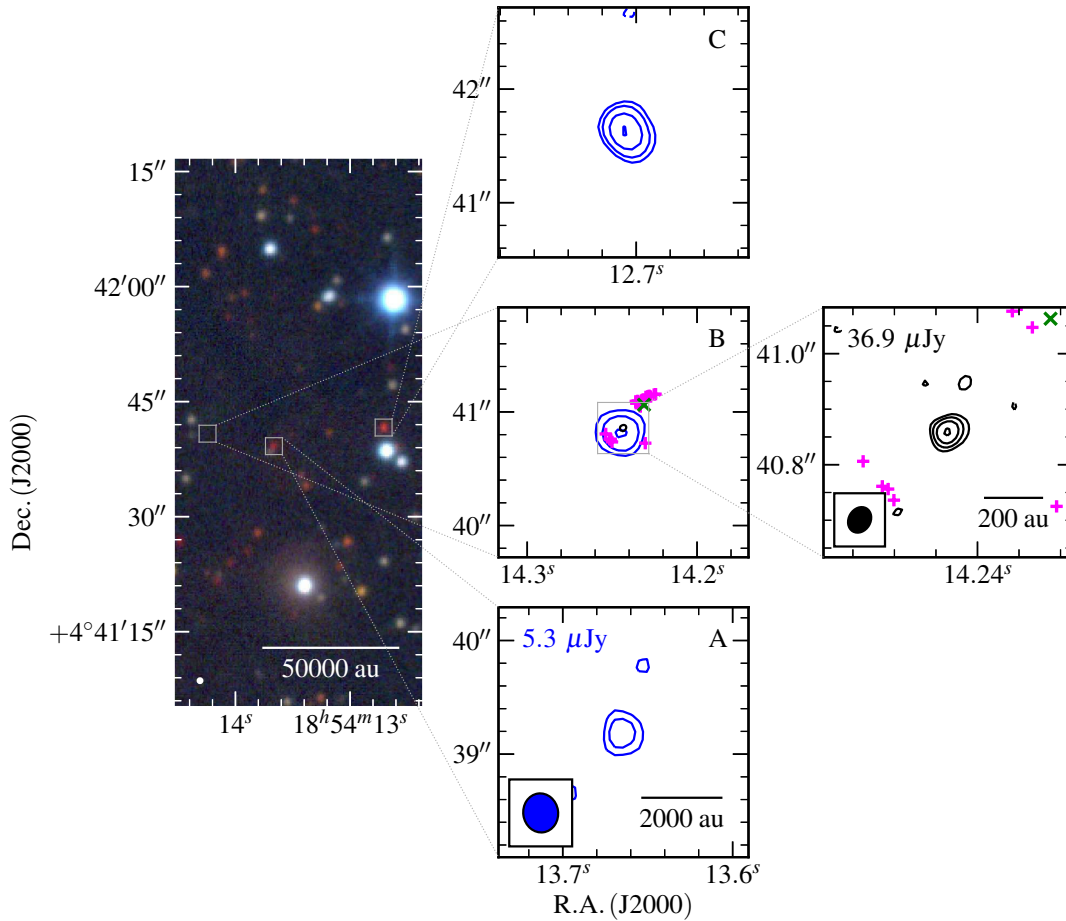


Figure A.54: Near-infrared (R, G, B colour-scale, left panel; 2MASS, K, H, J bands) and radio contour maps of IRAS 18517+0437 at C-band (bottom, blue contours) and Q-band (bottom, black contours). Restoring beams were $0.344'' \times 0.307''$ at 8° and $0.048'' \times 0.039''$ at -31° for the C and Q-band data respectively. The bottom panels show enlarged maps of components A, B and C at both bands. Contour levels are $(-3, 3, 5, 9, 15) \times \sigma$ and $(-3, 3, 5, 8, 13) \times \sigma$ for C and Q-band respectively. All other values have the usual meaning. Pink '+' markers represent the methanol masers detected by Surcis *et al.* (2015).

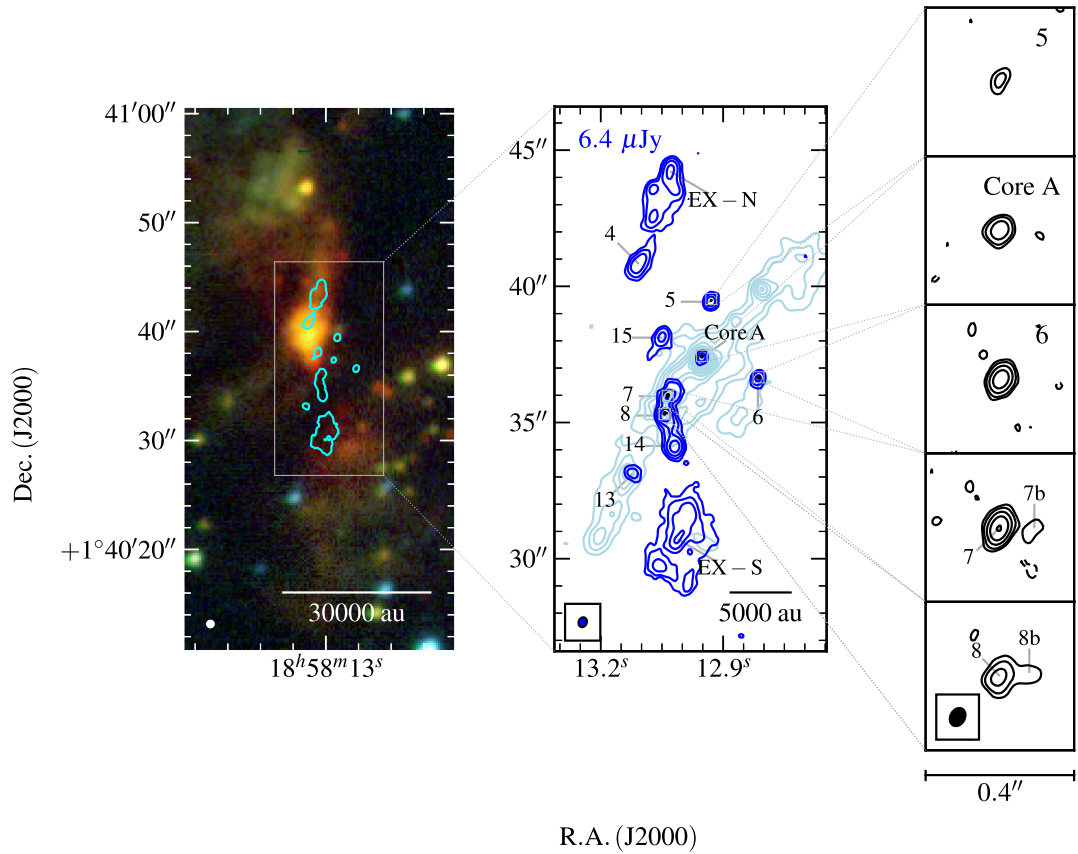


Figure A.55: Mid-infrared (GLIMPSE 8.0, 4.5, 3.6 μm R, G, B image; left panel), ALMA 343 GHz (Sánchez-Monge *et al.* 2014, light blue contours; middle panel), C-band (dark blue contours; middle panel) and Q-band (black contours; middle/right panels) images of IRAS 18556+0136. Restoring beams were $0.367'' \times 0.293''$ at -21° and $0.051'' \times 0.039''$ at -29° for the C and Q-band data respectively. The right panels show enlarged maps of components 5, 6, 7, 8 and Core A at Q-band. Contour levels are $(-4, 4, 11, 29, 78) \times \sigma$ and $(-3, 3, 6, 14, 29, 63) \times \sigma$ for C and Q-band respectively where $\sigma = 35.1 \mu\text{Jy}$ for the Q-band image. All other values have the usual meaning.

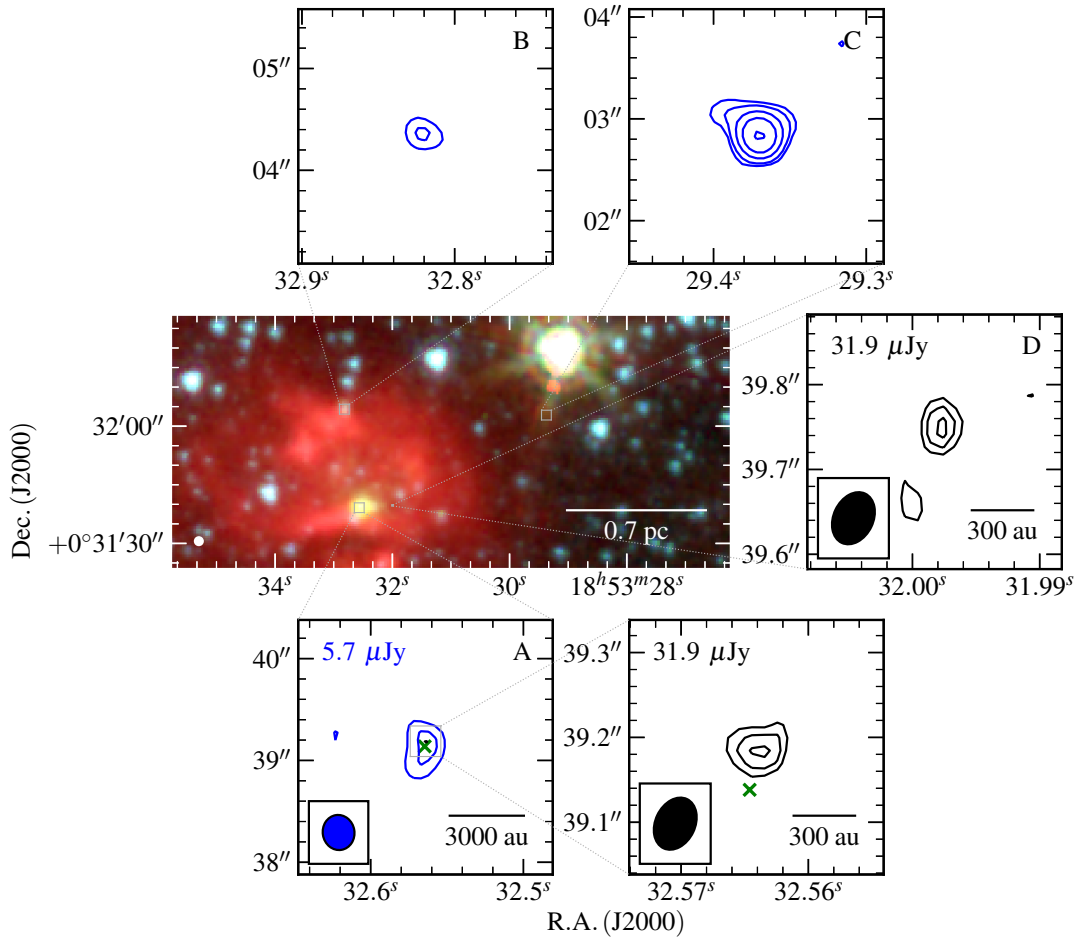


Figure A.56: Mid-infrared (GLIMPSE 8.0, 4.5, 3.6 μm R, G, B image; left panel) and radio maps of G033.6437–00.2277 at C-band (blue contours; top and bottom left panels) and Q-band (black contours; bottom right and right panels). Restoring beams were $0.346'' \times 0.311''$ at 9° and $0.064'' \times 0.047''$ at -26° , while contour levels are $(-3, 3, 5, 10, 18, 33) \times \sigma$ and $(-3, 3, 4, 5) \times \sigma$ for C and Q-band respectively. All other symbols/values have the usual meaning.

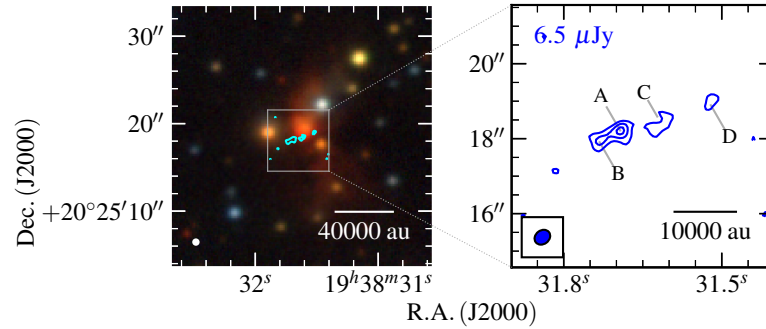


Figure A.57: Near-infrared (left panel; UKIDSS, K, H, J bands in R, G, B colour-scale) and C-band radio map (robustness of 2) of G056.3694–00.6333 (right panel). The restoring beams used was $0.445'' \times 0.364''$ at -53° , while contour levels are set to $(-3, 3, 5, 7) \times \sigma$. All other symbols/values have the usual meaning. To highlight the slight offset between the reddened UKIDSS source and radio lobes, the radio 3σ contour is overlaid upon the NIR image (cyan).

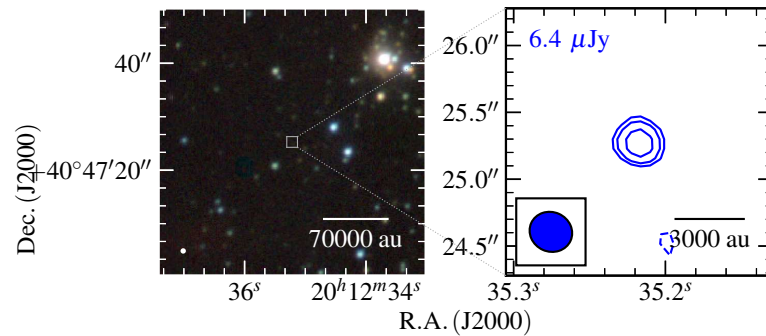


Figure A.58: Near-infrared (left panel; UKIDSS, K, H, J bands in R, G, B colour-scale) and C-band radio map of G077.5671–00.6333 (right panel). The restoring beams used was $0.323'' \times 0.295''$ at 66° . Contour levels are $(-3, 3, 5, 7) \times \sigma$. All other symbols/values have the usual meaning.

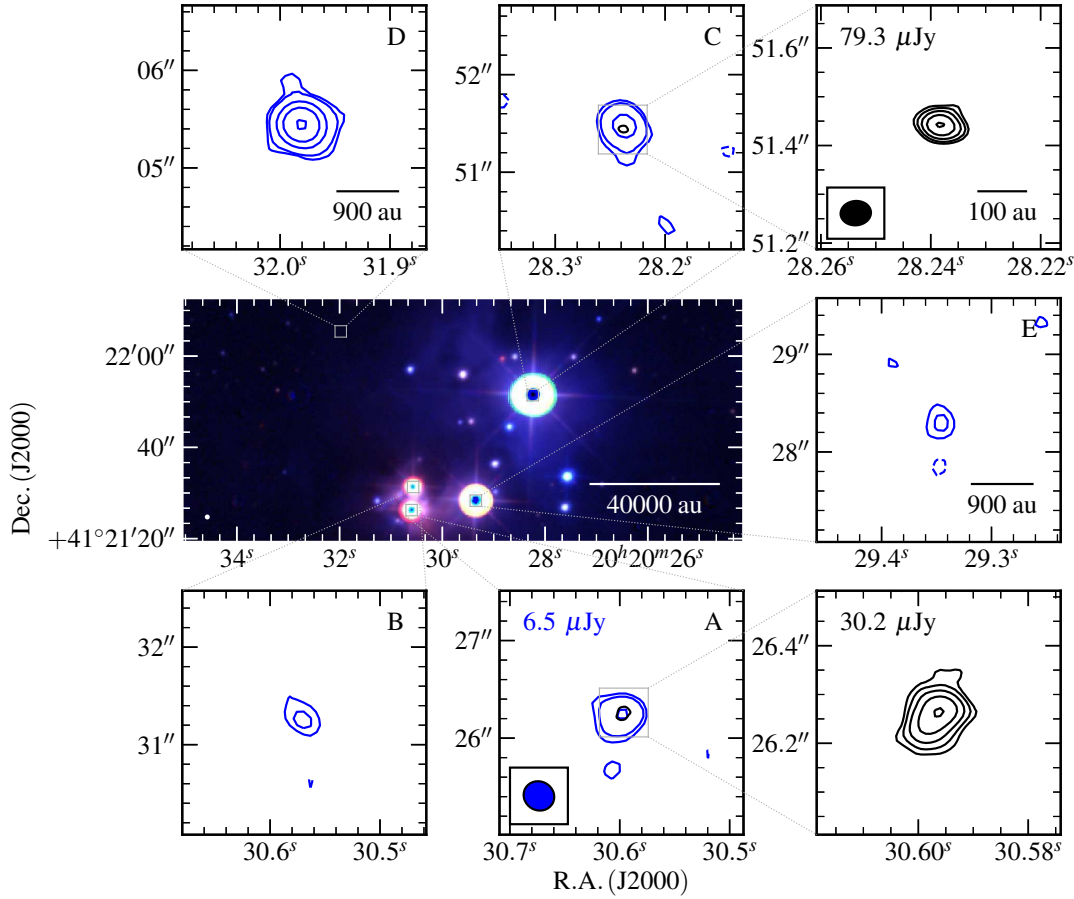


Figure A.59: Near-infrared (middle row, left panel; UKIDSS, K, H, J R, G, B colour-scale) and radio maps of G078.8699+02.7602 at C-band (blue contours; middle row and top right panels) and Q-band (black contours; bottom panels). Restoring beams were $0.319'' \times 0.295''$ at 61° and $0.062'' \times 0.050''$ at -85° for the C and Q-band data respectively. Contour levels are $(-3, 3, 6, 16, 35, 80) \times \sigma$ for C-band images, $(-3, 3, 5, 10, 20, 37) \times \sigma$ for the Q-band image of A and $(-3, 3, 5, 8, 12, 19) \times \sigma$ for the Q-band image of C (due to varying noise across the primary beam). All other symbols/values have the usual meaning.

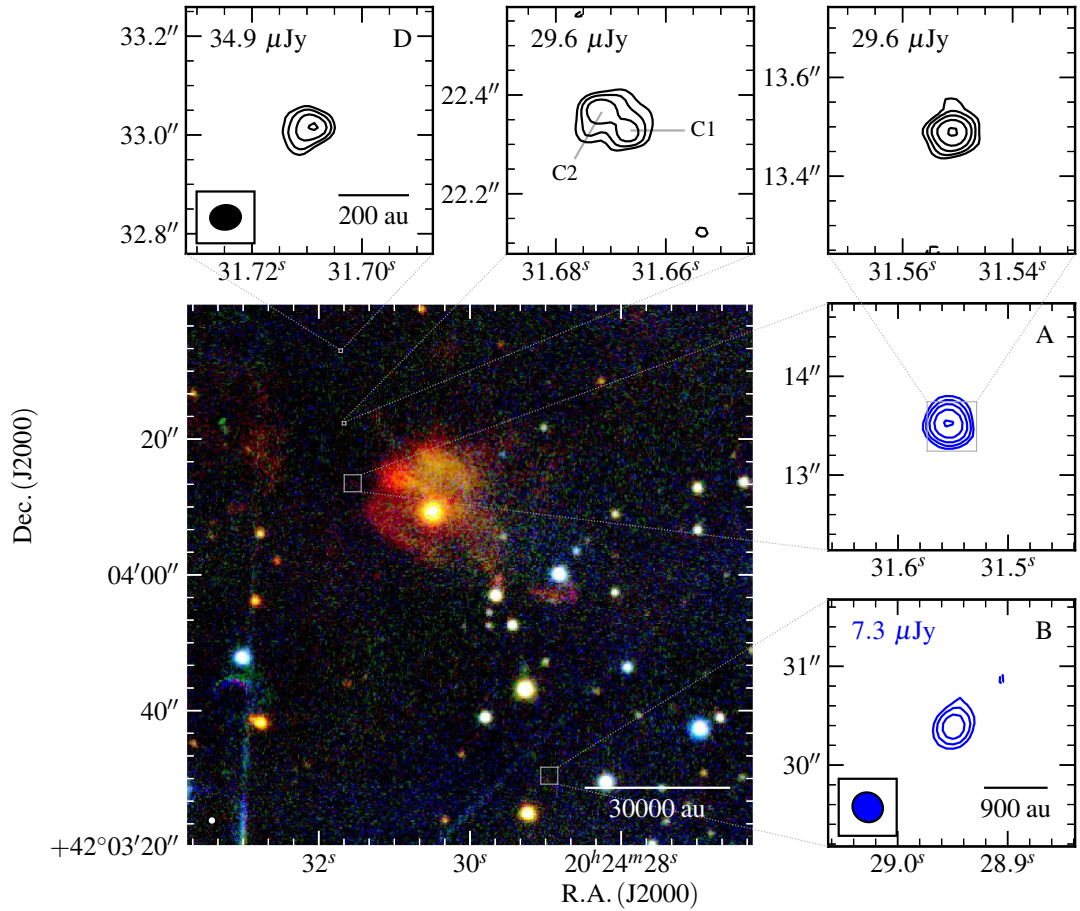


Figure A.60: Near-infrared (bottom left panel; UKIDSS, K, H, J bands in R, G, B colour-scale) and radio maps of G079.8855+02.5517 at C-band (blue contours; right panels) and Q-band (black contours; top panels). Restoring beams were $0.316'' \times 0.293''$ at 54° and $0.062'' \times 0.050''$ at -84° for the C and Q-band data respectively. Contour levels are $(-3, 3, 6, 11, 22) \times \sigma$ for C-band and Q-band images of lobes A, B and C1/C2, whilst being $(-3, 3, 4, 7, 10) \times \sigma$ for the Q-band image of D (due to varying noise across the primary beam). All other symbols/values have the usual meaning.

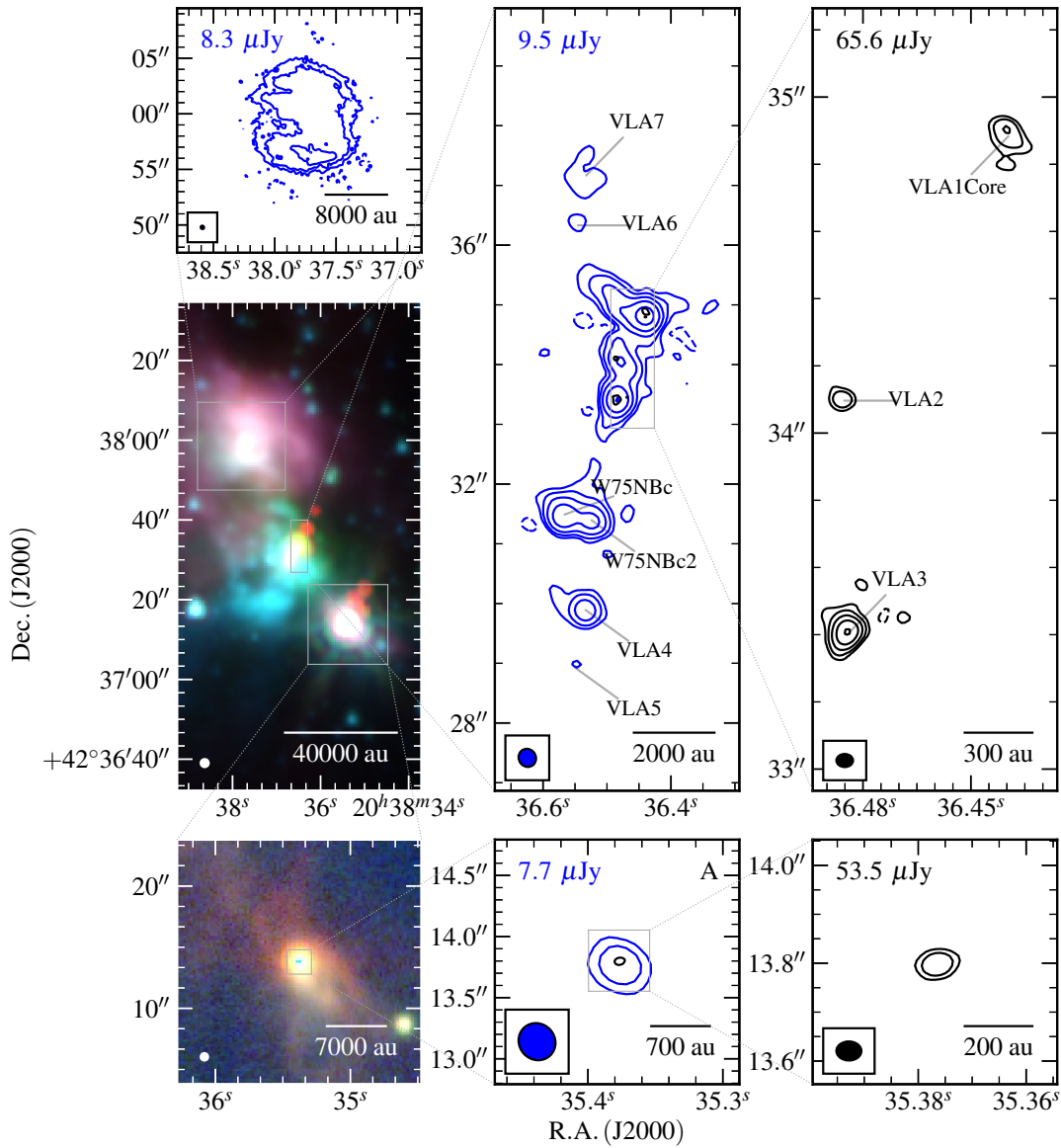


Figure A.61: Mid-infrared (middle, left panel; GLIMPSE, 8.0, 4.5, 3.6 μm R, G, B colour-scale), near-infrared (bottom left panel; UKIDSS, K, H, J bands in R, G, B colour-scale) and radio maps of G081.8652+00.7800 at C-band (blue contours; middle, central and bottom-middle) and Q-band (black contours; right and bottom right). Restoring beams were $0.313'' \times 0.293''$ at 43° and $0.051'' \times 0.039''$ at 89° , while contour levels are set at $(-4, 4, 9, 21, 49, 112)$ and $(-4, 4, 10, 25, 61, 153) \times \sigma$ for the C and Q-band data respectively. Varying noise levels are the result of dynamic range limitations leading to non-Gaussian noise as well as standard primary beam effects.

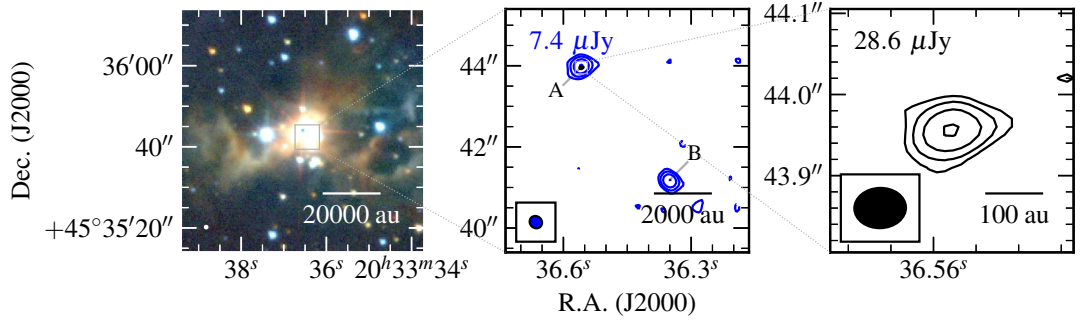


Figure A.62: Near-infrared (left panel; UKIDSS, K, H, J bands in R, G, B colour-scale) and radio maps of G083.7071+03.2817 at C-band (blue contours; middle) and Q-band (black contours; bottom). Restoring beams were $0.319'' \times 0.290''$ at 46° and $0.064'' \times 0.050''$ at -88° for the C and Q-band data respectively. Contour levels are $(-3, 3, 6, 13, 27) \times \sigma$ and $(-3, 3, 5, 10, 18) \times \sigma$ for C and Q-band respectively. All other symbols/values have the usual meaning.

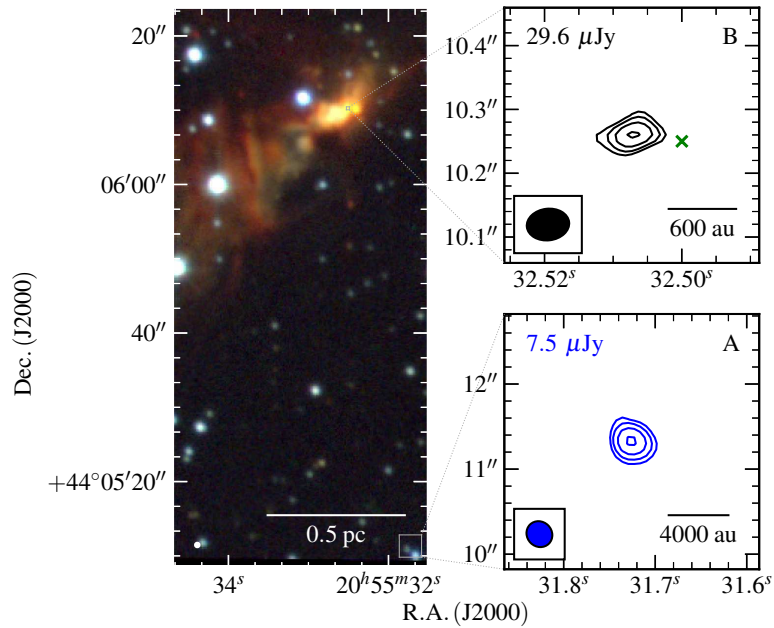


Figure A.63: Near-infrared (left panel; UKIDSS, K, H, J bands in R, G, B colour-scale) and radio maps of the G084.9505-00.6910 field at C-band (blue contours; bottom right) and Q-band (black contours; top right). Restoring beams were $0.316'' \times 0.292''$ at 45° and $0.067'' \times 0.050''$ at -83° for the C and Q-band (robustness of 2) data respectively. Contour levels are $(-3, 3, 5, 9, 16) \times \sigma$ and $(-3, 3, 4, 6, 8) \times \sigma$ for C and Q-band respectively. All other symbols/values have the usual meaning.

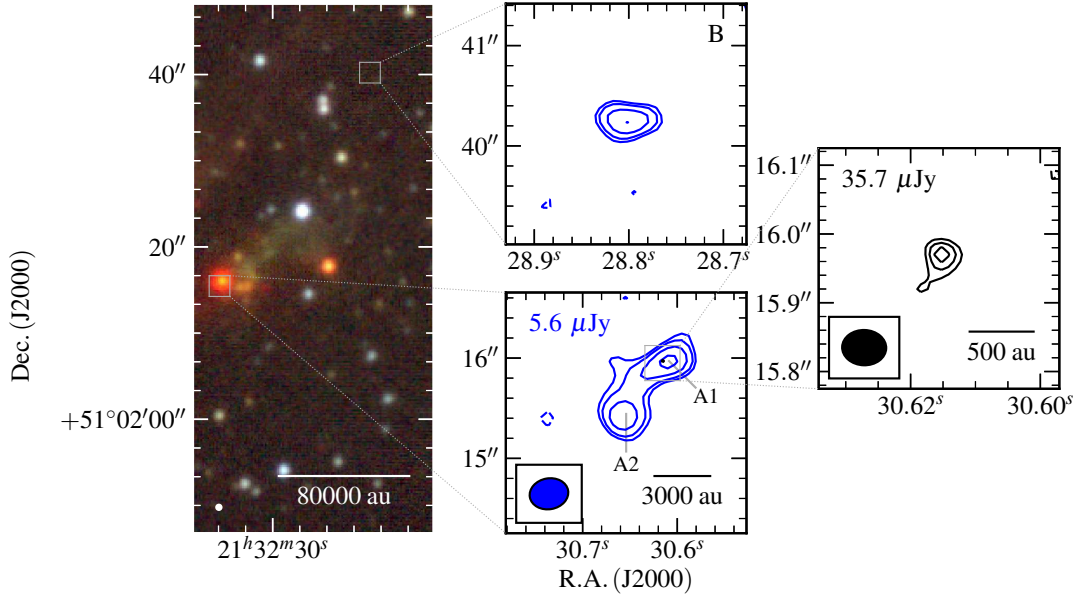


Figure A.64: Near-infrared (left panel; UKIDSS, K, H, J bands in R, G, B colour-scale) and radio maps of the G094.2615–00.4116 field at C-band (blue contours; middle) and Q-band (black contours; right). Restoring beams were $0.387'' \times 0.308''$ at -80° and $0.064'' \times 0.051''$ at 88° for the C and Q-band data respectively. Contour levels are $(-3, 3, 4, 6, 9) \times \sigma$ and $(-3, 3, 4, 5) \times \sigma$ for C and Q-band (robustness of 2) respectively. All other symbols/values have the usual meaning.

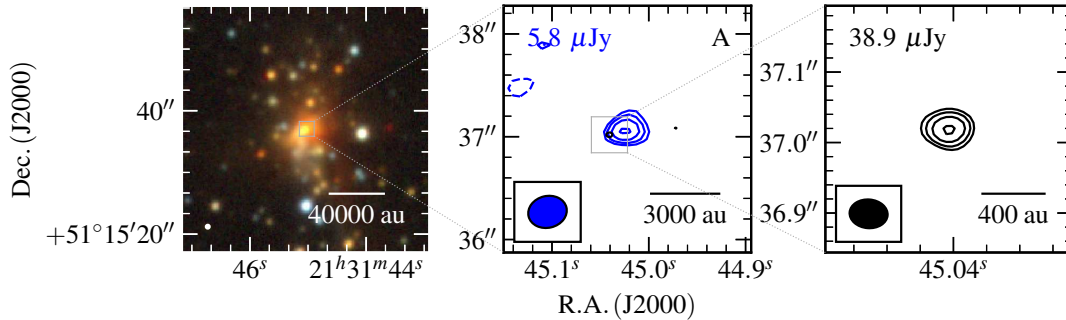


Figure A.65: Near-infrared (left panel; UKIDSS, K, H, J bands in R, G, B colour-scale) and radio maps of the G094.3228–00.1671 field at C-band (blue contours; middle) and Q-band (black contours; right). Restoring beams were $0.377'' \times 0.309''$ at -77° and $0.054'' \times 0.041''$ at -85° for the C and Q-band data respectively. Contour levels are $(-3, 3, 4, 6, 8) \times \sigma$ and $(-3, 3, 4, 7, 10) \times \sigma$ for C and Q-band respectively. All other symbols/values have the usual meaning.

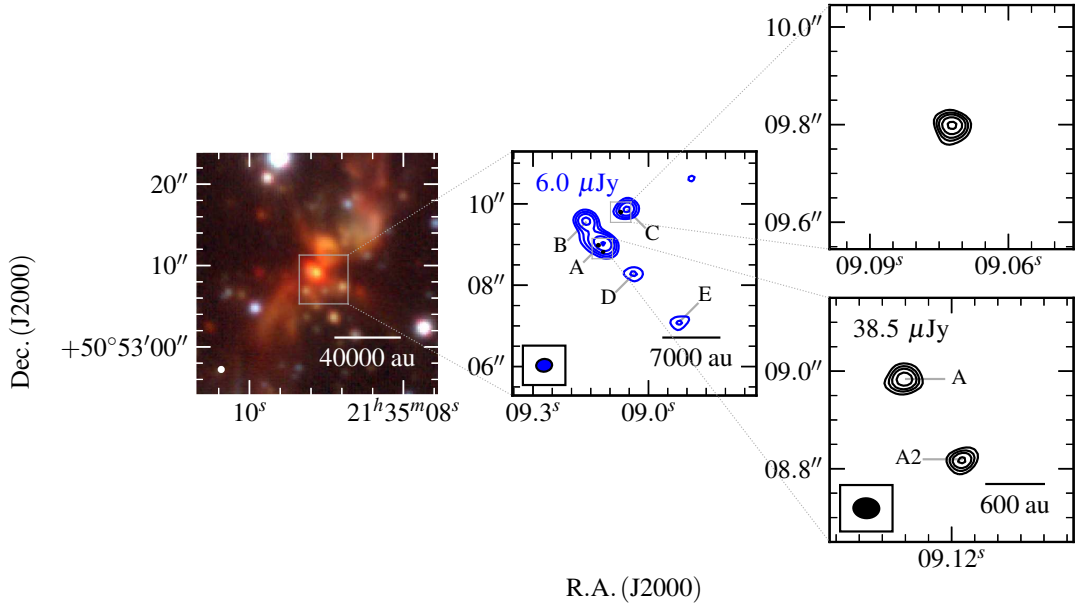


Figure A.66: Near-infrared (left panel; UKIDSS, K, H, J bands in R, G, B colour-scale) and radio maps of the G094.4637–00.8043 field at C-band (blue contours; middle) and Q-band (black contours; right). Restoring beams were $0.392'' \times 0.312''$ at -82° and $0.053'' \times 0.041''$ at 87° for the C and Q-band data respectively. Contour levels are $(-4, 4, 8, 15, 29) \times \sigma$ and $(-4, 4, 6, 8, 11, 15) \times \sigma$ for C and Q-band respectively. All other symbols/values have the usual meaning.

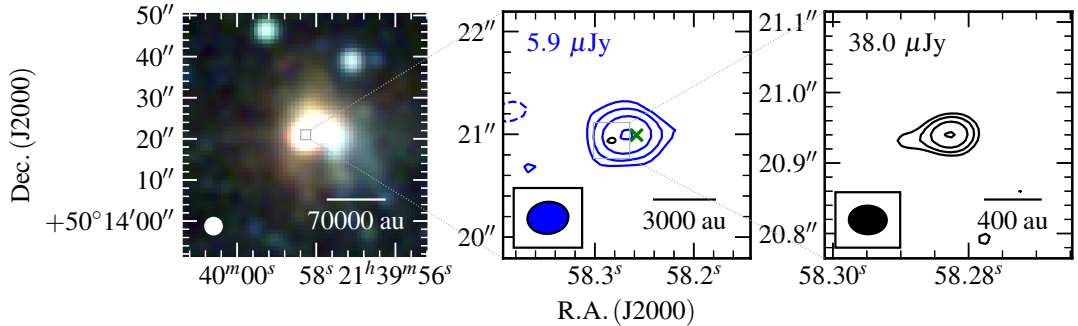


Figure A.67: Near-infrared (left panel; 2MASS, K, H, J bands in R, G, B colour-scale) and radio maps of G094.6028–01.7966 at C-band (blue contours; middle) and Q-band (black contours; bottom). Restoring beams were $0.399'' \times 0.311''$ at -84° and $0.054'' \times 0.041''$ at 88° for the C and Q-band data respectively. Contour levels are $(-3, 3, 7, 15, 32) \times \sigma$ and $(-3, 3, 5, 9, 15) \times \sigma$ for C and Q-band respectively. All other symbols/values have the usual meaning.

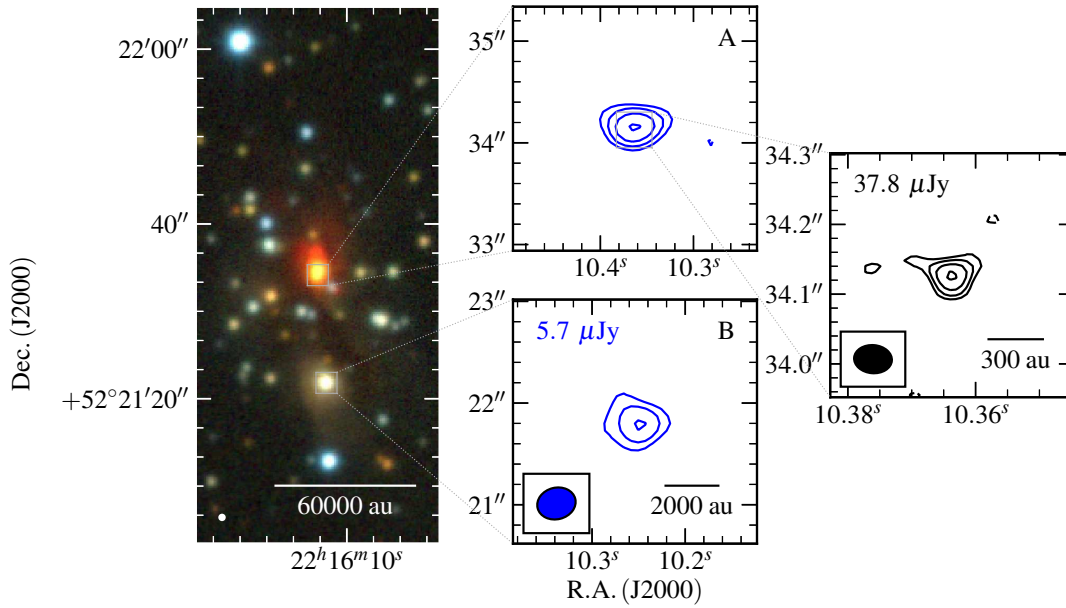


Figure A.68: Near-infrared (left panel; UKIDSS, K, H, J bands in R, G, B colour-scale) and radio maps of the G100.3779–03.5784 field at C-band (blue contours; middle) and Q-band (black contours; right). Restoring beams were $0.381'' \times 0.310''$ at -76° and $0.054'' \times 0.041''$ at 87° for the C and Q-band data respectively. Contour levels are $(-3, 3, 5, 8, 13) \times \sigma$ and $(-3, 3, 4, 7, 10) \times \sigma$ for C and Q-band (robustness of 2) respectively. All other symbols/values have the usual meaning.

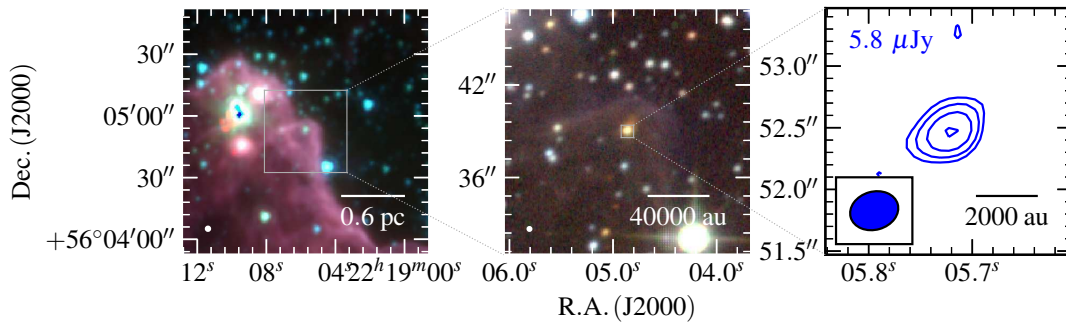


Figure A.69: Mid-infrared (left panel; GLIMPSE, 8.0, 4.5, $3.6 \mu\text{m}$ R, G, B colour-scale), near-infrared (middle panel; UKIDSS, K, H, J bands in R, G, B colour-scale) and C-band radio map of G102.8051–00.7184 (right panel). The restoring beams used was $0.395'' \times 0.309''$ at -75° . Contour levels are $(-3, 3, 5, 9, 14) \times \sigma$. All other symbols/values have the usual meaning.

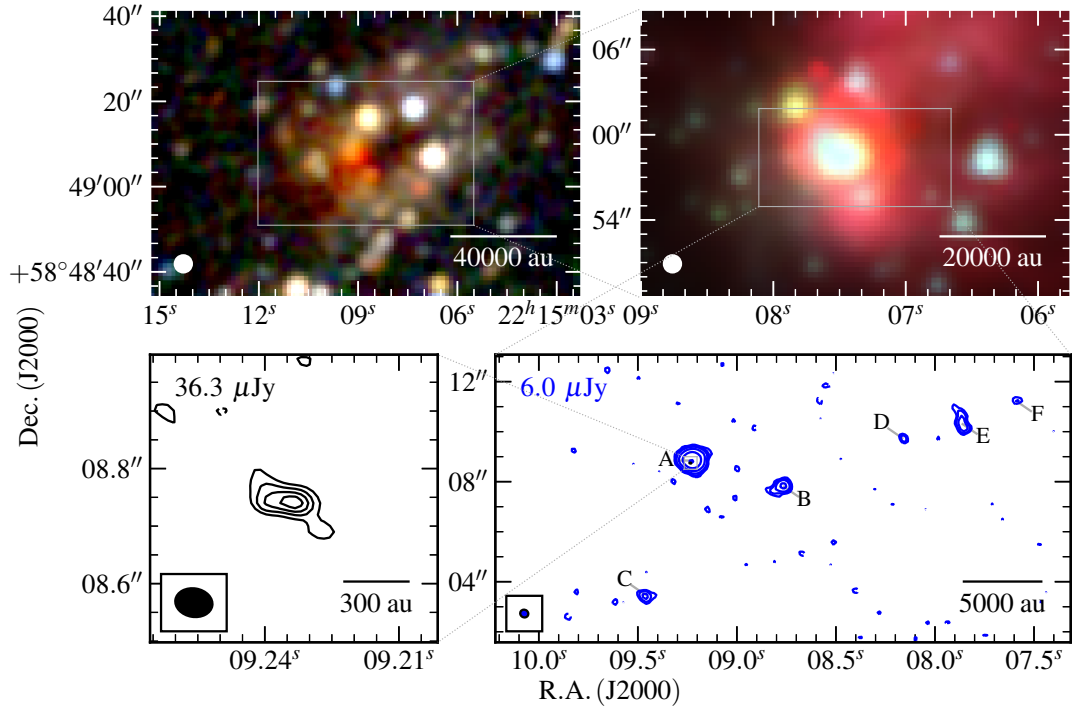


Figure A.70: Mid-infrared (top left panel; GLIMPSE, 8.0, 4.5, 3.6 μm R, G, B colour-scale), near-infrared (top right panel; 2MASS, K, H, J R, G, B colour-scale) and radio maps of G103.8744+01.8558 at C-band (blue contours; bottom-right) and Q-band (black contours; bottom left). Restoring beams were $0.327'' \times 0.302''$ at 54° and $0.065'' \times 0.050''$ at 80° , while contour levels are $(-3, 3, 5, 9, 24, 70, 199) \times \sigma$ and $(-3, 3, 4, 5, 6) \times \sigma$ for C and Q-band (robustness of 2) respectively. All other symbols have their usual meanings.

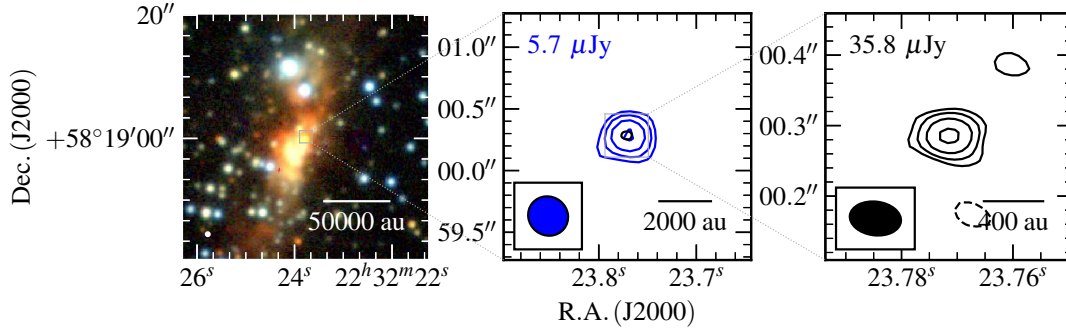


Figure A.71: Near-infrared (R, G, B colour-scale, left panel; UKIDSS, K, H, J bands) and radio maps of the G105.5072+00.2294 field at C-band (blue contours; middle) and Q-band (black contours; right). Restoring beams were $0.330'' \times 0.312''$ at 51° and $0.073'' \times 0.048''$ at 83° , while contour levels are $(-3, 3, 4, 6, 9) \times \sigma$ and $(-3, 3, 5, 7, 12) \times \sigma$ for C and Q-band (robustness of 2) respectively. All other symbols/values have the usual meaning.

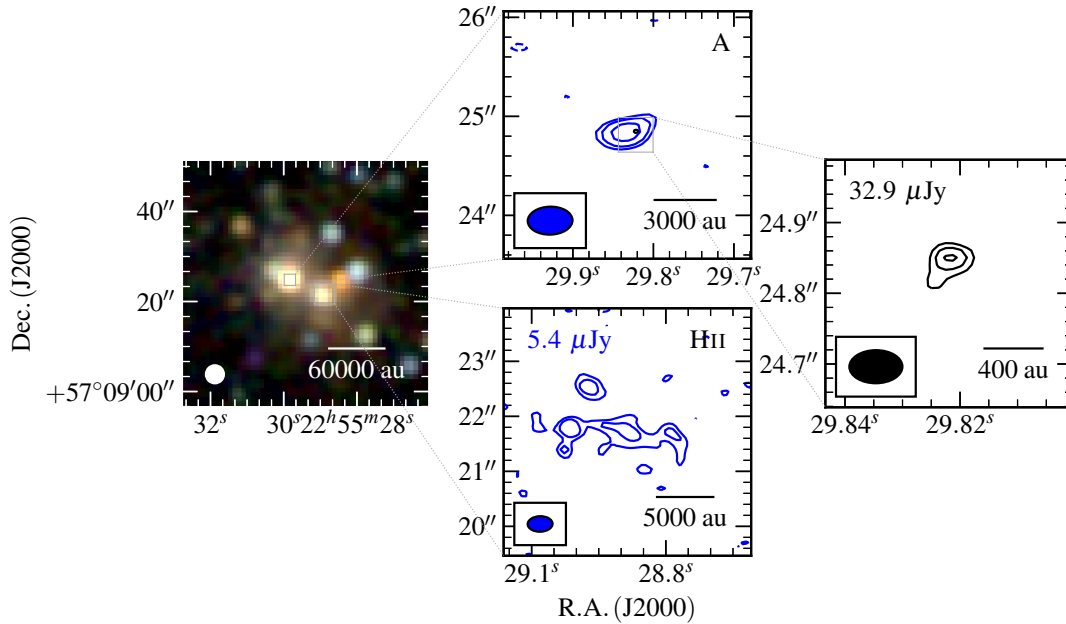


Figure A.72: Near-infrared (R, G, B colour-scale, left panel; 2MASS, K, H, J bands) and radio contour maps of G107.6823-02.2423A at C-band (top and bottom panels; blue contours) and Q-band (right panel; black contours). Restoring beams were $0.564'' \times 0.352''$ at -88° and $0.075'' \times 0.047''$ at -90° while contour levels are $(-3, 3, 4, 6, 8) \times \sigma$ and $(-3, 3, 4, 5) \times \sigma$ for C and Q-band respectively. A robustness of 2 was utilised for both sets of radio data. All other values have the usual meaning.

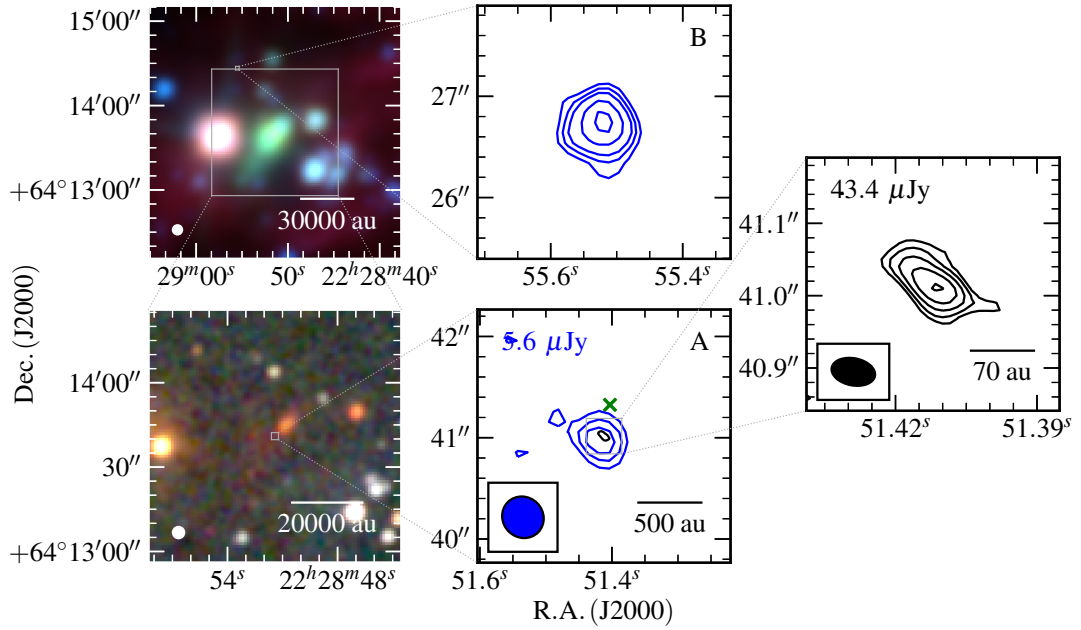


Figure A.73: Mid-infrared (R, G, B colour-scale, top-left panel; WISE, 12.0, 4.6, 3.4 μm), near-infrared (R, G, B colour-scale, bottom-left panel; 2MASS, K, H, J bands) and radio contour maps of G108.18+5.51 at C-band (top and bottom panels; blue contours) and Q-band (right panel; black contours). Restoring beams were $0.423'' \times 0.398''$ at 45° and $0.061'' \times 0.038''$ at 79° while contour levels are $(-3, 3, 4, 5, 7, 9) \times \sigma$ and $(-3, 3, 5, 7, 11, 16) \times \sigma$ for C and Q-band respectively. All other values have the usual meaning.

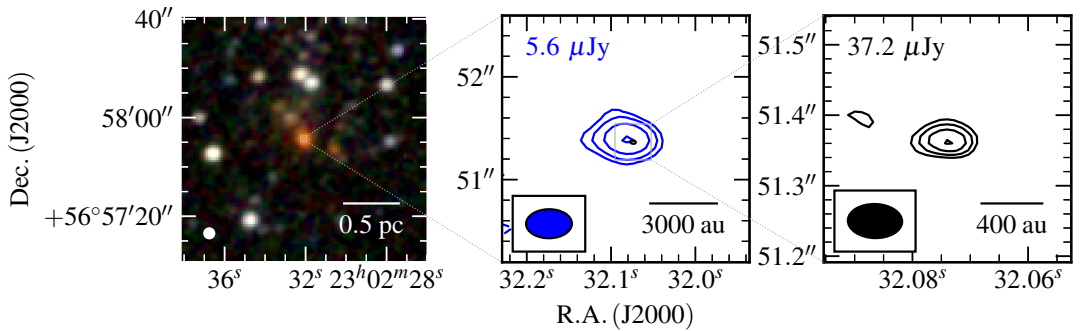


Figure A.74: Near-infrared (left panel; 2MASS, K, H, J bands R, G, B colour-scale) and radio maps of the G108.4714-02.8176 field at C-band (blue contours; middle) and Q-band (black contours; right). Restoring beams were $0.445'' \times 0.282''$ at -90° and $0.063'' \times 0.038''$ at 88° for the C and Q-band data respectively. Contour levels are $(-3, 3, 5, 10, 17) \times \sigma$ and $(-3, 3, 4, 5, 7) \times \sigma$ for C and Q-band respectively. All other symbols/values have the usual meaning.

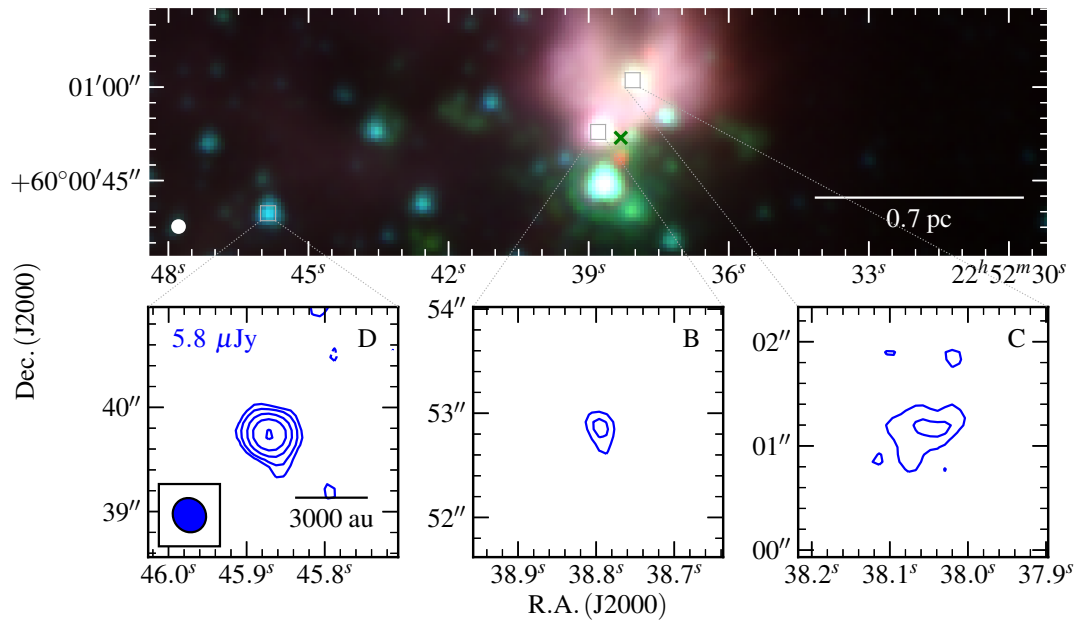


Figure A.75: Mid-infrared (R, G, B colour-scale, top panel; GLIMPSE 8.0, 4.5, 3.6 μm bands) and C-band (blue contours; bottom panels) images of G108.5955+00.4935B and G108.5955+00.4935C. The C-band restoring beam was $0.337'' \times 0.311''$ at 35° . Contour levels are $(-3, 3, 5, 9, 15, 26) \times \sigma$ and all other values have their usual meaning. It is important to note that the methanol maser indicated on the MIR plot isn't represented on radio images due to non-detection of continuum emission.

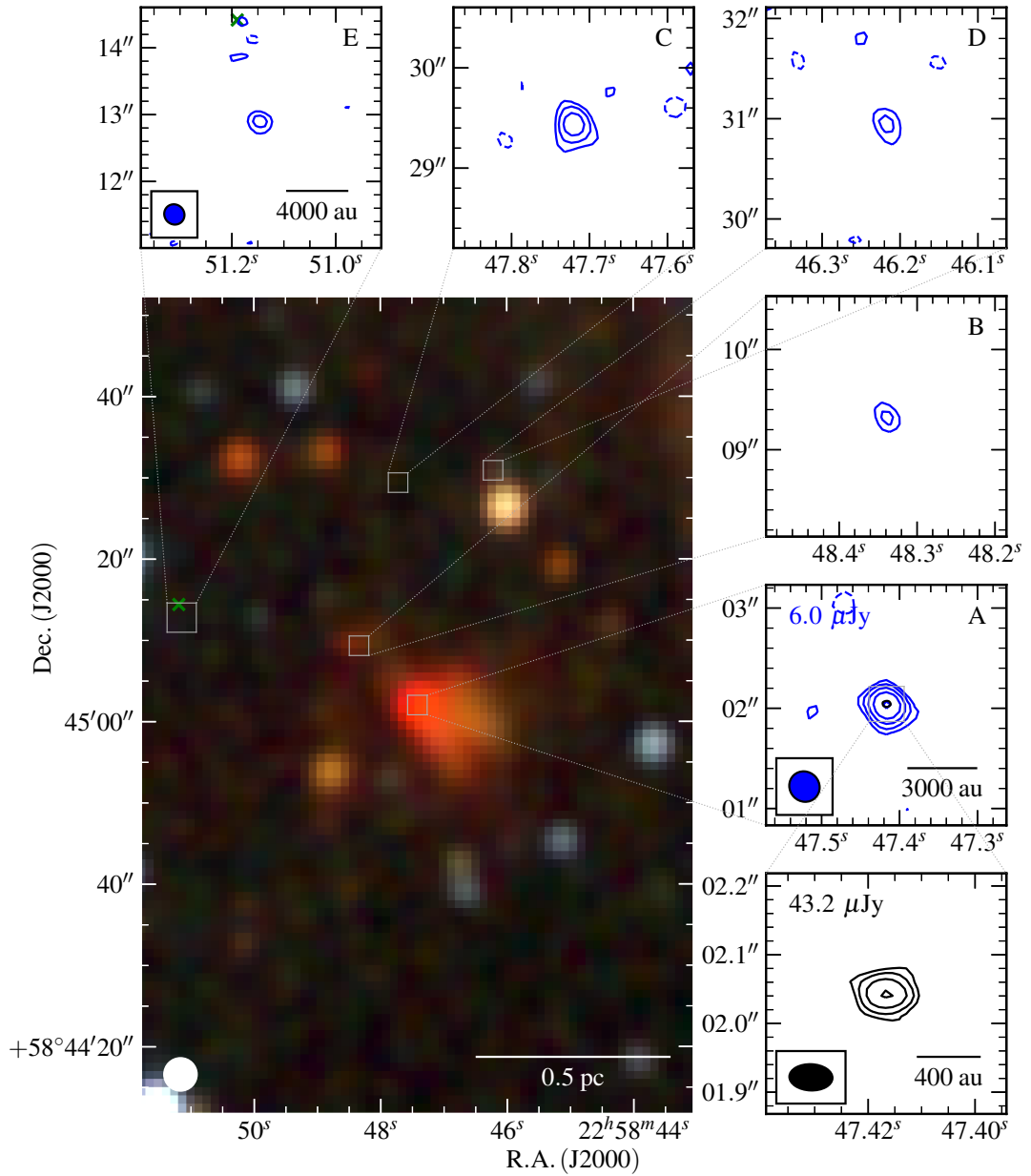


Figure A.76: Mid-infrared (R, G, B colour-scale, left panel; 2MASS, K, H, J bands R, G, B colour-scale) and radio maps of G108.7575–00.9863 at C-band (blue contours; top and middle-right panels) and Q-band (black contours; bottom right). Restoring beams were $0.312'' \times 0.295''$ at 44° and $0.063'' \times 0.038''$ at 88° , while contour levels were set at $(-3, 3, 5, 8, 12, 19)$ and $(-3, 3, 5, 9, 15) \times \sigma$ for the C and Q-band (robustness of 2) data respectively. Varying noise levels are the result of missing spatial scale information leading to non-Gaussian noise and primary beam effects.

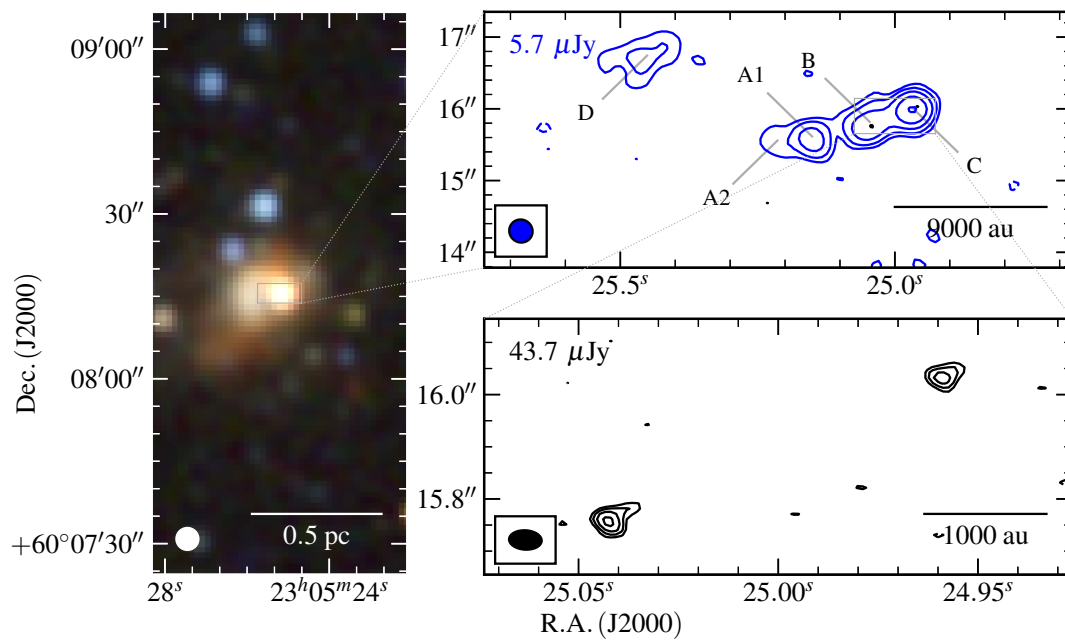


Figure A.77: Near-infrared (R, G, B colour-scale, left panel; 2MASS, K, H, J bands) and radio maps of the G110.0931–00.0641 field at C-band (blue contours; middle) and Q-band (black contours; right). Restoring beams were $0.326'' \times 0.314''$ at 36° and $0.063'' \times 0.038''$ at 86° , while contour levels are $(-3, 3, 7, 14, 32, 69) \times \sigma$ and $(-3, 3, 4, 5, 6) \times \sigma$ for C and Q-band respectively. All other symbols/values have the usual meaning.

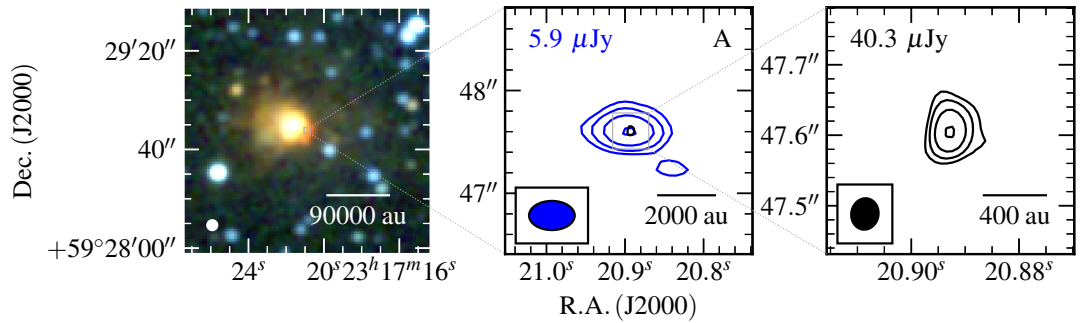


Figure A.78: Near-infrared (left panel; 2MASS, K, H, J bands R, G, B colour-scale) and radio maps of the G111.2348–01.2385 field at C-band (blue contours; middle) and Q-band (black contours; right). Restoring beams were $0.443'' \times 0.284''$ at 90° and $0.045'' \times 0.039''$ at -10° while contour levels are set at $(-3, 3, 6, 12, 24) \times \sigma$ and $(-3, 3, 6, 12, 25) \times \sigma$ for C and Q-band respectively. All other symbols/values have the usual meaning.

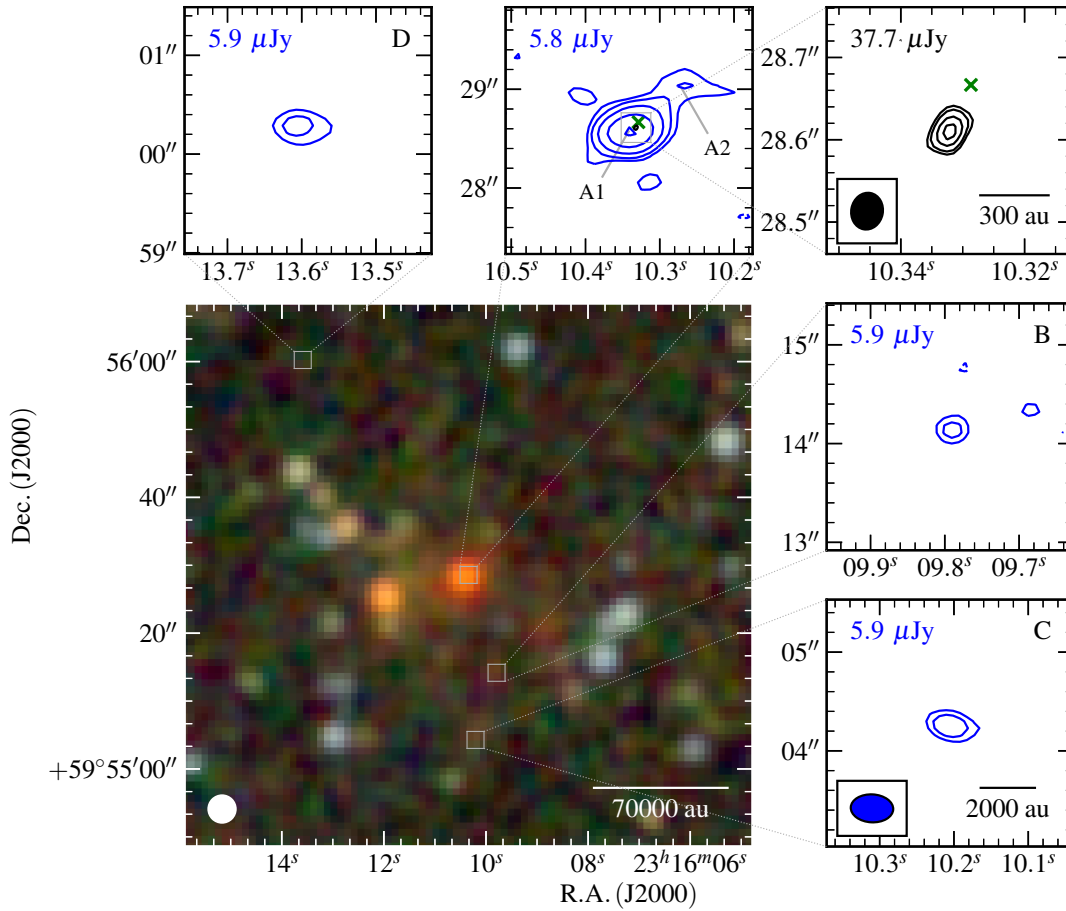


Figure A.79: Near-infrared (bottom left panel; 2MASS, K, H, J R, G, B colour-scale) and radio maps of G111.2552–00.7702 at C-band (blue contours; top left/middle and right middle/bottom panels) and Q-band (black contours; top right panel). Restoring beams were $0.430'' \times 0.283''$ at 87° and $0.045'' \times 0.038''$ at -11° while contour levels are set at $(-3, 3, 5, 9, 17, 30) \times \sigma$ and $(-3, 3, 4, 6, 8) \times \sigma$ for the C-band and Q-band images respectively. All other symbols/values have the usual meaning.

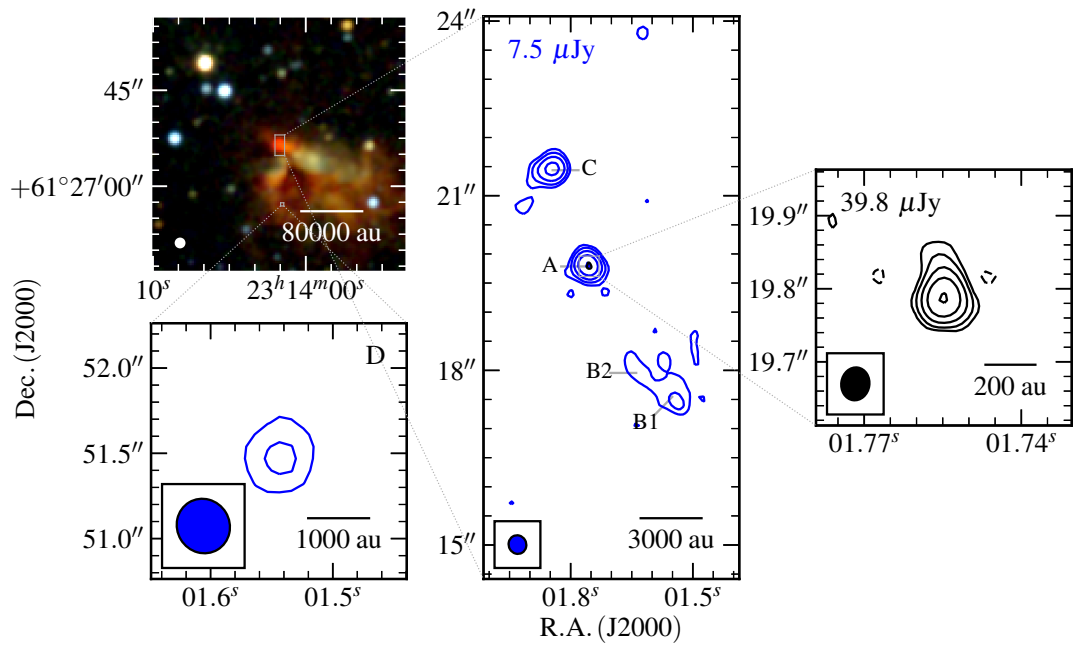


Figure A.80: Near-infrared (R, G, B colour-scale, left panel; 2MASS, K, H, J bands) and radio contour maps of G111.5671+00.7517 at C-band (middle and bottom left panels; blue contours) and Q-band (right panel; black contours). Restoring beams were $0.324'' \times 0.308''$ at 31° and $0.045'' \times 0.038''$ at -9° while contour levels are $(-3, 3, 6, 12, 24, 48) \times \sigma$ and $(-3, 3, 6, 12, 23, 46) \times \sigma$ for C and Q-band respectively. All other values have the usual meaning.

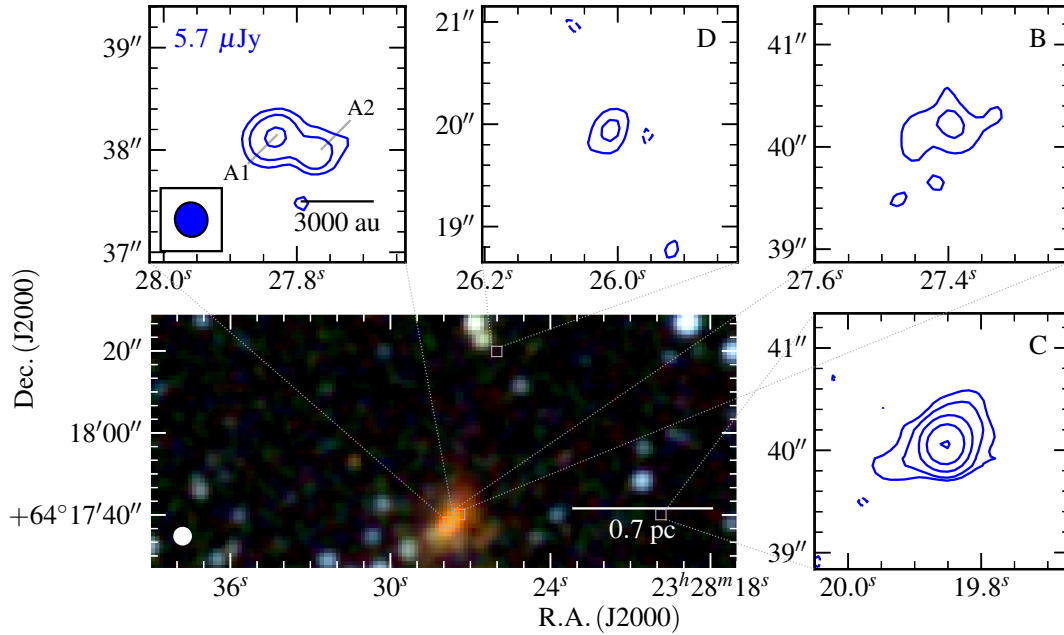


Figure A.81: Near-infrared colour-scale (R, G, B colour-scale, left panel; 2MASS, K, H, J bands) and radio contour maps of G114.0835+02.8568 at C-band (blue contours). The restoring beam and contour levels used were $0.337'' \times 0.317''$ at 13° and $(-3, 3, 6, 14, 30, 64) \times \sigma$. All other values have the usual meaning.

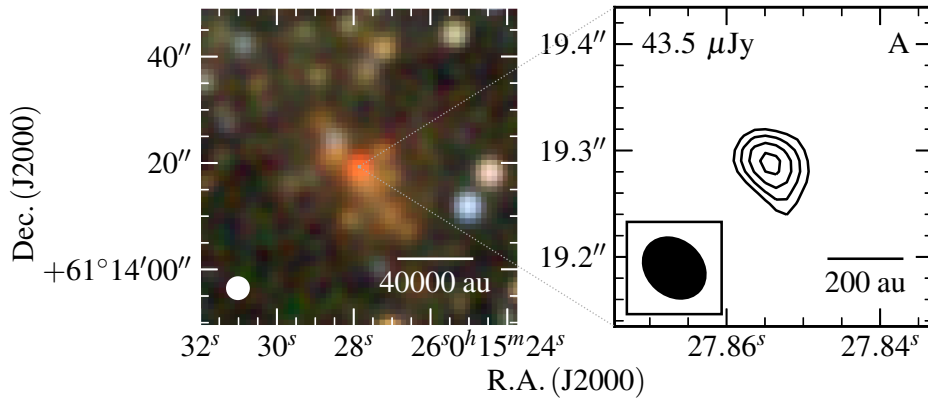


Figure A.82: Near-infrared colour-scale (R, G, B colour-scale, left panel; 2MASS, K, H, J bands) and radio contour map of G118.6172-01.3312 at Q-band (right panel). The restoring beam and contour levels used were $0.064'' \times 0.051''$ at 48° and $(-3, 3, 4, 5, 6) \times \sigma$ respectively. All other values have the usual meaning.

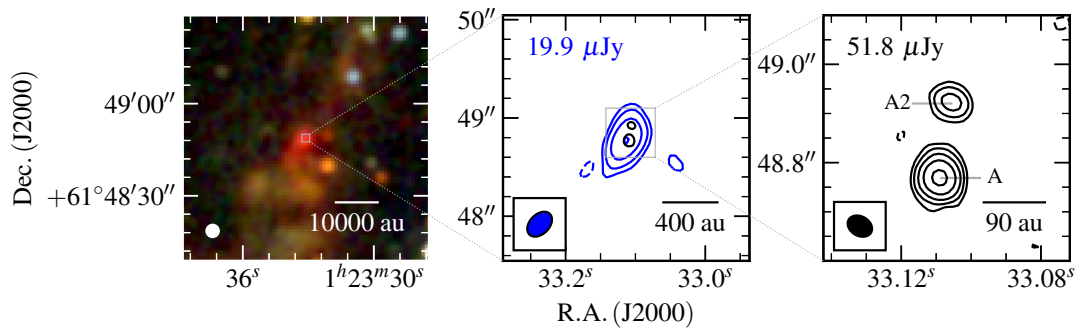


Figure A.83: Near-infrared (left panel; 2MASS, K,H,J bands R, G, B colour-scale) and radio maps of the G126.7144–00.8220 field at C-band (blue contours; middle) and Q-band (black contours; right). Restoring beams were $0.295'' \times 0.200''$ at -44° and $0.053'' \times 0.040''$ at 60° , while contour levels are $(-3, 3, 7, 18, 43) \times \sigma$ and $(-3, 3, 7, 16, 37, 86) \times \sigma$ for C (robustness of -1) and Q-band respectively. All other symbols/values have the usual meaning.

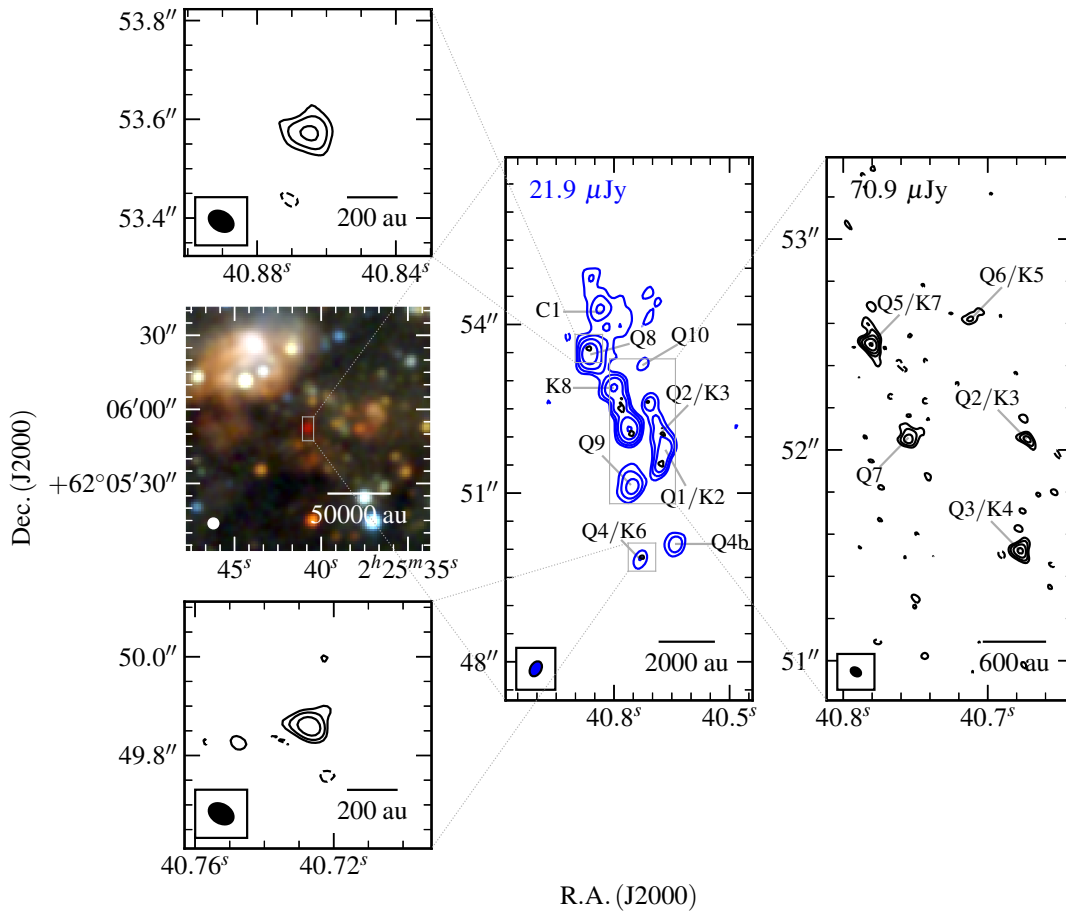


Figure A.84: Near-infrared (R, G, B colour-scale, middle left panel; 2MASS, K, H, J bands) and radio contour maps of G133.7150+01.2155 at C-band (middle, blue contours) and Q-band (top left, bottom right and right panels; black contours). Restoring beams were $0.287'' \times 0.197''$ at -31° and $0.054'' \times 0.038''$ at 59° with contour levels set to $(-4, 4, 9, 19, 42, 93) \times \sigma$ and $(-3, 3, 6, 12, 24, 48) \times \sigma$ for C (robust = -1) and Q-bands respectively. All other values have the usual meaning.

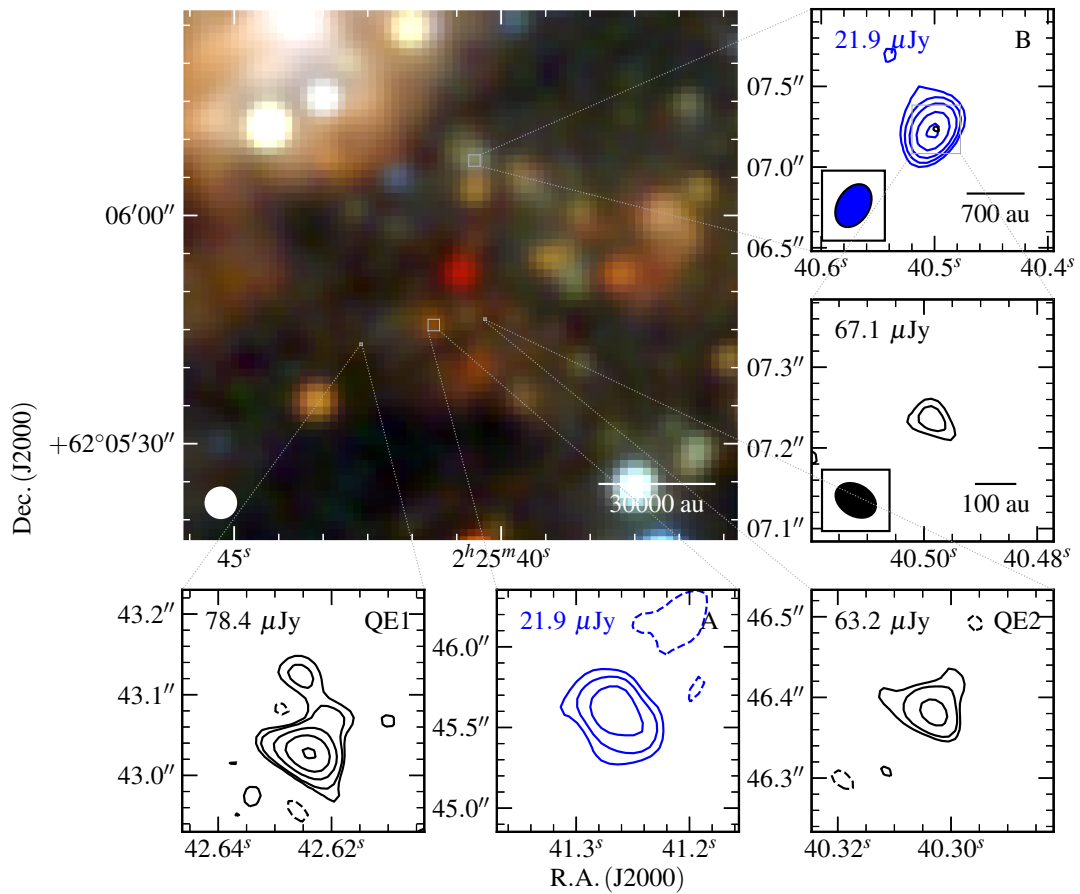


Figure A.85: Near-infrared (R, G, B colour-scale, middle left panel; 2MASS, K, H, J bands) and radio contour maps of the other detected sources in the G133.7150+01.2155 field. Restoring beams and contour colours are the same as in Figure A.84, with contour levels set to $(-3, 3, 5, 8, 14, 22) \times \sigma$ and $(-3, 3, 5, 12, 24, 47) \times \sigma$ for C (robust=-1) and Q-bands respectively.

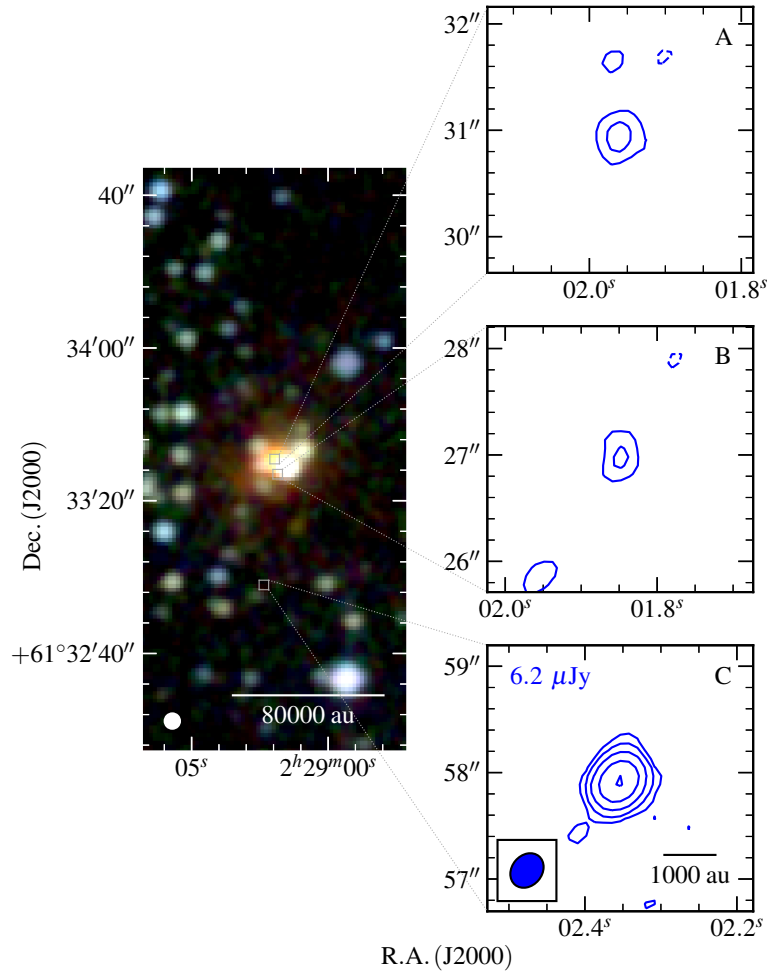


Figure A.86: Near-infrared (R, G, B colour-scale, left panel; 2MASS, K, H, J bands) and radio contour maps of G134.2792+00.8561 at C-band (right panels, blue contours). The restoring beam used was $0.350'' \times 0.284''$ at -40° , while contour levels are $(-3, 3, 7, 17, 41, 97) \times \sigma$. All other values have the usual meaning.

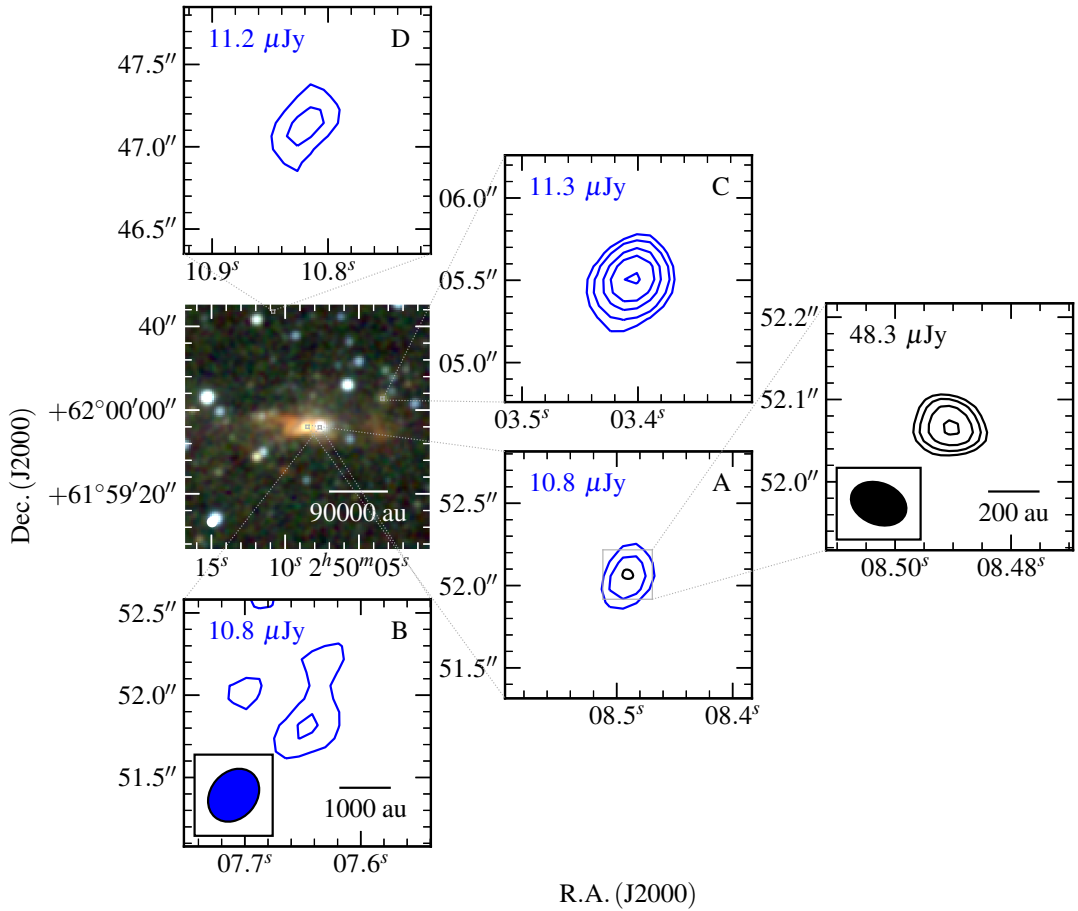


Figure A.87: Near-infrared (R, G, B colour-scale, left panel; 2MASS, K, H, J bands) and radio contour maps of G136.3833+02.2666 at C-band (top left, bottom left and middle panels, blue contours) and Q-band (right panel, black contours). Restoring beams were $0.349'' \times 0.279''$ at -40° and $0.070'' \times 0.050''$ at 69° utilising a robustness of 2 for the Q-band data. Contour levels are $(-3, 3, 5, 9, 13, 20) \times \sigma$ and $(-3, 3, 4, 6, 9) \times \sigma$ for C and Q-band respectively. Varying noises across the C-band primary beam are represented. All other values have the usual meaning.

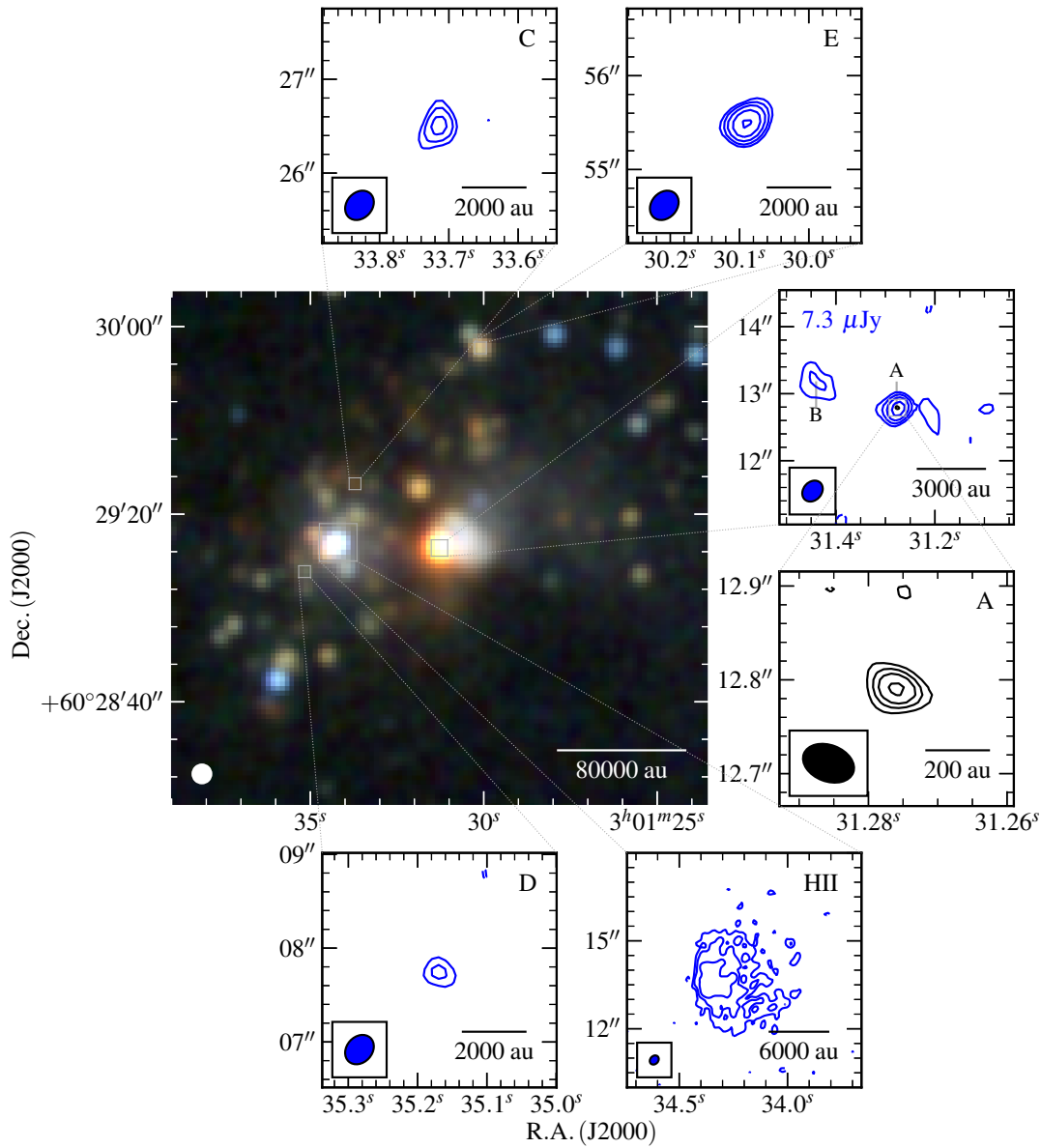


Figure A.88: Near-infrared (R, G, B colour-scale, central panel; 2MASS, K, H, J bands) and radio contour maps of G138.2957+01.5552 at C-band (top, bottom and top-right panels, blue contours) and Q-band (bottom-right panel, black contours). Restoring beams were $0.342'' \times 0.273''$ at -42° and $0.056'' \times 0.039''$ at 69° . Contour levels are $(-3, 3, 5, 8, 13, 22) \times \sigma$ and $(-3, 3, 5, 7, 10) \times \sigma$ for C and Q-band respectively. All other values have the usual meaning.

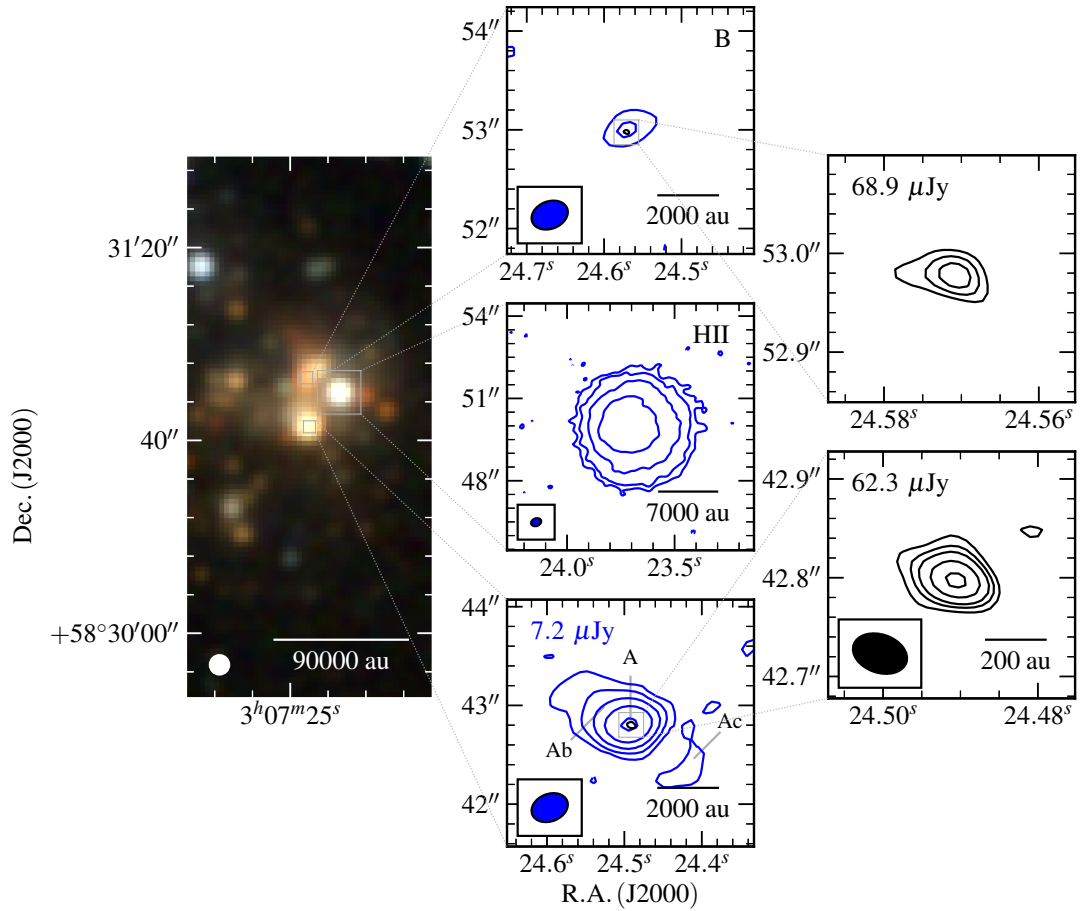


Figure A.89: Near-infrared (R, G, B colour-scale, left panel; 2MASS, K, H, J bands) and radio contour maps of G139.9091+00.1969A at C-band (centre-column panels, blue contours) and Q-band (right panels, black contours). Restoring beams were $0.379'' \times 0.278''$ at -69° and $0.056'' \times 0.039''$ at 71° . Contour levels are $(-3, 3, 7, 15, 32, 71) \times \sigma$ and $(-3, 3, 5, 7, 11, 16) \times \sigma$ for C and Q-band respectively. All other values have the usual meaning.

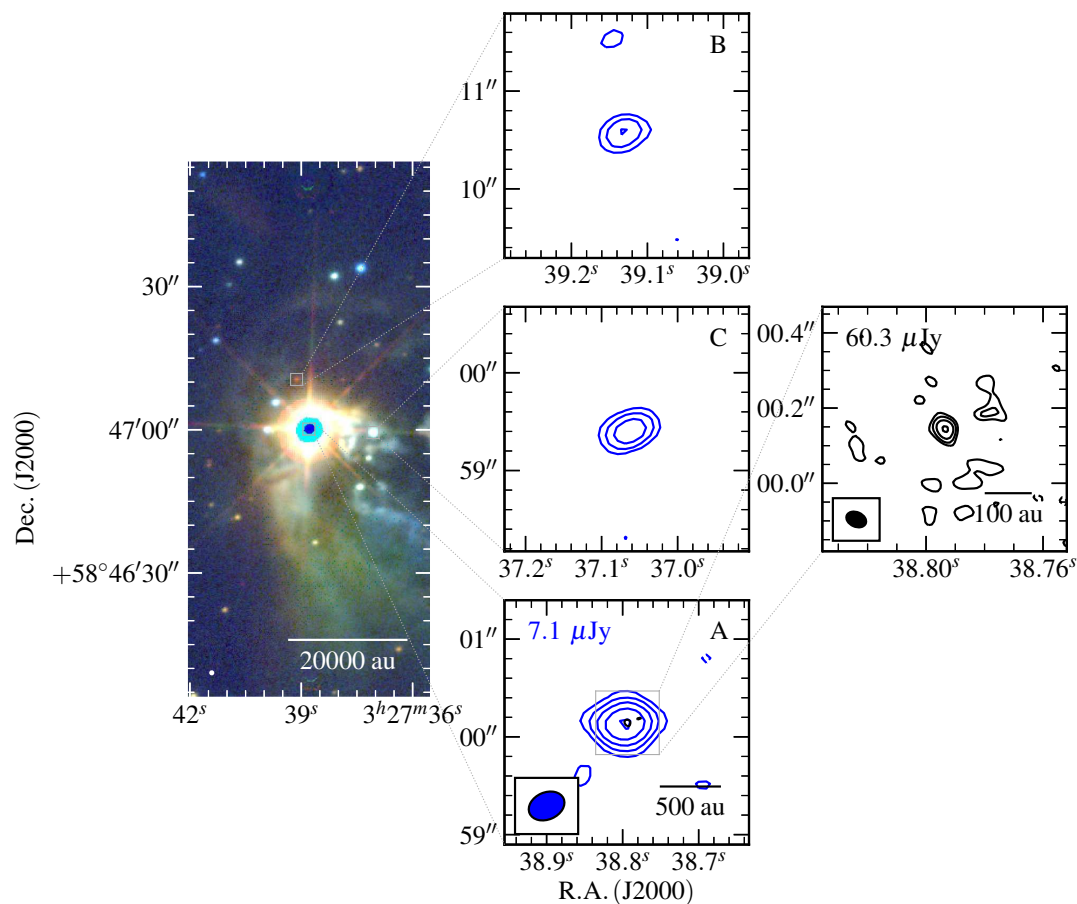


Figure A.90: Near-infrared (R, G, B colour-scale, left panel; UKIDSS, K, H, J bands) and radio contour maps of G141.9996+01.8202 at C-band (centre-column panels, blue contours) and Q-band (right panel, black contours). Restoring beams were $0.379'' \times 0.277''$ at -66° and $0.055'' \times 0.039''$ at 66° . Contour levels are $(-3, 3, 6, 11, 20, 37) \times \sigma$ and $(-3, 3, 5, 7, 12) \times \sigma$ for C and Q-band respectively. All other values have the usual meaning.

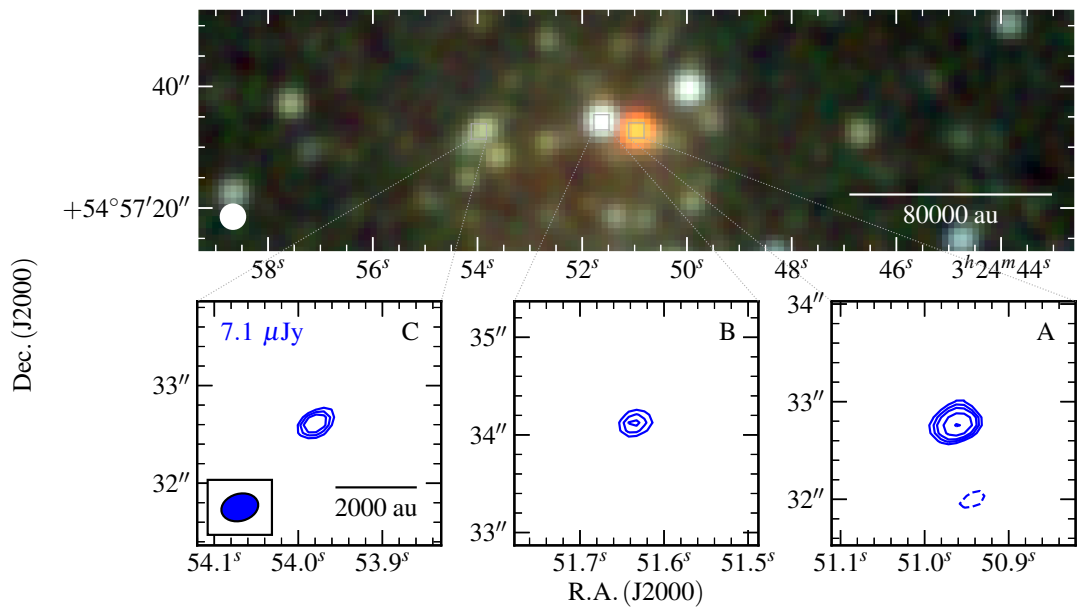


Figure A.91: Near-infrared (R, G, B colour-scale, top panel; 2MASS, K, H, J bands) and C-band contour maps of G143.8118–01.5699 (bottom panels; blue contours). The restoring beams used was $0.384'' \times 0.277''$ at -75° and contour levels are $(-3, 3, 4, 5, 7, 10) \times \sigma$. All other values have the usual meaning.

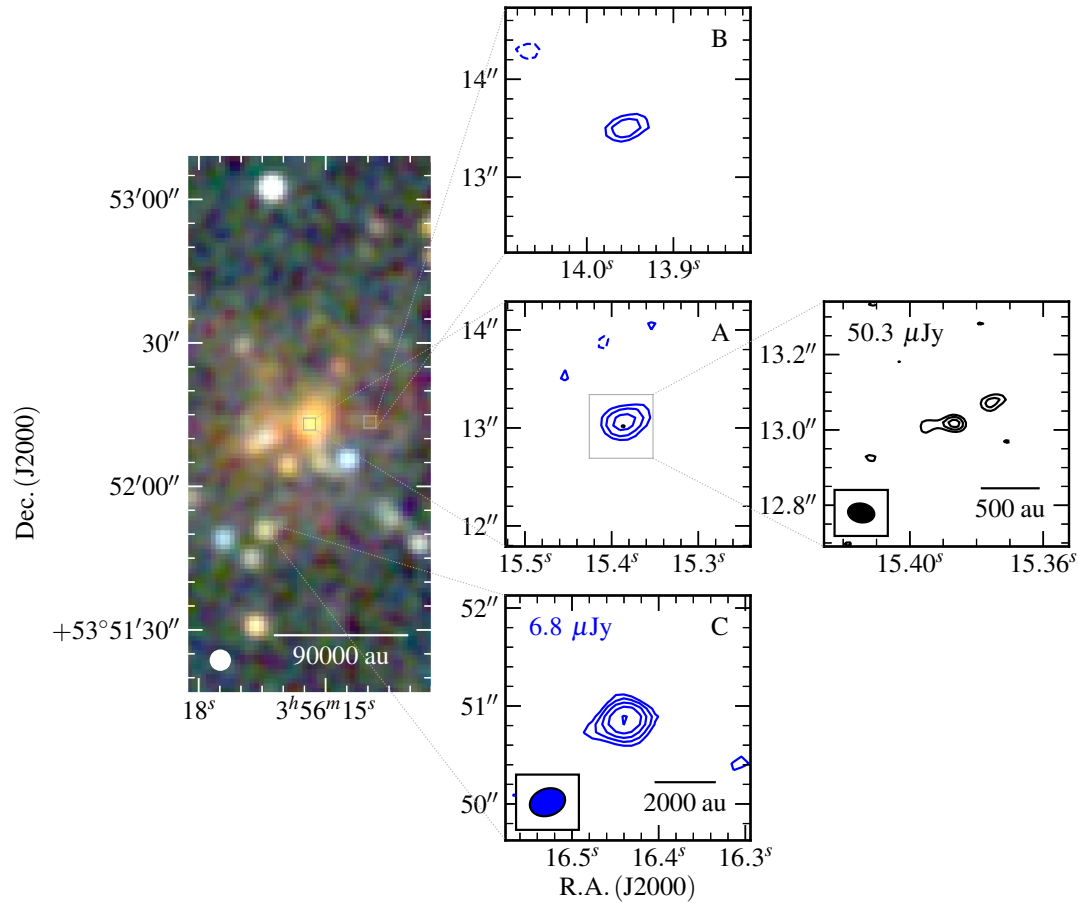


Figure A.92: Near-infrared (R, G, B colour-scale, left panel; 2MASS, K, H, J bands) and radio contour maps of G148.1201+00.2928 at C-band (centre-column panels, blue contours) and Q-band (right panel, black contours). Restoring beams were $0.368'' \times 0.275''$ at -71° and $0.070'' \times 0.050''$ at 80° . Contour levels are $(-3, 3, 5, 8, 12, 20) \times \sigma$ and $(-3, 3, 4, 5) \times \sigma$ for C and Q-band (robustness of 2) respectively. All other values have the usual meaning.

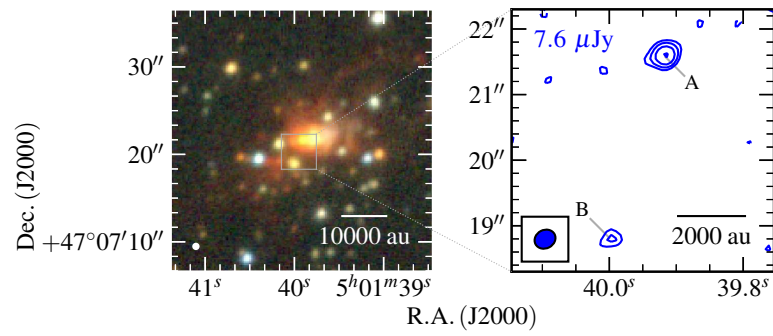


Figure A.93: Near-infrared (R, G, B colour-scale, left panel; UKIDSS, K, H, J bands) and radio contour maps of G160.1452+03.1559 at C-band (right panel, blue contours). The restoring beam for the C-band data was $0.328'' \times 0.280''$ at -62° , while contour levels are set at $(-3, 3, 5, 8, 13) \times \sigma$. All other values have the usual meaning.

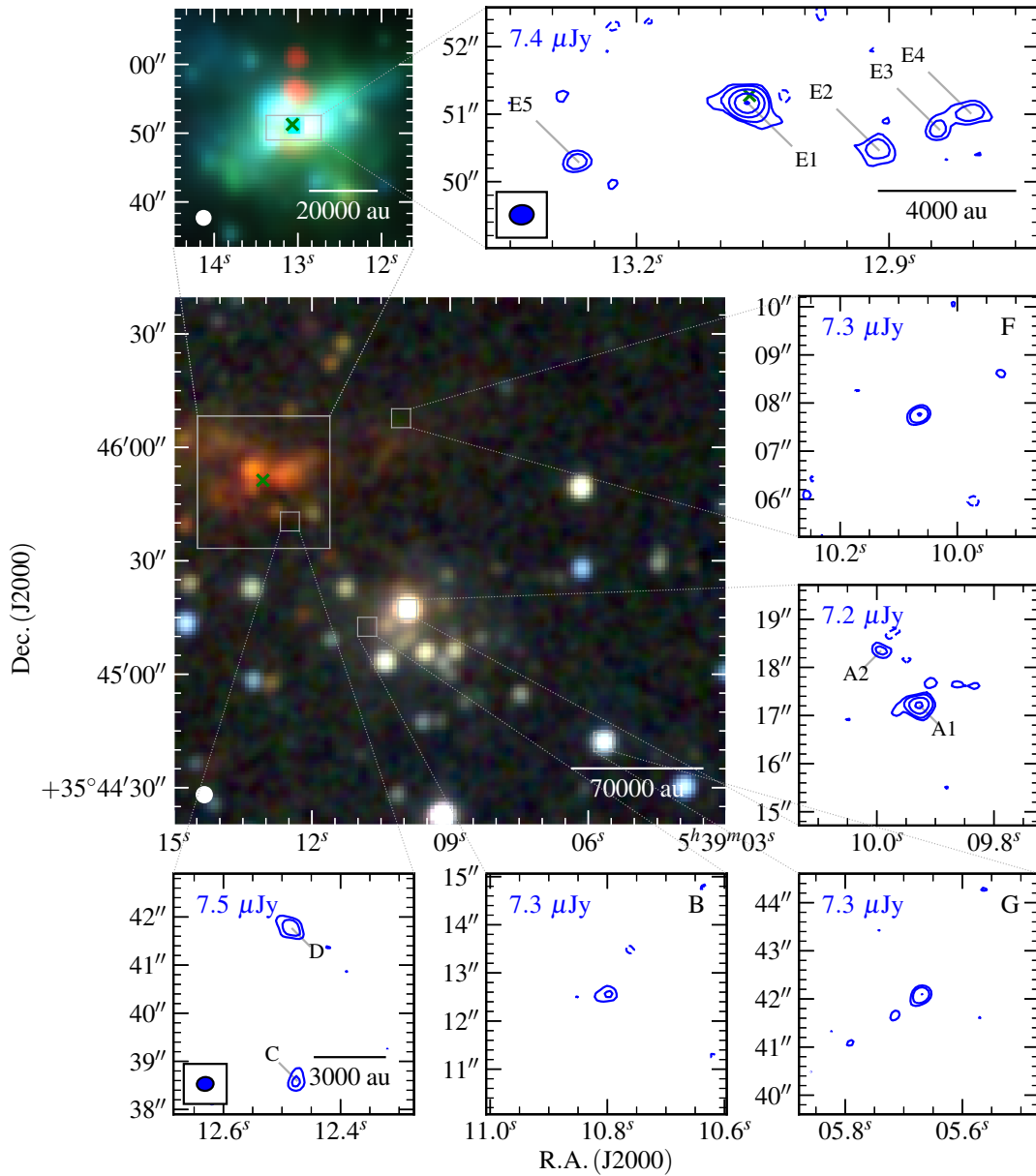


Figure A.94: Near-infrared (R, G, B colour-scale, central, large panel; 2MASS, K, H, J bands), mid-infrared (R, G, B colour-scale, top left panel; GLIMPSE 8.0, 4.5, 3.6 μm bands) and radio contour maps of G173.4839+02.4317 at C-band (other panels, blue contours). The restoring beam for the C-band data was $0.347'' \times 0.286''$ at -84° , while contour levels are set at $(-3, 3, 5, 8, 14, 24) \times \sigma$. All other values have the usual meaning.

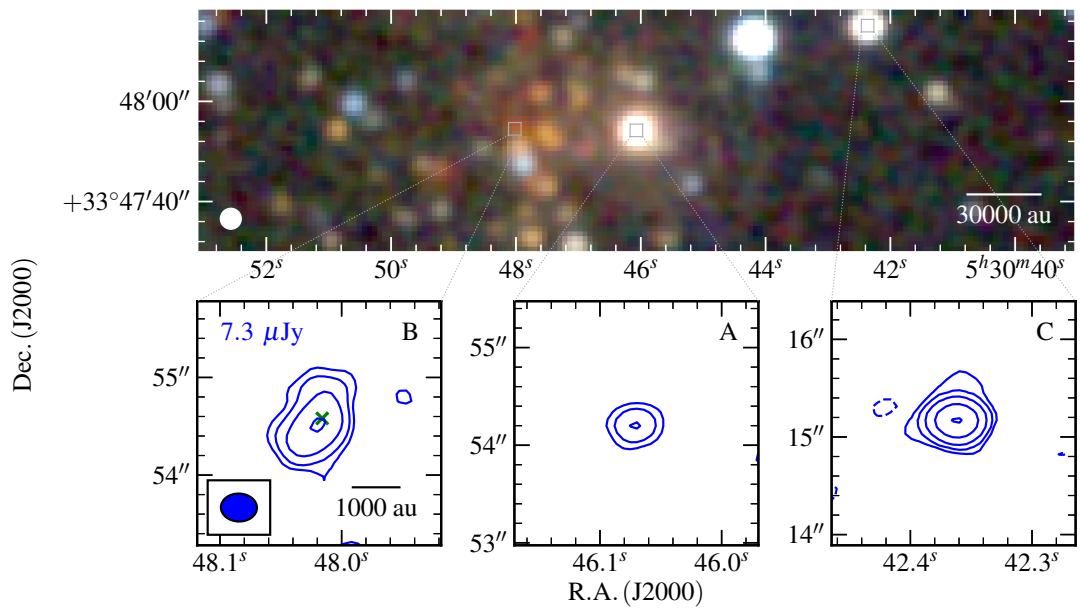


Figure A.95: Near-infrared (R, G, B colour-scale, central, large panel; 2MASS, K, H, J bands) and radio contour maps of G174.1974–00.0763 at C-band (other panels, blue contours). The restoring beam for the C-band data was $0.369'' \times 0.286''$ at 88° , while contour levels are set at $(-3, 3, 7, 17, 46, 114) \times \sigma$. All other values have the usual meaning.

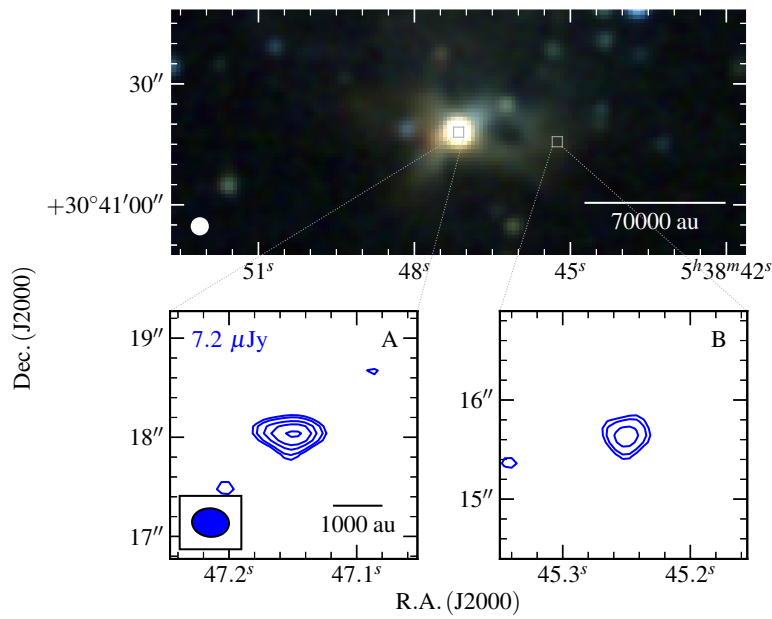


Figure A.96: Near-infrared (R, G, B colour-scale, central, large panel; 2MASS, K, H, J bands) and C-band (blue contours; bottom panels) images of G177.7291–00.3358. The C-band restoring beam was $0.374'' \times 0.288''$ at 84° . Contour levels are $(-3, 3, 4, 6, 8, 11) \times \sigma$ and all other values have their usual meaning.

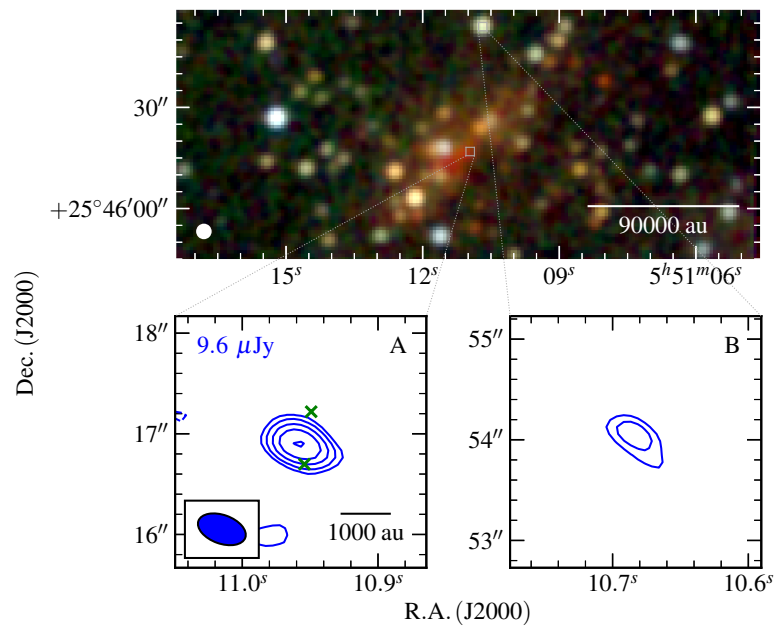


Figure A.97: Near-infrared (R, G, B colour-scale, central, large panel; 2MASS, K, H, J bands) and C-band (blue contours; bottom panels) images of G183.3485–00.5751. The C-band restoring beam was $0.495'' \times 0.285''$ at 70° . Contour levels are $(-3, 3, 5, 8, 12, 19) \times \sigma$ and all other values have their usual meaning.

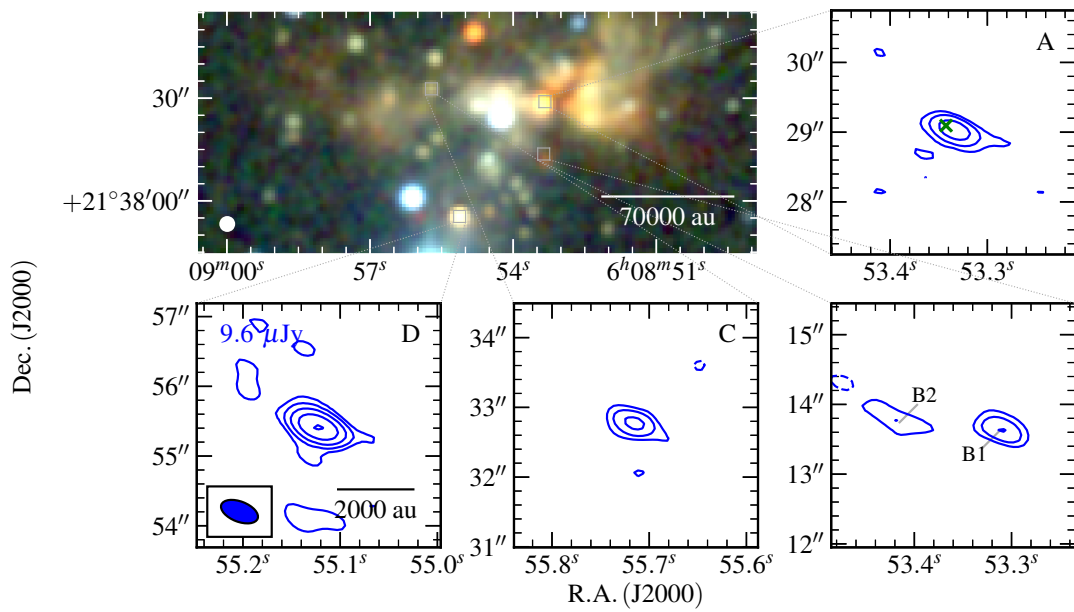


Figure A.98: Near-infrared (R, G, B colour-scale, top left panel; 2MASS, K, H, J bands) and C-band (blue contours; bottom and top right panels) images of G188.9479+00.8871. The C-band restoring beam was $0.558'' \times 0.290''$ at 69° . Contour levels are $(-3, 3, 6, 12, 24, 48) \times \sigma$ and all other values have their usual meaning.

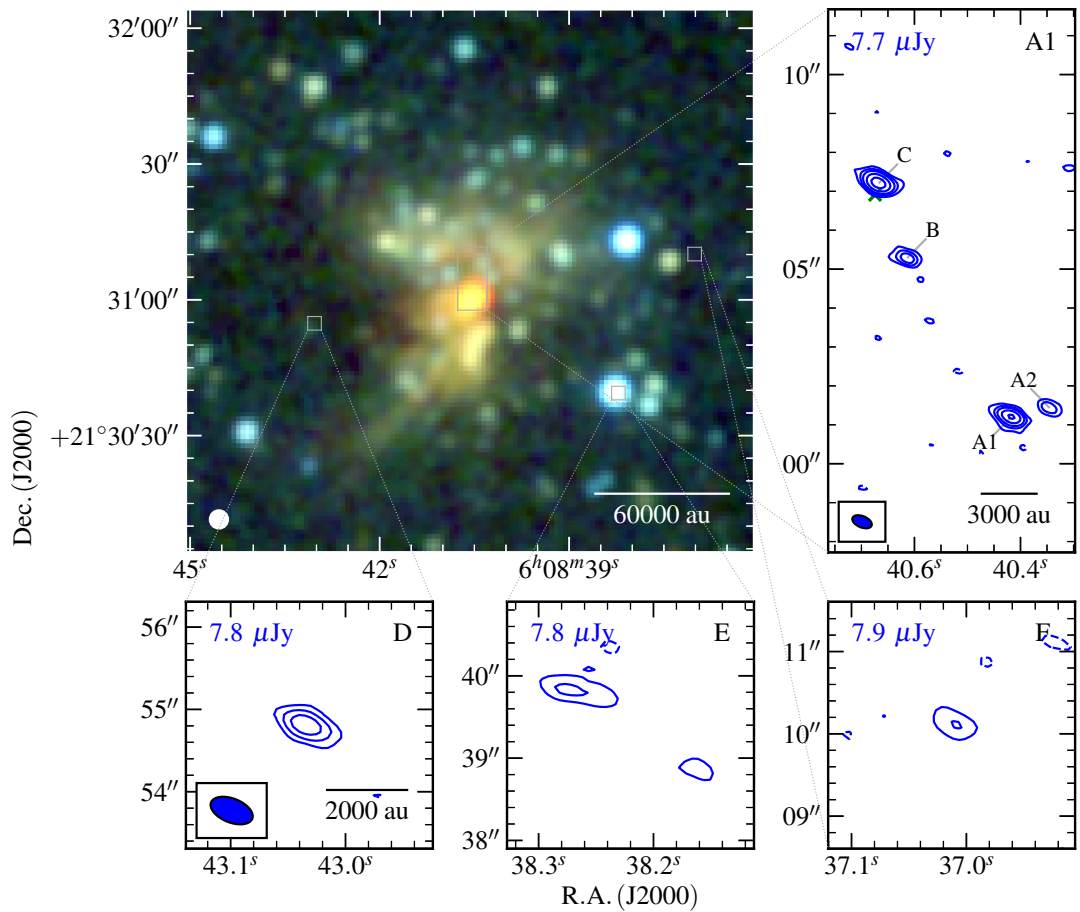


Figure A.99: Near-infrared (R, G, B colour-scale, top left panel; 2MASS, K, H, J bands) and C-band (blue contours; bottom and top right panels) images of G189.0307+00.7821. The C-band restoring beam was $0.539'' \times 0.291''$ at 68° . Contour levels are $(-3, 3, 6, 10, 19, 34) \times \sigma$ and all other values have their usual meaning.

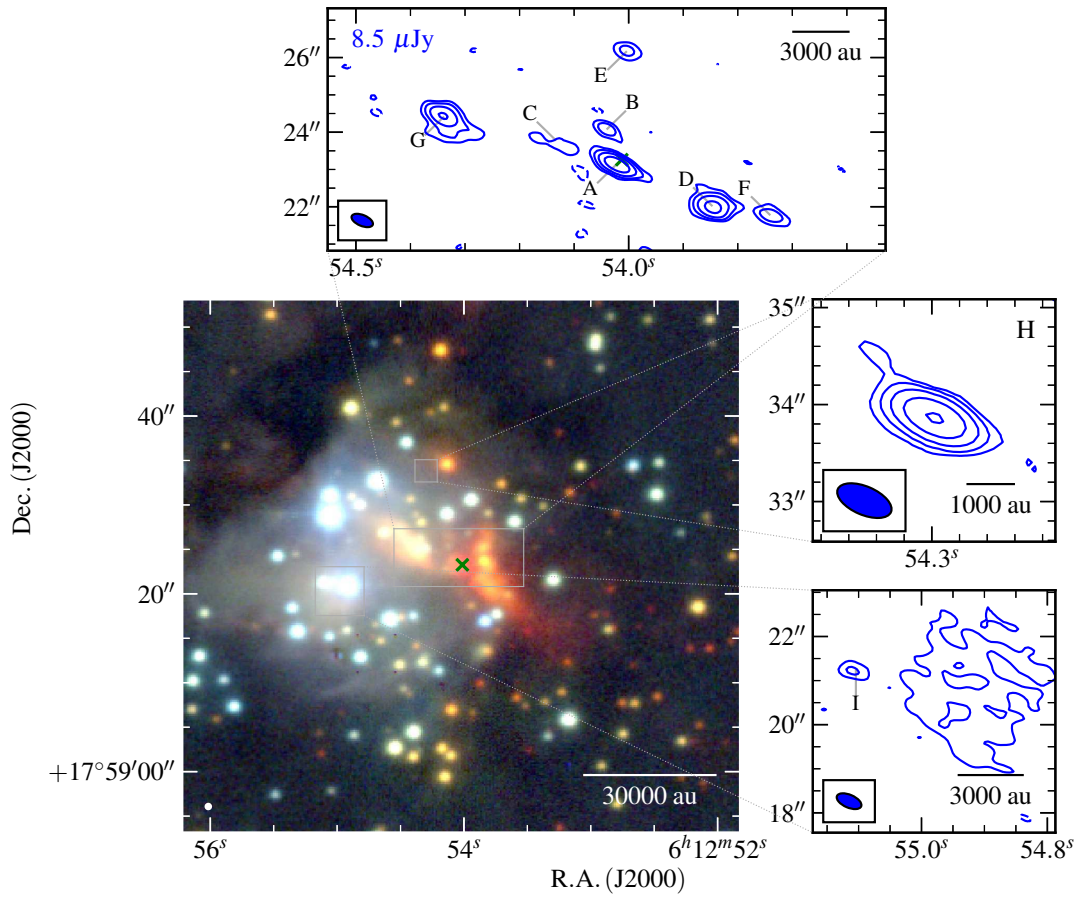


Figure A.100: Near-infrared (R, G, B colour-scale, bottom left panel; UKIDSS, K, H, J bands) and C-band (blue contours; other panels) images of G192.6005–00.0479. The C-band restoring beam was $0.597'' \times 0.292''$ at 67° . Contour levels are $(-3, 3, 7, 16, 38, 87) \times \sigma$ and all other values have their usual meaning.

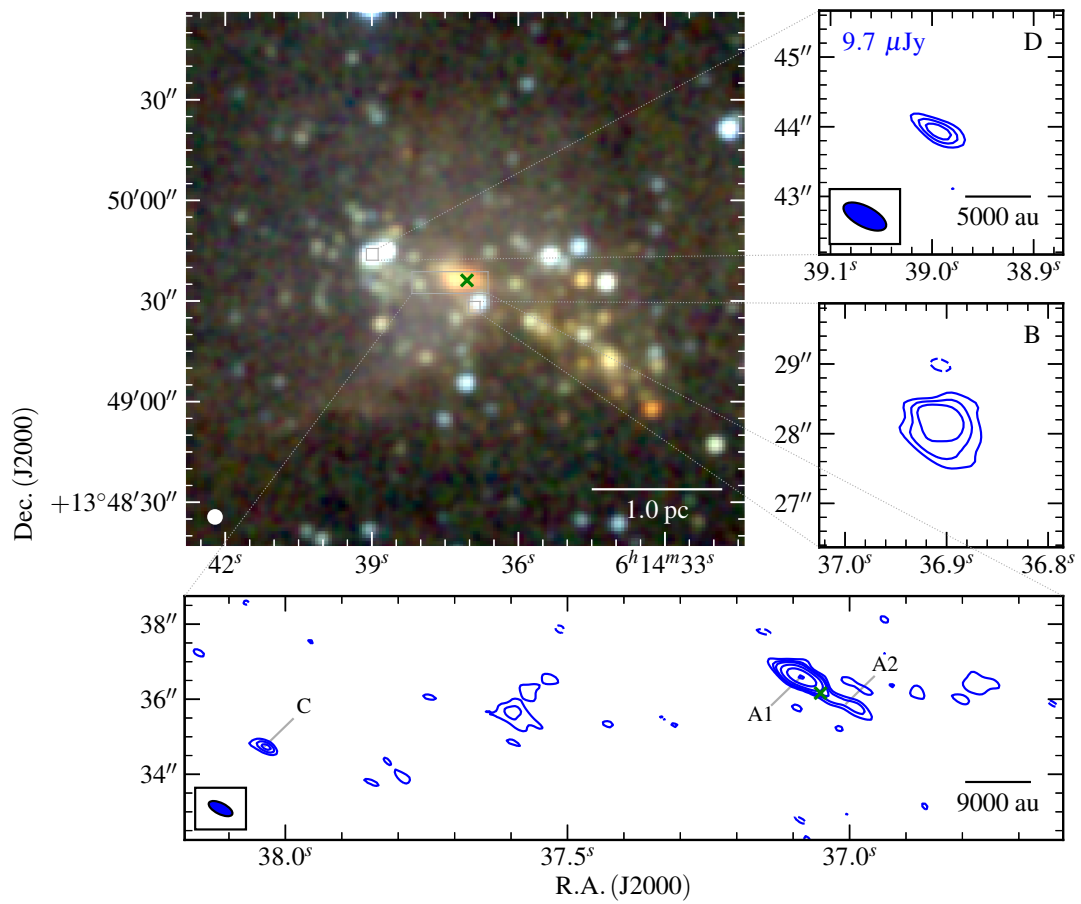


Figure A.101: Near-infrared (R, G, B colour-scale, top left panel; UKIDSS, K, H, J bands) and C-band (blue contours; other panels) images of G196.4542–01.6777. The C-band restoring beam was $0.674'' \times 0.293''$ at 63° . Contour levels are $(-3, 3, 5, 7, 13, 27, 55) \times \sigma$ and all other values have their usual meaning.

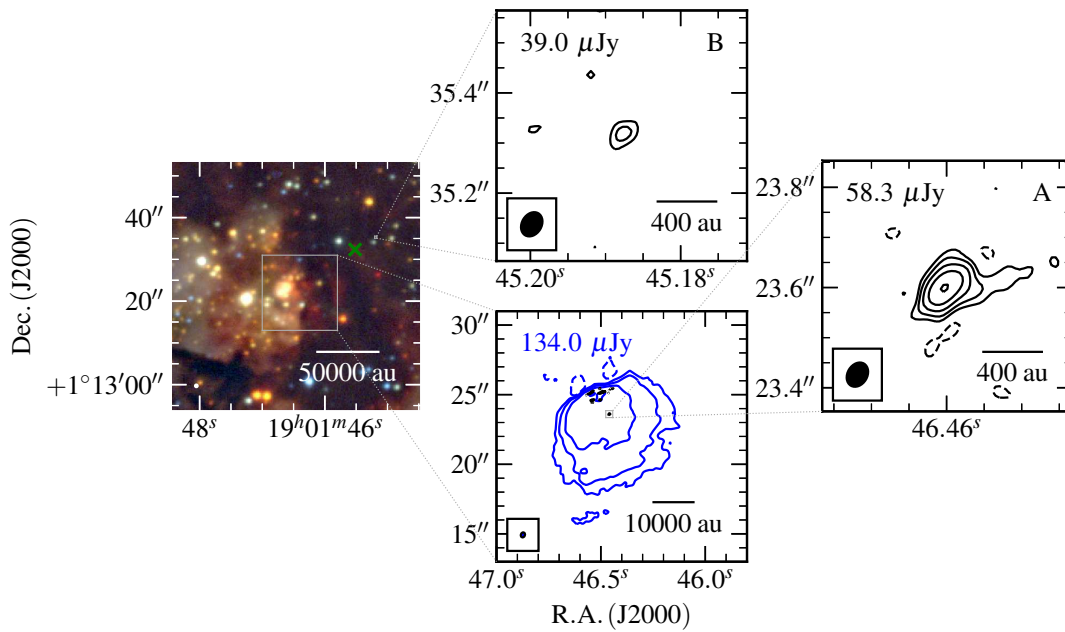


Figure A.102: Near-infrared (R, G, B colour-scale, top left panel; UKIDSS, K, H, J bands), C-band (blue contours; bottom panel) and Q-band (black contours; top and right panels) images of W48 (G035.1992-01.7424). The C-band restoring beam was $0.364'' \times 0.289''$ at -21° and $0.051'' \times 0.039''$ at -31° , while contour levels are $(-3, 3, 11, 40, 147) \times \sigma$ and $(-3, 3, 6, 11, 20, 38) \times \sigma$ for the C and Q-band data respectively. All other values have their usual meaning.

Appendix B

Supporting tables

Table B.1: The deconvolved positions of the MYSOs displaying characteristics of jets and/or disc-winds at 5.5 and 9 GHz, as well as their associated lobes. In cases where positions are given without errors, we fixed the positions to allow deconvolution solutions to converge (generally from the highest frequency where deconvolution with no fixed parameters is possible).

Name	Type	5.5 GHz				9 GHz				
		α (J2000)	$\Delta\alpha$	δ (J2000)	$\Delta\delta$	α (J2000)	$\Delta\alpha$	δ (J2000)	$\Delta\delta$	
G251.2337-01.9535	Jet(C)	08 ^h 02 ^m 42.98 ^s	0.030	-34°31'49.15''	0.082	08 ^h 02 ^m 42.98 ^s	0.021	-34°31'49.12''	0.051	
G254.0491-00.5615	Jet	08 ^h 15 ^m 57.12 ^s	0.077	-36°08'07.16''	0.196	08 ^h 15 ^m 57.13 ^s	0.040	-36°08'06.90''	0.085	
G254.0548-00.0961	C	Jet	08 ^h 17 ^m 52.55 ^s	0.044	-35°52'47.64''	0.115	08 ^h 17 ^m 52.56 ^s	0.029	-35°52'47.63''	0.067
	W	Lobe	08 ^h 17 ^m 52.31 ^s	0.131	-35°52'51.62''	0.340	08 ^h 17 ^m 52.27 ^s	0.130	-35°52'50.96''	0.298
G263.2283+01.5712	Jet	08 ^h 53 ^m 09.45 ^s	0.034	-42°13'07.72''	0.061	08 ^h 53 ^m 09.46 ^s	0.016	-42°13'07.85''	0.029	
G263.7434+00.1161	N	Lobe	08 ^h 48 ^m 48.47 ^s	0.033	-43°32'24.02''	0.057	08 ^h 48 ^m 48.47 ^s	0.026	-43°32'24.01''	0.042
	S	Jet	08 ^h 48 ^m 48.65 ^s	0.035	-43°32'28.58''	0.060	08 ^h 48 ^m 48.66 ^s	0.023	-43°32'28.70''	0.036
G298.2620+00.7394	DW	12 ^h 11 ^m 47.67 ^s	0.123	-61°46'20.86''	0.085	12 ^h 11 ^m 47.67 ^s	0.080	-61°46'20.98''	0.052	
G310.0135+00.3892	N	Lobe	13 ^h 51 ^m 37.84 ^s	0.078	-61°39'06.30''	0.207	13 ^h 51 ^m 37.85 ^s	0.019	-61°39'06.34''	0.048
	S	Jet	13 ^h 51 ^m 37.85 ^s	0.223	-61°39'07.94''	0.597	13 ^h 51 ^m 37.86 ^s	0.053	-61°39'07.80''	0.076
	SW	Lobe	13 ^h 51 ^m 37.66 ^s	0.735	-61°39'08.72''	0.441	13 ^h 51 ^m 37.73 ^s	0.182	-61°39'09.02''	0.254
G310.1420+00.7583	A1	Jet	13 ^h 51 ^m 58.39 ^s	-	-61°15'41.19''	-	13 ^h 51 ^m 58.38 ^s	-	-61°15'41.22''	-
	A2	Lobe	13 ^h 51 ^m 58.29 ^s	-	-61°15'41.40''	-	13 ^h 51 ^m 58.28 ^s	-	-61°15'41.37''	-
	A3	Lobe	13 ^h 51 ^m 58.17 ^s	-	-61°15'41.75''	-	13 ^h 51 ^m 58.15 ^s	-	-61°15'41.83''	-
	A4	Lobe	13 ^h 51 ^m 57.94 ^s	-	-61°15'42.20''	-	13 ^h 51 ^m 57.95 ^s	-	-61°15'42.26''	-

Table B.1: Continued

Name	Type	5.5 GHz				9 GHz				
		α (J2000)	$\Delta\alpha$	δ (J2000)	$\Delta\delta$	α (J2000)	$\Delta\alpha$	δ (J2000)	$\Delta\delta$	
	B	Lobe	13 ^h 51 ^m 58.70 ^s	0.069	−61°15′40.90″	0.069	13 ^h 51 ^m 58.73 ^s	-	−61°15′40.58″	-
	C	Lobe	13 ^h 51 ^m 59.10 ^s	0.016	−61°15′40.00″	0.021	13 ^h 51 ^m 59.07 ^s	-	−61°15′40.02″	-
	D	Lobe	13 ^h 51 ^m 59.54 ^s	0.009	−61°15′40.10″	0.011	13 ^h 51 ^m 59.55 ^s	-	−61°15′40.00″	-
G313.7654-00.8620	A1	Jet	14 ^h 25 ^m 01.59 ^s	0.021	−61°44′57.71″	0.026	14 ^h 25 ^m 01.59 ^s	0.016	−61°44′57.77″	0.019
	A2	Lobe	14 ^h 25 ^m 01.82 ^s	-	−61°44′58.96″	-	14 ^h 25 ^m 01.82 ^s	0.112	−61°44′58.96″	0.134
	B1	Lobe	14 ^h 25 ^m 01.10 ^s	0.050	−61°44′56.24″	0.061	14 ^h 25 ^m 01.10 ^s	0.061	−61°44′55.93″	0.073
	B2	Lobe	14 ^h 25 ^m 01.20 ^s	-	−61°44′57.92″	-	14 ^h 25 ^m 01.20 ^s	0.080	−61°44′57.92″	0.096
	C	Lobe	14 ^h 25 ^m 02.23 ^s	0.031	−61°45′01.36″	0.038	14 ^h 25 ^m 02.24 ^s	0.029	−61°45′01.34″	0.035
	D	Lobe	14 ^h 25 ^m 00.06 ^s	0.084	−61°44′53.17″	0.103	14 ^h 25 ^m 00.06 ^s	0.061	−61°44′53.35″	0.073
G318.9480-00.1969		Jet/DW	15 ^h 00 ^m 55.22 ^s	0.143	−58°58′53.02″	0.203	15 ^h 00 ^m 55.28 ^s	0.066	−58°58′52.84″	0.091
G327.1192+00.5103		Jet	15 ^h 47 ^m 32.78 ^s	0.057	−53°52′39.69″	0.073	15 ^h 47 ^m 32.79 ^s	0.054	−53°52′39.68″	0.071
G331.3576+01.0626		Jet(C)	16 ^h 06 ^m 25.79 ^s	0.063	−50°43′22.46″	0.085	16 ^h 06 ^m 25.82 ^s	0.029	−50°45′02.82″	0.040
G332.0939-00.4206	E	Lobe	16 ^h 16 ^m 16.73 ^s	0.064	−51°18′26.68″	0.100	16 ^h 16 ^m 16.75 ^s	0.055	−51°18′26.60″	0.080
	W	Jet	16 ^h 16 ^m 16.46 ^s	0.032	−51°18′25.21″	0.051	16 ^h 16 ^m 16.48 ^s	0.025	−51°18′25.35″	0.036
G332.9868-00.4871		Jet(C)	16 ^h 20 ^m 37.78 ^s	0.038	−50°43′49.47″	0.041	16 ^h 20 ^m 37.79 ^s	0.013	−50°43′49.51″	0.019
G338.9196+00.5495		Jet(C)	16 ^h 40 ^m 34.06 ^s	0.124	−45°42′07.21″	0.240	16 ^h 40 ^m 34.03 ^s	0.035	−45°42′07.61″	0.071

Table B.1: Continued

Name	Type		5.5 GHz				9 GHz			
			α (J2000)	$\Delta\alpha$	δ (J2000)	$\Delta\delta$	α (J2000)	$\Delta\alpha$	δ (J2000)	$\Delta\delta$
G339.6221-00.1209	E	Jet(C)	16 ^h 46 ^m 06.02 ^s	0.022	−45°36′43.63″	0.049	16 ^h 46 ^m 06.03 ^s	0.014	−45°36′43.75″	0.026
	W	Lobe	16 ^h 46 ^m 05.64 ^s	0.139	−45°36′45.52″	0.347	16 ^h 46 ^m 05.65 ^s	0.088	−45°36′45.42″	0.166
G339.8838-01.2588	C	Jet	16 ^h 52 ^m 04.69 ^s	0.056	−46°08′34.22″	0.085	16 ^h 52 ^m 04.67 ^s	0.016	−46°08′34.16″	0.035
	NE	Jet	16 ^h 52 ^m 04.94 ^s	0.014	−46°08′31.21″	0.021	16 ^h 52 ^m 04.94 ^s	0.009	−46°08′31.22″	0.019
	SW	Jet	16 ^h 52 ^m 04.17 ^s	0.043	−46°08′40.97″	0.065	16 ^h 52 ^m 04.20 ^s	0.049	−46°08′41.47″	0.107
G340.0543-00.2437	D	Jet(C)	16 ^h 48 ^m 13.84 ^s	0.060	−45°21′46.11″	0.110	16 ^h 48 ^m 13.82 ^s	0.029	−45°21′45.88″	0.045
G343.5213-00.5171	E	Lobe	17 ^h 01 ^m 34.11 ^s	0.348	−42°50′19.62″	0.336	17 ^h 01 ^m 34.10 ^s	0.186	−42°50′19.62″	0.321
	W	Jet(C)	17 ^h 01 ^m 33.94 ^s	0.087	−42°50′19.53″	0.097	17 ^h 01 ^m 33.94 ^s	0.047	−42°50′19.54″	0.076
G345.5043+00.3480		Jet(C)	17 ^h 04 ^m 22.91 ^s	0.070	−40°44′23.08″	0.116	17 ^h 04 ^m 22.90 ^s	0.061	−40°44′22.86″	0.100

Table B.2: The deconvolved positions of the MYSOs displaying characteristics of jets and/or disc-winds at 17 and 22.8 GHz, as well as their associated lobes at all 4 observing frequencies. In cases where positions are given without errors, we fixed the positions to allow deconvolution solutions to converge (generally from the highest frequency where deconvolution with no fixed parameters is possible).

Name	Type	17 GHz				22.8 GHz			
		α (J2000)	$\Delta\alpha$	δ (J2000)	$\Delta\delta$	α (J2000)	$\Delta\alpha$	δ (J2000)	$\Delta\delta$
G010.8411-02.5919	Jet	18 ^h 19 ^m 12.10 ^s	0.005	-20°47'30.99"	0.029	18 ^h 19 ^m 12.09 ^s	0.006	-20°47'31.01"	0.039
G012.9090-00.2607	Jet(C)	18 ^h 14 ^m 39.52 ^s	0.024	-17°51'59.69"	0.108	18 ^h 14 ^m 39.51 ^s	0.017	-17°51'59.87"	0.068
G014.9958-00.6732	Jet(C)	18 ^h 20 ^m 19.48 ^s	0.024	-16°13'29.77"	0.077	18 ^h 20 ^m 19.48 ^s	0.010	-16°13'29.95"	0.030
G251.2337-01.9535	Jet(C)	08 ^h 02 ^m 42.97 ^s	0.017	-34°31'48.83"	0.036	08 ^h 02 ^m 42.96 ^s	0.079	-34°31'48.47"	0.260
G254.0491-00.5615	Jet	08 ^h 15 ^m 57.12 ^s	0.063	-36°08'06.03"	0.161	-	-	-	-
G254.0548-00.0961	C Jet	08 ^h 17 ^m 52.55 ^s	0.041	-35°52'47.61"	0.075	08 ^h 17 ^m 52.54 ^s	0.051	-35°52'47.74"	0.156
G263.2283+01.5712	Jet	08 ^h 53 ^m 09.45 ^s	0.028	-42°13'08.21"	0.039	08 ^h 53 ^m 09.45 ^s	0.021	-42°13'08.09"	0.041
G263.7434+00.1161	N Lobe	08 ^h 48 ^m 48.48 ^s	0.020	-43°32'23.61"	0.046	-	-	-	-
	S Jet	08 ^h 48 ^m 48.65 ^s	0.011	-43°32'28.42"	0.025	08 ^h 48 ^m 48.65 ^s	0.021	-43°32'28.42"	0.046
G263.7759-00.4281	Jet	08 ^h 46 ^m 34.85 ^s	0.008	-43°54'30.24"	0.013	08 ^h 46 ^m 34.85 ^s	0.008	-43°54'30.33"	0.013
	NW Lobe	08 ^h 46 ^m 34.80 ^s	0.014	-43°54'29.35"	0.021	08 ^h 46 ^m 34.82 ^s	0.045	-43°54'29.69"	0.076
G265.1438+01.4548	Jet/DW	08 ^h 59 ^m 27.40 ^s	0.022	-43°45'03.75"	0.038	08 ^h 59 ^m 27.40 ^s	0.002	-43°45'03.75"	0.073
G286.2086+00.1694	B Jet(C)	10 ^h 38 ^m 32.15 ^s	0.039	-58°19'08.60"	0.084	10 ^h 38 ^m 32.16 ^s	0.033	-58°19'08.58"	0.044
	B2 Lobe	10 ^h 38 ^m 32.23 ^s	0.083	-58°19'08.62"	0.044	-	-	-	-

Table B.2: Continued

Name	Type	17 GHz				22.8 GHz				
		α (J2000)	$\Delta\alpha$	δ (J2000)	$\Delta\delta$	α (J2000)	$\Delta\alpha$	δ (J2000)	$\Delta\delta$	
G298.2620+00.7394	DW	12 ^h 11 ^m 47.69 ^s	0.042	-61°46'21.08''	0.043	12 ^h 11 ^m 47.69 ^s	0.042	-61°46'20.97''	0.047	
G310.0135+00.3892	N	Lobe	13 ^h 51 ^m 37.85 ^s	0.020	-61°39'06.25''	0.017	13 ^h 51 ^m 37.85 ^s	0.045	-61°39'06.25''	0.039
	S	Jet	13 ^h 51 ^m 37.85 ^s	0.016	-61°39'07.69''	0.014	13 ^h 51 ^m 37.86 ^s	0.012	-61°39'07.81''	0.014
G310.1420+00.7583	A1	Jet	13 ^h 51 ^m 58.39 ^s	-	-61°15'41.17''	-	13 ^h 51 ^m 58.39 ^s	0.009	-61°15'41.18''	0.017
	A2	Lobe	13 ^h 51 ^m 58.28 ^s	-	-61°15'41.35''	-	13 ^h 51 ^m 58.28 ^s	0.019	-61°15'41.35''	0.037
	A3	Lobe	13 ^h 51 ^m 58.16 ^s	-	-61°15'41.61''	-	13 ^h 51 ^m 58.16 ^s	0.026	-61°15'41.72''	0.050
	A4	Lobe	13 ^h 51 ^m 57.94 ^s	-	-61°15'42.14''	-	13 ^h 51 ^m 57.95 ^s	0.054	-61°15'42.10''	0.104
	B	Lobe	13 ^h 51 ^m 58.69 ^s	-	-61°15'40.48''	-	-	-	-	-
	C	Lobe	13 ^h 51 ^m 59.07 ^s	0.036	-61°15'39.95''	0.089	-	-	-	-
	D	Lobe	13 ^h 51 ^m 59.57 ^s	-	-61°15'40.02''	-	13 ^h 51 ^m 59.57 ^s	0.052	-61°15'39.82''	0.101
G318.9480-00.1969	Jet/DW	15 ^h 00 ^m 55.28 ^s	0.063	-58°58'52.72''	0.050	15 ^h 00 ^m 55.29 ^s	0.050	-58°58'52.80''	0.044	
G326.6618+00.5207	Jet(C)	15 ^h 45 ^m 02.84 ^s	0.017	-54°09'03.38''	0.036	15 ^h 45 ^m 02.83 ^s	0.017	-54°09'03.43''	0.040	
G327.1192+00.5103	Jet	15 ^h 47 ^m 32.80 ^s	0.026	-53°52'39.68''	0.053	15 ^h 47 ^m 32.80 ^s	0.024	-53°52'39.68''	0.054	
G331.3576+01.0626	Jet(C)	16 ^h 06 ^m 25.76 ^s	0.012	-50°43'22.47''	0.010	16 ^h 06 ^m 25.78 ^s	0.017	-50°43'22.55''	0.024	
G332.0939-00.4206	E	Lobe	-	-	-	-	-	-	-	
	W	Jet	16 ^h 16 ^m 16.44 ^s	0.002	-51°18'24.80''	0.004	16 ^h 16 ^m 16.44 ^s	0.004	-51°18'24.83''	0.009

Table B.2: Continued

Name	Type		17 GHz				22.8 GHz			
			α (J2000)	$\Delta\alpha$	δ (J2000)	$\Delta\delta$	α (J2000)	$\Delta\alpha$	δ (J2000)	$\Delta\delta$
G332.9868-00.4871		Jet(C)	16 ^h 20 ^m 37.80 ^s	0.002	-50°43'49.86''	0.004	16 ^h 20 ^m 37.80 ^s	0.004	-50°43'49.84''	0.007
G338.9196+00.5495		Jet(C)	16 ^h 40 ^m 34.01 ^s	0.039	-45°42'07.46''	0.052	16 ^h 40 ^m 34.01 ^s	0.022	-45°42'07.47''	0.029
G339.8838-01.2588	C	Jet	16 ^h 52 ^m 04.67 ^s	0.004	-46°08'34.07''	0.010	16 ^h 52 ^m 04.67 ^s	0.004	-46°08'34.07''	0.010
	NE	Jet	16 ^h 52 ^m 04.94 ^s	0.007	-46°08'31.10''	0.018	16 ^h 52 ^m 04.94 ^s	0.011	-46°08'31.03''	0.030
	SW	Jet	16 ^h 52 ^m 04.15 ^s	0.015	-46°08'39.97''	0.037	16 ^h 52 ^m 04.15 ^s	0.027	-46°08'39.95''	0.072
G343.1261-00.0623	C	Lobe	16 ^h 58 ^m 17.67 ^s	0.025	-42°52'12.60''	0.065	16 ^h 58 ^m 17.67 ^s	0.015	-42°52'12.57''	0.044
	Cen.	Jet	16 ^h 58 ^m 17.21 ^s	0.006	-42°52'07.16''	0.013	16 ^h 58 ^m 17.21 ^s	0.005	-42°52'07.15''	0.014
	N1	Lobe	16 ^h 58 ^m 16.82 ^s	0.019	-42°51'57.00''	0.051	16 ^h 58 ^m 16.81 ^s	0.030	-42°51'57.02''	0.087
	N2	Lobe	16 ^h 58 ^m 16.88 ^s	0.019	-42°51'58.41''	0.051	16 ^h 58 ^m 16.87 ^s	0.040	-42°51'58.39''	0.117
	N4	Lobe	16 ^h 58 ^m 16.99 ^s	0.013	-42°52'03.64''	0.035	16 ^h 58 ^m 16.99 ^s	0.012	-42°52'03.67''	0.035
	S1	Lobe	16 ^h 58 ^m 17.46 ^s	0.005	-42°52'16.48''	0.014	16 ^h 58 ^m 17.46 ^s	0.005	-42°52'16.44''	0.013
	S3	Lobe	16 ^h 58 ^m 17.25 ^s	0.071	-42°52'08.55''	0.095	16 ^h 58 ^m 17.24 ^s	0.062	-42°52'08.77''	0.128
	-	-	-	-	-	-	-	-	-	-
G343.5213-00.5171	E	Lobe	-	-	-	-	-	-	-	-
	W	Jet(C)	17 ^h 01 ^m 33.94 ^s	0.104	-42°50'19.27''	0.159	17 ^h 01 ^m 33.93 ^s	0.044	-42°50'20.02''	0.128
G345.4938+01.4677	C	Jet	16 ^h 59 ^m 41.63 ^s	0.002	-40°03'43.73''	0.005	16 ^h 59 ^m 41.63 ^s	0.001	-40°03'43.74''	0.004
	IE	Lobe	16 ^h 59 ^m 41.88 ^s	0.060	-40°03'44.28''	0.060	16 ^h 59 ^m 41.88 ^s	0.040	-40°03'44.11''	0.040

Table B.2: Continued

Name	Type	17 GHz				22.8 GHz			
		α (J2000)	$\Delta\alpha$	δ (J2000)	$\Delta\delta$	α (J2000)	$\Delta\alpha$	δ (J2000)	$\Delta\delta$
	IW Lobe	16 ^h 59 ^m 41.37 ^s	0.060	-40°03'42.95''	0.060	16 ^h 59 ^m 41.39 ^s	0.040	-40°03'43.38''	0.040
	OE Lobe	16 ^h 59 ^m 44.11 ^s	0.060	-40°03'51.89''	0.060	-	-	-	-
	OW Lobe	16 ^h 59 ^m 39.77 ^s	0.060	-40°03'41.66''	0.060	-	-	-	-
G345.5043+00.3480	Jet(C)	17 ^h 04 ^m 22.91 ^s	0.010	-40°44'22.81''	0.018	17 ^h 04 ^m 22.91 ^s	0.006	-40°44'22.89''	0.015

Table B.3: Fluxes and spectral indices of the MYSOs displaying the characteristics of jets and/or disc-winds in the sample, as well as their associated lobes. Hyphenated entries mean simply that particular source was not observed at that frequency and upper-limits to the flux are given where available.

Name	Type	S_ν (mJy)				α
		5.5 GHz	9.0 GHz	17.0 GHz	22.8 GHz	
G010.8411-02.5919	Jet	-	-	4.75±0.14	6.29±0.11	0.96±0.16
G012.9090-00.2607	Jet(C)	-	-	1.49±0.15	1.54±0.08	0.11±0.52
G014.9958-00.6732	Jet(C)	-	-	0.91±0.10	1.50±0.09	1.71±0.58
G251.2337-01.9535	Jet(C)	0.51±0.02	0.56±0.02	0.54±0.03	0.64±0.12	0.08±0.06

Table B.3: Continued

Name	Type		S_ν (mJy)				α
			5.5 GHz	9.0 GHz	17.0 GHz	22.8 GHz	
G254.0491-00.5615		Jet	0.30±0.03	0.34±0.03	0.58±0.10	< 0.31	0.56±0.19
G254.0548-00.0961	C	Jet	0.27±0.08	0.36±0.09	0.35±0.04	0.40±0.05	0.22±0.19
	W	Lobe	0.11±0.02	0.04±0.01	< 0.09	< 0.32	-2.09±0.92
G263.2283+01.5712		Jet	0.44±0.02	0.58±0.02	0.70±0.06	0.84±0.09	0.19±0.24
G263.7434+00.1161	S	Jet	0.73±0.03	0.87±0.04	1.01±0.04	1.43±0.16	0.39±0.18
G263.7434+00.1161	N	Lobe	0.58±0.02	0.56±0.03	0.44±0.03	< 0.37	-0.45±0.31
G263.7759-00.4281		Jet	-	-	1.70±0.05	1.98±0.17	0.52±0.39
	NW	Lobe	-	-	2.16±0.10	1.72±0.32	-0.78±0.80
G265.1438+01.4548		Jet/DW	-	-	0.60±0.05	0.70±0.10	0.54±0.79
G286.2086+00.1694	B	Jet(C)	-	-	1.20±0.10	1.51±0.24	0.78±0.61
	B2	Lobe	-	-	0.34±0.04	< 0.32	< -0.27
G298.2620+00.7394		DW	0.21±0.04	0.21±0.03	0.33±0.05	0.70±0.08	0.79±0.20
G305.5610+00.0124	C	HCHII	-	-	4.18±0.24	4.21±0.16	0.02±0.33
G310.0135+00.3892	S	Jet	0.27±0.16	0.42±0.08	0.91±0.07	1.35±0.07	1.27±0.18
	N	Lobe	0.81±0.10	0.82±0.07	0.74±0.07	0.54±0.14	-0.17±0.12
	SW	Lobe	0.12±0.08	0.16±0.07	-	-	0.70±1.66

Table B.3: Continued

Name	Type		S_ν (mJy)				α
			5.5 GHz	9.0 GHz	17.0 GHz	22.8 GHz	
G310.1420+00.7583A	A1	Jet	1.00±0.57	1.37±0.11	1.97±0.14	1.60±0.08	0.18±0.09
G310.1420+00.7583A	A2	Lobe	2.00±0.30	1.97±0.21	1.38±0.16	1.49±0.16	-0.28±0.11
	A3	Lobe	1.92±0.19	1.40±0.10	1.03±0.26	0.63±0.09	-0.76±0.12
	A4	Lobe	1.08±0.08	0.93±0.12	0.51±0.24	0.34±0.10	-0.70±0.16
	B	Lobe	0.26±0.02	0.39±0.35	0.85±0.03	< 0.22	1.04±0.07
	C	Lobe	1.40±0.03	1.05±0.56	0.21±0.03	< 0.22	-1.69±0.14
	D	Lobe	2.28±0.03	1.93±0.67	1.29±0.55	1.19±0.36	-0.46±0.18
	G313.7654-00.8620	A1	Jet	0.50±0.01	0.58±0.02	-	-
A2		Lobe	0.20±0.04	0.14±0.03	-	-	-0.68±0.86
B1		Lobe	0.45±0.03	0.28±0.03	-	-	-0.96±0.34
B2		Lobe	0.05±0.01	0.12±0.02	-	-	1.90±0.77
C		Lobe	0.41±0.01	0.41±0.02	-	-	0.04±0.18
D		Lobe	0.15±0.01	0.12±0.01	-	-	-0.32±0.42
G318.9480-00.1969A		Jet/DW	0.12±0.03	0.10±0.01	0.14±0.02	0.33±0.06	0.69±0.22
G326.6618+00.5207		Jet(C)	< 0.26	< 0.17	0.76±0.07	1.02±0.10	1.02±0.63
G327.1192+00.5103		Jet	0.33±0.02	0.47±0.05	0.35±0.04	0.56±0.08	0.16±0.09

Table B.3: Continued

Name	Type		S_ν (mJy)				α
			5.5 GHz	9.0 GHz	17.0 GHz	22.8 GHz	
G331.3576+01.0626		Jet(C)	1.55±0.19	1.91±0.17	2.70±0.14	2.94±0.24	0.48±0.09
G332.0939-00.4206	E	Lobe	0.32±0.04	0.47±0.09	< 0.14	< 0.34	1.24±0.65
G332.0939-00.4206	W	Jet	0.57±0.03	0.99±0.09	4.25±0.07	5.00±0.11	1.49±0.03
G332.9868-00.4871		Jet(C)	1.96±0.21	3.54±0.26	9.30±0.42	10.84±0.59	1.27±0.14
G338.9196+00.5495		Jet(C)	< 0.14	0.14±0.04	0.25±0.06	0.33±0.06	0.96±0.48
G339.6221-00.1209	E	Jet(C)	1.56±0.10	1.43±0.16	-	-	-0.17±0.16
	W	Lobe	0.22±0.05	0.13±0.03	-	-	-1.05±0.88
G339.8838-01.2588	C	Jet	0.88±0.06	1.58±0.05	2.44±0.05	3.01±0.07	0.77±0.04
	NE	Lobe	2.29±0.04	2.36±0.04	1.86±0.06	1.14±0.08	-0.39±0.07
	SW	Lobe	1.40±0.08	1.50±0.16	0.71±0.05	0.43±0.07	-0.72±0.11
G340.0543-00.2437D	D	Jet(C)	1.80±0.37	2.18±0.55	-	-	0.39±0.67
G343.1261-00.0623	Cen.	Jet	-	-	16.80±0.51	16.30±0.59	-0.10±0.23
	C	Lobe	-	-	1.49±0.17	1.00±0.09	-1.37±0.71
	N1	Lobe	-	-	1.07±0.09	0.52±0.09	-2.48±0.92
	N2	Lobe	-	-	1.58±0.14	0.85±0.20	-2.12±1.14
	N4	Lobe	-	-	1.80±0.11	1.48±0.11	-0.67±0.46

Table B.3: Continued

Name	Type		S_ν (mJy)				α
			5.5 GHz	9.0 GHz	17.0 GHz	22.8 GHz	
	S1	Lobe	-	-	4.72±0.11	4.13±0.11	-0.45±0.17
	S3	Lobe	-	-	0.96±0.32	0.67±0.38	-1.21±3.41
G343.5213-00.5171	W	Jet(C)	0.54±0.08	0.57±0.07	0.46±0.15	0.52±0.09	-0.05±0.15
	E	Lobe	0.14 ± 0.08	0.14 ± 0.08	< 0.09	< 0.20	0.04±1.56
G345.4938+01.4677	C	Jet	-	-	13.90±0.11	17.50±0.13	0.79±0.05
	IE	Lobe	-	-	1.93±0.13	1.97±0.50	0.07±1.11
	IW	Lobe	-	-	2.18±0.16	2.16±0.65	-0.03±1.31
	OE	Lobe	-	-	0.97±0.07	< 0.44	-
	OW	Lobe	-	-	1.84±0.07	< 0.44	-
G345.5043+00.3480		Jet(C)	0.82±0.12	1.55±0.30	2.93±0.17	3.24±0.18	0.92±0.10

Table B.4: A table of deconvolved, major axes of MYSOs in the sample displaying jet-like and/or disc-wind characteristics. Hyphenated entries denote where either the source was not observed, or the source was point-like after deconvolution.

Name	Type		$\theta_{\text{maj}} (")$			
			5.5 GHz	9.0 GHz	17.0 GHz	22.8 GHz
G010.8411-02.5919		Jet	-	-	0.95±0.24	0.60±1.70
G012.9090-00.2607		Jet(C)	-	-	-	-
G014.9958-00.6732		Jet(C)	-	-	0.34±0.04	-
G251.2337-01.9535		Jet(C)	-	-	0.41±0.08	-
G254.0491-00.5615		Jet	2.22±0.18	1.22±0.08	2.34±0.92	-
G254.0548-00.0961	C	Jet	0.94±0.12	-	-	-
	W	Lobe	2.95±0.76	-	-	-
G263.2283+01.5712		Jet	-	0.68±1.16	0.66±0.09	-
G263.7434+00.1161	S	Jet	2.11±0.36	1.92±0.20	0.94±0.14	0.54±0.23
	N	Lobe	-	1.23±0.26	-	-
G263.7759-00.4281		Jet	-	-	-	-
	NW	Lobe	-	-	1.64±0.04	-
G265.1438+01.4548		Jet/DW	-	-	0.62±0.19	-
G286.2086+00.1694	B	Jet(C)	-	-	1.08±0.05	0.90±0.36
	B2	Lobe	-	-	-	-
G298.2620+00.7394		DW	2.02±0.74	-	0.80±0.33	0.43±0.13
G310.0135+00.3892	S	Jet	-	-	0.17±0.03	-
	N	Lobe	-	-	-	-
	SW	Lobe	-	-	-	-
G310.1420+00.7583A	A1	Jet	-	0.73±0.15	-	0.34±0.02
	A2	Lobe	-	0.85±0.17	0.55±0.11	0.73±0.06
	A3	Lobe	1.31±0.26	0.94±0.19	-	-
	A4	Lobe	1.74±0.35	1.10±0.22	-	-
	B	Lobe	-	1.70±0.34	4.27±0.85	-

Table B.4: Continued

Name	Type	$\theta_{\text{maj}} (")$				
		5.5 GHz	9.0 GHz	17.0 GHz	22.8 GHz	
G313.7654-00.8620	C	Lobe	2.17±0.06	1.38±0.28	-	-
	D	Lobe	1.38±0.04	1.38±0.28	1.28±0.26	1.40±0.20
	A1	Jet	-	0.47±0.14	-	-
	A2	Lobe	3.49±0.41	1.78±0.23	-	-
	B1	Lobe	2.23±0.16	1.52±0.20	-	-
	B2	Lobe	-	-	-	-
	C	Lobe	0.86±1.16	0.81±0.14	-	-
	D	Lobe	0.80±0.17	-	-	-
G318.9480-00.1969A		Jet/DW	-	-	-	0.54±0.09
G326.6618+00.5207		Jet(C)	-	-	0.52±0.23	0.51±0.21
G327.1192+00.5103		Jet	-	1.68±0.35	-	-
G331.3576+01.0626		Jet(C)	-	< 0.56	-	0.28±0.11
G332.0939-00.4206	W	Jet	-	-	-	-
	E	Lobe	-	-	-	-
G332.9868-00.4871		Jet(C)	-	-	-	-
G338.9196+00.5495		Jet(C)	-	-	< 0.76	-
G339.6221-00.1209	E	Jet(C)	1.48±0.28	1.25±0.23	-	-
	W	Lobe	-	-	-	-
G339.8838-01.2588	C	Jet	1.87±0.30	1.13±0.08	-	-
	NE	Lobe	1.15±0.06	0.47±0.12	0.59±0.04	0.30±0.60
	SW	Lobe	3.07±0.11	5.33±0.14	-	-
G340.0543-00.2437D		D	Jet(C)	-	-	-
G343.1261-00.0623	Cen.	Jet	-	-	0.97±0.01	1.01±0.20
	C	Lobe	-	-	-	0.69±0.27
	N1	Lobe	-	-	0.57±0.59	-

Table B.4: Continued

Name	Type		$\theta_{\text{maj}} (")$			
			5.5 GHz	9.0 GHz	17.0 GHz	22.8 GHz
	N2	Lobe	-	-	0.84±0.07	1.10±0.19
	N4	Lobe	-	-	0.65±0.07	0.42±0.09
	S1	Lobe	-	-	0.64±0.03	0.70±0.02
	S3	Lobe	-	-	-	-
G343.5213-00.5171	W	Jet(C)	-	-	1.73±0.35	1.20±0.33
	E	Lobe	-	-	-	-
G345.4938+01.4677	C	Jet	-	-	0.24±0.02	0.32±0.01
	IE	Lobe	-	-	2.31±0.17	-
	IW	Lobe	-	-	1.15±0.07	1.46±0.13
	OE	Lobe	-	-	2.97±0.13	-
	OW	Lobe	-	-	3.20±0.11	-
G345.5043+00.3480		Jet(C)	-	-	0.32±0.07	< 0.37

Table B.5: A table of deconvolved, minor axes of MYSOs in the sample displaying jet-like and/or disc-wind characteristics. Hyphenated entries denote where either the source was not observed, or the source was point-like after deconvolution.

Name	Type	$\theta_{\text{min}} (")$			
		5.5 GHz	9.0 GHz	17.0 GHz	22.8 GHz
G010.8411-02.5919	Jet	-	-	0.19±0.07	0.10±0.22
G012.9090-00.2607	Jet(C)	-	-	-	-
G014.9958-00.6732	Jet(C)	-	-	0.05±0.16	-
G251.2337-01.9535	Jet(C)	-	-	0.26±0.05	-
G254.0491-00.5615	Jet	0.17±0.39	0.42±0.17	0.27±0.17	-

Table B.5: Continued

Name	Type		θ_{\min} (")			
			5.5 GHz	9.0 GHz	17.0 GHz	22.8 GHz
G254.0548-00.0961	C	Jet	0.34±0.30	-	-	-
	W	Lobe	1.91±1.15	-	-	-
G263.2283+01.5712		Jet	-	0.17±0.84	0.46±0.16	-
G263.7434+00.1161	S	Jet	0.67±0.40	0.50±0.15	0.21±0.04	0.19±0.11
	N	Lobe	-	0.36±0.24	-	-
G263.7759-00.4281		Jet	-	-	-	-
	NW	Lobe	-	-	0.34±0.12	-
G265.1438+01.4548		Jet/DW	-	-	0.19±0.17	-
G286.2086+00.1694	B	Jet(C)	-	-	0.65±0.08	0.26±0.15
	B2	Lobe	-	-	-	-
G298.2620+00.7394		DW	1.05±0.57	-	0.26±0.19	0.23±0.13
G310.0135+00.3892	S	Jet	-	-	0.06±0.04	-
	N	Lobe	-	-	-	-
	SW	Lobe	-	-	-	-
G310.1420+00.7583A	A1	Jet	-	0.13±0.03	-	0.09±0.04
	A2	Lobe	-	0.38±0.08	0.13±0.03	0.39±0.13
	A3	Lobe	0.80±0.16	0.28±0.06	-	-
	A4	Lobe	0.75±0.15	0.59±0.12	-	-
	B	Lobe	-	0.27±0.05	0.26±0.05	-
	C	Lobe	0.62±0.16	0.75±0.15	-	-
	D	Lobe	1.10±0.06	1.05±0.21	0.95±0.19	0.23±0.11
G313.7654-00.8620	A1	Jet	-	0.40±0.27	-	-
	A2	Lobe	1.95±0.63	0.42±0.26	-	-
	B1	Lobe	1.31±0.24	0.80±0.35	-	-
	B2	Lobe	-	-	-	-

Table B.5: Continued

Name			θ_{\min} (")			
			5.5 GHz	9.0 GHz	17.0 GHz	22.8 GHz
	C	Lobe	0.19±1.40	0.72±0.18	-	-
	D	Lobe	0.41±0.21	-	-	-
G318.9480-00.1969A		Jet/DW	-	-	-	0.25±0.18
G326.6618+00.5207		Jet(C)	-	-	0.24±0.11	0.10±0.14
G327.1192+00.5103		Jet	-	0.53±0.46	-	-
G331.3576+01.0626		Jet(C)	-	< 0.17	-	0.23±0.16
G332.0939-00.4206	W	Jet	-	-	-	-
	E	Lobe	-	-	-	-
G332.9868-00.4871		Jet(C)	-	-	-	-
G338.9196+00.5495		Jet(C)	-	-	< 0.14	-
G339.6221-00.1209	E	Jet(C)	0.22±0.12	0.20±0.11	-	-
	W	Lobe	-	-	-	-
G339.8838-01.2588	C	Jet	1.55±0.38	0.62±0.18	-	-
	NE	Lobe	0.73±0.11	0.38±0.20	0.30±0.09	0.12±0.22
	SW	Lobe	1.47±0.20	0.85±0.53	-	-
G340.0543-00.2437D	D	Jet(C)	-	-	-	-
G343.1261-00.0623	Cen.	Jet	-	-	0.16±0.05	0.15±0.03
	C	Lobe	-	-	-	0.18±0.20
	N1	Lobe	-	-	0.15±0.30	-
	N2	Lobe	-	-	0.62±0.15	0.32±0.41
	N4	Lobe	-	-	0.35±0.18	0.31±0.15
	S1	Lobe	-	-	0.35±0.06	0.27±0.07
	S3	Lobe	-	-	-	-
G343.5213-00.5171	W	Jet(C)	-	-	0.41±0.08	0.63±0.50
	E	Lobe	-	-	-	-

Table B.5: Continued

Name	Type		θ_{\min} (")			
			5.5 GHz	9.0 GHz	17.0 GHz	22.8 GHz
G345.4938+01.4677	C	Jet	-	-	0.12±0.06	0.13±0.02
	IE	Lobe	-	-	1.25±0.29	-
	IW	Lobe	-	-	0.90±0.15	0.86±0.33
	OE	Lobe	-	-	0.95±0.37	-
	OW	Lobe	-	-	1.51±0.29	-
G345.5043+00.3480		Jet(C)	-	-	0.12±0.09	< 0.04

Table B.6: A table of deconvolved, major-axis position angles and values for γ (power-law index for the relationship between major axis and frequency) of MYSOs in the sample displaying jet-like and/or disc-wind characteristics. Hyphenated entries denote where either the source was not observed, or the source was point-like after deconvolution.

Name	Type	$\theta_{\text{P.A.}}(^{\circ})$				γ
		5.5 GHz	9.0 GHz	17.0 GHz	22.8 GHz	
G010.8411-02.5919	Jet	-	-	1.4 \pm 20.3	7.2 \pm 9.8	-1.45 \pm 0.63
G012.9090-00.2607	Jet(C)	-	-	-	-	-
G014.9958-00.6732	Jet(C)	-	-	9.8 \pm 3.7	-	-
G251.2337-01.9535	Jet(C)	-	-	154.9 \pm 20.0	-	-
G254.0491-00.5615	Jet	169.7 \pm 4.9	3.0 \pm 3.0	164.9 \pm 4.0	-	-0.93 \pm 0.19
G254.0548-00.0961	C Jet	19.4 \pm 3.5	-	-	-	-
	W Lobe	78.0 \pm 165.0	-	-	-	-
G263.2283+01.5712	Jet	-	167.0 \pm 16.0	147.0 \pm 37.0	-	-
G263.7434+00.1161	S Jet	6.6 \pm 10.0	4.7 \pm 4.2	2.5 \pm 2.5	23.0 \pm 51.0	-0.84 \pm 0.16
	N Lobe	-	173.3 \pm 9.9	-	-	-
G263.7759-00.4281	Jet	-	-	-	-	-
	NW Lobe	-	-	141.1 \pm 1.5	-	-
G265.1438+01.4548	Jet/DW	-	-	51.0 \pm 27.0	-	-
G286.2086+00.1694	B Jet(C)	-	-	17.2 \pm 2.7	49.0 \pm 45.0	-0.59 \pm 1.36
	B2 Lobe	-	-	-	-	-

Table B.6: Continued

Name	Type		$\theta_{\text{P.A.}}(^{\circ})$				γ
			5.5 GHz	9.0 GHz	17.0 GHz	22.8 GHz	
G298.2620+00.7394		DW	78±65	-	106±30	103±32	-1.05±0.33
G310.0135+00.3892	S	Jet	-	-	113.8± 3.3	-	-
	N	Lobe	-	-	-	-	-
	SW	Lobe	-	-	-	-	-
G310.1420+00.7583A	A1	Jet	-	86.1±17.2	-	2.4± 0.8	-0.84±0.28
	A2	Lobe	-	85.4±17.1	-36.5± 7.3	25.0±10.0	-0.06±0.26
	A3	Lobe	85.1±17.0	80.6±16.1	-	-	-0.69±0.82
	A4	Lobe	-75.5±15.1	83.4±16.7	-	-	-0.93±0.82
	B	Lobe	-	-85.2±17.0	83.0±16.6	-	1.44±0.64
	C	Lobe	70.4± 1.9	60.4±12.1	-	-	-0.92±0.41
	D	Lobe	105.5± 7.8	-76.7±15.3	-46.0± 9.2	81.6± 5.6	-0.01±0.09
	G313.7654-00.8620	A1	Jet	-	106.0±159.0	-	-
A2		Lobe	24.2± 7.6	168.8± 5.1	-	-	-1.37±0.50
B1		Lobe	137.5± 8.3	128.0±13.0	-	-	-0.78±0.41
B2		Lobe	-	-	-	-	-
C		Lobe	123.0±72.0	98.0±170.0	-	-	-

Table B.6: Continued

Name	Type		$\theta_{\text{P.A.}}(^{\circ})$				γ
			5.5 GHz	9.0 GHz	17.0 GHz	22.8 GHz	
	D	Lobe	5.8± 4.5	-	-	-	-
G318.9480-00.1969A		Jet/DW	-	-	-	77.0±143.0	-
G326.6618+00.5207		Jet(C)	-	-	180.0±52.0	153.0±27.0	-0.07±2.42
G327.1192+00.5103		Jet	-	157.0±36.0	-	-	-
G331.3576+01.0626		Jet(C)	-	-	-	119.0±143.0	-
G332.0939-00.4206	W	Jet	-	-	-	-	-
	E	Lobe	-	-	-	-	-
G332.9868-00.4871		Jet(C)	-	-	-	-	-
G338.9196+00.5495		Jet(C)	-	-	-	-	-
G339.6221-00.1209	E	Jet(C)	7.5± 5.3	177.6±4.5	-	-	-0.33±0.52
	W	Lobe	-	-	-	-	-
G339.8838-01.2588	C	Jet	108.0±157.0	160.0±11.0	-	-	-1.02±0.36
G339.8838-01.2588	NE	Lobe	160.5± 6.4	36.0±50.0	5.8± 9.0	146.0±124.0	-0.59±0.07
	SW	Lobe	171.0± 2.3	160.1± 3.2	-	-	1.12±0.13
G340.0543-00.2437D	D	Jet(C)	-	-	-	-	-1.43±0.66
G343.1261-00.0623	Cen.	Jet	-	-	160.1± 0.8	161.6±20.0	0.16±0.72

Table B.6: Continued

Name	Type		$\theta_{\text{P.A.}}(^{\circ})$				γ
			5.5 GHz	9.0 GHz	17.0 GHz	22.8 GHz	
	C	Lobe	-	-	-	160.0 \pm 20.0	-0.61 \pm 1.82
	N1	Lobe	-	-	132.0 \pm 46.0	-	-
	N2	Lobe	-	-	9.3 \pm 30.9	132.0 \pm 48.0	0.91 \pm 0.90
	N4	Lobe	-	-	171.0 \pm 18.0	44.0 \pm 34.0	-1.48 \pm 1.05
	S1	Lobe	-	-	23.1 \pm 6.0	36.4 \pm 3.8	0.31 \pm 0.26
	S3	Lobe	-	-	-	-	-
G343.5213-00.5171	W	Jet(C)	-	-	-33.0 \pm 30.0	167.0 \pm 35.0	-1.25 \pm 1.65
	E	Lobe	-	-	-	-	-
G345.4938+01.4677	C	Jet	-	-	136.0 \pm 12.0	164.1 \pm 2.7	0.96 \pm 0.35
	IE	Lobe	-	-	145.5 \pm 7.5	-	-
	IW	Lobe	-	-	14.0 \pm 27.0	14.0 \pm 14.0	0.82 \pm 0.52
	OE	Lobe	-	-	175.2 \pm 5.7	-	-
	OW	Lobe	-	-	175.2 \pm 3.6	-	-
G345.5043+00.3480		Jet(C)	-	-	145 \pm 15	-	-

Table B.7: The deconvolved positions for sources of unknown classification.

Name	5.5 GHz				9 GHz			
	α (J2000)	$\Delta\alpha$	δ (J2000)	$\Delta\delta$	α (J2000)	$\Delta\alpha$	δ (J2000)	$\Delta\delta$
G305.2017+00.2072	-	-	-	-	-	-	-	-
G345.9561+00.6123	-	-	-	-	17 ^h 04 ^m 42.99 ^s	0.151	-40°13'14.82''	0.404
17 GHz				22.8 GHz				
G305.2017+00.2072	13 ^h 11 ^m 10.52 ^s	0.045	-62°34'38.70''	0.054	13 ^h 11 ^m 10.51 ^s	0.058	-62°34'38.70''	0.114
G345.9561+00.6123	17 ^h 04 ^m 43.00 ^s	0.134	-40°13'13.82''	0.22	-	-	-	-

Table B.8: Fluxes and spectral indices for sources of unknown classification.

Name	S_ν (mJy)				α
	5.5 GHz	9.0 GHz	17.0 GHz	22.8 GHz	
G305.2017+00.2072		-	0.61±0.16	0.44±0.15	-1.11±1.46
G345.9561+00.6123	< 0.07	0.09±0.03	0.28±0.07	< 0.14	1.78±0.89

Table B.9: Deconvolved sizes and position angles for sources of unknown classification. The 5.5 and 22.8 GHz bands are not listed since they were either not observed or no dimensions could be deconvolved.

Name	θ_{maj} (")		θ_{min} (")		$\theta_{\text{P.A.}}$ (°)		γ
	9.0 GHz	17.0 GHz	9.0 GHz	17.0 GHz	9.0 GHz	17.0 GHz	
G305.2017+00.2072	-	0.64±0.13	-	0.38±0.19	-	145.0±19.0	-
G345.9561+00.6123	1.57±1.98	2.70±1.51	0.39±0.36	0.95±0.48	174±10	168±50	0.85±2.17

Table B.10: A table of the positions, fluxes and deconvolved dimensions of the HII regions in the sample. Their apparent morphologies are given in the second column (B for bipolar, S for spherical, CH for core/halo, I for irregular and C for cometary). Fluxes, positions and dimensions were derived using the IMFIT task in CASA. Asterisked sources are extended and are poorly fitted by the IMFIT task, and their positions represent that of the peak flux at each frequency, their fluxes are those integrated over the 3σ areas of the clean maps and dimensions are their deconvolved sizes as calculated using Equation 2.1.

Name	M	Freq. (GHz)	α (J2000)	$\Delta\alpha$ (")	δ (J2000)	$\Delta\delta$ (")	S_ν (mJy)	$\theta_{\text{Maj.}}$ (")	$\theta_{\text{Min.}}$ (")
G274.0649-01.1460A	B	17.0	09 ^h 24 ^m 42.53 ^s	0.021	-52°01'51.00"	0.027	2.5 ± 0.2	0.84 ± 0.06	0.08 ± 0.44
		22.8	09 ^h 24 ^m 42.52 ^s	0.011	-52°01'50.71"	0.020	3.1 ± 0.2	0.49 ± 0.02	0.11 ± 0.04
G284.2438-01.1302	S	5.5	10 ^h 20 ^m 35.17 ^s	0.028	-58°25'07.06"	0.021	1.6 ± 0.1	2.05 ± 0.08	1.51 ± 0.08
		9.0	10 ^h 20 ^m 35.24 ^s	0.119	-58°25'07.54"	0.065	1.3 ± 0.1	2.54 ± 0.22	1.36 ± 0.66

Table B.10: Continued

Name	M	Freq. (GHz)	α (J2000)	$\Delta\alpha$ (")	δ (J2000)	$\Delta\delta$ (")	S_ν (mJy)	$\theta_{\text{Maj.}}$ (")	$\theta_{\text{Min.}}$ (")
		17.0	10 ^h 20 ^m 35.13 ^s	0.035	-58°25'06.88"	0.053	0.9 ± 0.1	1.48 ± 0.08	0.83 ± 0.13
		22.8	10 ^h 20 ^m 35.18 ^s	0.079	-58°25'06.57"	0.129	0.5 ± 0.2	< 2.15	< 0.38
G287.3716+00.6444 *	S	5.5	10 ^h 48 ^m 04.68 ^s	0.018	-58°27'02.22"	0.016	3.7 ± 0.1	1.63 ± 0.10	1.16 ± 0.14
		9.0	10 ^h 48 ^m 04.68 ^s	0.017	-58°27'02.23"	0.014	3.1 ± 0.1	1.35 ± 0.05	1.21 ± 0.06
		17.0	10 ^h 48 ^m 04.70 ^s	0.050	-58°27'01.90"	0.050	1.7 ± 0.1	1.54 ± 0.52	1.07 ± 0.49
		22.8	10 ^h 48 ^m 04.71 ^s	0.055	-58°27'02.15"	0.072	1.7 ± 0.4	1.09 ± 0.16	0.56 ± 0.19
G300.9674+01.1499 *	S	17.0	12 ^h 34 ^m 53.24 ^s	0.050	-61°39'39.98"	0.050	519 ± 39	0.57 ± 0.01	0.51 ± 0.01
		22.8	12 ^h 34 ^m 53.24 ^s	0.030	-61°39'39.88"	0.030	528 ± 28	0.57 ± 0.01	0.55 ± 0.01
G301.1364-00.2249	B	17.0	12 ^h 35 ^m 35.10 ^s	0.002	-63°02'31.89"	0.001	812 ± 5	0.67 ± 0.01	0.36 ± 0.01
		22.8	12 ^h 35 ^m 35.09 ^s	0.001	-63°02'31.88"	0.001	1100 ± 5	0.63 ± 0.01	0.36 ± 0.01
G305.5610+00.0124	CH	17.0	13 ^h 14 ^m 26.39 ^s	0.010	-62°44'30.30"	0.012	4.2 ± 0.2	0.42 ± 0.03	0.11 ± 0.22
		22.8	13 ^h 14 ^m 26.39 ^s	0.005	-62°44'30.29"	0.006	4.2 ± 0.2	< 0.23	< 0.05
G308.9176+00.1231A *	I	17.0	13 ^h 43 ^m 01.73 ^s	0.040	-62°08'55.28"	0.040	158 ± 2	3.19 ± 0.03	1.27 ± 0.03
		22.8	13 ^h 43 ^m 01.72 ^s	0.040	-62°08'55.12"	0.040	80.5 ± 1.2	3.49 ± 0.08	1.35 ± 0.06
G317.4298-00.5612	B	5.5	14 ^h 51 ^m 37.63 ^s	0.002	-60°00'20.68"	0.003	15.2 ± 0.3	0.77 ± 0.02	0.41 ± 0.03
		9.0	14 ^h 51 ^m 37.62 ^s	0.001	-60°00'20.66"	0.001	24.1 ± 0.1	0.45 ± 0.01	0.27 ± 0.01
G317.8908-00.0578	S	17.0	14 ^h 53 ^m 06.27 ^s	0.002	-59°21'00.00"	0.005	15.7 ± 0.2	0.47 ± 0.01	0.38 ± 0.02

Table B.10: Continued

Name	M	Freq. (GHz)	α (J2000)	$\Delta\alpha$ (")	δ (J2000)	$\Delta\delta$ (")	S_ν (mJy)	$\theta_{\text{Maj.}}$ (")	$\theta_{\text{Min.}}$ (")
		22.8	14 ^h 53 ^m 06.27 ^s	0.003	−59°21′00.28″	0.005	12.8 ± 0.2	0.44 ± 0.01	0.27 ± 0.02
G331.5414-00.0675	S	5.5	16 ^h 12 ^m 09.02 ^s	0.019	−51°25′47.65″	0.017	169 ± 4	1.08 ± 0.07	0.74 ± 0.09
		9.0	16 ^h 12 ^m 09.01 ^s	0.003	−51°25′47.81″	0.003	206 ± 1	0.77 ± 0.01	0.43 ± 0.02
G332.8256-00.5498A *	C	5.5	16 ^h 20 ^m 11.06 ^s	0.200	−50°53′16.20″	0.200	2490 ± 89	4.37 ± 0.14	3.67 ± 0.08
		9.0	16 ^h 20 ^m 11.06 ^s	0.100	−50°53′13.80″	0.100	3440 ± 67	3.42 ± 0.12	3.17 ± 0.04
		17.0	16 ^h 20 ^m 11.04 ^s	0.040	−50°53′13.56″	0.040	4090 ± 68	4.63 ± 0.28	2.98 ± 0.14
		22.8	16 ^h 20 ^m 11.06 ^s	0.040	−50°53′13.48″	0.040	4320 ± 58	3.19 ± 0.06	2.84 ± 0.06
G337.8442-00.3748	S	17.0	16 ^h 40 ^m 26.67 ^s	0.001	−47°07′13.11″	0.002	42.7 ± 0.1	0.23 ± 0.01	0.18 ± 0.01
		22.8	16 ^h 40 ^m 26.66 ^s	0.001	−47°07′13.02″	0.003	43.9 ± 0.3	0.23 ± 0.01	0.19 ± 0.01
G340.2480-00.3725 *	S	17.0	16 ^h 49 ^m 30.06 ^s	0.060	−45°17′44.75″	0.060	210 ± 19	0.70 ± 0.01	0.63 ± 0.02
		22.8	16 ^h 49 ^m 30.06 ^s	0.040	−45°17′44.73″	0.040	442 ± 41	0.65 ± 0.01	0.43 ± 0.01
G348.6972-01.0263 *	S	5.5	17 ^h 19 ^m 58.91 ^s	0.200	−38°58′15.22″	0.200	1830 ± 156	4.75 ± 0.06	3.40 ± 0.03
		9.0	17 ^h 19 ^m 58.88 ^s	0.150	−38°58′15.10″	0.150	2020 ± 154	3.63 ± 0.03	2.90 ± 0.04

Table B.11: A table of derived properties for the jets and ambiguous jet/disc wind sources. The 4th column shows whether the distance-luminosities have been extrapolated from data at other frequencies with derived spectral indices. The 6th column shows the infrared flux (from MSX) ratio between 21 μm and 8 μm , expressed logarithmically. Calculated mass loss rate is displayed in the final column. In the cases where an opening angle could not be calculated, a value of $\theta = 40 \pm 20^\circ$ was adopted.

Name	Type	$S_{9\text{GHz}}D^2$ (mJy kpc ²)	E?	M_{Clump} (M_\odot)	$\log \frac{S_{21\ \mu\text{m}}}{S_8\ \mu\text{m}}$	\dot{M}_{Jet} ($\times 10^{-6} M_\odot \text{km s}^{-1} \text{yr}^{-1}$)
Jets						
G010.8411-02.5919	Jet	$(9.30 \pm 0.62) \times 10^0$	Y	-	1.20	12.30 ± 8.04
G012.9090-00.2607	Jet(C)	$(8.01 \pm 1.73) \times 10^0$	Y	$(3.18 \pm 0.49) \times 10^3$	0.96	1.07 ± 2.46
G014.9958-00.6732	Jet(C)	$(1.22 \pm 0.30) \times 10^0$	Y	$(6.98 \pm 1.05) \times 10^3$	0.60	8.08 ± 20.72
G251.2337-01.9535	Jet(C)	$(1.19 \pm 0.05) \times 10^1$	N	-	0.86	2.79 ± 1.33
G254.0491-00.5615	Jet	$(1.69 \pm 0.15) \times 10^{-1}$	N	-	1.07	4.10 ± 3.04
G254.0548-00.0961C	Jet(L)	$(2.86 \pm 0.71) \times 10^0$	N	-	1.20	1.11 ± 1.26
G263.2283+01.5712	Jet	$(2.86 \pm 0.09) \times 10^{-1}$	N	-	0.97	0.33 ± 0.32
G263.7434+00.1161S	Jet(L)	$(4.26 \pm 0.18) \times 10^{-1}$	N	-	0.48	0.32 ± 0.20
G263.7759-00.4281	Jet(L)	$(5.98 \pm 1.07) \times 10^{-1}$	Y	-	0.94	0.67 ± 0.70
G286.2086+00.1694B	Jet(L,C)	$(3.90 \pm 1.45) \times 10^0$	Y	$(1.30 \pm 0.20) \times 10^3$	1.48	11.37 ± 13.01
G310.0135+00.3892S	Jet(L)	$(4.27 \pm 0.81) \times 10^0$	N	$(1.19 \pm 0.19) \times 10^3$	0.55	17.92 ± 13.38
G310.1420+00.7583A	Jet(L)	$(3.99 \pm 0.32) \times 10^1$	N	$(2.28 \pm 0.39) \times 10^3$	0.92	5.57 ± 3.84

Table B.11: Continued

Name	Type	$S_{9\text{GHz}}D^2$ (mJy kpc ²)	E?	M_{Clump} (M_{\odot})	$\log \frac{S_{21\ \mu\text{m}}}{S_{8\ \mu\text{m}}}$	\dot{M}_{Jet} ($\times 10^{-6} M_{\odot} \text{km s}^{-1} \text{yr}^{-1}$)
G313.7654-00.8620	Jet(L)	$(3.56 \pm 0.10) \times 10^1$	N	$(6.45 \pm 1.06) \times 10^3$	0.97	20.53 ± 11.39
G326.6618+00.5207	Jet(C)	$(1.28 \pm 0.35) \times 10^0$	Y	$(2.66 \pm 0.45) \times 10^2$	0.93	2.96 ± 3.25
G327.1192+00.5103	Jet	$(1.12 \pm 0.12) \times 10^1$	N	$(1.73 \pm 0.30) \times 10^3$	1.13	2.64 ± 2.10
G331.3576+01.0626	Jet(C)	$(5.26 \pm 0.47) \times 10^1$	N	$(1.95 \pm 0.32) \times 10^3$	0.50	38.38 ± 21.78
G332.0939-00.4206W	Jet(L)	$(1.59 \pm 0.08) \times 10^1$	N	$(2.41 \pm 0.40) \times 10^3$	0.33	43.89 ± 30.77
G332.9868-00.4871	Jet(C)	$(5.03 \pm 0.12) \times 10^1$	N	$(5.10 \pm 0.81) \times 10^3$	0.96	63.54 ± 45.69
G338.9196+00.5495	Jet(C)	$(3.69 \pm 0.60) \times 10^0$	N	$(1.21 \pm 0.19) \times 10^4$	1.88	4.02 ± 3.71
G339.6221-00.1209E	Jet(L)	$(1.24 \pm 0.04) \times 10^1$	N	$(8.74 \pm 1.48) \times 10^2$	0.84	5.78 ± 3.85
G339.8838-01.2588C	Jet(L)	$(1.15 \pm 0.04) \times 10^1$	N	$(1.95 \pm 0.32) \times 10^3$	1.59	26.53 ± 14.47
G340.0543-00.2437D	Jet(C)	$(3.15 \pm 0.79) \times 10^1$	N	$(4.43 \pm 0.71) \times 10^3$	1.45	8.12 ± 16.38
G343.1261-00.0623	Jet(L)	$(1.42 \pm 0.10) \times 10^2$	Y	$(2.94 \pm 0.47) \times 10^3$	1.51	17.50 ± 9.66
G343.5213-00.5171W	Jet(L,C)	$(5.84 \pm 0.77) \times 10^0$	N	$(1.16 \pm 0.20) \times 10^3$	1.47	2.38 ± 1.34
G345.4938+01.4677C	Jet(L)	$(4.84 \pm 0.10) \times 10^1$	Y	$(4.54 \pm 0.71) \times 10^3$	1.20	60.39 ± 32.10
G345.5043+00.3480	Jet(C)	$(6.20 \pm 1.20) \times 10^0$	N	$(3.03 \pm 0.48) \times 10^3$	1.04	13.56 ± 10.28
Jets/DWs						
G265.1438+01.4548	Jet/DW	$(2.07 \pm 0.73) \times 10^{-1}$	Y	-	0.83	0.47 ± 0.84

Table B.11: Continued

Name	Type	$S_{9\text{GHz}}D^2$ (mJy kpc ²)	E?	M_{Clump} (M_{\odot})	$\log \frac{S_{21\mu\text{m}}}{S_{8\mu\text{m}}}$	\dot{M}_{Jet} ($\times 10^{-6} M_{\odot} \text{km s}^{-1} \text{yr}^{-1}$)
G298.2620+00.7394	DW	$(2.96 \pm 0.29) \times 10^0$	N	$(6.76 \pm 1.25) \times 10^2$	1.68	11.02 ± 7.09
G318.9480-00.1969A	Jet/DW	$(5.59 \pm 0.75) \times 10^{-1}$	N	$(6.38 \pm 1.05) \times 10^2$	1.01	2.98 ± 2.37

Table B.12: A table of derived properties for HII regions. The fourth column (‘E’) denotes whether the flux (and hence $S_{9\text{GHz}}D^2$) has been directly measured at 9 GHz or extrapolated from the upper two frequencies (assuming a simple power law). The final column shows how the emission measures for the HII regions have been derived. If the row’s value is ‘M’, this indicates the data across all frequencies has been fitted with a model of an homogeneous HII region, and an emission measure has been inferred from the fit. If a frequency is shown, this is the frequency used to calculate the emission measure, assuming the ionized gas is not opaque to its own emission. If the type is given as ‘HCHII core’, this denotes that the properties derived are of the compact component located within the extended emission.

Name	Type	$S_{9\text{GHz}}D^2$ (mJy kpc ²)	E	M_{Clump} (M_{\odot})	$\log \frac{S_{21\mu\text{m}}}{S_{8\mu\text{m}}}$	Radius (pc)	EM (pc cm ⁻⁶)	M
G274.0649-01.1460A	CHII	$(4.77 \pm 0.96) \times 10^1$	Y	-	1.36	0.209 ± 0.010	$(5.70 \pm 0.60) \times 10^7$	5.5
G274.0649-01.1460	HCHII Core	$(2.15 \pm 0.05) \times 10^3$	N	-	1.36	0.009 ± 0.001	$(3.07 \pm 0.40) \times 10^7$	22.8
G284.2438-01.1302	CHII	$(2.26 \pm 0.16) \times 10^1$	N	-	0.97	0.037 ± 0.002	$(2.28 \pm 0.26) \times 10^5$	5.5

Table B.12: Continued

Name	Type	$S_{9\text{GHz}}D^2$ (mJy kpc ²)	E	M_{Clump} (M_{\odot})	$\log \frac{S_{21\mu\text{m}}}{S_{8\mu\text{m}}}$	Radius (pc)	EM (pc cm ⁻⁶)	M
G287.3716+00.6444	CHII	$(6.60 \pm 0.77) \times 10^1$	N	$(3.82 \pm 0.85) \times 10^2$	0.77	0.030 ± 0.002	$(8.99 \pm 1.89) \times 10^5$	5.5
G300.9674+01.1499	UCHII	$(9.23 \pm 1.67) \times 10^3$	Y	$(4.89 \pm 0.76) \times 10^3$	1.11	0.041 ± 0.005	$(1.02 \pm 0.32) \times 10^8$	M
G301.1364-00.2249N	UCHII	$(3.02 \pm 0.26) \times 10^3$	Y	$(5.98 \pm 0.93) \times 10^3$	1.93	0.029 ± 0.002	$(7.91 \pm 1.29) \times 10^7$	M
G301.1364-00.2249S	HCHII	$(7.81 \pm 0.13) \times 10^3$	Y	$(5.98 \pm 0.93) \times 10^3$	1.93	0.019 ± 0.001	$(1.19 \pm 0.17) \times 10^9$	M
G305.5610+00.0124C	HCHII	$(6.61 \pm 0.92) \times 10^1$	Y	$(2.42 \pm 0.39) \times 10^3$	0.93	< 0.004	> 4.28×10^8	22.8
	Core							
G308.9176+00.1231A	UCHII	$(1.44 \pm 0.08) \times 10^3$	Y	$(2.68 \pm 0.45) \times 10^3$	0.46	0.063 ± 0.001	$(1.94 \pm 0.20) \times 10^7$	17
G317.4298-00.5612	HCHII	$(4.86 \pm 0.01) \times 10^3$	N	$(8.71 \pm 1.60) \times 10^3$	0.76	0.017 ± 0.001	$(5.57 \pm 0.59) \times 10^8$	9
	Core							
G317.4298-00.5612 (SE)	Class. HII	$(4.86 \pm 0.01) \times 10^3$	N	$(8.71 \pm 1.60) \times 10^3$	0.76	0.599 ± 0.004	$(5.57 \pm 0.58) \times 10^8$	5.5
G317.8908-00.0578	UCHII	$(4.50 \pm 0.18) \times 10^3$	Y	$(6.23 \pm 1.19) \times 10^3$	0.99	0.028 ± 0.001	$(4.50 \pm 0.47) \times 10^7$	17
G331.5414-00.0675	UCHII	$(5.15 \pm 0.02) \times 10^3$	N	$(8.97 \pm 1.39) \times 10^3$	1.26	0.015 ± 0.001	$(8.74 \pm 1.17) \times 10^8$	9
G332.8256-00.5498A	UCHII	$(4.46 \pm 0.09) \times 10^4$	N	$(1.01 \pm 0.16) \times 10^4$	1.50	0.073 ± 0.009	$(1.82 \pm 0.53) \times 10^8$	M
G337.8442-00.3748	HCHII	$(3.60 \pm 0.05) \times 10^2$	Y	$(5.04 \pm 0.92) \times 10^2$	0.75	0.004 ± 0.001	$(6.05 \pm 0.53) \times 10^8$	M
G340.2480-00.3725	UCHII	$(3.51 \pm 0.86) \times 10^3$	Y	$(4.76 \pm 0.76) \times 10^3$	1.13	0.022 ± 0.003	$(8.84 \pm 3.59) \times 10^7$	M
G348.6972-01.0263	UCHII	$(1.70 \pm 0.04) \times 10^4$	N	$(2.06 \pm 0.33) \times 10^3$	1.46	0.035 ± 0.002	$(2.48 \pm 0.30) \times 10^8$	9

Table B.13: A table of properties for the additional sources detected in the primary beams (to the 20% level) of both 5.5 and 9.0 GHz images (except for G254.0819-00.5614A/B which were observed at 17 and 22.8 GHz). Names of the sources are either inferred from their galactic positions, or are the names of the sources given in the RMS survey (if present in the database). The second column shows the morphology for the sources (G for gaussian/compact and E for extended), which determined how fluxes and positions (at 9 GHz) were deduced. In the case of the Gaussian sources, position and fluxes were determined through the deconvolution of the source, by a Gaussian, in the image plane. For the extended sources, fluxes were determined by integrating over the 3σ areas, while the positions are for the peak pixel in the source's flux distribution. All images were corrected for the primary beam at each frequency.

Name	M	α (J2000)	$\Delta\alpha$ (")	δ (J2000)	$\Delta\delta$ (")	$S_{5.5\text{GHz}}$ (mJy)	$S_{9\text{GHz}}$ (mJy)	α
G251.2301-01.9918	G	08 ^h 02 ^m 33.12 ^s	0.011	-34°32'50.95''	0.027	2.28 ± 0.03	1.44 ± 0.05	-0.9 ± 0.2
G251.2414-01.9315	G	08 ^h 02 ^m 49.78 ^s	0.041	-34°31'30.35''	0.104	0.38 ± 0.02	0.22 ± 0.04	-1.1 ± 0.9
G254.0311-00.5793	G	08 ^h 15 ^m 49.78 ^s	0.058	-36°07'49.93''	0.131	0.25 ± 0.04	0.20 ± 0.02	-0.5 ± 0.8
G254.0364-00.5363	G	08 ^h 16 ^m 01.26 ^s	0.091	-36°06'39.52''	0.220	0.20 ± 0.03	< 0.09	< -1.6
G254.0819-00.5614A	G	08 ^h 16 ^m 02.61 ^s	0.015	-36°09'45.76''	0.035	0.86 ± 0.02	1.00 ± 0.03	0.3 ± 0.2
G254.0819-00.5614B	G	08 ^h 16 ^m 02.76 ^s	0.060	-36°09'46.82''	0.145	0.49 ± 0.05	0.71 ± 0.16	0.8 ± 1.1
G254.1113-00.1012	G	08 ^h 18 ^m 00.71 ^s	0.008	-35°55'46.24''	0.018	8.17 ± 0.04	4.59 ± 0.07	-1.2 ± 0.1
G263.7696+00.1347	G	08 ^h 48 ^m 58.97 ^s	0.003	-43°32'59.94''	0.005	14.70 ± 0.08	11.00 ± 0.06	-0.6 ± 0.1
G286.2074+00.1698A*	G	10 ^h 38 ^m 32.16 ^s	0.023	-58°19'08.52''	0.028	1.27 ± 0.10	1.89 ± 0.32	1.4 ± 1.5
G286.2074+00.1698B*	G	10 ^h 38 ^m 32.32 ^s	0.035	-58°19'08.75''	0.043	0.35 ± 0.04	< 0.31	< -0.4

Table B.13: Continued

Name	M	α (J2000)	$\Delta\alpha$ (")	δ (J2000)	$\Delta\delta$ (")	$S_{5.5\text{GHz}}$ (mJy)	$S_{9\text{GHz}}$ (mJy)	α
G287.3277+00.6608A	G	10 ^h 47 ^m 50.17 ^s	0.093	-58°24'56.27''	0.076	1.35 ± 0.05	0.99 ± 0.13	-0.6 ± 0.6
G287.3277+00.6608B	G	10 ^h 47 ^m 50.60 ^s	0.138	-58°24'53.73''	0.112	1.06 ± 0.06	0.77 ± 0.15	-0.7 ± 0.9
G287.4170+00.6473	G	10 ^h 48 ^m 23.77 ^s	0.053	-58°28'06.08''	0.043	0.76 ± 0.04	0.58 ± 0.04	-0.6 ± 0.4
G298.2481+00.7261	G	12 ^h 11 ^m 39.59 ^s	0.096	-61°47'00.04''	0.066	0.21 ± 0.02	0.18 ± 0.04	-0.2 ± 1.0
G298.2718+00.7520	G	12 ^h 11 ^m 53.49 ^s	0.022	-61°45'41.17''	0.015	0.94 ± 0.02	0.84 ± 0.02	-0.2 ± 0.2
G298.2744+00.7082	G	12 ^h 11 ^m 51.42 ^s	0.023	-61°48'18.26''	0.016	1.00 ± 0.02	0.89 ± 0.04	-0.2 ± 0.2
G305.3474-01.9987	G	13 ^h 14 ^m 07.01 ^s	0.100	-64°45'50.63''	0.100	9.71 ± 0.12	4.97 ± 0.04	-1.4 ± 0.1
G305.5367+00.0136	G	13 ^h 14 ^m 13.06 ^s	0.023	-62°44'34.53''	0.024	1.35 ± 0.06	1.41 ± 0.06	0.1 ± 0.3
G305.5528-00.0109	E	13 ^h 14 ^m 22.81 ^s	0.100	-62°46'00.17''	0.100	22.05 ± 0.80	16.90 ± 0.26	-0.6 ± 0.2
G309.9977+00.3960	G	13 ^h 51 ^m 29.28 ^s	0.053	-61°38'57.17''	0.057	0.28 ± 0.02	0.20 ± 0.02	-0.7 ± 0.5
G310.1380+00.7641	G	13 ^h 51 ^m 55.08 ^s	0.019	-61°15'31.16''	0.024	0.43 ± 0.02	0.39 ± 0.02	-0.2 ± 0.2
G310.1501+00.7313	G	13 ^h 52 ^m 04.74 ^s	0.056	-61°17'15.69''	0.071	0.24 ± 0.02	0.14 ± 0.02	-1.1 ± 0.6
G313.7293-00.8291	G	14 ^h 24 ^m 37.80 ^s	0.078	-61°43'53.37''	0.094	0.27 ± 0.02	0.20 ± 0.03	-0.6 ± 0.8
G313.7365-00.9279	G	14 ^h 24 ^m 58.93 ^s	0.063	-61°49'17.22''	0.076	0.95 ± 0.02	0.94 ± 0.10	-0.0 ± 0.5
G313.7514-00.8978	G	14 ^h 25 ^m 00.58 ^s	0.060	-61°47'17.03''	0.072	0.36 ± 0.03	0.31 ± 0.03	-0.3 ± 0.7
G313.7551-00.8195	G	14 ^h 24 ^m 48.30 ^s	0.087	-61°42'48.42''	0.104	0.28 ± 0.03	0.20 ± 0.03	-0.6 ± 0.9
G313.7628-00.9283	G	14 ^h 25 ^m 11.48 ^s	0.010	-61°48'45.14''	0.013	3.35 ± 0.03	4.51 ± 0.08	0.6 ± 0.1

Table B.13: Continued

Name	M	α (J2000)	$\Delta\alpha$ (")	δ (J2000)	$\Delta\delta$ (")	$S_{5.5\text{GHz}}$ (mJy)	$S_{9\text{GHz}}$ (mJy)	α
G317.4713-00.6210	G	14 ^h 52 ^m 08.82 ^s	0.046	-60°02'25.59''	0.068	2.47 ± 0.03	1.31 ± 0.12	-1.3 ± 0.4
G317.4745-00.5843	G	14 ^h 52 ^m 02.32 ^s	0.072	-60°00'22.27''	0.107	0.44 ± 0.03	0.63 ± 0.09	0.7 ± 0.8
G318.9238-00.1639	G	15 ^h 00 ^m 38.40 ^s	0.006	-58°57'51.90''	0.009	18.80 ± 0.24	7.07 ± 0.09	-2.0 ± 0.1
G318.9490-00.2321	G	15 ^h 01 ^m 03.84 ^s	0.008	-59°00'44.71''	0.011	3.03 ± 0.03	1.70 ± 0.03	-1.2 ± 0.1
G327.1052+00.5612	G	15 ^h 47 ^m 15.45 ^s	0.019	-53°50'47.84''	0.025	2.59 ± 0.04	1.56 ± 0.06	-1.0 ± 0.2
G327.1070+00.4933	G	15 ^h 47 ^m 33.11 ^s	0.010	-53°53'56.18''	0.013	2.36 ± 0.03	1.39 ± 0.03	-1.1 ± 0.1
G327.1160+00.4966	G	15 ^h 47 ^m 35.15 ^s	0.030	-53°53'26.52''	0.040	0.45 ± 0.02	0.46 ± 0.03	0.0 ± 0.4
G327.1306+00.5258	G	15 ^h 47 ^m 32.48 ^s	0.001	-53°51'31.69''	0.002	21.60 ± 0.05	18.40 ± 0.05	-0.3 ± 0.1
G327.1761+00.5137	G	15 ^h 47 ^m 50.05 ^s	0.003	-53°50'24.45''	0.005	20.30 ± 0.06	19.80 ± 0.14	-0.1 ± 0.1
G331.3546+01.0638	E	16 ^h 06 ^m 23.25 ^s	0.100	-50°43'28.83''	0.100	78.10 ± 0.69	86.20 ± 3.21	0.2 ± 0.2
G331.5131-00.1020	G	16 ^h 12 ^m 09.99 ^s	0.006	-51°28'37.67''	0.005	128.00 ± 2.20	170.00 ± 1.20	0.6 ± 0.1
G331.5582-00.1206	G	16 ^h 12 ^m 27.27 ^s	0.031	-51°27'32.64''	0.026	164.00 ± 8.50	103.00 ± 4.00	-0.9 ± 0.3
G331.5717-00.0498	G	16 ^h 12 ^m 12.90 ^s	0.124	-51°23'51.40''	0.104	7.41 ± 0.98	3.33 ± 0.51	-1.6 ± 0.9
G332.0625-00.4061	G	16 ^h 16 ^m 03.96 ^s	0.012	-51°19'05.31''	0.018	2.23 ± 0.09	1.93 ± 0.05	-0.3 ± 0.2
G333.0145-00.4438	E	16 ^h 20 ^m 33.19 ^s	0.150	-50°40'41.26''	0.150	101.00 ± 14.50	101.00 ± 4.12	0.0 ± 0.7
G338.9145+00.5470	G	16 ^h 40 ^m 33.58 ^s	0.038	-45°42'28.12''	0.084	3.44 ± 0.16	3.35 ± 0.26	-0.1 ± 0.4
G338.9195+00.5566	G	16 ^h 40 ^m 32.24 ^s	0.055	-45°41'51.92''	0.123	0.80 ± 0.07	0.81 ± 0.09	0.0 ± 0.7

Table B.13: Continued

Name	M	α (J2000)	$\Delta\alpha$ (")	δ (J2000)	$\Delta\delta$ (")	$S_{5.5\text{GHz}}$ (mJy)	$S_{9\text{GHz}}$ (mJy)	α
G338.9217+00.6233	E	16 ^h 40 ^m 15.52 ^s	0.150	−45°39′02.91″	0.150	214.00 ± 5.15	249.00 ± 5.75	0.3 ± 0.2
G338.9237+00.5618	G	16 ^h 40 ^m 31.90 ^s	0.066	−45°41′25.09″	0.146	1.55 ± 0.20	2.76 ± 0.38	1.2 ± 0.9
G338.9249+00.5563	G	16 ^h 40 ^m 33.55 ^s	0.018	−45°41′37.82″	0.040	1.35 ± 0.10	1.81 ± 0.07	0.6 ± 0.4
G338.9313+00.5296	G	16 ^h 40 ^m 41.90 ^s	0.045	−45°42′24.54″	0.101	0.74 ± 0.07	0.76 ± 0.07	0.1 ± 0.6
G339.5664-00.0866	G	16 ^h 45 ^m 44.61 ^s	0.007	−45°37′55.78″	0.014	24.60 ± 0.26	20.50 ± 0.34	−0.4 ± 0.1
G339.5878-00.0796	G	16 ^h 45 ^m 47.67 ^s	0.053	−45°36′41.25″	0.100	0.94 ± 0.08	0.55 ± 0.06	−1.1 ± 0.7
G339.6197-00.0994	G	16 ^h 45 ^m 59.96 ^s	0.020	−45°36′00.43″	0.038	0.72 ± 0.04	0.72 ± 0.03	0.0 ± 0.3
G339.6534-00.1602	G	16 ^h 46 ^m 23.31 ^s	0.061	−45°36′50.46″	0.115	0.93 ± 0.08	0.76 ± 0.10	−0.4 ± 0.8
G339.9059-01.2753	G	16 ^h 52 ^m 13.90 ^s	0.062	−46°08′11.26″	0.135	0.24 ± 0.07	0.26 ± 0.03	0.2 ± 1.4
G343.4717-00.5152	G	17 ^h 01 ^m 23.46 ^s	0.019	−42°52′36.32″	0.035	1.81 ± 0.03	1.24 ± 0.05	−0.8 ± 0.2
G343.5530-00.4503	G	17 ^h 01 ^m 23.03 ^s	0.024	−42°46′21.81″	0.045	17.10 ± 0.24	13.00 ± 0.61	−0.6 ± 0.2
G343.5539-00.4565	G	17 ^h 01 ^m 24.81 ^s	0.046	−42°46′33.02″	0.087	8.88 ± 0.27	6.39 ± 0.58	−0.7 ± 0.5
G345.4881+00.3148	E	17 ^h 04 ^m 28.04 ^s	0.100	−40°46′24.84″	0.100	2330.00 ± 31.40	1690.00 ± 51.90	−0.7 ± 0.2

Table B.14: A table of lobe positions, integrated fluxes and deconvolved dimensions at 6 GHz for the 2014 epoch. The final column indicates which robustness was employed in the clean map. Those components with a ¹ above their name are extended and therefore their peak flux positions are given, whose errors cover half of their 3σ spatial extent. Their provided fluxes are integrated over the 3σ contours.

Source	Lobe	α (J2000)	$\delta\alpha$ ($''$)	δ (J2000)	$\delta\delta$ ($''$)	S_6 (μJy)	θ_{Maj} ($''$)	θ_{Min} ($''$)	θ_{PA} ($^\circ$)	R
G263.7434+00.1161	N	08 ^h 48 ^m 48.48 ^s	0.005	-43°32'23.9 $''$	0.027	626 ± 43	1.40 ± 0.19	0.50 ± 0.03	177.1 ± 3.6	0.5
	S2	08 ^h 48 ^m 48.63 ^s	0.009	-43°32'57.7 $''$	0.050	319 ± 28	1.13 ± 0.49	0.35 ± 0.17	168.0 ± 21.0	0.5
	S	08 ^h 48 ^m 48.65 ^s	0.004	-43°32'28.5 $''$	0.029	767 ± 52	2.24 ± 0.13	0.62 ± 0.05	5.9 ± 2.0	0.5
	SE	08 ^h 48 ^m 48.83 ^s	0.035	-43°32'33.4 $''$	0.365	126 ± 22	5.18 ± 1.09	0.64 ± 0.23	178.7 ± 2.7	0.5
G310.0135+00.3892	N	13 ^h 51 ^m 37.87 ^s	0.005	-61°39'06.2 $''$	0.009	707 ± 53	0.28 ± 0.07	0.15 ± 0.12	87.0 ± 75.0	-1
	S	13 ^h 51 ^m 37.87 ^s	0.013	-61°39'07.7 $''$	0.022	347 ± 37	0.50 ± 0.16	0.35 ± 0.20	155.0 ± 89.0	-1
	SW	13 ^h 51 ^m 37.73 ^s	0.135	-61°39'09.3 $''$	0.168	126 ± 35	< 2.60	< 0.51	-	-1
	HH0*	13 ^h 51 ^m 41.84 ^s	2.4	-61°38'18.7 $''$	3.3	145 ± 19	-	-	-	0.5
	HH1*	13 ^h 51 ^m 48.13 ^s	2.7	-61°36'46.2 $''$	3.2	422 ± 48	-	-	-	0.5
	HH2*	13 ^h 51 ^m 55.35 ^s	1.6	-61°35'38.6 $''$	1.8	121 ± 21	-	-	-	0.5
G310.1420+00.7583A	A1+A2	13 ^h 51 ^m 58.33 ^s	0.004	-61°15'41.2 $''$	0.006	2744 ± 177	0.84 ± 0.03	0.55 ± 0.05	62.6 ± 5.4	-1
	A3	13 ^h 51 ^m 58.18 ^s	0.006	-61°15'41.7 $''$	0.010	2053 ± 144	1.09 ± 0.04	0.42 ± 0.06	37.5 ± 3.1	-1
	A4	13 ^h 51 ^m 57.96 ^s	0.011	-61°15'42.0 $''$	0.021	888 ± 83	0.93 ± 0.10	0.43 ± 0.15	37.8 ± 9.6	-1
	B	13 ^h 51 ^m 58.70 ^s	0.027	-61°15'41.0 $''$	0.102	369 ± 51	2.24 ± 0.36	0.71 ± 0.21	175.8 ± 6.6	0.5

Table B.14: Continued

Source	Lobe	α (J2000)	$\delta\alpha$ (")	δ (J2000)	$\delta\delta$ (")	S_6 (μ Jy)	θ_{Maj} (")	θ_{Min} (")	θ_{PA} ($^\circ$)	R
G313.7654–00.8620	C	13 ^h 51 ^m 59.12 ^s	0.018	–61 $^\circ$ 15'40.0''	0.020	1508 \pm 115	1.91 \pm 0.09	1.09 \pm 0.18	80.7 \pm 5.8	0.5
	D	13 ^h 51 ^m 59.55 ^s	0.006	–61 $^\circ$ 15'40.1''	0.011	2474 \pm 157	1.31 \pm 0.05	1.15 \pm 0.07	136.0 \pm 16.0	0.5
	A1	14 ^h 25 ^m 01.59 ^s	0.012	–61 $^\circ$ 44'57.9''	0.024	338 \pm 30	–	–	–	0.5
	A2	14 ^h 25 ^m 01.69 ^s	0.076	–61 $^\circ$ 44'58.2''	0.064	426 \pm 47	3.42 \pm 0.28	0.70 \pm 0.28	122.6 \pm 3.1	0.5
	B1	14 ^h 25 ^m 01.10 ^s	0.044	–61 $^\circ$ 44'56.0''	0.043	231 \pm 28	–	–	–	0.5
	B2	14 ^h 25 ^m 01.18 ^s	0.049	–61 $^\circ$ 44'57.5''	0.047	213 \pm 27	–	–	–	0.5
	B3	14 ^h 25 ^m 00.71 ^s	0.160	–61 $^\circ$ 44'54.6''	0.176	118 \pm 30	2.15 \pm 0.90	1.20 \pm 0.77	122.0 \pm 51.0	0.5
	D	14 ^h 25 ^m 00.09 ^s	0.043	–61 $^\circ$ 44'53.3''	0.060	165 \pm 24	< 1.20	< 0.84	–	0.5
	F	14 ^h 25 ^m 04.70 ^s	0.064	–61 $^\circ$ 44'50.3''	0.185	85 \pm 22	< 2.2	< 0.77	–	0.5
G	14 ^h 24 ^m 57.07 ^s	0.581	–61 $^\circ$ 44'53.2''	0.236	171 \pm 59	4.75 \pm 1.56	1.09 \pm 0.88	101 \pm 15	0.5	

Table B.15: A table of lobe positions, integrated fluxes and deconvolved dimensions at 9 GHz for the 2014 epoch. The final column indicates which robustness was employed in the clean map.

Source	Lobe	α (J2000)	$\delta\alpha$ ($''$)	δ (J2000)	$\delta\delta$ ($''$)	S_9 (μJy)	θ_{Maj} ($''$)	θ_{Min} ($''$)	θ_{PA} ($^\circ$)	R
G263.7434+00.1161	N	08 ^h 48 ^m 48.48 ^s	0.004	−43°32′23.8 $''$	0.026	594 ± 44	1.40 ± 0.14	0.39 ± 0.03	176.1 ± 2.0	0.5
	S2	08 ^h 48 ^m 48.63 ^s	0.007	−43°32′57.7 $''$	0.037	363 ± 31	1.04 ± 0.27	0.27 ± 0.07	167.8 ± 7.8	0.5
	S	08 ^h 48 ^m 48.66 ^s	0.003	−43°32′28.5 $''$	0.023	837 ± 58	1.85 ± 0.10	0.43 ± 0.04	5.8 ± 1.6	0.5
	SE	08 ^h 48 ^m 48.82 ^s	0.047	−43°32′33.1 $''$	0.468	135 ± 29	5.29 ± 1.27	0.73 ± 0.18	177.2 ± 2.4	0.5
G310.0135+00.3892	N	13 ^h 51 ^m 37.86 ^s	0.005	−61°39′06.2 $''$	0.013	695 ± 66	< 0.46	< 0.06	–	−1
	S	13 ^h 51 ^m 37.87 ^s	0.006	−61°39′07.6 $''$	0.018	481 ± 53	–	–	–	−1
	SW	13 ^h 51 ^m 37.75 ^s	0.045	−61°39′08.9 $''$	0.078	93 ± 32	–	–	–	−1
G310.1420+00.7583A	A1	13 ^h 51 ^m 58.39 ^s	0.006	−61°15′41.2 $''$	0.014	1462 ± 125	0.66 ± 0.07	0.28 ± 0.03	162.4 ± 4.3	−1
	A2	13 ^h 51 ^m 58.28 ^s	0.006	−61°15′41.4 $''$	0.012	1842 ± 149	0.61 ± 0.07	0.41 ± 0.03	171.0 ± 12.0	−1
	A3	13 ^h 51 ^m 58.14 ^s	0.024	−61°15′41.7 $''$	0.045	1295 ± 160	1.36 ± 0.14	0.81 ± 0.07	163.4 ± 8.0	−1
	A4	13 ^h 51 ^m 57.93 ^s	0.018	−61°15′41.9 $''$	0.058	570 ± 94	1.00 ± 0.22	0.32 ± 0.15	7.1 ± 13.9	−1
	B	13 ^h 51 ^m 58.72 ^s	0.055	−61°15′41.0 $''$	0.100	357 ± 69	1.40 ± 0.39	0.75 ± 0.64	35.0 ± 36.0	0.5
	C	13 ^h 51 ^m 59.13 ^s	0.037	−61°15′40.0 $''$	0.031	1154 ± 120	1.82 ± 0.15	0.82 ± 0.33	88.6 ± 8.8	0.5
	D	13 ^h 51 ^m 59.56 ^s	0.001	−61°15′40.0 $''$	0.013	2079 ± 151	1.13 ± 0.06	0.74 ± 0.11	95.8 ± 8.0	0.5
G313.7654−00.8620	A1	14 ^h 25 ^m 01.59 ^s	0.012	−61°44′57.9 $''$	0.015	451 ± 39	–	–	–	0.5
	A2	14 ^h 25 ^m 01.74 ^s	0.165	−61°44′58.4 $''$	0.150	469 ± 67	4.90 ± 0.56	1.09 ± 0.15	130.6 ± 2.1	0.5

Table B.15: Continued

Source	Lobe	α (J2000)	$\delta\alpha$ ($''$)	δ (J2000)	$\delta\delta$ ($''$)	S_9 (μJy)	θ_{Maj} ($''$)	θ_{Min} ($''$)	θ_{PA} ($^\circ$)	R
	B1	14 ^h 25 ^m 01.10 ^s	0.061	-61°44'56.2 $''$	0.071	277 ± 42	1.62 ± 0.34	0.99 ± 0.21	132.0 ± 25.0	0.5
	B2	14 ^h 25 ^m 01.18 ^s	0.068	-61°44'57.5 $''$	0.081	146 ± 26	< 1.70	< 0.29	–	0.5
	B3	14 ^h 25 ^m 00.72 ^s	0.195	-61°44'54.8 $''$	0.218	81 ± 27	1.97 ± 1.11	0.32 ± 0.34	134.0 ± 33.0	0.5
	C	14 ^h 25 ^m 02.25 ^s	0.023	-61°45'01.4 $''$	0.028	372 ± 38	0.87 ± 0.21	0.35 ± 0.11	125.0 ± 19.0	0.5
	D	14 ^h 25 ^m 00.08 ^s	0.038	-61°44'53.4 $''$	0.056	164 ± 24	–	–	–	0.5
	F	14 ^h 25 ^m 04.68 ^s	0.104	-61°44'50.1 $''$	0.105	85 ± 25	–	–	–	0.5
	G	14 ^h 24 ^m 57.04 ^s	0.130	-61°44'54.1 $''$	0.125	51 ± 18	–	–	–	0.5

Table B.16: A table containing the dates the sample was observed by the VLA, and the flux and bandpass calibrators used for each observing block.

Date	Epoch	Bandpass Cal.	Flux Cal.
C-Band			
13/10/2012	C1	3C286	3C286
04/11/2012	C2	3C48	3C48
17/11/2012	C3	3C286	3C286
19/11/2012	C4	3C286	3C286
15/12/2012	C5	3C286	3C286
27/12/2012	C6	3C48	3C48
29/12/2012	C7	3C286	3C286
Q-Band			
16/03/2014	Q1	J1357+1919	3C286
21/03/2014	Q2	J1357+1919	3C286
22/03/2014	Q3	J1357+1919	3C286
23/03/2014	Q4	J1357+1919	3C286
24/03/2014	Q5	J1357+1919	3C286
25/03/2014	Q6	J1357+1919	3C286
29/03/2014	Q7	J1357+1919	3C286
25/04/2014	Q8	J0237+2848	3C48
02/05/2014	Q9	J0237+2848	3C48
09/05/2014	Q10	J1357+1919	3C286
16/05/2014	Q11	J1357+1919	3C286
19/05/2014	Q12	J1357+1919	3C286
27/07/2015	Q13	J0237+2848	3C48

Table B.17: Phase calibrators used at C and Q-bands, and the quality and positional accuracy of each calibrator at C (columns 4 and 5) and Q-band (columns 8 and 9).

Object	C-band				Q-band			
	Calibrator	S_C	Qual.	Pos. Acc.	Calibrator	S_Q	Qual.	Pos. Acc.
18517+0437	J1804+0101	1.2	P	A	J1851+0035	0.7	S	C
18556+0136	J1824+1044	1.3	P	A	J1851+0035	0.7	S	C
G018.82−00.28	J1733−1304	5.0	P	B	J1832−1035	0.58	S	C
G024.08+00.04	J1804+0101	1.2	P	A	J1832−1035	0.58	S	C
G024.33+00.11	J1804+0101	1.2	P	A	J1832−1035	0.58	S	C
G024.60+00.08	J1804+0101	1.2	P	A	J1832−1035	0.58	S	C
G028.28−00.34	J1804+0101	1.2	P	A	J1851+0035	0.7	S	C
G028.37+00.07	J1804+0101	1.2	P	A	J1851+0035	0.7	S	C
G028.67+00.13	J1804+0101	1.2	P	A	J1851+0035	0.7	S	C
G33.64−0.21	J1804+0101	1.2	P	A	J1851+0035	0.7	S	C
G33.68−0.26	J1804+0101	1.2	P	A	J1851+0035	0.7	S	C
G033.6437−00.2277	J1804+0101	1.2	P	A	J1851+0035	0.7	S	C
G033.69−00.01	J1804+0101	1.2	P	A	J1851+0035	0.7	S	C
G41.34−0.14	J1824+1044	1.3	P	A	J1851+0035	0.7	S	C
G49.57−0.38	J1824+1044	1.3	P	A	J1925+2106	1.0	S	A

Table B.17: Continued

Object	C-band				Q-band			
	Calibrator	S_C	Qual.	Pos. Acc.	Calibrator	S_Q	Qual.	Pos. Acc.
G056.3694−00.6333	J1850+2825	1.0	P	A	J1925+2106	1.0	S	A
G077.5671+03.6911	J2007+4029	4.5	P	B	J2012+4628	1.5	S	A
G078.8699+02.7602	J2007+4029	4.5	P	B	J2012+4628	1.5	S	A
G079.8855+02.5517	J2007+4029	4.5	P	B	J2012+4628	1.5	S	A
G081.8652+00.7800	J2007+4029	4.5	P	B	J2012+4628	1.5	S	A
G083.7071+03.2817	J2007+4029	4.5	P	B	J2012+4628	1.5	S	A
G084.9505−00.6910	J2007+4029	4.5	P	B	J2012+4628	1.5	S	A
G094.2615−00.4116	J2202+4216	5.4	P	A	J2137+5101	0.7	S	C
G094.3228−00.1671	J2202+4216	5.4	P	A	J2137+5101	0.7	S	C
G094.4637−00.8043	J2202+4216	5.4	P	A	J2137+5101	0.7	S	C
G094.6028−01.7966	J2202+4216	5.4	P	A	J2137+5101	0.7	S	C
G100.3779−03.5784	J2202+4216	5.4	P	A	J2250+5550	0.46	W	A
G102.8051−00.7184	J2202+4216	5.4	P	A	J2250+5550	0.46	W	A
G103.8744+01.8558	J2230+6946	1.1	P	A	J2250+5550	0.46	W	A
G105.5072+00.2294	J2230+6946	1.1	P	A	J2250+5550	0.46	W	A
G107.6823−02.2423A	J2355+4950	1.6	P	B	J2250+5550	0.46	W	A

Table B.17: Continued

Object	C-band				Q-band			
	Calibrator	S_C	Qual.	Pos. Acc.	Calibrator	S_Q	Qual.	Pos. Acc.
G108.18+5.51	J2230+6946	1.1	P	A	J2250+5550	0.46	W	A
G108.4714−02.8176	J2355+4950	1.6	P	B	J2250+5550	0.46	W	A
G108.5955+00.4935A	J2230+6946	1.1	P	A	J2250+5550	0.46	W	A
G108.7575−00.9863	J2230+6946	1.1	P	A	J2250+5550	0.46	W	A
G110.0931−00.0641	J2230+6946	1.1	P	A	J2250+5550	0.46	W	A
G111.2348−01.2385	J2355+4950	1.6	P	B	J2250+5550	0.46	W	A
G111.2552−00.7702	J2355+4950	1.6	P	B	J2250+5550	0.46	W	A
G111.5671+00.7517	J2230+6946	1.1	P	A	J2250+5550	0.46	W	A
G114.0835+02.8568	J2230+6946	1.1	P	A	-	-	-	-
G118.6172−01.3312	J2355+4950	1.6	P	B	J0102+5824	2.4	S	A
G126.7144−00.8220	J0228+6721	1.15	P	A	J0102+5824	2.4	S	A
G133.7150+01.2155	J0228+6721	1.15	P	A	J0228+6721	1.4	S	A
G134.2792+00.8561	J0228+6721	1.15	P	A	J0228+6721	1.4	S	A
G136.3833+02.2666	J0228+6721	1.15	P	A	J0228+6721	1.4	S	A
G138.2957+01.5552	J0228+6721	1.15	P	A	J0306+6243	0.72	W	A
G139.9091+00.1969A	J0359+5057	10.1	S	B	J0306+6243	0.72	W	A

Table B.17: Continued

Object	C-band				Q-band			
	Calibrator	S_C	Qual.	Pos. Acc.	Calibrator	S_Q	Qual.	Pos. Acc.
G141.9996+01.8202	J0359+5057	10.1	S	B	J0359+6005	0.7	W	A
G143.8118−01.5699	J0359+5057	10.1	S	B	J0359+5057	5.5	S	B
G148.1201+00.2928	J0359+5057	10.1	S	B	J0359+5057	5.5	S	B
G160.1452+03.1559	J0359+5057	10.1	S	B	-	-	-	-
G173.4839+02.4317	J0555+3948	5.0	P	A	-	-	-	-
G174.1974−00.0763	J0555+3948	5.0	P	A	-	-	-	-
G177.7291−00.3358	J0555+3948	5.0	P	A	-	-	-	-
G183.3485−00.5751	J0559+2353	1.05	P	A	-	-	-	-
G188.9479+00.8871	J0559+2353	1.05	P	A	-	-	-	-
G189.0307+00.7821	J0559+2353	1.05	P	A	-	-	-	-
G192.6005−00.0479	J0559+2353	1.05	P	A	-	-	-	-
G196.4542−01.6777	J0559+2353	1.05	P	A	-	-	-	-
W48	J1824+1044	1.3	P	A	J1851+0035	0.7	S	C

Table B.18: Positions and fluxes at C-band for all detected sources derived from IMFIT. A ‘PA’ value in R.A. or Declination error columns indicates that the source is extended and listed positions are those of the pixel of peak-flux.

Object	Lobe	α (J2000) (hh:mm:ss)	$\delta\alpha$ (mas)	δ (J2000) (dd:mm:ss)	$\delta\delta$ (mas)	$S_{5.8}^{Peak}$ (μ Jy)	$\delta S_{5.8}^{Peak}$ (μ Jy)	$S_{5.8}$ (μ Jy)	$\delta S_{5.8}$ (μ Jy)
18517+0437	A	18:54:13.6643	12.6	+04:41:39.193	18.6	39	5	35	8
	B	18:54:14.2433	16.5	+04:41:40.821	13.1	50	5	51	9
	C	18:54:12.7075	8.2	+04:41:41.619	9.0	81	5	82	9
18556+0136	13	18:58:13.1204	15.3	+01:40:33.146	16.1	117	6	177	24
	14	18:58:13.0190	2.0	+01:40:34.141	3.3	818	6	1387	27
	15	18:58:13.0498	6.6	+01:40:38.118	9.7	245	6	401	26
	4	18:58:13.1067	5.5	+01:40:40.818	5.5	421	6	1009	33
	5	18:58:12.9305	3.2	+01:40:39.434	4.4	348	6	354	17
	6	18:58:12.8148	5.4	+01:40:36.613	7.2	224	6	238	17
	7	18:58:13.0336	5.4	+01:40:35.965	6.3	459	6	794	30
	8	18:58:13.0406	1.5	+01:40:35.256	2.4	1031	6	1433	24
	Core A	18:58:12.9525	8.9	+01:40:37.383	14.0	111	6	109	16
	EX-N	18:58:13.0300	PP	+01:40:44.225	PP	598	6	2130	140
EX-S	18:58:13.0120	PP	+01:40:30.722	PP	533	6	747	230	
G018.82-00.28	Core	18:26:23.6516	1.1	-12:39:37.549	1.4	18890	105	36620	250
	Extended	18:26:23.6250	PP	-12:39:38.860	PP	994	105	72800	2400

Table B.18: Continued

Object	Lobe	α (J2000) (hh:mm:ss)	$\delta\alpha$ (mas)	δ (J2000) (dd:mm:ss)	$\delta\delta$ (mas)	$S_{5.8}^{Peak}$ (μ Jy)	$\delta S_{5.8}^{Peak}$ (μ Jy)	$S_{5.8}$ (μ Jy)	$\delta S_{5.8}$ (μ Jy)
G024.08+00.04	A	18:34:57.1881	5.7	-07:43:26.234	5.8	1048	9	4547	81
	B	18:34:59.5980	PP	-07:43:00.433	PP	1475	9	-	-
	B1	18:34:59.6276	7.2	-07:43:01.633	8.9	769	9	1715	59
	B2	18:34:59.5937	5.0	-07:43:00.313	7.2	1475	9	5517	65
	B3	18:34:59.5918	25.3	-07:42:57.355	34.0	297	9	2470	130
G024.33+00.11	A	18:35:08.1393	3.6	-07:35:04.096	5.0	234	6	283	12
	B	18:35:10.9054	4.1	-07:34:22.083	8.0	137	6	136	10
	D	18:35:23.9255	1.5	-07:37:37.979	1.7	2183	19	3360	45
G024.60+00.08	A	18:35:43.7668	6.6	-07:19:25.809	10.4	120	6	148	13
	B	18:35:36.1054	9.4	-07:18:57.992	15.0	72	6	73	11
G028.28-00.34	A	18:44:09.8066	3.8	-04:18:00.120	4.1	1415	39	1597	72
	HII	18:44:15.1070	PP	-04:17:54.985	PP	9340	82	222100	4500
G028.37+00.07	A	18:42:51.9820	24.1	-03:59:54.609	20.9	44	6	41	10
	A3	18:42:51.9783	57.2	-03:59:53.814	51.8	24	6	47	15
	B	18:42:52.3941	1.4	-03:59:06.902	2.2	514	6	544	11
	C	18:42:50.2414	16.5	-03:59:16.450	16.6	51	6	53	11
	D	18:42:37.1243	3.2	-04:02:02.264	3.8	606	12	934	20

Table B.18: Continued

Object	Lobe	α (J2000) (hh:mm:ss)	$\delta\alpha$ (mas)	δ (J2000) (dd:mm:ss)	$\delta\delta$ (mas)	$S_{5.8}^{Peak}$ (μ Jy)	$\delta S_{5.8}^{Peak}$ (μ Jy)	$S_{5.8}$ (μ Jy)	$\delta S_{5.8}$ (μ Jy)
G028.67+00.13	HII	18:43:03.1780	PP	-03:41:46.484	PP	975	10	61950	780
G033.64-00.21	A	18:53:32.5641	22.6	+00:31:39.130	32.1	33	6	55	14
	B	18:53:32.8191	31.2	+00:32:04.333	18.4	31	6	32	9
	C	18:53:29.3719	4.4	+00:32:02.828	4.3	197	6	223	11
G033.68-00.26		-	-	-	-	26	5	-	-
G033.69-00.01	A	18:52:49.0900	15.9	+00:38:10.015	16.1	136	6	1533	56
G041.34-00.14		-	-	-	-	-	6	-	-
G049.57-00.38		-	-	-	-	-	7	-	-
G056.3694-00.6333	A	19:38:31.6920	33.5	+20:25:18.194	27.4	52	7	72	16
	B	19:38:31.7329	46.2	+20:25:17.929	32.8	38	7	55	16
	C	19:38:31.6215	120.2	+20:25:18.566	118.7	28	7	135	41
	D	19:38:31.5218	48.1	+20:25:18.916	69.1	28	7	45	17
G077.5671+03.6911	A	20:12:35.2170	18.3	+40:47:25.279	16.0	51	6	54	12
G078.8699+02.7602	A	20:20:30.5984	9.0	+41:21:26.260	7.5	110	7	126	13
	B	20:20:30.5689	32.9	+41:21:31.327	37.6	41	7	59	17
	C	20:20:28.2397	5.4	+41:21:51.460	5.9	157	7	163	12
	D	20:20:31.9780	1.7	+41:22:05.416	1.5	549	7	604	12

Table B.18: Continued

Object	Lobe	α (J2000) (hh:mm:ss)	$\delta\alpha$ (mas)	δ (J2000) (dd:mm:ss)	$\delta\delta$ (mas)	$S_{5.8}^{Peak}$ (μ Jy)	$\delta S_{5.8}^{Peak}$ (μ Jy)	$S_{5.8}$ (μ Jy)	$\delta S_{5.8}$ (μ Jy)
G079.8855+02.5517	E	20:20:29.3480	12.6	+41:21:28.327	18.6	38	7	33	9
	A	20:24:31.5514	4.9	+42:04:13.490	5.3	169	7	171	12
	B	20:24:28.9510	10.1	+42:03:30.426	12.8	85	7	89	13
	C1	-	-	-	-	-	7	-	-
	C2	-	-	-	-	-	7	-	-
G081.8652+00.7800	D	-	-	-	-	-	7	-	-
	A	20:38:35.3784	7.1	+42:37:13.792	5.7	161	8	169	14
	HII	20:38:37.6000	PP	+42:37:55.861	PP	366	8	89800	1400
	VLA1Core	20:38:36.4396	0.9	+42:37:34.827	0.9	2484	9	2739	28
	VLA1Jet	20:38:36.4752	8.6	+42:37:34.928	9.3	600	9	1866	59
	VLA2	20:38:36.4769	4.0	+42:37:34.057	6.4	646	9	1304	45
	VLA3	20:38:36.4842	1.2	+42:37:33.416	1.7	1521	9	1867	30
	VLA4	20:38:36.5345	5.2	+42:37:29.900	4.5	494	9	652	33
	VLA5	20:38:36.5509	79.4	+42:37:28.934	57.8	42	9	66	39
	VLA6	20:38:36.5469	35.5	+42:37:36.331	32.4	58	9	83	25
VLA7	20:38:36.5335	32.1	+42:37:37.156	47.9	77	9	337	53	
W75NBc	20:38:36.5676	2.1	+42:37:31.484	2.2	1175	9	1843	37	

Table B.18: Continued

Object	Lobe	α (J2000) (hh:mm:ss)	$\delta\alpha$ (mas)	δ (J2000) (dd:mm:ss)	$\delta\delta$ (mas)	$S_{5.8}^{Peak}$ (μ Jy)	$\delta S_{5.8}^{Peak}$ (μ Jy)	$S_{5.8}$ (μ Jy)	$\delta S_{5.8}$ (μ Jy)
	W75NBc2	20:38:36.5251	3.1	+42:37:31.402	2.9	841	9	1260	36
G083.7071+03.2817	A	20:33:36.5573	6.7	+45:35:43.975	5.2	207	7	265	17
	B	20:33:36.3512	5.2	+45:35:41.178	5.2	200	7	207	14
G084.9505-00.6910	A	20:55:31.7256	8.0	+44:05:11.323	7.7	127	8	160	14
G094.2615-00.4116	A1	21:32:30.6095	35.1	+51:02:15.978	16.4	58	6	93	14
	A2	21:32:30.6540	22.6	+51:02:15.454	249.0	47	6	71	14
	B	21:32:28.8028	29.6	+51:02:40.218	14.3	51	6	69	13
G094.3228-00.1671	A	21:31:45.0221	17.9	+51:15:37.074	11.9	46	6	37	8
G094.4637-00.8043	A	21:35:09.1203	9.0	+50:53:09.022	6.2	182	6	303	16
	B	21:35:09.1610	8.5	+50:53:09.561	8.3	127	6	160	13
	C	21:35:09.0566	9.0	+50:53:09.865	6.2	122	6	131	11
	D	21:35:09.0366	32.7	+50:53:08.288	19.8	46	6	64	14
	E	21:35:08.9195	31.6	+50:53:07.098	19.5	46	6	55	12
	SC1	21:35:11.1307	0.3	+50:52:13.253	0.2	8989	22	9164	29
G094.6028-01.7966	A	21:39:58.2677	6.3	+50:14:20.994	3.8	201	6	229	12
	SC1	21:40:00.8472	0.3	+50:13:39.486	0.2	6489	13	6924	17
G100.3779-03.5784	A	22:16:10.3628	17.3	+52:21:34.139	7.7	78	6	90	11

Table B.18: Continued

Object	Lobe	α (J2000) (hh:mm:ss)	$\delta\alpha$ (mas)	δ (J2000) (dd:mm:ss)	$\delta\delta$ (mas)	$S_{5.8}^{Peak}$ (μ Jy)	$\delta S_{5.8}^{Peak}$ (μ Jy)	$S_{5.8}$ (μ Jy)	$\delta S_{5.8}$ (μ Jy)
	B	22:16:10.2539	35.4	+52:21:21.817	25.0	48	6	88	18
G102.8051-00.7184	A	22:19:05.7223	11.4	+56:04:52.470	9.1	88	6	91	10
G103.8744+01.8558	A	22:15:09.2239	1.9	+58:49:08.847	1.6	1269	6	3625	36
	B	22:15:08.7668	9.8	+58:49:07.822	7.4	186	6	281	22
	C	22:15:09.4574	24.0	+58:49:03.453	14.9	65	6	120	18
	D	22:15:08.1600	12.1	+58:49:09.715	14.7	46	6	40	8
	E	22:15:07.8650	9.9	+58:49:10.328	26.0	87	6	225	21
	F	22:15:07.5911	38.0	+58:49:11.230	16.2	32	6	37	11
G105.5072+00.2294	A	22:32:23.7707	18.6	+58:19:00.275	14.8	55	6	65	12
G107.6823-02.2423A	A	22:55:29.8323	49.6	+57:09:24.812	26.4	43	5	54	12
	HII	22:55:28.8860	PP	+57:09:21.715	PP	39	5	850	84
G108.1844+05.5187	A	22:28:51.4743	103.4	+64:13:41.131	108.7	34	6	166	37
	B	22:28:55.5193	25.8	+64:14:26.645	31.6	52	6	126	18
G108.4714-02.8176	A	23:02:32.0825	12.9	+56:57:51.396	5.8	102	6	110	11
G108.5955+00.4935A	B	22:52:38.7975	12.9	+60:00:52.820	31.1	35	6	30	8
	C	22:52:38.0574	71.6	+60:01:01.133	65.2	32	6	147	35
	D	22:52:45.8662	5.8	+60:00:39.764	5.4	158	6	170	11

Table B.18: Continued

Object	Lobe	α (J2000) (hh:mm:ss)	$\delta\alpha$ (mas)	δ (J2000) (dd:mm:ss)	$\delta\delta$ (mas)	$S_{5.8}^{Peak}$ (μ Jy)	$\delta S_{5.8}^{Peak}$ (μ Jy)	$S_{5.8}$ (μ Jy)	$\delta S_{5.8}$ (μ Jy)	
G108.7575-00.9863	A	22:58:47.4172	7.0	+58:45:02.032	6.2	123	6	124	11	
	B	22:58:48.3396	13.7	+58:45:09.333	19.9	36	6	25	7	
	C	22:58:47.7203	12.2	+58:45:29.403	17.4	68	6	78	13	
	D	22:58:46.2177	13.3	+58:45:30.910	23.1	36	6	31	8	
	E	22:58:51.1438	21.3	+58:45:12.804	56.0	39	6	56	16	
G110.0931-00.0641	A1	23:05:25.1493	6.8	+60:08:15.604	6.8	137	6	179	13	
	A2	23:05:25.2124	32.8	+60:08:15.568	25.3	35	6	53	14	
	B	23:05:25.0444	8.4	+60:08:15.807	6.1	172	6	309	17	
	C	23:05:24.9678	2.2	+60:08:16.012	2.0	419	6	492	12	
	D	23:05:25.4498	50.0	+60:08:16.753	26.4	53	6	208	30	
G111.2348-01.2385	A	23:05:23.5920	17.2	+60:09:08.724	28.2	33	6	41	11	
	A	23:17:20.8952	10.3	+59:28:47.609	3.6	147	6	157	11	
	G111.2552-00.7702	A1	23:16:10.3413	9.6	+59:55:28.582	5.2	181	6	255	16
		A2	23:16:10.2717	90.3	+59:55:29.025	34.7	30	6	55	20
		B	23:16:09.7928	13.5	+59:55:14.170	11.9	38	6	23	6
C		23:16:10.2051	27.4	+59:55:04.281	10.4	47	6	43	9	
D	23:16:13.5915	57.3	+59:56:00.239	17.8	38	6	58	15		

Table B.18: Continued

Object	Lobe	α (J2000) (hh:mm:ss)	$\delta\alpha$ (mas)	δ (J2000) (dd:mm:ss)	$\delta\delta$ (mas)	$S_{5.8}^{Peak}$ (μ Jy)	$\delta S_{5.8}^{Peak}$ (μ Jy)	$S_{5.8}$ (μ Jy)	$\delta S_{5.8}$ (μ Jy)
G111.5671+00.7517	A	23:14:01.7570	3.2	+61:27:19.785	3.2	375	7	424	16
	B1	23:14:01.5487	34.5	+61:27:17.558	32.6	59	7	191	29
	B2	23:14:01.6363	40.4	+61:27:17.956	50.0	38	7	134	24
	C	23:14:01.8471	6.2	+61:27:21.438	5.1	241	7	317	18
	D	23:14:01.5441	16.5	+61:26:51.513	24.5	53	7	71	15
G114.0835+02.8568	A1	23:28:27.8290	11.2	+64:17:38.154	9.4	98	6	124	13
	A2	23:28:27.7639	16.9	+64:17:38.000	12.0	61	6	62	10
	B	23:28:27.4089	77.5	+64:17:40.123	48.9	43	6	172	34
	C	23:28:19.8581	2.6	+64:17:40.088	2.7	380	6	464	13
	D	23:28:26.0116	16.4	+64:18:19.902	23.7	42	6	45	10
G118.6172-01.3312		-	-	-	-	-	5	-	-
G126.7144-00.8220	A	01:23:33.1132	2.3	+61:48:48.795	4.0	895	20	1282	44
G133.7150+01.2155	A	02:25:41.2632	14.1	+62:05:45.603	14.0	265	22	690	77
	B	02:25:40.5017	3.5	+62:06:07.229	4.8	517	22	536	36
	C1	02:25:40.8263	40.5	+62:05:54.228	69.4	493	22	2990	420
	K8	02:25:40.8008	5.0	+62:05:52.872	5.7	1054	22	1510	100
	Q1/K2	02:25:40.6667	5.4	+62:05:51.772	8.7	864	22	845	72

Table B.18: Continued

Object	Lobe	α (J2000) (hh:mm:ss)	$\delta\alpha$ (mas)	δ (J2000) (dd:mm:ss)	$\delta\delta$ (mas)	$S_{5.8}^{Peak}$ (μ Jy)	$\delta S_{5.8}^{Peak}$ (μ Jy)	$S_{5.8}$ (μ Jy)	$\delta S_{5.8}$ (μ Jy)
	Q10	02:25:40.7262	40.8	+62:05:53.274	40.9	129	22	165	72
	Q2/K3	02:25:40.6824	7.9	+62:05:52.041	26.7	420	22	847	107
	Q3/K4	02:25:40.6805	3.9	+62:05:51.485	7.2	802	22	630	55
	Q4/K6	02:25:40.7317	9.6	+62:05:49.819	18.2	201	22	220	42
	Q4b	02:25:40.6417	6.7	+62:05:50.096	8.3	376	22	482	50
	Q5/K7	02:25:40.7838	3.8	+62:05:52.549	6.9	903	22	920	78
	Q6/K5	02:25:40.7074	9.3	+62:05:52.581	17.1	328	22	349	68
	Q7	02:25:40.7608	2.0	+62:05:52.144	3.2	2139	22	3380	110
	Q8	02:25:40.8616	2.5	+62:05:53.465	4.0	2035	22	3450	120
	Q9	02:25:40.7560	12.8	+62:05:51.144	14.7	651	22	940	139
	QE1	-	-	-	-	< 110	22	-	22
	QE2	-	-	-	-	< 110	22	-	22
G134.2792+00.8561	A	02:29:01.9594	16.8	+61:33:30.910	16.7	60	6	77	14
	B	02:29:01.8486	12.6	+61:33:26.961	27.9	53	6	61	13
	C	02:29:02.3535	1.4	+61:32:57.947	1.5	632	6	674	12
G136.3833+02.2666	A	02:50:08.4898	10.6	+61:59:52.065	17.7	84	11	73	14
	B	02:50:07.6460	PP	+61:59:51.831	PP	58	11	946	188

Table B.18: Continued

Object	Lobe	α (J2000) (hh:mm:ss)	$\delta\alpha$ (mas)	δ (J2000) (dd:mm:ss)	$\delta\delta$ (mas)	$S_{5.8}^{Peak}$ (μ Jy)	$\delta S_{5.8}^{Peak}$ (μ Jy)	$S_{5.8}$ (μ Jy)	$\delta S_{5.8}$ (μ Jy)
G138.2957+01.5552	C	02:50:03.4081	5.9	+62:00:05.510	6.6	240	11	250	20
	D	02:50:10.8178	22.3	+62:00:47.099	38.4	66	11	106	26
	E	02:50:12.0910	5.0	+61:57:07.558	5.9	326	13	326	22
	A	03:01:31.2773	9.9	+60:29:12.797	7.8	125	7	137	15
	B	03:01:31.4400	53.1	+60:29:13.185	43.2	39	7	123	32
	C	03:01:33.7136	9.8	+60:29:26.503	16.5	72	7	79	13
	D	03:01:35.1685	53.0	+60:29:07.765	16.9	43	7	57	16
	E	03:01:30.0932	5.5	+60:29:55.465	4.9	168	7	166	12
G139.9091+00.1969A	HII	03:01:34.3510	PP	+60:29:13.821	PP	90	7	3450	170
	A	03:07:24.4921	3.1	+58:30:42.821	1.9	537	7	595	16
	Ab	03:07:24.5258	42.1	+58:30:42.989	27.6	70	7	242	38
	Ac	03:07:24.4105	62.6	+58:30:42.460	148.0	31	7	97	35
	B	03:07:24.5659	34.1	+58:30:52.992	34.1	60	7	70	17
G141.9996+01.8202	HII	03:07:23.7050	8.3	+58:30:49.965	8.1	427	7	20470	170
	A	03:27:38.7946	5.4	+58:47:00.148	3.4	278	7	349	16
	B	03:27:39.1272	15.5	+58:47:10.543	8.0	80	7	79	12
	C	03:27:37.0669	10.0	+58:46:59.424	5.6	126	7	129	12

Table B.18: Continued

Object	Lobe	α (J2000) (hh:mm:ss)	$\delta\alpha$ (mas)	δ (J2000) (dd:mm:ss)	$\delta\delta$ (mas)	$S_{5.8}^{Peak}$ (μJy)	$\delta S_{5.8}^{Peak}$ (μJy)	$S_{5.8}$ (μJy)	$\delta S_{5.8}$ (μJy)
G143.8118-01.5699	A	03:24:50.9655	17.5	+54:57:32.778	11.5	73	7	80	13
	B	03:24:51.6329	41.4	+54:57:34.119	36.2	38	7	48	17
	C	03:24:53.9752	19.5	+54:57:32.613	14.9	49	7	38	9
G148.1201+00.2928	A	03:56:15.3811	16.7	+53:52:13.040	8.7	64	7	65	11
	B	03:56:13.9524	26.3	+53:52:13.480	10.3	52	7	42	10
	C	03:56:16.4354	9.1	+53:51:50.878	5.5	139	7	155	13
	D	03:56:05.4740	3.1	+53:52:04.960	2.0	366	7	447	13
G160.1452+03.1559	A	05:01:39.9173	12.6	+47:07:21.585	9.4	103	8	117	15
	B	05:01:39.9988	28.7	+47:07:18.805	20.0	43	8	39	12
G173.4839+02.4317	A1	05:39:09.9276	8.2						
	A2	05:39:09.9926	22.6	+35:45:18.349	14.5	45	7	43	11
	B	05:39:10.8015	40.4	+35:45:12.562	18.7	41	7	57	16
	C	05:39:12.4734	20.1	+35:45:38.587	28.6	44	7	59	15
	D	05:39:12.4835	25.6	+35:45:41.770	19.4	60	7	98	18
	E1	05:39:13.0663	4.1	+35:45:51.145	2.7	326	7	353	14
	E2	05:39:12.9114	25.7	+35:45:50.458	26.0	59	7	98	21
E3	05:39:12.8395	15.3	+35:45:50.764	14.6	53	7	48	11	

Table B.18: Continued

Object	Lobe	α (J2000) (hh:mm:ss)	$\delta\alpha$ (mas)	δ (J2000) (dd:mm:ss)	$\delta\delta$ (mas)	$S_{5.8}^{Peak}$ (μ Jy)	$\delta S_{5.8}^{Peak}$ (μ Jy)	$S_{5.8}$ (μ Jy)	$\delta S_{5.8}$ (μ Jy)
	E4	05:39:12.8024	41.6	+35:45:51.006	16.0	61	7	96	19
	E5	05:39:13.2682	18.3	+35:45:50.282	9.5	58	7	51	10
	E6	05:39:13.3321	37.9	+35:45:49.330	14.8	33	7	29	11
	F	05:39:10.0649	12.9	+35:46:07.721	9.1	85	7	81	12
	G	05:39:05.6736	11.2	+35:44:42.103	10.3	81	7	74	11
G174.1974-00.0763	A	05:30:46.0701	9.3	+33:47:54.225	5.8	133	7	130	12
	B	05:30:48.0185	4.2	+33:47:54.531	5.4	358	7	726	22
	C	05:30:42.3644	1.5	+33:48:15.140	0.9	874	7	886	13
G177.7291-00.3358	A	05:38:47.1493	26.2	+30:41:18.023	7.0	84	7	112	16
	B	05:38:45.2523	22.8	+30:41:15.647	16.8	53	7	67	14
G183.3485-00.5751	A	05:51:10.9569	11.5	+25:46:16.919	6.7	189	10	208	17
	B	05:51:10.6830	36.4	+25:46:53.978	30.1	69	10	83	19
G188.9479+00.8871	A	06:08:53.3351	18.0	+21:38:28.996	7.7	187	10	202	18
	B1	06:08:53.3116	22.9	+21:38:13.631	15.8	120	10	134	21
	B2	06:08:53.4159	51.1	+21:38:13.732	93.6	58	10	116	35
	C	06:08:55.7136	20.0	+21:38:32.743	9.1	144	10	146	17
	D	06:08:55.1220	6.0	+21:37:55.441	3.0	489	10	537	18

Table B.18: Continued

Object	Lobe	α (J2000) (hh:mm:ss)	$\delta\alpha$ (mas)	δ (J2000) (dd:mm:ss)	$\delta\delta$ (mas)	$S_{5.8}^{Peak}$ (μ Jy)	$\delta S_{5.8}^{Peak}$ (μ Jy)	$S_{5.8}$ (μ Jy)	$\delta S_{5.8}$ (μ Jy)
G189.0307+00.7821	A1	06:08:40.4176	7.9	+21:31:01.199	4.1	280	8	304	15
	A2	06:08:40.3450	30.0	+21:31:01.432	14.6	71	8	77	15
	B	06:08:40.6137	22.9	+21:31:05.283	9.6	54	8	122	15
	C	06:08:40.6675	6.2	+21:31:07.204	3.5	367	8	468	17
	D	06:08:43.0314	19.7	+21:30:54.808	10.4	114	8	116	14
	E	06:08:38.2673	57.5	+21:30:39.862	19.1	55	8	85	19
	F	06:08:37.0129	32.7	+21:31:10.105	19.2	49	8	47	12
G192.6005-00.0479	A	06:12:54.0224	5.4	+17:59:23.136	2.9	651	9	790	19
	B	06:12:54.0404	20.8	+17:59:24.072	12.3	114	9	94	14
	C	06:12:54.1330	164.0	+17:59:23.775	60.0	53	9	157	44
	D	06:12:53.8464	6.6	+17:59:22.016	3.5	464	9	692	23
	E	06:12:54.0033	32.3	+17:59:26.170	13.8	85	9	92	17
	F	06:12:53.7403	36.5	+17:59:21.773	17.7	109	9	146	22
	G	06:12:54.3384	9.7	+17:59:24.419	6.8	365	9	566	26
	H	06:12:54.2984	3.6	+17:59:33.836	1.8	785	9	801	16
	I	06:12:55.1043	41.7	+17:59:21.252	21.8	72	9	69	17
G196.4542-01.6777	A1	06:14:37.0870	8.0	+13:49:36.587	4.2	561	10	722	22

Table B.18: Continued

Object	Lobe	α (J2000) (hh:mm:ss)	$\delta\alpha$ (mas)	δ (J2000) (dd:mm:ss)	$\delta\delta$ (mas)	$S_{5.8}^{Peak}$ (μ Jy)	$\delta S_{5.8}^{Peak}$ (μ Jy)	$S_{5.8}$ (μ Jy)	$\delta S_{5.8}$ (μ Jy)
W48	A2	06:14:37.0074	105.7	+13:49:35.864	53.0	65	10	153	29
	B	06:14:36.9054	34.3	+13:49:28.121	26.0	113	10	301	38
	C	06:14:38.0374	38.8	+13:49:34.733	19.6	78	10	67	15
	D	06:14:38.9911	35.5	+13:49:43.917	18.7	89	10	74	14
	B	-	-	-	-	-	37	-	-
	HII	19:01:46.5000	PP	+01:13:25.023	PP	20700	134	2015000	39000

Table B.19: Positions and fluxes at Q-band for all detected sources derived from IMFIT. A ‘PA’ value in R.A. or Declination error columns indicates that the source is extended and listed positions are those of the pixel of peak-flux.

Object	Lobe	α (J2000) (hh:mm:ss)	$\delta\alpha$ (mas)	δ (J2000) (dd:mm:ss)	$\delta\delta$ (mas)	S_{44}^{Peak} (μ Jy)	δS_{44}^{Peak} (μ Jy)	S_{44} (μ Jy)	δS_{44} (μ Jy)
18517+0437	B	18:54:14.2435	1.5	+04:41:40.858	1.4	510	37	539	68
18556+0136	5	18:58:12.9294	2.0	+01:40:39.478	2.2	286	35	220	46
	6	18:58:12.8135	0.4	+01:40:36.661	0.5	1876	35	2121	71

Table B.19: Continued

Object	Lobe	α (J2000) (hh:mm:ss)	$\delta\alpha$ (mas)	δ (J2000) (dd:mm:ss)	$\delta\delta$ (mas)	S_{44}^{Peak} (μ Jy)	δS_{44}^{Peak} (μ Jy)	S_{44} (μ Jy)	δS_{44} (μ Jy)
	7	18:58:13.0357	0.3	+01:40:35.990	0.5	2327	35	2921	8
	7b	18:58:13.0295	8.6	+01:40:35.988	5.6	161	35	307	113
	8	18:58:13.0434	1.0	+01:40:35.337	1.3	760	35	1157	79
	8b	18:58:13.0381	5.3	+01:40:35.345	4.2	188	35	354	91
	Core A	18:58:12.9520	0.8	+01:40:37.430	0.8	965	35	1118	71
G018.82-00.28	Core	18:26:23.6570	5.0	-12:39:37.400	5.0	2372	57	51000	1096
G024.08+00.04		-	-	-	-	-	29	-	-
G024.33+00.11	A	18:35:08.1391	4.4	-07:35:04.122	3.1	506	37	1180	120
	C	18:35:07.9034	1.9	-07:35:01.104	4.4	340	37	365	66
G024.60+00.08		-	-	-	-	-	35	-	-
G028.28-00.34	HII	18:44:15.1103	5.0	-04:17:55.317	6.0	714	41	5170	480
G028.37+00.07	A	18:42:51.9768	21.7	-03:59:54.532	18.6	219	31	666	187
	A2	18:42:51.9833	2.9	-03:59:54.047	6.5	238	31	255	59
	A3	18:42:51.9878	5.3	-03:59:53.914	9.5	280	31	1200	160
G028.67+00.13		-	-	-	-	-	33	-	-
G033.64-00.21	A	18:53:32.5641	9.6	+00:31:39.188	6.1	169	32	343	106
	D	18:53:31.9983	10.3	+00:31:39.733	18.1	172	32	373	124

Table B.19: Continued

Object	Lobe	α (J2000) (hh:mm:ss)	$\delta\alpha$ (mas)	δ (J2000) (dd:mm:ss)	$\delta\delta$ (mas)	S_{44}^{Peak} (μ Jy)	δS_{44}^{Peak} (μ Jy)	S_{44} (μ Jy)	δS_{44} (μ Jy)
G033.66-00.25		-	-	-	-	-	31	-	-
G033.68-00.26		-	-	-	-	-	34	-	-
G033.69-00.01	E	18:52:50.5239	7.2	+00:37:53.806	3.9	152	27	134	44
G033.69-00.01ii		-	-	-	-	-	34	-	-
G033.69-00.01iii		-	-	-	-	-	25	-	-
G041.34-00.14		-	-	-	-	-	35	-	-
G049.57-00.38		-	-	-	-	-	33	-	-
G056.3694-00.6333		-	-	-	-	-	34	-	-
G077.5671+03.6911		-	-	-	-	-	30	-	-
G078.8699+02.7602	A	20:20:30.5963	1.0	+41:21:26.263	1.0	1165	30	2205	92
	B	20:20:30.5672	6.8	+41:21:31.282	7.7	123	32	218	75
	C	20:20:28.2386	1.5	+41:21:51.437	0.8	1625	79	1590	130
G079.8855+02.5517	A	20:24:31.5511	1.3	+42:04:13.493	1.1	691	30	847	63
	C1	20:24:31.6664	4.1	+42:04:22.328	3.1	310	30	427	72
	C2	20:24:31.6716	3.6	+42:04:22.366	2.7	369	30	571	79
	D	20:24:31.7096	4.3	+42:04:33.009	3.1	352	35	613	98
G081.8652+00.7800	A	20:38:35.3769	1.4	+42:37:13.803	0.7	1074	54	1290	100

Table B.19: Continued

Object	Lobe	α (J2000) (hh:mm:ss)	$\delta\alpha$ (mas)	δ (J2000) (dd:mm:ss)	$\delta\delta$ (mas)	S_{44}^{Peak} (μ Jy)	δS_{44}^{Peak} (μ Jy)	S_{44} (μ Jy)	δS_{44} (μ Jy)
	VLA1Core	20:38:36.4394	1.3	+42:37:34.885	1.4	1493	45	4010	200
	VLA2	20:38:36.4855	1.0	+42:37:34.096	0.7	1338	45	1620	100
	VLA3	20:38:36.4841	0.2	+42:37:33.403	0.2	7753	66	14690	150
G083.7071+03.2817	A	20:33:36.5578	2.1	+45:35:43.955	1.1	551	29	684	62
G084.9505-00.6910	B	20:55:32.5073	5.0	+44:06:10.259	1.9	252	30	285	54
G094.2615-00.4116	A1	21:32:30.6156	6.2	+51:02:15.950	9.0	198	36	243	83
G094.3228-00.1671	A	21:31:45.0406	2.0	+51:15:37.019	1.1	392	39	412	56
G094.4637-00.8043	A	21:35:09.1301	1.9	+50:53:08.984	1.4	540	38	663	81
	A2	21:35:09.1176	2.1	+50:53:08.819	1.6	452	38	473	71
	C	21:35:09.0723	1.4	+50:53:09.795	1.4	624	38	755	80
G094.6028-01.7966	A	21:39:58.2830	2.0	+50:14:20.940	0.8	601	38	622	66
G100.3779-03.5784	A	22:16:10.3637	2.6	+52:21:34.127	1.8	391	38	449	74
G102.8051-00.7184		-	-	-	-	-	36	-	-
G103.8744+01.8558	A	22:15:09.2335	29.6	+58:49:08.748	16.0	204	36	1560	340
G105.5072+00.2294	A	22:32:23.7715	3.2	+58:19:00.284	1.6	434	36	509	70
G107.6823-02.2423A	A	22:55:29.8219	25.6	+57:09:24.814	24.1	172	33	552	188
G108.1844+05.5187	A	22:28:51.4120	2.8	+64:13:41.016	2.3	747	43	1390	155

Table B.19: Continued

Object	Lobe	α (J2000) (hh:mm:ss)	$\delta\alpha$ (mas)	δ (J2000) (dd:mm:ss)	$\delta\delta$ (mas)	S_{44}^{Peak} (μ Jy)	δS_{44}^{Peak} (μ Jy)	S_{44} (μ Jy)	δS_{44} (μ Jy)
G108.4714-02.8176	A	23:02:32.0739	7.0	+56:57:51.366	2.7	263	37	335	96
G108.5955+00.4935A		-	-	-	-	-	44	-	-
G108.7575-00.9863	A	22:58:47.4166	2.0	+58:45:02.043	1.2	688	43	835	92
G110.0931-00.0641	B	23:05:25.0417	8.4	+60:08:15.756	5.1	272	44	612	159
	C	23:05:24.9591	5.3	+60:08:16.028	5.8	235	44	415	125
	F	23:05:25.2319	5.0	+60:08:14.691	1.7	226	44	199	61
G111.2348-01.2385	A	23:17:20.8927	0.6	+59:28:47.606	1.1	1045	40	1459	91
G111.2552-00.7702	A1	23:16:10.3320	2.1	+59:55:28.611	2.3	336	38	351	69
G111.5671+00.7517	A	23:14:01.7548	0.4	+61:27:19.788	0.6	1936	38	2460	100
	Disc	23:14:01.7552	0.4	+61:27:19.784	0.5	-	38	1705	72
	Jet	23:14:01.7539	1.7	+61:27:19.806	3.8	-	38	892	104
G118.6172-01.3312	A	00:15:27.8538	4.4	+61:14:19.285	5.7	271	44	381	100
	B	00:15:27.8247	10.3	+61:14:19.039	8.1	178	44	175	73
G126.7144-00.8220	A	01:23:33.1088	0.4	+61:48:48.769	0.5	4005	52	5500	180
	A2	01:23:33.1053	1.4	+61:48:48.920	1.8	1133	52	1360	160
G133.7150+01.2155	B	02:25:40.4985	3.1	+62:06:07.234	2.1	467	67	415	101
	Q2/K3	02:25:40.6731	1.6	+62:05:52.051	1.2	1144	71	1180	120

Table B.19: Continued

Object	Lobe	α (J2000) (hh:mm:ss)	$\delta\alpha$ (mas)	δ (J2000) (dd:mm:ss)	$\delta\delta$ (mas)	S_{44}^{Peak} (μ Jy)	δS_{44}^{Peak} (μ Jy)	S_{44} (μ Jy)	δS_{44} (μ Jy)
	Q3/K4	02:25:40.6778	0.8	+62:05:51.522	0.9	2056	71	2960	170
	Q4/K6	02:25:40.7274	1.1	+62:05:49.862	0.7	1450	71	1460	120
	Q5/K7	02:25:40.7810	0.5	+62:05:52.502	0.5	3607	71	5160	170
	Q6/K5	02:25:40.7101	9.6	+62:05:52.632	4.1	494	71	1140	250
	Q7	02:25:40.7548	1.8	+62:05:52.059	1.9	1271	71	2410	220
	Q8	02:25:40.8653	2.2	+62:05:53.573	1.7	1030	71	1960	210
	QE1	02:25:42.6240	0.5	+62:05:43.028	0.4	3912	78	4150	150
	QE2	02:25:40.3032	1.5	+62:05:46.383	1.4	1045	63	1200	130
G134.2792+00.8561	-	-	-	-	-	-	51	-	-
G136.3833+02.2666	A	02:50:08.4906	3.1	+61:59:52.067	2.2	433	48	472	85
G138.2957+01.5552	A	03:01:31.2759	2.2	+60:29:12.790	1.3	658	60	554	93
G139.9091+00.1969A	A	03:07:24.4912	1.8	+58:30:42.803	1.2	1072	62	1390	140
	B	03:07:24.5713	4.5	+58:30:52.974	1.6	601	69	696	136
G141.9996+01.8202	A	03:27:38.7937	1.8	+58:47:00.144	2.4	750	60	1040	140
G143.8118-01.5699	-	-	-	-	-	-	52	-	-
G148.1201+00.2928	A	03:56:15.3893	12.3	+53:52:13.015	2.1	283	50	393	106
	A2	03:56:15.3749	9.4	+53:52:13.074	2.5	228	50	244	82

Table B.19: Continued

Object	Lobe	α (J2000) (hh:mm:ss)	$\delta\alpha$ (mas)	δ (J2000) (dd:mm:ss)	$\delta\delta$ (mas)	S_{44}^{Peak} (μ Jy)	δS_{44}^{Peak} (μ Jy)	S_{44} (μ Jy)	δS_{44} (μ Jy)
W48	A	19:01:46.4599	0.9	+01:13:23.603	0.9	2316	58	4840	190
	B	19:01:45.1878	2.4	+01:13:35.315	2.6	303	39	293	61

Table B.20: Sizes and position angles at C-band for all detected sources derived from IMFIT.

Object	Lobe	θ_{maj} (mas)	$\delta\theta_{maj}$ (mas)	θ_{min} (mas)	$\delta\theta_{min}$ (mas)	θ_{PA} (mas)	$\delta\theta_{PA}$ (mas)
18517+0437	A	-	-	-	-	-	-
	B	-	-	-	-	-	-
	C	-	-	-	-	-	-
18556+0136	13	327	63	64	129	52	16
	14	382	12	207	12	16	3
	15	340	37	204	27	156	10
	4	606	25	232	14	145	2
	5	< 66	-	< 38	-	-	-
	6	89	70	16	69	136	38
	7	456	24	224	18	137	4
	8	314	10	134	15	24	3
	Core A	-	-	-	-	-	-
	EX-N	932	68	331	31	3	2
EX-S	784	282	281	263	115	20	
G018.82-00.28	Core	417	7	324	3	134	2
	Extended	4850	160	3240	110	74	3
G024.08+00.04	A	817	25	742	26	102	16
	B	-	-	-	-	-	-
	B1	641	35	367	21	137	4
	B2	1496	22	219	5	144	0
	B3	1765	97	650	51	36	2
G024.33+00.11	A	179	36	111	92	122	29
	B	-	-	-	-	-	-
	D	296	9	187	14	111	4
G024.60+00.08	A	194	76	124	76	149	63

Table B.20: Continued

Object	Lobe	θ_{maj} (mas)	$\delta\theta_{maj}$ (mas)	θ_{min} (mas)	$\delta\theta_{min}$ (mas)	θ_{PA} (mas)	$\delta\theta_{PA}$ (mas)
G028.28-00.34	B	< 180	-	< 88	-	-	-
	A	< 170	-	< 56	-	-	-
	HII	2750	56	1171	25	99	1
G028.37+00.07	A	-	-	-	-	-	-
	A3	< 740	-	< 180	-	-	-
	B	99	22	53	37	167	36
	C	-	-	-	-	-	-
	D	315	12	139	23	71	3
G028.67+00.13	HII	4044	51	3173	40	151	2
G033.64-00.21	A	271	122	182	82	2	50
	B	-	-	-	-	-	-
	C	160	33	36	80	83	27
G033.68-00.26		-	-	-	-	-	-
G033.69-00.01	A	1070	48	1049	47	39	86
G041.34-00.14		-	-	-	-	-	-
G049.57-00.38		-	-	-	-	-	-
G056.3694-00.6333	A	350	133	210	172	59	82
	B	359	179	202	176	76	67
	C	1100	360	800	290	135	41
	D	450	237	202	188	165	34
G077.5671+03.6911	A	80	145	60	66	106	74
G078.8699+02.7602	A	< 210	-	< 130	-	-	-
	B	361	137	112	112	36	64
	C	< 160	-	< 39	-	-	-
	D	96	22	60	50	95	38
	E	-	-	-	-	-	-

Table B.20: Continued

Object	Lobe	θ_{maj} (mas)	$\delta\theta_{maj}$ (mas)	θ_{min} (mas)	$\delta\theta_{min}$ (mas)	θ_{PA} (mas)	$\delta\theta_{PA}$ (mas)
G079.8855+02.5517	A	-	-	-	-	-	-
	B	-	-	-	-	-	-
	C1	-	-	-	-	-	-
	C2	-	-	-	-	-	-
	D	-	-	-	-	-	-
G081.8652+00.7800	A	-	-	-	-	-	-
	HII	7529	114	5589	84	7	2
	VLA1Core	124	9	109	11	103	35
	VLA1Jet	875	31	181	13	42	1
	VLA2	469	20	177	15	24	2
	VLA3	207	8	51	31	166	3
	VLA4	211	30	154	36	88	28
	VLA5	330	231	159	216	113	63
	VLA6	274	132	230	134	70	88
	VLA7	747	126	507	94	173	21
	W75NBc	238	11	223	10	35	69
W75NBc2	253	14	189	14	57	10	
G083.7071+03.2817	A	237	29	45	61	118	9
	B	-	-	-	-	-	-
G084.9505-00.6910	A	173	46	103	84	51	81
G094.2615-00.4116	A1	535	114	95	72	112	7
	A2	322	59	175	144	5	92
	B	302	111	101	91	81	68
G094.3228-00.1671	A	-	-	-	-	-	-
G094.4637-00.8043	A	413	34	144	52	54	6
	B	< 290	-	< 150	-	-	-

Table B.20: Continued

Object	Lobe	θ_{maj} (mas)	$\delta\theta_{maj}$ (mas)	θ_{min} (mas)	$\delta\theta_{min}$ (mas)	θ_{PA} (mas)	$\delta\theta_{PA}$ (mas)
	C	< 190	-	< 120	-	-	-
	D	279	130	176	81	102	86
	E	< 420	-	< 100	-	-	-
	SC1	< 62	-	< 17	-	-	-
G094.6028-01.7966	A	149	44	92	53	91	71
	SC1	94	4	54	5	122	4
G100.3779-03.5784	A	-	-	-	-	-	-
	B	399	144	288	175	69	61
G102.8051-00.7184	A	-	-	-	-	-	-
G103.8744+01.8558	A	464	6	393	6	90	4
	B	291	40	140	61	114	13
	C	381	82	206	85	84	23
	D	-	-	-	-	-	-
	E	675	71	141	58	13	3
	F	-	-	-	-	-	-
G105.5072+00.2294	A	208	79	51	128	113	31
G107.6823-02.2423A	A	< 650	-	< 240	-	-	-
	HII	2680	280	2290	240	101	41
G108.1844+05.5187	A	1410	330	830	200	42	18
	B	576	103	410	91	24	68
G108.4714-02.8176	A	< 190	-	< 120	-	-	-
G108.5955+00.4935A	B	-	-	-	-	-	-
	C	857	218	485	144	130	17
	D	< 170	-	< 100	-	-	-
G108.7575-00.9863	A	-	-	-	-	-	-
	B	-	-	-	-	-	-

Table B.20: Continued

Object	Lobe	θ_{maj} (mas)	$\delta\theta_{maj}$ (mas)	θ_{min} (mas)	$\delta\theta_{min}$ (mas)	θ_{PA} (mas)	$\delta\theta_{PA}$ (mas)
	C	< 300	-	< 98	-	-	-
	D	-	-	-	-	-	-
	E	< 610	-	< 140	-	-	-
G110.0931-00.0641	A1	195	37	138	50	49	82
	A2	287	116	136	110	68	31
	B	397	28	177	28	116	4
	C	170	13	57	49	116	7
	D	857	132	379	74	107	7
	E	-	-	-	-	-	-
G111.2348-01.2385	A	< 250	-	< 49	-	-	-
G111.2552-00.7702	A1	298	47	123	54	128	14
	A2	539	265	196	182	106	70
	B	-	-	-	-	-	-
	C	-	-	-	-	-	-
	D	473	216	100	88	78	27
G111.5671+00.7517	A	145	24	67	38	49	21
	B1	644	107	445	81	50	26
	B2	773	152	365	88	36	10
	C	249	26	77	41	117	8
	D	249	91	74	114	168	30
G114.0835+02.8568	A1	258	50	41	90	117	12
	A2	-	-	-	-	-	-
	B	1020	210	440	110	116	9
	C	215	15	104	27	131	7
	D	-	-	-	-	-	-
G118.6172-01.3312		-	-	-	-	-	-

Table B.20: Continued

Object	Lobe	θ_{maj} (mas)	$\delta\theta_{maj}$ (mas)	θ_{min} (mas)	$\delta\theta_{min}$ (mas)	θ_{PA} (mas)	$\delta\theta_{PA}$ (mas)
G126.7144-00.8220	A	252	16	14	43	170	4
G133.7150+01.2155	A	393	50	144	76	50	9
	B	< 74	-	< 58	-	-	-
	C1	1250	181	506	84	25	6
	K8	184	25	97	71	55	26
	Q1/K2	202	44	31	36	155	10
	Q10	< 430	-	< 98	-	-	-
	Q2/K3	< 560	-	< 68	-	-	-
	Q3/K4	-	-	-	-	-	-
	Q4/K6	-	-	-	-	-	-
	Q4b	145	42	63	60	51	57
	Q5/K7	-	-	-	-	-	-
	Q6/K5	< 200	-	< 110	-	-	-
	Q7	230	14	42	39	31	5
	Q8	261	16	128	26	24	6
	Q9	228	79	136	88	132	76
	QE1	-	-	-	-	-	-
	QE2	-	-	-	-	-	-
G134.2792+00.8561	A	167	110	119	109	63	43
	B	-	-	-	-	-	-
	C	82	26	38	30	169	36
G136.3833+02.2666	A	-	-	-	-	-	-
	B	2100	430	1730	350	23	42
	C	< 140	-	< 88	-	-	-
	D	366	157	58	115	161	30
	E	-	-	-	-	-	-

Table B.20: Continued

Object	Lobe	θ_{maj} (mas)	$\delta\theta_{maj}$ (mas)	θ_{min} (mas)	$\delta\theta_{min}$ (mas)	θ_{PA} (mas)	$\delta\theta_{PA}$ (mas)
G138.2957+01.5552	A	< 180	-	< 120	-	-	-
	B	565	169	310	153	57	24
	C	-	-	-	-	-	-
	D	-	-	-	-	-	-
	E	-	-	-	-	-	-
	HII	2426	118	1891	93	18	8
G139.9091+00.1969A	A	145	22	29	55	62	14
	Ab	686	128	336	105	61	14
	Ac	966	408	123	175	162	12
	B	< 410	-	< 71	-	-	-
	HII	2319	23	2256	22	74	19
G141.9996+01.8202	A	210	29	47	70	58	13
	B	-	-	-	-	-	-
	C	-	-	-	-	-	-
G143.8118-01.5699	A	112	124	21	116	157	75
	B	269	156	123	172	25	116
	C	-	-	-	-	-	-
G148.1201+00.2928	A	-	-	-	-	-	-
	B	-	-	-	-	-	-
	C	< 190	-	< 110	-	-	-
	D	< 150	-	< 10	-	-	-
G160.1452+03.1559	A	153	71	50	64	111	86
	B	-	-	-	-	-	-
G173.4839+02.4317	A1	187	46	95	68	87	34
	A2	-	-	-	-	-	-
	B	< 450	-	< 150	-	-	-

Table B.20: Continued

Object	Lobe	θ_{maj} (mas)	$\delta\theta_{maj}$ (mas)	θ_{min} (mas)	$\delta\theta_{min}$ (mas)	θ_{PA} (mas)	$\delta\theta_{PA}$ (mas)
	C	-	-	-	-	-	-
	D	352	99	72	118	49	22
	E1	< 180	-	< 58	-	-	-
	E2	318	112	231	219	165	86
	E3	-	-	-	-	-	-
	E4	< 600	-	< 140	-	-	-
	E5	-	-	-	-	-	-
	E6	-	-	-	-	-	-
	F	-	-	-	-	-	-
	G	-	-	-	-	-	-
G174.1974-00.0763	A	< 110	-	< 64	-	-	-
	B	487	18	124	30	153	2
	C	< 48	-	< 32	-	-	-
G177.7291-00.3358	A	-	-	-	-	-	-
	B	163	132	46	129	157	53
G183.3485-00.5751	A	-	-	-	-	-	-
	B	< 510	-	< 11	-	-	-
G188.9479+00.8871	A	< 390	-	< 68	-	-	-
	B1	-	-	-	-	-	-
	B2	< 1100	-	< 370	-	-	-
	C	116	157	28	84	103	41
	D	184	59	100	54	53	30
G189.0307+00.7821	A1	120	72	112	18	163	83
	A2	< 320	-	< 180	-	-	-
	B	245	119	60	84	92	19
	C	221	45	180	40	46	63

Table B.20: Continued

Object	Lobe	θ_{maj} (mas)	$\delta\theta_{maj}$ (mas)	θ_{min} (mas)	$\delta\theta_{min}$ (mas)	θ_{PA} (mas)	$\delta\theta_{PA}$ (mas)
G192.6005-00.0479	D	< 290	-	< 100	-	-	-
	E	506	246	130	119	85	31
	F	-	-	-	-	-	-
	A	< 410	-	< 24	-	-	-
	B	-	-	-	-	-	-
	C	1300	460	400	150	75	12
	D	333	26	87	86	133	8
	E	-	-	-	-	-	-
	F	444	178	156	72	67	24
G196.4542-01.6777	G	402	50	264	49	34	15
	H	-	-	-	-	-	-
	I	-	-	-	-	-	-
	A1	435	40	134	11	64	2
	A2	1191	333	152	79	64	3
	B	593	134	456	251	138	78
W48	C	-	-	-	-	-	-
	D	-	-	-	-	-	-
	B	-	-	-	-	-	-
	III	3860	79	3800	78	120	54

Table B.21: Sizes and position angles at Q-band for all detected sources derived from IMFIT.

Object	Lobe	θ_{maj} (mas)	$\delta\theta_{maj}$ (mas)	θ_{min} (mas)	$\delta\theta_{min}$ (mas)	θ_{PA} (mas)	$\delta\theta_{PA}$ (mas)
18517+0437	B	< 22	-	< 19	-	-	-
18556+0136	5	-	-	-	-	-	-
	6	20	4	12	4	158	30
	7	34	2	9	4	166	5
	7b	58	28	20	24	104	29
	8	40	6	29	5	161	35
	8b	51	26	30	21	92	52
	Core A	< 27	-	< 15	-	-	-
G018.82-00.28	Core	577	58	417	42	116	10
G024.08+00.04		0	0	0	0	0	0
G024.33+00.11	A	111	14	26	13	118	5
	C	77	11	33	2	158	3
G024.60+00.08		-	-	-	-	-	-
G028.28-00.34	HII	162	18	139	11	22	15
G028.37+00.07	A	220	70	63	28	129	10
	A2	55	29	4	18	164	56
	A3	176	26	72	15	25	7
G028.67+00.13		-	-	-	-	-	-
G033.64-00.21	A	79	27	31	32	80	31
	D	135	56	39	28	153	13
G033.66-00.25		-	-	-	-	-	-
G033.68-00.26		-	-	-	-	-	-
G033.69-00.01	E	-	-	-	-	-	-
G033.69-00.01ii		-	-	-	-	-	-
G033.69-00.01iii		-	-	-	-	-	-

Table B.21: Continued

Object	Lobe	θ_{maj} (mas)	$\delta\theta_{maj}$ (mas)	θ_{min} (mas)	$\delta\theta_{min}$ (mas)	θ_{PA} (mas)	$\delta\theta_{PA}$ (mas)
G041.34-00.14		-	-	-	-	-	-
G049.57-00.38		-	-	-	-	-	-
G056.3694-00.6333		-	-	-	-	-	-
G077.5671+03.6911		-	-	-	-	-	-
G078.8699+02.7602	A	71	4	36	5	149	6
	B	57	20	33	35	179	119
	C	-	-	-	-	-	-
G079.8855+02.5517	A	31	8	20	18	168	89
	C1	< 77	-	< 26	-	-	-
	C2	67	15	20	14	131	15
	D	64	18	37	20	123	45
G081.8652+00.7800	A	< 36	-	< 11	-	-	-
	VLA1Core	81	5	40	4	35	4
	VLA2	24	6	10	11	30	32
	VLA3	53	1	26	1	163	2
G083.7071+03.2817	A	44	10	12	10	111	18
G084.9505-00.6910	B	-	-	-	-	-	-
G094.2615-00.4116	A1	-	-	-	-	-	-
G094.3228-00.1671	A	< 26	-	< 9	-	-	-
G094.4637-00.8043	A	28	11	15	16	148	78
	A2	< 34	-	< 11	-	-	-
	C	< 38	-	< 13	-	-	-
G094.6028-01.7966	A	-	-	-	-	-	-
G100.3779-03.5784	A	< 40	-	< 3	-	-	-
G102.8051-00.7184		-	-	-	-	-	-
G103.8744+01.8558	A	334	77	118	28	66	7

Table B.21: Continued

Object	Lobe	θ_{maj} (mas)	$\delta\theta_{maj}$ (mas)	θ_{min} (mas)	$\delta\theta_{min}$ (mas)	θ_{PA} (mas)	$\delta\theta_{PA}$ (mas)
G105.5072+00.2294	A	25	20	22	16	106	46
G107.6823-02.2423A	A						
G108.1844+05.5187	A	79	11	16	10	42	7
G108.4714-02.8176	A	40	28	22	11	101	25
G108.5955+00.4935A		-	-	-	-	-	-
G108.7575-00.9863	A	< 35	-	< 18	-	-	-
G110.0931-00.0641	B	76	32	42	31	123	52
	C	53	15	8	41	173	124
	F	-	-	-	-	-	-
G111.2348-01.2385	A	35	4	16	5	173	9
G111.2552-00.7702	A1	-	-	-	-	-	-
G111.5671+00.7517	A	28	3	16	4	16	16
	Disc	-	-	-	-	-	-
	Jet	-	-	-	-	-	-
G118.6172-01.3312	A	48	24	21	21	15	57
	B	-	-	-	-	-	-
G126.7144-00.8220	A	< 38	-	< 11	-	-	-
	A2	-	-	-	-	-	-
G133.7150+01.2155	B	-	-	-	-	-	-
	Q2/K3	-	-	-	-	-	-
	Q3/K4	40	5	13	10	161	15
	Q4/K6	-	-	-	-	-	-
	Q5/K7	39	3	19	6	3	8
	Q6/K5	106	27	13	19	112	8
	Q7	54	6	38	8	149	215
	Q8	48	10	37	15	118	54

Table B.21: Continued

Object	Lobe	θ_{maj} (mas)	$\delta\theta_{maj}$ (mas)	θ_{min} (mas)	$\delta\theta_{min}$ (mas)	θ_{PA} (mas)	$\delta\theta_{PA}$ (mas)
	QE1	< 16	-	< 1	-	-	-
	QE2	< 34	-	< 1	-	-	-
G134.2792+00.8561		-	-	-	-	-	-
G136.3833+02.2666	A	-	-	-	-	-	-
G138.2957+01.5552	A	-	-	-	-	-	-
G139.9091+00.1969A	A	28	10	22	18	55	83
	B	-	-	-	-	-	-
G141.9996+01.8202	A	< 53	-	< 2	-	-	-
G143.8118-01.5699		-	-	-	-	-	-
G148.1201+00.2928	A	-	-	-	-	-	-
	A2	-	-	-	-	-	-
W48	A	65	4	33	2	131	4
	B	-	-	-	-	-	-

Table B.22: Spectral indices, major axis coefficients and changes in position angles from C to Q-band. $\text{Lim}(\alpha)$ and $\text{Lim}(\gamma)$ show if the calculated values for α and γ are upper or lower limits, if at all.

Object	Lobe	α	$\delta\alpha$	$\text{Lim}(\alpha)?$	γ	$\delta\gamma$	$\text{Lim}(\gamma)?$	$\Delta\theta_{PA}$ ($^{\circ}$)	$\delta\Delta\theta_{PA}$ ($^{\circ}$)
18517+0437	A	0.73	0.18	<	-	-	-	-	-
	B	1.16	0.16	False	-	-	-	-	-
	C	0.44	0.15	<	-	-	-	-	-
18556+0136	13	-0.10	0.15	<	-	-	-	-	-
	14	-1.13	0.13	<	-	-	-	-	-
	15	-0.52	0.14	<	-	-	-	-	-
	4	-0.97	0.13	<	-	-	-	-	-
	5	-0.23	0.16	False	-	-	-	-	-
	6	1.08	0.09	False	-0.74	0.40	False	-22	48
	7	0.64	0.07	False	-1.29	0.05	False	-29	6
	7b	1.22	0.26	>	-	-	-	-	-
	8	-0.11	0.09	False	-1.02	0.07	False	-136	35
	8b	1.29	0.22	>	-	-	-	-	-
	Core A	1.15	0.13	False	-	-	-	-	-
EX-N	-1.32	0.14	<	-	-	-	-	-	
EX-S	-0.81	0.22	<	-	-	-	-	-	

Table B.22: Continued

Object	Lobe	α	$\delta\alpha$	Lim(α)?	γ	$\delta\gamma$	Lim(γ)?	$\Delta\theta_{PA}$ ($^{\circ}$)	$\delta\Delta\theta_{PA}$ ($^{\circ}$)
G018.82-00.28	Core	0.16	0.07	False	0.16	0.05	False	18	10
	Extended	-2.84	0.13	<	-	-	-	-	-
G024.08+00.04	A	-1.81	0.13	<	-	-	-	-	-
	B1	-0.45	0.13	<	-	-	-	-	-
	B2	-1.02	0.13	<	-	-	-	-	-
	B3	-0.56	0.13	<	-	-	-	-	-
G024.33+00.11	A	0.70	0.11	False	-0.24	0.12	False	4	29
	B	1.61	0.14	<	-	-	-	-	-
	C	1.34	0.19	>	-	-	-	-	-
	D	31.96	0.13	<	-	-	-	-	-
G024.60+00.08	A	1.93	0.14	<	-	-	-	-	-
	B	2.95	0.16	<	-	-	-	-	-
G028.28-00.34	A	1.33	0.13	<	-	-	-	-	-
	HII	-1.86	0.10	False	-1.40	0.06	False	77	15
G028.37+00.07	A	1.38	0.24	False	-	-	-	-	-
	A2	1.14	0.20	>	-	-	-	-	-
	A3	1.60	0.22	False	-0.71	0.07	>	-	-

Table B.22: Continued

Object	Lobe	α	$\delta\alpha$	Lim(α)?	γ	$\delta\gamma$	Lim(γ)?	$\Delta\theta_{PA}$ ($^{\circ}$)	$\delta\Delta\theta_{PA}$ ($^{\circ}$)
	B	-0.12	0.13	<	-	-	-	-	-
	C	1.08	0.18	<	-	-	-	-	-
	D	27.74	0.13	<	-	-	-	-	-
G028.67+00.13	HII	-3.02	0.13	<	-	-	-	-	-
G033.64-00.21	A	0.90	0.25	False	-0.61	0.28	False	-78	59
	B	0.94	0.21	<	-	-	-	-	-
	C	0.91	0.13	<	-	-	-	-	-
	D	1.38	0.25	>	-	-	-	-	-
G033.69-00.01	A	-1.18	0.13	<	-	-	-	-	-
	E	0.86	0.24	>	-	-	-	-	-
G056.3694-00.6333	A	0.32	0.18	<	-	-	-	-	-
	B	0.45	0.21	<	-	-	-	-	-
	C	0.01	0.21	<	-	-	-	-	-
	D	0.55	0.24	<	-	-	-	-	-
G077.5671+03.6911	A	0.61	0.18	<	-	-	-	-	-
G078.8699+02.7602	A	1.41	0.10	False	-0.54	0.03	>	-	-
	B	0.64	0.28	False	-0.91	0.26	False	-143	135

Table B.22: Continued

Object	Lobe	α	$\delta\alpha$	Lim(α)?	γ	$\delta\gamma$	Lim(γ)?	$\Delta\theta_{PA}$ ($^{\circ}$)	$\delta\Delta\theta_{PA}$ ($^{\circ}$)
G079.8855+02.5517	C	1.12	0.11	False	-	-	-	-	-
	D	-0.07	0.13	<	-	-	-	-	-
	E	0.72	0.20	<	-	-	-	-	-
	A	0.79	0.10	False	-	-	-	-	-
	B	1.44	0.16	<	-	-	-	-	-
	C1	1.32	0.19	>	-	-	-	-	-
	C2	1.47	0.17	>	-	-	-	-	-
G081.8652+00.7800	D	1.50	0.18	>	-	-	-	-	-
	A	1.00	0.11	False	-	-	-	-	-
	HII	-2.87	0.13	<	-	-	-	-	-
	VLA1Core	0.19	0.08	False	-0.21	0.05	False	68	35
	VLA1Jet	-1.21	0.13	<	-	-	-	-	-
	VLA2	0.11	0.09	False	-1.46	0.12	False	-6	32
	VLA3	1.02	0.06	False	-0.67	0.02	False	4	3
	VLA4	-0.68	0.13	<	-	-	-	-	-
	VLA5	0.45	0.34	<	-	-	-	-	-
	VLA6	0.32	0.21	<	-	-	-	-	-

Table B.22: Continued

Object	Lobe	α	$\delta\alpha$	Lim(α)?	γ	$\delta\gamma$	Lim(γ)?	$\Delta\theta_{PA}$ ($^{\circ}$)	$\delta\Delta\theta_{PA}$ ($^{\circ}$)
	VLA7	-0.37	0.16	<	-	-	-	-	-
	W75NBc	-1.20	0.13	<	-	-	-	-	-
	W75NBc2	-1.01	0.13	<	-	-	-	-	-
G083.7071+03.2817	A	0.47	0.11	False	-0.83	0.13	False	7	20
	B	-0.29	0.14	<	-	-	-	-	-
G084.9505-00.6910	A	1.32	0.14	<	-	-	-	-	-
	B	1.11	0.19	>	-	-	-	-	-
G094.2615-00.4116	A1	0.47	0.24	False	-	-	-	-	-
	A2	0.39	0.17	<	-	-	-	-	-
	B	0.81	0.17	<	-	-	-	-	-
G094.3228-00.1671	A	1.19	0.18	False	-	-	-	-	-
G094.4637-00.8043	A	0.39	0.12	False	-1.33	0.20	False	-94	78
	A2	1.47	0.17	>	-	-	-	-	-
	B	-0.02	0.14	<	-	-	-	-	-
	C	0.86	0.12	False	-	-	-	-	-
	D	0.43	0.18	<	-	-	-	-	-
	E	0.51	0.18	<	-	-	-	-	-

Table B.22: Continued

Object	Lobe	α	$\delta\alpha$	Lim(α)?	γ	$\delta\gamma$	Lim(γ)?	$\Delta\theta_{PA}$ ($^{\circ}$)	$\delta\Delta\theta_{PA}$ ($^{\circ}$)
	SC1	-0.54	0.13	<	-	-	-	-	-
G094.6028-01.7966	A	0.49	0.11	False	-	-	-	-	-
	SC1	-0.90	0.13	<	-	-	-	-	-
G100.3779-03.5784	A	0.79	0.16	False	-	-	-	-	-
	B	0.31	0.18	<	-	-	-	-	-
G102.8051-00.7184	A	0.61	0.15	<	-	-	-	-	-
G103.8744+01.8558	A	-0.42	0.16	False	-0.16	0.11	False	24	8
	B	-0.32	0.14	<	-	-	-	-	-
	C	0.11	0.16	<	-	-	-	-	-
	D	0.65	0.17	<	-	-	-	-	-
	E	-0.18	0.14	<	-	-	-	-	-
	F	0.74	0.21	<	-	-	-	-	-
G105.5072+00.2294	A	1.02	0.16	False	-1.05	0.44	False	7	55
G107.6823-02.2423A	A	1.15	0.26	False	-	-	-	-	-
	HII	-0.89	0.14	<	-	-	-	-	-
G108.1844+05.5187	A	1.05	0.17	False	-1.42	0.13	False	0	19
	B	1.31	0.16	<	-	-	-	-	-

Table B.22: Continued

Object	Lobe	α	$\delta\alpha$	Lim(α)?	γ	$\delta\gamma$	Lim(γ)?	$\Delta\theta_{PA}$ ($^{\circ}$)	$\delta\Delta\theta_{PA}$ ($^{\circ}$)
G108.4714-02.8176	A	0.55	0.20	False	-0.77	0.35	>	-	-
G108.5955+00.4935A	B	0.91	0.20	<	-	-	-	-	-
	C	0.09	0.19	<	-	-	-	-	-
	D	1.62	0.14	<	-	-	-	-	-
G108.7575-00.9863	A	0.94	0.12	False	-	-	-	-	-
	B	1.01	0.21	<	-	-	-	-	-
	C	0.73	0.16	<	-	-	-	-	-
	D	1.26	0.20	<	-	-	-	-	-
	E	0.95	0.21	<	-	-	-	-	-
G110.0931-00.0641	A1	-0.01	0.14	<	-	-	-	-	-
	A2	0.59	0.20	<	-	-	-	-	-
	B	0.34	0.18	False	-0.82	0.21	False	-7	52
	C	-0.08	0.20	False	-0.58	0.14	False	-57	124
	D	-0.08	0.16	<	-	-	-	-	-
	E	1.96	0.20	<	-	-	-	-	-
	F	1.07	0.24	>	-	-	-	-	-
G111.2348-01.2385	A	1.10	0.10	False	-0.97	0.06	>	-	-

Table B.22: Continued

Object	Lobe	α	$\delta\alpha$	Lim(α)?	γ	$\delta\gamma$	Lim(γ)?	$\Delta\theta_{PA}$ ($^{\circ}$)	$\delta\Delta\theta_{PA}$ ($^{\circ}$)
G111.2552-00.7702	A1	0.16	0.16	False	-	-	-	-	-
	A2	0.50	0.24	<	-	-	-	-	-
	B	1.02	0.19	<	-	-	-	-	-
	C	0.86	0.18	<	-	-	-	-	-
	D	1.14	0.20	<	-	-	-	-	-
G111.5671+00.7517	A	0.87	0.08	False	-0.82	0.10	False	33	26
	B1	-0.09	0.16	<	-	-	-	-	-
	B2	0.09	0.17	<	-	-	-	-	-
	C	-0.34	0.13	<	-	-	-	-	-
	D	0.71	0.18	<	-	-	-	-	-
	Disc	2.00	0.14	>	-	-	-	-	-
	Jet	1.68	0.16	>	-	-	-	-	-
G118.6172-01.3312	A	1.45	0.22	>	-	-	-	-	-
	B	1.06	0.28	>	-	-	-	-	-
G126.7144-00.8220	A	0.72	0.08	False	-0.93	0.03	<	-	-
	A2	1.40	0.16	>	-	-	-	-	-
G133.7150+01.2155	A	-0.41	0.15	<	-	-	-	-	-

Table B.22: Continued

Object	Lobe	α	$\delta\alpha$	Lim(α)?	γ	$\delta\gamma$	Lim(γ)?	$\Delta\theta_{PA}$ ($^{\circ}$)	$\delta\Delta\theta_{PA}$ ($^{\circ}$)
	B	-0.13	0.18	False	-	-	-	-	-
	C1	-1.16	0.16	<	-	-	-	-	-
	K8	-0.83	0.14	<	-	-	-	-	-
	Q1/K2	-0.54	0.14	<	-	-	-	-	-
	Q10	0.27	0.27	<	-	-	-	-	-
	Q2/K3	0.16	0.13	False	-	-	-	-	-
	Q3/K4	0.76	0.10	False	-	-	-	-	-
	Q4/K6	0.93	0.15	False	-	-	-	-	-
	Q4b	-0.26	0.14	<	-	-	-	-	-
	Q5/K7	0.85	0.09	False	-	-	-	-	-
	Q6/K5	0.58	0.20	False	-0.31	0.13	>	-	-
	Q7	-0.17	0.10	False	-0.71	0.06	False	-118	215
	Q8	-0.28	0.11	False	-0.84	0.11	False	-94	54
	Q9	-0.59	0.16	<	-	-	-	-	-
	QE1	1.90	0.15	>	-	-	-	-	-
	QE2	1.29	0.17	>	-	-	-	-	-
G134.2792+00.8561	A	0.48	0.17	<	-	-	-	-	-

Table B.22: Continued

Object	Lobe	α	$\delta\alpha$	Lim(α)?	γ	$\delta\gamma$	Lim(γ)?	$\Delta\theta_{PA}$ ($^{\circ}$)	$\delta\Delta\theta_{PA}$ ($^{\circ}$)
G136.3833+02.2666	B	0.60	0.18	<	-	-	-	-	-
	C	-0.12	0.13	<	-	-	-	-	-
	A	0.92	0.18	False	-	-	-	-	-
	B	-0.78	0.17	<	-	-	-	-	-
	C	0.41	0.14	<	-	-	-	-	-
	D	1.71	0.19	<	-	-	-	-	-
G138.2957+01.5552	E	11.32	0.14	<	-	-	-	-	-
	A	0.69	0.15	False	-	-	-	-	-
	B	0.33	0.20	<	-	-	-	-	-
	C	0.76	0.16	<	-	-	-	-	-
	D	1.06	0.20	<	-	-	-	-	-
	E	0.96	0.14	<	-	-	-	-	-
G139.9091+00.1969A	HII	-1.10	0.13	<	-	-	-	-	-
	A	0.42	0.11	False	-0.81	0.19	False	7	84
	Ab	0.01	0.16	<	-	-	-	-	-
	Ac	0.47	0.24	<	-	-	-	-	-
	B	1.13	0.21	False	-	-	-	-	-

Table B.22: Continued

Object	Lobe	α	$\delta\alpha$	Lim(α)?	γ	$\delta\gamma$	Lim(γ)?	$\Delta\theta_{PA}$ ($^{\circ}$)	$\delta\Delta\theta_{PA}$ ($^{\circ}$)
G141.9996+01.8202	HII	-2.14	0.13	<	-	-	-	-	-
	A	0.54	0.13	False	-0.68	0.07	<	-	-
	B	0.60	0.16	<	-	-	-	-	-
G143.8118-01.5699	C	0.38	0.14	<	-	-	-	-	-
	A	0.47	0.16	<	-	-	-	-	-
	B	0.74	0.23	<	-	-	-	-	-
G148.1201+00.2928	C	1.11	0.19	<	-	-	-	-	-
	A	0.89	0.21	False	-	-	-	-	-
	A2	1.09	0.25	>	-	-	-	-	-
W48	B	0.84	0.19	<	-	-	-	-	-
	C	0.37	0.14	<	-	-	-	-	-
	D	2.81	0.13	<	-	-	-	-	-
	A	1.09	0.14	>	-	-	-	-	-
	B	0.34	0.20	>	-	-	-	-	-
	HII	-4.61	0.13	<	-	-	-	-	-

Appendix C

Object Notes

C.1 Southern MYSO sample

C.1.1 Jets, candidates and a disc wind

G010.8411–02.5919

Otherwise known as the Herbig-Haro object, HH 80-81, an outflow axis with a P.A. and spectral index for the central source of $\sim 20^\circ$ and $\alpha \sim -0.3$ respectively has been observed (Marti *et al.* 1993). Polarisation of the radio emission is also present (Carrasco-González *et al.* 2010a) inferring a magnetic field aligned with the jet axis and with a strength of ~ 0.2 mG. At 7mm, a disc with an orientation of $\sim -20^\circ$ (Linz *et al.* 2004) is seen as well as an SiO bipolar outflow whose axis lies at a P.A. of $\sim 70^\circ$ and a monopolar SiO outflow with $\theta_{\text{PA}} \sim -20^\circ$ (Fernández-López *et al.* 2011).

From the 17 and 22.8 GHz observations values of $\alpha = 0.23 \pm 0.14$ and $\gamma = -0.98 \pm 0.63$ are derived with water maser emission detected to the ENE (in

direction of bipolar SiO outflow). Considering the history of observations towards this object, it can be classified as an unambiguous ionised jet.

G012.9090–00.2607

More commonly known by the alias W33A, previous radio observations derive a spectral index for the central source of $\alpha \sim 1.5$ (from 8 to 15 GHz, Rengarajan & Ho 1996a). Q-band observations by van der Tak & Menten (2005) resolved W33A into 3 sources (Q1, Q2 and Q3) with a mean separation of $\sim 0.8''$. Galván-Madrid *et al.* (2010) resolved two previously established mm-cores (MM1 and MM2) ~ 0.1 pc apart, into multiple individual mm-sources. One ESE-WNW outflow centred on MM1-main (Q1) and a NNE-SSW outflow centred on the mm-core MM2. Davies *et al.* (2010) used resolved Br γ emission observations, to infer a fast bipolar wind aligned to the large scale outflow from Q1/MM1-main, with complimentary H₂ 2.12 μ m emission in the same orientation out to $1''$. A rotating disc structure perpendicular to the outflow was also detected in CO, orbiting a central mass of $10^{+9}_{-5} M_{\odot}$.

Water maser emission is detected coincident with the central continuum (~ 550 au SE of MM1-main) source, and $\sim 5''$ to the south, possibly due to collisional pumping from a rapidly moving outflow/jet. By splitting the 17 and 22.8 GHz data into two sub-bands each, the emission can be decomposed into 3 components with a value of $\alpha = 1.37 \pm 0.32$ derived for the emission coincident with Q1, $\alpha > 0.36 \pm 0.47$ for that coincident with Q2 and $\alpha > 0.19 \pm 0.51$ for that coincident with Q3. Without a value for γ for the jet this object must be classified as a jet candidate.

G014.9958–00.6732

Also known as the Kleinmann-Wright object (Kleinmann & Wright 1973). Previous observations in the near infrared (I-band, $0.81\ \mu\text{m}$, Chini *et al.* (2004)) resolved the KW-object into 2 separate early B-type stars (KW-1 and KW-2) separated by ~ 2600 au. Subsequent SED fitting by Povich *et al.* (2009), concluded that the object KW-1 was an early Herbig Be star, while KW-2 remained unresolved, yet coincident with X-ray emission. Radio data at 5.0 and 8.5 GHz by Rodríguez *et al.* (2012a) determined a spectral index of $\alpha = 0.9 \pm 0.6$ (JVLA number 3) for which the source remained unresolved.

An unresolved point source was detected at 17 and 22.8 GHz coincident with JVLA number 3 from Rodríguez *et al.* (2012a). Including the flux recorded at 8.46 GHz by Rodríguez *et al.* (2012a) yields a spectral index of $\alpha = 1.11 \pm 0.23$, indicative of thermal free-free emission. The emission is offset from the nearest source (KW-1) by $\sim 0.88''$ or 1700 au. Likely this indicates a third component absent at the NIR I-band due to heavy extinction, and therefore more embedded and younger. Radio fluxes recorded at 22.8 GHz are ~ 50 times less than that expected from an optically thin HII region of the same bolometric luminosity (Davies *et al.* 2011). Without a definite outflow or position angle, this is classified as a jet candidate.

G251.2337–01.9535

Both $\text{Br}\gamma$ and $[\text{FeII}]$ emission are present in NIR spectra (Lumsden *et al.*, in prep.) towards this MYSO.

From the ATCA observations, a spectral index of $\alpha = 0.08 \pm 0.06$ is derived

for the central object, however it remained unresolved at 3 out of the 4 frequencies. This spectral index suggests a highly collimated ionised jet from the central MYSO or an optically thin HII region, however it is under-luminous by a factor of 5 at 22.8 GHz compared to the flux expected from HII optically thin regions of the same luminosity (which is well constrained given the isolated nature of the source in the infrared). There are hints of more structure to the NNW though this may be an artefact of the deconvolution process. Confusing NIR spectra and under-luminosity of just less than 20% classifies this as a jet candidate.

G254.0491–00.5615

G254.0491–00.5615 looks like a point source at both 10 μm and K-band (with possibly a weak nebula surrounding it). Navarete *et al.* (2015) detect 2.12 μm H₂ emission at a position angle of 310°. NIR spectra (Lumsden *et al.*, in prep.) show no Br γ emission, ruling out a HII region.

The 17 GHz data was poor and affected by side-lobes with resulting derived (between 5.5 and 9 GHz) values of $\alpha = 0.3 \pm 0.3$ and $\gamma = -0.9 \pm 0.2$ found consistent with thermal emission from a collimated jet. Deconvolved position angles at 9 GHz are parallel with the 2.12 μm H₂ emission. This leads to the classification of this source as an ionised jet.

G254.0548–00.0961

Optical knots with velocities of $\sim 570 \text{ km s}^{-1}$ in the ENE-WSW direction (PA $\sim 60^\circ$) have been identified (Neckel & Staude 1995) hence the alias, HH 217. Felli *et al.* (1998) observed unresolved, free-free emission (8.4 and 15.0 GHz), and interpolated a spectral index of $\alpha = 0.3 \pm 0.5$. Emission at the [FeII] line is seen in

NIR spectra (Lumsden et al., in prep.).

Alignment of the central (thermal jet) and west (non-thermal) lobes is parallel to the previously established Herbig-Haro outflow axis. We calculate $\alpha = 0.19 \pm 0.20$, suggestive of collimated jet, therefore this is classified as a thermal jet with a non-thermal lobe.

G263.2283+01.5712

Ks band observations by Burkert *et al.* (2000) show a bipolar reflection nebula centred on their source 25 (Figure 1e in the reference) interpreted as the evacuated bipolar cavities emitting at NIR wavelengths after heating by the central source (the NE cavity is oriented towards us). High extinction at angles perpendicular to the cavities, and general morphology of the emission, are suggestive of a circumstellar accretion disc. From inspection of those images (figure 3b in Burkert *et al.* (2000)), an outflow axis with a P.A. $\sim 130^\circ$ is inferred.

The radio intensity contour maps presented in Figure A.7, show a confirmed radio detection coincident with source 25 of Burkert *et al.* (2000). The derived spectral index is $\alpha = 0.19 \pm 0.24$ indicating thermal free-free emission. From the models of Reynolds (1986), this suggests a thermal, collimated jet of ionised material. Deconvolved position angle at 17 GHz of P.A. = $147 \pm 37^\circ$ is aligned with the outflow cavities. On the basis of the radio emission being parallel with the cavities and perpendicular to the disc, we classify this as an ionised jet.

G263.7434+00.1161

‘Complex and intense’ H₂ emission at $2.12 \mu\text{m}$ (de Luca *et al.* 2007) is seen with no discernable orientation. Thi *et al.* (2010) inferred a jet-bow shock model and

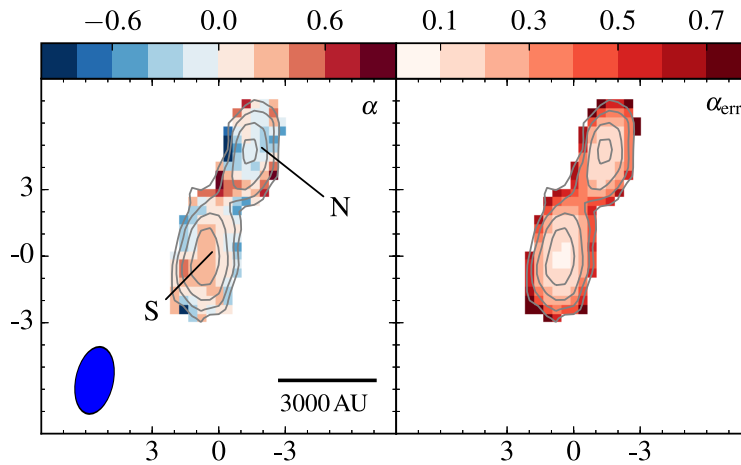


Figure C.1: A map of the spectral index (between 5.5 and 9GHz) for G263.7434+00.1161 (left) and the associated errors in the spectral index (right). The restoring beams (blue) used for both the 5 GHz and 9 GHz data were identical, in the production of the spectral index maps. Grey contours represent the flux densities at 9 GHz starting at 8.04×10^{-5} Jy/beam (4σ), and scaling by a factor of $\sqrt{3}$ for each subsequent contour.

wide-angle wind model to explain their observations of both $^{12}\text{CO}(1 \leftarrow 2)$ and $^{13}\text{CO}(1 \leftarrow 2)$ which both had large turbulent widths ($10 - 12 \text{ km s}^{-1}$).

Our observations of G263.7434+00.1161 reveal two distinct lobes of emission present (separated by ~ 3500 au for a distance of 0.7 kpc) at the lower 3 frequencies (northern lobe) and one detected at all frequencies (southern lobe), for which we find spectral indices of $\alpha = -0.45 \pm 0.31$ and $\alpha = 0.39 \pm 0.18$ respectively. We have also constructed a map of the spectral index variation across the source in Figure C.1, reflecting this thermal/non-thermal emission distribution. For γ , we find a value of -1.01 ± 0.24 for the southern lobe. Given the previous observational history and values for α/γ , we classify this as an ionised jet with a non-thermal lobe.

G263.7759–00.4281

Giannini *et al.* (2005) observed the region looking for $2.12\ \mu\text{m}$ H_2 emission, and identified two jets with NW-SE and ENE-WSW axes, with the first centred on G263.7759–00.4281 (source #57 in their paper) and the other a few tenths of an arcsecond to the NW of #57 (seen as an elongation in the broadband NIR images). Diffraction limited MIR imaging (Wheelwright *et al.* 2012) shows elongation of the MIR emission to the NW-SE, interpreted as emission from the cavity walls (also seen in 2MASS and GLIMPSE imagery). Asymmetry in the images supports the notion of multiplicity, with the second YSO (driving the ENE-WSW outflow) positioned to the NW of G263.7759–00.4281. IRAC GLIMPSE imaging shows 4 knots of excessive $4.5\ \mu\text{m}$ emission along an axis at a position angle of 155° , attributable to the jet (Giannini *et al.* 2013).

Our results show a compact source with extended emission to the NW at a rough position angle of $\sim 140^\circ$, parallel to the outflow axis seen in H_2 emission. Values of $\alpha = 0.52 \pm 0.39$ and -0.78 ± 0.80 are found for the central and NW components respectively. The likelihood that the NW source represents a second source is unlikely due to the probable non-thermal nature of its spectrum. Considering the observational history of this object, we believe this is good evidence for a jet with a non-thermal lobe.

G265.1438+01.4548

Wheelwright *et al.* (2012) observed this object using diffraction limited mid-infrared imaging and based upon SED modelling derived a low inclination angle of 32° , a mass loss rate, $2 \times 10^{-4}\ \text{M}_\odot\ \text{yr}^{-1}$ and an opening angle of $\theta_{\text{OA}} = 25^\circ$.

Considering the symmetrical morphology of the mid-infrared emission, the low inclination angle may in fact be head on to the outflowing material, within the constraints of the SED fitting procedure.

As for radio observations, this object was observed at 17 and 22.8 GHz and displayed maser emission $\sim 6''$ to the north of the source. Imaging of the continuum emission discarded baselines with a length of $< 22\text{k}\lambda$ due to the presence of partially resolved-out, strong and extended emission to the north east, the side lobes from which drowned out the relatively weak flux of the target. At the higher frequency band a relatively simple point like morphology is seen, while at 17 GHz the source is elongated to the NW. We derive a spectral index of $\alpha = 0.5 \pm 0.4$) and θ_{PA} at 17 GHz of $51 \pm 34^\circ$. At 22.8 GHz, we find the central source is over-luminous by a factor of ~ 4 compared to that expected of an optically thin HII region (Davies *et al.* 2011). These observations support the picture of both a disc wind and also a conical, non-collimated jet. It is worth noting that mid-infrared emission seen by Wheelwright *et al.* (2012) was symmetrical and interpreted as looking directly down the ionised flow. This favours the disc-wind picture, though observations at both sub-mm and mm would help eliminate one of these possibilities.

G286.2086+00.1694

GLIMPSE imagery show the MSX point source to be a combination of two red-dened infrared sources separated by $\sim 8''$. TIMMI2 $10\ \mu\text{m}$ emission is seen towards the SE IR source, with weaker $10\ \mu\text{m}$ emission to the NW source.

Radio observations show radio emission associated to the NW IR source, but not the SE source. The emission is comprised of two components (B and B2),

with $\alpha = 0.78 \pm 0.61$ ($\gamma = -0.6 \pm 1.4$) and $\alpha < -0.27$ respectively. Due to large errors and a lack of other observations we classify this as a jet candidate.

G298.2620+00.7394

GLIMPSE observations reveal two point sources within $2''$ of each other, with possible extended emission to the south. A ^{13}CO ($J2 \rightarrow 1$) outflow was seen by Henning *et al.* (2000b), oriented NNW (blue lobe) to SSE. A spectral type for the central MYSO of B0.5 was inferred. Walsh *et al.* (1998) also detected a methanol maser at $12^{\text{h}}11^{\text{m}}47.8^{\text{s}}$, $-61^{\circ}46'19''$ (J2000), slightly offset from an extended green object (EGO) at $12^{\text{h}}11^{\text{m}}47.7^{\text{s}}$, $-61^{\circ}46'21''$ (Cyganowski *et al.* 2008).

A single lobe of emission with $\alpha = 0.79 \pm 0.20$ and $\gamma = -1.09 \pm 0.33$ is detected at all frequencies. An average position angle of $(92 \pm 28)^{\circ}$ is also deduced. The spectral index of the emission can be modelled by a standard, bi-conical jet/wind (Reynolds 1986). Considering the shocked EGO emission and radio emission perpendicular to the outflow, this is classified as a disc wind.

G310.0135+00.3892

Kraus *et al.* (2010) used near-infrared interferometry to observe a hot, dusty, compact ($13 \text{ au} \times 19 \text{ au}$) disc with $\theta_{\text{PA}} = 114^{\circ}$. Sub-mm emission from a collimated (opening angle $\sim 6^{\circ}$) bipolar outflow (Kraus *et al.* 2010) is found perpendicular to the disc. Furthermore, investigations of IRAC images showed two lobes of excess emission at $4.5 \mu\text{m}$ separated by $7'$ (indicative of shocked molecular hydrogen) and aligned with the outflow axis. Corroborating these findings, diffraction limited mid-infrared imaging at $20 \mu\text{m}$ by Wheelwright *et al.* (2012) suggested that the dominant emission at $20 \mu\text{m}$ was due to the presence of cavities evacuated by out-

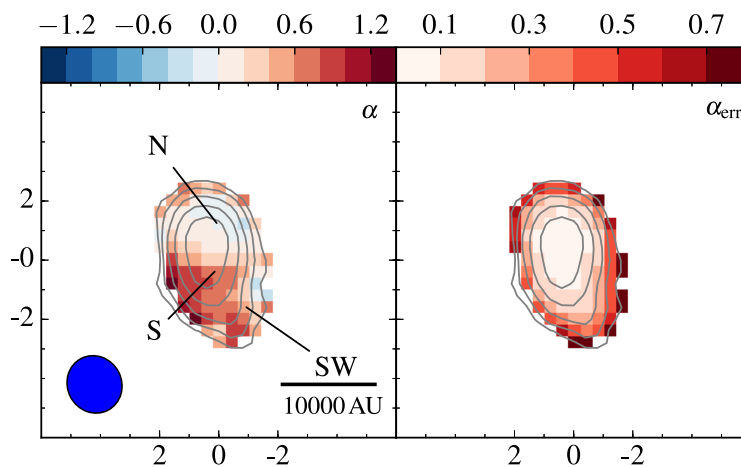


Figure C.2: A map of the spectral index (between 5.5 and 9GHz) for G310.0135+00.3892 (left) and the associated errors in the spectral index (right). The restoring beams (blue) used for both the 5 GHz and 9 GHz data were identical, in the production of the spectral index maps. Grey contours represent the flux densities at 9 GHz starting at $5.64 \times 10^{-5} \text{ Jy/beam}$ (4σ), and scaling by a factor of $\sqrt{3}$ for each subsequent contour.

flows (along a SW-NE axis). Ilee *et al.* (2013) observed CO bandhead emission indicative of entrained envelope material in an outflow, and subsequent modelling found temperature gradients consistent with Kraus *et al.* (2010) and with a flared, irradiated disc around a MYSO with $M_{\star} = 21.8 M_{\odot}$. Broad linewidths (25.5 km s^{-1}) in the CO are also present, as well as high-velocity wings attached to the P-cygni profile of the $\text{Br}\gamma$ line (Stecklum *et al.* 2012), suggestive of an ionised wind. Most recently Caratti o Garatti *et al.* (2015) observed the H_2 2.21 μm transition, detecting lobes of emission spread over 6.9 pc at a position angle of $\sim 206^\circ$, coincident with the SE–NW outflow.

Two distinct lobes of emission are detected at each frequency. The southern lobe is centred on the IRAS point source, whereas the northern lobe is offset to the north by $\sim 2''$. There is also an additional component to the SW, seen

at 5 GHz as a slight extension to the southern lobe, and at 9 GHz as distinct emission at a position angle of $\sim 215^\circ$ and separated by $1.5''$ (~ 4900 au) from the southern lobe. Spectral indices of $\alpha_N = -0.17 \pm 0.12$ and $\alpha_S = 1.27 \pm 0.18$ are derived for the north and south lobes respectively. A spectral index for the south west component of $\alpha_{SW} \sim 0.7$ is derived between 5.5 and 9 GHz. This SW component is also parallel with the observed outflow axis, and perpendicular to the disc inferred by Kraus *et al.* (2010), thus we conclude this to be part of the jet. Corroborating this scenario, the spectral index map in Figure C.2 shows an orientation for the thermal emission along the outflow axis. The southern component centred on the accretion disc, based on its spectral index, is likely to be a pressure confined ionised jet of material imaged close to the accretion disc. We interpret the northern source as a working surface located in the cavities upon which the edges of the ionised jet impinge upon. Thus we classify this as a jet with lobes.

G310.1420+00.7583A

This source is associated to IRAS 13484–6100 and is in close proximity ($\sim 8''$ offset) to a cometary UCHII (G310.1420+00.7583B). Different masing species (OH, H₂O and CH₃OH) have been detected towards this source (Walsh *et al.* (1998), Urquhart *et al.* (2009a) and Green *et al.* (2012) respectively). Caratti o Garatti *et al.* (2015) observed two knots of H₂ emission (blue circles in Figure C.3), one of which displayed Br γ emission indicative of strong dissociative shocks (‘knot 1’) where the shock velocities exceeded 90 km s^{-1} within a medium of density $\sim 10^5 \text{ cm}^{-3}$. Jet properties inferred included a length of 0.4 pc, precession of 17° and electron density of $n_e = (4 \pm 1) \times 10^4 \text{ cm}^{-3}$. An extended green object was

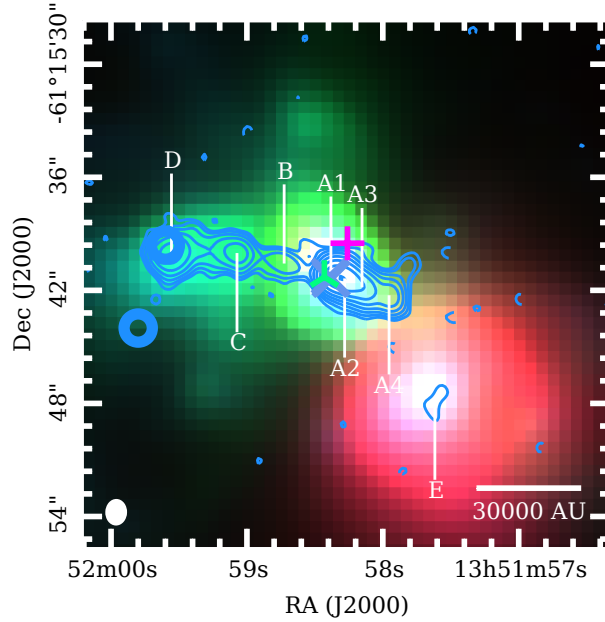


Figure C.3: The 9GHz radio contours overlaid on an RGB ($8.0\ \mu\text{m}$, $4.5\ \mu\text{m}$ and $3.6\ \mu\text{m}$) composite image of existing GLIMPSE data for G310.1420+00.7583A. Contours step up from 4σ by a factor of $\sqrt{3}$ per level and negative (-4σ) contours are dashed. Other annotations have the same meanings as in Figure A.22.

detected offset to knot 1 by $\sim 16''$ at a PA of 57° (Cyganowski *et al.* 2008).

Morphologically, the emission forms a string of at least 7 lobes whose axis lies at a position angle of $\sim 77^\circ$, with the eastern lobes of emission becoming weaker with increasing frequency. A knot of H_2 emission (knot 1 from Caratti o Garatti *et al.* 2015) coincides with the most easterly radio lobe of the eastern emission. Component A1 (centred on the observed water masers) has a thermal, slightly positive spectral index of $\alpha = 0.18 \pm 0.09$. The rest of the derived parameters are shown in Tables B.4–B.6 and due to the complex morphological nature of the target, we plot a map of the spectral index in Figure C.4. This is indicative of thermal emission processes for lobes A1 and B. Component D becomes resolved at the upper two frequencies, and possibly is comprised of

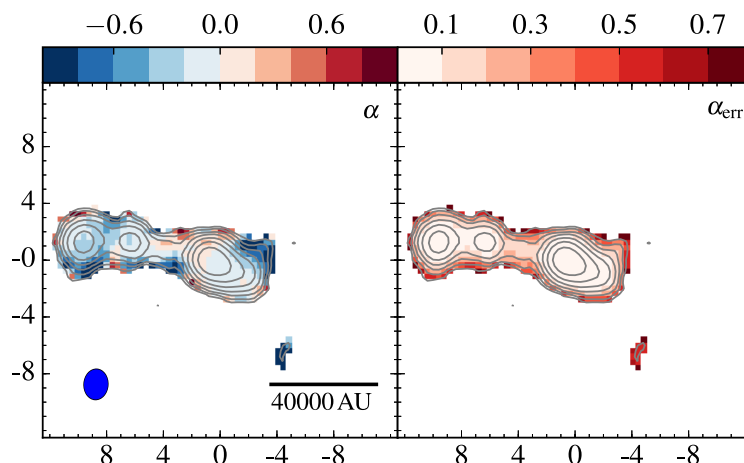


Figure C.4: A map of the spectral index (between 5.5 and 9GHz) for G310.1420+00.7583A (left) and the associated errors in the spectral index (right). The restoring beams (blue) used for both the 5 GHz and 9GHz data were identical, in the production of the spectral index maps. Grey contours represent the flux densities at 9GHz starting at 8.0×10^{-5} Jy/beam (5σ), and scaling by a factor of $\sqrt{5}$ for each subsequent contour.

multiple sources. Considering the orientation of the two knots of H₂ emission with the apparent orientation of the resolved emission of D (especially at 17 GHz), this complicates the picture. From the observations presented here, we believe this to be an ionised jet displaying both thermal and non-thermal emission.

G313.7654–00.8620

Associated to the IRAS point source IRAS 14212–6131, this object has a ¹³CO outflow detection (Urquhart *et al.* 2007b) and masers (OH and methanol). Caratti o Garatti *et al.* (2015) detected 4 knots of H₂ emission which, if tracing a jet, show evidence of a precession in the jet’s axis of 32°. Knot 1 (closest to the MSX point source) has an inferred electron density of $(1 \pm 0.5) \times 10^4$ cm⁻³, while knot 4 (most distant) displays Br γ emission indicative of strong J-type shocks with a

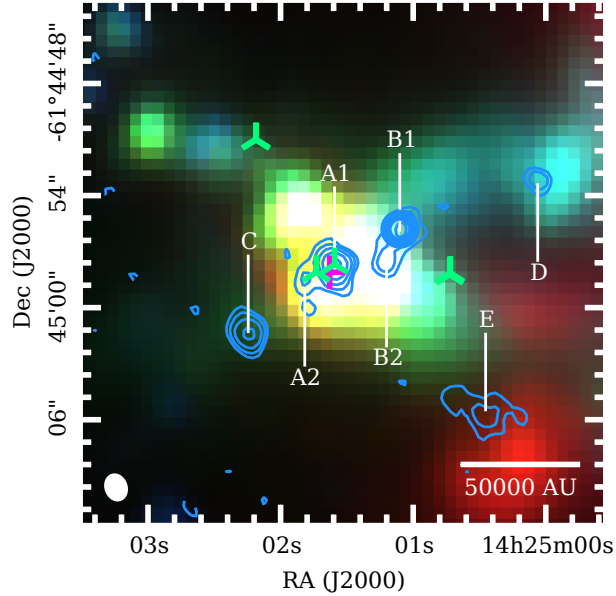


Figure C.5: The 9 GHz radio contours overlaid on an RGB ($8.0\ \mu\text{m}$, $4.5\ \mu\text{m}$ and $3.6\ \mu\text{m}$) composite image of existing GLIMPSE data for G313.7654–00.8620. Contours step up from 3σ (where $\sigma = 1.58 \times 10^{-5}\text{ Jy/beam}$ by a factor of $\sqrt{3}$ per level.

shock speed of $\sim 60\text{ km s}^{-1}$. Currently the jet axis is defined at a position angle of 125° , with a length (on one side) of 1.4 pc. GLIMPSE images show diffuse emission in the direction of the H₂ knot 1, an extended HII region to the south and two point sources within $5''$ of the MSX point source position.

Our observations show at least 7 distinct lobes of emission at both observing frequencies. Lobe B1 coincides with a H₂ emission knot (Caratti o Garatti *et al.* 2015), while A1 is coincident with both methanol (Purser *et al.*, in prep.) and hydroxyl maser emission (Caswell 1998). The NW string of emission (i.e. B1/B2 and D) coincide with extended MIR emission potentially tracing outflow cavities (see Figure C.5). All emission (apart from E) is sited in a linear distribution with the brightest emission (A1) being co-located with the MSX point source’s peak position. A large range of spectral indices are present as shown in Figure C.6 with

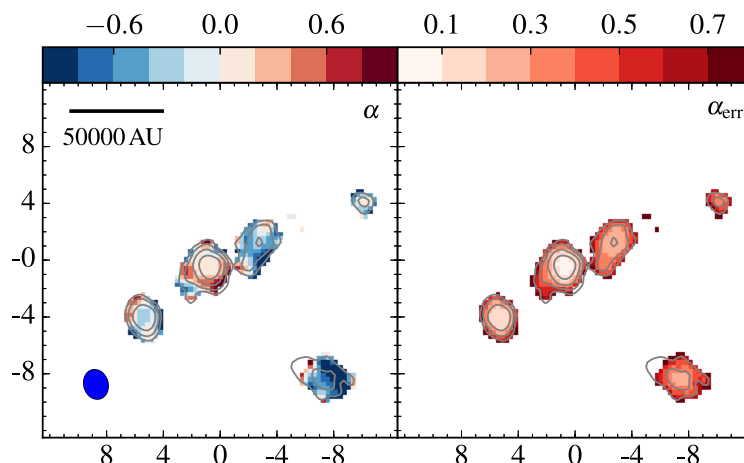


Figure C.6: A map of the spectral index (between 5.5 and 9 GHz) of G313.7654–00.8620 (left) and the map of errors in the spectral index (right). Grey contours represent the flux densities at 9GHz starting at 7.40×10^{-5} Jy/beam (5σ), and scaling by a factor of $\sqrt{5}$ for each subsequent contour.

spectral indices of 0.3, -0.7 , -0.96 , 1.9, 0.04, -0.32 and 0.29 calculated for lobes A1, A2, B1, B2, C, D and E respectively. B1 has the steepest negative spectral index and is coincident with an H_2 knot (knot 1 in Caratti o Garatti *et al.* 2015). The current position angle of this jet from our observations (from the alignment of A1, A2 and B1) is 121° , close to that derived by Caratti o Garatti *et al.* (2015). We classify this as an ionised jet with lobes.

G318.9480–00.1969A

Lee *et al.* (2001) detected H_2 line emission with two H_2 knots present (linearly distributed with the MYSO) separated from the target by $\sim 15''$ to the WNW and ESE. De Buizer (2003) also found 5 knots oriented on the same axis. Methanol masers are distributed in a linear fashion and offset from the centre of $11.7 \mu\text{m}$ emission which is elongated in the direction of the knots ($\text{PA} \sim 145^\circ$), as well as an SiO outflow (blue lobe to the WNW, red to the ESE, De Buizer *et al.* 2009).

Considering the apparent misalignment of the methanol masers with the outflow, the hypothesis of the methanol masers residing in the disc was rejected by De Buizer *et al.* (2009). However, considering that discs can span up to 30000 au in some cases (see the review by Cesaroni *et al.* (2007)), with a flared cross-section, an alternate interpretation is that the masers are residing in the flared outer region of a disc around 1500-2000AU from the central object.

With the observations presented in this work (Figure A.26), radio continuum from this object is detected at all 4 observing frequencies. The emission is point like and unresolved, offset from the $11.7 \mu\text{m}$ emission by $1''$ (3000 au) to the ESE. With a derived spectral index of $\alpha = 0.69 \pm 0.22$, this fits Reynold's model of a conical, non-collimated jet. Lower limits on the deconvolved sizes infer a value for $\gamma > -0.9$, while the deconvolved position angle of $\sim 80^\circ$ (at 22.8 GHz) is parallel with the observed H_2 emission. We dismiss the possibility of a HII region on the basis of the radio luminosity (at 22.8 GHz) being 1.4% of that expected for $L_{\text{bol}} = 1 \times 10^4 \text{ au}$. However, without more information on the deconvolved properties, we must classify this as a jet/disc wind.

G326.6618+00.5207

The 1.2mm emission in this region (Miettinen *et al.* 2006) revealed a complex large-scale morphology. This complexity continues on the smaller core/clump scale with IRAS 15412–5359 being a compact site of massive star formation surrounded by an ionised region powered by several massive stars, one O9V and several B0V type (Barres de Almeida *et al.* 2006). Ellingsen (2006) detected 6.7GHz methanol maser activity centred on the continuum emission presented in this work (see Figure A.27).

We derive $\alpha = 1.0 \pm 0.6$ (between 17 and 22.8 GHz), the emission for which is resolved with an angular size of $(0.51 \pm 0.29)'' \times (0.10 \pm 0.14)''$ at 22.8 GHz and position angle of $153^\circ \pm 20^\circ$. It is also coincident with water maser emission detected in the highest frequency band. A wide range of scenarios are compatible with the relatively large errors on the spectral index. The elongation of the radio emission hints at elongated morphology for the deconvolved emission, though the errors are too large to conclude this. At 22.8 GHz, the flux is 0.78% that expected from the bolometric flux assuming a HII region. On this basis, we classify it as a jet candidate.

G327.1192+00.5103

Phillips *et al.* (1998) detected a weak 0.5 mJy source, which was classified as a HII region powered by a B1 type star (though this is underluminous to the flux expected for $L_{\text{bol}} = 3.7 \times 10^4 L_\odot$ by a factor of ~ 500). Previously, both methanol and hydroxyl masers have been detected close to the MSX point source position with the methanol masers aligned in a linear arrangement with a position angle of $\sim 80^\circ$ (Walsh *et al.* 1998). An extended green object is detected at $15^{\text{h}}45^{\text{m}}32.7^{\text{s}} - 53^\circ 52' 39.4''$ and is listed as a ‘likely MYSO candidate’ by Cyganowski *et al.* (2008). Br γ emission is absent from NIR spectra (Lumsden *et al.*, in prep.).

A single lobe with $\alpha = 0.16 \pm 0.09$ is detected at all frequencies with water masers $\sim 1''$ to the NW. All species of maser are aligned in a roughly linear configuration with a position angle of $\sim 125^\circ$. At 22.8 GHz, there are hints of emission detected toward the water masers at the 3σ level. The source is underluminous at radio frequencies compared to the bolometric flux (0.18% of that expected for a HII region). Since it cannot be a HII region, or a disc wind

($\alpha \neq 0.6$), we classify this as an ionised jet.

G331.3576+01.0626

We derive $\alpha = 0.47 \pm 0.09$ for the single component, typical of a collimated jet (Reynolds 1986). The presence of a strong HII region $25''$ to the West necessitated the neglect of baselines shorter than $40 \text{ k}\lambda$ at 5.5 and 9 GHz. Deconvolved dimensions at 22.8 GHz show a spherical structure (with admittedly large errors), and consequent fitting with a model for a homogeneous HII region yields an emission measure of $2.4 \times 10^8 \text{ pc cm}^{-3}$ over an area of $\sim 0.08''^2$ or 400 au^2 , however this is poorly fitted and radio flux at 22.8 GHz is underluminous by a factor ~ 17 compared to the bolometric luminosity. Considering the lack of historical observations, we can only classify this object as a jet candidate.

G332.0939–00.4206

One of the brightest objects in our sample with $L_{\text{bol}} = 9.3 \times 10^4 L_{\odot}$, it shows a slight extension in K-band in the SE/NW direction (2MASS images). In GLIMPSE imagery it is heavily saturated in all filters, with extended red emission still discernible to the NE. Weak $\text{Br}\gamma$ is present in NIR spectra (Lumsden et al., in prep.) as well as faint CO bandhead emission, too weak to be fitted (Ilee *et al.* 2013). A methanol maser has been detected close ($< 1''$) to the source position (Ellingsen 2006) also.

Between 5.5/9 GHz and 17/22.8 GHz, $\alpha = 0.9 \pm 0.5$ and $\alpha = 0.6 \pm 0.3$ are derived respectively, while across all frequencies we derive $\alpha = 1.80 \pm 0.14$. We believe the steep overall index when compared to the values for α calculated across the two spectral bands indicate significant variability between the two epochs. In

this case the fluxes at 17 and 22.8 GHz are overluminous by a factor of ~ 2.7 , when compared to that expected from the fluxes at 5.5 and 9 GHz (using $\alpha = 0.9 \pm 0.5$). Comparing the bolometric flux to the radio flux at 22.8 GHz indicates the radio flux at 22.8 GHz to be 0.17% of that expected. Together with faint CO bandhead emission indicating an accretion disc, this indicates a ionised jet.

G332.9868–00.4871

CO bandhead emission attributable to an accretion disc around a central source of $16.6 M_{\odot}$ was detected by Ilee *et al.* (2013). Diffraction limited MIR observations (Wheelwright *et al.* 2012) showed a spherically symmetric and compact morphology. NIR observations revealed weak Br γ emission also (Lumsden *et al.*, in prep.).

This source has a confirmed detection at all four observing frequencies, and was too compact to be deconvolved. The radio spectrum itself displays possible evidence for a turnover at higher frequencies, and when fitted with a homogeneous HII region model, an emission measure of $(1.17 \pm 0.28) \times 10^9 \text{ pc cm}^{-3}$, a size of ($\sim 330 \text{ au}$) and $n_e = (8 \pm 1) \times 10^5 \text{ cm}^{-3}$ is derived. Fitting with a simple power-law yield a spectral index of $\alpha = 1.27 \pm 0.14$. Optically thin radio flux (as fitted by simple HII models) is 18% of that expected from the bolometric flux, which works against the HII region picture. Thus we classify this object as a jet candidate on account of uncertainty in deconvolved dimensions and orientations.

G338.9196+00.5495

In K-band 2MASS images, an infrared point source is present with a tail of diffuse emission to the SE which is not detected at longer infrared wavelengths. The

MSX source position itself is coincident with a $4.5 \mu\text{m}$ excess (EGO) indicative of shocks (Cyganowski *et al.* 2008) and outflow activity.

The detection of multiple, bright, extended HII regions meant image quality was reduced at the lower frequencies due to residual side lobes. By neglecting baselines $< 30\text{k}\lambda$, a spectral index of ~ 1 is derived. Water maser activity is detected, offset $1''$ ($\sim 5000 \text{ au}$) to the south of the free-free emission. At 22.8 GHz , the radio flux is a factor of ~ 800 times weaker than that expected from an optically thin HII region. The presence of shocks in the MIR, and weak radio flux would classify this as a jet, however without reliable estimates for γ or direct outflow observations, we must classify this as a candidate.

G339.6221–00.1209

Diffraction-limited mid-infrared imaging of this object by Wheelwright *et al.* (2012) showed a bi-polar, cometary morphology whose major axis is oriented NE-SW. Modelled with a high bolometric luminosity ($L_{\text{bol}} = 5.2 \times 10^5 L_{\odot}$) in this reference, yet with a radio-quiet profile, this object was postulated to be a weak, distant, extended HII region. However recent revisions of its bolometric luminosity (see Table 2.2) fit in more with an MYSO picture. With this in mind, the mid-infrared emission may trace the warm dust in the outflow cavities assuming a single MYSO at the MSX point source position. Navarete *et al.* (2015) observed $2.12 \mu\text{m}$ H_2 emission coincident with the source, indicative of shock emission from outflows.

Observations of G339.6221–00.1209 at 5.5 and 9 GHz show the detection of two components of free-free emission in the (robustness of 0.5) clean maps. The east component has a thermal, flat spectral index of $\alpha = 0$ and coincides with

OH maser emission whilst offset from a string of methanol maser spots residing $2''$ to the east of the lobe's centroid. The west lobe of emission is relatively weak and has a negative spectral index of $\alpha = -1$. Because of interference from strong HII regions in the area, re-imaging was performed neglecting shorter baselines ($< 12.5 \text{ k}\lambda$) and a robustness of -1 to suppress residual side lobes. This yielded $\alpha = -0.17 \pm 0.26$ and $\gamma = -0.33 \pm 0.25$ for E, however W was not detected. From Equations 1.8 and 1.5, these are incompatible assuming an ionised jet picture. However, considering the deconvolved position angle is roughly oriented with the major axis of the beam, deconvolved dimensions may be compromised by the low signal to noise of the target combined with the elongated beam. Flux densities of the source are more certain and are ~ 110 times too weak compared to the flux expected of an optically thin HII region of the same bolometric luminosity. Although the observations in the literature show jet activity in the area, our radio images cannot definitely classify this source as an ionised jet, only as a candidate.

G339.8838–01.2588

Associated to the object IRAS 16484–4603, this MYSO has an extensive observational history. Ellingsen *et al.* (1996) observed elongated, ionised emission at a position angle of -45° which, within astrometrical errors, was coincident with the position of, and perpendicular to, the distribution of multiple, linearly-distributed (both spatially and in velocity) CH_3OH maser spots. Stecklum & Kaufl (1998) also observed $10 \mu\text{m}$ emission elongated at the same position angle as the masers, leading to an interpretation of a disc/jet model with irradiated masers in Keplerian rotation, embedded in the circumstellar disc. However, further observations at $10 \mu\text{m}$ and $18 \mu\text{m}$ by De Buizer *et al.* (2002) resolved the elongated MIR emis-

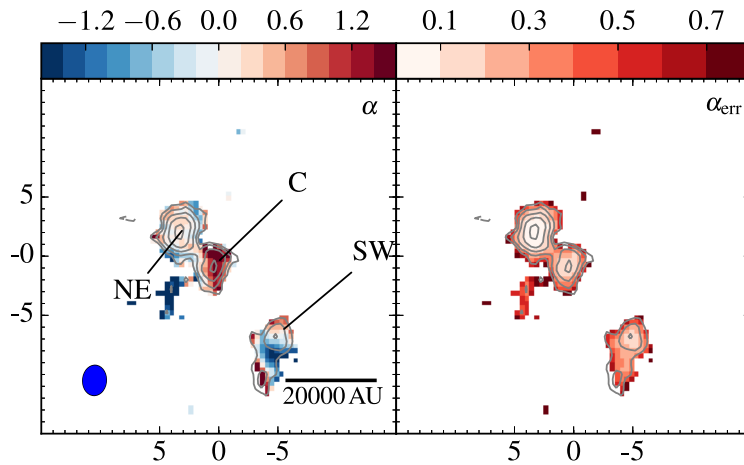


Figure C.7: A map of the spectral index (between 5.5 and 9GHz) for G339.8838–01.2588 (left) and the associated errors in the spectral index (right). The restoring beams (blue) used for both the 5 GHz and 9GHz data were identical, in the production of the spectral index maps. Grey contours represent the flux densities at 5 GHz starting at 1.40×10^{-4} Jy/beam (4σ), and scaling by a factor of $\sqrt{3}$ for each subsequent contour.

sion into three sources, whose temperature profile peaked with the radio emission spatially, however the resolved point source, 1B, was offset $\sim 0.4''$ to the SE, and coincident with the outflow axis of the radio knots from Ellingsen *et al.* (1996). De Buizer *et al.* (2002) further concluded that there are two sources at work, one massive, unobscured star with an extended HII region (partially resolved out in existing radio data) and a second, which is embedded and centred on the previously detected radio emission and also responsible for outflow activity in the region.

The nature of the observations in this paper preclude the detection of extended emission on the scales discussed in the above references (some extended emission is partially resolved out at 5 GHz). Therefore it is safe to assume that any flux imaged comes from free-free emission associated to compact sources (i.e. radio

lobes/central jets/HCHIIIs).

From the radio flux contour maps in Figure A.37, 3 compact components are present through all 4 observing frequencies. A range of spectral indices are seen over these components as illustrated in Figure C.7. Calculated values for α and γ (component C) are 0.77 ± 0.04 and $\gamma = -1.0 \pm 0.5$ respectively indicate either a conical, thermal jet undergoing some degree of recombination and/or acceleration in the flow (Reynolds 1986) or an optically thick HCHII. At 5 GHz, the central source also becomes slightly extended. Considering the turn-off at higher frequencies, it is possible that this represents a young, optically thick HCHII region of small spatial extent, as well as an ionised jet, however it is underluminous by a factor of ~ 1800 to that expected from the bolometric luminosity, supporting the ionised jet picture which is our final classification.

G340.0543–00.2437A

Though observations of this region are sparse in the literature, this is none-the-less a very active region with star formation at a variety of stages. Within $10''$ there are 5 separate objects registered as HII regions or YSOs in the RMS database with G340.0543–00.2437D overlapping the extended green object determined from GLIMPSE.

Due to the large fluxes and extended emission of G340.0543–00.2437E (the UCHII in Figure A.38), robustness of the images was reduced to -1 to counter its strong sidelobes. Noise in the images is still relatively high as a result of this but also due to partially resolved out extended emission in the general area. As a result, fitting of a Gaussian to the image plane was ineffectual and a spectral index of $\alpha = 0.4 \pm 0.7$ is calculated from the integrated flux within the 3σ con-

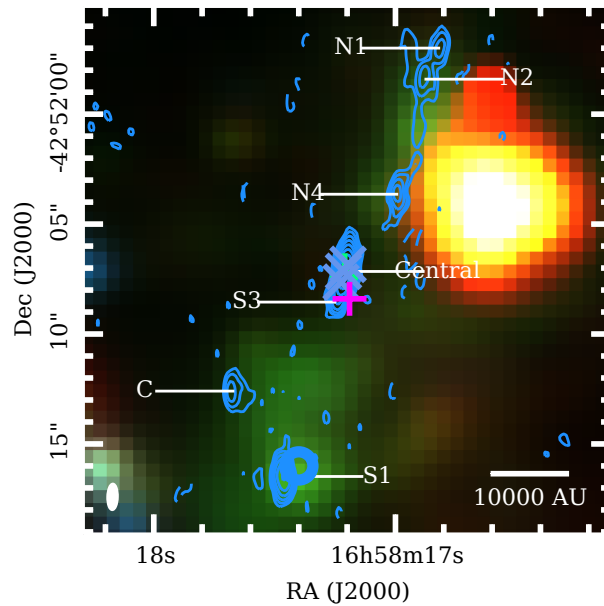


Figure C.8: The 17 GHz radio contours overlaid on an RGB ($8.0\ \mu\text{m}$, $4.5\ \mu\text{m}$ and $3.6\ \mu\text{m}$) composite image of existing GLIMPSE data for G343.1261–00.0623. Contours step up from 5σ by a factor of $\sqrt{3}$ per level. Arrows represent the proper motions derived from our data and that found in Rodríguez *et al.* (2005), who’s lengths are relative and in proportion.

tours of G340.0543–00.2437D. The radio emission coincides with the EGO and is probably associated with outflow activity because of its coincidence with this $4.5\ \mu\text{m}$ excess and underluminosity compared to HII regions of similar luminosities. Through a lack of observations in the literature as well the results presented here, we classify this object as a jet candidate.

G343.1261–00.0623

Associated to the object IRAS 16547–4247, this source has an extensive observational history. Most recently, cycle-0 ALMA observations at $880\ \mu\text{m}$ have revealed two dust cores separated by $\sim 5000\ \text{au}$, Core A (closest to IR source) and Core B (masses $15\ M_{\odot}$ and $12\ M_{\odot}$ respectively, Higuchi *et al.* 2015). The same set of

observations showed two, perpendicular, bi-polar molecular outflows in $^{12}\text{CO}(3-2)$ (one NNE-SSW, the other WNW-ESE for the red-blue lobe alignment axis), which are both separate again to a larger-scale bi-polar outflow detected with the Atacama Pathfinder EXperiment (Garay *et al.* 2007a) with a N-S alignment. This larger scale outflow is slightly misaligned to the previously established radio jet of Rodríguez *et al.* (2005) which is comprised of at least 9 components, the central thermal jet being deduced to have a spectral index of $\alpha = 0.33 \pm 0.05$ (between 8.46 and 14.9 GHz). The thermal jet also displays evidence for precession (Rodríguez *et al.* 2008) which is likely caused by the proximity of the two cores. Other ALMA observations of spectral lines associated to CH_3SH and CH_3OH (Zapata *et al.* 2015) reveal a compact disc and display Keplerian rotation profiles (along a position angle of $\sim 40^\circ$, perpendicular to the free-free thermal jet). These findings lead to a conclusion of a central MYSO with a mass of $\sim 20 M_\odot$ and disc mass of $\sim 6 M_\odot$, calculated from concurrent observations of 0.86mm continuum emission.

Taking the terminology from Rodríguez *et al.* (2005), lobes of emission are detected towards the positions of components C, N2, N1, S-1 and the central source. Source B was not detected but is known to be time variable. New lobes of emission are detected, dubbed N-4 and S-3, of which the first was detected by Rodríguez *et al.* (2005) but not named. At 17 GHz there is some weak, diffuse emission connecting the northern lobes which is either resolved out or too weak at 22.8 GHz to be detected. The central component appears to be comprised of multiple components for which a 2-component model best fits the 17 GHz and 3-component model best fits the 22.8 GHz data. For consistency, spectral indices derived were taken from the 2-component model (S-3 and central lobes) at each

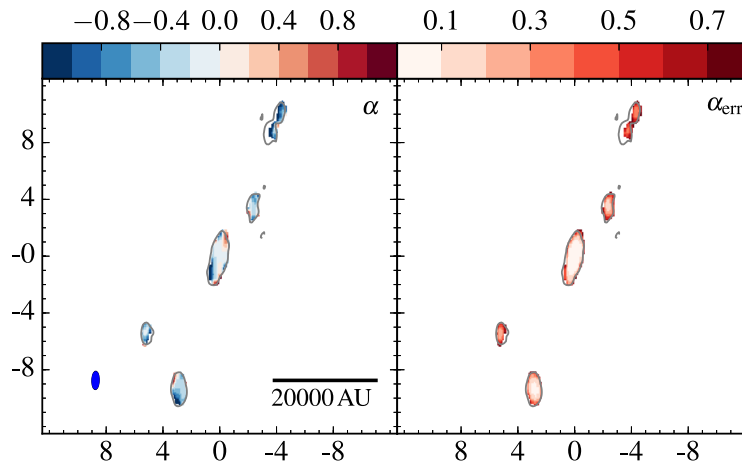


Figure C.9: A map of the spectral index (between 17 and 22.8 GHz) for G343.1261–00.0623 (left) and the map of errors in the spectral index (right). The grey contour represents a flux density, at 17 GHz, of 3.03×10^{-4} Jy/beam (5σ). For clarity, no further contouring has been included.

frequency, however flux is left over at 22.8 GHz (with an integrated value of ~ 1 mJy) in the residual map which cannot be fitted without an extra component. Spectral indices derived are -0.1 for the central source, and -1.2 for the second component, indicating thermal and non-thermal emission respectively, though the reliability of these is unknown requiring higher resolutions. Considering the relatively large errors at 22.8 GHz, these spectral indices have inherently large errors. For the other lobes, spectral indices of -1.4 , -0.45 , -2.5 , -2.1 and -0.7 are derived for lobes C, S-1, N-1, N-2 and N-4 respectively. Because of the diffuse emission resolved out at 22.8 GHz, the spectral indices for the northern components and component C should be taken as lower limits. Lobe S-1 has a spectral index consistent with that found by Rodríguez *et al.* (2005). With expected fluxes from Rodríguez *et al.* (2005) at 17 and 22.8 GHz of 10.9 and 12.3 mJy respectively, and measured fluxes of 16.8 and 16.3 mJy, the central source appears to display a degree of time variability. Water maser emission is also

detected across a broad range of channels, with the maser spots arranged in a linear pattern parallel to the major axis of the central component. This would indicate they are excited in the outflow cavities rather than the accretion disc. This source is classified as a jet with lobes.

G343.5213–00.5171

Modelling of the SED profile by Wheelwright *et al.* (2012) suggested an MYSO inclined 57° to the line of sight with a mass loss rate of $2.5 \times 10^{-4} M_\odot \text{ yr}^{-1}$ and opening angle of 10° , however the confused nature of the source detrimentally influenced the reliability of the fit. No other significant previous observations of this object are present in the literature other than an extended green object detected by Cyganowski *et al.* (2008) offset $30''$ to the north. Whether this is directly related to this particular source, and not the star formation region in general, is unknown. No $\text{Br}\gamma$ emission is seen, however $[\text{FeII}]$ emission is present (Lumsden *et al.*, in prep.).

The detection of 2 components at lower frequencies, and 1 component at higher frequencies are made for this source. At the risk of inconsistency, the robustness parameter was increased to 4 at 22.8 GHz due to the point like nature of the source and also the very low signal to noise ratio present at this frequency. This allowed a more reliable fit to the spectral index for the west component of $\alpha = -0.05 \pm 0.15$. The east component yielded a spectral index of ~ 0 for the two frequencies it was detected at. The SW extension of the emission at 5 GHz, and west/east lobes of emission are coincident with the MIR emission in figure 3K of Wheelwright *et al.* (2012). The possibility of both components representing separate MYSOs is considered, which would mean the accepted bolometric luminosity

would be split between the two, potentially explaining the lower than expected fluxes for the main component. However, no $\text{Br}\gamma$ emission is seen (Lumsden *et al.*, in prep.), ruling out the possibility of a HII region. As such, we classify this as a jet candidate.

G345.4938+01.4677

A paper by Guzmán *et al.* (2010) detected 5 distinct lobes of thermal free-free emission associated to this object, and promoted an episodic accretion/ejection scenario. The central source was inferred to be an ionised jet with a spectral index of $\alpha = 0.85 \pm 0.15$, and a position angle for the jet of $\sim 99^\circ$. Emission in the inner/outer lobes was optically thin with flat spectral indices of $\alpha \sim -0.1$, and was associated to excess emission at $4.5 \mu\text{m}$ due to shocks in the flow. K_s band images show enhanced emission, as a result of the excitation of the $2.12 \mu\text{m}$ line, parallel to the jet on both sides of the source, and also perpendicular to it with a N-S alignment. The N-S emission displayed a morphology similar to that seen in the bow-shocks of Herbig-Haro objects, suggesting a second outflow in the region. Emission at $10 \mu\text{m}$ (Mottram *et al.* 2007) coincided with the I-E lobe (terminology as in Guzmán *et al.* (2010)) and central source, with the prior being associated to warm dust in the outflow cavity. Follow up observations of the lines $\text{CO } J = 3 \rightarrow 2, 6 \rightarrow 5$ and $7 \rightarrow 6$ (with APEX) showed a quadrupolar morphology (more distinctive in the two higher excitation temperature transitions), with one red-blue lobe pair aligned with the radio jet and the other aligned with the N-S K_s band emission (Guzmán *et al.* 2011). The velocity range of the outflows was $\sim 60 \text{kms}^{-1}$, with collimation factors of ~ 1 and 2 for the N-S (P.A. of 7°) and SE-NW (P.A. of 107°) outflows respectively, as expected with MYSOs. GLIMPSE

images show the walls of an outflow cavity aligned with the eastern jet.

The radio lobes detected in previous works are all detected at 17 GHz, however at 22.8 GHz only the central component and components I-E and I-W are detected. The jet is aligned with the outflow cavities seen in GLIMPSE imagery. Water maser activity is detected towards at least 5 separate sites in the field of view, and is probably associated to radiative processes on material in the west outflow cavity walls. The spectral index of the central source (derived from our observations alone) is $\alpha \sim 0.8$, in close agreement with Guzmán *et al.* (2010). However the fluxes recorded at both frequencies are $\sim 30\%$ lower than expected, suggesting the central source's flux may be time variable (absolute flux calibration errors of $< 10\%$ are expected with the ATCA). We classify this source as a jet with lobes.

G345.5043+00.3480

Outflow activity is detected in MOPRA observations of HCO^+ , however it is relatively uncollimated with a rough S-N (red-blue) configuration centred on G345.5043+00.3480 (Yu & Wang 2014).

Observations detect a radio source offset by less than $1''$ to the NE of the phase centre (at all frequencies), as well as an extremely strong HII region located $\sim 130''$ to the SE (RMS survey designation, G345.4881+00.3148). Due to the limited dynamic range of the observations, strong side lobes were present at the lower two frequencies, which interfered with the deconvolution of the target of interest. A robustness of -1 was therefore used to suppress the side lobes as well as neglecting baselines $< 40 \text{ k}\lambda$ at the cost of higher noise levels in the resultant images. Large errors on the deconvolved size at 17 GHz prohibit a

power-law index for the deconvolved major axis being derived, however a spectral index of $\alpha = 0.92 \pm 0.10$ is calculated, indicative of thermal free-free emission. At 22.8 GHz, water maser emission is detected in two spots, one coincident with and the second offset $\sim 3''$ to the SE (previously seen by Forster & Caswell (1989)) from, the target. It is underluminous at 22.8 GHz by a factor of ~ 3000 , however without more information on the behaviour of the major axis with frequency, we can only classify this object as jet candidate.

C.1.2 ‘Embedded’ HCHII regions

From the 14 HII regions which were identified in our sample, three displayed a compact, optically thick core, centred on the MSX point source position. These cores were embedded in an optically thin region of extended emission and generally qualify for HCHII regions, as opposed to jets, based on their radio fluxes and high-frequency turnovers present in their spectra (jet turnover frequencies are likely $\nu_m > 50$ GHz). All of these examples are discussed below in further detail.

G274.0649–01.1460A

Our observations show a compact, bipolar HII region with a bright core which becomes more prominent at 17 and 22.8 GHz. From the morphology alone, this object is similar to bipolar HCHII regions like NGC 7538 IRS1 (Campbell (1984); Sandell *et al.* (2009)). It is thought that these objects may be a transitional phase between MYSOs and an expanding HII region, as the ionised front moves along the density gradient of the evacuated cavities previously cleared by outflows and jets (which may still be active), to produce the bipolar morphology. How-

ever considering the distance-luminosity expected at 22.8 GHz ($\sim 25 \text{ mJy kpc}^2$), G274.0649–01.1460A is ~ 4 times too luminous suggesting either other ionisation processes may be responsible for the flux observed or simply that the bolometric luminosity has been underestimated due to the complex environment. The fluxes of the core were fitted with a Gaussian profile and had a spectral index (between 17 and 22.8 GHz) of $\alpha = 0.81 \pm 0.81$, for a robustness of 0.5. However, the extended emission affected the fitting of the central component as they could not be separated effectively. Therefore, we re-imaged the object using a robustness of -1 at 9 (neglecting baselines $< 50\text{k}\lambda$), 17 and 22.8 GHz (5 GHz imaging was ineffective at separating the extended and compact components), yielding a more reliable value for the spectral index of $\alpha = 0.37 \pm 0.17$ (γ could not be determined as the central component remained unresolved at all frequencies). It is worth noting there was no sign of a turnover and the fluxes remained within errors for a standard power-law profile. The spectral index of the emission as a whole (between 5.5 and 9GHz since much emission is resolved out at the upper two frequencies) is $\alpha \sim -0.1$, indicative of optically thin free-free emission from a HII region.

Two other HII regions were detected within $20''$ of the central source, G274.0649–01.1460B (most southerly in Figure A.11) and G274.0649–01.1460C. These two HII regions have spectral indices of $\alpha \sim 0.1$ and $\alpha = -0.06 \pm 0.06$ for G274.0649–01.1460B (2 frequencies) and G274.0649–01.1460C (4 frequencies) respectively, both indicative of optically thin emission from a HII region. The reason for using differing numbers of frequencies for the derivation of spectral indices was based upon whether or not extended emission was becoming resolved out (as in A/B's case) or not (as in C's case). Based upon the 9 GHz flux densities, emission

measures of $1.47 \times 10^6 \text{ pc cm}^{-3}$, $2.30 \times 10^6 \text{ pc cm}^{-3}$ and $2.83 \times 10^6 \text{ pc cm}^{-3}$ are derived for A, B and C respectively. All of these regions would be powered by a B0.5 ZAMS type star (Davies *et al.* 2011). The compact core seen towards the target is of particular interest, and its exact nature remains undetermined. Considering the spectral index of the extended emission, and bipolar morphology, a young HCHII region expanding down the outflow cavities previously cleared by jet activity is likely.

G305.5610+00.0124

TIMMI2 observations of this source (Mottram *et al.* 2007) show bright, compact $10.4 \mu\text{m}$ emission, coincident with the MSX point source position. Faint, extended emission is also seen to the north and east of the bright source. GLIMPSE imaging is saturated, while 2MASS shows a reddened point source with extended faint emission in the background.

Flux density contour maps presented in Figure A.19 show a complicated picture. An apparent UCHII is present, which becomes resolved out at higher frequencies. One compact component coincident with the MSX point source is persistent at all frequencies and likely represents the position of the MYSO. Undoubtedly this source displays characteristics of multiplicity from the distribution of ionised material since the morphology does not fit in with those expected for a HII region powered by a single source. The water maser spots detected are located on opposite sides of the UCHII region, suggesting excitation via shocks at the ionisation front of the overall expanding HII region. The compact source at the phase centre of the observations holds a spectral index of $\alpha \sim 0.8$, which was derived from the upper two frequencies where the extended emission had

been resolved out enough to enable fitting by a Gaussian profile. However this spectral index will have large inherent errors due to the morphology of the region itself. The spectral index plot in The north east emission has a spectral index of $\alpha = -0.14 \pm 0.06$ from the 5.5, 9.0 and 17 GHz (using a robustness of 0.5) data. If this were a separate, optically thin HII region, we derive an emission measure of $5.44 \times 10^6 \text{ pc cm}^{-3}$, a Lyman continuum flux of $2.27 \times 10^{46} \text{ s}^{-1}$ and a ZAMS spectral type of B0.5 (Davies *et al.* 2011). Using the deconvolved size at 9 GHz, the size of the north east component is found to be 0.03 pc, which in combination with the other derived physical parameters is suggestive of an UCHII region.

The central, compact source could represent an ionised jet (considering a radio under-luminosity of 25% that expected from the bolometric luminosity) or an early-stage HCHII region, embedded in extended HII regions from other young massive stars in the environment. Deconvolution at 22.8 GHz of the central source yields a source size of $(0.48 \pm 0.02)'' \times (0.17 \pm 0.08)''$, oriented at a position angle of $(171 \pm 4)^\circ$. This position angle is oriented towards the extended emission to the SE (which is apparent at all observing frequencies) and NW, suggesting a density gradient in these directions. Considering the optically thick nature of the emission and only slight under-luminosity, it is most likely this core is in fact an embedded HCHII region.

G317.4298-00.5612

Guzmán *et al.* (2012) observed this object at similar frequencies to this paper and concluded, from radio spectral analysis, that this was a HCHII with an emission measure of $1.9 \times 10^8 \text{ pc cm}^{-3}$, an effective area of 0.08 arcsec^2 and powered by an O6/5.5 ZAMS type star. Morphologically, two lobes of radio emission were

detected, one centred on the MSX source position and the other offset $\sim 4''$ to the SE. The second source was concluded to be an optically thin UCHII region powered by a O9.5 type ZAMS star.

This source was observed at 5.5 and 9 GHz, for which a central compact source and diffuse emission to its south east are detected. At 9 GHz, the diffuse emission looks partially resolved out by the smaller synthesised beam, and at both frequencies the central compact source is resolved. Fitting a Gaussian profile to the central source in the image domain yields a spectral index of $\alpha = 0.9$, indicative of thermal free-free emission, and a power law constant of $\gamma = -1.1$ for the variation of the deconvolved major axis with frequency. It is important to note that the deconvolved dimensions may be affected by the diffuse emission to the south east. Since we do not have observations at higher frequencies, it is hard to tell whether this is an HCHII region approaching its turnover frequency in our observations, or an extremely bright ionised jet. The deconvolved size at 9 GHz of $0.45'' \times 0.27''$ (or $0.024 \text{ pc} \times 0.005 \text{ pc}$ for a distance of 14.2 kpc) and emission measure of $5.57 \times 10^8 \text{ pc cm}^{-3}$ are suggestive of a HCHII/UCHII region around a B0 type ZAMS star. The calculated emission measure assumed an optically thin regime at 9 GHz and is thus a lower limit. The deconvolved position angles of $136.0 \pm 2.6^\circ$ and $136.6 \pm 1.6^\circ$ at 5.5 and 9 GHz respectively, align the major axis with the diffuse emission to the south east, approximately bisecting it. One interpretation of these results would be a MYSO with a HCHII region which is expanding down the evacuated cavities in the circumstellar envelope (explaining the elongated deconvolved dimensions). The diffuse emission to the south east is possibly the expansion of the HII region down these outflow cavities, which possess relatively wide opening angles. However, considering the scale of the extended

emission (~ 0.65 pc) this is unlikely. Instead this is probably a separate, classical HII region. In this case, we derive an emission measure (using 5 GHz images, and assuming this is in the optically thin regime) of $(1.26 \pm 0.09) \times 10^5$ pc cm $^{-3}$ and Lyman flux of $(8.79 \pm 1.36) \times 10^{47}$ s $^{-1}$. These are indicative of a classical HII region powered by an O9.5 type ZAMS star (Davies *et al.* 2011) with $L_{\text{bol}} \sim 4 \times 10^4 L_{\odot}$. Comparing the combination of the two massive stars contributing to the bolometric luminosity ($3.5 \times 10^5 L_{\odot}$), there is a distinct under-luminosity ($\sim 7\%$ of that expected) lending some support to the core being in the jet phase. However since the core is still optically thick and extremely bright compared to the rest of the jets, we classify it to be a HCHII.

C.1.3 A curious case - G301.1364-00.2249

Walsh *et al.* (1998) detect the radio emission from two UCHII regions associated with IRAS 12326–6245, both coincident with excess $4.5 \mu\text{m}$ emission/EGOs in GLIMPSE RGB images. Both UCHII regions were inferred to be powered by B0 type stars, which are both members of a deeply embedded proto-cluster, with a NE-SW outflow detected in molecular line maps (though the $23''$ beam was too coarse to resolve the origin). Inferred parameters for the outflow include mass loss rates of $\sim 0.02 M_{\odot} \text{yr}^{-1}$ and a momentum rate of $\sim 0.15 M_{\odot} \text{km s}^{-1} \text{yr}^{-1}$ (from Henning *et al.* 2000a, where it was named MIR1). H_2 ($2.122 \mu\text{m}$) emission is detected to the SE and W of G301.1364–00.2249 and loosely associated with the other UCHII. A 6.7 GHz methanol maser with a peak velocity of -39.6 km s^{-1} is also detected coincident with the southern UCHII (Urquhart, private communication). Class I methanol maser emission (36 and 44 GHz) is also detected

coincident with the southern HII region, displaying a ‘remarkable’ absorption feature (Voronkov *et al.* 2014).

Our observations at 17 and 22.8 GHz show the presence of two apparent HII regions, G301.1364–00.2249 (phase centre) and G301.1364–00.2235 ($\sim 7''$ north). Spectral indices of $\alpha = 1.0 \pm 0.1$ and $\alpha = 0.3 \pm 0.2$ are calculated between the two observed frequencies, for the target and HII region to the north respectively. At 22.8 GHz, extensive water maser activity is detected, coincident with each HII region, to the south of the target and in at least 8 other spots spread between the HII regions. Archival ATCA data at 2, 5.5, 9, 33 and 46 GHz was reduced (taken on the 29th January 2011 for the 2, 5.5 and 9 GHz data and 16th August 2009 otherwise) providing a dataset from which (for G301.1364–00.2235) we calculate an emission measure of $(7.91 \pm 1.29) \times 10^7 \text{ pc cm}^{-3}$, a size of $1.25'' \times 0.45''$ (or a diameter, assuming spherical morphology, of $0.03 \pm 0.01 \text{ pc}$, for a distance of 4.3 kpc), and an inferred ZAMS spectral type of B0. This classifies it as a UCHII. Given the deconvolved size for G301.1364–00.2249 of $0.67'' \times 0.36''$ ($2800 \times 1500 \text{ au}$), and derived emission measure of $(1.19 \pm 0.17) \times 10^9 \text{ pc cm}^{-3}$, this can be classified as an elongated (potentially bipolar at higher resolutions) HCHII region. At 22.8 GHz, there is also a (relatively) weak extension to the emission of G301.1364–00.2249 to the NW, with an integrated flux of $21.4 \pm 1.7 \text{ mJy}$, a deconvolved size of $0.86'' \times 0.18''$ and a position angle of $150 \pm 3^\circ$.

Figure C.10 shows four hydrogen recombination lines detected during observations of this region (using the pixels with values greater than 5σ in each channel, within a bounding box for each HII region). These radio recombination lines (RRLs) display broad line-widths in excess of 60 km s^{-1} for G301.1364–00.2249 and narrower line-widths of $\sim 30 \text{ km s}^{-1}$ for G301.1364–00.2235, further clarify-

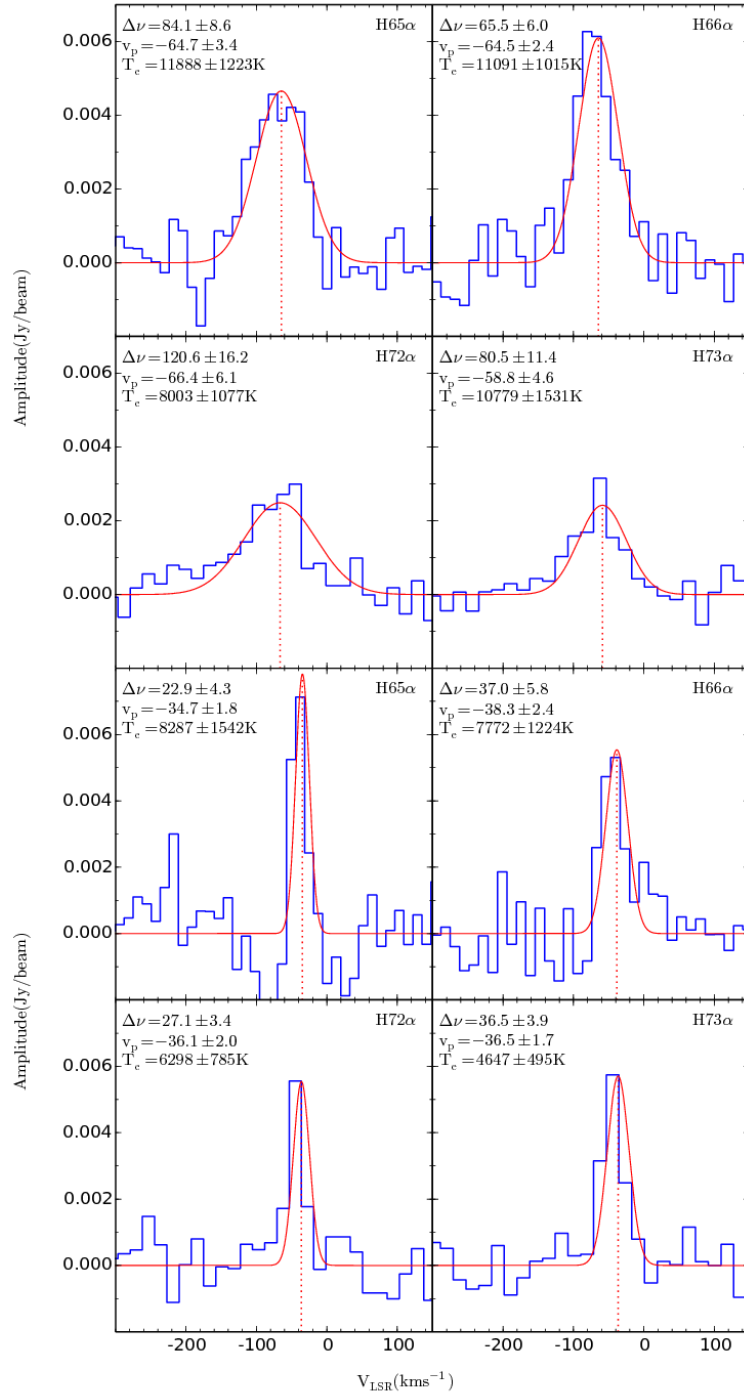


Figure C.10: A spectral plot of the hydrogen recombination lines detected during our observations of G301.1364–00.2235 (bottom 4 plots) and G301.1364–00.2249 (top 4 plots). The transition name is annotated in the top right of each plot, while fitted parameters are annotated in the top left, where $\Delta\nu$ and v_p are the line-width and peak velocity respectively (both in km s^{-1}). The fitted Gaussian profile is indicated by the solid, red line, while the peak velocity is illustrated by the dotted, red line.

ing their status as HCHII and UCHII regions respectively. The peak velocities for the two HII regions do, however, differ considerably. The southern HCHII has RRLs which consistently peak at $\sim -64 \text{ km s}^{-1}$, while the northern UCHII data peaks at $\sim -36 \text{ km s}^{-1}$. To have members of the same clump with velocities differing by $> 10 \text{ km s}^{-1}$ is unusual. For this clump ($M_{\text{clump}} \sim 6000 M_{\odot}$), the virial velocity at a separation of $2.2''$ for a distance of 4.3 kpc is $\sim 24 \text{ km s}^{-1}$, and since the velocity difference is of this order, a scenario whereby this source was recently ejected from the cluster is possible. From the archived data, hydrogen recombination lines at 34.6 GHz ($\text{H}57\alpha$) and 45.5 GHz ($\text{H}52\alpha$) were also analysed. Both the $\text{H}52\alpha$ and $\text{H}57\alpha$ RRLs showed a similar profile to those lines in the 17 and 22.8 GHz data. Many individual channels were pre-flagged by the CABB correlator during these observations, some of which lie on the $\text{H}52\alpha$ RRL itself, however the fitted data adheres closely to a Gaussian.

The clear offset in the v_{LSR} cannot be explained by the observations presented here. A possible, speculative explanation for the observations would be an optically thick HCHII region expanding down previously evacuated outflow cavities which are oriented towards the observer. This would explain both the classical HII region spectral profile (i.e. with an optically thick spectral index of ~ 2 rather than ~ 1 typical of HCHII regions) and broad linewidths offset from the LSR velocity of the source itself (Lizano 2008). Further observations of RRLs at higher spectral resolutions would help to definitively resolve this situation.

C.2 Northern IRDC/MYSO sample

Throughout this section we discuss each field with detected emission in both/either C-band or Q-band imagery. Subsequently the detected radio emission is then compared to previous observations in the literature across all wavelengths, to both decide upon the classification of each individual radio source and also to discern the overall star formation picture towards each core/clump.

C.2.1 IRDC Sample

G018.82–00.28

Within the C-band primary beam, there are three, classified cores from Rathborne *et al.* (2010), MM2, MM4 and MM5. Another core, MM6 lies approximately halfway between MM4 and MM5, however it remained unclassified. Only MM2 is classified as containing a red MIR source, which is identified as IRAS 18236–1241 and also as G018.8330–00.3004 from the RMS survey where it is classified as a HII region. Follow up radio observations with the VLA as part of the CORNISH survey (Purcell *et al.* 2013) do indeed detect an extended HII region possessing an integrated flux of 131.4 mJy.

Approximately $3''$ to the east of the pointing centre, coincident with MM2, a reddened, extended GLIMPSE source and the catalogued RMS HII region, we detect a cometary UCHII region approximately $0.4'' \times 0.6''$ in (FWHM) size (or $0.024 \text{ pc} \times 0.037 \text{ pc}$ for a distance of 12.6 kpc) and with a Q-band integrated flux (over the 3σ contours) of $51 \pm 4 \text{ mJy}$. Since a C-band flux of 108 mJy was found, it is highly likely considering the spectral index between 5.8 and 44 GHz of -0.4 that some flux has been resolved out at Q-band. Unfortunately the HII region

limited the image in dynamic range around the pointing centre and no other emission is detected.

G024.08+00.04

Rathborne *et al.* (2010) observed 5, 1.2 mm cores (MM1 – 5) all of which are quiescent apart from MM1 which contains a reddened MIR source and is hosted by the brightest sub-mm clump in the complex.

At C-band we detect a cometary HII region (designated A) $3''$ to the east of the pointing centre (coincident with core MM1) and a bright C-band source $45''$ to the NE comprised of at least 3 separate components in elongated morphology. Both sources were not detected at Q-band, whereby we do not detect any significant flux in the primary beam. With a physical, FWHM size of 0.015×0.014 pc for the distance of 3.8 kpc, A is a typical UCHII region. We believe that B (collective term for B1, B2 and B3) is emission from an AGN on account of upper-limits to the (non-thermal) spectral indices of $\alpha < -0.4$, however the calculated upper limits may be affected by loss of flux at Q-band considering the extended nature at 5.8 GHz. Since B is not coincident with any IR source, or sub-mm, continuum emission, and is located away from MIR extinction patches, the extragalactic classification is extremely likely. No radio emission was detected towards any of the other cores within the C-band primary beam.

G024.33+00.11

VLA, 3.6 cm observations showed a 0.33 mJy radio source (VLA1) at $\alpha(\text{J2000}) = 18^{\text{h}}35^{\text{m}}08.1^{\text{s}}$, $\delta(\text{J2000}) = -07^{\circ}35'04''$ and a 0.29 mJy source (VLA2) at $\alpha(\text{J2000}) = 18^{\text{h}}35^{\text{m}}24.0^{\text{s}}$, $\delta(\text{J2000}) = -07^{\circ}37'38''$ (Battersby *et al.* 2010). VLA1 and VLA2

are coincident with the mm-cores, MM1 (15'' in diameter) and MM8 (40'' in diameter) respectively, observed by Rathborne *et al.* (2006). Unusually, MM1 is determined to be at the kinematic far-distance (6.3 kpc) unlike the other mm-cores of Rathborne *et al.* (2010) (which are at distances of 3.7 kpc). Near-infrared H₂, 2.122 μ m images show two lobes of shock H₂ emission (B and C) aligned along a position angle of 125° and separated by $\sim 6''$, (described as a bipolar H₂ outflow by Lee *et al.* 2013). López-Sepulcre *et al.* (2010) detect a wide angle, bipolar outflow centred on MM1 whose outflow axis is not well defined in channel intensity maps.

At C-band we detect three radio sources, A, B and D, one of which (A) is located at the centre of MM1 coincident with an MIR ‘yellowball’, whilst B is distinctly positioned away from the patch of mid-infrared extinction. No mid-infrared source is seen coincident with B, however in UKIDSS imagery, it is possibly co-located with a faint red source in close proximity/confusion with a bright blue star. As for source D, it is located within the MM8 core (18'' SE of its peak position), however considering its relatively large flux, does not possess a corresponding mid-infrared source. Comparing our C-band flux with the 8.33 GHz flux obtained by Battersby *et al.* (2010), we see a large amount of variability (inferred spectral indices of $\alpha \sim -6$ are not realistic). We therefore classify D to be extragalactic, and only by chance does it is positioned on our line of sight towards MM8 (an otherwise quiescent core). Only source A is detected at Q-band, however another compact Q-band source, C, is detected 4.6'' to the NW of A. Source C does not have a C-band counterpart, giving a lower limit on its spectral index (assuming this is not a variability effect) of $\alpha > 1.2$. Both A and C are resolved at Q-band, while only A is resolved at C-band. As mentioned

previously, a bipolar H_2 outflow is present which is associated to our source A. In combination with its spectral index of $\alpha = 0.70 \pm 0.11$, we determine this to be an ionised jet, especially given its elongated radio morphology, with C and Q band major axes that are parallel, showing minimal dust contributions at Q-band. Interestingly A seems to have a western extension to its Q-band emission, the exact nature of which remains undetermined.

G024.60+00.08

Rathborne *et al.* (2010) detect 4 mm-cores in total towards this IRDC (MM1–4) of which MM4 remains unclassified. An earlier work (Rathborne *et al.* 2006) determined that the complex itself was comprised of two separate complexes at different distances from us. The furthest distance, 6.3 kpc, was obtained for MM2 while for the rest of the cores, a distance of 3.7 kpc was adopted. Interestingly, the same work used PdBI observations at 1.2 and 3 mm to show that MM1 and MM2 are actually composed of 3 and 5 separate condensations respectively. Towards both MM1 and MM2 López-Sepulcre *et al.* (2010) detect bipolar outflows in $\text{HCO}^+(1-0)$ whose red lobes are oriented at position angles of $\sim 280^\circ$ and $\sim 10^\circ$ respectively. Previous radio observations (Battersby *et al.* 2010) at 8.3 GHz revealed two point-like sources, one distinctly offset from the IRDC ($\sim 4'$ to the south of MM1) and the other closer, but still outside, the obvious mid-infrared extinction. Each source had peak fluxes of $90 \mu\text{Jy}$ measured at X-band.

Two C-band continuum sources are detected within the primary beam. Source A is not coincident with any near, or mid, infrared source and is distinctly located away from the mid-infrared extinction of the IRDC. It is identified as VLA1 from Battersby *et al.* (2010) and consequently we calculate a spectral index of

$\alpha = -0.8 \pm 0.4$ between the peak fluxes at their (8.3 GHz) and our frequencies, determining it to be extragalactic in nature. In contrast, Source B is located on a western filament of the cloud and is coincident with a reddened, UKIDSS source and white, GLIMPSE source. On this basis, it is determined that A is not associated with the IRDC and is likely extra-galactic, while B represents a reddened main sequence star located on the near-side of the IRDC on account of its mid-infrared colours. At Q-band no significant radio emission was detected across the primary beam. A methanol maser was also observed and located within the NW armature of the IRDC's extinction coincident with both a GLIMPSE point source, the mm-core MM2 and one of the bipolar outflows, but with no associated, C-band, continuum emission (5σ upper limit of $30.6 \mu\text{Jy}$).

G028.28–00.34

A deep radio survey by Cyganowski *et al.* (2011) detected a 4σ , unresolved, radio-continuum source (EGO G28.28–0.36–CM1) with a peak flux at 8.3 GHz of 0.21 mJy, centred on the EGO at $18^{\text{h}}44^{\text{m}}13.33^{\text{s}}$, $-04^{\circ}18'04.3''$. Three other sources were detected (F G28.28–0.36–CM1, CM2 and CM3) in their field of view, two of which (CM1 and CM3) were coincident with extended, reddened, GLIMPSE sources and the other isolated from any infrared emission. No evidence for a molecular outflow (López-Sepulcre *et al.* 2010) or H_2 line emission (Lee *et al.* 2013) was found in the region however, suggesting minimal outflow or jet activity. At 1.2 mm Rathborne *et al.* (2010) detected 4 cores, of which 3 have classifications (all 'R'), which are contained within 2 ATLASGAL clumps at $870 \mu\text{m}$.

For the obvious HII region, Q-band imaging resolves out much of the extended emission, leaving a compact, but resolved, source of an IMFIT derived size of

1900 au \times 1600 au. Since the extended emission was not resolved out in the C-band images, the Q-band data was split in to two sub-bands (with central frequencies of 42 GHz and 46 GHz), reimaged and fluxes for the compact source recorded. Using the peak fluxes in both sub-bands derives a spectral index of $\alpha \sim -0.1$, which likely indicates optically thin free-free emission, therefore ruling out a stellar or disc wind. A C-band source (outside the Q-band primary beam) was detected (Source A) coincident with G28.28–0.36–CM2 from Cyganowski *et al.* (2011), but has no near, or mid-infrared counterpart and lies outside the IRDC’s extinction and ATLASGAL, sub-mm, continuum emission. Deconvolved dimensions at 8.33 GHz show A to be resolved with a size of $0.69'' \times 0.54''$, whereas in our C-band data only upper limits on A’s physical size could be determined. This tends to suggest that our A-configuration observations have likely resolved out any extended flux detected in Cyganowski *et al.* (2011). Therefore, comparing their peak flux to our peak flux to determine a rough spectral index yields $\alpha = -0.2 \pm 0.2$, supporting our extragalactic classification. At a robustness of 0.5 without removing short baselines, no source is detected coincident with the EGO, however this is most likely due to the anticipated, weak cm-emission and residual sidelobe dominated image.

G028.37+00.07

Within our C-band primary beam Rathborne *et al.* (2010) used the IRAM at 1.2 mm to observe 11 cores of a wide range in evolutionary classes (Q, I and A). Their MM1 and MM2 were determined to possess luminosities of $\sim 25000 L_{\odot}$ with both being members of clumps containing EGOs and HII regions from inspection of GLIMPSE imagery. At $870 \mu\text{m}$ MM1’s parental clump is the most luminous

and has the widest $\text{NH}_3(1,1)$ line widths (4.3 km s^{-1}) and rotational temperatures of the entire complex (clump P2 of Wang *et al.* 2008), likely a consequence of internal heating. No previous cm-emission, excluding the HII regions detected by Battersby *et al.* (2010), has been detected towards MM1. Towards MM2, however, a point-like (with a $2.4''$ C-configuration, VLA, synthesised beam) radio source with an 8.3 GHz flux of $1.7 \pm 0.2 \text{ mJy}$ was observed to be coincident with a possibly extended, reddened, GLIMPSE source (VLA4 of Battersby *et al.* 2010). No sub-mm, line observations are found in the literature targeting molecular outflow activity and therefore no comment can be made on the presence of large-scale outflows.

Radio images in Figure A.51 show the detection of four C-band sources, designated A, B, C and D, and three Q-band sources, A (co-located with the C-band source), A2 and A3. A CH_3OH maser is detected and coincident with A, which possesses a spectral index of $\alpha = 1.38 \pm 0.24$. Source B is resolved in C-band and coincident with a $\sim 2.6 \text{ mJy}$ source from archival, 20 cm, GPS images, indicating a non-thermal spectral index of $\alpha \simeq -1$ (assuming minimal resolving out effects). Comparison with the observations of Battersby *et al.* (2010), show that B is registered as their point-like VLA6 with a 3.6 cm flux of $380 \pm 40 \mu\text{Jy}$ yielding a value for α of -1.0 ± 0.5 , agreeing with the GPS comparison. In conjunction with its non-detection at Q-band (4σ upper limit of $360 \mu\text{Jy}$), location away from cold-dust, sub-mm emission (ATLASGAL $870 \mu\text{m}$) and lack of a MIR-counterpart, this confirms its extragalactic nature (rather than resolved out HII region). From our data alone, component C's nature can not be determined due to its high upper limit for spectral index ($\alpha < 1.1$) and ambiguous positioning on the edge of sub-mm continuum emission. Source A3 from Q-band is

coincident with a 3σ , C-band source which looks slightly extended at a position angle of $\sim -45^\circ$. Using an IMFIT derived flux of $47 \pm 15 \mu\text{Jy}$ for the C-band, 3σ emission, a spectral index of $\alpha = 1.60 \pm 0.22$ is calculated. A Q-band, IMFIT-derived position angle for A3 show it to be elongated at an angle of $25 \pm 7^\circ$, while the C-band, IMFIT derived centroid of emission is offset to the Q-band's at a position angle of $\sim -55^\circ$ (i.e. roughly perpendicular to the Q-band elongation axis). This suggests that A3 may be dominated by thermal, free-free emission from an ionised jet at C-band (ejection axis at $\theta_{PA} \sim -50^\circ$), but by dust from an accretion disc (~ 800 au in diameter) at Q-band. Source A2, which is offset by 750 au at a position angle of -154° from A3, is likely to be the dust emission from a close-by, coeval YSO/core. We therefore believe A, A2 and A3 represent a triple system of YSOs. Component D is the same source as VLA4 from Battersby *et al.* (2010) and in conjunction with their flux at X-band we derive a spectral index of 1.7 ± 0.5 indicating optically thick, free-free emission. From its MIR colour/morphology, deconvolved size ($0.007 \text{ pc} \times 0.003 \text{ pc}$) and radio spectral index, D is likely a HCHII for which we calculate a powering star of ZAMS type B2, corresponding to a mass of $11 M_\odot$ and luminosity of $6600 L_\odot$. This estimate is based upon the assumption that the emission is optically thin at 3.6 cm which is wrong, however it does provide a lower limit for the bolometric luminosity, in agreement with that derived by Rathborne *et al.* (2010) of $23329 L_\odot$.

G028.67+00.13

At C-band we detect one source, being the HII region coincident with the mm-core MM1 from Rathborne *et al.* (2010). We measure an integrated flux of 62 mJy and deconvolved size of $4.0'' \times 3.2''$ (or $0.09 \text{ pc} \times 0.07 \text{ pc}$ at the distance of 4.8 kpc),

typical of a compact HII region. From the flux, and assuming optically thin emission at 5.8 GHz, we infer a powering star of ZAMS type B1 equivalent to a mass of $15 M_{\odot}$ or luminosity of $20000 L_{\odot}$ (Davies *et al.* 2011), in rough agreement with $12000 L_{\odot}$ derived for MM1. We establish a 5σ upper flux limit for C-band emission towards MM2 of $40 \mu\text{Jy}$

G33.69–0.01

Mid-IR images show a filamentary structure extending along a rough N-S axis along which Rathborne *et al.* (2010) classify 10 cores with a wide range in evolutionary status. The most luminous of these cores are MM2 and MM5, which possess red and active classifications respectively. From inspection of GLIMPSE images, the reddened MIR source associated to MM2 is likely an HII region on account of its extended morphology. Comparison with ATLASGAL images show that MM2 lies approximately halfway between two $870 \mu\text{m}$ emission peaks, both of which are likely associated to extended HII regions. The northern part of the overall filamentary complex appears less evolved and quiescent, but harbours the highest mass core (MM1 at $750 M_{\odot}$) which itself harbours a reddened MIR source.

Only a cometary HII region (A) is detected $18''$ to NW of MM2's given position with a flux of $\sim 1.5 \text{ mJy}$ at C-band, indicative of a ZAMS B1 powering star with a mass between $12 - 15 M_{\odot}$ and equivalent to a luminosity of $9 - 18 \times 10^3 L_{\odot}$ (Davies *et al.* 2011). No Q-band emission is detected across any of the 3 pointings towards this complex. Source A is also located $8''$ to the north and $37''$ to the NW of more expanded, resolved out HII regions which show prominently in the GLIMPSE, RGB images of Figure A.53. Core MM2 is offset from A by $17''$ to

the SE but still encompasses the detected HII region due to its large diameter (41'' Rathborne *et al.* 2007). Considering its radio-derived bolometric luminosity, it is likely to be the major contributor to the IR derived luminosity of $22373 L_{\odot}$.

C.2.2 MYSO Sample

18517+0437

López-Sepulcre *et al.* (2010) detect a N-S oriented molecular outflow in C¹⁸O(2 – 1). Subsequently Surcis *et al.* (2015) used VLBI to identify 19 CH₃OH maser spots divided into two groups, A and B, to the NW and SE of G37.43+1.51's position. No clear velocity gradients existed in the masers however group A shared their velocity with the blue lobe of the outflow's blue lobe and therefore the maser emission was associated with the N-S molecular outflow of López-Sepulcre *et al.* (2010).

We detect one Q-band, ~ 0.5 mJy point-like source offset $\sim 11''$ to the north east of the pointing centre, which coincides with both a mid-infrared (in WISE imagery) source and B at C-band (which also has a CH₃OH maser spot associated to it). Two more C-band sources are detected, A and C, which both have red, NIR counterparts. All source have thermal spectral indices of 0.73 ± 0.18 , 1.16 ± 0.16 and 0.44 ± 0.15 for A, B and C respectively. No physical dimensions could be deconvolved using IMFIT and therefore we can only classify these three sources as jet candidates.

18556+0136

Better known as G35.20–0.74N, Sánchez-Monge *et al.* (2014) used ALMA observations at 350 GHz to detect 6 evenly-spaced, dense cores (labelled as cores A to F) aligned along a position angle of $\sim 140^\circ$ over an extent of $\sim 15''$ (0.15 pc at 2.19 kpc). Cores A and B showed coherent velocity structures indicative of Keplerian discs in rotation around central objects of mass $4 - 18 M_\odot$, as well as harbouring precessing jets perpendicular to the suspected discs. Previous to that work, Gibb *et al.* (2003) analysed 5 and 8.5 GHz VLA observations, detecting 11 radio sources at either/both frequencies. Of these 11 sources, 1 – 4 and 7 – 11 appeared to be aligned along a N-S axis, with 7 (or G35.2N) and 8 coincident with core B from Sánchez-Monge *et al.* (2014). Fits to the SED yielded ranges in bolometric luminosity from $(0.7 - 2.2) \times 10^5 L_\odot$, dependent upon cavity opening angle and inclination (Zhang *et al.* 2013).

Q-band images show 5 compact radio sources in the field of view, all of which coincide with, and maintain the naming of, the previously detected sources in Gibb *et al.* (2003), apart from the source we designate as ‘Core A’ (see Figure A.55) which inherits its name from the sub-mm source by the same name (Sánchez-Monge *et al.* 2014). Sources 7 and 8 both show lobes of faint radio emission $\sim 0.09''$ (or 200 au) to the west of their peaks, which are recorded as 7b and 8b respectively. At C-band we detect all Q-band sources, as well as five more designated 4, 13, 14, 15, EX–S and EX–N (i.e. extended south/north). Lobes 13, 14 and 15 are new detections, while EX–S and EX–N are comprised of sources 9, 10, 11 and 1, 2, 3 from Gibb *et al.* (2003) respectively.

Comparison with the ALMA image of Sánchez-Monge *et al.* (2014) (central

panel of Figure A.55) show 4, 5, 14, 15, EX–S and EX–N are not associated with any sub-mm continuum sources, but are with the diffuse emission from cavity walls in both near and mid-infrared images. From UKIDSS imagery, 5 is possibly associated with a NIR source and, like 6, is probably more evolved than the radio sources associated to strong sub-mm emission. Considering their flat spectral indices and non-association with sub-mm emission, 5 and 6 are likely small, compact HII regions. Due to its jet-like spectral index of 0.65 ± 0.08 and perfect alignment with 14 and 15, we determine that 7 is the driving jet behind the precessing axis defined by 4, 7, 8, 14, 15, EX–S and EX–N. Assuming a velocity of 500 km s^{-1} for the jet, we determine a rough precession period of $150 \pm 50 \text{ yr}$ from fitting a simple jet model to the lobe positions (Figure C.11). Assuming this motion has a simple relation to the period of a possible, binary companion, we determine (for a $19 M_{\odot}$ central object) that the companion should orbit at a distance of $80 \pm 20 \text{ au}$. Although the nature of 8 may appear ambiguous as a HII region, jet or optically thin lobe of shocked emission ($\alpha = -0.11 \pm 0.09$), its position relative to 7 changes significantly ($\sim 0.24''$) in comparison with the results of Gibb *et al.* (2003), indicating a more transient phenomena. Therefore, we split the bolometric luminosity of $150000 L_{\odot}$ evenly between Core A and 7 for any further analysis.

G033.6437–00.2277

Classified as a diffuse HII region in the RMS survey, from inspection of GLIMPSE imagery a ‘yellowball’ coincides with the diffuse PAH, $8 \mu\text{m}$ emission from the extended HII region (G033.6437–00.2277 in the RMS survey). Towards the MYSO, methanol maser emission is detected (Bartkiewicz *et al.* 2009) in an arc along a

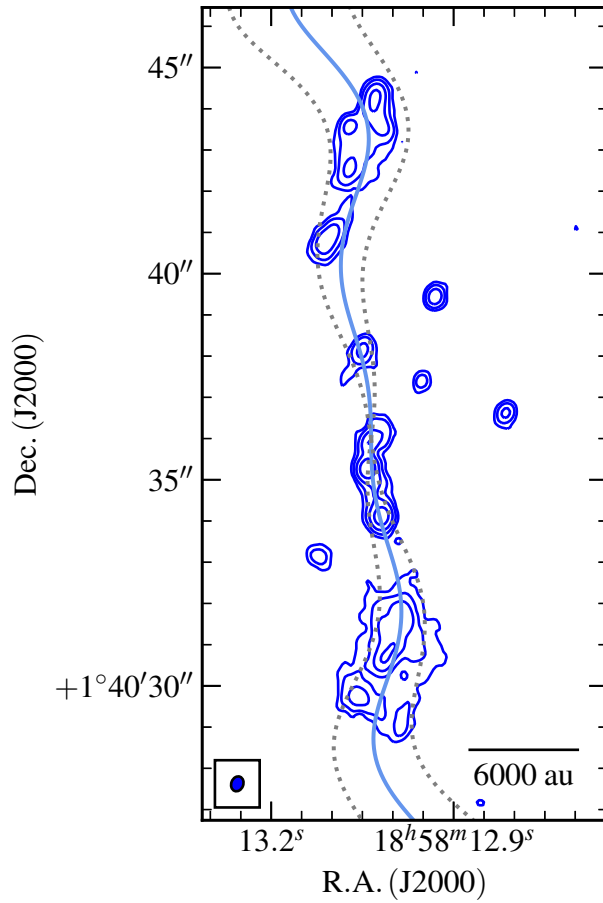


Figure C.11: A radio contour map of G35.20–0.74N with a fitted jet model overlaid (light blue line), with the derived, minimum jet opening angle defined by the grey, dotted lines. Contour levels are the same as in Figure A.55.

rough position angle of 70° . These masers are known to periodically flare (Fuji-sawa *et al.* 2012) on short timescales (~ 1 day).

At C-band we detect 3 sources names A, B and C of which only A has a corresponding Q-band detection associated to it. Approximately $8.5''$ to the west of A, a Q-band only radio object is detected (D) to a 5σ level. Methanol maser emission is also detected at A’s position, which itself is situated at the centre of the HII region’s diffuse $8\mu\text{m}$ emission with a mid-infrared ‘yellowball’ (see RGB

image of Figure A.56). Without any further information in terms of previously detected outflows or other indicators of jet activity, we classify A to be a jet candidate. Source B is coincident with a blue source in UKIDSS, with an upper limit to its radio spectral index of < 0.94 . We believe it to be more evolved than the YSO stage on account of its non-reddened NIR profile and therefore classify it with an evolved status. Due to its isolated nature and absence of a mid-infrared detection, C is classified to be extragalactic, although it has an ambiguous upper limit to its spectral index ($\alpha < 0.91$). Unusually D was only detected at Q-band, and a spectral index lower limit of $\alpha > 1.4$ is deduced. We believe this to be a YSO in the vicinity of G033.6437–00.2277, and due to its high spectral index, may display variability.

G056.3694–00.6333

Near-infrared UKIDSS imagery shows a reddened point source at the centre of some nebulosity towards the south west and north of the point source.

At C-band we detect a lobe/jet-like morphology slightly offset to the reddened, UKIDSS point source. Considering the string like morphology, this is likely an ionized jet with lobes, however a lack of results from other wavelengths in the literature means we must classify this as a candidate. Due to its proximity to the near-infrared source, C is assumed to be the YSO where the base of the jet is located, while A, B and D are shock-ionized lobes associated to the jet's flow. Ideally high-resolution mm-observations would help to establish which components are affiliated with cores to clarify the picture further. In the case that C is indeed a jet, while A, B and D are shock-ionized radio lobes, mm sources should only be associated to C.

G077.5671+03.6911

Near infrared 2MASS images show this object to be at the centre of a possible cluster. Previous ammonia and water maser observations failed to detect significant emission (Urquhart *et al.* 2011b), unusual for our sample of MYSOs.

One source, unrelated to the MYSO, was detected 23'' to the SE of the pointing centre in the C-band clean images, however nothing was detected at Q-band. Considering that it has no associated near or mid-infrared source, it is most likely extragalactic in origin though its non-thermal or thermal nature can not be constrained ($\alpha < 0.6 \pm 0.2$).

G078.8699+02.7602

Another well studied region in our sample, and containing 3 Herbig Ae/Be stars named BD+40°4124, V1686 Cygni and V1318 Cygni. Observed in both optical and NIR regimes, it was determined that V1318 Cygni was composed of 3 separate optical sources dubbed north, middle and south (Aspin *et al.* 1994), of which ‘south’ was concluded to be a very young, intermediate-mass, Herbig Ae/Be star with a low-mass binary companion, ‘north’, separated by ~ 5000 au and connected via the diffuse optical source ‘middle’. At sub-mm wavelengths, V1318 Cygni is by far the dominant source (see Figure 22 of Sandell *et al.* 2011). Navarete *et al.* (2015) observed this region in both K-band continuum ($2.2 \mu\text{m}$) and H₂ line ($2.122 \mu\text{m}$) NIR filters. They detected a bipolar outflow in shocked H₂ emission consisting of 4 lobes (sources 1a, 1b, 1c and 1d) roughly aligned at a position angle of $\sim 150^\circ$ and extending over a length of 0.78 pc. The approximate midpoint of these lobes is located at $\alpha(\text{J2000}) = 20^{\text{h}}20^{\text{m}}30.6^{\text{s}}$, $\delta(\text{J2000}) = 41^\circ22'06''$.

Two more lobes (2 and 3) of shock emission were detected $\sim 2'$ from their pointing centre (which coincides that of our observations) at a position angle of 10° .

UKIDSS imagery shows 4 bright sources within $1'$ of our field centre (Figure A.59), the most easterly two being separated from each other by $\sim 5''$, displaying red NIR colours and coincident with V1318 Cygni's 'north' and 'south' source from Aspin *et al.* (1994) respectively. A less reddened source can be seen $\sim 14''$ to their east (V1686 Cygni) and the brightest source, blue in colour, is located $\sim 40''$ to the NE (BD+40°4124). At C-band we detect radio emission from all of these NIR sources (A, B, C and E), as well as from a NIR dark source located $47''$ NNW of the pointing centre with profiterole-like morphology (D). Only sources A, B and C are detected at Q-band.

Source A is clearly resolved at Q-band with dimensions of $(99 \pm 6 \times 50 \pm 7)$ au for the listed distance of 1.4 kpc, while possessing values for α and γ of 1.41 ± 0.10 and > -0.54 respectively. Its deconvolved position angle of $-31 \pm 6^\circ$ aligns it with the shocked emission lobes, 1c and 1d, of Navarete *et al.* (2015). Source B is extremely low signal to noise (3σ level at Q-band) and is listed as a Q-band detection on the basis of its coincidence with the corresponding C-band source but does remain consistent with the standard jet model of Reynolds (1986) whereby $\alpha = 0.64 \pm 0.28$ and $\gamma = -0.91 \pm 0.26$. Without more supporting evidence however, we must classify it as a jet candidate. Source C remains unresolved at both frequencies and we calculate a spectral index of $\alpha = 1.12 \pm 0.11$ for it, but given its bright, blue NIR colours it has clearly evolved past the MYSO stage. For D we determine it to be extragalactic on account of its IR dark nature mixed with a limit to its spectral index of $\alpha < -0.07 \pm 0.13$. Our radio object E is not detected at Q-band and we establish an upper limit on α of < 0.72 and although

definitely galactic, its more specific nature can not be determined. Considering the fact that optical counterparts exist to these objects, it is highly likely that some are Herbig Ae/Be stars. As for the bolometric luminosities of each object, based on correction for the more accurate distance of Rygl *et al.* (2012), we adopt $5972 L_{\odot}$ and $528 L_{\odot}$ for A and B respectively (from Aspin *et al.* 1994), while for C we adopt a luminosity of $1080 L_{\odot}$ (Lumsden *et al.* 2012).

G079.8855+02.5517

Previous $^{12}\text{CO} (3 - 2)$ maps detect an outflow with red and blue lobes along a position angle of $\sim 120^{\circ}$ and roughly centred on the RMS source G079.8855+02.5517B (Gottschalk *et al.* 2012).

Within the RMS database, our C-band and Q-band detected source A is designated as G079.8855+02.5517C, while our Q-band-only source C1/C2 corresponds to RMS source G079.8855+02.5517B (the more luminous of the two by an order of magnitude). None of our sources are detected in UKIDSS, but A and C1/C2 are strongly saturated in GLIMPSE imagery. With a separation of just 97 ± 29 au, C1 and C2 may be a young binary object. Considering that C2 is elongated along a position angle of $131 \pm 16^{\circ}$, parallel with the molecular outflow observed by Gottschalk *et al.* (2012), we believe that it is an ionized jet whose flux is contributed to by dust emission (hence the steep spectral index of $\alpha > 1.5 \pm 0.2$).

Other detected emission in the field is the C-band source B (outside the Q-band primary beam) and Q-band source D. Since B has no near or mid-infrared counterpart, its most likely classification is extragalactic, while source D, with its steep ($\alpha > 1.5 \pm 0.2$) thermal spectral index and mid IR-dark appearance, is

most probably a YSO at the beginning of its evolution.

G081.8652+00.7800 (W75N)

W75N is arguably the most well-studied region of our sample. Our C-band field of view encompasses 3 significant objects, one being an HII region (RMS designation G081.8789+00.7822), another being the string of radio lobes (Carrasco-González *et al.* 2010b) with confusing outflow morphology (Shepherd *et al.* 2003) and the last being a reddened MIR source (RMS designation G081.8652+00.7800) to the SW of the well studied radio object. The string of 5 radio lobes is oriented at a position angle of $\sim 170^\circ$ from the clean maps of Carrasco-González *et al.* (2010b) who determined their source VLA3 to be a thermal jet ($\alpha = 0.6 \pm 0.1$) powering the Herbig-Haro object, Bc, with the natures of VLA1, VLA2 and VLA4 uncertain. Significant radio flux variability was detected towards Bc over the period encapsulating all of their studied, archival observations (~ 13 yr).

At both C and Q-bands we detect an unresolved source coincident with the RMS source G081.8652+00.7800, possessing a spectral index of $\alpha = 1.00 \pm 0.11$ indicative of thermal free-free emission. Upper limits on A's physical dimensions of ($< 50 \times < 24$) au are established from the higher frequency images indicating an extremely compact source. As a result, we can only classify this object to be a jet candidate as both its spectral index and extremely small dimensions lend themselves to interpretation as a small HCHII.

Approximately $24''$ to the NE of A we detect at least 9 sources in the C-band maps and 3 in the Q-band images. These form the well-studied jet/lobes of the W75N region and we report VLA5, VLA6 and VLA7 to be new sources previously undetected. VLA 1 is elongated at a position angle of $\sim 80^\circ$, which is parallel with

the large CO outflow reported in Shepherd *et al.* (2003), however IMFIT requires a two-component model at C-band which we report as components VLA1Core and VLA1Jet. VLA1Core is also detected at Q-band and a spectral index of $\alpha = 0.19 \pm 0.08$ is derived, while for VLA1Jet we calculate $\alpha = -1.21 \pm 0.07$. The accuracy of these indices is, however, debatable considering resolving out effect at Q-band and accurate deconvolution of VLA1 into two sources at C-band. Due to its strong alignment with an outflow, but uncertain spectral indices we assign in the classification of jet candidate.

VLA2 possesses values for α and γ of 0.11 ± 0.09 and -1.46 ± 0.12 respectively, with deconvolved position angles of $\sim 20^\circ$ at both frequencies. It is highly likely this is another YSO driving a thermal jet, however given the confusing picture of outflow and low signal to noise, we must classify VLA2 as a jet candidate.

VLA4 is seen to possibly be another lobe of shocked emission by Carrasco-González *et al.* (2010b) who required longer time baselines to see if proper motions were significant or not. Taking advantage of the larger time baselines between our 5.8 GHz and their 2006, 8.46 GHz observations we derive proper motions of $0.13 \pm 0.04''$, or $126 \pm 42 \text{ km s}^{-1}$, at a position angle of $-178 \pm 24^\circ$. We believe that due to the $> 3\sigma$ detection of this proper motion, this source is another radio lobe induced by jet shocks.

VLA5, VLA6 and VLA7 all fall well below the detection thresholds of previous radio observations and are both unresolved (VLA5) and distinctly extended (VLA6 and VLA7) in their morphology. Considering the overall morphology of the region, we assume these sources to be radio lobes, much like VLA4, Bc and Bc2, as the result of jet shocks.

The source W75NBc was detected to have proper motions of $\sim 220 \pm 70 \text{ km s}^{-1}$

by Carrasco-González *et al.* (2010b), however the positions they catalogue for source Bc assume that our sources W75NBc and W75NBc2 (see Figure A.61) are one and the same. Therefore to recalculate proper motions using our data, we used a deconvolved position derived from IMFIT assuming Bc and Bc2 to be the same source. It is important to note that we use the same phase calibrator (J2007+4029) as that of Carrasco-González *et al.* (2010b). At 5.8 GHz, this gives a 2012 epoch position of $\alpha(\text{J2000}) : 20^{\text{h}}38^{\text{m}}36.5525^{\text{s}}$, $\delta(\text{J2000}) : 42^{\circ}37'31.4585''$ (with uncertainties in position of 24.9 and 9.8 mas in $\alpha(\text{J2000})$ and $\delta(\text{J2000})$ respectively) translating to a proper motion of $0.12 \pm 0.05''$ ($\theta_{\text{PA}} = 161 \pm 27^{\circ}$) or $114 \pm 46 \text{ km s}^{-1}$ for the more accurate distance of $1.32 \pm 0.11 \text{ kpc}$ from Rygl *et al.* (2010) ($173 \pm 69 \text{ km s}^{-1}$ using the distance of 2 kpc adopted by Carrasco-González *et al.* (2010b)). Considering this evidence for proper motions in both current and previous data, Bc2/Bc are classified as lobes representing the shocked surfaces of an ionized jet impinging upon its surroundings.

We also detect (C-band only) the HII region (RMS designation G081.8789+00.7822) whose material stretches across a region approximately $9.5 \times 8.6''$ in angular size, or $0.064 \times 0.058 \text{ pc}$, classifying it as an ultracompact HII region. Considering its flux, assuming optically thin emission and using the models of Davies *et al.* (2011) we estimate it to have a bolometric luminosity (from its derived Lyman flux) of $6600 L_{\odot}$, mass of $11 M_{\odot}$ and therefore equivalent ZAMS type of B1.

G083.7071+03.2817

Apart from galactic plane surveys, no previous significant observations targeting this MYSO exist in the literature. UKIDSS NIR images show extended nebulosity

in a bipolar configuration, characteristic of cavities, at a position angle of $\sim 120^\circ$ and more diffuse emission to the south west.

Towards this source we detect two C-band radio objects, A and B, and one Q-band source coincident with A. Source A is resolved with dimensions of $(0.237 \pm 0.029 \times 0.045 \pm 0.061)''$ at $118 \pm 9^\circ$ and $(0.044 \pm 0.01 \times 0.012 \pm 0.01)''$ at $111 \pm 18^\circ$ at C and Q-bands respectively. In turn we calculate spectral index values of $\alpha = 0.47 \pm 0.11$ and $\gamma = -0.83 \pm 0.11$, in line with the models of Reynolds (1986) and A is therefore a thermal jet, especially given its alignment with NIR reflection nebulae in UKIDSS images (see left panel of Figure A.62). Source B has an upper limit to its spectral index of $\alpha < -0.43 \pm 0.17$ and, considering its unresolved dimensions at C-band and position angle with respect to A of $\sim -140^\circ$ (i.e. perpendicular to A's major axis), is most likely extragalactic in origin.

G084.9505–00.6910

Near infrared RGB images from UKIDSS show a well defined example of a bipolar reflection nebulae at a position angle of $\sim 120^\circ$, centred on the MYSO, however no other previous targeted observations of this object are present in the literature.

At Q-band we detect one source, B, which is not resolved using IMFIT but does appear slightly elongated along a position angle of $\sim 120^\circ$, parallel to what appears to be reflection nebulae (likely cavity walls) in UKIDSS imagery (left panel, Figure A.63). At C-band no continuum source is detected coincident with the B, but a methanol maser is detected whose IMFIT derived position is offset to B's Q-band peak by $\sim 0.8''$. Without further information we classify this to be a jet candidate, especially given its unusually steep (but still consistent with the models of Reynolds 1986) spectral index of $\alpha > 1.25$ suggesting flux contribution

from dust emission. One source is detected only at C-band, A, which is outside of the Q-band primary beam and so no further analysis can be conducted leaving it with an unknown classification. However, it does not have either a UKIDSS (NIR) or WISE (MIR) counterpart meaning it is likely extragalactic.

G094.2615–00.4116

A knot of H₂ 2.122 μ m emission is detected to the SE of our source A1 (Varricatt *et al.* 2010, source 1 of A from) and associated to a molecular outflow oriented NW to SE at an angle of 141° (Fontani *et al.* 2004).

We detect 3 sources within 50'' of the pointing centre, A1, A2 and B. Source B is only detected at C-band ($\alpha < 0.81 \pm 0.17$), does not have an NIR counterpart and, from WISE imagery, probably does not have a MIR counterpart either (its position is on the limit of source confusion). Therefore B is classified as extragalactic in origin. A1 has both a C-band and Q-band detection inferring a spectral index of $\alpha = 0.47 \pm 0.24$, however no value for γ could be obtained due to the relatively low (5σ) SNR at Q-band. However, considering A1's obvious elongation at C-band, apparent NIR cavities oriented at the same position angle and a parallel outflow, we classify it as a thermal jet. A2 is likely to be a lobe associated to A1's jet, produced via shock emission. However its extended morphology (1700 ± 300 au by 900 ± 700 au) and unknown MIR status make it a possibility that it is a small HII region of a B3, ZAMS-type star (mass of $\sim 8 M_{\odot}$, for the calculated value $\log(N_i) = 44.23 \pm 0.09$, or $L_{\star} = 2300 \pm 180 L_{\odot}$, from the models of Davies *et al.* 2011).

G094.3228–00.1671

Knots of H₂, 2.122 μ m emission were detected by Navarete *et al.* (2015) and classified to be bipolar in distribution. Their orientation with respect to the RMS source are at position angles of 355°, 185°, 290° and 165° for H₂ lobes 1a, 1b, 1c and 1d respectively.

At both frequencies we detect an unresolved radio source designated as A $\sim 2''$ to the NW of the pointing centre and coincident with the reddened NIR source apparent in the left panel of Figure A.65. At Q-band, A's position is separated from that at C-band by 0.18'' at a position angle of 107°, however the positional accuracy code of the Q-band phase calibrator is 'C' and therefore we can not say if this offset is real. We derive a spectral index of $\alpha = 1.19 \pm 0.18$ between C and Q-bands, with an upper limit on the physical size of the emission at Q-band of $< 114 \text{ au} \times < 40 \text{ au}$. Due to the unresolved nature of the radio source, it can not be determined if the emission is parallel, or perpendicular, to the previously recorded outflow axes from Navarete *et al.* (2015). We therefore classify A as a jet candidate.

G094.4637–01.7966

Observations by Smith & Fischer (1992) used near-infrared line and continuum observations to show that multiple jets were likely to exist from this region, considering the wide range in outflow axes seen in their H₂, 2.12 μ m images. More recent H₂ line observations (Navarete *et al.* 2015) showed 5 distinct regions of emission, with what appears to be 2 bipolar outflows at position angles of 355/180° (1a, 1b) and 210/30° (2a, 2b), and a monopolar outflow (3a) at a

position angle of -60° . The monopolar outflow is also aligned with the obvious NE/SW bipolar reflection nebula in NIR images, and the 2a/2b outflow was aligned with another, fainter, NIR reflection nebula (see left panel of Figure A.66).

In standard images with a robustness of 0.5 (Figure A.66), source A at C-band is coincident with A and A2 at Q-band, with an average spectral index (combining the two Q-band fluxes) of $\bar{\alpha} = 0.65 \pm 0.10$, typical of ionised jets. However considering their separation of 990 ± 210 au (202 ± 9 mas) and current theoretical ranges of jet launching radii between 10 – 100 au, we believe that A1 and A2 are close binaries. Imaging the C-band data with a more uniform robustness of -2 (increasing the effective resolution) shows that C-band source A is most likely the same source as Q-band source A, while A2 appears more separate from the C-band lobe. Using this approach, A's spectral index is derived to be 0.39 ± 0.12 , while for A2 it is calculated to be $\alpha > 1.36 \pm 0.12$ (which takes the 5σ level for C-band as a conservative estimate, due to source confusion). Both A and A2 are roughly aligned with components B, D and E at a position angle of $\sim 45^\circ$, for which we calculate spectral index upper limits of < 0.0 , < 0.4 and < 0.5 respectively. Component C is detected at both bands and has a jet-like spectral index of 0.86 ± 0.12 , and although IMFIT was unable to deconvolve any sizes, at Q-band the emission looks slightly elongated along a position angle of $\sim 10^\circ$.

Comparing our results to those of Navarete *et al.* (2015) who detects three distinct directions of collimated outflow, we detect 3 heavily thermal components (A, A2 and C). Although no definitive spectral indices could be deduced for B, D or E, we believe that due to their alignment with A, they represent shocked surfaces of optically thin and/or non-thermal emission from a thermal jet ejected

at a position angle of $\sim 45^\circ$ from A. The H_2 bipolar outflow components 2a and 2b are aligned along this axis and therefore likely more distant jet-shock features. A2 is likely a close binary to A, though its possible association with an outflow is unknown. The thermal jet at C also has a 4σ component to its WNW, in line with the monopolar outflow 3a, however without more information, we can not be sure as to C's exact nature. We therefore classify A to be a jet with lobes and both A2 and C as jet candidates.

G094.6028–01.7966

More popularly known as V645 Cygni, this object has a rich observational history. Notably Murakawa *et al.* (2013) detected $\text{Br}\gamma$ emission with a P-Cygni profile and a blue absorption feature in HeI strongly shifted in velocity by -800 km s^{-1} . This implies fast moving gas in the line of sight towards us. Modelling CO bandhead emission detected during their K-band spectroscopic analysis showed that the accretion disc in the system was almost pole-on, reinforcing the theory that a stellar wind/ionized jet was oriented towards the observer. Previous to this, a bipolar CO $J = 3 - 2$ outflow was detected by Schulz *et al.* (1989), centred on V645 Cygni.

At both C-band and Q-band we detect a compact source at the pointing centre. Although no physical dimensions could be deconvolved, we derive a spectral index for the emission of 0.49 ± 0.11 . Considering the observational history and compatibility with either a disc-wind, or a thermal jet, we classify this object as a jet candidate.

G100.3779–03.5784

This YSO was observed by Moscadelli *et al.* (2016) at frequencies of 6.2, 13.1 and 21.7 GHz with the VLA in its A-configuration. They detect a compact source which is slightly resolved at the upper two frequency bands with a spectral index of $\alpha = 0.84 \pm 0.25$. Previously Anglada & Rodríguez (2002) also observed the same object (their VLA2, which also had a NW extension to its emission), as well as another radio lobe $\sim 10''$ to the south (VLA1). In UKIDSS imagery, a red source is coincident with the previous radio detection, which appears extended in the N-S direction.

At C-band we detect two radio object, which we designate A and B. A coincides with VLA2 from Anglada & Rodríguez (2002) and therefore the same radio source from Moscadelli *et al.* (2016). We derived a spectral index of $\alpha = 0.79 \pm 0.16$, in line with that estimated previously. Combining our data with that from Moscadelli *et al.* (2016), we derive a more accurate spectral index of $\alpha = 0.80 \pm 0.09$ (neglecting their C-band result due to poor image quality). Although no deconvolved dimensions could be established, A does look extended in a NW direction in Q-band images in line with the extension of 3.6 cm emission in Anglada & Rodríguez (2002), while B is not detected likely owing to an optically thin spectral index and the loss of flux with the smaller synthesised beam. Due to the near IR colours presented in UKIDSS RGB images, we classify B as an HII region. On the other hand, source A, displays many characteristics of a jet, and due to the apparent non-contribution of dust emission to Q-band fluxes, we classify it as an ionized jet.

G102.8051–00.7184

The RMS survey catalogues three red MSX sources, G102.8051–00.7184A, B and C, within $15''$ of each other, with bolometric luminosities of $2300 L_{\odot}$, $2300 L_{\odot}$ and $1300 L_{\odot}$ respectively. Four millimetric sources were found by Palau *et al.* (2013), with their MM2 being the only possibly massive ($2 - 10 M_{\odot}$) core in the region ($22^{\text{h}}19^{\text{m}}08.974^{\text{s}}$, $56^{\circ}05'02.97''$) and the only one driving a CO(2 – 1) bipolar outflow (position angle of -20°). Fontani *et al.* (2004) detected a CO(1 – 0) outflow at a position angle of $\sim 10^{\circ}$ with the NE blue lobe coincident with both [FeII] and H₂ line emission indicative of shocks from protostellar outflows. GLIMPSE imagery shows a reddened, extended source with all the typical characteristics of an HII region approximately $15''$ NE of G102.8051–00.7184B and with a luminosity of $660 L_{\odot}$ (from the RMS survey).

At C-band we detect one source, however it is not coincident with any reddened, MIR source in GLIMPSE, with colours (in near and mid-infrared images) more attributable to a more evolved phase. Further to this, no corresponding source was detected at Q-band, establishing an upper limit to the spectral index of $< 0.61 \pm 0.15$.

G103.8744+01.8558

Previous PdBI (2mm) and VLA observations (multiple frequencies) detect 6 mm-cores associated to the IRAS source (22134+5834), one of which (MM2) is coincident with a detected UCHII region, VLA1 (Wang *et al.* 2016) which was calculated to be powered by a B1 ZAMS type star. Of the 6 detected cores, MM1 was both the brightest and heaviest with a 2mm flux of 9.3 ± 2.0 mJy and inferred

mass of $6.1 \pm 1.3 M_{\odot}$.

At C-band, we detect 5 sources which we label A, B, C, D and E, of which only A is detected at Q-band. From the derived sizes of $\sim 0.3 - 0.4''$ for A, B and C, resolving out effects become significant at the upper frequency band and therefore their non-detection is not surprising. In terms of C-band radio flux, A is the brightest and a spectral index of $\alpha = -0.41 \pm 0.16$ is derived for A, however we believe that this is a symptom of flux-loss due to resolving out effects at Q-band. This is supported by the decrease in deconvolved major axis length with frequency (HII regions should not change in size). From the optically thin (verified by the previous observations of Wang *et al.* 2016) 5.8 GHz emission, the models of Davies *et al.* (2011) predict a bolometric luminosity of $4200 L_{\odot}$. In comparison to the infrared derived bolometric luminosity of $6800 L_{\odot}$, we believe that the difference of $2600 L_{\odot}$ is supplied by the other 5 cores in the vicinity, most of which comes from MM1, which is coincident with our source B. Our only other detected radio source with a corresponding mm-core is C which is associated to MM4 of Wang *et al.* (2016). From the general morphology, we believe D, E and F (which have no IR or mm counterparts) to be shock sites whereby ejected material from B is impacting the surrounding dust/gas. We classify B as a jet with lobes on the basis of its elongated morphology along a position angle of 114° which is aligned with the string of lobes, D, E and F. Although source C is almost certainly a YSO, its exact classification is unknown and we therefore classify it as a jet candidate.

G105.5072+00.2294

Molinari *et al.* (2002) detected a 0.12 ± 0.03 mJy 3.6 cm radio source (VLA1)

coincident with a ‘ring’ of $\text{HCO}^+(1-0)$ line emission towards the MSX source. A CO $J = 2 - 1$ molecular outflow has also been observed whose emission peaks $\sim 10''$ to the NW of the MSX position (Zhang *et al.* 2005). A definitive position angle for the outflow is difficult to establish with the red lobe elongated at a position angle of $\sim 90^\circ$ and the blue lobe at an angle of -160° . Later H_2 $2.122 \mu\text{m}$ observations by Varricatt *et al.* (2010) showed three distinct patches of shock emission aligned along a position angle of $\sim 15^\circ$ and separated from the infrared source by $20''$ to the NNW.

One, elongated radio source is detected at both frequencies (A) with values for α and γ of 1.02 ± 0.16 and -1.05 ± 0.44 respectively. Deconvolved position angles for the major axis agree at both frequencies with a value of $\sim 110^\circ$ parallel with the NIR reflection nebulae of the outflow cavities apparent in the left panel of Figure A.71. Confusingly this position angle does not align well with the H_2 emission or blue CO $J = 2 - 1$ lobe, but is parallel with the elongated red CO $J = 2 - 1$ emission. Assuming the radio source is a jet, it is possible that the outflow axis has precessed towards the west considering the trail of H_2 emission and the elongation of the radio source at 110° . However, further observations will be needed to clarify this picture and A is assigned a classification of jet candidate.

G107.6823–02.2423A

Previous near-infrared spectroscopic observations detected both $\text{Br}\gamma$ and $[\text{FeII}]$ emission (Cooper *et al.* 2013) with a slit positioned over both G107.6823–02.2423A and its neighbouring HII region G107.6823–02.2423B. While the strong $\text{Br}\gamma$ is attributable to the HII region, the $1.64 \mu\text{m}$ $[\text{FeII}]$ emission is a consequence of shocked material, possibly attributable to jet activity. Diffuse $2.122 \mu\text{m}$ H_2 emis-

sion is detected by Navarete *et al.* (2015) over ranges in position angle from the central source of $210 - 240^\circ$ and $250 - 360^\circ$.

Coincident with two NIR 2MASS sources are two C-band detections, one of which is extended and resolved out (HII, coincident with G107.6823–02.2423B) and the other (A) which is located at the pointing centre and is also detected at Q-band. For the latter we derive a spectral index of $\alpha = 1.15 \pm 0.26$, however the source could not be deconvolved at any frequency (which may be due to the low SNR or it possessing a true, unresolved nature). Due to the lack of further information, this source is classified as a jet candidate.

G108.1844+05.5187

One of the nearest objects in our sample at a distance of $0.776_{-0.083}^{+0.104}$ pc (Rygl *et al.* 2010), Beltrán *et al.* (2006) detected a CO outflow at a position angle of 140° centred on their source, OVRO 2 (mass of $14.2 M_\odot$), with the (weak) red lobe towards the SE and (strong) blue to the NW. Surcis *et al.* (2013) used polarimetric, VLBI observations to detect 29 methanol masers aligned along the same position angle ($145 \pm 11^\circ$) as the molecular outflow and derived a magnetic field position angle of $9 \pm 15^\circ$. For this source we adopt a bolometric luminosity of $873 L_\odot$ based on the luminosity found by Sugitani *et al.* (1989) of $1100 L_\odot$, corrected for the more recent distance found by maser parallax (Rygl *et al.* 2010).

Towards the mm-emission of previous observations, we detect source A to be coincident with OVRO 2 from Beltrán *et al.* (2006). The emission is elongated along a position angle of $42 \pm 18^\circ$ and $42 \pm 7^\circ$ at C (which is embedded in diffuse emission) and Q-band respectively, giving an offset to the magnetic field position angles of $33 \pm 18^\circ$. Considering that the radio emission is almost perpendicular

$(82 \pm 18^\circ)$ to the outflow, which itself is significantly offset to the magnetic field direction, a confusing picture is established. However, given the overwhelming evidence for an outflow from source A (and the elongation of a reddened 2MASS source along the outflow axis), we believe that the Q-band emission is tracing a disc of dimensions $(61 \pm 12) \times (12 \pm 8)$ au. We therefore conclude that source A traces an ionized jet (candidate) at C-band, but is dominated by disc emission at Q.

Source B is not coincident with any near or mid-infrared emission, was not detected at Q-band (though was located far out in the primary beam) and does not display any mm-emission at all. Considering these facts, we conclude it to be extragalactic in origin.

G108.4714–02.8176

Navarete *et al.* (2015) detect a bipolar H_2 outflow at a position angle of 15° centred on a reddened 2MASS point source (left panel of Figure A.74).

We detect one component at both bands, centred on the red 2MASS source, with a spectral index of $\alpha = 0.55 \pm 0.20$. While not at C-band, it is resolved at Q-band ($\gamma > -0.77 \pm 0.35$), with a major axis aligned along a position angle of $\theta_{\text{PA}} = 101 \pm 25^\circ$, perpendicular to the H_2 outflow's direction. With the spectral index indicative of a typical ionised jet or disc wind, we classify this as a disc wind on the basis of its Q-band elongation perpendicular to the established outflow. It is worth noting that the C-band image shows a slight elongation at a position angle parallel with the H_2 bipolar outflow.

G108.5955+00.4925A

Associated to the infrared source, IRAS 22506+5944, the RMS survey lists two more MYSOs within $60''$ of G108.5955+00.4925A, being G108.5955+00.4925B and G108.5955+00.4925C, owing to this being a cluster of at least 15 members (Kumar *et al.* 2006). GLIMPSE imagery shows diffuse $8\mu\text{m}$ emission centred on G108.5955+00.4925C, characteristic of a HII region, however it is categorised as an MYSO based on NIR spectral features (Cooper *et al.* 2013). G108.5955+00.4925A itself is centred on a green (but not extended) MIR object and G108.5955+00.4925B is centred on a reddened MIR compact source. Previous mm observations (Su *et al.* 2004) detected a 3 mm core, which appeared to be driving a bipolar CO outflow at a position angle of $\sim 90^\circ$ but was not positioned over any of the three RMS MYSOs.

Three C-band radio sources were identified from the radio clean maps, however we did not detect any at Q-band. In light of the RMS survey's naming schemes, we dub them B, C (G108.5955+00.4925B and G108.5955+00.4925C respectively) and D (not in the RMS database). All are coincident with mid-infrared sources, however D's source is not reddened and therefore is likely of a more evolved evolutionary status. Our source B has a very low flux ($30 \pm 8\mu\text{Jy}$), and therefore a non-restrictive upper limit to its spectral index of $\alpha < 0.91 \pm 0.20$. Without more information, we classify B to be a jet candidate. On the other hand, C is classified as a HII region due to its extended morphology, coincidence with a diffuse MIR source and radio flux which matches that expected of a HII region with a bolometric luminosity of $2700L_\odot$ (Davies *et al.* 2011), which agrees with the $3000L_\odot$ derived from infrared SED fitting. A CH_3OH maser was detected

at $\alpha(\text{J2000}) = 22^{\text{h}}52^{\text{m}}38.3110^{\text{s}}$, $\delta(\text{J2000}) = 60^{\circ}00'51.885''$ (with positional uncertainties of 7 and 9 mas in α and δ respectively) but was not coincident with any RMS source, or infrared/radio continuum source. However, it was coincident with the 3 mm core/CO outflow detected by Su *et al.* (2004). It is therefore likely that this maser reveals the position of a deeply embedded, relatively unevolved MYSO, considering the already clustered environment towards this source.

G108.7575–00.9863

While GLIMPSE images are completely saturated, 2MASS (left panel of Figure A.76) shows a reflection nebula centred on G108.7575–00.9863 with its diffuse emission extending over a position angle range of $225 - 280^{\circ}$, with respect to the MYSO which lies at the heart of a cluster of 38 members (Chen *et al.* 2009). NIR observations (Cooper *et al.* 2013) show a relatively featureless spectra, with only a weak Br γ line present. Approximately $130''$ to the NNW is the classical HII region, Sh2-152, which harbours a cluster and is a well studied object. Navarete *et al.* (2015) detect H₂ 2.122 μm emission dispersed widely over a wide area, including diffuse/knotted emission towards Sh2-152 and bipolar outflows centred on G108.7575–00.9863 and to the W and ESE of it. No obvious driving force can be determined for the source of the shocking material, though the obvious candidate is G108.7575–00.9863, especially due to its coincidence with the bipolar H₂ emission, BP1.

We report the detection of 5 C-band, compact sources within $1'$ of the pointing centre (i.e. G108.7575–00.9863). These are labelled A→E, of which A and B have near-infrared counterparts (NIRS 172 and NIRS 182 from Chen *et al.* 2009, respectively). Source A is also situated on a heavily saturated GLIMPSE

source, is the only detection at Q-band within the primary beam, possesses a spectral index of 0.94 ± 0.12 and remains unresolved at all frequencies. Without further information, we consequently classify it to be a jet candidate. Due to B's reddened near infrared colours, it is determined to be a cluster member though its evolutionary status remains ambiguous without further information. Source C through E all suffer from the same classification issues of non-restrictive, thermal upper limits to spectral indices and lack of information at other wavelengths and we therefore classify them all to be of unknown nature. A methanol maser coincident with small 3σ source $1.5''$ to the north of E is also detected suggestive of a well-embedded YSO.

G110.0931–00.0641

K-band images from 2MASS show diffuse emission to the east and north-east of a bright point source centred on G110.0931–00.0641's position. A bipolar H_2 $2.122 \mu\text{m}$ outflow is detected at a position angle of 125° and centred on the MYSO (Navarete *et al.* 2015). Radio observations conducted in 2007 at 3.6 cm (8.33 GHz) using the VLA in its A-configuration detected 3 lobes of emission arranged along an axis at a position angle of $\sim 110^\circ$ (Rodríguez *et al.* 2012b). López-Sepulcre *et al.* (2010) detect a $\text{HCO}^+(1-0)$ outflow at a rough position angle of 45° and elongated emission in $\text{C}^{18}\text{O}(2-1)$ (tracing dense material) perpendicular to it. Both types of emission were centred on G110.0931–00.0641.

At C-band we detect 5 radio components named A1 (VLA3 from Rodríguez *et al.* 2012b), A2, B (VLA2 from Rodríguez *et al.* 2012b), C (VLA1 from Rodríguez *et al.* 2012b) and D, all of which are within $3''$ of the pointing centre. Both B and C are detected at Q-band and B's morphology is elongated in the direction of C.

Spectral indices were therefore only established for B and C, and were calculated to be 0.34 ± 0.18 and -0.08 ± 0.20 respectively, indicative of optically thin free-free emission. Components A1, A2, B and C are all approximately aligned on a position angle of 110° , while D is located $2.5''$ to the NE of A1.

Under the assumption that A1, A2, B and C are all HII regions, the sum of the radio flux-inferred bolometric luminosities of $(1.2 \pm 0.1) \times 10^4 L_\odot$, is slightly under-luminous for that derived from SED fits of infrared data ($1.7 \times 10^4 L_\odot$). However, B is optically thick and therefore under-luminosity is expected, meaning that a quadruple system of neighbouring HII regions is still possible at this point. Considering the alignment with previously established outflows, proper motions and changes in physical size from C to Q-bands, an alternative explanation is that of a radio jet/lobe system. Considering the high-positional accuracy quality code of the phase calibrators used at C-band (J2230+6946) and Q-band (J2250+5550), for the optically thin radio lobe, C, any positional change between frequencies should be solely due to proper motions (which we do not expect to see in the HII region case). For C, an angular shift of 67 ± 3 mas, at a position angle of $283 \pm 5^\circ$ (along the axis joining the lobes), is deduced from C to Q-bands corresponding to a proper motion of $988 \pm 255 \text{ km s}^{-1}$ (using a distance of 4.3 ± 1.0 kpc and $\Delta t = 508 \pm 52$ days). This is typical of observed velocities for radio lobes detected towards MYSOs and serves to strengthen the case that C is an optically-thin, shock-ionized lobe. On the basis of the excellent agreement of spectral indices with the models of Reynolds (1986), proper motions observed towards C and the general alignment of the radio lobes with outflows, we classify B as a radio jet with lobes (A1, A2 and C). As for D, in light of the HII region-like infrared K-band morphology, we believe it is an extended HII region whereby resolving

out is starting to affect recovered flux/morphology at C-band and resulted in a non-detection at Q.

G111.2348–01.2385

Near-infrared (2MASS) images show a point source embedded in a reflection nebula extending to the east of it. Beuther *et al.* (2002b) detected a CO (2 – 1) molecular outflow oriented east to west. Previously, this source was observed by the VLA at both 8.44 GHz and 43.4 GHz by Garay *et al.* (2007b), who observed a compact source centred on the MYSO’s location, with a spectral index of 1.1 ± 0.2 , and a large, cometary HII region whose peak is located $15''$ to the north west. That work concluded the compact source to be a HCHII region around the MYSO, which was still undergoing accretion. Later 3.6 cm (8.33 GHz) radio observations using the VLA in its A-configuration detected one radio component elongated at a position angle of 97° with a line of 8 H₂O maser spots roughly perpendicular to it (Rodríguez-Esnard *et al.* 2014). Sub-mm observations show two cores in the continuum ($875 \mu\text{m}$), one centred on G111.2348–01.2385 and the other located $\sim 2''$ to its south west, with an east-west SiO(8 – 7) outflow centred on G111.2348–01.2385 (Beuther *et al.* 2007b) and another in the north east-south west direction, presumably from the other core.

At both frequencies we detect one radio lobe coincident with the NIR point source. A spectral index of 1.10 ± 0.10 (in agreement with that calculated by Garay *et al.* 2007b) is calculated, and interestingly the deconvolved dimensions of the emission show it to be elongated at a position angle of $173 \pm 9^\circ$ at Q-band (unresolved at C-band). This position angle is perpendicular to that derived by previous 8.33 GHz observations of 97° (Rodríguez-Esnard *et al.* 2014) which, cou-

pled with the steep spectral index, suggests that at Q-band, dust emission starts to dominate over the (perpendicular) ionized component. However, contrary to this, if we take fluxes from the variety of frequencies present in the literature, the spectral index remains steady across all bands. Considering the history of previous observations, an ionized jet may be located at the single radio component we detect, however it is equally likely the emission stems from a HCHII region. Without further radio information, we can not establish the dust's flux contribution and therefore can not elucidate the nature of the radio object further. Consequently, we assign the classification of jet candidate to this object.

G111.2552–00.7702

Radio observations at 8.66 GHz (Tofani *et al.* 1995; Sridharan *et al.* 2002) imaged a compact source at the position of G111.2552–00.7702 with time-variable flux. Later, higher resolution observations (Trinidad *et al.* 2006) showed the previous compact source (labelled I23139) and an unresolved 3.5 cm source 0.5'' to its SSW. I23139 was deduced to be an ionized jet on the basis of its spectral index (0.64 ± 0.36) and masers tracing an outflow (Goddi *et al.* 2005, who derived maser proper motions along a position angle of $\sim -70^\circ$). Varricatt *et al.* (2010) showed that the MYSO is centred on a K-band source which is resolved as a binary (separation of 0.4'') in their images. Further to this they also detected a H₂ 2.122 μ m knot at a position angle of 65° from the MYSO. A molecular outflow was detected in CO (2–1) but with no discernible outflow axis since the red and blue lobes lay on top of each other (Beuther *et al.* 2002b), suggesting a head on orientation.

Within 1' of the pointing centre, we detect 5 compact, C-band radio objects,

which we label A1, A2, B, C and D. Component A1 has a Q-band counterpart with a spectral index, between the two frequencies, of $\alpha = 0.16 \pm 0.16$. The spectral index may be steeper however considering A2's close proximity at C-band which, when using IMFIT, can lead to flux being wrongly allocated from A2 to A1. Considering the spectral index previously found ($\alpha = 0.64 \pm 0.36$, Trinidad *et al.* 2006), this may indeed be the case. Because A1's major axis and A2's θ_{PA} , with respect to A1, is oriented at a position angle parallel to that of maser proper motions (Goddi *et al.* 2005) resulting from an outflow, we suggest A2 is a shock-excited lobe of emission, with the jet source located at A1. We therefore classify A1 as a thermal jet with lobes.

A CH₃OH maser is also detected offset from the continuum at C-band by $0.13''$ at a position angle of -48° . Components B and C appear to have near-infrared counterparts from 2MASS images, while D does not. However, because the spectral indices of these three components is not constrained, we must assign them an unknown classification. Further to those sources reported above, a 4σ source is detected $0.6''$ SW of A1 and coincident with I23139S. With an IMFIT derived flux of $15.5 \pm 7.6 \mu\text{Jy}$ and in combination with the flux at 8.6 GHz derived by Trinidad *et al.* (2006), we calculate a spectral index of 6.8 ± 1.5 , which is clearly not realistic. We therefore propose that I23139S is another time variable (over the 11 yr period between their observations and ours) object.

G111.5671+00.7517

One of the best examples of a NIR reflection nebulae is seen in 2MASS images of this source (also known as NGC7548–IRS9), which extends towards the south west of the redenned MYSO. Previous 3.6 and 1.3 cm radio obser-

vations by Sánchez-Monge *et al.* (2008) detected two compact radio components at 1.3 cm associated to NGC7548–IRS9. While their VLA3 is coincident with G111.5671+00.7517, VLA2 was offset approximately $5''$ to the west, yet both sources were coincident with K-band NIR (2MASS) point sources. At 3.6 cm, their images were affected by a bright, extended HII region’s sidelobes from the NW resulting in a non-detection. Navarete *et al.* (2015) resolved a bipolar H₂, 2.122 μm outflow at a position angle of $\sim 155^\circ$ with respect to the MYSO, and another in an east-west direction. Sub-mm observations of HCO⁺ and CO (1 – 0) have shown two outflows, one coincident with the H₂ jet and driven by VLA2 (Sánchez-Monge *et al.* 2008) and the other associated to VLA3 and driven along a position angle of $\sim 70^\circ$.

In our C-band images, we detect 5 radio components within $60''$ of G111.5671+00.7517, labelled, in order of distance from the centre, A (coincident with VLA3), C, B2, B1 and D. Of these 5 components, only A has a NIR or Q-band counterpart. The Q-band counterpart of A is distinctly elongated at a position angle of 19° , pointing towards C, and has a spectral index of 0.87 ± 0.08 . Since there are no NIR source associated with C, B1 or B2 by inspection of the high-resolution ($\theta = 0.4''$) RGB, J, H and K-band images of Mallick *et al.* (2014), we believe them to be shock-ionized lobes, especially given their optically thin spectral indices. From the morphology of the emission, we believe the jet is launched and collimated at A. On this basis we therefore classify A to be a jet with lobes. Also, considering the position angles of lobes B1, B2 and C with respect to A (in order of separation) of 214° , 205° and 21° respectively, in conjunction with the wide angle reflection nebula at K-band, the molecular outflow at 70° and the current jet’s major axis defined by the Q-band data (19°), we believe A’s jet axis to be

undergoing rapid, clockwise (on the plane of the sky) precession. Assuming a jet velocity of 500 km s^{-1} and inclination of 90° (i.e. jet lies in the plane of the sky) this indicates a shift of 12.5° over 23.2 yr, or a precession rate of $\sim 0.5^\circ \text{ yr}^{-1}$. This would also explain why the molecular outflow being driven from A is outflowing at a position angle of 70° . As for source D, because of its non-detection and location on the edge of the Q-band's primary beam, a non-restrictive upper limit of the spectral index was deduced ($\alpha < 0.71 \pm 0.18$) and therefore we classify as unknown in nature.

G114.0835+02.8568

Being a relatively unstudied object within our sample, the only relevant observations are those of Navarete *et al.* (2015) who observed a bipolar H_2 outflow along a rough north-south axis and centred on the MYSO's position. In near infrared RGB images, the MYSO is centred on an extended (in the north west-south east direction), reddened source.

Only C-band observations of this field were observed in which we detect 5 radio sources, labelled A1, A2, B, C and D, of which A1 and A2 are spatially coincident with G114.0835+02.8568 and the only sources associated to a NIR point source. Component B looks spatially extended/resolved out and lies within the K-band nebulosity seen in 2MASS images, whereas C (the strongest source in the field) and D are located distinctly away from the central MYSO. For A1/A2, because of the lack of Q-band images, spectral indices can not be established and therefore either component could be a YSO, or a lobe of shocked emission. Without further information, we can not constrain the natures of the radio objects and therefore assign them all with an unknown classification.

G118.6172–01.3312

Aside from the usual surveys of the whole galactic plane, no observations towards this source are present in the literature. In 2MASS near-infrared images, the MYSO presents itself as a red source in a cluster of other, slightly less reddened, point sources. GLIMPSE images are verging on saturation at $8\mu\text{m}$ over the MYSO's position, with diffuse $8\mu\text{m}$ (presumably PAH emission) to the north and north east spread across a wide area.

Unusually we only detect one source at Q-band which is not detected at C-band, therefore we establish a lower limit to the spectral index of $> 1.45 \pm 0.22$, which is unusually high for the sample in general. The radio source is just resolved with dimensions of 48×21 mas, corresponding to 134×56 au, with the major axis oriented at a position angle of 15° . However, the errors on these derived quantities are large due to the low SNR of this source. Considering the lack of any data at other wavelength regimes, as well as at C-band, we classify this as a jet candidate.

G126.7144–00.8220

G126.7144–00.8220 is situated at the centre of a bipolar, near-infrared nebula aligned at a rough position angle of -10° , typical of outflow cavities. A $2.122\mu\text{m}$ H_2 bipolar outflow centred on the MYSO and driven along a north-south axis $\theta_{\text{PA}} \sim -10^\circ$ was observed by Navarete *et al.* (2015). The same work also detected knots of H_2 emission to the west and north west. No other relevant, high-resolution observations exist in the literature for this object.

Centred on the reddened 2MASS object, we detect an elongated source at

C-band, which splits into two Q-band sources (A and A2) separated by $0.15''$ (~ 110 au at the RMS survey's distance of 0.7 pc). We calculate an overall spectral index of 0.83 ± 0.06 using the C-band flux for A and the combined fluxes of both sources at Q-band. For this object, two scenarios fit the radio data we have obtained. The first scenario is that the Q-band sources are a close binary of two YSOs, one of which is driving the previously detected $2.122 \mu\text{m}$ H_2 outflow. On the other hand, due to their combined, jet-like spectral index and small separation, this could in fact be a biconical jet, whereby we are seeing the direct emission from the launching site of the jet and counter-jet, with a launching radius of 55 au (assuming symmetry). This second scenario is supported by the alignment of the two sources with the H_2 outflow, however it must be conceded that this is in fact a serendipitous alignment. With the equal likelihood of both scenarios, we classify both objects as jet candidates.

G133.7150+01.2155

An extremely well studied object with the alias W3 IRS5, previous radio observations at K and Q-bands by van der Tak *et al.* (2005) detected 5 sources (labelled Q1 \rightarrow 5) at Q-band and 8 sources (labelled K1 \rightarrow 8) at K-band. Of these, Q1/K2, Q2/K3, Q3/K4, Q4/K6, Q5/K7 and Q6/K5 were determined to be the same Q-band/K-band sources, with ranges in thermal spectral indices of $0.5 \leq \alpha \leq 1.4$ determining them to be YSOs and therefore highlighting the tight clustered environment. Using speckle MIR imaging, the same work determined Q3/K4, Q4/K6 and Q5/K7 to have mid-infrared counterparts. In comparison with previous radio observations (Tieftrunk *et al.* 1997; Wilson *et al.* 2003, the latter of which also detected proper motions of $\sim 130 \text{ km s}^{-1}$ for K8 and Q2/K3), Q2/K3, Q3/K4,

Q5/K7 and K8 showed flux variability over time. PdBI 1.3/3.4 mm imaging by Rodón *et al.* (2008) detected 6 mm-cores towards W3 IRS5, separated by $< 2''$, MM1→6, of which MM1 was coincident with Q5/K7, MM2 with Q3/K4, MM3 with Q1/K2 (or possibly Q2/K3) and MM6 with Q4/K6. Simultaneous SiO (2–1) and (5–4) line imaging was conducted identifying 5 outflows, one driven by MM1 (SIO-a) in a north-east/south-west direction, one by MM2 (SIO-b) which is head on and one by MM4 (SIO-c) aligned east to west, with the other outflows not having any identified driving source. Line emission from SO₂ (22_{2,20} – 22_{1,21}) showed overall rotation with a velocity gradient over the whole cluster at a position angle of $\sim 130^\circ$, with the blue shifted gas towards the south-east. Diffuse 2.122 μm H₂ emission containing knots was also detected towards this region (Navarete *et al.* 2015), though no specific position angle for this emission was given.

Imaging at C-band was dominated by 4 large, extended and bright HII regions to the West, East and South of the pointing centre. Consequently a uv-range of $> 60\text{k}\lambda$ and robustness of -1 were employed to minimise the detrimental effects of bright, extended emission close to the science target.

At C-band we detect emission (left panel of Figure A.84) from 7 previously observed lobes (van der Tak *et al.* 2005) labelled Q1/K2, Q2/K3, Q3/K4, Q4/K6, Q5/K7 (MYSO), Q6/K5 and K8, as well as 5 new lobes labelled, Q4b, Q8, Q9, Q10 and C1 (in accordance with previous naming systems) in the immediate vicinity (within $3''$) of Q5/K7. At Q-band (right panel of Figure A.84) we detect emission coincident with C-band positions for Q2/K3, Q3/K4, Q4, Q5/K7, Q6/K5, Q7 and Q8.

Due to its elongated morphology, jet-like spectral index ($\alpha = 0.85 \pm 0.09$) and positioning relative to its associated lobes parallel to the SIO-a outflow, Q5/K7

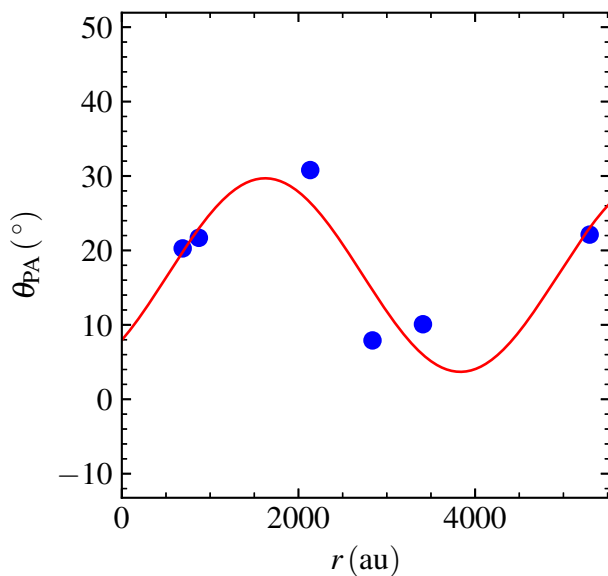


Figure C.12: A plot of the radii and position angles of lobes Q4b, Q7, Q8, Q9, K8 and C1, with respect to Q5/K7, for the MYSO G133.7150+01.2155. Least squares fitting of these points is shown in red, which represents a simple precession model.

is determined to be a thermal jet with lobes. Shock emission as a result of the jet from Q5/K7 impacting on surrounding material are present in lobes Q4b, Q7, Q8, Q9, K8 and C1. Due to a range in position angle with respect to Q5/K7 we estimate the precession angle, and period, using least squares fitting of a simple, sinusoidal, precession model to the positions (with respect to Q5/K7) for Q4b, Q7, Q8, Q9, K8 and C1 (Figure C.12). The inclination and velocity were assumed to be 90° (i.e. jet is pointed away from the observer) and 500 km s^{-1} respectively. This resulted in a derived precession period of $43 \pm 6 \text{ yr}$ and precession angle of $37 \pm 15^{\circ}$, around an axis oriented at a position angle of $16 \pm 5^{\circ}$. Our derived period should be taken as a lower limit if an inclination of the precession axis towards the observer exists. Interestingly the IMFIT-derived positions for both Q7 and Q8 change from C to Q band, which is likely due to proper motions if both lobes

are optically thin shocks as discussed above. Considering that the C and Q-band observations were taken ~ 2.7 yr apart and assuming these to be shock surfaces of the jet (from Q5/K7) upon ambient material, proper motions (in the plane of the sky) are derived to be $303 \pm 26 \text{ km s}^{-1}$ at $154 \pm 1^\circ$ and $353 \pm 30 \text{ km s}^{-1}$ at $14 \pm 1^\circ$ for Q7 and Q8 respectively (adopting a distance of $1.83 \pm 0.14 \text{ kpc}$, Imai *et al.* 2000), consistent with the derived precession model. These velocity magnitudes are often seen in ionised jets towards MYSOs adding to the case that these changes are proper motion based. It must be conceded that due to the extended nature of these lobes at both C and Q-bands, these motions may in fact be due to resolving-out effects, however the facts that the two proper motions are equal in magnitude but opposite in direction, the ionized gas is optically thin and that the precession model is consistent with these positional changes adds weight to the proper motion interpretation.

From the spectral index of Q3/K4 (0.76 ± 0.10), and the position angle of its major axis at $\theta_{161 \pm 15}$ which points at the non-thermal lobe Q1/K2, we classify it as a jet with lobes. As for its northern neighbours, Q2/K3 and Q6/K5, we believe one of them to be driving a jet which is powering lobe Q10 due to positional alignment of the C-band emission. From the C-band images, emission appears to be present between Q2/K3 and Q6/K5, which was associated to Q2/K3 by IMFIT. We therefore believe Q6/K5 to be another jet candidate in the vicinity, while Q2/K3 is classified as a candidate jet with associated lobes, Q10 and the emission between Q2/K3 and Q6/K5. Q4/K6 possesses a steep spectral index ($\alpha = 0.93 \pm 0.15$) and is coincident with MM6 from Rodón *et al.* (2008), and we therefore classify it as a jet candidate, due to its ambiguous properties as either a jet or small HCHII region.

Outside the immediate vicinity of G133.7150+01.2155, we also detect two more C-band sources, A and B (the latter of which is also detected at Q), and two sources solely detected at Q-band, QE1 and QE2. Both A and B have near-infrared counterparts in 2MASS imagery, and we determine spectral indices of -0.41 ± 0.15 and -0.13 ± 0.18 respectively. Considering the IMFIT derived C-band dimensions of A, this spectral index results from the loss of extended flux at Q-band. Due to its extended nature, we classify it as a UCHII region powered by a B3 ZAMS type star ($L_{\text{bol}} = 2500 L_{\odot}$, $EM = (5.5 \pm 3.1) \times 10^6 \text{ pc cm}^{-3}$). Source B remains point-like at all frequencies, and due to its optically thin spectral index and unreddened NIR colour we classify it as a small HCHII region powered by a B3 type ZAMS star ($L_{\text{bol}} = 2300 L_{\odot}$, $EM > 7.4 \times 10^7 \text{ pc cm}^{-3}$) or later. As for the Q-band only sources, QE1 and QE2, we derived steep, thermal spectral indices of 1.90 ± 0.15 and 1.29 ± 0.17 respectively. We believe them to be deeply embedded YSOs on account of their non-detection at near-infrared wavelengths and therefore members of the cluster associated to W3 IRS5.

G134.2792+00.8651

In the RGB, 2MASS images of Figure A.86, G134.2792+00.8651 is centred on a reddened, elongated (along a position angle of $\sim 110^\circ$) source, which itself is spatially confused with a bright, white source. At $11.6 \mu\text{m}$, MICHELLE images show the 2MASS source to break up into 2, possibly 3, sources oriented east to west. Ogura *et al.* (2002) detect a HH object (HH 586) in images of $\text{H}\alpha$ emission at coordinates, $\alpha(\text{J2000}) = 02^{\text{h}}29^{\text{m}}01.1^{\text{s}}$, $\delta(\text{J2000}) = 61^{\circ}33'33''$ offset from the MYSO's coordinates by $6.3''$ at a position angle, $\theta_{\text{PA}} = 103^\circ$. A bipolar CO molecular outflow is also detected, centred on G134.2792+00.8651, with an

outflow position angle and dynamical timescale of -30° and 15000 yr respectively (Lefloch *et al.* 1997). Images of continuum-subtracted, $2.122 \mu\text{m}$, H_2 emission, show diffuse, knotted and bipolar morphologies predominantly to the west and south-east of the central source (Navarete *et al.* 2015).

At the MYSO's position, we detect a barely resolved source ($167 \times 119 \text{ mas}$ at $\theta_{\text{PA}} = 109 \pm 63^\circ$), labelled as A, with no corresponding detection at Q-band thereby giving an upper limit to its spectral index of $< 0.48 \pm 0.17$. Due to the alignment of A's major axis with the Herbig-Haro object, HH 586, it is most likely a thermal jet, however without further information we classify it to be a jet candidate. Approximately $4''$ to the south of A is an unresolved, 7σ source at C-band whose established upper limit of $\alpha < 0.60 \pm 0.18$ fails to constrain its nature. Similarly, the brightest C-band radio source is located $33''$ south of the MYSO, named C, which has an upper limit to its spectral index of $< -0.12 \pm 0.13$. Considering the fact that C does not have a NIR or MIR counterpart, we deduce it to be extragalactic in nature. As for B however, mid-infrared saturation of GLIMPSE images by G134.2792+00.8651 prohibits us from ascertaining its MIR profile and therefore we classify it as unknown in nature. No source was detected over the primary beam in the Q-band image.

G136.3833+02.2666

Relevant previous observations towards this source are limited in the literature, with only millimetric and low-resolution outflow studies being prevalent. Saito *et al.* (2006) used high resolution mm-studies at 100 GHz to resolve three mm-cores within $20''$ of each other. The most massive core, core A, is associated to the MYSO, with the other two cores located $15''$ and $20''$ to its north east.

In the near-infrared, an elongated reflection nebula emanating from the central, reddened source is seen at K-band along an approximate east-west axis. A non-reddened 2MASS source is located $\sim 6''$ to the west of the MYSO.

At C-band we detect four sources, A, B, C and D, of which only D is not associated to a near-infrared source. Q-band images only detect one source at the same position as the C-band source A, yielding a spectral index of $\alpha = 0.92 \pm 0.18$. Unfortunately A remains unresolved at both frequencies and without further studies, is classified as a jet candidate. Due to B's coincidence with a unreddened 2MASS source, and absence of mm-emission (Saito *et al.* 2006) we classify it to be a partially resolved out HII region. For both C and D we can not make a definite classification and therefore assign them an unknown status.

G138.2957+01.5552

Also known as AFGL 4029-IRS1, this MYSO's parental clump harbours a dense cluster of at least 30 B-type stars (Deharveng *et al.* 1997). Remarkably, a previous optical study of this object exists and established velocities of 500 km s^{-1} for the highly-inclined [SII] optical jet emanating from this MYSO (Ray *et al.* 1990). Previous A-configuration, VLA, 3.6 cm observations by Zapata *et al.* (2001) detected a cometary UCHII region (AFGL 4029-IRS2) to the south of G138.2957+01.5552, two compact sources (S and N) separated by $0.6''$ in the north-south direction (at the MSX source position) and elongated/extended emission along a position angle of 80° relative to S, which they concluded to be an ionized jet. The radio source N was determined to be a time-variable, low-mass T-Tauri star close to S. A bipolar $2.122 \mu\text{m}$ outflow has previously been detected, comprised of arc-like eastern ($\theta_{PA} = 90^\circ$) and more compact western emission

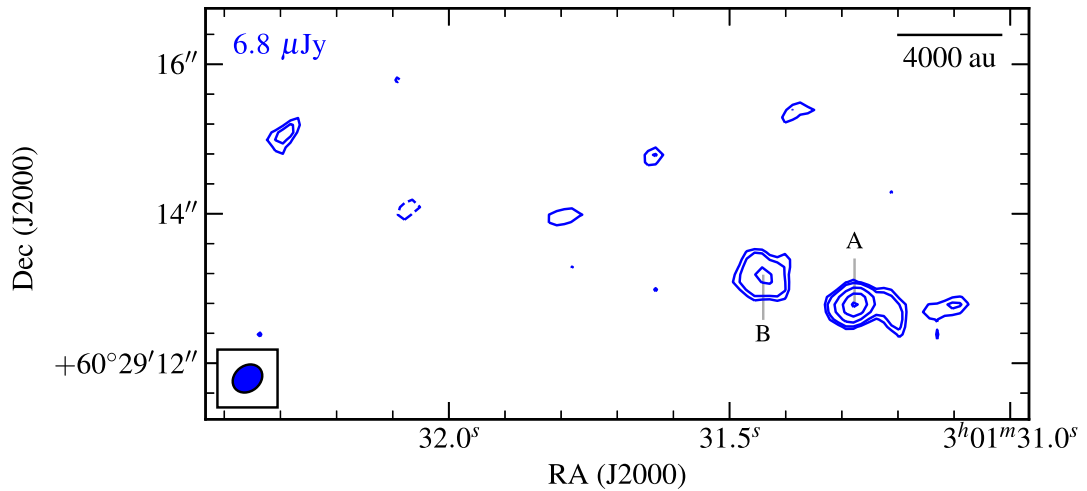


Figure C.13: C-band image of G138.2957+01.5552, utilising a robustness of 2 and a restoring beam of $0.421'' \times 0.340''$ at -50° . Contour levels are set to $(-3, 3, 4, 7, 12, 18) \times \sigma$.

$(\theta_{PA} = 270^\circ)$, both of which are separated by $\sim 12''$ (0.24 pc) from the MSX source (Navarete *et al.* 2015).

Our C-band radio images shown in Figure A.88 detect 6 objects within a $1'$ field of view. Near-infrared, 2MASS, reddened point sources are associated to C, D and E, meaning they are likely YSOs/T-tauri stars which are members of the cluster established by Deharveng *et al.* (1997). A resolved out HII region is detected, associated to a bright 2MASS source, which is the previously detected cometary UCHII region. Source A is centred at the pointing centre and is the only radio object also detected in our Q-band images. It is separated from B by $1.3''$, which lies at a position angle of 72° relative to A. Considering the alignment with the established outflow axis we determine B (which appears partially resolved out) to be a lobe of shock emission, especially given its lack of an infrared counterpart. Being located at the MYSO's position and with its spectral index typical of an ionized jet of 0.69 ± 0.15 , A is classified as a thermal jet with lobes. In our images

however, we detect no emission from the position of source N from Zapata *et al.* (2001), which is not due to resolving out effects (our beam is practically identical to theirs) or sensitivity issues (image RMS noise is ~ 2 times lower). We believe that the previously established time-variability is the reason for our non-detection of N.

Considering the absence of previously detected emission (N) and apparent resolving out effects towards A2, the field was re-imaged with a robustness of 2, the results of which are shown in Figure C.13. The new, more sensitive robustness shows how B was indeed resolved out in the images of Figure A.88, but also that significant ($> 5\sigma$), arc-like emission is also detected at a position angle of -100° from A with an IMFIT derived flux of $128 \pm 21 \mu\text{Jy}$. With this measurement, the flux of A decreases to $71 \pm 10 \mu\text{Jy}$, giving a spectral index of $\alpha = 1.0 \pm 0.1$. For consistency however, we use the value for flux and spectral index from the clean maps with a robustness of 0.5 in the analysis within the main body of this work. A 4σ component is also detected $4''$ to the ENE of A, in line with the jet's outflow axis which, if real, is likely to be another shock surface interacting with the jet.

G139.9091+00.1969A

Associated to the cluster AFGL437 of at least 60 members, this is a well studied object. At the centre of the cluster, three near-infrared sources dominate in terms of flux with both diffuse, knotted and bipolar $2.122 \mu\text{m}$, H_2 emission detected at a variety of position angles (Navarete *et al.* 2015) with respect to the MYSO. A relatively uncollimated, CO, molecular outflow was detected oriented roughly on a north (red) - south (blue) axis (Gomez *et al.* 1992), whose material was hypothesised to be sourced from laminar flow of dragged gas from outflow cavity

walls. Weintraub & Kastner (1996) resolved the northern-most of the three NIR sources into two, dubbed WK34 and WK35, of which WK34 was determined to be a low-luminosity protostar driving the north-south molecular outflow and located at the centre of a similarly oriented reflection nebula (Meakin *et al.* 2005). From those works, the other NIR sources were dubbed S and W for the southern and western bright NIR sources respectively

We detect three C-band sources, all of which are associated with near-infrared objects in 2MASS imagery and only one of which (the HII region) is not detected at Q-band. The radio object A (the southern-most NIR source, S, from Weintraub & Kastner 1996) is extended at a position angle of 62° in the direction of Ab, which is located $0.3''$ from A at a position angle of 58° . To the south-west of A is the low-SNR source, Ac, separated by $0.7''$ (at $\theta_{PA} = 241^\circ$). Calculated values of α and γ , for A, are 0.42 ± 0.11 and -0.81 ± 0.18 respectively, which agree well with the models of Reynolds (1986) and therefore we determine A to be a jet with lobes (Ab and Ac). It is interesting to note that the Q-band image shows a potentially quadrupolar morphology, which may indicate a certain degree of dust contribution to both A's morphology and flux.

Approximately $9''$ north-west of A is a spherical HII region (the NIR source, W), with a C-band flux of 20.5 ± 1.2 mJy which is therefore (assuming it is optically thin at C-band) powered by a B1 type star with a bolometric luminosity of $11000 L_\odot$ (Davies *et al.* 2011). This agrees well with the $10000 L_\odot$ (Lumsden *et al.* 2013) calculated from the infrared SED of its alias in the RMS survey.

Located $10''$ north of A is the weakest C/Q-band source, B (also known as WK34), which is unresolved at both frequencies. Derived to have a spectral index of $\alpha = 1.13 \pm 0.21$, it is classified as a nearby YSO, which may be powering a

small HCHII region, or an ionized jet.

G141.9996+01.8202

Near and mid-infrared surveys show a bright source which saturates in 2MASS, UKIDSS and GLIMPSE images. Mitchell *et al.* (1992) observed a CO $J = 2 \rightarrow 1$ outflow, with G141.9996+01.8202 (alias AFGL490) at the centre of the red and blue lobes. The molecular outflow's red lobe peaked $\sim 20''$ to the north-west but extended in an arc round to the north east of AFGL490, with the blue lobe situated at a position angle of 225° (i.e. anti-parallel to the arc of red emission). A cold envelope elongated at a position angle of $\sim -45^\circ$ was observed in the sub-mm continuum, while simultaneous observations of CS $J = 2 \rightarrow 1$ showed evidence for multiple outflows driven by low-mass sources in the envelope (Schreyer *et al.* 2002). Further PdBI observations of C¹⁷O ($2 - 1$) revealed a rotating, clumpy, molecular disc with an inclination of 35° and major axis oriented at a position angle of 105° (Schreyer *et al.* 2006).

In our C-band images, we detect 3 compact sources labelled A (the MYSO), B and C, all of which are coincident with a NIR source. Only A was detected at Q-band, the images of which show an interesting morphology with a compact radio 'core' embedded in (partially) resolved-out emission. Initially it was thought that the extended component was the dominant emission detected at C-band, however A's C-band dimensions ($0.21'' \times 0.06''$ at 58°) do not coincide with the patches of extended emission at Q-band. Values derived for α and γ closely agree to those of a spherical, stellar wind (Panagia & Felli 1975), thermal jet or disc wind, all of which are supported by the presence of the shock tracer [FeII] at $1.64 \mu\text{m}$ in NIR spectra (Cooper *et al.* 2013). Since the derived position angle of

the C-band component is as equally aligned with the inferred disc's major axis, as it is with the molecular outflow, we classify this as a jet candidate. As a further note, considering its relatively evolved status in the literature (in comparison to this sample), it is likely that the stellar wind (especially given IR recombination line profiles seen by Bunn *et al.* 1995), or photo-evaporative disc wind picture is correct, however more observations are required to distinguish between all three possibilities. As for the nature of the extended emission, under the assumption that the central object has evolved past the MYSO stage and is beginning to produce appreciable Lyman fluxes, it could be sources from ionized cavity walls, disc surfaces or an optically thick HII region. Both B and C are almost certainly members of the same cluster, however their classification, although almost certainly not extragalactic, is unknown.

G143.8118–01.5699

Near-infrared images show a reddened source at the MYSO position which is embedded in a cluster $1.8' \times 1.4'$ in size (Bica *et al.* 2003). Navarete *et al.* (2015) detect no emission in $2.122 \mu\text{m}$ H_2 towards this object.

Although we do not detect anything at 44 GHz, we see three, low-flux, compact sources in C-band images, A (G143.8118–01.5699), B and C, of which all have near-infrared counterparts. Although A and B are resolved according to IMFIT routines, their signal to noise is low and consequently the errors on deconvolved position angles/dimensions are large. Considering the relatively unconstrained nature of the emission detected towards all C-band sources, we therefore classify A to be a jet candidate, while B and C, although certainly no extragalactic, are of unknown classification.

G148.1201+00.2928

Another object with a small observation history, the most relevant of which were the H₂, 2.122 μm observations which detected diffuse, knotted and bipolar, shock emission at position angles ranging from 160 – 215° at separations between 0.27 and 1.08 pc. In 2MASS images, the MYSO is situated in a cluster, with a diffuse reflection nebula emanating from it towards the north-west ($\theta_{\text{PA}} \sim 110^\circ$).

At 5.8 GHz, we detect 3 sources within the inner 60'' of the field of view. One of these sources (A) is coincident with the MYSO from the RMS survey, while the other 2 are coincident with other near-infrared objects in the field. The C-band radio source A breaks up into 2 Q-band sources whose peaks are separated by 0.1'' (320 au), with the weaker lobe (A2) located at a position angle of 295° from the other (A), roughly aligned with the NIR reflection nebula. Because both Q-band sources (A and A2) are coincident with the C-band image of A, we combine the Q-band fluxes of A and A2 and find a spectral index of $\alpha = 1.13 \pm 0.18$ for the MYSO. From this information, A and A2 may be a jet/counter-jet system, or a close binary system. If a jet/counterjet, from the models of Reynolds (1986), the derived spectral index would suggest some degree of recombination, or acceleration, in the flow which if the separation represents the collimation radius (i.e. where the toroidal become dominant over the poloidal component in the launching magnetic field), would be more likely from acceleration. A piece of evidence against the biconical jet scenario would be the position angles of shocked H₂ emission observed by Navarete *et al.* (2015), which are misaligned with the apparent jet's axis. Due to these considerations, we define A/A2 to be a jet candidate. As for B and C, upper limits on the spectral indices of $< 0.84 \pm 0.19$

and $< 0.37 \pm 0.14$ do not constrain their natures much and therefore, although not extragalactic, are assigned the unknown classification.

G160.1452+03.1559

Near-infrared UKIDSS images (colourscale in Figure A.93 respectively) show that the reddened MYSO is extended in the NIR (especially UFTI imagery), highlighting the possibility of cavities at a position angle of $\sim 100^\circ$, an interpretation backed up by the detection of a parallel ^{12}CO ($2 - 1$) outflow by Xu *et al.* (2012). Radio observations by Sánchez-Monge *et al.* (2008) detect a compact radio source centred on the MYSO at 3.6 cm, 1.3 cm, 7 mm and 1.2 mm (IRAM) with a spectral index between 3.6 cm and 1.3 cm of $\alpha = 1.1 \pm 0.4$. Targeted, near-infrared observations showed a H_2 , $2.122 \mu\text{m}$, collimated outflow parallel to both the molecular outflow's, and radio source's major, axes at a position angle of 126° which extended over a length of $> 0.35 \text{ pc}$ (Varricatt *et al.* 2010).

This source was only observed at C-band, the images of which show two compact sources in the field of view, one situated on the MYSO (A) and the other (B) offset $\sim 3''$ to the SSE. Although B was too low in terms of signal to noise for its dimensions to be derived by IMFIT, A has a major axis aligned along a position angle of $\sim 110^\circ$, parallel with the apparent outflow cavities seen in NIR images. In order to try to discern A's nature, the data from Sánchez-Monge *et al.* (2008) was combined with our C-band result and fitted with a power law consisting of a dust, and ionized, component (assuming no flux variability between the two datasets). The resulting fit has been plotted in Figure C.14, deriving a spectral index for the ionized component of $\alpha = 0.74 \pm 0.48$, expected of a typical ionized jet. Using the derived power law we calculate a flux contribution from the ionized

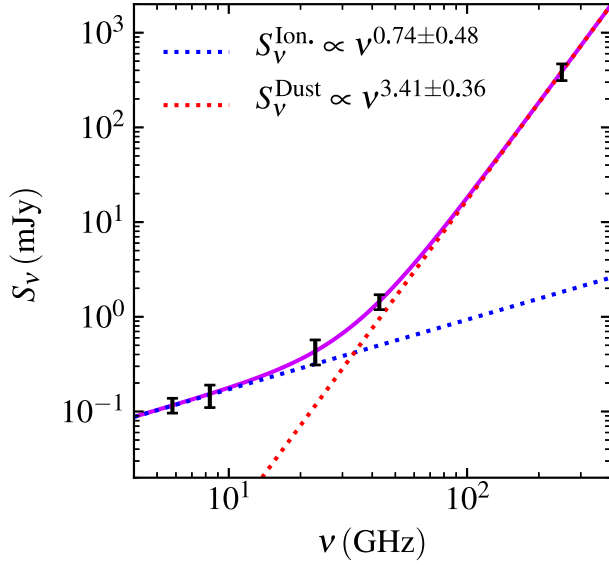


Figure C.14: Plot of flux against frequency for source ‘A’ of G160.1452+03.1559, utilising data at 8 GHz, 23 GHz, 43 GHz and 250 GHz from Sánchez-Monge *et al.* (2008). The least squares fit is plotted as the purple line for a double power law, with each power law component plotted as a dotted red (dust) and blue (ionized) line. Derived power laws for the dust and ionized contributions are indicated in the top left corner.

component, at 43 GHz, of $500 \mu\text{Jy}$ which is equivalent to an optically thin HII region powered by a ZAMS type B3 star with a luminosity of $\sim 2500 \pm 2000 L_{\odot}$. Comparing this to the IR derived flux of $2100 L_{\odot}$, it appears that the radio flux is also compatible with a HCHII region with an average electron density of $8 \pm 7 \times 10^4 \text{ cm}^{-3}$. However, because of its extensive observational history, with collimated, H_2 , shock features, molecular outflows and a full sampling of its radio spectrum, the ionized jet scenario is extremely likely. We therefore have classified A as an ionized jet. Component B, being associated with a reddened near-infrared source is likely a coeval low-mass YSO, however more observations are needed to clarify this.

G173.4839+02.4317

Our field of view contains two MYSOs from the RMS database, G173.4839+02.4317 and G173.4815+02.4459. In 2MASS images (middle panel of Figure A.94), G173.4839+02.4317 displays as a relatively unreddened, bright source surrounded by a small, young cluster (Ginsburg *et al.* 2009), while the reddened, near-infrared source, G173.4815+02.4459 shows significant, EGO emission at $4.5\ \mu\text{m}$ (see GLIMPSE inset of Figure A.94) whose diffusivity extends along a rough north-west to south-east axis. The EGO emission is embedded in a protocluster according to Ginsburg *et al.* (2009) who also inferred that G173.4815+02.4459 was, in fact, a massive binary system with a separation of 400 au. H_2 , $2.122\ \mu\text{m}$ observations show an outflow at a position angle of $\sim 150^\circ$ centred on G173.4839+02.4317 (components 7/8 and 1a/b/c from Varricatt *et al.* 2010; Navarete *et al.* 2015, respectively). Most other observations concentrate on G173.4815+02.4459, for example Beuther *et al.* (2002a) detect 3 condensations in H^{13}CO^+ ($1-0$), condensation ‘1’ being centred on G173.4815+02.4459, and condensations ‘2’ and ‘3’ located $16''$ and $25''$ to the west of condensation ‘1’ respectively. A highly collimated outflow in CO ($1-0$), at a position angle of $\sim 165^\circ$, which terminates in H_2 bow-shocks, is detected centred on condensation ‘1’ which is also at the centre of a high-velocity CO ($1-0$) outflow at a position angle of $\sim 130^\circ$, parallel to the EGO’s diffuse emission. Core ‘2’ powers an SiO ($2-1$) outflow at a position angle of $\sim 15^\circ$. Simultaneous 2.6 mm observations showed condensation ‘1’ to break into 3 mm-cores, with the brightest core, mm1, being centred on the MYSO and the other two mm-cores, mm2 and mm3, positioned $4''$ to the east and $8''$ to the north-west of mm1 respectively. Further sub-mm observations (Beuther *et al.* 2007b) resolved mm1 into

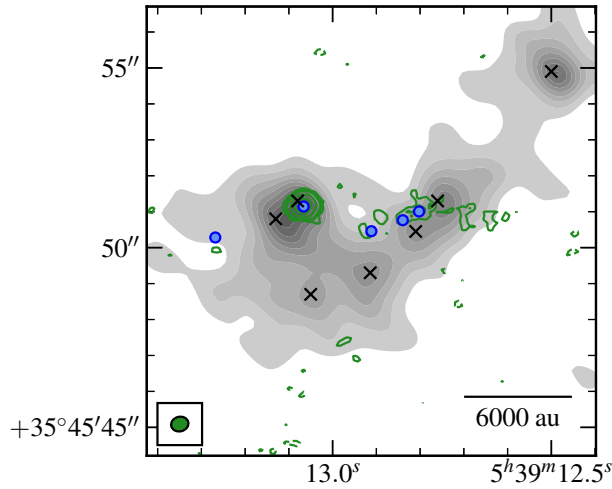


Figure C.15: Sub-mm continuum image of G173.4815+02.4459 at 1.2 mm (PdBI, greyscale) with 8.4 GHz VLA data overlaid (green contours). The ‘x’ markers show the position of the 5 cores from Beuther *et al.* (2007b) and the blue ‘o’ markers show the positions of the 5 sources, E1, E2, E3, E4 and E5, that we detected at C-band. Grey-scale increases by 10% from 10% to 90% of the peak flux ($58.9 \text{ mJy beam}^{-1}$), while green contours are set at $-3, 3, 4, 5, 10$ and 20σ ($\sigma = 16.4 \mu\text{Jy beam}^{-1}$). Both the 8.4 GHz VLA and 1.2 mm PdBI data are from Beuther *et al.* (2007b).

two further sub-cores (one of which was detected by the VLA at X-band), and mm2 into 4 further sub-cores, creating a complicated picture of this particular massive star-forming site. From the spectral energy distribution across cm, mm and sub-mm wavelengths, mm2 was also hypothesised to be emission from an outflow/jet. At other wavelengths, both the collimated, and high-velocity, molecular outflows are also seen in line emission in the near-infrared (Varricatt *et al.* 2010; Navarete *et al.* 2015). Perpendicular to the established H_2 , and high-velocity molecular, outflows, a line of CH_3OH masers ($\theta_{\text{PA}} \sim 35^\circ$), along a velocity gradient suggestive of Keplerian rotation in an accretion disc, were detected by VLBI observations (taken in 1997, Minier *et al.* 2000).

Within $1'$ of the two MYSOs in our field of view, we detect a total of 12 differ-

ent C-band radio sources. Component E1→E5 are associated with G173.4815+02.4459, while A1 and A2 are associated to G173.4839+02.4317. Components B, C, D, E and F are not associated to any infrared source, while G is coincident with a bright, unreddened 2MASS source. We detect a methanol maser located at E1's position which is coincident with the EGO from GLIMPSE images (top left panel in Figure A.94). High-resolution NIR images show that E2, E3, E4 and E5 are not associated with any near-infrared point sources, only diffuse emission (Figure 1c of Yan *et al.* 2010). Those same NIR images were however saturated around our component A1 and therefore we are unable to discern if A2 has its own infrared source. In order to better understand the natures of E1→E5, we plotted their positions on top of previous mm and radio observations in Figure C.15 from Beuther *et al.* (2007b). E1 is located at the position of core mm1a from Beuther *et al.* (2007b) and is also detected at X-band (we calculate $\alpha = 1.5 \pm 0.4$ between C and X-band), while E2 and E5 are not co-located with any 1.2 mm emission. There is also diffuse, low-SNR, X-band emission coincident with E2, E3 and E4 with a rough spectral index of ~ 0 . E3 and E4 are located towards the mm-core, mm2b, which was the core with an inferred emission contribution from a jet/outflow. Considering the wealth of previous observations, it is clear that E1 is driving a collimated, outflow and therefore harbours an ionized jet with associated lobes. We believe that E5 is a lobe as a result of jet-shocks on surrounding material, considering its position angle from the MYSO (along which there is another 3σ lobe $\sim 1.1''$ ESE of E5). As for E2, E3 and E4, there is a variety in position angle offsets from E1. If the massive binary scenario from Ginsburg *et al.* (2009) is accurate, large precessional shifts may be affecting the north-western side of the jet, providing a mechanism to alter the jet's outflow axis and we tentatively

classify E2, E3 and E4 as shock-excited lobes on this basis. Interestingly our source F is also located along a similar axis from E1 as E5 and therefore may be another lobe, however this is uncertain. Sources A2, B, C and D are not easy to classify considering their absence of previous detections and are therefore of unknown classification. From its near-infrared profile and evolved status in the literature, G173.4839+02.4317 is almost certainly a HII region, especially considering both its strong Br γ emission in the near-infrared (Cooper *et al.* 2013) and C-band, radio-inferred bolometric luminosity of $2450 L_{\odot}$ which agrees with that derived from IR studies ($2900 L_{\odot}$). As for G, due to its bright, main sequence near-infrared profile, it is likely to be a main-sequence star.

G174.1974–00.0763

Located in an active star formation region with a rich observational history, the MSX source G174.1974–00.0763 is a relatively unreddened, bright near-infrared 2MASS source, with a saturated mid-infrared profile surrounded by diffuse $8 \mu\text{m}$ PAH emission, typical of HII regions. Carral *et al.* (1999) detect a faint radio source at 8.4 GHz with a flux of 0.30 ± 0.06 mJy. Within $60''$ of the pointing centre is another MYSO, at an earlier stage in evolution, referred to in the literature as AFGL 5142 (α (J2000) = $05^{\text{h}}30^{\text{m}}48.02^{\text{s}}$, δ (J2000) = $33^{\circ}47'54.5''$). In GLIMPSE images, it is at the heart of a dense cluster, while at near-infrared, dust extinction gives it a faint, reddened profile in 2MASS images. AFGL 5142 is listed as possessing a bolometric luminosity of $2300 L_{\odot}$ (Palau *et al.* 2011), which is revised to $3300 L_{\odot}$ in light of the more accurate distance estimate of $2.14_{-0.049}^{+0.051}$ kpc by Burns *et al.* (2017). AFGL 5142 is positioned at the centre of collimated HCO $^{+}$ ($1 - 0$) and SiO($v = 0, 2 - 1$) outflows, along a position angle of $\sim 5^{\circ}$ (Hunter

et al. 1999), as well as co-located with a compact radio source (0.83 ± 0.15 mJy at 8.4 GHz using the VLA in A-configuration, Hunter *et al.* 1995). However, it appears this source may be prone to resolving out effects and/or variability at radio wavelengths (see Figure 2 of Goddi & Moscadelli (2006) for a summary), for example a higher flux of 1 mJy was reported by Carpenter *et al.* (1990) for D-configuration 4.86 GHz observations (performed 1989), and 1.5 ± 0.3 mJy reported by Hunter *et al.* (1995) at 8.6 GHz which used B-configuration observations (taken 1998). Later studies at 8.4 GHz show that the continuum source breaks down into 2 separate sources named, CM-1A and CM-1B, and also appears to power a further two molecular outflows at position angles of 35° and -60° (Zhang *et al.* 2007). PdBI, 1.3 mm observations by Palau *et al.* (2011) showed that two mm-cores were located with the MYSO. Of these, MM1 is attributed to the previous radio detections of the literature, and is elongated at a position angle of 94° (perpendicular to the north-south outflow), whereas MM2 is situated $\sim 1''$ to its south and may have been previously detected at 8.4 GHz (with a peak flux of 0.35 ± 0.09 mJy, Zhang *et al.* 2007).

From the C-band data, we report the detection of 3 radio sources, A, B and C, of which A is located at the same position as G174.1974–00.0763, and both B and C are colocated with near-infrared/mid-infrared sources, $24''$ to the east and $51''$ to the WNW respectively. Using the radio flux at 8.4 GHz of 0.30 ± 0.06 mJy from Carral *et al.* (1999), we calculate a spectral index for A of $\alpha = 2.3 \pm 0.7$, typical of optically thick emission from a HII region. It must be conceded that the flux from the literature used observations from 1994 with the VLA in its most compact configuration, therefore the resolving out of flux and/or variability may affect this calculated value. However, considering its near and mid-infrared

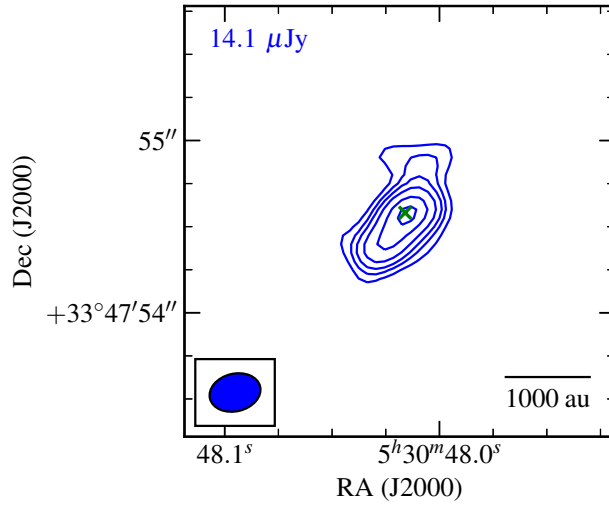


Figure C.16: Re-imaged C-band data of source B (AFGL 5172) from the G174.1974–00.0763 field, utilising a robustness of -1 . Contours are set at $-3, 3, 5, 7, 10, 15$ and 20σ where $\sigma = 14.1 \mu\text{Jy beam}^{-1}$. The restoring beam’s dimensions were $0.299'' \times 0.218''$ at $\theta_{\text{PA}} = 104^\circ$.

appearance, likely optically thick radio spectrum and diffuse $8 \mu\text{m}$ emission, it is determined that A is a HCHII region. As for B, in combination with our C-band flux of $726 \pm 22 \mu\text{Jy}$, we calculate a spectral index for B of 0.4 ± 0.5 . However, as previously discussed, this derived spectral index is not very useful in trying to establish whether or not the emission stems from an ionized jet on account of resolving out/variability issues apparent in the literature. Since Zhang *et al.* (2007) resolve B into two sources, we reimaged the field using a robustness of -1 , in order to increase the effective resolution. The results are plotted in Figure C.16 which more reliably shows two components, one elongated at a position angle of $\sim 0^\circ$ from the peak emission, and the other elongated at a position angle of $\sim -50^\circ$. Zhang *et al.* (2007) recorded almost equal fluxes at 8.4 GHz for both of these sources, whereas our 5.8 GHz data shows the most southern to be the strongest. This may be due to spectral index effects, or

variability, however further observations are required to clarify this. It is believed however that the northern elongation is an ionized jet driving the well established north-south outflows and we therefore classify B to be an ionized jet. Our detected source C has no previous detections present in the literature, however considering its coincidence with a bright main-sequence star in the near-infrared, it is likely a stellar wind, however more radio observations will be required to determine this.

G177.7291–00.3358

K-band, near-infrared, continuum images show a bright point source at the centre of a quadrupolar patch of extended emission with a UIB feature indicative of UV excitation (see Figure 1y of Ishii *et al.* 2002, who associated the morphology to tracing cavity walls). Low-resolution, near-infrared spectra taken with a slit alignment of $\theta_{\text{PA}} = -70^\circ$ (i.e. along the NW-SE, K-band diffusivity) shows shocked, [FeII] emission, a weak Br γ line and CO ($v = 2 - 0$) bandhead emission (Cooper *et al.* 2013), presumably from an accretion disc (Ilee *et al.* 2013). Non-detection of both methanol (where $3\sigma = 150$ mJy), and water, masers towards this source has been recorded by Fontani *et al.* (2010).

Two C-band sources are detected in the inner $60''$ of our field of view, labelled A (the MYSO) and B (located $25''$ west of A). Component A is completely unresolved at C-band, whereas B has dimensions of $0.16'' \times 0.13''$ with large errors on account of low signal to noise and barely extended structure. Assuming an optically thin HII region, from the C-band flux for A we infer a bolometric luminosity of $1300 L_\odot$ (Davies *et al.* 2011), close to that derived from the infrared ($2300 L_\odot$), especially considering the radio emission is likely still partially optically thick. Therefore neither jet, nor compact HII, gains precedence and therefore we clas-

sify A as a jet candidate. As for B, it is aligned with the outflow cavities' central axis seen at near-infrared wavelengths yet lacks an (mid or near) infrared counterpart, and therefore could be a shocked, Herbig-Haro type object (especially given its resolved dimensions) from a jet. However without more spectral information we must determine it to be of an unknown nature due to its similarity to extragalactic phenomena.

G183.3485–00.5751

Near-infrared, K-band images show diffuse emission elongated along a NW-SE axis, with the MYSO's reddened source at its centre. From C¹⁸O observations, a clump 0.76 pc (75'') in diameter was detected with a mass of 250 M_⊙ (Wu *et al.* 2011), whose peak is offset to the MYSO's position by 14'' to the south-west. No other relevant observations are present in the literature.

Our observations detect two, point-like, C-band sources, one (A) is roughly positioned at the MYSO's location, while the second (B) is co-located with a main sequence (from its near-infrared colours) star. We also detect two methanol maser spots separated from A's location by 0.22'' and 0.32'', at position angles of 189° and 341° respectively. The positioning of the methanol masers, along the edges of the diffuse emission, would suggest them to reside in the cavity walls, rather than in the disc (which would need to be at least 1000 au in diameter). From the sparsity of information on this source, it is impossible to definitively classify A and we assign it candidacy as a jet. Source B's positioning with a main sequence star means it is likely a stellar wind, though further radio data, at a variety of frequencies, are needed to clarify this.

G188.9479+00.8871

Located in the star formation region AFGL 5180, G188.9479+00.8871 is commonly referred to as NIRS1 (following the work of Tamura *et al.* 1991, who identified 11 K-band point sources in its proximity) and has an established, bipolar, CO outflow at a P.A. of $\sim 130^\circ$ detected by Snell *et al.* (1988). The RMS source is at the centre of a bipolar, $2.122\ \mu\text{m}$, H_2 outflow at a position angle of 110° (1a/1b from Navarete *et al.* 2015) as well as two diffuse, bipolar, K-band, reflection nebula at position angles of 90° and 110° (Tamura *et al.* 1991). Saito *et al.* (2006) detect 11 cores in C^{18}O , with core F associated to NIRS1, and two continuum sources at 98 GHz, of which core F is coincident with one (MCS B) and core E with the other (MCS A, the brightest), which in turn is located with the NIR source, NIRS5. Both of the continuum sources were previously detected as 1.2 mm cores by Minier *et al.* (2005), with bolometric luminosities of $7.0 \times 10^3 L_\odot$ and $2.4 \times 10^4 L_\odot$ for NIRS1 and NIRS5 respectively (reduced following the more accurate distance estimate of 1.76 ± 0.11 kpc by Oh *et al.* 2010). VLBI observations of CH_3OH masers show a linear arrangement of maser spots along a position angle of $78 \pm 7^\circ$, with an inferred magnetic field direction parallel to the CO outflow (Surcis *et al.* 2013).

At C-band we detect 5 distinct radio sources. Sources A and B1/B2 are unresolved and coincident with the C^{18}O cores F and E, from Saito *et al.* (2006), respectively, while C and D are resolved and have no mm-counterparts in the literature but are associated to near-infrared sources. A methanol maser is also detected to be coincident with continuum source A. Considering the wide variety of outflow phenomena seen, we believe A to be a jet, however without more

information at a range of frequencies we can only classify it as a candidate. As for B1 and B2, interestingly the axis running through them in a direction parallel to extended 98 GHz emission from Saito *et al.* (2006), which may include contribution from an ionised jet assuming B1/B2 are a jet/lobe pair. As with A, more information is required, and consequently B1 is determined to be a candidate jet with lobes (B2). Component C's coincidence with a near-infrared source classifies it as a cluster member, but the origin of its radio emission is unclear. Due to its extended nature, presence of resolved out emission and mid-infrared appearance in GLIMPSE images, we classify D to be a HII region.

G189.0307+00.7821

Also known as AFGL 6366S, this source is located with a K-band, reflection nebula, indicative of outflow cavities, along a rough north-west to south-east axis. Approximately $100''$ to the ENE another YSO, G189.0323+00.8092 (alias AFGL 6366N) from the RMS database ($L_{\text{bol}} = 1.1 \times 10^4 L_{\odot}$), is within our C-band field of view and is another YSO which has diffuse NIR emission towards its east. Kurtz *et al.* (1994) detect a 0.6 ± 0.06 mJy, unresolved, 8.4 GHz source at α (J2000) = $06^{\text{h}}08^{\text{m}}40.66^{\text{s}}$, δ (J2000) = $21^{\circ}31'07.3''$ (slightly offset to G189.0307+00.7821's position), with an unlisted ~ 0.25 mJy source $\sim 2''$ south west of it. Observations at 98 and 110 GHz show that there are two mm-cores (also detected in C^{18}O), one centred on G189.0307+00.7821's coordinates (MCS A) and the other (MCS B) located approximately $8''$ to it north-east (Saito *et al.* 2008). Two molecular clumps, one coincident with G189.0307+00.7821 (clump 3a) and the other located $\sim 140''$ to its ENE (clump 3b, positioned with G189.0323+00.8092) were detected in single dish ^{13}CO ($J = 1 - 0$) observations

by Shimoikura *et al.* (2013). Along a position angle of $\sim 100^\circ$, Wu *et al.* (2010) detected a bipolar, ^{12}CO (1 – 0) outflow, centred on G189.0307+00.7821, with the blue lobe towards the west, along the same position angle that Navarete *et al.* (2015) detect a knot of H_2 emission, as well as a bipolar H_2 outflow at a position angle of $\sim 130^\circ$.

Within $60''$ of the pointing centre we detect 7 radio sources in our C-band image. Four of these are located within $8''$ of the reddened 2MASS source shown in the top left panel of Figure A.99, named A1, A2, B and C, the last of which we also detect a methanol maser towards. Comparing to NIR, UIST images, A1 is associated to the bright K-band source, while A2, B and C do not have a NIR counterpart. In $12\ \mu\text{m}$ MICHELLE images however, it can be seen that both A1 and C have mid-infrared counterparts, suggesting that C's YSO is more deeply embedded in the natal clump (clump 3a from Shimoikura *et al.* 2013). It is also relevant to note that component C was previously detected by Kurtz *et al.* (1994) (see above) and, assuming no variability, therefore has a spectral index of $\alpha = 0.4 \pm 0.4$ between 5.8 and 8.4 GHz. As for the natures of these central components, given the CO ($\theta_{\text{PA}} \sim 100^\circ$) and H_2 outflows centred on A1, a strong case could be made for A2 being a shocked lobe along the jets path. We therefore (through lack of more radio information), classify A1 to be a candidate jet with lobes. Due to C's coincidence with both a methanol maser and mid-infrared source, it is almost certainly another MYSO in the vicinity of G189.0307+00.7821, however the nature of its radio emission is unconstrained. Due to C's deconvolved dimensions, the major axis of which is aligned along a position angle parallel to the axis through B and C, B may be a shocked lobe of emission related to a jet at C. However more information is again needed and we

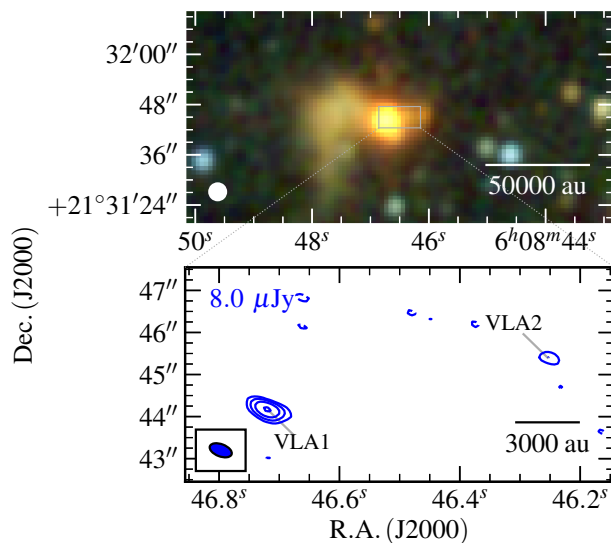


Figure C.17: Near-infrared (top panel; 2MASS, K, H, J, R, G, B colour-scale) and C-band radio map (bottom) of G189.0323+00.8092. Restoring beams are the same as in Figure A.99, while contour levels are set at $(-3, 3, 6, 11, 21) \times \sigma$.

therefore designate C as a candidate jet with lobes. As for the other three sources, both D and F have no near, or mid, infrared counterparts and are located away from the clump’s sub-mm emission, but are aligned along the same position angle as A2, relative to A1. Therefore it is quite possible that these are also lobes of shocked emission significantly more separated from the jet’s launching site than A2. However, considering the speculative nature of this and that a serendipitous alignment of background sources is a possibility, we therefore classify them as unknown sources. Due to its clear near-infrared profile as a blue, main-sequence star, we classify E as a likely stellar wind.

As previously mentioned, another MYSO (G189.0323+00.8092) is registered in the RMS database 100'' to the ENE of G189.0307+00.7821, and coincident with another molecular clump. Inspection of the C-band data outside the central 1', shows a radio source coincident with the second YSO’s position (VLA1) and

a 6σ source $\sim 7''$ to its east (VLA2). In Figure C.17 these sources are presented in conjunction with a 2MASS, NIR image. Using IMFIT, we derive VLA1's right ascension to be $06^{\text{h}}08^{\text{m}}46.7192^{\text{s}} \pm 0.014''$, declination to be $+21^{\circ}31'44.164'' \pm 0.007''$, with a flux of $212 \pm 16 \mu\text{Jy}$ and dimensions $(287 \pm 84 \text{ mas}) \times (76 \pm 67 \text{ mas})$ at $\theta_{\text{PA}} = 69 \pm 13^{\circ}$. Those same properties derived for the unresolved source VLA2 are $\alpha(\text{J2000}) = 06^{\text{h}}08^{\text{m}}46.2528^{\text{s}} \pm 0.054''$, $\delta(\text{J2000}) = +21^{\circ}31'45.383'' \pm 0.015''$ and a flux of $43 \pm 13 \mu\text{Jy}$. For VLA1, the radio flux is equivalent to an optically thin HII region powered by a central object with a bolometric luminosity of $1700 L_{\odot}$. Considering the emission is likely still optically thick, this under-luminosity is expected should VLA1 be a HII region. However it is elongated towards VLA2, and therefore a jet/lobe pair in VLA1/VLA2 is also a plausible scenario. The presence of [FeII] and relatively weak $\text{Br}\gamma$ in the NIR spectrum (Cooper *et al.* 2013) would favour this. We therefore classify VLA1 to be a candidate jet with lobes (VLA2), with a better determination of its radio spectral characteristics required for a more definitive conclusion about the radio emission's origin.

G192.6005–00.0479

Also referred to as S255IR-IRS3, this is another of our sample with a relatively rich observational history and lies in the massive star forming clump, S255IR, itself sandwiched between two, large, classical HII regions, S255 and S257. Previously, a $1.97 \pm 0.32 \text{ mJy}$ source was detected at 15 GHz with VLA, B-configuration data taken in 1984 (Rengarajan & Ho 1996b) on the MYSO's position, though remained unresolved. From near-infrared speckle imaging, two YSOs were apparent, IRS3 and IRS1 ($2.4''$ to the WNW of IRS1), which powered a bipolar reflection nebulae, IRN 1 (along a NE-SW axis) and IRN 2 (along a north-

south axis) respectively. While Heyer *et al.* (1989) observed a north-south, ^{12}CO ($J = 1 - 0$) outflow, Zinchenko *et al.* (2015) detected an extremely collimated, bipolar, CO ($J = 3 - 2$) outflow, centred on G192.6005–00.0479, at a position angle of 67° . Concurrent continuum observations at 1.3 mm, showed three cores, SMA1 (G192.6005–00.0479), SMA2 and SMA3, the latter two of which are separated from the MYSO by $2''$ and $5''$ respectively, to the north-west. Multi-epoch VLBI observations by Burns *et al.* (2016) both refined distance estimates for this object ($D = 1.78_{0.11}^{0.12}$ kpc) and observed a jet-driven bow-shock of water maser spots moving in a direction parallel to the overall outflow. The NIR, H_2 , $2.122 \mu\text{m}$ survey of Navarete *et al.* (2015) showed a large amount of diffuse emission associated to the two neighbouring, classical HII regions, however a collimated, bipolar outflow was seen centred on G192.6005–00.0479 at a position angle of 70° (their lobes 1a, 1b and 1c). A north/south alignment of H_2 shock features was also observed, but their direct association to S255IR-SMA1 is less certain.

Our C-band images show the presence of 7 radio sources within $5''$ of the MYSO, denoted as A→G, whereby A is positioned at the MYSO's coordinates and was also detected to have a methanol maser. Lobes C, D, F and G are all aligned along an average position angle of 70° with A, whilst B and E are positioned north of A by $1''$ and $3''$ respectively. From the overwhelming evidence for a collimated jet from studies in the literature, A is classified as a jet with lobes. Subsequently, least squares fitting of a simple sinusoid to the separations/position angles of C, D, F and G with respect to A, derives an approximate precession period and angle of 190 yr and 21° respectively. As for the natures of B and E, it is possible, given the north-south outflow detected by Heyer *et al.* (1989), that this may be tracing a second jet, possibly from a close binary near A's location.

However, higher resolution observations are required to establish this and B and E are therefore unknown in nature.

Away from the central object, we detect 2 more compact sources, H and I, the latter of which is separated by $\sim 2''$ from a large extended HII region $\sim 3''$ in diameter. While I has a near infrared counterpart, H does not, and neither does it have one in mid-infrared images therefore we can not determine its nature. Because component I has its own UKIDSS source ahead of a bright NIR source which is clearly the extended HII region, it is possible that it is a wind from an main-sequence cluster member, and therefore we classify it as stellar in origin.

G196.4542–01.6777

More commonly referred to as S269 IRS2, the reddened, near-infrared emission is comprised of two sources separated by $4.1''$, designated as IRS 2e and IRS 2w (G196.4542–01.6777) by Eiroa *et al.* (1994). The same work also discovered a HH object (HH 191 at α (J2000) = $06^{\text{h}}14^{\text{m}}37.8^{\text{s}}$, δ (J2000) = $+13^{\circ}49'38''$) separated from IRS 2w, its powering source, by $10''$ at a position angle of 82° , with an inferred shock velocity of 570 km s^{-1} . Jiang *et al.* (2003) detect one, possibly two, H_2 , $2.122 \mu\text{m}$ outflows along a south-east/north-west direction from IRS 2e, IRS 2w, or both. Near infrared spectroscopy of IRS 2w reveal H_2 and [FeII] shock emission, as well as relatively weak (in comparison to typical UCHII regions) $\text{Br}\gamma$ emission (Cooper *et al.* 2013) from the MYSO.

Our C-band maps of flux show 5 distinct components labelled A1, A2, B→D, with A1 and A2 centred on the MYSO's (IRS 2w) position. Both A1 and A2 are aligned and elongated at a position angle of 64° , with relatively small errors on deconvolved dimensions. However, considering the fact that the restoring beam

itself is oriented at a position angle of 64° , this may be an effect of elongated beams and imperfect cleaning/calibration. That being said, A2 looks unquestionably extended along this position angle and inspection of images show them to be noise-limited rather than dynamic range limited by the presence of residual side lobes. It is worth noting that this alignment is also roughly aligned with the Herbig-Haro object HH 191, but not the H_2 outflows. Without significantly more spectral information, we classify A1 to be a candidate jet with lobes (A2). The detected component B is at first glance, coincident with source 47 from Eiroa & Casali (1995), however it is in fact offset by $2''$ to its south-east and likely associated with a nearby cluster member. By its extended morphology ($\sim 0.015 \text{ pc} \times 0.012 \text{ pc}$) B is likely to be a small HII region powered by a $4000 L_\odot$ B2 type star (assuming optically thin emission, Davies *et al.* 2011). Source C is separated from A1 by $14''$ to the east and is coincident with the near infrared source 63 from Eiroa & Casali (1995), which looks like a typical, more-evolved cluster member. As for source D, it is coincident with a bright NIR source and is likely to be a stellar wind, or other relatively evolved phenomena.

W48 (G035.1992–01.7424)

Our RMS source is also known as the UCHII region, W48A, located in the W48 massive-star forming complex. Rygl *et al.* (2014) detected 3 FIR clumps towards the W48 region, one (H1) centred on the UCHII region and the other two, H2 and H3, located $16''$ and $63''$ to the west respectively. Both H1 and H2 have one 2.3 mm-core each, named H1a and H2a respectively, while H3 has two 2.3 mm-cores (H3a and H3b). Clump H2 was associated with methanol, hydroxyl and water maser activity, while clump H3 displayed a roughly north-east to south-

west outflow traced by the CO (3–2) transition. Ultimately this work concluded that sequential star formation from (in order of most to least evolved) H1, to H2 and lastly to H3 explained their observations, with H2 bordering the UCHII’s PDR and therefore being pressured into collapse by the expanding HII region. Most recently, 22 GHz radio images employing uv -cuts of $> 320\text{k}\lambda$ by Masqué *et al.* (2017) resolved out much of the emission and detected a compact source at $\alpha(\text{J2000}) = 19^{\text{s}}01^{\text{m}}46.460^{\text{s}}$, $\delta(\text{J2000}) = 01^{\circ}13'23.60''$ (centre of W48A) with a flux of $5.24 \pm 0.14\text{ mJy}$ and deconvolved size of $(67 \pm 3\text{ mas}) \times (39 \pm 3\text{ mas})$, at a position angle of $131 \pm 5^{\circ}$.

At C-band we detect a cometary UCHII, W48A, which limits the image in dynamic range due to its extended, bright emission. When moving to Q-band, the lack of short uv -spacings filtered out much of the extended structure and we detect partially resolved out emission at the location of the cometary HII region’s bow shock. Further to this, we detect a compact source roughly at the HII region’s geometric centre (i.e. at the location of the compact source detected by Masqué *et al.* 2017). From the K-band, radio flux previously recorded by Masqué *et al.* (2017), we derive a spectral index of -0.11 ± 0.17 with no change in deconvolved position angle or size (which makes the hypothesis of an ionized jet unlikely). From the models of a spherical, ionized wind (Panagia & Felli 1975), this looks like an unlikely candidate for an ionized, stellar wind. To investigate this possibility however, from the measured flux at 44 GHz of $4.84 \pm 0.19\text{ mJy}$, we infer a mass loss rate of (assuming $v = 3000\text{ km s}^{-1}$) of $5.6 \times 10^{-5}\text{ M}_{\odot}\text{ yr}^{-1}$ (Wright & Barlow 1975). From the models of Vink *et al.* (2001), we can infer a mass loss rate expected for a source of given luminosity/mass. For W48’s luminosity of $1.5 \times 10^5\text{ L}_{\odot}$ we expect a mass loss rate of $\sim 2.5 \times 10^{-6}\text{ M}_{\odot}\text{ yr}^{-1}$ at best, which is around 20 times

too small, compared to our measured flux at 44 GHz, which consequently rules out the stellar wind picture. With the calculated, optically-thin, spectral index, we can accurately calculate an emission measure of $(1.32 \pm 0.14) \times 10^9 \text{ pc cm}^{-6}$, an average electron density of $(1.24 \pm 0.14) \times 10^6 \text{ cm}^{-3}$ and a B1 type ($7600 L_{\odot}$, $11 M_{\odot}$) powering star, assuming it is a small HII region. Considering W48A is powered by a star (or cluster) with a bolometric luminosity of $170000 L_{\odot}$, we can say that A is not powering the overall region. Therefore we deduce A to be a gravitationally trapped HII region, since half the major axis size ($106 \pm 20 \text{ au}$) is smaller than the gravitational radius ($r_g = 122 \text{ au}$ for $M_{\star} = 11.3 M_{\odot}$).

Source B has no obvious K-band, or WISE $3/4 \mu\text{m}$ counterpart though we can not pass comment for longer wavelengths due to saturation of the WISE images at $12 \mu\text{m}$ and $22 \mu\text{m}$. Although not detected at C-band, we establish a dynamic range limited, 4σ , upper limit on its flux of $147 \mu\text{m}$ and therefore a lower limit on its spectral index of $\alpha > 0.34 \pm 0.20$. Assuming no variability in the source, this would suggest a thermal object, likely a deeply embedded, extremely young YSO. With the limitations to radio interferometric imaging from W48A, K or Ku-band observations would likely be needed to adequately establish the spectral index of B and therefore provide a firmer classification.

A methanol maser was detected which is co-located with a reddened source in UKIDSS NIR imagery, however no continuum emission is detected in C (dynamic range limited) or Q-band (with 4σ upper flux limits of $210 \mu\text{Jy}$ and $150 \mu\text{Jy}$ respectively) images. This methanol maser is located within clump H2/core H2a from Rygl *et al.* (2014) and likely points to a young MYSO on account of its non-detection at radio wavelengths.

References

- AINSWORTH, R.E., SCAIFE, A.M.M., SHIMWELL, T., TITTERINGTON, D. & WALDRAM, E. (2012). AMI radio continuum observations of young stellar objects with known outflows. *MNRAS*, **423**, 1089–1108. 37, 70, 72
- AMI CONSORTIUM, SCAIFE, A.M.M., HATCHELL, J., DAVIES, M., FRANZEN, T.M.O., GRAINGE, K.J.B., HOBSON, M.P., HURLEY-WALKER, N., LASENBY, A.N., OLAMAIE, M., PERROTT, Y.C., POOLEY, G.G., RODRÍGUEZ-GONZÁLVIZ, C., SAUNDERS, R.D., SCHAMMEL, M.P., SCOTT, P.F., SHIMWELL, T., TITTERINGTON, D. & WALDRAM, E. (2011). AMI-LA radio continuum observations of Spitzer c2d small clouds and cores: Perseus region. *MNRAS*, **415**, 893–910. 33, 37, 59, 60, 82, 163
- ANDRE, P., WARD-THOMPSON, D. & BARSONY, M. (1993). Submillimeter continuum observations of Rho Ophiuchi A - The candidate protostar VLA 1623 and prestellar clumps. *ApJ*, **406**, 122–141. 7
- ANGLADA, G. (1995). Centimeter Continuum Emission from Outflow Sources. In S. Lizano & J.M. Torrelles, eds., *Revista Mexicana de Astronomía y Astrofísica Conference Series*, vol. 1 of *Revista Mexicana de Astronomía y Astrofísica*, vol. 27, 67. 20, 33, 59, 60, 61, 162, 163, 164

- ANGLADA, G. (1996). Radio Jets in Young Stellar Objects. In A.R. Taylor & J.M. Paredes, eds., *Radio Emission from the Stars and the Sun*, vol. 93 of *Astronomical Society of the Pacific Conference Series*, 3–14. 37
- ANGLADA, G. & RODRÍGUEZ, L.F. (2002). VLA Detection of the Exciting Sources of the Molecular Outflows Associated with L1448 IRS2, IRAS 05327+3404, L43, IRAS 22142+5206, L1211, and IRAS 23545+6508. *RMAA*, **38**, 13–21. 430
- ANGLADA, G., VILLUENDAS, E., ESTALELLA, R., BELTRÁN, M.T., RODRÍGUEZ, L.F., TORRELLES, J.M. & CURIEL, S. (1998). Spectral Indices of Centimeter Continuum Sources in Star-forming Regions: Implications on the Nature of the Outflow Exciting Sources. *ApJ*, **116**, 2953–2964. 48
- ARCE, H.G., SHEPHERD, D., GUETH, F., LEE, C.F., BACHILLER, R., ROSEN, A. & BEUTHER, H. (2007). Molecular Outflows in Low- and High-Mass Star-forming Regions. *PPV*, 245–260. 11
- ASPIN, C., SANDELL, G. & WEINTRAUB, D.A. (1994). The remarkable pre-main sequence object V1318 Cygni. *A&A*, **282**, L25–L28. 152, 419, 420, 421
- BARRES DE ALMEIDA, U., ABRAHAM, Z. & ROMAN-LOPES, A. (2006). Radio observations of the HII region complex RCW 95. *Mem. S.A.It.*, **77**, 1158. 382
- BARTKIEWICZ, A., SZYMCZAK, M., VAN LANGEVELDE, H.J., RICHARDS, A.M.S. & PIHLSTRÖM, Y.M. (2009). The diversity of methanol maser morphologies from VLBI observations. *A&A*, **502**, 155–173. 416

- BATTERSBY, C., BALLY, J., JACKSON, J.M., GINSBURG, A., SHIRLEY, Y.L., SCHLINGMAN, W. & GLENN, J. (2010). An Infrared Through Radio Study of the Properties and Evolution of IRDC Clumps. *ApJ*, **721**, 222–250. 406, 407, 408, 411, 412
- BELTRÁN, M.T., BRAND, J., CESARONI, R., FONTANI, F., PEZZUTO, S., TESTI, L. & MOLINARI, S. (2006). Search for massive protostar candidates in the southern hemisphere. II. Dust continuum emission. *A&A*, **447**, 221–233. 434
- BEUTHER, H., SCHILKE, P., GUETH, F., MCCAUGHREAN, M., ANDERSEN, M., SRIDHARAN, T.K. & MENTEN, K.M. (2002a). IRAS 05358+3543: Multiple outflows at the earliest stages of massive star formation. *A&A*, **387**, 931–943. 461
- BEUTHER, H., SCHILKE, P., SRIDHARAN, T.K., MENTEN, K.M., WALMSLEY, C.M. & WYROWSKI, F. (2002b). Massive molecular outflows. *A&A*, **383**, 892–904. 10, 11, 54, 440, 441
- BEUTHER, H., ZHANG, Q., GREENHILL, L.J., REID, M.J., WILNER, D., KETO, E., SHINNAGA, H., HO, P.T.P., MORAN, J.M., LIU, S.Y. & CHANG, C.M. (2005). Line Imaging of Orion KL at 865 μm with the Submillimeter Array. *ApJ*, **632**, 355–370. 4
- BEUTHER, H., CHURCHWELL, E.B., MCKEE, C.F. & TAN, J.C. (2007a). The Formation of Massive Stars. *Protostars and Planets V*, 165–180. 4

- BEUTHER, H., ZHANG, Q., HUNTER, T.R., SRIDHARAN, T.K. & BERGIN, E.A. (2007b). The $10^5 L_{\odot}$ high-mass protostellar object IRAS 23151+5912. *A&A*, **473**, 493–500. 440, 461, 462, 463
- BICA, E., DUTRA, C.M., SOARES, J. & BARBUY, B. (2003). New infrared star clusters in the Northern and Equatorial Milky Way with 2MASS. *A&A*, **404**, 223–232. 457
- BLANDFORD, R.D. & PAYNE, D.G. (1982). Hydromagnetic flows from accretion discs and the production of radio jets. *MNRAS*, **199**, 883–903. 12, 16
- BLITZ, L. & WILLIAMS, J.P. (1999). Molecular Clouds (a review). *ArXiv Astrophysics e-prints*. 3
- BOLEY, P.A., KRAUS, S., DE WIT, W.J., LINZ, H., VAN BOEKEL, R., HENNING, T., LACOUR, S., MONNIER, J.D., STECKLUM, B. & TUTHILL, P.G. (2016). A multi-wavelength interferometric study of the massive young stellar object IRAS 13481-6124. *A&A*, **586**, A78. 126
- BONNELL, I.A., BATE, M.R., CLARKE, C.J. & PRINGLE, J.E. (1997). Accretion and the stellar mass spectrum in small clusters. *MNRAS*, **285**, 201–208. 9
- BONNELL, I.A., BATE, M.R. & ZINNECKER, H. (1998). On the formation of massive stars. *MNRAS*, **298**, 93–102. 10
- BONNELL, I.A., BATE, M.R., CLARKE, C.J. & PRINGLE, J.E. (2001). Competitive accretion in embedded stellar clusters. *MNRAS*, **323**, 785–794. 37

- BONTEMPS, S., ANDRE, P., TEREBEY, S. & CABRIT, S. (1996). Evolution of outflow activity around low-mass embedded young stellar objects. *A&A*, **311**, 858–872. 63
- BORNANCINI, C.G., O’MILL, A.L., GUROVICH, S. & LAMBAS, D.G. (2010). Radio galaxies in the Sloan Digital Sky Survey: spectral index-environment correlations. *MNRAS*, **406**, 197–207. 47
- BRIGGS, D.S. (1995). *High Fidelity Deconvolution of Moderately Resolved Sources*. Ph.d. thesis, The New Mexico Institute of Mining and Technology. 102
- BROOS, P.S., FEIGELSON, E.D., TOWNSLEY, L.K., GETMAN, K.V., WANG, J., GARMIRE, G.P., JIANG, Z. & TSUBOI, Y. (2007). The Young Stellar Population in M17 Revealed by Chandra. *ApJS*, **169**, 353–385. 19
- BUNN, J.C., HOARE, M.G. & DREW, J.E. (1995). Observations of the IR recombination line emission from massive young stellar objects. *MNRAS*, **272**, 346–354. 457
- BURKERT, A., STECKLUM, B., HENNING, T. & FISCHER, O. (2000). Multi-wavelength imaging of the peculiar Vela Molecular Ridge nebula BBW 192E. *A&A*, **353**, 153–162. 371
- BURNS, R.A., HANDA, T., NAGAYAMA, T., SUNADA, K. & OMODAKA, T. (2016). H₂O masers in a jet-driven bow shock: episodic ejection from a massive young stellar object. *MNRAS*, **460**, 283–290. 142, 474

- BURNS, R.A., HANDA, T., IMAI, H., NAGAYAMA, T., OMODAKA, T., HIROTA, T., MOTOGI, K., VAN LANGEVELDE, H.J. & BAAN, W.A. (2017). Trigonometric distance and proper motions of H₂O maser bowshocks in AFGL 5142. *MNRAS*, **467**, 2367–2376. 142, 464
- BURROWS, C.J., STAPELFELDT, K.R., WATSON, A.M., KRIST, J.E., BALLESTER, G.E., CLARKE, J.T., CRISP, D., GALLAGHER, J.S., III, GRIFFITHS, R.E., HESTER, J.J., HOESSEL, J.G., HOLTZMAN, J.A., MOULD, J.R., SCOWEN, P.A., TRAUGER, J.T. & WESTPHAL, J.A. (1996). Hubble Space Telescope Observations of the Disk and Jet of HH 30. *ApJ*, **473**, 437. 27
- CABRIT, S. & BERTOUT, C. (1992). CO line formation in bipolar flows. III - The energetics of molecular flows and ionized winds. *A&A*, **261**, 274–284. 11, 71
- CAMPBELL, B. (1984). VLA observations of collimated outflow at NGC 7538 IRS 1. *ApJ*, **282**, L27–L30. 396
- CARATTI O GARATTI, A., STECKLUM, B., LINZ, H., GARCIA LOPEZ, R. & SANNA, A. (2015). A near-infrared spectroscopic survey of massive jets towards extended green objects. *A&A*, **573**, A82. 18, 25, 54, 105, 106, 108, 113, 114, 115, 130, 202, 376, 377, 378, 379, 380, 381
- CARATTI O GARATTI, A., STECKLUM, B., WEIGELT, G., SCHERTL, D., HOFMANN, K.H., KRAUS, S., OUDMAIJER, R.D., DE WIT, W.J., SANNA, A., GARCIA LOPEZ, R., KREPLIN, A. & RAY, T.P. (2016). Tracing jet emission

at the base of a high-mass YSO. First AMBER/VLTI observations of the Br γ emission in IRAS 13481-6124. *A&A*, **589**, L4. 105

CARATTI O GARATTI, A., STECKLUM, B., GARCIA LOPEZ, R., EISLÖFFEL, J., RAY, T.P., SANNA, A., CESARONI, R., WALMSLEY, C.M., OUDMAIJER, R.D., DE WIT, W.J., MOSCADELLI, L., GREINER, J., KRABBE, A., FISCHER, C. & KLEIN (2017). Disk-mediated accretion burst in a high-mass young stellar object. *Nature Physics*, **13**, 276–279. 192, 195

CARPENTER, J.M., SNELL, R.L. & SCHLOERB, F.P. (1990). Molecular clouds associated with luminous far-infrared sources in the outer Galaxy. *ApJ*, **362**, 147–164. 465

CARRAL, P., KURTZ, S., RODRÍGUEZ, L.F., MARTÍ, J., LIZANO, S. & OSORIO, M. (1999). VLA Continuum Observations of Suspected Massive Hot Cores. *hRev. Mex. Astron. Astr.*, **35**, 97–108. 464, 465

CARRASCO-GONZÁLEZ, C., RODRÍGUEZ, L.F., ANGLADA, G., MARTÍ, J., TORRELLES, J.M. & OSORIO, M. (2010a). A Magnetized Jet from a Massive Protostar. *Science*, **330**, 1209–. 28, 367

CARRASCO-GONZÁLEZ, C., RODRÍGUEZ, L.F., TORRELLES, J.M., ANGLADA, G. & GONZÁLEZ-MARTÍN, O. (2010b). A Bright Radio HH Object with Large Proper Motions in the Massive Star-forming Region W75N. *ApJ*, **139**, 2433–2439. 422, 423, 424

CARRASCO-GONZÁLEZ, C., GALVÁN-MADRID, R., ANGLADA, G., OSORIO, M., D’ALESSIO, P., HOFNER, P., RODRIGUEZ, L.F., LINZ, H. & ARAYA,

- E.D. (2012). Resolving the circumstellar disk around the massive protostar driving the hh 80-81 jet. *The ApJ Journal Letters*, **752**, L29. 25
- CARRASCO-GONZÁLEZ, C., TORRELLES, J.M., CANTÓ, J., CURIEL, S., SURCIS, G., VLEMMINGS, W.H.T., VAN LANGEVELDE, H.J., GODDI, C., ANGLADA, G., KIM, S.W., KIM, J.S. & GÓMEZ, J.F. (2015). Observing the onset of outflow collimation in a massive protostar. *Science*, **348**, 114–117. 13, 23
- CASWELL, J.L. (1998). Positions of hydroxyl masers at 1665 and 1667 MHz. *MNRAS*, **297**, 215–235. 107, 202, 380
- CESARONI, R., GALLI, D., LODATO, G., WALMSLEY, C.M. & ZHANG, Q. (2007). Disks Around Young O-B (Proto)Stars: Observations and Theory. *Protostars and Planets V*, 197–212. 8, 382
- CHAMBERS, E.T., JACKSON, J.M., RATHBORNE, J.M. & SIMON, R. (2009). Star Formation Activity of Cores within Infrared Dark Clouds. *ApJS*, **181**, 360–390. 138, 160
- CHEN, H.R.V., KETO, E., ZHANG, Q., SRIDHARAN, T.K., LIU, S.Y. & SU, Y.N. (2016). A Hot and Massive Accretion Disk around the High-mass Protostar IRAS 20126+4104. *ApJ*, **823**, 125. 167
- CHEN, Y., YAO, Y., YANG, J., ZENG, Q. & SATO, S. (2009). Near-Infrared Imaging of the Star-Forming Regions Sh2-157 and Sh2-152. *ApJ*, **693**, 430–446. 437

- CHINI, R., HOFFMEISTER, V.H., KÄMPGEN, K., KIMESWENGER, S., NIELBOCK, M. & SIEBENMORGEN, R. (2004). The nature of the KW object. *A&A*, **427**, 849–853. 369
- CODELLA, C., CABRIT, S., GUETH, F., CESARONI, R., BACCIOTTI, F., LEFLOCH, B. & McCAUGHREAN, M.J. (2007). A highly-collimated SiO jet in the HH212 protostellar outflow. *A&A*, **462**, L53–L56. 24
- CODELLA, C., BELTRÁN, M.T., CESARONI, R., MOSCADELLI, L., NERI, R., VASTA, M. & ZHANG, Q. (2013). SiO collimated outflows driven by high-mass YSOs in G24.78+0.08. *A&A*, **550**, A81. 24
- COOPER, H.D.B., LUMSDEN, S.L., OUDMAIJER, R.D., HOARE, M.G., CLARKE, A.J., URQUHART, J.S., MOTTRAM, J.C., MOORE, T.J.T. & DAVIES, B. (2013). The RMS survey: near-IR spectroscopy of massive young stellar objects. *MNRAS*, **430**, 1125–1157. 17, 146, 179, 184, 185, 433, 436, 437, 456, 464, 467, 473, 475
- CURIEL, S., CANTO, J. & RODRIGUEZ, L.F. (1987). A model for the thermal radio continuum emission produced by a shock wave and its application to the Herbig-Haro objects 1 and 2. *RMAA*, **14**, 595–602. 20, 59, 61
- CURIEL, S., HO, P.T.P., PATEL, N.A., TORRELLES, J.M., RODRÍGUEZ, L.F., TRINIDAD, M.A., CANTÓ, J., HERNÁNDEZ, L., GÓMEZ, J.F., GARAY, G. & ANGLADA, G. (2006). Large Proper Motions in the Jet of the High-Mass YSO Cepheus A HW2. *ApJ*, **638**, 878–886. 22, 23, 29, 83
- CYGANOWSKI, C.J., WHITNEY, B.A., HOLDEN, E., BRADEN, E., BROGAN, C.L., CHURCHWELL, E., INDEBETOUW, R., WATSON, D.F., BABLER,

- B.L., BENJAMIN, R., GOMEZ, M., MEADE, M.R., POVICH, M.S., ROBITAILLE, T.P. & WATSON, C. (2008). A Catalog of Extended Green Objects in the GLIMPSE Survey: A New Sample of Massive Young Stellar Object Outflow Candidates. *ApJ*, **136**, 2391–2412. 26, 39, 42, 107, 375, 378, 383, 386, 393
- CYGANOWSKI, C.J., BROGAN, C.L., HUNTER, T.R. & CHURCHWELL, E. (2011). Deep Very Large Array Radio Continuum Surveys of GLIMPSE Extended Green Objects (EGOs). *ApJ*, **743**, 56. 409, 410
- DAME, T.M., HARTMANN, D. & THADDEUS, P. (2001). The Milky Way in Molecular Clouds: A New Complete CO Survey. *ApJ*, **547**, 792–813. 5
- DAVIES, B., LUMSDEN, S.L., HOARE, M.G., OUDMAIJER, R.D. & DE WIT, W.J. (2010). The circumstellar disc, envelope and bipolar outflow of the massive young stellar object W33A. *MNRAS*, **402**, 1504–1515. 8, 368
- DAVIES, B., HOARE, M.G., LUMSDEN, S.L., HOSOKAWA, T., OUDMAIJER, R.D., URQUHART, J.S., MOTTRAM, J.C. & STEAD, J. (2011). The Red MSX Source survey: critical tests of accretion models for the formation of massive stars. *MNRAS*, **416**, 972–990. 18, 33, 38, 52, 58, 59, 60, 86, 126, 162, 163, 172, 179, 186, 187, 369, 374, 398, 399, 401, 413, 424, 426, 432, 436, 455, 467, 476
- DE BUIZER, J.M. (2003). Testing the circumstellar disc hypothesis: a search for H₂ outflow signatures from massive young stellar objects with linearly distributed methanol masers. *MNRAS*, **341**, 277–298. 381

- DE BUIZER, J.M., WALSH, A.J., PIÑA, R.K., PHILLIPS, C.J. & TELESKO, C.M. (2002). High-Resolution Mid-Infrared Imaging of G339.88-1.26. *ApJ*, **564**, 327–332. 387, 388
- DE BUIZER, J.M., REDMAN, R.O., LONGMORE, S.N., CASWELL, J. & FELDMAN, P.A. (2009). SiO outflow signatures toward massive young stellar objects with linearly distributed methanol masers. *A&A*, **493**, 127–143. 381, 382
- DE LUCA, M., GIANNINI, T., LORENZETTI, D., MASSI, F., ELIA, D. & NISINI, B. (2007). Near- and far-infrared counterparts of millimeter dust cores in the Vela molecular ridge cloud D. *A&A*, **474**, 863–872. 103, 126, 371
- DEHARVENG, L., ZAVAGNO, A., CRUZ-GONZALEZ, I., SALAS, L., CAPLAN, J. & CARRASCO, L. (1997). AFGL 4029: a cluster of massive young stars. *A&A*, **317**, 459–475. 452, 453
- DRAINE, B.T. (2006). On the Submillimeter Opacity of Protoplanetary Disks. *ApJ*, **636**, 1114–1120. 166
- DUCHÊNE, G. & KRAUS, A. (2013). Stellar Multiplicity. *ARAA*, **51**, 269–310. 82
- DYSON, J.E. & WILLIAMS, D.A. (1980). *Physics of the Interstellar Medium*. Manchester University Press. 11
- EGAN, M.P., SHIPMAN, R.F., PRICE, S.D., CAREY, S.J., CLARK, F.O. & COHEN, M. (1998). A Population of Cold Cores in the Galactic Plane. *ApJ*, **494**, L199–L202. 4

- EIROA, C. & CASALI, M.M. (1995). The S 269 stellar cluster. *A&A*, **303**, 87.
476
- EIROA, C., CASALI, M.M., MIRANDA, L.F. & ORTIZ, E. (1994). S269-IRS2:
a massive young stellar object powering Herbig-Haro emission. *A&A*, **290**,
599–604. 475
- EISLOFFEL, J., MUNDT, R., RAY, T.P. & RODRIGUEZ, L.F. (2000). Colli-
mation and Propagation of Stellar Jets. *Protostars and Planets IV*, 815–840.
67
- ELIAS, J.H. (1980). H₂ emission from Herbig-Haro objects. *ApJ*, **241**, 728–735.
114
- ELLINGSEN, S.P. (2006). Methanol Masers: Reliable Tracers of the Early Stages
of High-Mass Star Formation. *ApJ*, **638**, 241–261. 382, 384
- ELLINGSEN, S.P., NORRIS, R.P. & MCCULLOCH, P.M. (1996). Continuum
emission associated with 6.7-GHz methanol masers. *MNRAS*, **279**, 101–107.
387, 388
- ELMEGREEN, B.G. & LADA, C.J. (1977). Sequential formation of subgroups in
OB associations. *ApJ*, **214**, 725–741. 3
- FEIGELSON, E.D. & MONTMERLE, T. (1999). High-Energy Processes in Young
Stellar Objects. *ARA&A*, **37**, 363–408. 7
- FELLI, M., TAYLOR, G.B., NECKEL, T. & STAUDE, H.J. (1998). The ionized
wind of IRAS 08159-3543. *A&A*, **329**, 243–248. 370

- FERNÁNDEZ-LÓPEZ, M., CURIEL, S., GIRART, J.M., HO, P.T.P., PATEL, N. & GÓMEZ, Y. (2011). Millimeter and Submillimeter High Angular Resolution Interferometric Observations: Dust in the Heart of IRAS 18162-2048. *ApJ*, **141**, 72. 367
- FONTANI, F., CESARONI, R., TESTI, L., MOLINARI, S., ZHANG, Q., BRAND, J. & WALMSLEY, C.M. (2004). Nature of two massive protostellar candidates: IRAS 21307+5049 and IRAS 22172+5549. *A&A*, **424**, 179–195. 426, 431
- FONTANI, F., CESARONI, R. & FURUYA, R.S. (2010). Class I and Class II methanol masers in high-mass star-forming regions. *A&A*, **517**, A56. 467
- FORSTER, J.R. & CASWELL, J.L. (1989). The spatial relationship of OH and H₂O masers. *A&A*, **213**, 339–350. 396
- FORSTER, J.R. & CASWELL, J.L. (1999). OH and H₂O masers in 74 star-forming regions. The FC89 database. *A&AS*, **137**, 43–49. 66
- FRANK, A., RAY, T.P., CABRIT, S., HARTIGAN, P., ARCE, H.G., BACCIOTTI, F., BALLY, J., BENISTY, M., EISLÖFFEL, J., GÜDEL, M., LEBEDEV, S., NISINI, B. & RAGA, A. (2014). Jets and Outflows from Star to Cloud: Observations Confront Theory. *Protostars and Planets VI*, 451–474. 67
- FRATER, R.H., BROOKS, J.W. & WHITEOAK, J.B. (1992). The Australia Telescope - Overview. *Journal of Electrical and Electronics Engineering Australia*, **12**, 103–112. 39

- FUJISAWA, K., SUGIYAMA, K., AOKI, N., HIROTA, T., MOCHIZUKI, N., DOI, A., HONMA, M., KOBAYASHI, H., KAWAGUCHI, N., OGAWA, H., OMODAKA, T. & YONEKURA, Y. (2012). Bursting Activity in a High-Mass Star-Forming Region G33.64-0.21 Observed with the 6.7GHz Methanol Maser. *PASJ*, **64**, 17. 142, 152, 417
- FURUYA, R.S., KITAMURA, Y., WOOTTEN, A., CLAUSSEN, M.J. & KAWABE, R. (2003). Water Maser Survey toward Low-Mass Young Stellar Objects in the Northern Sky with the Nobeyama 45 Meter Telescope and the Very Large Array. *ApJS*, **144**, 71–134. 37, 60, 163
- GALVÁN-MADRID, R., ZHANG, Q., KETO, E., HO, P.T.P., ZAPATA, L.A., RODRÍGUEZ, L.F., PINEDA, J.E. & VÁZQUEZ-SEMADENI, E. (2010). From the Convergence of Filaments to Disk-outflow Accretion: Massive Star Formation in W33A. *ApJ*, **725**, 17–28. 167, 368
- GARAY, G., BROOKS, K.J., MARDONES, D. & NORRIS, R.P. (2003). A Triple Radio Continuum Source Associated with IRAS 16547-4247: A Collimated Stellar Wind Emanating from a Massive Protostar. *ApJ*, **587**, 739–747. 29, 54
- GARAY, G., FAÚNDEZ, S., MARDONES, D., BRONFMAN, L., CHINI, R. & NYMAN, L.Å. (2004). Discovery of Four New Massive and Dense Cold Cores. *ApJ*, **610**, 313–319. 4
- GARAY, G., MARDONES, D., BRONFMAN, L., BROOKS, K.J., RODRÍGUEZ, L.F., GÜSTEN, R., NYMAN, L.Å., FRANCO-HERNÁNDEZ, R. & MORAN, J.M. (2007a). Discovery of an energetic bipolar molecular outflow towards IRAS 16547-4247. *A&A*, **463**, 217–224. 391

- GARAY, G., RODRÍGUEZ, L.F. & DE GREGORIO-MONSALVO, I. (2007b). Very Large Array Observations of Candidate High-Mass Protostellar Objects at 7 Millimeters. *ApJ*, **134**, 906–911. 440
- GIANNINI, T., MASSI, F., PODIO, L., LORENZETTI, D., NISINI, B., CARATTI O GARATTI, A., LISEAU, R., LO CURTO, G. & VITALI, F. (2005). Star formation in the Vela Molecular Clouds: A new protostar powering a bipolar jet. *A&A*, **433**, 941–954. 373
- GIANNINI, T., LORENZETTI, D., DE LUCA, M., STRAFELLA, F., ELIA, D., MAIOLO, B., MARENGO, M., MARUCCIA, Y., MASSI, F., NISINI, B., OLMI, L., SALAMA, A. & SMITH, H.A. (2013). Spitzer-IRAC Survey of Molecular Jets in Vela-D. *ApJ*, **767**, 147. 373
- GIBB, A.G., HOARE, M.G., LITTLE, L.T. & WRIGHT, M.C.H. (2003). A detailed study of G35.2-0.7N: collimated outflows in a cluster of high-mass young stellar objects. *MNRAS*, **339**, 1011–1024. 415, 416
- GINSBURG, A.G., BALLY, J., YAN, C.H. & WILLIAMS, J.P. (2009). Outflows and Massive Stars in the Protocluster IRAS 05358+3543. *ApJ*, **707**, 310–327. 461, 463
- GODDI, C. & MOSCADELLI, L. (2006). Tracing the base of protostellar wind(s) towards the high-mass star forming region AFGL 5142: VLA continuum and VLBA H₂O maser observations. *A&A*, **447**, 577–587. 465
- GODDI, C., MOSCADELLI, L., ALEF, W., TARCHI, A., BRAND, J. & PANI, M. (2005). Kinematics of H₂O masers in high-mass star forming regions. *A&A*, **432**, 161–173. 441, 442

- GOMEZ, J.F., TORRELLES, J.M., ESTALELLA, R., ANGLADA, G., VERDESMONTENEGRO, L. & HO, P.T.P. (1992). On the nature of the bipolar molecular outflow in AFGL 437. *ApJ*, **397**, 492–499. 454
- GÓMEZ, J.F., SARGENT, A.I., TORRELLES, J.M., HO, P.T.P., RODRÍGUEZ, L.F., CANTÓ, J. & GARAY, G. (1999). Disk and Outflow in Cepheus A-HW2: Interferometric SiO and HCO⁺ Observations. *ApJ*, **514**, 287–295. 29
- GOTTSCHALK, M., KOTHES, R., MATTHEWS, H.E., LANDECKER, T.L. & DENT, W.R.F. (2012). The JCMT ¹²CO(3-2) survey of the Cygnus X region. I. A pathfinder. *A*, **541**, A79. 421
- GREEN, J.A., CASWELL, J.L., FULLER, G.A., AVISON, A., BREEN, S.L., ELLINGSEN, S.P., GRAY, M.D., PESTALOZZI, M., QUINN, L., THOMPSON, M.A. & VORONKOV, M.A. (2012). The 6-GHz methanol multibeam maser catalogue - IV. Galactic longitudes 186deg - 330deg including the Orion-Monoceros region. *MNRAS*, **420**, 3108–3125. 106, 107, 377
- GUZMÁN, A.E., GARAY, G. & BROOKS, K.J. (2010). A String of Radio Emission Associated with IRAS 16562-3959: A Collimated Jet Emanating from a Luminous Massive Young Stellar Object. *ApJ*, **725**, 734–741. 30, 54, 82, 118, 394, 395
- GUZMÁN, A.E., GARAY, G., BROOKS, K.J., RATHBORNE, J. & GÜSTEN, R. (2011). A Hot Molecular Outflow Driven by the Ionized Jet Associated with IRAS 16562-3959. *ApJ*, **736**, 150. 30, 394

- GUZMÁN, A.E., GARAY, G., BROOKS, K.J. & VORONKOV, M.A. (2012). Search for Ionized Jets toward High-mass Young Stellar Objects. *ApJ*, **753**, 51. 31, 37, 39, 42, 399
- GUZMÁN, A.E., GARAY, G., RODRÍGUEZ, L.F., CONTRERAS, Y., DOUGADOS, C. & CABRIT, S. (2016). A Protostellar Jet Emanating from a Hypercompact Hii Region. *ApJ*, **826**, 208. 61, 192
- HACHISUKA, K., BRUNTHALER, A., MENTEN, K.M., REID, M.J., IMAI, H., HAGIWARA, Y., MIYOSHI, M., HORIUCHI, S. & SASAO, T. (2006). Water Maser Motions in W3(OH) and a Determination of Its Distance. *ApJ*, **645**, 337–344. 142
- HARTIGAN, P., MORSE, J.A. & RAYMOND, J. (1994). Mass-loss rates, ionization fractions, shock velocities, and magnetic fields of stellar jets. *ApJ*, **436**, 125–143. 67, 180
- HATCHELL, J., FULLER, G.A. & LADD, E.F. (1999). Temperature predictions for protostellar outflows. *A&A*, **344**, 687–695. 11
- HEATHCOTE, S., MORSE, J.A., HARTIGAN, P., REIPURTH, B., SCHWARTZ, R.D., BALLY, J. & STONE, J.M. (1996). Hubble Space Telescope Observations of the HH 47 Jet: Narrowband Images. *ApJ*, **112**, 1141. 27
- HENNING, T., LAPINOV, A., SCHREYER, K., STECKLUM, B. & ZINCHENKO, I. (2000a). IRAS 12326-6245: Luminous very young stellar objects with a massive molecular outflow. *A&A*, **364**, 613–624. 401

- HENNING, T., SCHREYER, K., LAUNHARDT, R. & BURKERT, A. (2000b). Massive young stellar objects with molecular outflows. *A&A*, **353**, 211–226. 375
- HERNANDEZ, A.K. & TAN, J.C. (2015). The Giant Molecular Cloud Environments of Infrared Dark Clouds. *ApJ*, **809**, 154. 4
- HESTER, J.J., STAPELFELDT, K.R. & SCOWEN, P.A. (1998). Hubble Space Telescope Wide Field Planetary Camera 2 Observations of HH 1-2. *ApJ*, **116**, 372–395. 27
- HEYER, M.H., SNELL, R.L., MORGAN, J. & SCHLOERB, F.P. (1989). A CO and far-infrared study of the S254-S258 region. *ApJ*, **346**, 220–231. 474
- HIGUCHI, A.E., SAIGO, K., CHIBUEZE, J.O., SANHUEZA, P., TAKAKUWA, S. & GARAY, G. (2015). IRAS 16547-4247: A New Candidate of a Protocluster Unveiled with ALMA. *ApJ*, **798**, L33. 390
- HILDEBRAND, R.H. (1983). The Determination of Cloud Masses and Dust Characteristics from Submillimetre Thermal Emission. *QJRAS*, **24**, 267. 62
- HOARE, M.G. (2006). An Equatorial Wind from the Massive Young Stellar Object S140 IRS 1. *ApJ*, **649**, 856–861. 11
- HOARE, M.G. & FRANCO, J. (2007). Massive Star Formation. *ArXiv e-prints*. 40, 54
- HOARE, M.G., KURTZ, S.E., LIZANO, S., KETO, E. & HOFNER, P. (2007). Ultracompact Hii Regions and the Early Lives of Massive Stars. *Protostars and Planets V*, 181–196. 76

- HOLLENBACH, D. & MCKEE, C.F. (1989). Molecule formation and infrared emission in fast interstellar shocks. III - Results for J shocks in molecular clouds. *ApJ*, **342**, 306–336. 52
- HONMA, M., BUSHIMATA, T., CHOI, Y.K., HIROTA, T., IMAI, H., IWADATE, K., JIKE, T., KAMEYA, O., KAMOHARA, R., KAN-YA, Y., KAWAGUCHI, N., KIJIMA, M., KOBAYASHI, H., KUJI, S., KURAYAMA, T., MANABE, S., MIYAJI, T., NAGAYAMA, T., NAKAGAWA, A., OH, C.S., OMODAKA, T., OYAMA, T., SAKAI, S., SATO, K., SASAO, T., SHIBATA, K.M., SHINTANI, M., SUDA, H., TAMURA, Y., TSUSHIMA, M. & YAMASHITA KAZUYOSHI (2007). Astrometry of Galactic Star-Forming Region Sharpless 269 with VERA: Parallax Measurements and Constraint on Outer Rotation Curve. *PASJ*, **59**, 889–895. 142
- HOSOKAWA, T. & OMUKAI, K. (2009). Evolution of Massive Protostars with High Accretion Rates. *ApJ*, **691**, 823–846. 15, 18
- HOYLE, F. (1954). On Nuclear Reactions Occuring in Very Hot STARS.I. the Synthesis of Elements from Carbon to Nickel. *ApJS*, **1**, 121. 1
- HUNTER, T.R., TESTI, L., TAYLOR, G.B., TOFANI, G., FELLI, M. & PHILLIPS, T.G. (1995). A multiwavelength picture of the AFGL 5142 star-forming region. *A&A*, **302**, 249. 465
- HUNTER, T.R., TESTI, L., ZHANG, Q. & SRIDHARAN, T.K. (1999). Molecular Jets and H₂O Masers in the AFGL 5142 Hot Core. *ApJ*, **118**, 477–487. 464
- ILEE, J.D., WHEELWRIGHT, H.E., OUDMAIJER, R.D., DE WIT, W.J., MAUD, L.T., HOARE, M.G., LUMSDEN, S.L., MOORE, T.J.T.,

- URQUHART, J.S. & MOTTRAM, J.C. (2013). CO bandhead emission of massive young stellar objects: determining disc properties. *MNRAS*, **429**, 2960–2973. 17, 105, 146, 376, 384, 385, 467
- IMAI, H., KAMEYA, O., SASAO, T., MIYOSHI, M., DEGUCHI, S., HORIUCHI, S. & ASAKI, Y. (2000). Kinematics and Distance of Water Masers in W3 IRS 5. *ApJ*, **538**, 751–765. 142, 449
- ISELLA, A. (2006). *Interferometric observations of pre-main sequence disks*. Ph.d. thesis, Università degli Studi di Milano. 7
- ISHII, M., HIRAO, T., NAGASHIMA, C., NAGATA, T., SATO, S. & YAO, Y. (2002). A Survey of Near Infrared Nebulosities around Luminous Young Stellar Objects: J, H, and K' Imaging. *ApJ*, **124**, 430–444. 467
- JACKSON, C.A. (2004). Deep radio continuum studies with the SKA: evolution of radio AGN populations. *NAR*, **48**, 1187–1193. 47
- JIANG, Z., YAO, Y., YANG, J., BABA, D., KATO, D., KURITA, M., NAGASHIMA, C., NAGATA, T., NAGAYAMA, T., NAKAJIMA, Y., ISHII, M., TAMURA, M. & SUGITANI, K. (2003). A Near-Infrared Study of the Star-forming Region S269. *ApJ*, **596**, 1064–1079. 475
- KAWAMURA, A., ONISHI, T., YONEKURA, Y., DOBASHI, K., MIZUNO, A., OGAWA, H. & FUKUI, Y. (1998). A ^{13}CO Survey of Molecular Clouds in Gemini and Auriga. *ApJS*, **117**, 387–425. 142
- KENDALL, M.G. (1938). A new measure of rank correlation. *Biometrika*, **30**, 81–93. 57

- KETO, E. (2002). On the Evolution of Ultracompact H II Regions. *ApJ*, **580**, 980–986. 184, 187
- KLAASSEN, P.D., GALVÁN-MADRID, R., PETERS, T., LONGMORE, S.N. & MAERCKER, M. (2013). Ionization driven molecular outflow in K3-50A. *A&A*, **556**, A107. 11
- KLASSEN, M., PUDRITZ, R.E., KUIPER, R., PETERS, T. & BANERJEE, R. (2016). Simulating the Formation of Massive Protostars. I. Radiative Feedback and Accretion Disks. *ApJ*, **823**, 28. 194
- KLEINMANN, D.E. & WRIGHT, E.L. (1973). A New Infrared Source in M17. *ApJ*, **185**, L131. 69, 369
- KRATTER, K.M. & MATZNER, C.D. (2006). Fragmentation of massive protostellar discs. *MNRAS*, **373**, 1563–1576. 194
- KRAUS, S., HOFMANN, K.H., MENTEN, K.M., SCHERTL, D., WEIGELT, G., WYROWSKI, F., MEILLAND, A., PERRAUT, K., PETROV, R., ROBBERDUBOIS, S., SCHILKE, P. & TESTI, L. (2010). A hot compact dust disk around a massive young stellar object. *Nature*, **466**, 339–342. 16, 104, 105, 375, 376, 377
- KRUMHOLZ, M.R., KLEIN, R.I., MCKEE, C.F., OFFNER, S.S.R. & CUNNINGHAM, A.J. (2009). The Formation of Massive Star Systems by Accretion. *Science*, **323**, 754–. 8

- KUMAR, M.S.N., KETO, E. & CLERKIN, E. (2006). The youngest stellar clusters. Clusters associated with massive protostellar candidates. *A&A*, **449**, 1033–1041. 436
- KURTZ, S., CHURCHWELL, E. & WOOD, D.O.S. (1994). Ultracompact H II regions. 2: New high-resolution radio images. *ApJS*, **91**, 659–712. 470, 471
- LADA, C.J. (1987). Star formation - From OB associations to protostars. In M. Peimbert & J. Jugaku, eds., *Star Forming Regions*, vol. 115 of *IAU Symposium*, 1–17. 7
- LEE, H.T., LIAO, W.T., FROEBRICH, D., KARR, J., IOANNIDIS, G., LEE, Y.H., SU, Y.N., LIU, S.Y., DUAN, H.Y. & TAKAMI, M. (2013). Near-infrared H₂ and Continuum Survey of Extended Green Objects. II. Complete Census for the Northern Galactic Plane. *ApJS*, **208**, 23. 407, 409
- LEE, J.K., WALSH, A.J., BURTON, M.G. & ASHLEY, M.C.B. (2001). Discovery of molecular hydrogen line emission associated with methanol maser emission. *MNRAS*, **324**, 1102–1108. 381
- LEFLOCH, B., LAZAREFF, B. & CASTETS, A. (1997). Cometary globules. III. Triggered star formation in IC 1848. *A&A*, **324**, 249–262. 451
- LINZ, H., HOFNER, P., ARAYA, E., RODRÍGUEZ, L.F., KURTZ, S., MARTÍ, J., STECKLUM, B. & HENNING, T. (2004). VLA 7mm Observations Toward the Pumping Heart of GGD27. *Astronomische Nachrichten Supplement*, **325**, 11. 367

- LISEAU, R., LORENZETTI, D., NISINI, B., SPINOGLIO, L. & MONETI, A. (1992). Star formation in the VELA molecular clouds. I - The IRAS-bright Class I sources. *A&A*, **265**, 577–596. 116
- LIZANO, S. (2008). Hypercompact HII Regions. In H. Beuther, H. Linz & T. Henning, eds., *Massive Star Formation: Observations Confront Theory*, vol. 387 of *Astronomical Society of the Pacific Conference Series*, 232. 404
- LÓPEZ-SEPULCRE, A., CESARONI, R. & WALMSLEY, C.M. (2010). A comparative study of high-mass cluster forming clumps. *A&A*, **517**, A66. 407, 408, 409, 414, 438
- LU, X., ZHANG, Q., LIU, H.B., WANG, J. & GU, Q. (2014). Very Large Array Observations of Ammonia in High-mass Star Formation Regions. *ApJ*, **790**, 84. 142, 152
- LUMSDEN, S.L., WHEELWRIGHT, H.E., HOARE, M.G., OUDMAIJER, R.D. & DREW, J.E. (2012). Tracers of discs and winds around intermediate- and high-mass young stellar objects. *MNRAS*, **424**, 1088–1104. 153, 421
- LUMSDEN, S.L., HOARE, M.G., URQUHART, J.S., OUDMAIJER, R.D., DAVIES, B., MOTTRAM, J.C., COOPER, H.D.B. & MOORE, T.J.T. (2013). The Red MSX Source Survey: The Massive Young Stellar Population of Our Galaxy. *ApJS*, **208**, 11. 2, 32, 33, 42, 83, 135, 142, 192, 455
- LYNCH, C., MUTEL, R.L., GÜDEL, M., RAY, T., SKINNER, S.L., SCHNEIDER, P.C. & GAYLEY, K.G. (2013). Very Large Array Observations of DG Tau's Radio Jet: A Highly Collimated Thermal Outflow. *ApJ*, **766**, 53. 83

- MALLICK, K.K., OJHA, D.K., TAMURA, M., PANDEY, A.K., DIB, S., GHOSH, S.K., SUNADA, K., ZINCHENKO, I., PIROGOV, L. & TSUJIMOTO, M. (2014). NGC 7538: multiwavelength study of stellar cluster regions associated with IRS 1-3 and IRS 9 sources. *MNRAS*, **443**, 3218–3237. 443
- MARTI, J., RODRIGUEZ, L.F. & REIPURTH, B. (1993). HH 80-81: A Highly Collimated Herbig-Haro Complex Powered by a Massive Young Star. *ApJ*, **416**, 208. 16, 27, 113, 367
- MARTI, J., RODRIGUEZ, L.F. & REIPURTH, B. (1995). Large Proper Motions and Ejection of New Condensations in the HH 80-81 Thermal Radio Jet. *ApJ*, **449**, 184. 28, 118
- MARTÍ, J., RODRÍGUEZ, L.F. & REIPURTH, B. (1998). Proper Motions of the Inner Condensations in the HH 80-81 Thermal Radio Jet. *ApJ*, **502**, 337–341. 83
- MARTINS, F., POMARÈS, M., DEHARVENG, L., ZAVAGNO, A. & BOURET, J.C. (2010). Near-IR integral field spectroscopy of ionizing stars and young stellar objects on the borders of H II regions. *A&A*, **510**, A32. 2
- MASQUÉ, J.M., RODRÍGUEZ, L.F., ARAUDO, A., ESTALELLA, R., CARRASCO-GONZÁLEZ, C., ANGLADA, G., GIRART, J.M. & OSORIO, M. (2015). Proper Motions of the Outer Knots of the HH 80/81/80N Radio-jet. *ApJ*, **814**, 44. 193
- MASQUÉ, J.M., RODRÍGUEZ, L.F., TRINIDAD, M.A., KURTZ, S., DZIB, S.A., RODRÍGUEZ-RICO, C.A. & LOINARD, L. (2017). Searching for Compact Radio Sources Associated with UCHII Regions. *ApJ*, **836**, 96. 477

- MASSI, F., DE LUCA, M., ELIA, D., GIANNINI, T., LORENZETTI, D. & NISINI, B. (2007). Star formation in the Vela molecular ridge. Large scale mapping of cloud D in the mm continuum. *A&A*, **466**, 1013–1023. 103
- MAUD, L.T., HOARE, M.G., GIBB, A.G., SHEPHERD, D. & INDEBETOUW, R. (2013). High angular resolution millimetre continuum observations and modelling of S140-IRS1. *MNRAS*, **428**, 609–624. 23
- MAUD, L.T., MOORE, T.J.T., LUMSDEN, S.L., MOTTRAM, J.C., URQUHART, J.S. & HOARE, M.G. (2015). A distance-limited sample of massive molecular outflows. *MNRAS*, **453**, 645–665. 11, 71, 181, 182, 183, 185
- MCKEE, C.F. & TAN, J.C. (2002). Massive star formation in 100,000 years from turbulent and pressurized molecular clouds. *Nature*, **416**, 59–61. 8, 78
- MCKEE, C.F. & TAN, J.C. (2003). The Formation of Massive Stars from Turbulent Cores. *ApJ*, **585**, 850–871. 8, 37, 181
- MCMULLIN, J.P., WATERS, B., SCHIEBEL, D., YOUNG, W. & GOLAP, K. (2007). CASA Architecture and Applications. In R.A. Shaw, F. Hill & D.J. Bell, eds., *Astronomical Data Analysis Software and Systems XVI*, vol. 376 of *Astronomical Society of the Pacific Conference Series*, 127. 41, 148
- MEAKIN, C.A., HINES, D.C. & THOMPSON, R.I. (2005). Young Stars and Dust in AFGL 437: Hubble Space Telescope NICMOS Polarimetric Imaging of an Outflow Source. *ApJ*, **634**, 1146–1154. 455

- MEYER, D.M.A., VOROBYOV, E.I., KUIPER, R. & KLEY, W. (2017). On the existence of accretion-driven bursts in massive star formation. *MNRAS*, **464**, L90–L94. 10, 82, 193
- MEZGER, P.G., ALTENHOFF, W., SCHRAML, J., BURKE, B.F., REIFENSTEIN, E.C., III & WILSON, T.L. (1967). A New Class of Compact H II Regions Associated with OH Emission Sources. *ApJ*, **150**, L157. 76
- MIETTINEN, O., HARJU, J., HAIKALA, L.K. & POMRÉN, C. (2006). SiO and CH₃CCH abundances and dust emission in high-mass star-forming cores. *A&A*, **460**, 721–731. 382
- MINH, Y.C., SU, Y.N., CHEN, H.R., LIU, S.Y., YAN, C.H. & KIM, S.J. (2010). Submillimeter Array Observations Toward the Massive Star-forming Core MM1 of W75N. *ApJ*, **723**, 1231–1240. 5
- MINIER, V., BOOTH, R.S. & CONWAY, J.E. (2000). VLBI observations of 6.7 and 12.2 GHz methanol masers toward high mass star-forming regions. I. Observational results: protostellar disks or outflows? *A&A*, **362**, 1093–1108. 462
- MINIER, V., ELLINGSEN, S.P., NORRIS, R.P. & BOOTH, R.S. (2003). The protostellar mass limit for 6.7 GHz methanol masers. I. A low-mass YSO survey. *A&A*, **403**, 1095–1100. 23
- MINIER, V., BURTON, M.G., HILL, T., PESTALOZZI, M.R., PURCELL, C.R., GARAY, G., WALSH, A.J. & LONGMORE, S. (2005). Star-forming protoclusters associated with methanol masers. *A&A*, **429**, 945–960. 142, 158, 469

- MITCHELL, G.F., HASEGAWA, T.I. & SCHELLA, J. (1992). A CO $J = 2 - 1$ study of the outflow sources GL 490, GL 2591, M8E-IR, and W3 IRS 5. *ApJ*, **386**, 604–617. 456
- MOLINARI, S., TESTI, L., RODRÍGUEZ, L.F. & ZHANG, Q. (2002). The Formation of Massive Stars. I. High-Resolution Millimeter and Radio Studies of High-Mass Protostellar Candidates. *ApJ*, **570**, 758–778. 432
- MORAGHAN, A., LEE, C.F., HUANG, P.S. & VAIDYA, B. (2016). A study of the wiggle morphology of HH 211 through numerical simulations. *MNRAS*, **460**, 1829–1838. 81
- MOSCADELLI, L., REID, M.J., MENTEN, K.M., BRUNTHALER, A., ZHENG, X.W. & XU, Y. (2009). Trigonometric Parallaxes of Massive Star-Forming Regions. II. Cep A and NGC 7538. *ApJ*, **693**, 406–412. 142
- MOSCADELLI, L., SÁNCHEZ-MONGE, Á., GODDI, C., LI, J.J., SANNA, A., CESARONI, R., PESTALOZZI, M., MOLINARI, S. & REID, M.J. (2016). Outflow structure within 1000 au of high-mass YSOs. I. First results from a combined study of maser and radio continuum emission. *A&A*, **585**, A71. 31, 37, 60, 68, 72, 430
- MOTTE, F., BONTEMPS, S., SCHILKE, P., SCHNEIDER, N., MENTEN, K.M. & BROGUIÈRE, D. (2007). The earliest phases of high-mass star formation: a 3 square degree millimeter continuum mapping of Cygnus X. *A&A*, **476**, 1243–1260. 5
- MOTTRAM, J.C., HOARE, M.G., LUMSDEN, S.L., OUDMAIJER, R.D., URQUHART, J.S., SHERET, T.L., CLARKE, A.J. & ALLSOPP, J. (2007).

The RMS survey: mid-infrared observations of candidate massive YSOs in the southern hemisphere. *A&A*, **476**, 1019–1111. 394, 398

MOTTRAM, J.C., HOARE, M.G., LUMSDEN, S.L., OUDMAIJER, R.D., URQUHART, J.S., MEADE, M.R., MOORE, T.J.T. & STEAD, J.J. (2010). The RMS survey: far-infrared photometry of young massive stars. *A&A*, **510**, A89. 42

MOTTRAM, J.C., HOARE, M.G., DAVIES, B., LUMSDEN, S.L., OUDMAIJER, R.D., URQUHART, J.S., MOORE, T.J.T., COOPER, H.D.B. & STEAD, J.J. (2011a). The RMS Survey: The Luminosity Functions and Timescales of Massive Young Stellar Objects and Compact H II Regions. *ApJ*, **730**, L33. 181

MOTTRAM, J.C., HOARE, M.G., URQUHART, J.S., LUMSDEN, S.L., OUDMAIJER, R.D., ROBITAILLE, T.P., MOORE, T.J.T., DAVIES, B. & STEAD, J. (2011b). The Red MSX Source survey: the bolometric fluxes and luminosity distributions of young massive stars. *A&A*, **525**, A149. 42, 76, 179

MURAKAWA, K., LUMSDEN, S.L., OUDMAIJER, R.D., DAVIES, B., WHEELWRIGHT, H.E., HOARE, M.G. & ILEE, J.D. (2013). Near-infrared integral field spectroscopy of massive young stellar objects. *MNRAS*, **436**, 511–525. 429

NAVARETE, F., DAMINELI, A., BARBOSA, C.L. & BLUM, R.D. (2015). A survey of extended H₂ emission from massive YSOs. *MNRAS*, **450**, 4364–4398. 25, 370, 386, 419, 420, 427, 428, 434, 435, 437, 438, 443, 444, 445, 447, 451, 453, 454, 457, 458, 461, 462, 469, 471, 474

- NECKEL, T. & STAUDE, H.J. (1995). IRAS 08159-3543: Optical Detection of the Dusty, Neutral Bipolar Wind of a Luminous Young Stellar Object. *ApJ*, **448**, 832. 370
- OGURA, K., SUGITANI, K. & PICKLES, A. (2002). H α Emission Stars and Herbig-Haro Objects in the Vicinity of Bright-rimmed Clouds. *ApJ*, **123**, 2597–2626. 450
- OH, C.S., KOBAYASHI, H., HONMA, M., HIROTA, T., SATO, K. & UENO, Y. (2010). VERA Observations of H₂O Maser Sources in Three Massive Star-Forming Regions and Galactic Rotation Measurements. *PASJ*, **62**, 101–114. 142, 469
- PALAU, A., FUENTE, A., GIRART, J.M., FONTANI, F., BOISSIER, J., PIÉTU, V., SÁNCHEZ-MONGE, Á., BUSQUET, G., ESTALELLA, R., ZAPATA, L.A., ZHANG, Q., NERI, R., HO, P.T.P., ALONSO-ALBI, T. & AUDARD, M. (2011). Intermediate-mass Hot Cores at ~ 500 AU: Disks or Outflows? *ApJL*, **743**, L32. 158, 464, 465
- PALAU, A., FUENTE, A., GIRART, J.M., ESTALELLA, R., HO, P.T.P., SÁNCHEZ-MONGE, Á., FONTANI, F., BUSQUET, G., COMMERÇON, B., HENNEBELLE, P., BOISSIER, J., ZHANG, Q., CESARONI, R. & ZAPATA, L.A. (2013). Early Stages of Cluster Formation: Fragmentation of Massive Dense Cores down to 1000 AU. *ApJ*, **762**, 120. 431
- PANAGIA, N. & FELLI, M. (1975). The spectrum of the free-free radiation from extended envelopes. *A&A*, **39**, 1–5. 23, 456, 477

- PARKIN, E.R., PITTARD, J.M., HOARE, M.G., WRIGHT, N.J. & DRAKE, J.J. (2009). The interactions of winds from massive young stellar objects: X-ray emission, dynamics and cavity evolution. *MNRAS*, **400**, 629–645. 19
- PATEL, N.A., CUIEL, S., SRIDHARAN, T.K., ZHANG, Q., HUNTER, T.R., HO, P.T.P., TORRELLES, J.M., MORAN, J.M., GÓMEZ, J.F. & ANGLADA, G. (2005). A disk of dust and molecular gas around a high-mass protostar. *Nature*, **437**, 109–111. 25, 29
- PELLETIER, G. & PUDRITZ, R.E. (1992). Hydromagnetic disk winds in young stellar objects and active galactic nuclei. *ApJ*, **394**, 117–138. 13, 14
- PHILLIPS, C.J., NORRIS, R.P., ELLINGSEN, S.P. & MCCULLOCH, P.M. (1998). Methanol masers and their environment at high resolution. *MNRAS*, **300**, 1131–1157. 383
- POVICH, M.S., CHURCHWELL, E., BIEGING, J.H., KANG, M., WHITNEY, B.A., BROGAN, C.L., KULESA, C.A., COHEN, M., BABLER, B.L., INDEBETOUW, R., MEADE, M.R. & ROBITAILLE, T.P. (2009). The Extended Environment of M17: A Star Formation History. *ApJ*, **696**, 1278–1306. 369
- PUDRITZ, R.E. & NORMAN, C.A. (1983). Centrifugally driven winds from contracting molecular disks. *ApJ*, **274**, 677–697. 13
- PUDRITZ, R.E., OUYED, R., FENDT, C. & BRANDENBURG, A. (2007). Disk Winds, Jets, and Outflows: Theoretical and Computational Foundations. *Protostars and Planets V*, 277–294. 16

- PURCELL, C.R., HOARE, M.G., COTTON, W.D., LUMSDEN, S.L., URQUHART, J.S., CHANDLER, C., CHURCHWELL, E.B., DIAMOND, P., DOUGHERTY, S.M., FENDER, R.P., FULLER, G., GARRINGTON, S.T., GLEDHILL, T.M., GOLDSMITH, P.F., HINDSON, L., JACKSON, J.M., KURTZ, S.E., MARTÍ, J., MOORE, T.J.T., MUNDY, L.G., MUXLOW, T.W.B., OUDMAIJER, R.D., PANDIAN, J.D., PAREDES, J.M., SHEPHERD, D.S., SMETHURST, S., SPENCER, R.E., THOMPSON, M.A., UMANA, G. & ZIJLSTRA, A.A. (2013). The Coordinated Radio and Infrared Survey for High-mass Star Formation. II. Source Catalog. *ApJS*, **205**, 1. 405
- PURSER, S.J.D., LUMSDEN, S.L., HOARE, M.G., URQUHART, J., S., CUNNINGHAM, N., PURCELL, C.R., BROOKS, K.J., GARAY, G., GÚZMAN, A.E. & VORONKOV, M.A. (2016). A search for ionized jets towards massive young stellar objects. *MNRAS*, **460**, 1039–1053. 18
- RATHBORNE, J.M., JACKSON, J.M. & SIMON, R. (2006). Infrared Dark Clouds: Precursors to Star Clusters. *ApJ*, **641**, 389–405. 168, 407, 408
- RATHBORNE, J.M., SIMON, R. & JACKSON, J.M. (2007). The Detection of Protostellar Condensations in Infrared Dark Cloud Cores. *ApJ*, **662**, 1082–1092. 414
- RATHBORNE, J.M., JACKSON, J.M., CHAMBERS, E.T., STOJIMIROVIC, I., SIMON, R., SHIPMAN, R. & FRIESWIJK, W. (2010). The Early Stages of Star Formation in Infrared Dark Clouds: Characterizing the Core Dust Properties. *ApJ*, **715**, 310–322. 137, 138, 139, 151, 160, 161, 194, 405, 406, 407, 408, 409, 410, 412, 413

- RAY, T.P., POETZEL, R., SOLF, J. & MUNDT, R. (1990). Optical jets from the high-luminosity young stars LkH-alpha 234 and AFGL 4029. *ApJL*, **357**, L45–L48. 452
- REIPURTH, B., HARTIGAN, P., HEATHCOTE, S., MORSE, J.A. & BALLY, J. (1997). Hubble Space Telescope Images of the HH 111 Jet. *ApJ*, **114**, 757–780. 27
- REIPURTH, B., YU, K.C., RODRÍGUEZ, L.F., HEATHCOTE, S. & BALLY, J. (1999). Multiplicity of the HH 111 jet source: it Hubble Space Telescope NICMOS images and VLA maps. *A&A*, **352**, L83–L86. 26, 195
- RENGARAJAN, T.N. & HO, P.T.P. (1996a). Search for Optically Thick H II Regions and Ionized Stellar Wind from Luminous Embedded Infrared Sources. *ApJ*, **465**, 363. 368
- RENGARAJAN, T.N. & HO, P.T.P. (1996b). Search for Optically Thick H II Regions and Ionized Stellar Wind from Luminous Embedded Infrared Sources. *ApJ*, **465**, 363. 473
- REYNOLDS, S.P. (1986). Continuum spectra of collimated, ionized stellar winds. *ApJ*, **304**, 713–720. 22, 27, 28, 54, 66, 73, 81, 112, 169, 195, 196, 371, 375, 384, 389, 420, 425, 439, 455, 458
- ROBITAILLE, T.P., WHITNEY, B.A., INDEBETOUW, R. & WOOD, K. (2007). Interpreting Spectral Energy Distributions from Young Stellar Objects. II. Fitting Observed SEDs Using a Large Grid of Precomputed Models. *ApJS*, **169**, 328–352. 122

- RODÓN, J.A., BEUTHER, H., MEGEATH, S.T. & VAN DER TAK, F.F.S. (2008). Millimeter interferometry of W3 IRS5: a trapezium in the making. *A&A*, **490**, 213–222. 156, 447, 449
- RODRIGUEZ, L.F., MORAN, J.M., HO, P.T.P. & GOTTLIEB, E.W. (1980). Radio observations of water vapor, hydroxyl, silicon monoxide, ammonia, carbon monoxide, and compact H II regions in the vicinities of suspected Herbig-Haro objects. *ApJ*, **235**, 845–865. 27
- RODRIGUEZ, L.F., GARAY, G., CUIEL, S., RAMIREZ, S., TORRELLES, J.M., GOMEZ, Y. & VELAZQUEZ, A. (1994). Cepheus A HW2: A powerful thermal radio jet. *ApJ*, **430**, L65–L68. 28
- RODRÍGUEZ, L.F., GARAY, G., BROOKS, K.J. & MARDONES, D. (2005). High Angular Resolution Observations of the Collimated Jet Source Associated with a Massive Protostar in IRAS 16547-4247. *ApJ*, **626**, 953–958. 29, 82, 390, 391, 392
- RODRÍGUEZ, L.F., MORAN, J.M., FRANCO-HERNÁNDEZ, R., GARAY, G., BROOKS, K.J. & MARDONES, D. (2008). The Collimated Jet Source in IRAS 16547-4247: Time Variation, Possible Precession, and Upper Limits to the Proper Motions Along the Jet Axis. *ApJ*, **135**, 2370–2379. 30, 82, 118, 391
- RODRÍGUEZ, L.F., GONZÁLEZ, R.F., MONTES, G., ASIRI, H.M., RAGA, A.C. & CANTÓ, J. (2012a). Compact Radio Sources in M17. *ApJ*, **755**, 152. 369

- RODRÍGUEZ, T., TRINIDAD, M.A. & MIGENES, V. (2012b). Search for Circumstellar Disks and Radio Jets in the Massive Star-formation Region IRAS 23033+5951. *ApJ*, **755**, 100. 438
- RODRÍGUEZ-ESNARD, T., MIGNES, V. & TRINIDAD, M.A. (2014). Accretion disks in the iras 23151+5912 region. *ApJ*, **788**, 176. 440
- ROSOLOWSKY, E., DUNHAM, M.K., GINSBURG, A., BRADLEY, E.T., AGUIRRE, J., BALLY, J., BATTERSBY, C., CYGANOWSKI, C., DOWELL, D., DROSBACK, M., EVANS, N.J., II, GLENN, J., HARVEY, P., STRINGFELLOW, G.S., WALAWENDER, J. & WILLIAMS, J.P. (2010). The Bolocam Galactic Plane Survey. II. Catalog of the Image Data. *ApJS*, **188**, 123–138. 168
- RYAN, S. & NORTON, A. (2010). *Stellar Evolution and Nucleosynthesis*. Cambridge University Press. 1
- RYBICKI, B.G. & LIGHTMAN, P.A. (1979). *Radiative Processes in Astrophysics*. Wiley. 23
- RYGL, K.L.J., BRUNTHALER, A., REID, M.J., MENTEN, K.M., VAN LANGEVELDE, H.J. & XU, Y. (2010). Trigonometric parallaxes of 6.7 GHz methanol masers. *A&A*, **511**, A2. 142, 424, 434
- RYGL, K.L.J., BRUNTHALER, A., SANNA, A., MENTEN, K.M., REID, M.J., VAN LANGEVELDE, H.J., HONMA, M., TORSTENSSON, K.J.E. & FUJISAWA, K. (2012). Parallaxes and proper motions of interstellar masers toward the Cygnus X star-forming complex. I. Membership of the Cygnus X region. *A&A*, **539**, A79. 142, 421

- RYGL, K.L.J., GOEDHART, S., POLYCHRONI, D., WYROWSKI, F., MOTTE, F., ELIA, D., NGUYEN-LUONG, Q., DIDELON, P., PESTALOZZI, M., BENEDETTINI, M., MOLINARI, S., ANDRÉ, P., FALLSCHEER, C., GIBB, A., GIORGIO, A.M.D., HILL, T., KÖNYVES, V., MARSTON, A., PEZZUTO, S., RIVERA-INGRAHAM, A., SCHISANO, E., SCHNEIDER, N., SPINOGLIO, L., WARD-THOMPSON, D. & WHITE, G.J. (2014). A Herschel and BIMA study of the sequential star formation near the W 48A H II region. *MNRAS*, **440**, 427–447. 476, 478
- SAITO, H., SAITO, M., MORIGUCHI, Y. & FUKUI, Y. (2006). High-Resolution Studies of the Dense Molecular Cores toward Massive Star-Forming Regions. *PASJ*, **58**, 343–359. 451, 452, 469, 470
- SAITO, H., SAITO, M., YONEKURA, Y. & NAKAMURA, F. (2008). High-Resolution Studies of the Multiple-Core Systems toward Cluster-forming Regions Including Massive Stars. *ApJS*, **178**, 302–329. 470
- SÁNCHEZ-MONGE, Á., PALAU, A., ESTALELLA, R., BELTRÁN, M.T. & GIRART, J.M. (2008). Survey of intermediate/high mass star-forming regions at centimeter and millimeter wavelengths. *A&A*, **485**, 497–515. 443, 459, 460
- SÁNCHEZ-MONGE, Á., BELTRÁN, M.T., CESARONI, R., ETOKA, S., GALLI, D., KUMAR, M.S.N., MOSCADELLI, L., STANKE, T., VAN DER TAK, F.F.S., VIG, S., WALMSLEY, C.M., WANG, K.S., ZINNECKER, H., ELIA, D., MOLINARI, S. & SCHISANO, E. (2014). A necklace of dense cores in the high-mass star forming region G35.20-0.74 N: ALMA observations. *A&A*, **569**, A11. 239, 415

- SANDELL, G., GOSS, W.M., WRIGHT, M. & CORDER, S. (2009). NGC 7538 IRS 1: An Ionized Jet Powered by Accretion. *ApJ*, **699**, L31–L34. 198, 396
- SANDELL, G., WEINTRAUB, D.A. & HAMIDOUCHE, M. (2011). A Submillimeter Mapping Survey of Herbig AeBe Stars. *ApJ*, **727**, 26. 419
- SANNA, A., SURCIS, G., MOSCADELLI, L., CESARONI, R., GODDI, C., VLEMINGS, W.H.T. & CARATTI O GARATTI, A. (2015). Velocity and magnetic fields within 1000 AU of a massive YSO. *A&A*, **583**, L3. 24
- SANNA, A., MOSCADELLI, L., CESARONI, R., CARATTI O GARATTI, A., GODDI, C. & CARRASCO-GONZÁLEZ, C. (2016). Momentum-driven outflow emission from an O-type YSO. Comparing the radio jet with the molecular outflow. *A&A*, **596**, L2. 11, 180, 182
- SAULT, R.J. & WIERINGA, M.H. (1994). Multi-frequency synthesis techniques in radio interferometric imaging. *AaPS*, **108**, 585–594. 44
- SAULT, R.J., TEUBEN, P.J. & WRIGHT, M.C.H. (1995). A Retrospective View of MIRIAD. In R.A. Shaw, H.E. Payne & J.J.E. Hayes, eds., *Astronomical Data Analysis Software and Systems IV*, vol. 77 of *Astronomical Society of the Pacific Conference Series*, 433. 41, 87
- SCAIFE, A. (2012). Radio Emission from Young Stellar Objects. *The Astronomical Review*, **7**, 26–32. 63
- SCAIFE, A.M.M., CURTIS, E.I., DAVIES, M., FRANZEN, T.M.O., GRAINGE, K.J.B., HOBSON, M.P., HURLEY-WALKER, N., LASENBY, A.N. & ZWART,

- J.T.L. (2011). AMI Large Array radio continuum observations of Spitzer c2d small clouds and cores. *MNRAS*, **410**, 2662–2678. 37, 63
- SCHREYER, K., HENNING, T., VAN DER TAK, F.F.S., BOONMAN, A.M.S. & VAN DISHOECK, E.F. (2002). The young intermediate-mass stellar object AFGL 490 - A disk surrounded by a cold envelope. *A&A*, **394**, 561–583. 456
- SCHREYER, K., SEMENOV, D., HENNING, T. & FORBRICH, J. (2006). A Rotating Disk around the Very Young Massive Star AFGL 490. *ApJL*, **637**, L129–L132. 456
- SCHULZ, A., BLACK, J.H., LADA, C.J., ULICH, B.L., MARTIN, R.N., SNELL, R.L. & ERICKSON, N.J. (1989). The bipolar molecular outflow of V645 Cygni. *ApJ*, **341**, 288–292. 429
- SEIFRIED, D., PUDRITZ, R.E., BANERJEE, R., DUFFIN, D. & KLESSEN, R.S. (2012). Magnetic fields during the early stages of massive star formation - II. A generalized outflow criterion. *MNRAS*, **422**, 347–366. 13
- SHAKURA, N.I. & SUNYAEV, R.A. (1973). Black holes in binary systems. Observational appearance. *A&A*, **24**, 337–355. 17, 19
- SHEIKHNEZAMI, S. & FENDT, C. (2015). Wobbling and Precessing Jets from Warped Disks in Binary Systems. *ApJ*, **814**, 113. 82
- SHEPHERD, D.S., TESTI, L. & STARK, D.P. (2003). Clustered Star Formation in W75 N. *ApJ*, **584**, 882–894. 422, 423
- SHIMOIKURA, T., DOBASHI, K., SAITO, H., MATSUMOTO, T., NAKAMURA, F., NISHIMURA, A., KIMURA, K., ONISHI, T. & OGAWA, H. (2013). Molec-

- ular Clumps and Infrared Clusters in the S247, S252, and BFS52 Regions. *ApJ*, **768**, 72. 471
- SHIRLEY, Y.L., CLAUSSEN, M.J., BOURKE, T.L., YOUNG, C.H. & BLAKE, G.A. (2007). The Detection and Characterization of Centimeter Radio Continuum Emission from the Low-Mass Protostar L1014-IRS. *ApJ*, **667**, 329–339. 33, 59, 60, 163
- SHU, F., NAJITA, J., OSTRIKER, E., WILKIN, F., RUDEN, S. & LIZANO, S. (1994). Magnetocentrifugally driven flows from young stars and disks. 1: A generalized model. *ApJ*, **429**, 781–796. 13, 15
- SHU, F.H., ADAMS, F.C. & LIZANO, S. (1987). Star formation in molecular clouds - Observation and theory. *Annual Review of Astronomy*, **25**, 23–81. 6
- SHU, F.H., NAJITA, J.R., SHANG, H. & LI, Z.Y. (2000). X-Winds Theory and Observations. *Protostars and Planets IV*, 789–814. 16
- SIMON, R., RATHBORNE, J.M., SHAH, R.Y., JACKSON, J.M. & CHAMBERS, E.T. (2006). The Characterization and Galactic Distribution of Infrared Dark Clouds. *ApJ*, **653**, 1325–1335. 139
- SMITH, H.A. & FISCHER, J. (1992). Multiple jets from the young star IRAS 21334 + 5039. *ApJL*, **398**, L99–L102. 427
- SMITH, M.D. & ROSEN, A. (2005). Synthetic Spitzer Infrared Array Camera band maps from simulations of protostellar jets. *MNRAS*, **357**, 1370–1376. 39

- SNELL, R.L., HUANG, Y.L., DICKMAN, R.L. & CLAUSSEN, M.J. (1988). Molecular outflows associated with bright far-infrared sources. *ApJ*, **325**, 853–863. 469
- SRIDHARAN, T.K., BEUTHER, H., SCHILKE, P., MENTEN, K.M. & WYROWSKI, F. (2002). High-Mass Protostellar Candidates. I. The Sample and Initial Results. *ApJ*, **566**, 931–944. 441
- STAHLER, S. & PALLA, F. (2008). *The Formation of Stars*. Wiley-VCH. 4, 21
- STAHLER, S.W. (1988). Deuterium and the stellar birthline. *ApJ*, **332**, 804–825. 15
- STECKLUM, B. & KAUFL, H. (1998). ESO Press Release, pR 08/98. 387
- STECKLUM, B., CARATTI O GARATTI, A. & LINZ, H. (2012). Integral-Field Spectroscopy of the Young High-Mass Star IRAS 13481-6124. In A.C. Carciofi & T. Rivinius, eds., *Circumstellar Dynamics at High Resolution*, vol. 464 of *Astronomical Society of the Pacific Conference Series*, 369. 105, 376
- SU, Y.N., ZHANG, Q. & LIM, J. (2004). Bipolar Molecular Outflows from High-Mass Protostars. *ApJ*, **604**, 258–271. 436, 437
- SUGITANI, K., FUKUI, Y., MIZUNI, A. & OHASHI, N. (1989). Star formation in bright-rimmed globules - Evidence for radiation-driven implosion. *ApJL*, **342**, L87–L90. 142, 154, 434
- SURCIS, G., VLEMMINGS, W.H.T., VAN LANGEVELDE, H.J., HUTAWARAKORN KRAMER, B. & QUIROGA-NUÑEZ, L.H. (2013). EVN

- observations of 6.7 GHz methanol maser polarization in massive star-forming regions. II. First statistical results. *A&A*, **556**, A73. 434, 469
- SURCIS, G., VLEMMINGS, W.H.T., VAN LANGEVELDE, H.J., HUTAWARAKORN KRAMER, B., BARTKIEWICZ, A. & BLASI, M.G. (2015). EVN observations of 6.7 GHz methanol maser polarization in massive star-forming regions. III. The flux-limited sample. *A&A*, **578**, A102. 24, 238, 414
- TAMURA, M., GATLEY, I., JOYCE, R.R., UENO, M., SUTO, H. & SEKIGUCHI, M. (1991). Infrared polarization images of star-forming regions. I - The ubiquity of bipolar structure. *ApJ*, **378**, 611–627. 469
- TAN, J.C., BELTRAN, M.T., CASELLI, P., FONTANI, F., FUENTE, A., KRUMHOLZ, M.R., MCKEE, C.F. & STOLTE, A. (2014). Massive Star Formation. *Protostars and Planets VI*. 4, 8, 9
- THI, W.F., VAN DISHOECK, E.F., PONTOPPIDAN, K.M. & DARTOIS, E. (2010). Evidence for episodic warm outflowing CO gas from the intermediate-mass young stellar object IRAS 08470-4321. *MNRAS*, **406**, 1409–1424. 371
- THOMPSON, R.I. (1984). Lyman and Balmer continuum ionization in zero-age main-sequence stars - Applications to the line excess phenomenon. *ApJ*, **283**, 165–168. 33, 60, 163
- TIEFTRUNK, A.R., GAUME, R.A., CLAUSSEN, M.J., WILSON, T.L. & JOHNSTON, K.J. (1997). The H II/molecular cloud complex W3 revisited: imaging the radio continuum sources using multi-configuration, multi-frequency observations with the VLA. *A&A*, **318**, 931–946. 446

- TOFANI, G., FELLI, M., TAYLOR, G.B. & HUNTER, T.R. (1995). Exploring the engines of molecular outflows. Radio continuum and H₂O maser observations. *A&AS*, **112**, 299–441.
- TRINIDAD, M.A., CURIEL, S., TORRELLES, J.M., RODRÍGUEZ, L.F., MIGENES, V. & PATEL, N. (2006). Interferometric Observations toward the High-Mass Young Stellar Object IRAS 23139+5939: Radio Continuum and Water Maser Emission. *ApJ*, **132**, 1918–1922. 441, 442
- TSINGANOS, K., RAY, T. & STUTE, M. (2009). *Protostellar Jets in Context*. Astrophysics and Space Science Proceedings, Springer Berlin Heidelberg. 68
- URQUHART, J.S., BUSFIELD, A.L., HOARE, M.G., LUMSDEN, S.L., CLARKE, A.J., MOORE, T.J.T., MOTTRAM, J.C. & OUDMAIJER, R.D. (2007a). The RMS survey. Radio observations of candidate massive YSOs in the southern hemisphere. *A&A*, **461**, 11–23. 33, 38, 106
- URQUHART, J.S., BUSFIELD, A.L., HOARE, M.G., LUMSDEN, S.L., OUDMAIJER, R.D., MOORE, T.J.T., GIBB, A.G., PURCELL, C.R., BURTON, M.G. & MARECHAL, L.J.L. (2007b). The RMS survey. ¹³CO observations of candidate massive YSOs in the southern Galactic plane. *A&A*, **474**, 891–901. 34, 379
- URQUHART, J.S., HOARE, M.G., LUMSDEN, S.L., OUDMAIJER, R.D., MOORE, T.J.T., BROOK, P.R., MOTTRAM, J.C., DAVIES, B. & STEAD, J.J. (2009a). The RMS survey. H₂O masers towards a sample of southern hemisphere massive YSO candidates and ultra compact HII regions. *A&A*, **507**, 795–802. 66, 106, 377

URQUHART, J.S., HOARE, M.G., PURCELL, C.R., LUMSDEN, S.L., OUDMAIJER, R.D., MOORE, T.J.T., BUSFIELD, A.L., MOTTRAM, J.C. & DAVIES, B. (2009b). The RMS survey. 6 cm continuum VLA observations towards candidate massive YSOs in the northern hemisphere. *A&A*, **501**, 539–551. 33, 146

URQUHART, J.S., MOORE, T.J.T., HOARE, M.G., LUMSDEN, S.L., OUDMAIJER, R.D., RATHBORNE, J.M., MOTTRAM, J.C., DAVIES, B. & STEAD, J.J. (2011a). The Red MSX Source survey: distribution and properties of a sample of massive young stars. *MNRAS*, **410**, 1237–1250. 38

URQUHART, J.S., MORGAN, L.K., FIGURA, C.C., MOORE, T.J.T., LUMSDEN, S.L., HOARE, M.G., OUDMAIJER, R.D., MOTTRAM, J.C., DAVIES, B. & DUNHAM, M.K. (2011b). The Red MSX Source survey: ammonia and water maser analysis of massive star-forming regions. *MNRAS*, **418**, 1689–1706. 419

URQUHART, J.S., FIGURA, C.C., MOORE, T.J.T., HOARE, M.G., LUMSDEN, S.L., MOTTRAM, J.C., THOMPSON, M.A. & OUDMAIJER, R.D. (2014a). The RMS survey: galactic distribution of massive star formation. *MNRAS*, **437**, 1791–1807. 34

URQUHART, J.S., MOORE, T.J.T., CSENGERI, T., WYROWSKI, F., SCHULLER, F., HOARE, M.G., LUMSDEN, S.L., MOTTRAM, J.C., THOMPSON, M.A., MENTEN, K.M., WALMSLEY, C.M., BRONFMAN, L., PFALZNER, S., KÖNIG, C. & WIENEN, M. (2014b). ATLASGAL - towards

- a complete sample of massive star forming clumps. *MNRAS*, **443**, 1555–1586.
2, 6, 24, 62, 70, 168
- VAIDYA, B., FENDT, C., BEUTHER, H. & PORTH, O. (2011). Jet Formation from Massive Young Stars: Magnetohydrodynamics versus Radiation Pressure. *ApJ*, **742**, 56. 172, 173
- VAN DER TAK, F.F.S. & MENTEN, K.M. (2005). Very compact radio emission from high-mass protostars. II. Dust disks and ionized accretion flows. *A&A*, **437**, 947–956. 69, 368
- VAN DER TAK, F.F.S., TUTHILL, P.G. & DANCHI, W.C. (2005). Subarcsecond mid-infrared and radio observations of the W3 IRS5 protocluster. *A&A*, **431**, 993–1005. 446, 447
- VARRICATT, W.P. (2011). A parsec-scale outflow from the luminous YSO IRAS 17527-2439. *A&A*, **527**, A97. 16
- VARRICATT, W.P., DAVIS, C.J., RAMSAY, S. & TODD, S.P. (2010). A near-IR imaging survey of intermediate- and high-mass young stellar outflow candidates. *MNRAS*, **404**, 661–720. 426, 433, 441, 459, 461, 462
- VINK, J.S., DE KOTER, A. & LAMERS, H.J.G.L.M. (2001). Mass-loss predictions for O and B stars as a function of metallicity. *A&A*, **369**, 574–588. 477
- VITI, S., COLLINGS, M.P., DEVER, J.W., MCCOUSTRA, M.R.S. & WILLIAMS, D.A. (2004). Evaporation of ices near massive stars: models based

- on laboratory temperature programmed desorption data. *Monthly Notices of the Royal Astronomical Society*, **354**, 1141–1145. 161
- VORONKOV, M.A., CASWELL, J.L., ELLINGSEN, S.P., GREEN, J.A. & BREEN, S.L. (2014). Southern class I methanol masers at 36 and 44 GHz. *MNRAS*, **439**, 2584–2617. 402
- WALL, J.V. & JENKINS, C.R. (2012). *Practical Statistics for Astronomers*. Cambridge University Press. 123
- WALSH, A.J., BURTON, M.G., HYLAND, A.R. & ROBINSON, G. (1998). Studies of ultracompact HII regions - II. High-resolution radio continuum and methanol maser survey. *MNRAS*, **301**, 640–698. 106, 202, 375, 377, 383, 401
- WANG, P., LI, Z.Y., ABEL, T. & NAKAMURA, F. (2010). Outflow Feedback Regulated Massive Star Formation in Parsec-Scale Cluster-Forming Clumps. *ApJ*, **709**, 27–41. 10
- WANG, Y., ZHANG, Q., PILLAI, T., WYROWSKI, F. & WU, Y. (2008). NH₃ Observations of the Infrared Dark Cloud G28.34+0.06. *ApJL*, **672**, L33. 411
- WANG, Y., AUDARD, M., FONTANI, F., SÁNCHEZ-MONGE, Á., BUSQUET, G., PALAU, A., BEUTHER, H., TAN, J.C., ESTALELLA, R., ISELLA, A., GUETH, F. & JIMÉNEZ-SERRA, I. (2016). Ongoing star formation in the protocluster IRAS 22134+5834. *A&A*, **587**, A69. 431, 432
- WEINTRAUB, D.A. & KASTNER, J.H. (1996). Betrayed: Using Near-Infrared Imaging Polarimetry to Locate the Sources of YSO Molecular Outflows. In

- W.G. Roberge & D.C.B. Whittet, eds., *Polarimetry of the Interstellar Medium*, vol. 97 of *Astronomical Society of the Pacific Conference Series*, 345. 455
- WHEELWRIGHT, H.E., DE WIT, W.J., OUDMAIJER, R.D., HOARE, M.G., LUMSDEN, S.L., FUJIYOSHI, T. & CLOSE, J.L. (2012). Probing the envelopes of massive young stellar objects with diffraction limited mid-infrared imaging. *A&A*, **540**, A89. 104, 127, 373, 374, 375, 385, 386, 393
- WILSON, T.L., BOBOLTZ, D.A., GAUME, R.A. & MEGEATH, S.T. (2003). High-Resolution Continuum Imaging at 1.3 and 0.7 Centimeters of the W3 IRS 5 Region. *ApJ*, **597**, 434–442. 446
- WILSON, W.E., FERRIS, R.H., AXTENS, P., BROWN, A., DAVIS, E., HAMPSON, G., LEACH, M. & ROBERTS, P. (2011). The Australia Telescope Compact Array Broad-band Backend: description and first results. *MNRAS*, **416**, 832–856. 39
- WOLFIRE, M.G. & KONIGL, A. (1991). Molecular line emission models of Herbig-Haro objects. I - H₂ emission. *ApJ*, **383**, 205–225. 54, 103
- WOOD, D.O.S. & CHURCHWELL, E. (1989). The morphologies and physical properties of ultracompact H II regions. *ApJS*, **69**, 831–895. 55, 76
- WOOD, D.O.S., HANDA, T., FUKUI, Y., CHURCHWELL, E., SOFUE, Y. & IWATA, T. (1988). Flux densities of ultracompact H II regions at 7 millimeters. *ApJ*, **326**, 884–888. 59
- WRIGHT, A.E. & BARLOW, M.J. (1975). The radio and infrared spectrum of early-type stars undergoing mass loss. *MNRAS*, **170**, 41–51. 477

- WU, Y.W., XU, Y., PANDIAN, J.D., YANG, J., HENKEL, C., MENTEN, K.M. & ZHANG, S.B. (2010). Ammonia and CO Observations Toward Low-luminosity 6.7 GHz Methanol Masers. *ApJ*, **720**, 392–408. 471
- WU, Y.W., XU, Y. & YANG, J. (2011). Multiwavelength study of low-luminosity 6.7-GHz methanol masers. *Research in Astronomy and Astrophysics*, **11**, 137–155. 468
- XU, J.L., WANG, J.J. & QIN, S.L. (2012). Outflow and accretion detections in the young stellar object IRAS 04579+4703. *A&A*, **540**, L13. 459
- YAN, C.H., MINH, Y.C., WANG, S.Y., SU, Y.N. & GINSBURG, A. (2010). Star-forming Region Sh 2-233IR. I. Deep Near-infrared Observations toward the Embedded Stellar Clusters. *ApJ*, **720**, 1–8. 463
- YU, N. & WANG, J.J. (2014). Molecular line study of massive star-forming regions from the Red MSX Source survey. *MNRAS*, **440**, 1213–1224. 395
- ZANNI, C., FERRARI, A., ROSNER, R., BODO, G. & MASSAGLIA, S. (2007). MHD simulations of jet acceleration from Keplerian accretion disks. The effects of disk resistivity. *A&A*, **469**, 811–828. 16
- ZAPATA, L.A., RODRÍGUEZ, L.F. & KURTZ, S.E. (2001). A Subarcsecond Radio Binary Associated with AFGL 4029-IRS1. *hRev. Mex. Astron. Astr.*, **37**, 83–86. 452, 454
- ZAPATA, L.A., PALAU, A., GALVÁN-MADRID, R., RODRÍGUEZ, L.F., GARAY, G., MORAN, J.M. & FRANCO-HERNÁNDEZ, R. (2015). ALMA reveals a

- candidate hot and compact disc around the O-type protostar IRAS 16547-4247. *MNRAS*, **447**, 1826–1833. 30, 391
- ZHANG, B., ZHENG, X.W., REID, M.J., MENTEN, K.M., XU, Y., MOSCADELLI, L. & BRUNTHALER, A. (2009). Trigonometric Parallaxes of Massive Star-Forming Regions. IV. G35.20-0.74 and G35.20-1.74. *ApJ*, **693**, 419–423. 142
- ZHANG, Q., HUNTER, T.R., BRAND, J., SRIDHARAN, T.K., CESARONI, R., MOLINARI, S., WANG, J. & KRAMER, M. (2005). Search for CO Outflows toward a Sample of 69 High-Mass Protostellar Candidates. II. Outflow Properties. *ApJ*, **625**, 864–882. 433
- ZHANG, Q., HUNTER, T.R., BEUTHER, H., SRIDHARAN, T.K., LIU, S.Y., SU, Y.N., CHEN, H.R. & CHEN, Y. (2007). Multiple Jets from the High-Mass (Proto)stellar Cluster AFGL 5142. *ApJ*, **658**, 1152–1163. 167, 465, 466
- ZHANG, Y., TAN, J.C., DE BUIZER, J.M., SANDELL, G., BELTRAN, M.T., CHURCHWELL, E., MCKEE, C.F., SHUPING, R., STAFF, J.E., TELESCO, C. & WHITNEY, B. (2013). A Massive Protostar Forming by Ordered Collapse of a Dense, Massive Core. *ApJ*, **767**, 58. 142, 152, 415
- ZINCHENKO, I., LIU, S.Y., SU, Y.N., SALII, S.V., SOBOLEV, A.M., ZEMLYANUKHA, P., BEUTHER, H., OJHA, D.K., SAMAL, M.R. & WANG, Y. (2015). The Disk-outflow System in the S255IR Area of High-mass Star Formation. *ApJ*, **810**, 10. 474
- ZINNECKER, H. & YORKE, H. (2007). Toward Understanding Massive Star Formation. *Annual Review of Astronomy*, **45**, 481–563. 3, 4, 8